Lecture Notes in Networks and Systems 944

Duy Cuong Nguyen · Do Trung Hai ·
Ngoc Pi Vu · Banh Tien Long ·
Horst Puta · Kai-Uwe Sattler *Editors*

Advances in Engineering Research and Application

Proceedings of the International Conference on Engineering Research and Applications, ICERA 2023, Volume 2

Springer

Lecture Notes in Networks and Systems 944

The series "Lecture Notes in Networks and Systems" publishes the latest developments in Networks and Systems—quickly, informally and with high quality. Original research reported in proceedings and post-proceedings represents the core of LNNS.

Volumes published in LNNS embrace all aspects and subfields of, as well as new challenges in, Networks and Systems.

The series contains proceedings and edited volumes in systems and networks, spanning the areas of Cyber-Physical Systems, Autonomous Systems, Sensor Networks, Control Systems, Energy Systems, Automotive Systems, Biological Systems, Vehicular Networking and Connected Vehicles, Aerospace Systems, Automation, Manufacturing, Smart Grids, Nonlinear Systems, Power Systems, Robotics, Social Systems, Economic Systems and other. Of particular value to both the contributors and the readership are the short publication timeframe and the world-wide distribution and exposure which enable both a wide and rapid dissemination of research output.

The series covers the theory, applications, and perspectives on the state of the art and future developments relevant to systems and networks, decision making, control, complex processes and related areas, as embedded in the fields of interdisciplinary and applied sciences, engineering, computer science, physics, economics, social, and life sciences, as well as the paradigms and methodologies behind them.

Indexed by SCOPUS, EI Compendex, INSPEC, WTI Frankfurt eG, zbMATH, SCImago.

All books published in the series are submitted for consideration in Web of Science.

For proposals from Asia please contact Aninda Bose (aninda.bose@springer.com).

Duy Cuong Nguyen · Do Trung Hai ·
Ngoc Pi Vu · Banh Tien Long · Horst Puta ·
Kai-Uwe Sattler
Editors

Advances in Engineering Research and Application

Proceedings of the International Conference on Engineering Research and Applications, ICERA 2023, Volume 2

Springer

Editors
Duy Cuong Nguyen
Faculty of Electronic Engineering
Thai Nguyen University of Technology
Thai Nguyen, Vietnam

Do Trung Hai
Faculty of Electronic Engineering
Thai Nguyen University of Technology
Thai Nguyen, Vietnam

Ngoc Pi Vu
Faculty of Mechanical Engineering
Thai Nguyen University of Technology
Thai Nguyen, Vietnam

Banh Tien Long
Vietnam Association for Science Editing
Hanoi University of Science and Technology
Hanoi, Vietnam

Horst Puta
Institute for Automation and Systems Engineering
Ilmenau University of Technology (IUT)
Ilmenau, Germany

Kai-Uwe Sattler
Ilmenau University of Technology (IUT)
Ilmenau, Germany

ISSN 2367-3370 ISSN 2367-3389 (electronic)
Lecture Notes in Networks and Systems
ISBN 978-3-031-62234-2 ISBN 978-3-031-62235-9 (eBook)
https://doi.org/10.1007/978-3-031-62235-9

This Springer imprint is published by the registered company Springer Nature Switzerland AG
The registered company address is: Gewerbestrasse 11, 6330 Cham, Switzerland

Preface

This book covers the proceedings of the 6th International Conference on Engineering Research and Application 2023 (ICERA 2023) that was organized by Thai Nguyen University of Technology (TNUT), Vietnam, and cooperated with Ilmenau University of Technology, Germany. In 2018, the first conference was held. Thus far, the conference has attracted a lot of contributions from researchers of many different universities around the world.

This conference aims to bring together researchers from many fields related to engineering research and applications, theories, and practices. This volume covers the following subjects: Mechanical Engineering, Materials and Mechanics of Materials, Mechatronics and Micromechatronics, Automotive Engineering, Electrical and Electronics Engineering, and Information and Communication Technology.

The up-to-date contributions reported in this book were carefully reviewed by experts and also approved by editors for the last review. All 103 accepted papers were presented and discussed on ICERA 2023, held in Thai Nguyen City, Vietnam, on December 1–2, 2023. The total papers sent to this conference are 232 papers. As a result of the two-stage review process, only 103 excellent contributions were selected for the presentation at the conference and publication in this book. The readers will find here representative samples of the most modern techniques available nowadays for the solution of challenging problems arising in engineering research and application.

We extend our sincere gratitude to the writers for their insightful articles that they contributed to the conference. Also, we sincerely appreciate the reviewers' assessments and suggestions for raising the caliber of the chosen papers. Moreover, we would like to specially thank to our Keynote speakers, Prof. Kai-Uwe Sattler (Ilmenau University of Technology, Germany), Prof. Tuan Le Anh (Ha Noi University of Sciences and Technology, Vietnam), Prof. S.A. Sherif (University of Florida, USA), Prof. Roger A. Sauer (RWTH Aachen University, Germany/Gdansk University of Technology), and Prof. Minh T. Nguyen (Thai Nguyen University of Technology, Vietnam), for their valuable and inspiring contributions to scientists, researchers, and listeners. We also thank to the members of the Organizing Committee of ICERA 2023 for their excellent technical and editorial support.

Last but not least, we would like to deeply thank to Springer Publishers and its Editor staff for helping us in the publication of the proceeding volume of this book.

December 2023

Duy Cuong Nguyen
Do Trung Hai
Ngoc Pi Vu
Banh Tien Long
Horst Puta
Kai-Uwe Sattler

Contents

Experimental Study for Superheated Steam Drying of Apple Slice

Thi Thu Hang Tran[1], Tien Cong Do[1], Thi Hanh Nguyen[2], Thi Hang Bui[3], and Kieu Hiep Le[1](✉)

[1] School of Mechanical Engineering, Hanoi University of Science and Technology, Hanoi, Vietnam
hiep.lekieu@hust.edu.vn

[2] School of Chemistry and Life Sciences, Hanoi University of Science and Technology, Hanoi, Vietnam

[3] Thermal Refrigeration Engineering, Hanoi College of Electronics and Refrigeration, Hanoi, Vietnam

Abstract. Superheated steam drying is an advanced drying technology in the food processing field. In this study, experimental studies at different drying conditions of superheated steam drying for apple slice are presented. It is observed that the evaporation is faster at higher temperature and higher gas velocity but the effects of temperature are smoother at fast gas velocity. One empirical model is built based on Page's model; this model enables to calculate the average moisture content versus time. The validation results show that the model yields high calculation so this can be applied to simulate the whole drying system. Product quality is also tested in terms of color change, sugar content and acid content to evaluate the application ability of superheated steam drying. Acid content and sugar content lost maximum at 130 °C and 140 °C, respectively.

Keywords: drying · apple · superheated steam · product quality · drying kinetic

1 Introduction

Drying technology is one of heat treatments that are widely applied in agriculture, especially in the post-harvest preservation field [1]. Due to the huge energy consumption of drying process so the continuous improvement of drying in terms of energy efficient and product quality have been received much attention [2]. Using super - heated steam replaces for air to avoid the oxidation and combustion reaction [2]. Thus, super – heated steam drying is the potential drying method to improve the dried product quality. Superheated steam drying (SSD) has been applied for wide range of product likes paddy, wood, soybean, durian, pork, banana, potato, milk, etc. [3–7].

Drying is also the common method to process apples, in which there are several applied dry methods likes hot air drying, freeze drying, hot air drying combined with puffing drying [2]. While hot air drying (HAD) causes negative effects on the apple slice, other methods are complicated and high energy consumption. To evaluate the application

D. C. Nguyen et al. (Eds.): ICERA 2023, LNNS 944, pp. 1–8, 2024.
https://doi.org/10.1007/978-3-031-62235-9_1

ability of SSD for apple slice in terms of drying kinetic and quality, the experiment work will be carried out for small drying sample at different drying conditions. The evaporation speed and product appearance are examined then one empirical model is built and validated. Additionally, dried products are also collected to analyze the quality in terms of appearance, acid content and sugar content. The study results will contribute to evaluate the application ability of SSD for apple slice.

2 Experiment Description

2.1 Experiment System

The experiment system is built for studying of drying kinetic of small fruit samples are shown in Fig. 1. The main part is one drying chamber which is insulated to prevent the heat loss. Drying sample is put one a tray containing big holes which allow gas flows on both sides of sample. Evaporation is monitored by the decrease of sample mass which is displayed by the sensitive balance 5. The feed water is pumped from (1) to the evaporator (2) then the dry vapor blows to the heater to be heated up to the setup temperature. This superheated steam flows to dry the sample in the dryer then one part blows to the heater to reheat up to the setup temperature and other part is released to the ambience.

Experiment is conducted for apple slice in range of temperature from 110 °C–150 °C and gas velocity from 3 m/s–6 m/s. In this work, the sample thickness is kept constant. Apple is the Breeze New Zealand kind which is bought from local Vinmart, Hanoi.

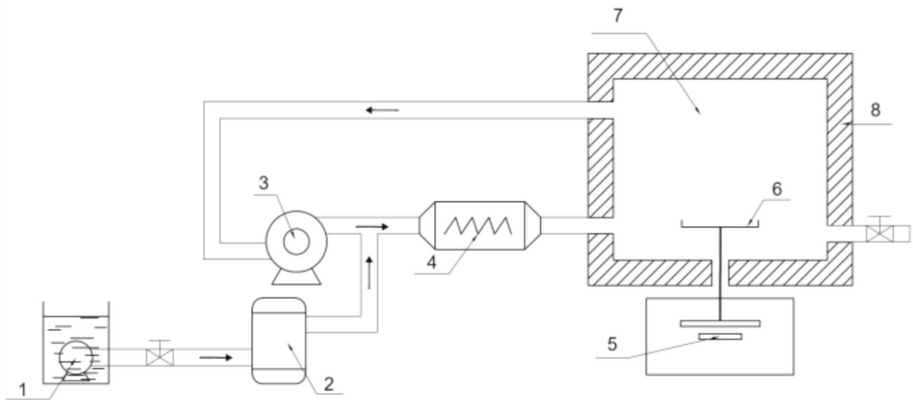

Fig. 1. Diagram of drying system: (1): feed water pump, (2): evaporator, (3): centrifugal fan, (4): electrical heater, (5): balance, (6): sample tray, (7): drying chamber, (8): insulated layer

2.2 Experiment Procedure

Each experiment is conducted for at least three times to make sure the accuracy of data. Experiments are done by seven following:

- Material preparation: Breeze New Zealand apple is chosen from Vinmart, Hanoi. It is cleaned and cut into 2 mm thickness slice.
- Drying system is setup, after drying conditions are reached to the stable status, 1 apple slice is put on the tray.
- Mass of sample is recorded continuously during the drying process until it is almost constant.
- Drying product is collected to analyze the product quality. The total acid content is determined by titration method [8], total sugar and reducing sugar contents are found by Graxianop method.
- Experiment is also conducted parallelly with the drying experiment to predict the initial water content. Several apple slices are checked the mass then they are put into one thermo-plus device for a long time at high temperature to get the solid mass. From the initial mass m_i and solid mass m_s, the initial water content is calculated as:

$$X_i = \frac{m_i - m_s}{m_s} \tag{1}$$

2.3 Data Evaluation

Evaporation
Moisture ratio is a dimensionless function which is expressed as:

$$MR = \frac{X_t - X_e}{X_i - X_e} \tag{2}$$

Where X_i, X_t, X_e are the initial, temporary and equilibrium water contents, kgw/kgs. The equilibrium water content X_e is the final water content of experiment so this is extracted corresponding to the particular experiment. The initial water content X_{in} is 6.7 kgw/kgs.

Color Change
Color change is evaluated based on the lightness, green and red indices of fresh apple and dried apple taken photo by Canon camera. Total difference of dried sample and fresh sample are determined by:

$$\Delta E = \sqrt{\left(c_{i,r} - c_{\mathrm{ex},r}\right)^2 + \left(c_{i,g} - c_{\mathrm{ex},g}\right)^2 + \left(c_{i,w} - c_{\mathrm{ex}}\right)^2} \tag{3}$$

In which, $c_{i,r}$, $c_{i,g}$, $c_{i,w}$ are red, green, lightness indices of initial samples. $c_{ex,r}$, $c_{ex,g}$, $c_{ex,w}$ are initial red, green, lightness indices of dried samples.

3 Result

3.1 Effect of Drying Conditions on the Evaporation

Changes of moisture rate over time at different temperature and gas velocity are shown in Figs. 2, 3, 4 and 5. For all cases, drying time is about 18–57 min, there are no constant drying period. In one hand, at all gas velocity, evaporation is faster at higher temperature but this effect is significant only at low velocity. In case of 3 m/s, drying time is 30 min at temperature of 110 °C while this time is about 12 min at temperature of 150 °C. However, at 6 m/s, drying time at 110 °C and 150 °C is 22 min and 11 min respectively. On the other hand, at the same temperature, drying is faster at higher gas velocity. The effect of gas velocity at high temperature is weaker than that at low temperature. These results are because the evaporation is the result of heat and mass transfer between sample surface and bulk vapor. At high temperature results in high temperature difference between sample and bulk gas so the temperature controls this heat and mass transfer. In case of fast velocity, the high gas velocity gives the high heat and mass transfer coefficient so the gas velocity dominates the evaporation in this case.

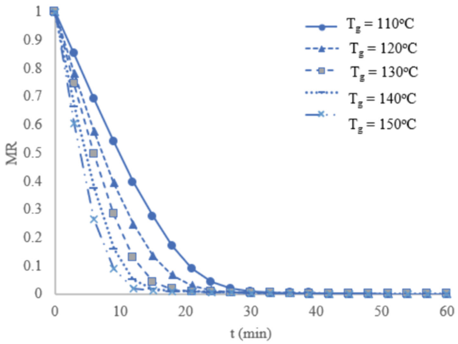

Fig. 2. Evaporation of apple slice at gas velocity of vg = 3 m/s

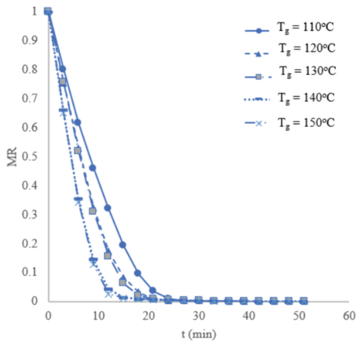

Fig. 3. Evaporation of apple slice at gas velocity of vg = 5 m/s

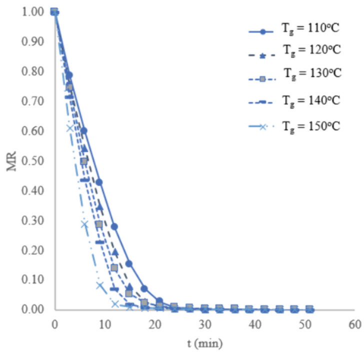

Fig. 4. Evaporation of apple slice at gas velocity of $v_g = 5.5$ m/s

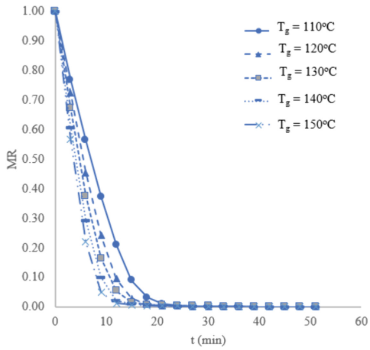

Fig. 5. Evaporation of apple slice at gas velocity of $v_g = 6$ m/s

3.2 Empirical Model

In this section, Page's model is applied to describe the drying kinetic as [9]:

$$MR = \exp(-kt^n) \tag{4}$$

Where a, b, k, n are parameters determined by fitting MR and experiment data based on square error R^2. Results show that Page model is the most accurate and the simplest model. The obtained parameters k and n of Page model at individual drying condition are listed as Table 1.

Table 1. Parameters of the empirical model

v_g	T_g	k	n	R^2
3	110	0.02407	1.491	0.9982
3	120	0.04754	1.375	0.9991
3	130	0.05412	1.454	0.9989
3	140	0.09464	1.397	0.9992
3	150	0.1054	1.421	0.9997
5	110	0.03737	1.411	0.9967
5	120	0.0532	1.407	0.999
5	130	0.05141	1.443	0.999
5	140	0.08457	1.422	0.9996
5	150	0.08369	1.452	0.9992
5.5	110	0.04005	1.418	0.9977
5.5	120	0.0493	1.424	0.9984
5.5	130	0.05663	1.423	0.999
5.5	140	0.06092	1.478	0.999
5.5	150	0.09816	1.445	0.9993
6	110	0.0443	1.449	0.998
6	120	0.06186	1.449	0.9992
6	130	0.07855	1.432	0.9993
6	140	0.1034	1.404	0.9996
6	150	0.1098	1.478	0.9998

Comparison of experiment and model is shown in Fig. 6 for selective drying conditions. It is observed that there is much good agreement so the established model is an accurate model and it can be applied for the simulation of the drying system.

3.3 Product Quality

Color Change

Pictures and color change of dried product compared with fresh sample are presented in Table 2 and Fig. 7. It can be observed that at temperature above 130 °C products are burned with the very high color difference. At lower temperatures, the difference

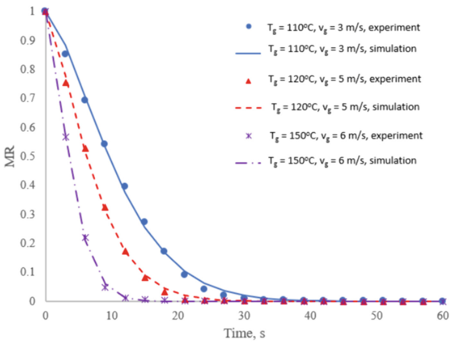

Fig. 6. Comparison of experimental data and simulation

between fresh sample and dried product increases with the increase in temperature but these changes are few. Thus, gas temperature below 130 °C is recommended for drying.

Table 2. Pictures of fresh slice and dried product

Fresh sample	$T_g = 110^oC$	$T_g = 120^oC$
	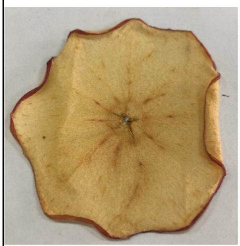	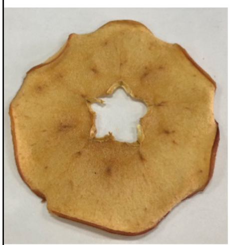
$T_g = 130^oC$	$T_g = 140^oC$	$T_g = 150^oC$
		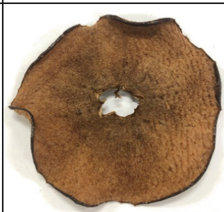

Marlic Acid Content and Reducing Sugar Content
Mass of marlic acid contained in 100 g basis solid is shown in Table 3. In the superheated steam drying, effects of drying temperature on the marlic acid and reducing sugar contents are significant but not much. The maximum acid content reduction occurs at 130 °C with 30.2% and this content reduces minimum at 110 °C with 18.9%. For the reducing sugar content, the maximum content reduction is at 140 °C with 27.4% and the sugar content decreases at least at 120 °C with 6.7%.

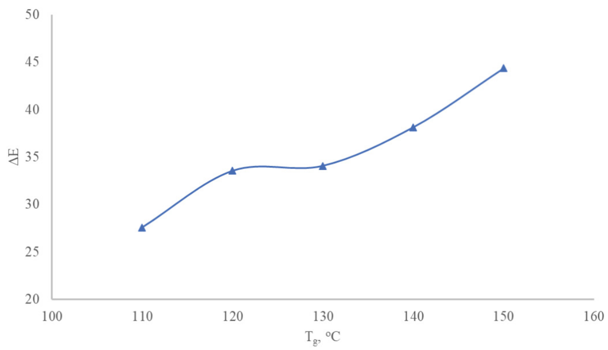

Fig. 7. Color change of product

Table 3. Product quality contents

Gas temperature	Acid content g/100g dried basis	Sugar content g/100 g dried basis
Fresh	2.96	59.41
110 °C	2.43	51.26
120 °C	2.25	55.31
130 °C	2.06	53.17
140 °C	2.39	43.08
150 °C	2.28	50.63

4 Conclusion

Experimental studies of apple slice dried in super-heated steam are presented in terms of evaporation kinetic and product quality. Results show that evaporation speed is faster at higher gas velocity and gas temperature. However, the effect of velocity on the drying kinetic reduces at higher temperature. The empirical model is simple and it gives high accuracy in compared with experiment data. Regarding to product quality, at temperature below 130 °C, color changes not much. Besides, the effects of temperature on the acid content and sugar contents are not clear. Acid content reduced most at 130 °C while the remained sugar content reaches the minimum value at 140 °C. In next step, the theoretical model should be developed to study the spatial distributions of moisture and temperature inside the sample. The morphology of dried product is also necessary to evaluate in order to find the optimization drying conditions. Besides, the sample thickness is also the important parameter which may prolong the drying time; so, this parameter should be also concerned.

Acknowledgement. This research is funded by the Vietnamese Ministry of Education and Training under grant number B2022-BKA-11.

References

1. Jangam, S.V., Law, C.L., Mujumdar, A.S.: Drying of Foods, Vegetables and Fruits, Singapore (2010)
2. Zhu, J., Yuan, Z., Min, C.W.: Effects of different drying methods on the physical properties and sensory characteristics of apple chip snacks. Lwt Food Sci. Technol. **154** (2022)
3. Alfy, A., Kiran, B.V., Jeevitha, G.C., Hebbar, H.U., et al.: Recent developments in superheated steam processing of foods-a review. Crit. Rev. Food Sci. Nutr. **56**(13), 2191–208 (2016)
4. Le, K.H., Tsotsas, E., Kharaghani, A.: Continuum-scale modeling of superheated steam drying of cellular plant porous media. Int. J. Heat Mass Transf. **124**, 1033–1044 (2018)
5. Linke, T., Happe, J., Kohlus, R.: Laboratory-scale superheated steam spray drying of food and dairy products. Dry. Technol. **40**(8), 1703–1714 (2021)
6. Patel, S.K., Bade, M.H.: Superheated steam drying and its applicability for various types of the dryer: the state of art. Dry. Technol. **39**(3), 284–305 (2020)
7. Lum, A., Mansouri, S., Hapgood, K., Wo, M.W.: Single droplet drying of milk in air and superheated steam: particle formation and wettability. Dry. Technol. **36**(15), 1802–1813 (2018)
8. Pierre, D.: Acid-base titration. Undergrad. J. Math. Model. One Two **10**(1) (2018)
9. Midilli, A., Kucuk, H., Yapar, Z.: A new model for single-layer drying. Dry. Technol. **20**(7), 1503–1513 (2007)

High Quality Torque for Five-Phase Open-End Winding Non-sinusoidal PMSM Drives

Hai T. Do[1], Tan D. Vu[1], Ky N. Nguyen[2], Eric Semail[2], and Minh T. Nguyen[1](✉)

[1] Thai Nguyen University of Technology, Thai Nguyen University, Thai Nguyen 240000, Vietnam
nguyentuanminh@tnut.edu.vn

[2] Univ. Lille, Arts et Metiers Institute of Technology, Central Lille, Junia, ULR 2697 - L2EP, 59000 Lille, France

Abstract. This paper presents a novel control scheme using the well-known field-oriented control (FOC) technique and a simple adaptive linear neuron (Adaline) to obtain smooth torque with a five-phase open-end winding non-sinusoidal permanent magnet synchronous machine (PMSM). For a given supply voltage value, the open-end winding structure results in higher allowable phase voltages, leading to a higher maximum rotating speed. Compared to a sinusoidal back electromotive force (back-EMF), a non-sinusoidal back-EMF leads to lower manufacturing costs and higher torque density. Nevertheless, unexpected current harmonics and torque ripples are consequently generated by the harmonics in back-EMFs, reducing control quality of the electric drive. In this study, the Adaline-FOC-based control scheme is proposed to eliminate the unwanted current harmonics and especially the torque ripples for a high-quality torque machine drive. Numerical results are presented to prove the effectiveness of the proposed scheme.

Keywords: Multiphase machine · non-sinusoidal back-EMF · torque ripple elimination · adaptive linear neuron

1 Introduction

With high functional reliability, multiphase drives have been a suitable choice in many applications such as transportation, submarine, and wind turbines [1]. Compared to the conventional three-phase topology, multiphase one (the number of phases $n > 3$) has more degrees of freedom for machine design and control. Accordingly, several advantages of the multiphase structure can be listed as fault tolerance, low power per phase rating, and smooth torque [2, 3].

The multi-reference-frame theory is a base to analyze an electric machine, especially multiphase ones [4]. For example, a machine with n phases is characterized by $(n - 1)/2$ (n is odd) and $(n - 2)/2$ (n is even) two-dimensional planes (reference frames). One plane is associated with a harmonic group. Ideally, in each plane, there is only one harmonic of back-EMF (or current). In this case, constant torque is perfectly generated

D. C. Nguyen et al. (Eds.): ICERA 2023, LNNS 944, pp. 9–19, 2024.
https://doi.org/10.1007/978-3-031-62235-9_2

by constant dq currents, facilitating popular proportional-integral (PI) controllers [5]. An increase in n leads to having more reference frames and more harmonics are allowable in back-EMFs. This characteristic cannot be found in a three-phase machine with only one two-dimensional frame, requiring sinusoidal back-EMFs and currents. Therefore, the multiphase topology has fewer constraints on design than a three-phase counterpart.

Nevertheless, the machine manufacturing could unprecedentedly generate more harmonics (>1 harmonic per frame), conflicting the multi-reference-frame theory. Possible impacts of these unexpected harmonics on current control have been discussed and solved in several recent studies. Indeed, one of the negative impacts is the appearance of unwanted current harmonics appear, resulting in time-variant dq currents. The approach in [6] for a high-speed three-phase machine drive, or in [7, 8] for five- and seven-phase machines could eliminate unwanted current harmonics, improving current control quality. However, in this case, torque pulsation still exists due to the interaction between the desired current harmonics and unwanted back-EMF harmonics.

Maximum torque per ampere (MTPA) in [9] applied for arbitrary waveforms of back-EMFs has been used to theoretically obtain the constant torque. However, varying current references for control in [9] require high bandwidth controllers but not PI controllers such as hysteresis controllers with high switching losses. Study [10] presents another approach but its results and those of [9] are similar. Several control techniques, such as model predictive control [11, 12] or pulse width modulation (PWM) carrier phase shift [13], have been applied to reduce torque ripples. However, torque ripples caused by unexpected back-EMF harmonics cannot be eliminated. Notably, in [14], an Adaline has been applied to eliminate torque ripples caused by unwanted back-EMF harmonics for a seven-phase star-connected winding machine without the use of Adalines for current harmonic eliminations.

In this study, an adaptive control scheme is introduced to derive smooth torque under the existence of plenty of harmonics in back-EMFs. Besides five Adalines used to eliminate unwanted current harmonics as proposed in [6–8], an additional Adaline is used for torque ripple eliminations. The conventional FOC technique and the Adaline are properly combined. Knowledge of machines such as harmonic components is used to optimize the Adaline, avoiding the calculation burden. The proposed Adaline-FOC-based scheme is validated with numerical results on a five-phase open-end winding non-sinusoidal PMSM drive.

This paper is organized as follows. Section 2 presents the mathematical modeling of a five-phase open-end winding PMSM; a solution to eliminate current harmonics is discussed in Sect. 3. Section 4 proposes a control scheme to obtain high quality torque. Finally, Sect. 5 presents numerical results.

2 Modeling of a Five-Phase Open-End Winding PMSM

A five-phase PMSM with non-sinusoidal back-EMF and equally shifted phases in the open-end winding configuration is considered in this study. Hypotheses for the back-EMF are described as follows: 3^{rd} harmonic has the second highest proportion after 1^{st} harmonic; the unwanted harmonics (5^{th}, 7^{th}, 9^{th}, and 15^{th}) have modest proportions.

The schematic diagram of the considered drive is presented in Fig. 1. One DC-bus voltage supplies two inverters VSI_1 and VSI_2. Notably, each leg in VSI_1 and its

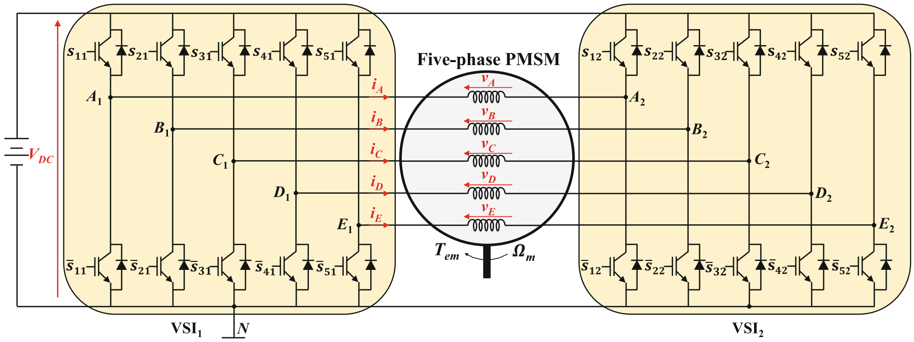

Fig. 1. Schematic diagram of a five-phase open-end winding PMSM supplied by two VSIs.

corresponding leg in VSI_2 are used to feed one phase of the machine, representing the open-end winding structure. The maximum allowable voltage of one machine phase is V_{DC} that is two times higher than the star connection.

In general, the voltages applied to the machine phases can be written as

$$\begin{aligned} \underline{v} = \left[v_A \; v_B \; v_C \; v_D \; v_E \right]^{\mathrm{T}} = \left[v_{A_1N} \; v_{B_1N} \; v_{C_1N} \; v_{D_1N} \; v_{E_1N} \right]^{\mathrm{T}} \\ - \left[v_{A_2N} \; v_{B_2N} \; v_{C_2N} \; v_{D_2N} \; v_{E_2N} \right]^{\mathrm{T}} \end{aligned} \tag{1}$$

where $\underline{v}$ is the 5-dimensional vector referring to five phase voltages of the machine; $(v_{A_1N}, \ldots, v_{E_1N})$ and $(v_{A_2N}, \ldots, v_{E_2N})$ are leg voltages of VSI_1 and VSI_2 compared to the neutral point N, respectively.

The calculation of phase voltages and electromagnetic torque can be expressed as

$$\underline{v} = R\underline{i} + [L]\frac{d\underline{i}}{dt} + \underline{e} \tag{2}$$

$$T_{em} = \underline{e}^T \underline{i} \tag{3}$$

where $\underline{i}$ and $\underline{e}$ are the 5-dimensional vectors of phase currents and back-EMFs, respectively; R is the resistance of one phase; $[L]$ is a 5 by 5 stator inductance matrix; T_{em} is the electromagnetic torque.

Table 1. Fictitious machines and odd harmonics of a five-phase machine.

Fictitious machine	dq frame	Associated harmonic in natural frame ($m \in \mathbb{N}_0$)
The first machine (FM1)	d_1–q_1	$\underline{1}, \underline{9}, 11, \ldots, 5m \pm 1$
The second machine (FM2)	d_3–q_3	$\underline{3}, \underline{7}, 13, \ldots, 5m \pm 2$
Zero-sequence machine (ZM)	z	$\underline{5}, \underline{15}, \ldots, 5m$

With the FOC technique, Clarke [*Clarke*] and Park [*Park*] matrices [8] are applied to convert parameters of the machine from natural frame into rotating frames (dq frames).

The transformation for phase currents is presented as

$$\left[i_{d1}\ i_{q1}\ i_{d3}\ i_{q3}\ i_z \right]^T = [Park][Clarke]\left[i_A\ i_B\ i_C\ i_D\ i_E \right]^T. \tag{4}$$

In dq frames, the machine can be represented by two fictitious 2-phase machines FM1 (with frame d_1–q_1) and FM2 (with frame d_3–q_3), and one zero-sequence machine ZM (with axis z). Each fictitious machine is associated with a group of harmonics in natural frame as presented in Table 1 [4]. The subscripts “1” and “3” in dq frames (d_1–q_1 and d_3–q_3) refer to the ranks of main harmonics in these frames. Notably, values of machine parameters, such as currents and back-EMFs, are expected to be constant in dq frames to facilitate current control as well as to obtain high quality torque. In other words, there are no harmonics in dq frames.

3 Elimination of Current Harmonics

According to [6–8], the low-frequency current harmonics in dq frames are generated by the unwanted back-EMF harmonics (5^{th}, 7^{th}, 9^{th}, and 15^{th}) and the inverter nonlinearity (dead-time voltages). These current harmonics have frequencies of 10θ (for i_{d1}, i_{q1}, i_{d3}, i_{q3}), 5θ and 15θ (for i_z) in dq frames as described in Table 2 where θ is the electrical position of the machine. Current harmonic amplitudes depend on several parameters such as the harmonic distribution in back-EMF, rotating speed, switching period, inverter dead time, and DC-bus voltage. Due to the complication of the real-time drive systems, these parameters need to be automatically identified in real time to correctly eliminate the current harmonics. Therefore, five Adalines have been proposed in [6] for five dq currents in three frames (d_1–q_1), (d_3–q_3), and z. The combination between the five Adalines and back-EMF harmonics can effectively eliminate current harmonics.

Table 2. Unwanted current harmonics of a non-sinusoidal five-phase machine.

Fictitious machine	dq frame	Current harmonics by unwanted back-EMFs	Current harmonics by dead-time voltages
FM1	d_1–q_1	10θ	10θ
FM2	d_3–q_3	10θ	10θ
ZM	z	5θ, 15θ	0

From [8], the i_{q1} current control scheme with current harmonic eliminations is described in Fig. 2a with the Adaline for current in Fig. 2b. Current i_{q1} is controlled by a PI controller. An adaptive compensating voltage v_{q1_com} generated by the Adaline and the estimated q_1-axis back-EMF $Eq.\ 1_{\_com}$ are used to eliminate a harmonic of 10θ in dq frame. In a five-phase open-end winding machine, there are five dq currents, leading to five Adalines for current harmonic eliminations.

However, the elimination of current harmonics in [6–8] cannot guarantee a constant torque because the interaction between the main harmonics of currents (1^{st} and 3^{rd})

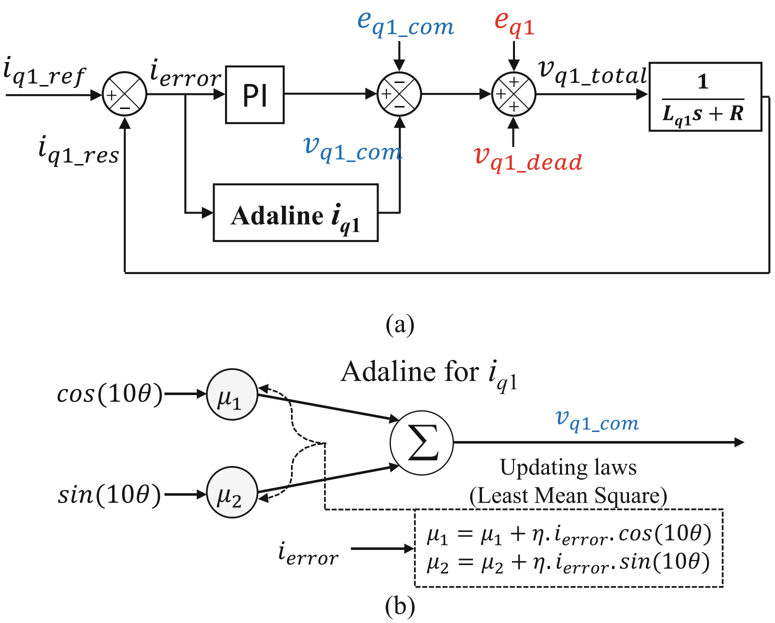

Fig. 2. Current harmonic elimination: (a) Control scheme of one of five dq currents, (b) Adaline structure.

and the unwanted back-EMF harmonics (5^{th}, 7^{th}, 9^{th}, and 15^{th}), causing the torque harmonic of 10θ. Table 3 describes the rank of torque ripples generated by the imposed current harmonics and unwanted back-EMF harmonics. Figure 3 shows the elimination of current harmonics (i_{q1} and phase current i_A from 0.015 s) and the existence of torque ripples with harmonic 10θ (about 18%) even when the current harmonics in dq frames have been eliminated [8].

Table 3. Torque ripples generated by unwanted back-EMF harmonics in fictitious machines.

Fictitious machine	Current harmonics after compensation	Unwanted back-EMF harmonics	Torque harmonics
ZM1	1θ	9θ	10θ
ZM2	3θ	7θ	10θ
ZM	0	5θ, 15θ	0

4 Eliminations of Torque Ripples

The proposed Adaline-FOC-based control scheme is described in Fig. 4 with the Adaline for torque described in Fig. 5. The purpose of the Adaline for torque in the control scheme is to determine compensating torque T_{emcom}. Then, the compensating currents

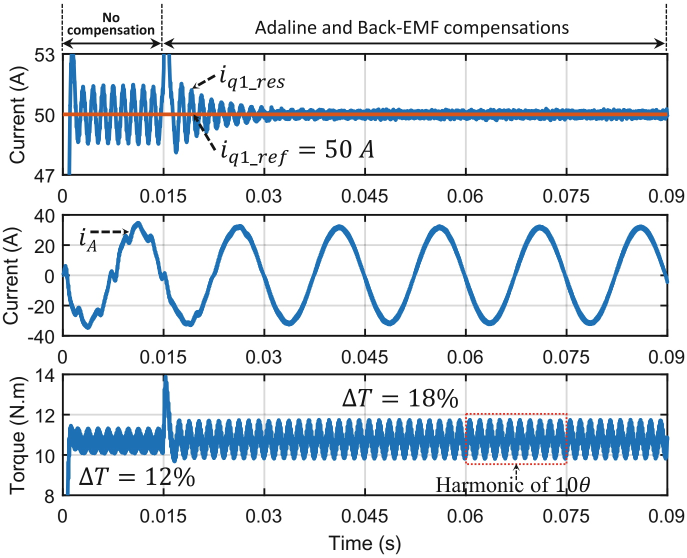

Fig. 3. Elimination of harmonics in i_{q1}, phase-A current, and torque at 60 rad/s.

$\underline{i}_{com}$ ($\underline{i}_{dqcom}$) can be calculated form T_{emcom} by using Maximum Torque Per Ampere (MTPA) [14]. However, only main harmonics (1$^{\text{st}}$ and 3$^{\text{rd}}$) of the speed normalized back-EMF are considered to calculate currents, the original MTPA becomes simplified MTPA in this study. Finally, the error between T_{em} and its reference value T_{emref} is minimized. The desired compensating torque can be expressed as

$$T^*_{emcom} = T_{emref} - T_{em} = \mu^*_0 + \mu^*_1 \cos(10\theta) + \mu^*_2 \sin(10\theta) \tag{5}$$

where μ^* is the constant term of the compensating torque; (μ^*_1, μ^*_2) are respectively coefficients representing torque harmonics 10θ. Therefore, the compensating torque T^*_{emcom} is expressed by three coefficients (μ^*_0, μ^*_1, μ^*_2).

The output of the Adaline in Fig. 5 is given by

$$y = \mu_0 + [\mu_1 \cos(10\theta) + \mu_2 \sin(10\theta)] \tag{6}$$

where θ is the electrical position; (μ_0, μ_1, μ_2) are three weights corresponding to the three coefficients of the desired compensating torque in (5).

The Adaline weights are updated by Least Mean Square rule [14, 15] at each sampled time k. An example for weight updating with μ_1 is expressed by

$$\mu_1(k+1) = \mu_1(k) + \eta\left[T_{emref} - T_{em}(k)\right]\cos(10\theta) = \mu_1(k) + \eta T_{error}(k)\cos(10\theta) \tag{7}$$

where η is the learning rate; T_{error} is the error between reference torque T_{emref} and total torque T_{em}; T_{em} is derived from phase currents and estimated back-EMFs in "Torque estimation" block in Fig. 4 using (3).

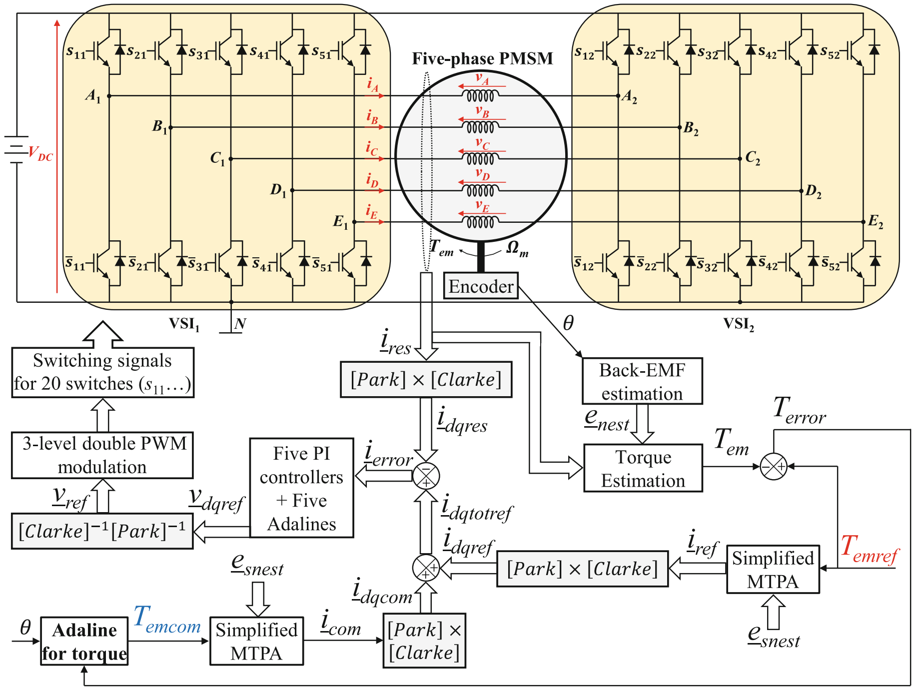

Fig. 4. The proposed Adaline-FOC-based control structure to eliminate torque ripples.

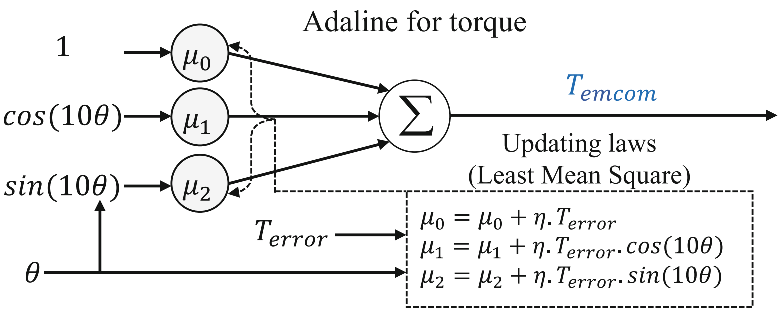

Fig. 5. Adaline structure to eliminate torque ripples.

Learning rate η needs be properly chosen and within [0, 1] to guarantee the system stability. Its value mainly depends on the sample time, amplitudes and phases of harmonics of the learned signal (T_{emcom}). The Adaline weights are updated to converge to the desired coefficients of the compensating torque in (5) as follows

$$\left\langle \mu_0(k) \underset{k\to\infty}{\to} \mu_0^*; \quad \mu_1(k) \underset{k\to\infty}{\to} \mu_1^*; \quad \mu_2(k) \underset{k\to\infty}{\to} \mu_2^* \right\rangle . \tag{8}$$

Finally, the torque ripples are eliminated by the proposed control scheme.

5 Numerical Results

Numerical results to verify the effectiveness of the Adaline-FOC-based scheme (Fig. 4) are obtained with MATLAB Simulink. Parameters of the studied drive are described in Table 4. Two VSIs are controlled with the 3-level double modulation PWM (at 15 kHz). Five dq currents are controlled by five PI controllers and five Adalines for current harmonic eliminations as described in [6].

As previously assumed, six back-EMF harmonics (1st, 3rd, 5th, 7th, 9th, 15th) with the proportions in Fig. 6 are used to model the 5-phase machine. The reference torque T_{emref} of 10 N.m (rated torque) is imposed at 750 r/min to verify the proposed scheme.

Table 4. Electrical parameters of the studied five-phase PMSM drive.

Parameter	Unit	Value
Stator resistance R	mΩ	9.1
Self-inductance L	mH	0.09
Mutual inductance M_1	mH	0.02
Mutual inductance M_2	mH	−0.01
1st harmonic of speed-normalized back-EMF	V/rad/s	0.1358
Number of pole pairs p		7
Rated torque	N.m	10
DC-bus voltage V_{DC}	V	48
PWM switching frequency	kHz	15
Learning rate of Adaline for torque η		0.00001

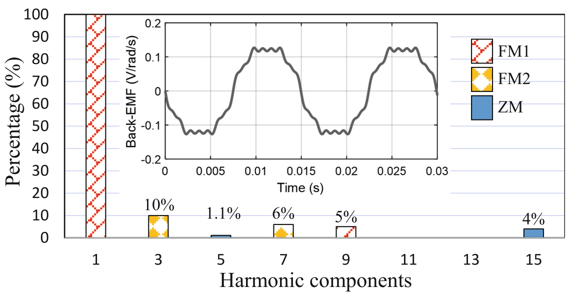

Fig. 6. Speed-normalized back-EMF and harmonic components of the studied five-phase PMSM.

The numerical results are shown in Fig. 7 including the electromagnetic torque, weights of Adaline for torque, dq currents, phase-A current. “No comp.” means that there are no compensations for both unwanted current harmonics and torque ripples. “EMF comp. for current” implies that only estimated back-EMFs are used to eliminate unwanted current harmonics. “EMF+Adalines comp. for current” expresses that both

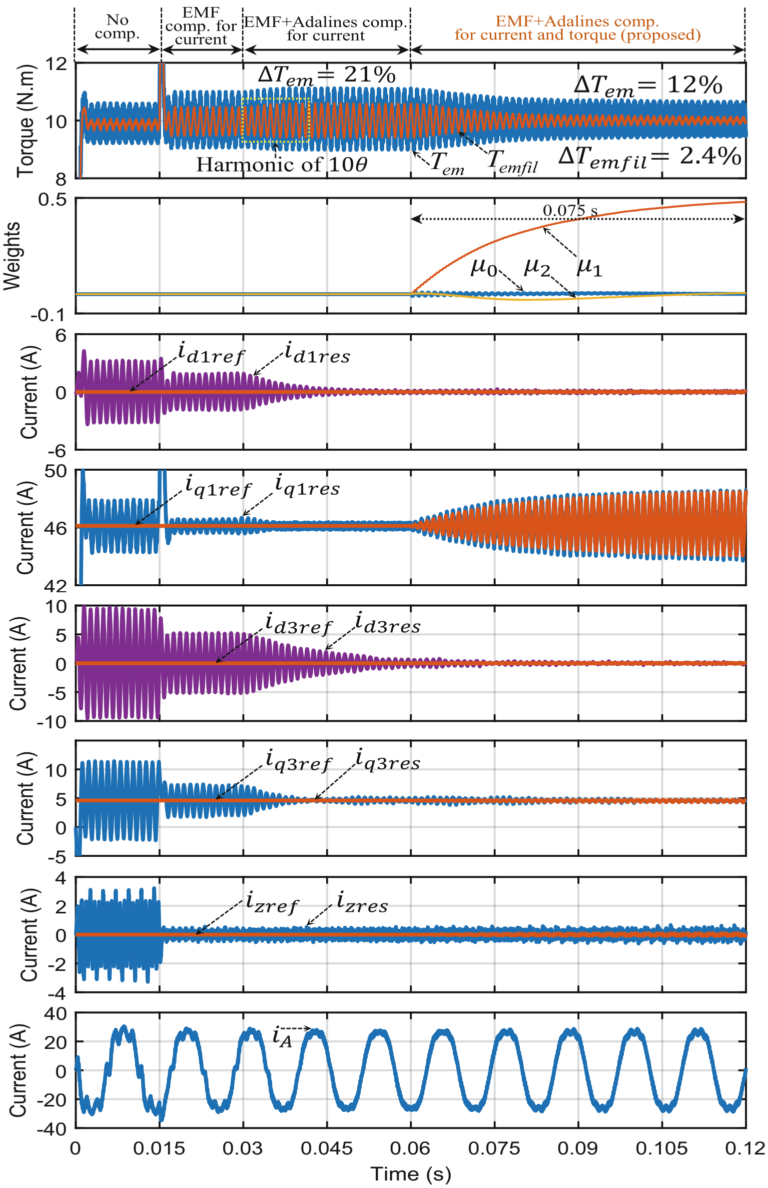

Fig. 7. Numerical results with the electromagnetic torque, weights of Adaline for torque, dq currents, and a phase current at 750 r/min.

estimated back-EMFs and five Adalines are applied to current harmonic eliminations. These first three stages have been discussed in [6]. The last stage presents the addition of the Adaline for torque in the proposed Adaline-FOC-based scheme.

Specifically, the torque ripple can be effectively reduced from 21 to 12% after using the Adaline for torque. The ripple of 12% almost comes from the switching-frequency zero-sequence components of the open-end winding structure. If the high-frequency components are filtered, the torque ripple is equal to only 2.4%. The convergence time of the Adaline weights is 0.075 s. Compared to the third stage, only the reference value of i_{q1} becomes time-variant to generate constant torque in the last stage. Current of phase A is presented in the bottom of Fig. 7. By using Adalines for unwanted current harmonics from the second stage to the last stage, the phase current waveform becomes smoother without unexpected current harmonics.

6 Conclusions

The Adaline-FOC-based control scheme for five-phase non-sinusoidal back-EMF machine drives has been proposed and validated in this study. Smooth torque has been generated with a low-cost machine having undesired back-EMFs. Only knowledge of torque harmonics enables the Adaline to be optimized, reducing the calculation burden. The combination of Adalines for current and Adaline for torque not only guarantees pure phase currents but also smooth torque. With the simplicity of Adaline, the Adaline-FOC-based scheme can be effectively used in industry.

Acknowledgments. The authors would like to thank Thai Nguyen University of Technology (TNUT), Viet Nam for the support.

References

1. Yepes, A., Lopez, O., Gonzalez Prieto, I., Duran, M.J., Doval-Gandoy, J.: A comprehensive survey on fault tolerance in multiphase AC drives, Part 1: general overview considering multiple fault types. Machines (2022)
2. Ala, G., et al.: Stability of microgrids: an application of virtual synchronous generator. In: Nguyen, D.C., Vu, N.P., Long, B.T., Puta, H., Sattler, K.U. (eds) ICERA 2022. LNNS, vol. 602, pp. 873–880. Springer, Cham (2023). https://doi.org/10.1007/978-3-031-22200-9_92
3. Yepes, A., Gonzalez Prieto, I., Lopez, O., Duran, M.J., Doval-Gandoy, J.: A comprehensive survey on fault tolerance in multiphase AC drives, Part 2: phase and switch open-circuit faults. Machines (2022)
4. Semail, E., Kestelyn, X., Bouscayrol, A.: Right harmonic spectrum for the back-electromotive force of an n-phase synchronous motor. In: the 39th IEEE Industry Applications Conference, Seattle, WA, USA, vol. 1, pp. 71–78, October 2004
5. Tran, H.T., Tran, D.L.T., Nguyen, V.Q., Do, H.T., Nguyen, M.T.: A novel framework of modelling, control, and simulation for autonomous quadrotor UAVs utilizing Arduino mega. Wirel. Commun. Mob. Comput. **2022** (2022)
6. Wang, L., Zhu, Z.Q., Bin, H., Gong, L.M.: Current harmonics suppression strategy for PMSM with non-sinusoidal back-EMF based on adaptive linear neuron method. IEEE Trans. Ind. Electron. **67**(11), 9164–9173 (2020)
7. Vu, D.T., Nguyen, N.K., Semail, E., Nguyen, T.T.N.: Current harmonic eliminations for seven-phase non-sinusoidal PMSM drives applying artificial neurons. In: The International Conference on Engineering and Research Application (ICERA), Thai Nguyen, Vietnam, pp. 270–279 (2020)

8. Vu, D.T., Nguyen, N.K., Semail, E.: Eliminations of low-frequency current harmonics for five-phase open-end winding non-sinusoidal machine drives applying neural networks. In: The 46th Annual Conference of the IEEE Industrial Electronics Society (IECON), Singapore, pp. 4839–4844 (2020)
9. Kestelyn, X., Semail, E.: A vectorial approach for generation of optimal current references for multiphase permanent-magnet synchronous machines in real time. IEEE Trans. Ind. Electron. **58**(11), 5057–5065 (2011)
10. Flieller, D., Nguyen, N.K., Wira, P., Sturtzer, G., Abdeslam, D.O., Mercklé, J.: A self-learning solution for torque ripple reduction for nonsinusoidal permanent-magnet motor drives based on artificial neural networks. IEEE Trans. Ind. Electron. **61**(2), 655–666 (2014)
11. Li, G., Hu, J., Li, Y., Zhu, J.: An improved model predictive direct torque control strategy for reducing harmonic currents and torque ripples of five-phase permanent magnet synchronous motors. IEEE Trans. Ind. Electron. **66**(8), 5820–5829 (2019)
12. Tran, D.L.T., Do, H.T., Tran, H.T., Hoang, T., Nguyen, M.T.: A design and implement of fuzzy controller for taking-off and landing for unmanned aerial vehicles. In: Nguyen, D.C., Vu, N.P., Long, B.T., Puta, H., Sattler, K.U. (eds.) ICERA 2022. LNNS, vol. 602, pp. 13–22. Springer, Cham (2023). https://doi.org/10.1007/978-3-031-22200-9_2
13. Wang, X., et al.: Selective torque harmonic elimination for dual three-phase PMSMs based on PWM carrier phase shift. IEEE Trans. Power Electron. **35**(12), 13255–13269 (2020)
14. Vu, D.T., Nguyen, N.K., Semail, E., Wu, H.: Adaline-based control schemes for non-sinusoidal multiphase drives-Part I: torque optimization for healthy mode. Energies **14**(24), Article no. 8302 (2021)
15. Widrow, B., Lehr, M.A.: Adaptive neural networks and their applications. Int. J. Intell. Syst. **8**(4), 453–507 (1993)

Physico–mechanical Properties and Carrier Mobility of HfS_2 Monolayer

Nguyen Hoang Linh[1], Nguyen Minh Son[1], Tran The Quang[2], To Toan Thang[1], Vuong Van Thanh[1], Dinh The Hung[3], and Do Van Truong[1](✉)

[1] School of Mechanical Engineering, Hanoi University of Science and Technology, Hanoi 100000, Vietnam
truong.dovan@hust.edu.vn
[2] Department of Basic Engineering, Faculty of Technology, Thai Binh University, Thai Binh 410000, Vietnam
[3] Faculty of Mechanical Engineering and Mechatronics, Phenikaa University, Hanoi 100000, Vietnam

Abstract. Our research focuses on determining the physico-mechanical properties and carrier mobility of HfS_2 monolayer using first-principles calculations. The results obtained indicate that HfS_2 monolayer possesses a highly stable structure based on both dynamical and mechanical criteria. The relatively small Young's modulus suggests that this structure exhibits flexible mechanical properties. Furthermore, the calculated energy band structures confirm that HfS_2 monolayer is a semiconductor material. Additionally, the electron mobility of HfS_2 is found to be flexible, with a value of $\mu_e \sim 1580\ cm^2V^{-1}s^{-1}$. This study provides valuable information for the potential application of HfS_2 monolayer in advanced technologies in the near future.

Keywords: DFT · mechanical properties · energy band structure · carrier mobility · HfS_2 monolayer

1 Introduction

In the 21st century, the exploration of graphene has revolutionized the materials science field and opened up countless orientations for the application of two-dimensional materials in practice. Owing to the outstanding advantages in physical and mechanical properties, monolayer materials have occupied an important position in the applications of photovoltaic, photocatalysis, power transmission, nanoelectronics, etc. [1–5]. Several two-dimensional materials have been successfully synthesized and applied widely such as Janus, transition metal dichalcogenides (TMDs), germanium, stenen, and so on [2, 6–8]. Through theoretical simulations and experiments, some TMDs have demonstrated their interesting properties and high potential application in reality like MoS_2, NiS_2, PbSe, SiS_2, HfS_2, etc. [4, 9–12]. Therein, HfS_2 has been investigated in a few studies but still has not been explored in detail. Previous studies have shown that HfS_2 is a semiconductor material with electronic properties sensitive to strain. Under biaxial strain,

D. C. Nguyen et al. (Eds.): ICERA 2023, LNNS 944, pp. 20–26, 2024.
https://doi.org/10.1007/978-3-031-62235-9_3

the optical absorption coefficient is significantly improved, which has many promising potentials for optical applications [13]. Besides, vertical strains in the in-plane could modulate the electronic properties of HfS_2 material very well and it is proved that the process controlling material's properties is possible [12]. Moreover, the heterostructure of $HfS_2/MoTe_2$ also has high potential in the applications of photovoltaic cells, and piezoelectric devices [14].

However, several important properties still lack information. In this study, we shed light on the physico–mechanical properties and transport properties for carrier mobility of HfS_2 material. These are special properties that need to be studied carefully, as they affect the quality and performance of devices made from this material. The obtained results show that HfS_2 material has the flexibility of mechanical properties and high fracture strain. Furthermore, the energy band structure and the state density of electronics have shown the distribution of energy bands. Finally, calculated transport properties have taken out potential applications in power transmission with high mobility carriers. This study has provided useful information to apply materials to advanced technologies in the near future.

2 Methodology

The calculations of mechanical, electronic properties and carrier mobility of HfS_2 monolayer were performed by density functional theory (DFT) through Quantum ESPRESSO package [15]. The interactions between atoms were described by the Perdew-Burke-Ernzerhof functional (PBE) using generalized gradient approximation (GGA). The kinetic energy cutoff was chosen as 700 Ry for the charge density to achieve the energy convergence conditions. The k–point grid in the Brillouin zone was represented by Monkhorst-Pack with $15 \times 15 \times 1$ [16]. Figure 1(a) shows the natural structure of monolayer HfS_2 at temperature of 0K, with the conditions of stress lower than 5.10^{-2} GPa and force lower than 10^{-6} Ry/a.u.

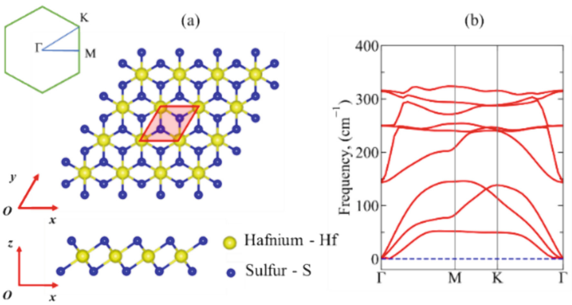

Fig. 1. (a) Atomic structure of HfS_2 monolayer along the boundaries in the x and y directions, (b) Phonon dispersion curves of HfS_2 monolayer in Brillouin zone

Young's modulus and Poisson's ratio of HfS_2 monolayer were calculated by the Eq. (1) based on Hooke's law:

$$Y = \frac{C_{11}C_{22} - C_{12}^2}{C_{11}}; v = \frac{C_{11}}{C_{12}} \tag{1}$$

3 Results and Discussions

3.1 Optimize Structures and Stable Conditions

HfS_2 monolayer is equilibrated at the temperature of 0K by the minimum energy Broyden–Fletcher–Goldfarb–Shanno method (BFGS) for the lattice crystal. On the top view, monolayer HfS_2 structure is analogous to the honeycomb one with sulfur atom (S) located in the center of the hexagon, Fig. 1(a). HfS_2 structure has only a single-layer structure, so the mechanical parameter is adjusted according to the *z*–dimension. The lattice parameters, elastic constants, Young's modulus, and Poisson's ratio are listed in Table 1. These obtained results are consistent with the previous studies [17].

This study uses two distinct criteria to demonstrate the stability of HfS_2 monolayer. Firstly, we inspect dynamic stability based on phonon dispersions. Figure 1(b) illustrates the phonon spectra of HfS_2 monolayer, with the nine oscillation branches analyzed, including three acoustic branches at the low frequencies and six optical ones at high frequencies. Through analysis of the vibration spectrum, HfS_2 monolayer has high stability, with the largest frequency of vibration reaching 325 cm^{-1} and there are not any negative phonon frequencies in the Brillouin zone. Therefore, the material is wholly stable based on dynamic criteria. Then, we use mechanical criteria to demonstrate the stability of the structure through elastic constants. The results of calculated elastic constants show that the structure is completely stable according to Born's criterion for hexagonal structure with $C_{11} > |C_{12}| > 0$ and $C_{66} > 0$ [18]. Thus, HfS_2 structure is entirely stable and has interesting potential for practical applications.

Table 1. Lattice constants *a* (Å), thickness *h* (Å), elastic constant C_{ij} (N/m), Young's modulus *Y* (N/m), Poisson's ratio υ

a	h	$C_{11} = C_{22}$	C_{12}	C_{66}	Y	υ
3.64	1.45	77.54	11.00	31.32	75.98	0.14

3.2 Physico–mechanical Properties

The mechanical strain is calculated by changing the parameters of the lattice as $\varepsilon = (\mathscr{A} - \mathscr{A}_0)/\mathscr{A}_0$, where $\mathscr{A}_0$ and $\mathscr{A}$ are the sizes of the lattice crystal at equilibrium and strained states, respectively. Figure 2(a) shows the relationship between tensile strain and stress of HfS_2 monolayer. The obtained results reveal that HfS_2 monolayer is capable of withstanding tensile strain fairly well in all three directions, up to $\varepsilon = 0.16$. The ideal strength of the tensile strain ε_{bia} is the highest, with fracture strain reaching at $\varepsilon_{bia} = 0.22$ and the critical stress close to 9 N/m.

To have a clear understanding of the electronic properties, we use the exchange–correlation potential energy PBE and Heyd-Scuseria-Ernzerhof functional (HSE) to calculate the energy band structure. Figure 2(b) describes the energy band structure of the HfS_2 structure with the exchange–correlation energy functionals having the same profile. The distribution of conduction band minimum (CBM) is located at Γ point and the valence band maximum (VBM) is distributed at M point. The different distributions of the two points show that they have no equilibrium in angular momentum, and electronic properties are easily sensitive to external impacts.

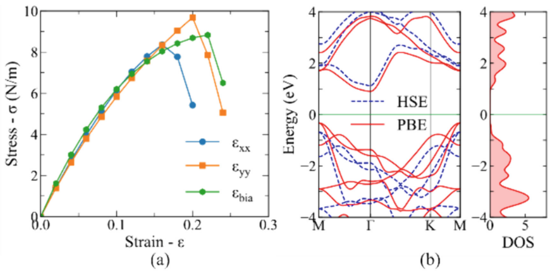

Fig. 2. (a) Relationship between mechanical strains and stress, (b) Energy band structure and density of state of HfS_2 monolayer

The band gap of the material calculated through two exchange-correlation functionals exhibits direct semiconductor properties. The band gap of HfS_2 monolayer is computed by the two functionals are 1.23 eV (for PBE) and 1.78 (for HSE), respectively. In general, the results are similar to the values of previous studies [13, 20]. In addition, Fig. 2(b) also shows the density of states of electrons. The density of electrons is high at the energy region of large absolute value. In contrast, at the positions near CBM and VBM points, the appearance of electrons is low, due to the possibility that it is difficult to exist around the band gap without the necessary energy level.

3.3 Carrier Mobility

To satisfy the conditions in the applications of electronic devices, it is required that the carrier mobility of the material should be flexible. Transport properties of carrier mobility are determined by their mobility, which depends on many factors described in Eq. (2) based on the theory of Bardeen and Shockley [20]:

$$\mu = \frac{e\hbar^3 C_{2D}}{k_B T m^* \sqrt{m_x m_y} E_d^2} \tag{2}$$

$$C_{2D} = \frac{1}{V}\frac{\partial^2 E}{\partial \varepsilon_{uni}^2}; \; E_d = \frac{E_{edge}}{\varepsilon_{uni}} \tag{3}$$

where, e is the elementary charge, $\hbar$ is the Planck constant, k_B is the Boltzmann constant, T is room temperature, m^* and $m_{x(y)}$ are effective masses. Moreover, the small deformation elastic coefficient C_{2D} and deformation potential are performed by two Eqs. (3) at small strain $\varepsilon_{uni} \leq 0.01$ as shown in Fig. 3.

Based on the relationship between stress and uniaxial strain at small levels, Table 2 shows the calculated results of small deformation elastic coefficient, effective mass, deformation potential and carrier mobility of particles following x and y directions. The results show that HfS_2 monolayer has good mobility, especially since the electrons can be very motive flexible. Besides, the carrier mobility of HfS_2 is almost similar in all directions. In the equilibrium state, the mobility of electrons is about 8 times that of holes. The reason is that the effective mass of the electrons is quite slight and there is enough potential energy for the moving process. Our results are suitable with some previous research such as Zang et al. [21], Kanazawa et al. [22]. Compared to the other popular 2D materials such as SnSO [6], and NiS_2 [4], the electron mobility of HfS_2 monolayer is about 7 times higher. Thus, this material has great potential in the electric transmission applications. Besides, the difference in the electron particles easily separates them to serve the needs of electric transmission [23].

Table 2. Elastic coefficients (N/m), effective mass (m/m_0), deformation potential (eV) and carrier mobility at room temperature ($cm^2V^{-1}s^{-1}$)

Particle	$C_{2D}^{xx} = C_{2D}^{yy}$	m_x	m_y	E_d^{xx}	E_d^{yy}	μ^{xx}	μ^{yy}
Electron	51.4	0.26	0.24	–3.40	3.40	1580.6	1580.6
Hole	51.4	0.30	2.30	3.12	2.76	193.5	247.4

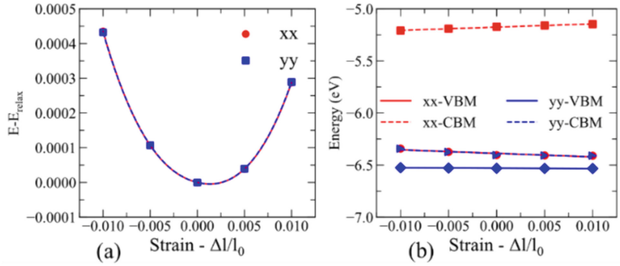

Fig. 3. (a) Relationship between strains along $x(y)$-direction and energy of system (b) Band edges positions CBM (VBM) under uniaxial strain

4 Conclusion

Our research reveals that HfS_2 monolayer exhibits small elastic constants, indicating its ability to withstand significant strain and display flexible mechanical properties in the different directions. By calculating the energy band structure, we find that HfS_2

monolayer possesses the characteristics of a semiconductor material, with a band gap of 1.78 eV, making it suitable for absorption in the visible light range. Additionally, the HfS_2 structure demonstrates nearly isotropic mobility, with electrons exhibiting approximately eight times higher mobility than holes. These findings suggest that HfS_2 structure holds great potential for wide-ranging applications in electronics and charge carrier devices.

References

1. Han, W., et al.: Graphene spintronics. Nat. Nanotechnol. **9**(10), 794–807 (2014)
2. Kandemir, A., et al.: Stability, electronic and phononic properties of β and 1T structures of SiTex(x=1,2) and their vertical heterostructures. J. Phys. Condens. Matter **29**(39), 1–8 (2017)
3. Linh, N.H., et al.: First-principles study of electronic and optical properties and photocatalytic performance of MS monolayer under strain. J. Sci. Technol. Tech. Univ. **33**(2), 44–51 (2023)
4. Linh, N.H., et al.: Theoretical computational of electronic and transport properties and optical conductivity of monolayer NiS_2 under mechanical strain. J. Sci. Technol. Tech. Univ. **33**(1), 34–41 (2023)
5. Nayak, D., Thangavel, R.: A density functional theory study on the strain modulated electronic and photocatalytic properties of a GaSe monolayer for photocatalytic water splitting and artificial photosynthesis. New J. Chem. **46**(23), 11447–11461 (2022)
6. Vu, T.V., et al.: A theoretical study on elastic, electronic, transport, optical and thermoelectric properties of Janus SnSO monolayer. J. Phys. D Appl. Phys. **54**(47), 1–11 (2021)
7. Wang, S., Ukhtary, M.S., Saito, R.: Strain effect on circularly polarized electroluminescence in transition metal dichalcogenides. Phys. Rev. Res. **2**(3), 1–7 (2020)
8. Liu, N., et al.: Recent progress on germanene and functionalized germanene: preparation, characterizations, applications, and challenges. Small **15**(32), 1–11 (2019)
9. Linh, N.H., et al.: First-principles investigation on the electromechanical properties of monolayer 1H Pb-dichalcogenides. Mater. Res. Soc. Korea **33**(5), 189–194 (2023)
10. Hung, N.T., Nugraha, A.R.T., Saito, R.: Two-dimensional MoS2 electromechanical actuators. J. Phys. D Appl. Phys. **51**(7), 075306–075316 (2018)
11. Linh, N.H., et al.: Prediction of mechanical, electronic and optical properties of monolayer 1T Si-dichalcogenides via first-principles theory. Mater. Today Commun. **36**, 1–16 (2023)
12. Wu, N., et al.: Strain effect on the electronic properties of 1T-HfS_2 monolayer. Phys. E Low-Dimens. Syst. Nanostruct. **93**, 1–5 (2017)
13. Hoat, D.M., et al.: Theoretical analysis of the HfS_2 monolayer electronic structure and optical properties under vertical strain effects. Optik (Stuttg). **225**, 165718–165727 (2021)
14. Yang, X., et al.: HfS_2/$MoTe_2$ vdW heterostructure: bandstructure and strain engineering based on first-principles calculation. RSC Adv. **10**(5), 2615–2623 (2020)
15. Giannozzi, P., et al.: QUANTUM ESPRESSO: a modular and open-source software project for quantum simulations of materials. J. Phys. Condens. Matter **21**(39) (2009)
16. Monkhorst, H.J., Pack, J.D.: Special points for Brillonin-zone integrations. Phys. Rev. B **13**(12), 5188–5192 (1976)
17. Faghihnasiri, M., et al.: A first-principles study of nonlinear elastic behavior and anisotropic electronic properties of two-dimensional HfS_2. Nanomaterials **10**(3), 1–13 (2020)
18. Mouhat, F., Coudert, F.X.: Necessary and sufficient elastic stability conditions in various crystal systems. Phys. Rev. B Condens. Am. Phys. Soc. **90**(22), 224104–4 (2014)
19. Zhao, Q., et al.: Elastic, electronic, and dielectric properties of bulk and monolayer ZrS_2, $ZrSe_2$, HfS_2, $HfSe_2$ from van der Waals density-functional theory. Phys. Status Solidi **254**(9), 1–11 (2017)

20. Bardeen, J., Shockley, W.: Deformation potentials and mobilities in non-polar crystals. Phys. Rev. **80**(1), 72–80 (1950)
21. Zhang, W., Huang, Z., Zhang, W., Li, Y.: Two-dimensional semiconductors with possible high room temperature mobility. Nano Res. **7**(12), 1731–1737 (2014)
22. Kanazawa, T., et al.: Few-layer HfS_2 transistors. Sci. Rep. **6**, 1–9 (2016)
23. Dai, J., Zeng, X.C.: Titanium trisulfide monolayer: theoretical prediction of a new direct-gap semiconductor with high and anisotropic carrier mobility. Angew. Chemie Int. Ed. **54**, 7572–7576 (2015)

Hybrid Energy Storage on Electric Vehicles

Denis Endachev[1], Alexey Terenchenko[1], Kirill Karpukhin[1], Aleksey Kolbasov[1], Andrey Povaliaev[1], Pablo Iturralde[2], and Nguyen Khac Minh[3](✉)

[1] NAMI Russian State Scientific Research Center, 2 Avtomotornaya Street, Moscow 125438, Russia

[2] Moscow Polytechnic University, Bolshaya Semyonovskaya Street, 38, Moscow 107023, Russia

[3] Faculty of Automotive and Power Machinery Engineering, Thai Nguyen University of Technology, № 666 Tich Luong Ward, Thai Nguyen 24131, Vietnam

khacminhcdl@tnut.edu.vn

Abstract. This scientific paper demonstrates options for improving traction batteries of electric vehicles. The use of energy storage batteries in vehicles requires continuous improvement of these systems, as the weakest link in their design. In addition to improving the chemical composition of the batteries used, new methods are being sought to improve the characteristics of the storage device. One of them is the use of a hybrid energy storage system. This paper analyzes the advantages of a hybrid drive over a traditional lithium battery.

Keywords: Vehicle · electric vehicle · hybrid vehicle · energy storage · ecology · energy efficiency · electric drive · supercapacitor · battery power

1 Introduction

Due to the changeable and unstable characteristics of wind and solar energy, the problems associated with the integration of renewable energy sources and the management of the stability of the energy system are becoming more and more noticeable. Meanwhile, the serious consequences caused by accidents in large power systems emphasize the acute the need for highly efficient large-scale energy storage technologies. Consequently, through the use of energy storage, it is possible to accumulate excess wind and solar energy, and the power grid, in turn, is able to provide a more stable output power, which provides rapid support for active power, expands the possibilities of regulating the frequency of the network, and leads to large-scale wind and solar generation connected to the network, stable and reliable.

Since hybrid energy storage systems have proven themselves well in the energy sector. Then it is advisable to consider similar storage schemes in relation to road transport. This is especially true if the vehicles will be equipped with solar energy converters in the form of solar panels.

With the growing environmental problems on our planet, the topic of electric vehicles has become actively developed. Most of the world's vehicle manufacturers confidently

D. C. Nguyen et al. (Eds.): ICERA 2023, LNNS 944, pp. 27–35, 2024.
https://doi.org/10.1007/978-3-031-62235-9_4

position moving away from internal combustion engine systems and a complete transition to electric traction in the near future. The most problematic and relevant in this aspect is the topic of creating energy storage devices for these vehicles, which are becoming more and more demanding with the development of scientific and technological progress. The main problem when creating these drives is that you need to combine quite contradictory parameters in one block, namely:

1. The supply of energy to ensure long run on 1 charge.
2. High power to ensure the vehicle's dynamic performance and charge speed.
3. Wide operating temperature range.
4. Mechanical stability and safety.
5. Low cost.
6. Low weight and volume to increase the load capacity and capacity.
7. Low self-discharge level for vehicle storage and Parking.
8. High cyclability (resource) to increase battery life.

Here, the choice of the battery type to create the battery comes to the fore. However, among the variety of existing and currently used batteries, it is impossible to find an absolute leader in all parameters. In any case, we always have to be guided by what is most important in this application, and, as a rule, we are forced to choose some compromise solution between technical parameters, cost and safety. The most promising direction for today is lithium batteries, but even here, depending on the chemistry and composition used, we have a very large range of contradictory characteristics. As an example, when choosing batteries LTO get good power and temperature readings with a very high resource and security, but it's fairly high mass and cost, when selecting the NMC battery get high power density with reasonable power and high value, and average resource when choosing LiFePO4 batteries get high power at low energy density and cost. There is a desire to collect all the best indicators in one source, but unfortunately, this is not possible. One of the ways out of this situation is to use hybrid energy storage devices, which will allow you to combine, at least partially, the best parameters of worthy representatives of the family of energy accumulators.

2 The Choice of Components

Currently, one of the main global trends in the development of the automotive industry is the development of environmentally friendly vehicles. They are developed by almost all the leading automakers in the world. It is believed that the most environmentally friendly Vehicles are electric vehicles [1]. One of the main components of an electric vehicle is a high-voltage battery [2].

The most popular and actively developing direction is hybridization, which combines high energy intensity and battery power [3]. And this is not accidental, because in transport, in addition to the primary task of providing a power reserve with a small mass, we are dealing with high starting currents of power plants, steadily growing capacities, requirements for vehicle dynamics, charging speed and energy recovery during braking. The choice of components for a hybrid drive in this case is quite obvious-lithium NMC batteries that provide energy reserves and supercapacitors, characterized by unsurpassed power, but practically not used separately in transport due to the characteristic feature – very low energy consumption [4] (Fig. 1).

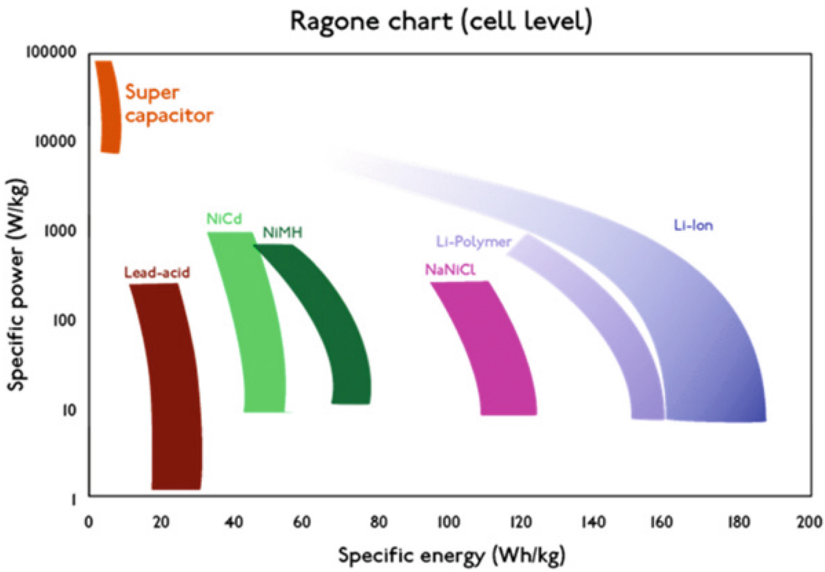

Fig. 1. Ragone chart. Comparison of characteristics of supercapacitors and batteries

It should be noted that hybrid battery systems have been used serially by automakers in practice for quite a long time and very successfully. One of the most popular options is a fairly common START-STOP system for cars with internal combustion engines. An example is the e-HDi engines equipped with the PSA stop & Start system Fig. 2.

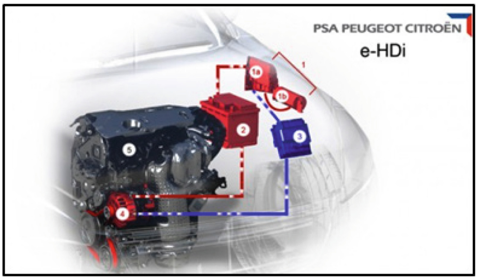

Fig. 2. START-STOP system e-HDi from PSA.

Frequent starts of the internal combustion engine caused by the operation algorithm in this case do not have a strong negative impact on the service life of the regular battery due to the use of a supercapacitor block, which levels the current loads on the regular battery. In addition to the supercapacitor, a generator in reverse mode is used to speed up the launch.

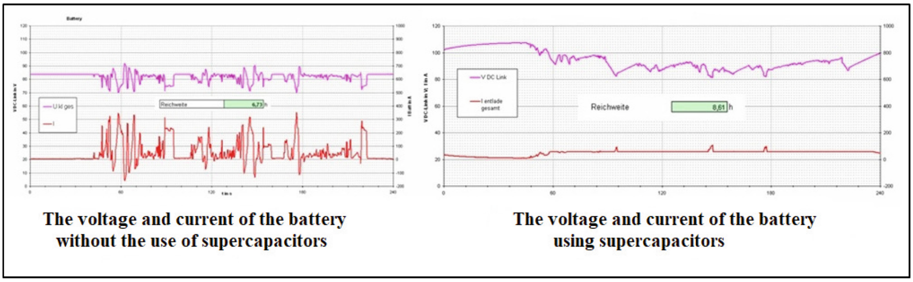

Fig. 3. Changing the battery load using a supercapacitor.

Thus, due to the lower internal resistance, the supercapacitor block takes on all the pulse surges of the charge-discharge current that are most harmful to the battery Fig. 3 [5].

3 Justification

Looking at the graph of the battery current, for example, the real cycle of an electric bus, it is easy to notice the impulse nature of the power plant's energy consumption and return during movement. A similar pattern will be observed in any electric or hybrid vehicle Fig. 4.

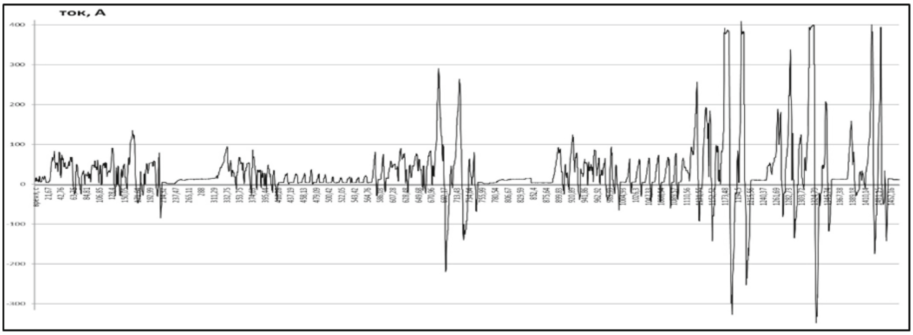

Fig. 4. Current consumption of the electric bus battery in the real cycle.

Analysis of the advantages of using a supercapacitor in a hybrid storage device on an electric vehicle.

1. High system life and battery life.

In this point, there are 2 main aspects:

A) the process of charge/discharge during the movement of the vehicle is cyclical, the supercapacitor taking over part of the cycle reduces the degree of cyclability of the battery, thereby increasing its resource.

B) Pulse loads on the battery have a rather negative impact and have a direct impact on its degradation and service life. The supercapacitor takes the pulse component of the cycle on itself in view of the lower internal resistance, thereby extending the life of the battery.

2. Safety of operation.

The most dangerous link in an electric vehicle is the battery energy storage. In the case of a hybrid storage system, the currents flowing directly through the battery are reduced, and the probability of its temperature reaching a critical level is reduced.

3. Improve dynamic characteristics.

Due to the ability of the supercapacitor to instantly transfer energy to the load, the improvement in dynamics is an indisputable fact.

4. Reducing the current load on the vehicle's power wiring. Possibility to reduce the cross-section of the power wiring harness.

When the supercapacitor is placed in close proximity to the inverter, the current load on the battery - Inverter power harness is reduced.

5. Reducing the load on the power plant and improving its reliability.

Since the supercapacitor gives off energy instantly, the voltage drawdown decreases under peak and dynamic loads, respectively, the currents flowing through the inverter and power plant will be slightly lower, which in turn will reduce heat generation and increase the reliability of the inverter and power plant.

6. Reducing the level of interference radiation.

Given the peculiarity of placing the supercapacitor in close proximity to the inverter, it can be argued that the battery–inverter power harness, having a certain resistance, will get rid of peak current surges, which are a source of interference in the vehicle.

7. Greater cost-effectiveness due to the efficiency of energy recovery.

Due to the ability of the supercapacitor to instantly receive a charge, it is possible to completely save all the energy of regenerative braking of the vehicle's power plant and increase the braking efficiency.

8. The main battery capacity requirements are Reduced.

Naturally, in each case, the parameters of batteries and supercapacitors must correspond to the vehicle's operating mode and operating conditions. The most reliable data on the capacitance values can be obtained empirically, after analyzing the actual current characteristics of the vehicle.

9. Thermostabilization.

Due to the fact that hybrid batteries based on supercapacitors have a wider operating temperature range relative to lithium-ion batteries, the requirements for the temperature control system can be significantly reduced, which will lead to greater reliability due to the lack of additional systems [6].

10. Fire in case of an accident

Since the volume of lithium-ion batteries is reduced with the same battery efficiency, the risk of fire in a road accident is also reduced. As a rule, lithium-ion batteries with NMC composition begin the process of thermal acceleration in case of mechanical damage or overheating. At the same time, supercapacitors do not react to mechanical damage in this way and in case of a short circuit, they do not cause ignition.

4 Problems

The main problem of using supercapacitors in hybrid drives is the need to use a bidirectional DC-DC Converter. The wide voltage range of the supercapacitor causes problems with the use of stored energy. The total energy stored in the Etot supercapacitor is the ratio of the capacitance C and the square of the voltage V.

$$\mathrm{Etot} = 1/2\mathrm{CxV}^2$$

In practice, in an energy storage system that includes a battery and a supercapacitor, the energy stored in the supercapacitor can almost never be fully used due to the fact that providing the Converter with such a wide range of voltage changes is too difficult for most applications. Moreover, when the supercapacitor is discharged to 50% of the rated voltage, up to 75% of the energy stored in the supercapacitor is released. Taking into account the limits of the voltage change, the useful energy will be:

$$\mathrm{E} = 1/2\mathrm{CxV}^2\mathrm{max} - 1/2\mathrm{CxV}^2\mathrm{min}$$

A fairly detailed comparative study of the practical implementation of a hybrid drive can be found in the article "Supercapacitor Enhanced Battery Traction Systems-Concept Evaluation" [7–9], the results of which confirm all the previously mentioned arguments.

5 Examples of Using Hybrid Energy Storage on Electric Vehicles

Currently, hybrid energy storage are beginning to be introduced into electric vehicles. As a rule, these are urban electric buses.

Belarusian "Belkommunmash" in 2017 presented the AKSM-E433 Vitovt electric bus equipped with supercapacitor (Fig. 5). It is able to travel 12 km on a single charge, and the time to fully charge the battery from supercapacitors is 7 min. Considering that the city bus stops every few hundred meters, and its route rarely exceeds a couple of tens of kilometers, you can charge it at the final stops.

Fig. 5. Electric bus AKSM-E433 (Minsk, Belarus)

The traction battery of an electric bus AKSM-E433 weighs about 1.5 tons, which is a lot by the standards of an electric vehicle. At the same time, the supercapacitors included in the composition allow you to travel no more than 5% of the total range of the electric bus. At the same time, if scientists achieve an increase in the capacity of supercapacitor by an order of magnitude, then a similar assembly of supercapacitor will be able to travel not 12 km, but 120 km, or have the same range, but with the mass of the hybrid energy storage up to 150 kg.

In 2016, electric buses HIGER powered by supercapacitors were put into operation in Serbia (Fig. 6). After charging with a pantograph, an electric bus with HIGER supercapacitors can travel up to 20 km. Due to its high environmental friendliness, the vehicle will help significantly reduce operating costs. In addition, supercapacitor buses are equipped with the latest electric control systems, fully developed by HIGER.

The Russian Federation is also conducting research on the introduction of hybrid energy storage in electric vehicles, mainly in Russian electric buses.

Fig. 6. Electric bus HIGER (Belgrade, Serbia)

6 Conclusion

The feasibility of using a hybrid energy storage system in cases of electric vehicles from a technical point of view is not in doubt. The only thing that remains behind the scenes is the economic component of the issue, which in turn changes greatly over time due to scientific achievements, technological progress and market development. Supercapacitors will not replace lithium-ion traction batteries, because batteries are also progressing. But they are capable of acting as a buffer power source and can also be used in urban electric transport. Similar solutions are already being developed and produced in the world. Therefore, research on the creation of hybrid energy storage is extremely relevant.

References

1. Tuan, N.Kh., Karpukhin, K.E., Terenchenko, A.S., Kolbasov, A.F.: World trends in the development of vehicles with alternative energy sources. ARPN J. Eng. Appl. Sci. **13**(7), 2535–2542 (2018)
2. Kamenev, V.F., Terenchenko, A.S., Karpukhin, K.E., Kolbasov, A.F.: The strategy of creating urban electric vehicle: challenges and solutions. Int. J. Civ. Eng. Technol. **8**(12), 895–905 (2017)
3. Karpukhin, K.E., Shorin, A.A., Terenchenko, A.S., Kondrashov, V.N.: The steps of creating an experimental system for accumulation and storage of electrical energy. ARPN J. Eng. Appl. Sci. **12**(13), 4189–4195 (2017)

4. Omar, N., et al.: Standardization work for BEV and HEV applications: critical appraisal of recent traction battery. Energies **5**(1), 138–156 (2012)
5. Burke, A.: Batteries and ultracapacitors for electric, hybrid, and fuel cell vehicles. University of California, Davis
6. Karpukhin, K.E., Terenchenko, A.S., Shorin, A.A., Bakhmutov, S.V., Kurmaev, R.Kh.: Temperature control of the battery for hybrid or electric vehicle. Biosci. Biotechnol. Res. Asia **12**(2), 1297–1301 (2015)
7. Van Mulders, F., Timmermans, J.M., McCaffrey, Z., Van Mierlo, J., Van den Bossche, P.: Supercapacitor enhanced battery traction systems – concept evaluation. World Electr. Veh. J. (2008)
8. Saykin, A.M., Buznikov, S.E., Endachev, D.V., Karpukhin, K.E., Terenchenko, A.S.: Development of Russian driverless electric vehicle. Int. J. Mech. Eng. Technol. **8**(12), 955–965 (2017)
9. Prakht, V., Dmitrievskii, V., Kazakbaev, V., Anuchin, A.: Comparative study of electrically excited conventional and homopolar synchronous motors for the traction drive of a mining dump truck operating in a wide speed range in field-weakening region. Mathematics **10**(18), 3364 (2022)

Identifying Best Input Elements in PMEDM 90CrSi Steel by MAIRCA Method

Dinh Van Thanh[1], Tran Huu Danh[2], Bui Thanh Danh[3], Nguyen Van Chien Thang[4], Nguyen Van Tung[5], and Do Thi Tam[5](✉)

[1] East Asia University of Technology, Ho Chi Minh City, Vietnam
[2] Vinh Long University of Technology Education, Vĩnh Long, Vietnam
[3] University of Transport and Communications, Hanoi, Vietnam
[4] Nguyen Tat Thanh University, Ho Chi Minh City, Vietnam
[5] Thai Nguyen University of Technology, Thai Nguyen, Vietnam
dothitam@tnut.edu.vn

Abstract. To find the optimal powder-mixed electrical discharge machining (PMEDM) option, this research defines a multi-criterion decision-making (MCDM) process. The 90CrSi steel workpieces in this project have a cylindrical shape. Additionally, five input variables—powder concentration, pulse duration, pulse off time, pulse current, and servo voltage—were picked for the examination. Additionally, the experimental design used the Taguchi approach. Additionally, the MCDM problem was addressed using the MAIRCA (Multi-Attributive Ideal-Real Comparative Analysis) technique in order to achieve both a low electrode wear rate (EWR) and a high material removal speed (MRS). The MEREC (Method based on the Removal Effects of Criteria) technique was also used to determine creation weights. Lastly, the most suitable option for PMEDM cylindrically shaped pieces is provided.

Keywords: MCDM · MAIRCA method · PMEDM · Electrode wear rate · Material removal speed · 90CrSi

1 Introduction

PMEDM is a technique for increasing the efficiency of the EDM process. It aids in increasing MRS, decreasing RS, and decreasing EWR. Consequently, various studies on this process have been conducted.

PMEDM process optimization has been the subject of various studies to date. The impact of input elements of PMEDM process on the output results including the machining time [1], the material removal rate (MRR) [2–4], EWR [5], or the surface roughness [6] were investigated. It was reported that, the SR can be reduced more than 30% when used the SiC powder in PMEDM. Optimal input parameters for achieving various goals were also investigated. For example, for minimum SR and maximum MRS [3, 7], minimal EWR and maximal MMR [8]; Various materials such as 90CrSi [1, 2, 6], SKD11 [4, 5, 7, 8]. Were also studied during PMEDM. Different electrode materials such as copper [1, 2, 6, 7] and graphite [3] have been investigated.

D. C. Nguyen et al. (Eds.): ICERA 2023, LNNS 944, pp. 36–43, 2024.
https://doi.org/10.1007/978-3-031-62235-9_5

In addition to optimization processes, the MCDM method was employed to figure out the optimal alternative when PMEDM. Three MCDM methods—Multi-Attributive Ideal-Real Comparative Analysis (MAIRCA), Measurement of Alternatives and Ranking according to Compromise Solution (MARCOS), and Technique for Order of Preference by Similarity to Ideal Solution (TOPSIS), were used in [9] to determine the best strategy when machining 90CrSi steel to achieve minimal SR and maximal MRS simultaneously. The MCDM method was used in [10] to determine the ideal input parameters for PMEDM SKD11 steel. The findings of an MCDM investigation in PMEDM cylindrically shaped pieces are presented in this publication. Minimum RS and maximum MRS were chosen as the two criteria. The MCDM problem was also solved using the MAIRCA approach, and the MEREC method was utilized to determine the weights of the criterion. It was advised to choose the option that would produce the lowest EWR and highest MRS simultaneously.

2 Methodology

2.1 Method for MCDM

For the MCDM problem, the MAIRCA approach was utilized. The phases listed below must be completed in order to use this approach [12]:

Step 1: Creating the initial matrix by:

$$X = \begin{bmatrix} x_{11} & \cdots & x_{1n} \\ x_{21} & \cdots & x_{2n} \\ \vdots & \cdots & \vdots \\ x_{mn} & \cdots & x_{mn} \end{bmatrix} \tag{1}$$

Where x_{mn} represents the outcome of criterion n in variant m. Step 2: Identifying choices based on different selection P_{A_j} by:

$$P_{A_j} = \frac{1}{m}, j = 1, 2, \ldots, \text{ n} \tag{2}$$

Step 3: Computing the components $\mathrm{t_{pij}}$ by:

$$t_{pij} = P_{A_j} \cdot \mathrm{w_j},\ \mathrm{i} = 1, 2, \ldots, \mathrm{m}; \mathrm{j} = 1, 2, \ldots \tag{3}$$

Where, $\mathrm{w_j}$ is the weight of the $\mathrm{j^{th}}$ criterion.
Step 4: Computing $\mathrm{t_{rij}}$ by:

+) If the condition j is as large as possible:

$$t_{r_{ij}} = t_{p_{ij}} \cdot \left(\frac{x_{ij} - x_i^-}{x_i^+ - x_i^-}\right) \tag{4}$$

+) If the condition j is as small as possible:

$$t_{r_{ij}} = t_{p_{ij}} \cdot \left(\frac{x_{ij} - x_i^+}{x_i^- - x_i^+} \right) \tag{5}$$

Step 5: Finding the complete gap matrix g_{ij} by:

$$g_{ij} = t_{p_{ij}} - t_{r_{ij}} \tag{6}$$

Step 6: Using the available options, establish the criterion functions' ultimate values (Qi):

$$Q_i = \sum\nolimits_{i=1}^{m} g_{ij} \tag{7}$$

2.2 Method for Computing the Weight of Criteria

The weights of the criteria can be found for this study using the MEREC method. The following steps are taken when using this method [13]:

Step 1: As in the first phase of the MAIRCA method, build the initial matrix.
Step 2: Locating the normalized matrix elements by:

– If the condition j is as large as possible:

$$h_{ij} = \frac{minx_{ij}}{x_{ij}} \tag{8}$$

– If the condition j is as small as possible:

$$h_{ij} = \frac{x_{ij}}{maxx_{ij}} \tag{9}$$

Step 3: The effectiveness of the options S_i is established by:

$$S_i = ln\left[1 + \left(\frac{1}{n}\sum\nolimits_j \left|ln\left(h_{ij}\right)\right|\right)\right] \tag{10}$$

Step 4: Identifying the efficiency of the ith option S'_{ij} in terms of removing the jth criterion by:

$$S'_{ij} = Ln\left[1 + \left(\frac{1}{n}\sum\nolimits_{k,k\neq j} \left|ln\left(h_{ij}\right)\right|\right)\right] \tag{11}$$

Step 5: Using the following formula to figure out the elimination effect of the jth criterion E_j:

$$E_j = \sum\nolimits_i \left|S'_{ij} - S_i\right| \tag{12}$$

Step 6: Obtaining the criteria's weight by:

$$w_j = \frac{E_j}{\sum_k E_k} \tag{13}$$

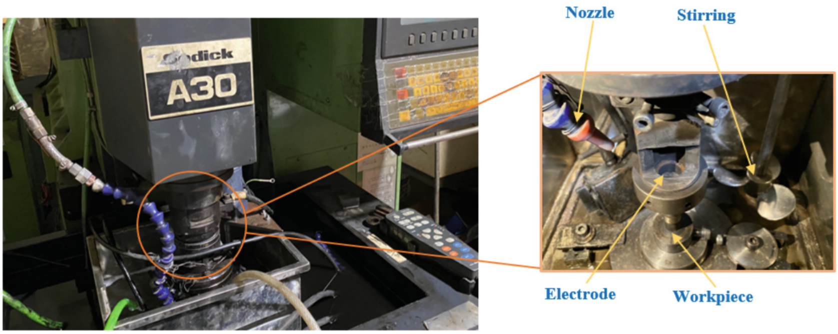

Fig. 1. Setup of experiment

3 Experimental Setup

An experiment was performed to address the MCDM issue. The investigation's input parameters are shown in Table 1. For the experiment, the technique known as Taguchi with L18 ($2^1 + 3^4$) design was also determined. Figure 1 presents the experimental configuration. Graphite electrodes from TOKAI Carbon Co., LTD in Japan, 90CrSi tool steel workpieces from China, 100 nm SiC powder from China, and Total Diel MS 7000 dielectric solution from France were all used in the experiment. EWR and MRS are calculated using the electrode mass, sample mass before and after cutting, and machining time recorded using the CNC milling machine's memory. Table 2 provides the experimental matrix as well as the outcomes (EWR and MRS) of the experiment.

Table 1. Input factors and their levels

No.	Input parameters	Unit	Level		
			1	2	3
1	Powder concentration C_p	g/l	0	0.5	1
2	Pulse on time T_{on}	μs	8	12	16
3	Pulse off time T_{off}	μs	8	12	16
4	Peak current I_p	A	5	10	15
5	Servo voltage SV	V	4	5	–

Table 2. Experimental matrix and output results

No.	Input factors					Output factors	
	C_p	S_p	T_{on}	T_{off}	SV	EWR (g/h)	MRS (g/h)
1	0.0	8	8	5	4	22.3049	0.7306
2	0.0	12	12	10	4	25.5724	1.3441

(continued)

Table 2. (*continued*)

No.	Input factors					Output factors	
	C_p	S_p	T_{on}	T_{off}	SV	EWR (g/h)	MRS (g/h)
3	0.0	16	16	15	4	33.0783	3.8894
4	0.5	8	8	10	4	74.0077	0.7992
5	0.5	12	12	15	4	78.9780	7.0694
6	0.5	16	16	5	4	16.9566	0.8136
7	1.0	8	12	5	4	114.3392	1.3978
8	1.0	12	16	10	4	30.2637	3.8204
9	1.0	16	8	15	4	34.3570	4.4114
10	0.0	8	16	15	5	143.7481	6.9694
11	0.0	12	8	5	5	33.6556	1.9435
12	0.0	16	12	10	5	13.4498	1.4282
13	0.5	8	12	15	5	148.4736	7.1003
14	0.5	12	16	5	5	28.2640	2.3283
15	0.5	16	8	10	5	16.5338	1.2479
16	1.0	8	16	10	5	83.4345	2.0881
17	1.0	12	8	15	5	88.0550	7.1046
18	1.0	16	12	5	5	17.6557	2.5645

4 Determining the Best Option

4.1 Calculating the Criteria's Weights

The MEREC method is used for estimating the weights for the criteria, which is performed in the steps outlined in Sect. 2.2. As a result, Formulas (8) and (9) are used to arrive at the normalized values h_j. Equation (10) can also be used to calculate the alternative performance S_i. (11) is then used to compute S'_{ij}. The criterion removal effect is then calculated using Eq. (12). Finally, the weight of the criterion wj is determined by Eq. (13). The reported Ra and MRR weights were 0.4619 and 0.5381, respectively.

4.2 Determination of the Best Option

Taking the actions suggested in Sect. 2.1, specifically: The priority or criterion P_{A_j} is obtained by using the Eq. (2) after the initial matrix is set up. Since both Ra and MRS are given identical importance, their priority is 1/18 = 0.0556. Furthermore, Eq. (3) is used to find the value of parameter $t_{p_{ij}}$, with the weight of the criterion identified in Sect. 2.2. Ra and MRS obtained $t_{p_{ij}}$ values of 0.0257 and 0.0299, respectively. Equations (4) and (5) are then used to obtain the values of $t_{r_{ij}}$, and Eq. (6) is used to calculate the values of g_{ij}. Finally, using Eq. (7), we can find the values of the criterion functions Q_i. The obtained characteristics and ratings for the different rating options when utilizing the MAIRCA approach are shown in Table 5. Besides, the values of Qi of each solution are presented through Fig. 2.

Table 3. Several calculated results and ranking of options

Trial.	t_{rij}		g_{ij}		Qi	Rank
	Ra	MRR	Ra	MRR		
1	0.0240	0.0000	0.0017	0.0299	0.0316	15
2	0.0234	0.0029	0.0023	0.0270	0.0293	13
3	0.0219	0.0148	0.0037	0.0151	0.0188	5
4	0.0142	0.0003	0.0115	0.0296	0.0411	17
5	0.0132	0.0297	0.0125	0.0001	0.0126	1
6	0.0250	0.0004	0.0007	0.0295	0.0302	14
7	0.0065	0.0031	0.0192	0.0268	0.0459	18
8	0.0225	0.0145	0.0032	0.0154	0.0186	4
9	0.0217	0.0173	0.0040	0.0126	0.0166	3
10	0.0009	0.0293	0.0248	0.0006	0.0254	8
11	0.0218	0.0057	0.0038	0.0242	0.0280	11
12	0.0257	0.0033	0.0000	0.0266	0.0266	10
13	0.0000	0.0299	0.0257	0.0000	0.0257	9
14	0.0228	0.0075	0.0028	0.0224	0.0252	7
15	0.0251	0.0024	0.0006	0.0275	0.0281	12
16	0.0124	0.0064	0.0133	0.0235	0.0368	16
17	0.0115	0.0299	0.0142	0.0000	0.0142	2
18	0.0249	0.0086	0.0008	0.0213	0.0221	6

Option 5 is the best choice, according to Table 3 and Fig. 2. This is because it has the smallest value of Q (Q5 = 0.0126). As a result, the ideal solution incorporates the following parameters: $C_p = 0.5$ (g/l), $T_{on} = 8$, $T_{off} = 12$, IP = 15 (A), and SV = 5 (V).

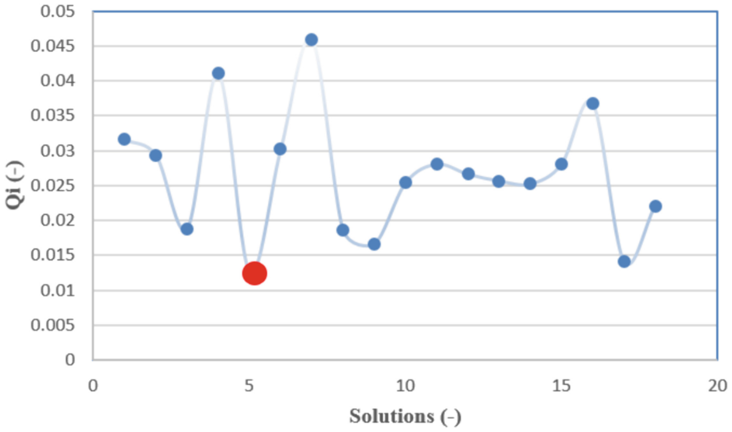

Fig. 2. Q_i values of different solutions

5 Conclusions

This work discusses the findings of an MCDM study conducted on PMEDM cylindrical pieces produced of 90CrSi tool steel. In this study, the MCDM problem was resolved using the MAIRCA approach, and the weights of the criteria were determined using the MEREC method. The Diel MS 7000 dielectric was additionally combined with a 100 nm SiC powder. In addition, five process variables including C_p, T_{on}, T_{off}, SV and IP were picked for the experiment. The experiment has an L18 (21 + 34) design and was constructed using the Taguchi method. It has been discovered that the following input factor configuration works best when processing cylindrically shaped parts to concurrently produce the lowest EWR and maximum MRS: Cp = 0.5 (g/l); Ton = 8 (s); Toff = 12 (s); IP = 15 (A); and SV = 4 (V).

Acknowledgment. This work was supported by Thai Nguyen University of Technology.

References

1. Hong, T.T., et al.: Effect of process parameters on machining time in PMEDM cylindrical shaped parts with silicon carbide powder suspended dielectric. Mater. Sci. Forum (2021)
2. Cuong, N.M., et al.: Influence of input factors on material removal rate in PMEDM cylindrical shaped parts with silicon carbide powder suspended dielectric. Key Eng. Mater. **861**, 129–135 (2020)
3. Quang, N.H., et al.: Multi-objective optimization of PMEDM of cylindrical parts with graphite electrodes. In: Li, X., Rashidi, M.M., Lather, R.S., Raman, R. (eds.) Emerging Trends in Mechanical and Industrial Engineering. LNME, pp. 677–688. Springer, Singapore (2023). https://doi.org/10.1007/978-981-19-6945-4_50
4. Anh, L.H., et al.: Impact of input parameters on material removal speed when PMEDM SKD11 tool steel. In: Nguyen, D.C., Vu, N.P., Long, B.T., Puta, H., Sattler, K.U. (eds.) ICERA 2021. LNNS, vol. 366, pp. 459–467. Springer, Cham (2022). https://doi.org/10.1007/978-3-030-92574-1_48

5. Nguyen, A.T., et al.: Optimization of PMEDM parameters for minimizing electrode wear rate when processing SKD11 steel. In: Nguyen, D.C., Vu, N.P., Long, B.T., Puta, H., Sattler, K.U. (eds.) ICERA 2021. LNNS, vol. 366, pp. 731–738. Springer, Cham (2022). https://doi.org/10.1007/978-3-030-92574-1_75
6. Tran, T.-H., et al.: Electrical discharge machining with SiC powder-mixed dielectric: an effective application in the machining process of hardened 90CrSi steel. Machines **8**(3), 36 (2020)
7. Nguyen, H.Q., et al.: Multi-objective optimization of PMEDM process for minimum surface roughness and maximum material removal speed when processing SKD11 steel. In: Nguyen, D.C., Vu, N.P., Long, B.T., Puta, H., Sattler, K.U. (eds.) ICERA 2021. LNNS, vol. 366, pp. 634–644. Springer, Cham (2022). https://doi.org/10.1007/978-3-030-92574-1_66
8. Nguyen, A.T., et al.: Multi-objective optimization of PMEDM process for maximum material removal speed and minimum electrode wear rate when machining SKD11 steel. In: Nguyen, D.C., Vu, N.P., Long, B.T., Puta, H., Sattler, K.U. (eds.) ICERA 2021. LNNS, vol. 366, pp. 623–633. Springer, Cham (2022). https://doi.org/10.1007/978-3-030-92574-1_65
9. Nguyen, H.-Q., et al.: Multi-criteria decision making in the PMEDM process by using MARCOS, TOPSIS, and MAIRCA methods. Appl. Sci. **12**(8), 3720 (2022)
10. Danh, T.H., et al., A study on multi-criteria decision-making in powder mixed electric discharge machining cylindrical shaped parts. EUREKA Phys. Eng. (5), 123–129 (2022)

Improvement of Motion Stability for AGV Using Pure-Pursuit Path Tracking Algorithm

Khong Minh and Vu Thi Lien(✉)

Faculty of Mechanical Engineering and Mechatronics, Phenikaa University, Hanoi, Vietnam
lien.vuthi@phenikaa-uni.edu.vn

Abstract. This study has improved Pure-Pursuit path tracking algorithm for automated guided vehicle (AGV) to obtain the motion stability. Pure-Pursuit algorithm is the most commonly used in path tracking. This algorithm computes the linear velocity and angular velocity of the robot to move it from its current position to reach a designated look-ahead point. Pure-Pursuit and its modified algorithms have been developed to improve tracking accuracy and maintain the stability of the AGV. With the same objectives, this paper has developed a path tracking algorithm in which the position error of the AGV is related directly to the velocity functions during tracking process. The results show that the proposed method not only improves the tracking accuracy but also increases stability of the AGV. This method can be applied in path tracking for AGV in reality.

Keywords: Automated guided vehicle (AGV) · Pure Pursuit · Path tracking algorithm · Path Panning · Motion stability

1 Introduction

For recent decades, autonomous cars and autonomous robots are applications that have received a lot of attention from researchers because they can replace human labor or perform tasks that are not suitable for humans, such as in harsh environments or tight spaces [1–3]. Along with the continuous development of controllers, sensor systems and other hardware systems have facilitated the development of AGV.

In order to control AGV or robots, it is necessary to have a path tracking algorithms to help them plan the trajectory, locate the AVG's position on the map, make digital maps, and move follow trajectory etc. [4–6].

The operating environment of the robot is very variable such as ground, water, space. The robot's operating space needs to be digitized under digital maps by different types of sensors such as laser sensors, digital cameras, ultrasonic sensors. These digital maps are provided to the robot during operation and it will move in real space based on the information of these digital maps [4–6]. The robot must move through one or more routes that defined geometric shapes with kinematics requirements such as position, velocity, acceleration. This type of movement is called trajectory movement. It is necessary to have an algorithm help the robot implements the give path plan, called the path tracking algorithm [4]. During the path tracking control, the robot always has to update its real

D. C. Nguyen et al. (Eds.): ICERA 2023, LNNS 944, pp. 44–51, 2024.
https://doi.org/10.1007/978-3-031-62235-9_6

position on the map by the positioning algorithms and the sensor system mounted on the robot.

Thus, the path tracking algorithm is one of the important algorithms to control AGV to move follow a predetermined trajectory [6–9]. Normally, the input of the path tracking control algorithm is the output of the path planning algorithm and the result of the AGV or robots positioning system. The output of this algorithm is the input of the motion control system for the motors that drive the AGV or robots. Since the data of the AGV or robot navigation system is continuous and high frequency, the path tracking algorithm also requires fast computation so that the system can respond in real time. Although the computational speed of the controller hardware has been greatly improved, it is always necessary to optimize the algorithm so that the computation quantity is reasonable for AGV or robots.

As one of the early path tracking algorithms, Pure-Pursuit method provides a simple mathematical expression to describe the geometric relationship between the goal point on the desired path and the front wheel angle of the vehicle [4–9]. For the Pure Pursuit algorithm, the look-ahead distance determines the selection of the goal point and thus directly affects the tracking effect, so many scholars have conducted more in-depth research on the determination of the look-ahead distance [6–9]. In order to improve the tracking accuracy and the stability of AGV, this paper presents a method in which the position error is used as a parameter of the input velocity functions during path tracking control process.

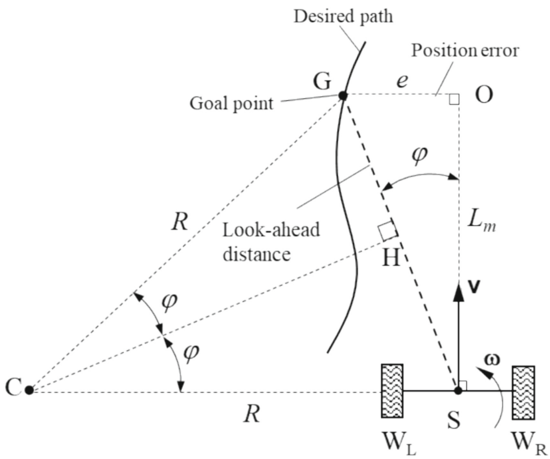

Fig. 1. Description of the Pure Pursuit algorithm

2 The Proposed Path Tracking Algorithm

2.1 Pure Pursuit Algorithm Analysis

The description of Pure Pursuit path tracking algorithm is presented in Fig. 1 in which the reference point S is the midpoint of the axe (rear axle) of the two drive wheels W_L and W_R of the robot. The goal point of the robot is G on the desired path. The tracking algorithm is applied to move the reference point S from this current position to reach the goal point G. Since the robot is a rigid body having general plane motion, the movement of the robot from S to G can be divided into two motions i.e. translational motion (linear velocity **v**) and rotation (angular velocity $\boldsymbol{\omega}$) around the instantaneous center of rotation C as shown in Fig. 1. The instantaneous center of rotation C is determined by the intersection of the rear axle and the perpendicular bisector of the line SG.

From Fig. 1, e is the tracking distance error from the linear velocity vector **v** to the goal point G, and O is the intersection point of **v** and the line passing through G and perpendicular to **v**.

Since GSO is a right triangle, so:

$$\sin\varphi = \frac{e}{SG} \tag{1}$$

Similarly, from right triangle CGH (H is the midpoint of SG), so:

$$\sin\varphi = \frac{GH}{R} = \frac{SG}{2R} \tag{2}$$

From Eq. (1) and Eq. (2):

$$\sin\varphi = \frac{e}{SG} = \frac{SG}{2R} \tag{3}$$

$$2eR = SG^2 \tag{4}$$

In right triangle GOS, the look-ahead distance SG is:

$$SG^2 = GO^2 + SO^2 = e^2 + {L_m}^2 \tag{5}$$

where $L_m = SO$

From Eq. (3) and Eq. (4):

$$2eR = e^2 + {L_m}^2 \tag{6}$$

$$R = \frac{e^2 + {L_m}^2}{2e} \tag{7}$$

Then, the angular velocity of the robot is:

$$\omega = \frac{v}{R} \tag{8}$$

where the linear velocity is a given function of time or $v = v(t)$:

$$\omega = \frac{v(t)}{R} = \frac{2e.v(t)}{e^2 + {L_m}^2} \tag{9}$$

Thus, the input control velocities of Pure-Pursuit algorithm is:

$$\begin{cases} v = v(t) \\ \omega = \frac{2e.v(t)}{e^2+L_m^2} \end{cases} \tag{10}$$

Pure-Pursuit method provides a simple path tracking algorithm in which the angular velocity is calculated based on the given linear velocity **v** and tracking distance *e*. Then, the orientation angle of robot is determined to reach the robot to the target point. However, the linear velocity function is not depended the position error during the tracking process. Since the linear velocity should be adjusted according to the position error to provide stable motion of robot. Thus, this paper presents a proposed method in which the position error is concerned in the input velocity functions to obtain stable motion for robot.

2.2 The Proposed Algorithm

According to Eq. (10), the magnitude of the linear velocity (v) does not depend on the distance error (e) between the robot and the desired path. Therefore, it is necessary to develop a relationship between v and e so that the robot can follow close to the desired path. In order to maintain the motion stability of the robot, four constraints of the linear velocity of the robot are listed in Table 1.

Table 1. Constraints of the linear velocity (v) of the robot

Constraint # 1	$e \rightarrow emax$ where e_{max} is a limited value of sensor)	$v \rightarrow 0$
Constraint # 2	$e \rightarrow 0$	$v \rightarrow \mathrm{v}(t)$
Constraint # 3	v is a bounded harmonic function	
Constraint # 4	$\frac{\lvert e\rvert}{\lvert e_{max}\rvert} < 1$	

Based on these constraints, the linear velocity function can be presented as a bounded harmonic function:

$$v = v(t)\cos(\frac{|e|}{|e_{max}|}\frac{\pi}{2}) \tag{11}$$

Substituting Eq. (11) into Eq. (10) in Pure-Pursuit method, the input velocity functions of the path tracking algorithm are rewritten as follows:

$$\begin{cases} v = v(t)\cos(\frac{|e|}{|e_{max}|}\frac{\pi}{2}) \\ \omega = \frac{2e.v(t)\sin(\frac{|e|}{|e_{max}|}\frac{\pi}{2})}{e^2+L_m^2} \end{cases} \tag{12}$$

The constraints in Table 1 show that, when $e \to e_{max}$, then $v \to 0$. At this position, $\omega \to 0$ and the robot cannot return to the desired path. Therefore, the angular velocity (ω) should be rewritten as:

$$\omega = \frac{2e.v(t)\sin(\frac{|e|}{|e_{max}|}\frac{\pi}{2})}{e^2 + {L_m}^2} \tag{13}$$

When $e \to e_{max}$, then:

$$\omega_{e \to e_{max}} \approx \frac{2e_{max}v(t)}{{e_{max}}^2 + {L_m}^2} \approx \frac{2v(t)}{e_{max} + \frac{{L_m}^2}{e_{max}}} \tag{14}$$

In order to ensure that at the position $e \to e_{max}$ and the angular velocity ω of the robot approaches the maximum angular velocity ω_{max}, it is necessary to multiply a coefficient k_ω into Eq. (14), then:

$$\omega_{max} = k_\omega \frac{2v(t)}{e_{max} + \frac{{L_m}^2}{e_{max}}} \; or \; k_\omega = \frac{\omega_{max}(e_{max} + \frac{{L_m}^2}{e_{max}})}{2v(t)} \tag{15}$$

ω_{max} is the maximum angular velocity for the robot to rotate without affecting the sensor and actuator operations.

Hence Eq. (13) becomes:

$$\omega = k_\omega \frac{2e.v(t)\sin(\frac{|e|}{|e_{max}|}\frac{\pi}{2})}{e^2 + {L_m}^2} \tag{16}$$

Thus, the proposed input control law is:

$$\begin{cases} v = v(t)\cos(\frac{|e|}{|e_{max}|}\frac{\pi}{2}) \\ \omega = \ k_\omega \frac{2e.v(t)\sin(\frac{|e|}{|e_{max}|}\frac{\pi}{2})}{e^2 + L_m^2} \end{cases} \tag{17}$$

3 Results and Discussion

The AGV model used in the experiment is an AGV250 model of PhenikaaX company. AGV uses two drive wheels to control. The motion of the two wheels simultaneously is controlled through the linear and angular velocity. These wheels with the size of 150 mm are driven by two 24 V and 200 W BLDC motors through a planet gear reducer with gear ratio of 30. AGV has four self-aligning wheels, including two self-aligning wheels at the front and rear of the vehicle. Two drive engines are controlled via the controller driver, which obtains control information from the PC mounted on the AGV via RS485 communication. The control signal from the PC sent to the motor control driver is the speed of the two wheels in front of the reducer at 40 Hz. The MLSE sensor is a magnetic field sensor fixed to the top of the AGV, used to measure the relative position of the AGV relative to the magnetic field path mounted on the floor. The output data of the sensor is sent to the central control PC via CAN Open communication at 100 Hz.

AGV250 with self-mass of 120 kg (including battery) and load mass of 250 kg, is tested on the same hardware to run both Pure-Pursuit and the proposed algorithms as shown in Fig. 2. The desired path of AGV is a straight line pasted on the floor by a magnetic line with a width of 3 cm. MLSE sensor has a resolution of 1 mm and frequency signal returns from the center of the sensor to the centerline of the magnetic line is 100 Hz. This is a standard sensor, commonly used in common AGVs in the world.

Fig. 2. Prototype AGV250.

The measurement results returned by the MLSE sensor with two algorithms on the same path are presented in Fig. 3, 4 and 5. In Fig. 3, the average distance error around the center of the magnetic line path is the same, but the number of oscillations is 3 when using the proposed method while this number is 12 for Pure-Pursuit.

In Fig. 4, the response linear velocity is equivalent in the two algorithms. However, the proposed algorithm provides smooth transition position. Thus, the acceleration and deceleration of the velocity are smoother and less sudden.

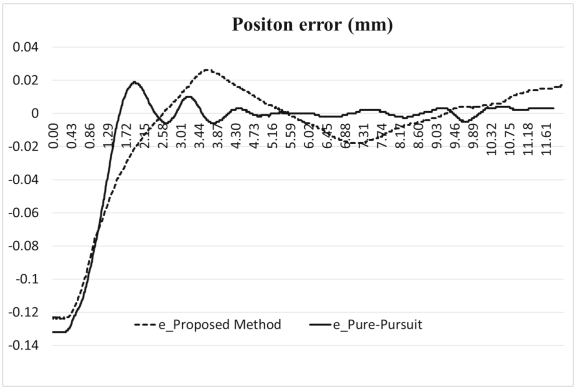

Fig. 3. Position error curves of the AGV using both Pure-Pursuit and the proposed methods

The improvement of the proposed is also shown for the angular velocity in Fig. 5. The angular velocity according to the proposed algorithm changes direction less. Thus, the robot is less sway around the center of the magnetic line path and runs more.

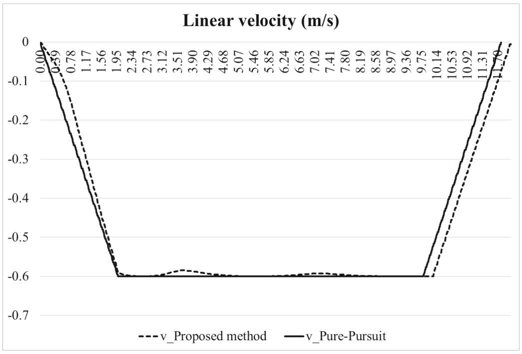

Fig. 4. Linear velocity curves of the AGV using both Pure-Pursuit and the proposed methods

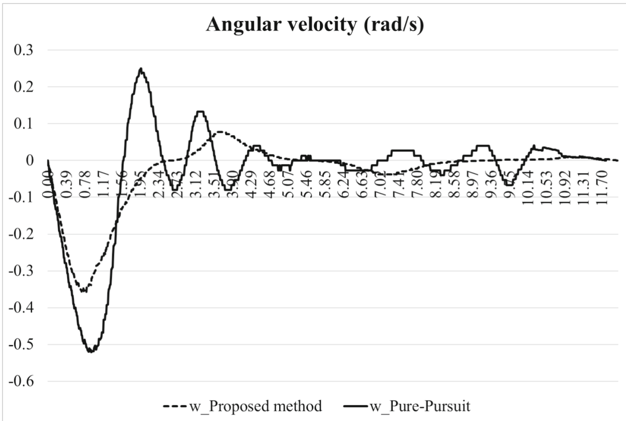

Fig. 5. Angular velocity curves of the AGV using both Pure-Pursuit and the proposed methods

4 Conclusion

This paper has updated the path tracking Pure-Pursuit to obtain the motion stability of AGV. The position error of robot is added to the input velocity functions. These functions have been developed based on four constraints for stable motion. The experimental results show that the linear velocity and angular velocity curves are quite smooth and less oscillation. These mean the robot maintains a stable posture during operation process. Thus, this proposed algorithm can be applied for path tracking in reality.

References

1. Coulter, C.: Implementation of the pure pursuit path tracking algorithm. Comput. Sci. (1992)
2. Hellström, T., Ringdahl, O.: Follow the past: a path-tracking algorithm for autonomous vehicles. Int. J. Veh. Auton. Syst. **4**(2/3/4) (2006)
3. Heredia, G., Ollero, A.: Stability of autonomous vehicle path tracking with pure delays in the control loop. Adv. Robot. **21**, 23–50 (2007)
4. Patle, B.K., Ganesh Babu, L., Pandey, A., Parhi, D.R.K., Jagadeesh, A.: A review: on path planning strategies for navigation of mobile robot. Def. Technol. **15**(4), 582–606 (2019)
5. Samuel, M., Hussein, M., Mohamad, M.: A review of some pure-pursuit based path tracking techniques for control of autonomous vehicle. Int. J. Comput. Appl. **135**, 35–38 (2016)
6. Rubio, F., Valero, F., Llopis-Albert, C.: A review of mobile robots: concepts, methods, theoretical framework, and applications. Int. J. Adv. Robot. Syst. **16**(2) (2019)
7. Ahn, J., Shin, S., Kim, M., Park, J.: Accurate path tracking by adjusting look-ahead point in pure pursuit method. Int. J. Automot. Technol. **22**, 119–129 (2021)
8. Rokonuzzaman, M., Mohajer, N., Nahavandi, S., Mohamed, S.M.K.: Review and performance evaluation of path tracking controllers of autonomous vehicles. IET Intell. Transp. Syst. (2021)
9. Yang, Y., et al.: An optimal goal point determination algorithm for automatic navigation of agricultural machinery: improving the tracking accuracy of the Pure Pursuit algorithm. Comput. Electron. Agric. **194**, 10676 (2022)

Influence of Dressing Parameters on Wheel Life in Surface Grinding Hardox 500

Dinh Van Thanh[1], Tran Huu Danh[2], Vi Le The Anh[3], Nguyen Van Trang[4], Le Xuan Hung[4], Vu Ngoc Pi[4], and Luu Anh Tung[4](✉)

[1] East Asia University of Technology, Ho Chi Minh City, Vietnam
[2] Vinh Long University of Technology Education, Vĩnh Long, Vietnam
[3] Nguyen Tat Thanh University, Ho Chi Minh City, Vietnam
[4] Thai Nguyen University of Technology, Thai Nguyen, Vietnam
luuanhtung@tnut.edu.vn

Abstract. This report presents the results of a study on the effect of dressing factors on wheel life in surface grinding Hardox 500. The study looked at five dressing factors to do this: rough dressing depth T_r, rough dressing times N_r, fine dressing depth T_f, fine dressing times N_f, and non-feeding dressing N_{non}. The effect of these elements on the grinding process's wheel life was evaluated. In addition, an optimal dressing mode was recommended to maximize wheel life. It was also mentioned that the proposed model may be used.

Keywords: Grinding · Surface grinding · Optimal dressing mode · Wheel life · Hardox 500

1 Introduction

Grinding is a popular machining procedure for material removal roughing as well as high-quality finishing. The dressing plays a significant part in wheel preparation throughout this process. It is used to sharpen abrasive particles as well as remove loads and built-up workpiece material from the grinding wheel's surface [1]. The grinding wheel is constantly worn while functioning, affecting the process's quality and productivity. As a result, the dressing process is required to ensure the grinding wheel's original specification. As a result, the dressing has a substantial impact on the performance of the grinding wheel [2].

There have been numerous attempts to optimize the dressing process and identify the impact of dressing parameters on machining quality or grinding wheel [2–6].

X.T. Hoang et al. investigated the effect of dressing factors on roughness in the grinding of 9XC tool steel [3]. For improving surface roughness, the authors suggested an optimization of dressing parameters such as rough dressing, final dressing, and dressing without the depth of cut. The authors of [5] studied the impact of dressing operation factors such as dressing depth of cut, dressing cross feed rate, dresser drag angle, and number of passes on surface roughness.

D. C. Nguyen et al. (Eds.): ICERA 2023, LNNS 944, pp. 52–60, 2024.
https://doi.org/10.1007/978-3-031-62235-9_7

A.T. Luu et al. used the Taguchi technique and Grey Relational Analysis to optimize the dressing parameters of a grinding wheel made of 9CrSi tool steel in order to decrease roughness average and flatness tolerance [4]. Rabiey M et al. [7] investigated the effect of dressing parameters of hybrid bond CBN grinding wheels on roughness, grinding forces, and wheel wear. I. Aleksandrova created a simulation model for the grinding process's wheel life, cutting ability, production rate, and cutting forces [8]. Fritz Klocke et al. [2] proposed a mathematical model for the first wear of vitrified bonded grinding wheels.

The life of a grinding wheel is an important indicator that represents both the physical characteristics of grinding and the economic and technological concerns. It exemplifies one of the fundamental properties of a grinding wheel [9]. T. Yu's research [10] developed a predicted model for total wheel life that is congruent with experimental findings. Hwang [11, 12] proposed that ongoing grit dulling and incremental increases in grinding pressures and specific energy had a significant impact on grinding wheel life. [13] established a relationship between wheel file variation and grinding ratio and static grinding force. [14] discovered that decreasing the dressing depth increases wheel life.

As previously discussed, despite numerous studies on optimizing the dressing process, there is still no publication on the ideal dressing mode for surface grinding Hardox 500. The findings of a study on the effect of dressing parameters on wheel life in surface grinding Hardox 500 are presented in this paper. When processing Hardox 500, optimal dressing mode was also recommended to enhance wheel life.

2 Experimental Work

Fig. 1. Experimental setup

An experiment was carried out in order to solve the investigation of the effect of dressing parameters on the wheel life when processing Hardox 500. This experiment was designed using the Minitab R19 software with L16 (44 × 21) design and 16 experimental runs were conducted. The input factors and their levels are shown in Table 1. Figure 1 depicts the experimental setup. The setup consists of: Surface machine: PSG-CL3060AH (Taiwan); grinding wheel: Cn60MV1G V1 350 × 40 × 127 35 (m/s); dressing tool: 3908-0088C type 2 (Russian); piezoelectric dynamometer: Kistler 9257BA (Germany). The experiment was carried out as follows: Each experiment was repeated three times. The time between starting of grinding after dressing and the usual Py spike determines the wheel life. Table 2 shows the experimental plan and results (the wheel life).

The Taguchi technique was chosen because of its ease of use and robustness in optimizing process parameters, resulting in significant cost and processing time savings [15]. The orthogonal array is used in the Taguchi method's experimental design to achieve the best results with the fewest number of experiments. An S/N ratio is chosen for assessing performance characteristics and calculating the percent contribution of each process parameter using analysis of variance. There are three sorts of S/N ratios in the Taguchi method: "the bigger the better," "the smaller the better," and "the nominal is the better". As a result, the proper type is used in each circumstance. To maximize wheel life, the "bigger is better" kind was chosen, as stated in the following equation:

$$\frac{S}{N} = -10\log\frac{1}{n}\sum\nolimits_{i=1}^{n}\frac{1}{y_i^2} \tag{1}$$

Where y_i is the observed data and n is the number of repeated experiments.

Table 1. Input parameters and their levels

No.	Parameters	Symbol	Level			
			1	2	3	4
1	Rough dressing depth (mm)	T_r	0.015	0.02	0.025	0.03
2	Rough dressing times	Nr	1	2	3	4
3	Fine dressing depth (mm)	T_f	0.005	0.01	–	–
4	Fine dressing times	N_f	0	1	2	3
5	Non-feeding dressing	Nnon	0	1	2	3

3 Results and Analysis

The Minitab software is used to calculate the S/N ratios. Table 2 displays the experimental outcomes as well as the S/N ratios. Table 3 shows the average wheel life ANOVA ((WL)). It was noted from the table that rough dressing times have the highest influence on WL (31.11%), followed by rough dressing depth (23.08%), non-feeding dressing (19.44%), fine dressing times (18.55%), and fine dressing depth (1.99%). Table 4 also shows the order of importance of dressing elements on wheel life.

Table 2. Experimental plan and output results

No.	T_r	N_r	N_f	N_{non}	T_f	Wheel life (WL) (min)			Means	S/N
						Trial 1	Trial 2	Trial 3		
1	0.015	1	0	0	0.005	23.10	22.3	23.8	23.07	27.25
2	0.015	2	1	1	0.005	33.60	34.6	31.4	33.20	30.40
3	0.015	3	2	2	0.010	5.05	5.3	4.8	5.05	14.04
4	0.015	4	3	3	0.010	1.90	1.7	2.1	1.90	5.48
5	0.020	1	1	2	0.010	19.40	19.8	20.5	19.90	25.97
6	0.020	2	0	3	0.010	41.60	39.8	42.2	41.20	32.29
7	0.020	3	3	0	0.005	44.30	44.8	42.9	44.00	32.86
8	0.020	4	2	1	0.005	23.70	22.9	24.6	23.73	27.50
9	0.025	1	2	3	0.005	5.20	4.8	5.7	5.23	14.31
10	0.025	2	3	2	0.005	36.80	35.2	38.0	36.67	31.27
11	0.025	3	0	1	0.010	28.80	27.4	27.9	28.03	28.95
12	0.025	4	1	0	0.010	35.70	35.9	40.2	37.27	31.39
13	0.030	1	3	1	0.010	26.50	25.7	27.2	26.47	28.45
14	0.030	2	2	0	0.010	35.50	34.8	35.2	35.17	30.92
15	0.030	3	1	3	0.005	41.70	42.2	41.4	41.77	32.42
16	0.030	4	0	2	0.005	16.90	17.6	16.4	16.97	24.58

Table 3. Analysis of variance for means

Analysis of Variance for Means

Source	DF	SeqSS	Adj SS	Adj MS	F	P	C%
T_r	3	638.70	638.70	212.90	2.64	0.287	23.08
N_r	3	860.94	860.94	286.98	3.56	0.227	31.11
N_f	3	513.37	513.37	171.12	2.12	0.336	18.55
N_{non}	3	537.86	537.86	179.29	2.22	0.325	19.44
T_f	1	54.95	54.95	54.95	0.68	0.496	1.99
Residual Error	2	161.44	161.44	80.72			5.83
Total	15	2767.27					100.00

Model Summary

S	R-Sq	R-Sq(adj)
8.9845	94.17%	56.25%

Figure 2 depicts the main effects plot for means. From the figure, it was found that as the rough dressing depth Tr increases, the wheel life WL reduces until it reaches its maximum value of 2 (0.02 mm). As an example, consider the following: Initially, Tr raises the grinding wheel's initial undulating height. This increases blade sharpness, making the stone easier to cut into the material and extending WL. If Tr continues to rise due to the abrasive's random fracture, WL may also rise or fall at random.

As Tf increases, WL drops until it reaches a minimum of 1 (0.005 mm). The reason behind this is that as Tf grows, so does the initial undulating height of the abrasives. The abrasive, on the other hand, has a high hardness and wear resistance, so the cutting edges will be shattered to return the little stone to its original undulating form. This makes it more difficult for the chip to escape, resulting in a drop in WL.

Increase the amount of time spent on fine dressing. Nf, WL reduces before increasing. This is explained by the fact that the initial undulation height of the grinding wheel is reduced after fine dressing compared to rough dressing. The grinding wheel surface is now smoother, the chip spacing is smaller, and the WL is lower. However, as Nf increases, so does the number of dynamic cutting edges, enhancing the cutting ability and durability of the grinding wheel. WL fell dramatically and subsequently increased somewhat as the number of times of non-feeding dressing was increased. This is explained by the fact that after numerous non-feeding dressings, the stone surface is smoother and the space for holding chips is narrower, limiting durability.

To figure out the best dressing mode to produce the highest WL, assess the variation of the WL's S/N ratio to discover a fair amount of the researched rock correction parameters. Figure 3 depicts the ANOVA findings for the WL S/N value. This figure clearly shows that rough dressing twice (Nr2) with a roughing depth of 0.02 mm (Tr2), fine dressing level 2 (Nf2) with a refining depth of 0.005 (Tf1), and the same feed rate of 1.2 (m/ph) are the dressing levels and values for the maximum S/N ratio. This is the appropriate dressing mode level and value for maximizing grinding wheel life.

Table 4. Response table for means

Response Table for Means

Level	Tr	Nr	Nf	Nnon	Tf
1	15.80	18.67	27.32	34.88	28.08
2	32.21	36.56	33.03	27.86	24.37
3	26.80	29.71	17.30	19.65	
4	30.09	19.97	27.26	22.53	
Delta	16.40	17.89	15.74	15.23	3.71
Rank	2	1	3	4	5

As noticed above (from Table 3), fine dressing depth has no effect on grinding wheel durability (just 1.99%). As a result, this parameter is included from the error analysis, and the results are displayed in Table 5.

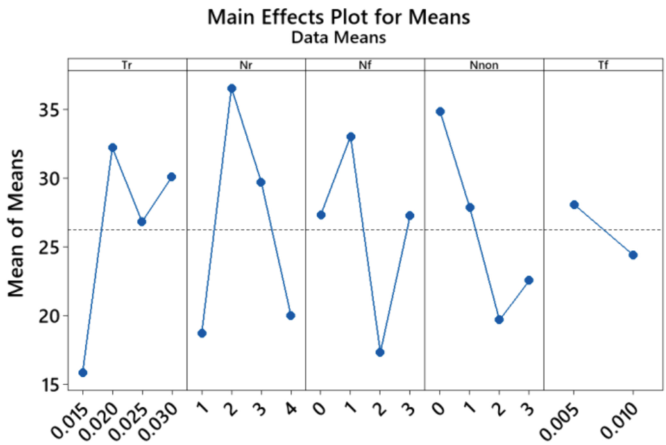

Fig. 2. Main effects plot for means

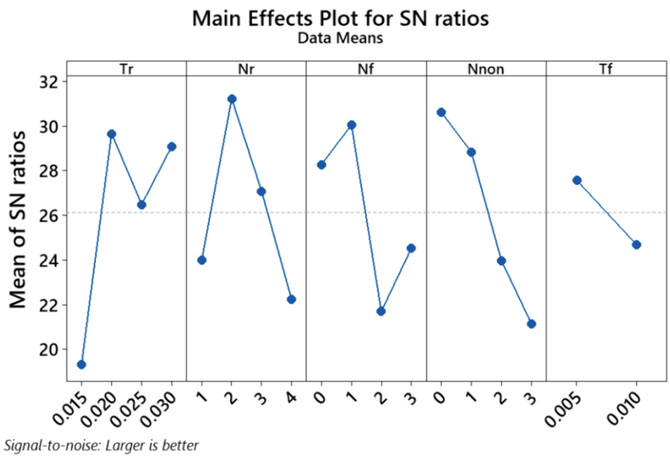

Fig. 3. Main effects plot for S/N ratios

According to the following formula, the anticipated mean wheel life ($\overline{WL}_{OP}$) is defined by the levels of the parameters that have a substantial influence on the S/N ratio of WL:

$$\overline{WL}_{OP} = \overline{T}_{r2} + \overline{N}_{r2} + \overline{N}_{non1} + \overline{N}_{f2} - 3 * \overline{T}_{WL} \tag{2}$$

Where, according to Table 5, $\overline{T}_{r2}$ is the average age of the grinding wheel for Tr at level 2: $\overline{T}_{r2} = 32.21$; $\overline{N}_{r2}$ is the grinding wheel's average age equivalent to Nr at level 2: $\overline{N}_{r2}$ =3 6.56; $\overline{N}_{non1}$ is the grinding wheel's average age equivalent to N_{non} at level 1: $\overline{N}_{non1} = 34.88$ (min); $\overline{N}_{f2}$ is the average age of the grinding wheel that corresponds to

Table 5. ANOVA of WL included the error analysis

Analysis of Variance for Means

Source	DF	SeqSS	Adj SS	Adj MS	F	P	C%
Tr	3	638.7	638.7	212.90	2.95	0.199	23.08
Nr	3	860.9	860.9	286.98	3.98	0.143	31.11
Nf	3	513.4	513.4	171.12	2.37	0.248	18.55
Nnon	3	537.9	537.9	179.29	2.49	0.237	19.44
Residual Error	3	216.4	216.4	72.13			7.82
Total	15	2767.3					100.00

Nf at level 2: $\overline{N}_{f2} = 33.03$ (min). The average wheel life for the entire experiment is $\overline{T}_g$:

$$\overline{T}_{Ra} = \frac{\sum_{i=1}^{16} WL_I + \sum_{i=1}^{16} WL_{II} + \sum_{i=1}^{16} WL_{III}}{48} = 26.22\,(\text{min}) \quad (3)$$

Substituting the values of the preceding quantities into (2) yields:

$$\overline{WL}_{OP} = 32.21 + 36.56 + 34.88 + 33.03 - 3 * 26.22 = 58\,(\text{min}) \quad (4)$$

The CI confidence interval is calculated as follows:

$$CI = \pm\sqrt{F_\alpha(1, f_e).V_e.(\frac{1}{N_e} + \frac{1}{R})} \quad (5)$$

Where fe = 3 is the degrees of freedom of error, Ve = 72.13 is the mean error of error (Table 5), $F_\propto(1, 3) = 5.5383$ is the coefficient of table lookup with 90% significance level, Ne is the effective number of iterations, and R is the number of experiment repetitions.

$$N_e = \frac{\text{Total number of experiments}}{1 + \text{Averaging the degrees of freedom of all parameters}} = \frac{48}{1+3+3+3+3} = 3.6923 \quad (6)$$

Substituting numbers, we have:

$$CI = \pm\sqrt{5.5383 * 72.13 * \left(\frac{1}{3{,}6923} + \frac{1}{3}\right)} = \pm 15.3 \quad (7)$$

As a result, with a significance level of α = 90%, the grinding wheel life is estimated using the ideal level of input parameters ar = 0.02 (mm), Nr = 1 (times), Nf = 2 (times), $a_{edf1} = 0.01$ (mm), $n_{non} = 3$ (times), and S = 1.2 (m/min) as follows:

$$(58 - 15.3\,min \le \overline{WL}_{op} \le 58 + 15.3\,(\text{min}) \quad (8)$$

To verify the aforementioned optimal set of parameters, an experiment was carried out using the following parameters: Tr = 0.02 (mm), Nr = 2 (times), Nf = 1 (times),

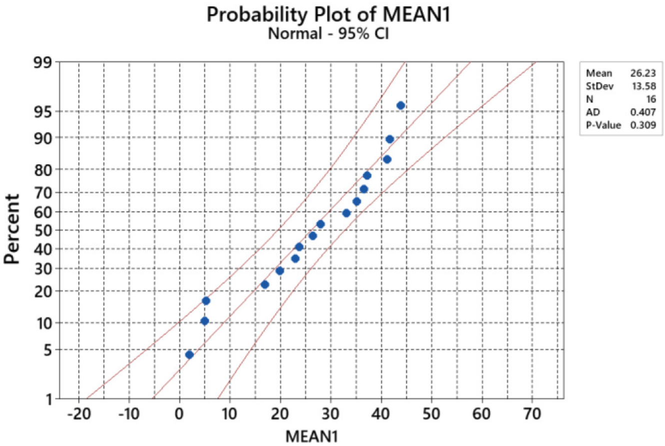

Fig. 4. Probability distribution graph of the data set

Tf = 0.005 (mm), and the same S = 1.2 (m/min). After three tests, the average grinding wheel life is 54.4 (minutes). This number falls entirely inside the anticipated range.

The Anderson-Darling approach was employed to justify the experimental model's fit (Fig. 4). The graph shows that all of the experimental data (blue dots) are inside a 95% confidence interval specified by two limit lines. Furthermore, P = 0.309 is greater than $\alpha = 0.05$, indicating that the proposed model is suitable.

4 Conclusions

The outcomes of a study on the effect of dressing conditions on wheel life in surface grinding Hardox 500 are presented in this publication. Five dressing parameters were explored in this study: rough dressing depth T_r, rough dressing times N_r, fine dressing depth T_f, fine dressing times N_f, and non-feeding dressing N_{non}. The impact of these components on wheel life was assessed. It was reported that N_r has the highest impact on WL (31.11%), followed by T_r (23.08%), N_{non} (19.44%), N_f (18.55%), and T_f (1.99%). Furthermore, the following optimal dressing mode was suggested to maximize wheel life: $T_r = 0.02$ (mm), $N_r = 2$ (times), $N_f = 1$ (times), $T_f = 0.005$ (mm), and the same S = 1.2 (m/min). The proposed model might also be used, it was stated.

Acknowledgment. This work was supported by Thai Nguyen University of Technology.

References

1. Rowe, W.B.: Principles of Modern Grinding Technology. William Andrew (2013)
2. Klocke, F., Thiermann, J., Mattfeld, P.: Influence of the dressing process on grinding wheel wear. Prod. Eng. **9**, 563–568 (2015)

3. Tu, H.X., et al.: Influence of dressing parameters on surface roughness of workpiece for grinding hardened 9XC tool steel. In: IOP Conference Series: Materials Science and Engineering. IOP Publishing (2019)
4. Tung, L.A., et al.: Optimization of dressing parameters of grinding wheel for 9CrSi tool steel using the Taguchi method with grey relational analysis. In: IOP Conference Series: Materials Science and Engineering. IOP Publishing (2019)
5. Mohite, D.D., Jadhav, S.: An investigation of effect of dressing parameters for minimum surface roughness using CNC cylindrical grinding machine. IJREAS **6**(6), 59–68 (2015)
6. Novák, M., Naprstkova, N., Kasuga, H.: Influence of grinding wheel dressing on the roughness of final surface and cutting force during GGG60 grinding. Key Eng. Mater. **686**, 218–223 (2016)
7. Rabiey, M., et al.: Dressing of hybrid bond CBN wheels using short-pulse fiber laser. J. Mech. Eng. **58**(7–8), 462–469 (2012)
8. Aleksandrova, I.: Optimization of the dressing parameters in cylindrical grinding based on a generalized utility function. Chin. J. Mech. Eng. **29**(1), 63–73 (2016)
9. Trmal, G., Kaliszer, H.: Optimization of a grinding process and criteria for wheel life. In: Tobias, S.A., Koenigsberger, F. (eds.) Proceedings of the Fifteenth International Machine Tool Design and Research Conference, pp. 311–315. Palgrave, London (1975). https://doi.org/10.1007/978-1-349-01986-1_37
10. Yu, T., Bastawros, A.F., Chandra, A.: Experimental and modeling characterization of wear and life expectancy of electroplated CBN grinding wheels. Int. J. Mach. Tools Manuf. **121**, 70–80 (2017)
11. Hwang, T., et al.: High speed grinding of silicon nitride with electroplated diamond wheels, Part 1: wear and wheel life. J. Manuf. Sci. Eng. **122**(1), 32–41 (2000)
12. Hwang, T., Evans, C.J., Malkin, S.: High speed grinding of silicon nitride with electroplated diamond wheels, Part 2: wheel topography and grinding mechanisms. J. Manuf. Sci. Eng. **122**(1), 42–50 (2000)
13. Kwak, J.-S., Ha, M.-K.: Evaluation of wheel life by grinding ratio and static force. KSME Int. J. **16**(9), 1072–1077 (2002)
14. Chen, X., Rowe, W., Cai, R.: Precision grinding using CBN wheels. Int. J. Mach. Tools Manuf. **42**(5), 585–593 (2002)
15. Phadke, M.S.: Quality engineering using design of experiments. In: Dehnad, K. (eds.) Quality Control, Robust Design, and the Taguchi Method, pp. 31–50. Springer, Boston (1989). https://doi.org/10.1007/978-1-4684-1472-1_3

Influence of the NdFeB Permanent Magnet on Working Characteristics of LSPMSM

Trinh Bien Thuy[1,2], Le Anh Tuan[3], Do Nhu Y[1], and Ngo Xuan Cuong[4](✉)

[1] Hanoi University of Mining and Geology, Hanoi, Vietnam
[2] Vietnam - Korea College of Quang Ninh, Ha Long, QuangNinh, Vietnam
[3] Faculty of Electrical Engineering, Hanoi University of Industry, Hanoi, Vietnam
[4] School of Engineering and Technology, Hue University, Hue, Thua Thien Hue, Vietnam
ngoxuancuong@hueuni.edu.vn

Abstract. Nowadays, the rapid development of neodymium rare earth (NdFeB) permanent magnet technology has promoted the creation of high-efficiency motors to replace the traditional low-efficiency induction motors (IM). In line-start permanent magnet synchronous motors (LSPMSM), the NdFeB permanent magnet acts as a source of flux. The calculation of permanent magnet depends on a large number of coefficients, which have a large range of variation and whose choice is largely dependent on experience. It is these factors that lead to the preliminary selection of the permanent magnet type, which can be inaccurate and greatly affect the working characteristics of the LSPMSM. The content of the article analyzes the influence of the selection of NdFeB permanent magnet types on starting speed characteristics, torque characteristics, current characteristics, and no-load dynamic forces in the design of an LSPMSM with a speed of 3000 rpm. Research results also show that, for each type of permanent magnet, there are some parameters or better working characteristics. Depending on the task required in the design of the LSPMSM, it is possible to select the type of permanent magnet suitable for the requirements.

Keywords: LSPMSM · NdFeB · line-start · permanent magnet

1 Introduction

The rapid development of NdFeB permanent magnet (PM) technology with high magnetic field density and a large energy product has spurred the development of high-efficiency motors, including LSPMSM [1]. The LSPMSM is a hybrid between an IM and a synchronous motor by placing PM rods in the rotor of the IM. As a result, LSPMSM has a high power factor and direct self-start capability; thus, LSPMSM emerges as an alternative to IM to save energy [2]. Although LSPMSM is claimed to be a motor with high efficiency and a large power factor, the design calculation for LSPMSM is very complicated. If the design of the LSPMSM is not good, the performance and performance parameters will be poor, even if they do not meet the standards of IM [3].

D. C. Nguyen et al. (Eds.): ICERA 2023, LNNS 944, pp. 61–67, 2024.
https://doi.org/10.1007/978-3-031-62235-9_8

In the LSPMSM, the NdFeB PM acts as a source of flux. Currently, the calculation of NdFeB PM depends on many coefficients, these coefficients have a large range of variation when the selection mainly depends on experience [4, 5]. While designing many parameters, the values have been rounded and normalized. It is these factors that lead to the preliminary selection of the initial NdFeB PM which can be inaccurate and greatly affect the starting characteristics, torque characteristics, current characteristics as well as no-load dynamic strength, performance of LSPMSM. In order for the LSPMSM to work with the best parameters, the selection of NdFeB PM must be re-evaluated after preliminary selection [6, 7].

The above studies have shown the outstanding characteristics and difficulties in the design of LSPMSM. Our research focuses on two aspects. First, analyze the basic characteristics of NdFeB PM types. Second, build a motor simulation model through Ansys/Maxwell software, thereby evaluating the influence of the basic characteristics of PM on the working characteristics of the motor. The rest of the paper is arranged as follows: Sect. 2 selects NdFeB PM for the LSPMSM design. Section 3 presents research on the effect of PM on LSPMSM. Our conclusions were drawn in the final section.

2 Selection of NdFeB PM for LSPMSM Design

The parameters of PM: coercive force, residual magnetic force, energy product from Curie temperature, effective magnetic flux density in Table 1 [8].

Table 1. Parameters of NdFeB PM.

Type	B_r (mT)	H_{cB} (kA/m)	H_{cJ} (kA/m)	BH_{max} (kJ/m^3)
N35SH	1.170	876	1.590	263
N38SH	1.220	907	1.590	286
N40SH	1.220	939	1.590	302
N42SH	1.280	987	1.590	318

where, B_r - Residual magnetic flux density; H_{cB} - Minimum magnetic field strength; H_{cJ} - Maximum magnetic field strength; BH_{max} - maximum energy product.

The selection of NdFeB PM must avoid demagnetization [4], the size calculation of the NdFeB PM in the LSPMSM design is usually done as follows [9]:

Step 1. Preliminary selection of the type of PM used to design the motor to determine the initial parameters (B_r, H_{cB}, H_{cJ}, BH_{max}).
Step 2: Calculate the preliminary selection of the maximum width W_{max}:

$$W_{max} = \sqrt{2}R_{1max} \tag{1}$$

Step 3. Calculate the minimum volume of PM used:

$$V_m = \frac{2.k_{ocf}.k_{fd}.(1 + k_{EC}).P_n}{\pi^2.\xi.2.p.f.B_r.H_c} \tag{2}$$

Step 4: Calculate the minimum thickness of the PM L_m:

$$L_m = \frac{V_m}{H_m.W_m} \tag{3}$$

where, R_{1max} - the distance from the center to the bottom of the rotor groove; k_{ocf} - Overload factor; k_{fd} - magnetization form factor; k_{EC} - Electromotive force factor (0.6 ÷ 0.95); P_n - Nominal power; ξ - Magnet utilization factor (0.3 ÷ 0.7); B_r - Residual magnetic flux density; H_c - Maximum magnetic field strength; H_m - Length of PM.

Formulas (1), (2) and (3) depend on many coefficients (k_{fd}, k_{EC}, k_{ocf}, ξ-…), These coefficients have a large range of variation, the choice mainly depends on experience. It is these factors that lead to the preliminary selection of NdFeB PM in step 1 which may be inaccurate and greatly affect the working parameters of the LSPMSM.

3 Study on the Effect of PM on LSPMSM

3.1 Research Motor Structure

Research LSPMSM is designed on the prototype IM with a power of 15 kW, a speed of 3,000 rpm and nominal voltage of 380/660 V. Preliminary selection of the N38SH type initial PM, the PM structure in the motor rotor uses a 3-bar construction type, using formulas (1), (2) and (3) to determine the preliminary size of the N38SH PM to use is: $W.L = 9 \times 35$ (mm). Structural parameters of LSPMSM were modeled on Ansys/Maxwell software comparative analysis of starting characteristics, torque characteristics, current characteristics as well as no-load dynamic magnetism, efficiency of LSPMSM using PM (N35SH, N38SH, N40SH, N42SH, N38SH).

3.2 Research Results

Magnetic Field Distribution

The magnetic field distribution in the LSPMSM in Fig. 1.

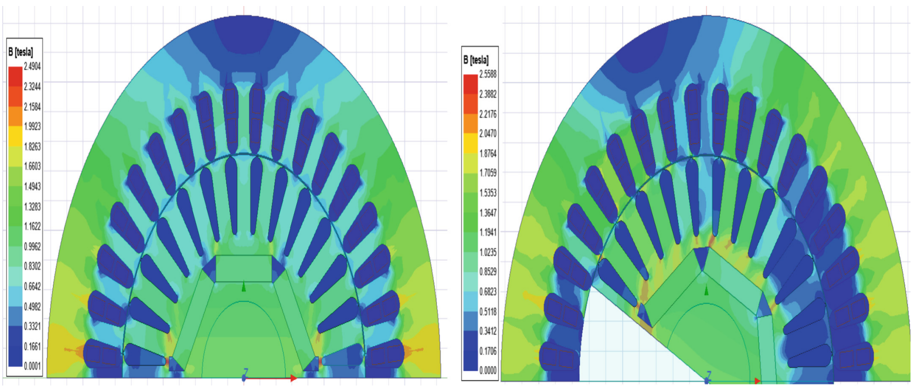

Fig. 1. Magnetic field distribution in the motor.

Table 2. Efficiency value and power factor of the motor.

Type	B_{max} (T)	η (%)	cos φ
N35SH	1.8	95.7	0.956
N38SH	1.9	96.3	0.961
N40SH	2.05	96.6	0.967
N42SH	2.2	95.6	0.953

The research results can calculate the parameters: The largest magnetic field in the magnetic circuit (B_{max}), efficiency (η) and power factor (cos φ) presented as Table 2.

From Fig. 1 and Table 2, it is shown that when using N38SH, the magnetic field in the magnetic circuit has not reached the saturation point (Steel 1008 allows 2.1 T), using N42SH swell in a saturated magnetic circuit (2.2 T), using N35SH, the magnetic field of the magnetic circuit is oversaturated, using N40SH will reach the allowable magnetic field value of the magnetic circuit, then the efficiency (96.6%), power factor (0.961) is higher than the case of using N38SH PM.

Starting and Torque Characteristics of the LSPMSM

The starting characteristics and operating characteristics of the LSPMSM in Fig. 2.

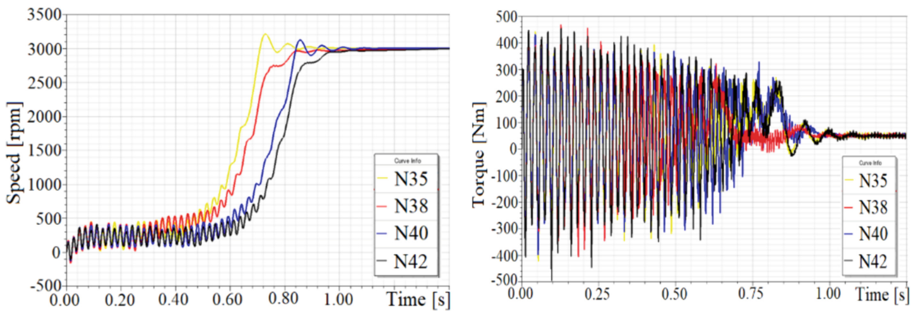

Fig. 2. Starting and torque characteristics of the LSPMSM.

Simulation results allow to analyze the starting parameters of the motor: time to reach synchronous speed (t_s), transient time (t_{trans}), speed (ω), maximum torque (M_{max}) and Torque ripple ($RipT$). Torque ripple of LSPMSM in one cycle is calculated [10]:

$$RipT = \frac{T_{\max} - T_{\min}}{T_e} \quad (4)$$

where, T_{max} – maximum torque value; T_{min} – minnimum torque value; T_e – average torque value of electric motor, Mm; $RipT$ – torque ripple, %.

From the results in Fig. 2 and Table 3, it can be seen that: The minimum synchronous input time ($t_s = 0.71$ s) is when using the N35SH PM, longest synchronization time is

Table 3. Torque characteristics of the LSPMSM.

Type	t_s (s)	t_{trans} (s)	$RipT$ (%)	M_{max} (Nm)
N35SH	0.71	1.12	26.1	420
N38SH	1.14	1.14	23.6	415
N40SH	0.84	1.12	26.3	435
N42SH	1.33	1.33	29.8	428

when using N42SH PM (t_s = 1.33 s); minimum transient time (t_{trans} = 1.12 s) when using N35SH and N40SH PM; greatest transient time (t_{trans} = 1.33 s) when using N42SH PM. In case of using N35SH PM, when entering synchronously, torque ripple reached 26.1%, smallest torque ripple (23.6%) when using N38SH PM, the largest (29.8%) when using N42SH PM.

Current and Dynamic Characteristics of the LSPMSM

The no-load current and electromotive force (E) characteristics in Fig. 3.

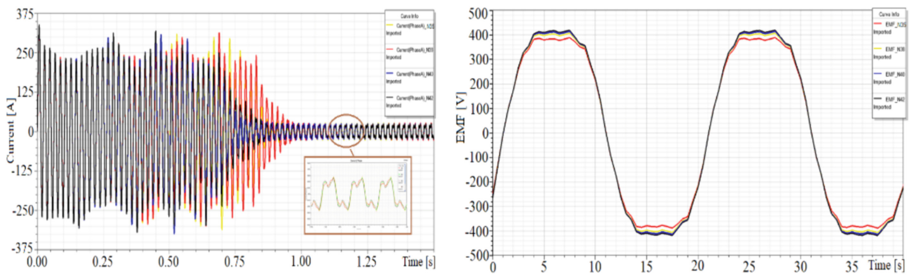

Fig. 3. Current and dynamic characteristics of the LSPMSM.

Total harmonic distortion (THD) in the current can be calculated to that given as follows [10] and value of no-load electromotive force (E) is also different in different cases of using different types of PM, the following formula is used:

$$THD_i = \frac{\sqrt{\sum_{n=2}^{\infty} I_n^2}}{I_1} = \frac{\sqrt{I_2^2 + I_3^2 + I_4^2 + I_5^2 + I_6^2 + \ldots}}{I_1} \tag{5}$$

$$\Delta E\% = \frac{E_{1NB} - 380}{E_{1NB}} 100\% \tag{6}$$

where, E_{1NB} is the RMS value of the 1st harmonic of the no-load electromotive force.

The research results of Fig. 3 and Table 4 show that the transient time (t_{trans}) of the current has the smallest value when using the N40SH type of PM. (t_{trans} = 0.8 s), followed by N42SH (t_{trans} = 0.85 s), N35SH (t_{trans} = 0.9 s) and the largest for N38SH

Table 4. Calculation results of no-load dynamic current and magnetic force characteristics.

Type	t_{trans} (s)	I_{max} (A)	THD_i (%)	E_{1NB} (V)	ΔE (%)
N35SH	0.90	308	17.8	389	+2.3
N38SH	0.95	314	16.1	400	+5.2
N40SH	0.80	312	14.3	410	+7.1
N42SH	0.85	337	17.6	420	+10.5

($t_{trans} = 0.95$ s). Minimum starting current when using N35SH ($I_{max} = 308$ A), followed by N40SH ($I_{max} = 312$ A), N38SH ($I_{max} = 314$ A) and the largest for N42SH ($I_{max} = 337$ A). The smallest *THDi* index corresponds to N40SH, followed by N38SH, N42SH and the largest is N35SH. For no-load electromotive force, the largest value is when using N42SH ($E_{1NB} = 420$ V) followed by N40SH, N38SH and the smallest is N35SH.

4 Conclusion

The article's content examines the selection of NdFeB PM in the LSPMSM of 3000 rpm. The effect of PM on the starting characteristics, torque characteristics, current characteristics, and no-load electromotive force in LSPMSM is evaluated. The research findings indicate that after preliminary PM type selection and calculating PM length and width in the LSPMSM design, the selected type of PM may not provide the best working characteristics due to the influence of the coefficients as well as rounding in the calculation. The research results also show that there are some parameters or better working characteristics for each type of PM. To calculate the working parameters of the LSPMSM, it is necessary to survey and evaluate the neighboring PM based on the preliminary selection of the NdFeB PM.

References

1. Do, N.Y, Le, T.A., Ngo, X.C.: Effect of permanent magnet structure on the performance of LSPMSM with a power of 22 kW and 3000 rpm. In: IOP Conference Series: Earth and Environmental Science, vol. 1111, no. 1, p. 012047. IOP Publishing, December 2022
2. Elistratova, V.: Optimal design of line-start permanent magnet synchronous motors of high efficiency (Doctoral dissertation, Ecole Centrale de Lille) (2015)
3. Do, N.Y., et al.: Design of high-performance explosion proof motor of 3,000 rpm for local exhaust ventilation in underground mining. Version B Vietnam J. Sci. Technol. **64**(10DB), 43–45 (2022)
4. Rao, D., Bagianathan, M.: Selection of optimal magnets for traction motors to prevent demagnetization. Machines **9**(6), 124 (2021)
5. Zijlstra, H.: Application of permanent magnets in electromechanical power converters; the impact of Nd-Fe-B magnets. J. Phys. Colloq. **46**(C6), C6-3 (1985)
6. Yun, J.B., et al.: A study on the starting characteristics in single-phase line-start permanent magnet motor. In: 2008 International Conference on Electrical Machines and Systems, pp. 3090–3093. IEEE, October 2008

7. Thurston, M.O.: Permanent magnet motor technology. Department of Electrical Engineering (2002)
8. Neodymium iron boron magnets Catalog. https://www.arnoldmagnetics.com/. Accessed 21 June 2023
9. Gieras, J.F., Wing, M.: Permanent Magnet Motor Technology, Design and Applications, 2nd edn. Revised and Expanded. Marcel Dekker, Inc. (2002)
10. Do, N.Y., Ngo, X.C.: Effects of voltage unbalance on matrix converter induction motor drive. In: Nguyen, D.C., Vu, N.P., Long, B.T., Puta, H., Sattler, K.U. (eds.) ICERA 2022. LNNS, vol. 602, pp. 468–476. Springer, Cham (2023). https://doi.org/10.1007/978-3-031-22200-9_53

Interative Learning Control (ILC) for Nonlinear System with Slow Variable Parameter and Noise, Applications for Wastewater Treatment Plantcontribution

Bach Van Nam[1(✉)], Đo Trung Hai[1], and Nguyen Quang Hung[2]

[1] Thai Nguyen University, Thai Nguyen City, Vietnam
bachvannam@tnut.edu.vn
[2] East Asia University of Technology, Hanoi, Vietnam

Abstract. This study focuses on developing algorithm and control structure for managing dissolved oxygen (DO) levels in tank 5 at a wastewater treatment plant using the Benchmark Simulation Model No.1 (BSM1). Initially, the paper outlines the principles of Iterative Learning Control (ILC), including its basic principles and its applications to nonlinear objects. It then introduces the wastewater treatment system and the standard BSM1 simulation model, a nonlinear object with slow variable parameters and noise. The emphasis is on proposing a control solution that combines feedforward Iterative Learning Control (ILC) with feedback PI control for the BSM1 wastewater treatment system. Results indicate that the control of dissolved oxygen levels in tank 5 has been significantly optimized, particularly as the number of learning iterations increases and the K_p, K_d parameters of the PD learning function are appropriately selected.

Keywords: Wastewater treatment · PID control · iterative learning control (ILC) · BSM1 model · dissolved oxygen (DO)

1 Introduction

The wastewater treatment plant is a nonlinear system affected by many complex disturbances with many biological and hydrodynamic phenomena occurring within. Because of nonlinearity, it may not be possible to derive the transfer function of the object, but the process controllers inside conventional wastewater treatment plants are still chosen as traditional controllers with control laws Proportional integral (PI) [1, 2], due to its simple design and popularity, it is easy to implement using electronic circuits. However, from the point of view of the control theory, the wastewater treatment plant is a nonlinear system with large size, slow variable parameter, easily perturbed by the speed of internal flows, the rate of contamination of wastewater, instability related to the components of input wastewater. Therefore, it is difficult for wastewater after treatment to achieve the goal of both meeting EQI quality standards and minimizing OCI operating costs at the same time (costs for aeration energy, mixing energy, total sludge production, etc.).

D. C. Nguyen et al. (Eds.): ICERA 2023, LNNS 944, pp. 68–77, 2024.
https://doi.org/10.1007/978-3-031-62235-9_9

On the other hand, the wastewater treatment process is slow and cyclical; Under such conditions, traditional control systems after a long enough period of work. Certainly in the materials used to manufacture the control device, as well as in the object, mechanical and physical fatigue will occur, leading to the control quality is no longer guaranteed as before. A simple solution to support the traditional system in which the same errors occur, that is the iterative learning control method. With iterative learning control (ILC), one does not need to re-configure the traditional controller, no need to interfere deeply in the existing system, because ILC is an intelligent control solution that does not need to the mathematical model of the object and is obviously applicable to nonlinear objects.

2 Introduction to Iterative Learning Control

2.1 The Iterative Learning Control Principle

The concept of iterative learning control (ILC) was introduced by Arimoto in 1990 [3] for systems where the operation is repetitive or batch. The quality of the control system can then be gradually improved by using the results of the previous batch operation to update the control signal for the next operation. ILC was first applied mainly for industrial robot control, then it was developed to apply for a variety of different fields such as process control, assembly, etc. [4]. With the assumption for a system with a transfer function of G(s), the block diagram of ILC is shown in Fig. 1.

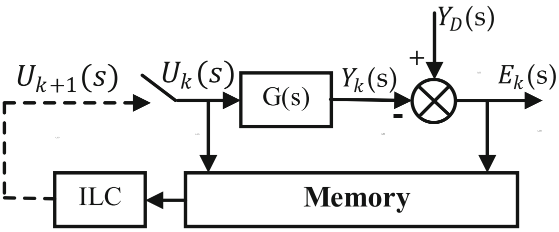

Fig. 1. The block diagram of ILC

In Fig. 1, the control signal $U_k(s)$ is fed to the system and the control error signal $E_k(s)$ between the desired value $Y_D(s)$ and the system output $Y_k(s)$ at the present iteration k is stored in memory. The control signal for the next $k + 1$ iteration is calculated so that the control error is gradually decrease or makes $E_{k+1} \le E_k$,

with $k = 0,1, 2, \ldots, \infty$. This algorithm is called a learning algorithm, and it often has the following form [5]:

$$U_{k+1}(s) = U_k(s) + L_e(s)E_k(s) \tag{1}$$

where $L_e(s)$ is a learning function, which has a linear relationship with $E_k(s)$.

Based on the principle of ILC, we see that ILC is an open-loop control structure, therefore, ILC does not have a feedback mechanism to minimize the effects of non-repetitive and unpredictable noise. We will combine ILC with feedback control to overcome this drawback.

From formula (1), we see that ILC is a part of intelligent control, since ILC does not use a mathematical model of the object (In the above formula, the presence of the function G(s) is not required), and it is applicable for cyclic systems with given period ΔT. In Fig. 1, we illustrate the ILC in the complex domain. To clarify the ILC, we will describe ILC in the time domain, as shown in Fig. 2 [4].

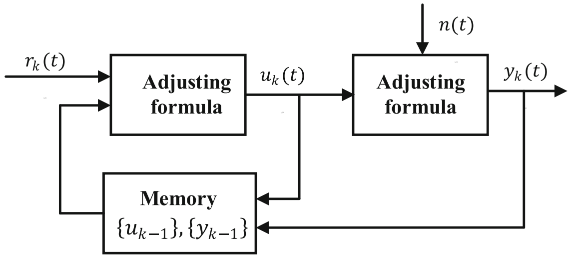

Fig. 2. The block diagram of ILC in the time domain

In Fig. 2, $r_k(t)$ is the time signal corresponding to $Y_D(s)$ in Fig. 1 (that is, $Y_D(s)$ is the Laplace conversion of $r_k(t)$, or $Y_D(s) = \boldsymbol{L}\{r_k(t)\}$), similarly $u_k(t)$, $y_k(t)$ and $e_k(t)$ are functions in time domain of $U_k(s)$, $Y_k(s)$ and $E_k(s)$; and n(t) represents the external noise affecting the system. So, the formulation corresponding to (1) in the time domain will be:

$$u_{k+1}(t) = u_k(t) + l_e(t) * e_k(t) \tag{2}$$

where $l_e(t) = \boldsymbol{L}^{-1}\{L_e(S)\}$, the symbol * represents convolution between two functions.

The working principle of ILC is based on the control signal $u(t)$ and error signal $e(t) = r(t) - y(t)$ in the previous cycle to adjust u(t) at the present cycle, called kth

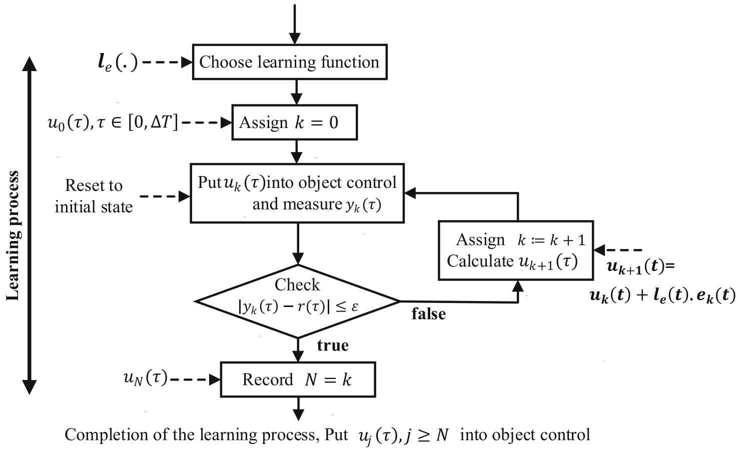

Fig. 3. The block diagram of ILC in the time domain

cycle, without mathematical model, so that the error signal at the present k period is smaller than in previous cycles and approaches e $\rightarrow$ 0 or $|e(t)| < \varepsilon$ after a finite number of duty cycles.

According to [1], we can summarize the training process of the iterative learning controller as shown in Fig. 3.

2.2 ILC with Nonlinear Objects

In Sect. 2.1, we describe ILC for linear objects, there exists a transfer function of the object G(s); and the relationship between the learning function and the error function is also a linear relationship, expressed by formula (1).

In the nonlinear case, the object is described by the equation:

$$y(t) = f(u(t)) \tag{3}$$

or in the form of state equation:

$$\begin{cases} \dot{x}(t) = f_x(x, u(t)) + d \\ y(t) = g(x) \end{cases} \tag{4}$$

with d is the external noise, and f(.) is a nonlinear function. The learning function can also be a nonlinear function for $e_k(t)$ in the form of:

$$l_e(t) = f_L(e_k(t)) \tag{5}$$

Here, because of the nonlinearity, we cannot derive the transfer functions G(s) and $L_e(s)$ from the above equations.

In this case, we can still apply the ILC following the block diagram in Fig. 2 and the adjusting algorithm as in Fig. 3, the only one difference is that the adjusting formula is in the time domain and will be more general as follows:

$$u_{k+1}(\tau) = u_k(\tau) + f_L(e_k(\tau)) \tag{6}$$

The convergence condition in general form for $e_k(\tau) \rightarrow 0$ is as follows [4]:

$$|1 - f \circ f_L| < 1 \tag{7}$$

where $\circ$ is the symbol of composite function.

Condition (7) asserts that for the case of nonlinear objects, we may still apply ILC to obtain $e_k(\tau) \rightarrow 0$. (Even according to the algorithm in Fig. 3, ILC can be used without a mathematical model of the object. Since the output of the system cannot be determined using the formula, we must measure it). Reality shows that it is difficult to check condition (7), even in the linear case when $f = G(s)$ and $f_L = L_e(s)$ are explicit, the choice of the coefficients of $L_e(s)$ to satisfy (7) is not simple. The general solution for (9) is still an unsolved issue at this time. However, ILC is still effectively applied by selecting the learning function $f_L(.)$ based on practical experience.

3 Proposal Feedback Control Solution Combined with Feedforward ILC Control for Wastewater Treatment Plant

3.1 Wastewater Treatment Plant and Standard Model BMS1

Wastewater treatment process with activated sludge is one of the most popular methods in the world and is also widely applied in Vietnam because it is highly effective in treating wastewater containing organic matter and can also handle other contaminants such as nitrates, nitrites and phosphates [5, 6]. It is also considered a reliable, scalable method to meet rising wastewater treatment needs, and can recycle sludge into fertilizer, reducing the amount of waste that needs to be treated [7].

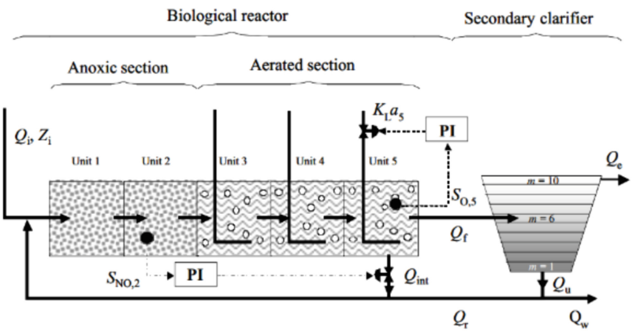

Fig. 4. Overview of BSM1 wastewater treatment model [6]

From the control point of view, in order to facilitate research as well as teaching and testing before commercialization, a number of models and protocols have been developed to simulate wastewater treatment plant, which are standardized models – "Benchmark Simulation Model No. 1- BSM1" [8] and "Benchmark Simulation Model No. 2 – BSM2" [9], in which the model BSM1 is used in this paper [8].

The standard wastewater treatment plant according to BSM1 [8] includes activated sludge tanks (or biological treatment tanks) and secondary settling tanks as shown in the Fig. 4. There are 5 activated sludge tanks including two anaerobic tanks, followed by three aerobic tanks, after the activated sludge tanks is a settling tank.

Controlling the aeration process is a very important part of the activated sludge wastewater treatment plant, the important task of that process is to maintain the desired concentration of Oxygen (DO) in the biological tank, ensuring aerobic conditions to promote the growth of biomass. Lack of oxygen in the aeration tank will lead to degradation of the activated sludge. The control system of aeration process consists of two control loops: the inner loop controls the DO level in the 5th tank and the outer loop controls the nitrate removal through controlling the flow of wastewater flows inside the tanks. According to [8], there are two PI controllers to control these two control loops, that is: The first control loop is to stabilize the concentration of Nitrogen SNO, 2 in the second tank with the desired value of 1 g/m^3 and the second control loop is to maintain the dissolved oxygen concentration in the fifth tank SO, 5 with the desired value of

$2\,g(COD)/m^3$. This reaseach will propose a control solution, which is the feedforward ILC combined with PI controller to improve the DO control quality of the 5th tank.

3.2 Feedforward ILC Control Combined with PI Feedback Control for Wastewater Treatment Plant

According to the BSM1 model [8], the kinetics of the dissolved oxygen concentration DO is described by the equation:

$$\begin{aligned}\frac{dS_{O,5}}{dt} =& -\frac{1}{V_5}Q_5 S_{O,5} + \frac{1}{V_5}\left(S_O^* - S_{o,5}\right)K_{La,5} \\ &+ \left[\frac{1}{V_5}Q_4 S_{O,4} - 1.972\frac{S_S}{10+S_S}\cdot\frac{S_O}{0.2+S_O}.X_{B,H}\right. \\ &\left.-9.02\rho_3\frac{S_{NH}}{1+S_{NH}}\cdot\frac{S_O}{0.4+S_O}.X_{B,A}\right]. \end{aligned} \tag{8}$$

where: $Q_5 = Q_4$ is the wastewater flow in tank 4 and tank 5; $S_{O,4}$ represents dissolved oxygen concentration DO of tank 4; $S_{O,5}$ represents dissolved oxygen concentration DO of tank 5; $K_{La,5}$ is the oxygen transmission coefficient, determining the dissolved oxygen concentration DO ($S_{O,5}$) in tank 5; S_O^* is the saturation concentration of Oxygen $S_O^* = 8\text{g.m}^{-3}$; $X_{B,A}$ and $X_{B,H}$ are the active autotrophic and heterotrophic biomass of tank 5, respectively; S_S is the easily decomposable substrate of tank 5; and S_{NH} represents nitrogen NH4+ and NH3 of tank 5.

Let $x = S_{O,5}$ be the state variable; $u = K_{La,5}$ be the control variable; And $d = \left[\frac{1}{V_5}Q_4 S_{O,4} - 1.972\frac{S_S}{10+S_S}\cdot\frac{S_O}{0.2+S_O}.X_{B,H} - 9.02\rho_3\frac{S_{NH}}{1+S_{NH}}\cdot\frac{S_O}{0.4+S_O}.X_{B,A}\right]$ is noise.

From (10), we have state equation system of the DO control loop of tank 5 as:

$$\begin{cases} \dot{x}(t) = f_x(x(t), u(t)) + d(t) \\ y(t) = x(t) \end{cases} \tag{9}$$

where:

$$f_x(x, u) = -\frac{1}{V_5}Q_5 x + \frac{1}{V_5}\left(S_O^* - x\right)u. \tag{10}$$

Suppose that from (11) we can solve the solution $x(t)$ in terms of u(t):

$y(t) = x(t) = f_y(u(t))$, the condition for the error of ILC to converge to 0, according to (7) will be:

$$\left|1 - f_y \circ f_L\right| < 1 \tag{11}$$

In the case of not finding a solution $f_y(u(t))$, we will check (11) by numerical method, then we must discretize (11) and calculate by loop index k and sample index i.

In this research, the traditional controller is a PI with transfer function $f_{PI}(e(\tau))$:

$$f_{PI}(e_k(\tau)) = k_{pi}e_k(\tau) + k_i\int e_k(\tau)d\tau \tag{12}$$

And the learning function of ILC is the PD expressed by the formula [10]:

$$l_e(\tau) = f_L(e_k(\tau)) = k_p e_k(\tau) + k_d \frac{de_k(\tau)}{d\tau} \tag{13}$$

with k_{PI}, k_i, k_p, k_d are appropriately chosen constants.

The block diagram of this controller is shown in Fig. 5, where $f_y(u(t))$ is transfer function of object.

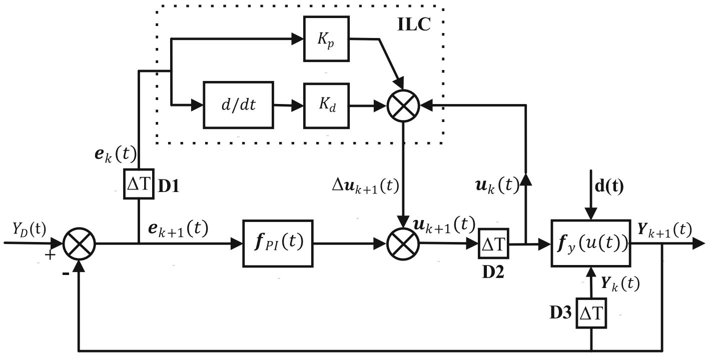

Fig. 5. Structure diagram of feedforward iterative learning controller combined with PI control to control DO concentration in tank 5

In Fig. 5, D1 and D2 And D3 are one-cycle delayed blocks ΔT, the input of this delayed block is the signal in the present cycle, the output is the same signal but in the previous cycle.

From the above diagram, the control signal at iterative step $k + 1$, $k = 0,1, 2, .., \infty$, $u_{k+1}(\tau)$ is the sum of two components: the first component is the output of the feedback controller $f_{PI}(\tau)$ at step $k + 1$ and the second component is the feedforward control $\Delta u_{k+1}(\tau)$, which is determined based on the iterative learning principle from control error signals $\Delta u_{k+1}(\tau)$, and control signal $u_k(\tau)$ at previous iteration k:

$$\Delta u_{k+1}(\tau) = u_k(\tau) + k_p e_k(\tau) + k_d \frac{de_k(\tau)}{d\tau} \tag{14}$$

In order to apply ILC, we proceed to discretize the system, that is, convert the ordinary differential equations into the form of differential equations.

Discrete (11) and (12) and then combine, we have:

$$y_{k+1}(i) = -\frac{1}{V_5} Q_5.y_k(i) + \frac{1}{V_5}[S_O^* - y_k(i)].u_k(i) + d(t) \tag{15}$$

where k is the loop index and i is the sample index, that is the function $f_y(u(t))$.

From (16), we have the output differential equation of the ILC as follows:

$$\Delta u_{k+1}(i) = u_k(i) + k_p.e_k(i) + k_d.e_k(i+1) \tag{16}$$

From Fig. 6 and Eq. (14), we can calculate:

$$\begin{aligned} u_{k+1}(i) &= \Delta u_{k+1}(i) + f_{PI}(e_{k+1}(t)) \\ &= \Delta u_{k+1}(i) + k_{PI}.e_{k+1}(i) + k_i.e_{k+1}(i-1) \end{aligned} \tag{17}$$

Equations (15), (16) and (17) are the basis for establishing the ILC algorithm.

Next, we choose the sample time T and calculate the number of samples for each loop:

M = ΔT/T, from i = 0, 1, 2,…., M-1 and set the vector variables:

$$\begin{cases} \boldsymbol{y}_k(i) = \left[y_k(0), y_k(1), y_k(2), \ldots\ldots, y_k(M-1)\right]^T \\ \boldsymbol{y}_{k+1}(i) = \left[y_{k+1}(0), y_{k+1}(1), \ldots\ldots, y_{k+1}(M-1)\right]^T \end{cases} \tag{18}$$

$$\begin{cases} \boldsymbol{e}_k(i) = [e_k(0), e_k(1), e_k(2), \ldots\ldots, e_k(M-1)]^T \\ \boldsymbol{e}_{k+1}(i) = \left[e_{k+1}(0), e_{k+1}(1), \ldots\ldots, e_{k+1}(M-1)\right]^T \end{cases}; \tag{19}$$

$$\begin{cases} \boldsymbol{\Delta u}_k(i) = [\Delta u_k(0), \Delta u_k(1), \Delta u_k(2), \ldots\ldots, \Delta u_k(M-1)]^T \\ \boldsymbol{\Delta u}_{k+1}(i) = \left[\Delta u_{k+1}(0), \Delta u_{k+1}(1), \ldots\ldots, \Delta u_{k+1}(M-1)\right]^T \end{cases} \tag{20}$$

$$\begin{cases} \boldsymbol{u}_k(i) = [u_k(0), u_k(1), u_k(2), \ldots\ldots, u_k(M-1)]^T \\ \boldsymbol{u}_{k+1}(i) = \left[u_{k+1}(0), u_{k+1}(1), \ldots\ldots, u_{k+1}(M-1)\right]^T \end{cases} \tag{21}$$

The ILC algorithm suggested is as follows:

Step 1:

+Set k = 0; choose ε;

+Set initial values; + $\Delta u_0(i) = [0, 0, \ldots, 0]^T$; + $e_0(i) = [Y_D, Y_D, \ldots, Y_D]^T$

+$y_0(i) = [0, 0, \ldots, 0]^T$; + $u_0(i) = [u_0(0, u_0(1), \ldots, u_0(M-1)]^T$;

Step 2:

+Calculate $y_{k+1}(i)$ from (17); and calcute: $e_{k+1}(i) = Y_D - y_{k+1}(i)$;

+Calculate $\Delta u_{k+1}(i)$ from (18); and calcule $u_{k+1}(i)$ from (19);

+Check condition:

$$\|Y_D - y_{k+1}(i)\| < \varepsilon;\ i = 0,1, \ldots, M-1 \tag{22}$$

If (22) is satisfied, the learning process is stopped.

If (22) is not satisfied then:

+Assign (k: = k + 1);

+Push the data of vector with index (k + 1) into the vector with index k and add 1 to the index of the vectors in formulas (18), (19), (20) and (21); + Go back to Step 2.

3.3 Simulation and Verification of the Proposed Control Solution

In this paper, only some simulation results are presented on matlab instead of the entire simulation.

Figure 6 is the simulation results for the following cases: Using only traditional PI controller and using proposed controller by the reasearch: Using ILC feedforward control combined with PI feedback control (with the same $K_p = 30$, $K_d = 10$ values of the PD learning function).

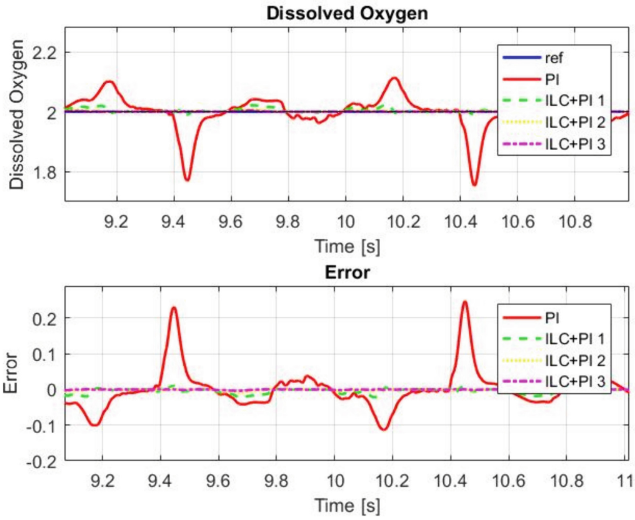

Fig. 6. Simulation results of feedforward iterative learning control combined with PI control

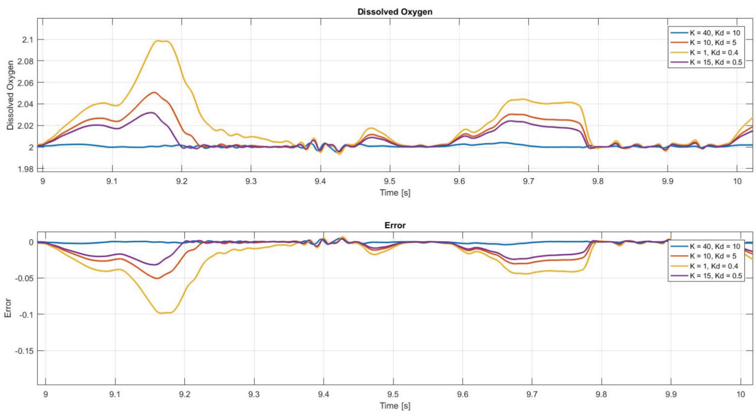

Fig. 7. Iterative learning process with 04 different values K_p and K_d

From Fig. 6, it can be seen that: After only 2 cycles of iterative learning, the results of ILC + PI control were much better than those of PI only, and after 3 cycles of iterative learning, the output has accurately followed the input set point.

Figure 7 shows the impact of the selection the K_p, K_d parameters of the PD learning function on the output has accurately followed the input set point, also compared with the case of using only PI control. Selections are: Case 1: $K_p = 40, K_d = 10$; Case 2: $K_p = 10, K_d = 5$; Case 3: $K_p = 1, K_d = 0{,}4$ và $K_p = 15, K_d = 0.5$. Simulation results show that the third case 1 the best results in the four selected cases.

4 Conclusion

The research presents a solution that combines a modern and intelligent control method - ILC - with the classical control method PI to improve the quality of the DO concentration of wastewater treatment plant with activated sludge. ILC analysis, design steps and some simulation results have been verified. The results show that the solution can be applied to slow-changing physicochemical processes operating in cycles, having nonlinear mathematical model, variable parameters and external noise.

Acknowledgements. The authors acknowledge Thai Nguyen University of Technology for their financial support in our project.

References

1. Henze, M., van Loosdrecht, M.C.C., Brdjanovic, D., Ekama, G.A.: Biological Wastewater Treatment: Principles. Modelling and Design. IWA Publishing, London (2008)
2. Mhaskar, P., El-Farra, N.H., Christofides, P.D.: A method for PID controller tuning using nonlinear control techniques. AIChE J. **51**(12), 3292–3299 (2005)
3. Arimoto, S., Kawamura, S., Miyazaki, F.: Bettering operation of robots by learning. J. Rob. Syst. **1**(2), 123–140 (1984)
4. Hà, N.T., Nam, N.H., Phư´ơc, N.D.: Điều khiển học lặp, Nhà xuất bản Bách khoa Hà Nội (2021)
5. Anders, R.: Automatic control of an activated sludge process in a wastewater treatment planta benchmark study. M. S. thesis, School of Engineering, Uppasala University, Sweden (2000)
6. Nhân, T.V., Nga, N.T.: Giáo trình công nghệ xử lý nư´ơc thải. (in lần th´ư 4), Nhà xuất bản Khoa học và Kỹ thuật, Hà nội (2006)
7. Kaplan, M.A.: Multiobjective analysis in water resource planning and management: A framework for policy evaluation. In: Decision and Control including the 14th Symposium on Adaptive Processes, pp. 145–147. IEEE (1975)
8. Alex, J., et al.: Benchmark Simulation Model. 1 (BSM1). Report by the IWA Taskgroup on Benchmarking of Control Strategies for WWTPs (2008)
9. Jeppsson, U., et al.: Benchmark simulation model no 2 – general protocol and exploratory case studies. Water Sci. Technol. **56**(8), 67–78 (2007)
10. Bristow, D.A., Tharayil, M., Alleyne, A.G.: A survey of Iterative learning control, a learning method for high-performance tracking control. IEEE Control Syst. Maga. **26**, 96–114 (2006)

Interface Formation Induced by Friction Stir Welded Tool Offset in T-lap Joint of AA7075 and AA5083

Hao Dinh Duong, Quan Minh Nguyen, Vu Anh Nguyen Le, Thuyen Van Phi, Vu Van Huynh, Nam Hoai Quach, Xuan-Phuong Dang, and Tra Hung Tran(✉)

Nha Trang University, 02 Nguyen Dinh Chieu Street, Nha Trang City, Vietnam
tra@ntu.edu.vn

Abstract. The goal of this work is to reveal the interface formation of T-lap joint of AA7075/AA5083 induced by friction stir welded tool offset. The distance from the tool axis to the center of the T-joint was defined as the tool offset. The results verified that the welding interface included kissing bond (KB) defects was significantly sensitive to the eccentric position of tool pin. Increasing the tool offset decreased the KBs at advancing side but increasing the KBs at retreating side. The influence of this type of defects on the joint tensile strength was evaluated in digital image correlation (DIC) technology.

Keywords: FSW · tool offset · aluminum alloys · interface formation · tensile strength

1 Introduction

The aerospace, automotive, railway, and shipbuilding industries encounter significant challenges in their efforts to decrease structural weight, conserve fuel, and mitigate greenhouse gas emissions [1]. Using lightweight alloys, hybrid structure, T-joint… were noted in recent years [2]. Nevertheless, the substantial disparity in material properties among various alloys presents a considerable challenge to conventional fusion welding [3]. Friction stir welding (FSW) technology has been recognized as an efficient solid-state welding method in metalworking, offering significant economic benefits. [4, 5]. Due to its low welding temperature, this technique could be effectively employed for dissimilar joints [5, 6].

T-joints play a crucial role as connections in structure, finding widespread applications in various industries. The limited weldability of conventional fusion welding is a big challenge due to the undesirable occurrence of defects like porosity, inadequate wetting, and coarse microstructure grain formation [7, 8]. Therefore, the FSW method can be regarded as a potential candidate for producing T-joints with high strength. In previous researches, the most significant difficulty in this method applied the T-lap joints could be associated with the formation of welded defects along the joint interface [9–11]. In order to improve the T-lap joint, some methods were mentioned such as controlling

D. C. Nguyen et al. (Eds.): ICERA 2023, LNNS 944, pp. 78–84, 2024.
https://doi.org/10.1007/978-3-031-62235-9_10

welding speed [9, 11, 12], moving pin location [13], using pin length [14], and applying multiple pass [2, 10, 15–17]. Nevertheless, the impact of tool offsets on the interface formation has not been thoroughly understood in these studies.

In this study, the interface formation of the T-lap joints of AA7075/AA5083 was produced by the FSWed tool offset. Its influence on the joint tensile strength and the fracture behavior was also clarified due to digital image correlation (DIC) technology.

2 Experiment and Methods

Dissimilar AA5083 and AA7075 alloys were welded by the FSW technology via a T-lap configuration (Fig. 1(a)). The dimension and position of two plates are showed in Fig. 1(a). The distance of tool offset *d* was setup from 0.0 mm to 0.8 mm toward advancing side (AS). The welding speed of 100 mm/min and rotational speed of 400 rpm was constant. A cylindrical and thread pin with the diameter of 8.5 mm was used in this work. The shoulder diameter and pin length were 24.0 mm and 3.7 mmm, respectively. The fixture and fabrication of the FSWed T-lap joint are showed in Fig. 1(b).

The joint interface and the KB defects are observed by microscope. The tensile strength of both the skin and stringer tests was measured, as depicted in Fig. 2(a,b), respectively. The geometry of tensile specimen might be seen in [10]. Testing process was carried out by the tensile machine of Instron 3366 model under the rate of 2.0 mm/min. The local strain during tensile testing process was recorded by digital image correlation technology (DIC), as seen in Fig. 2(a).

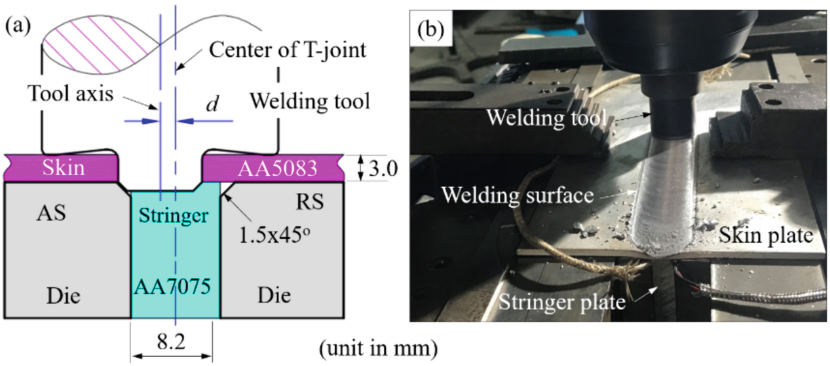

Fig. 1. (a) T-lap joint configuration and (b) FSWed T-lap joint process.

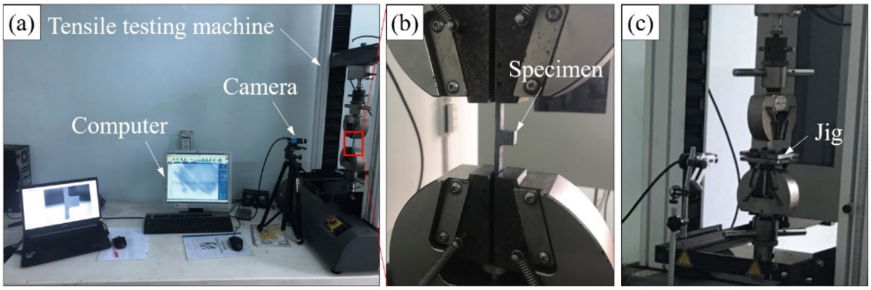

Fig. 2. Overview of (a,b) skin tensile test and DIC setup, and (c) stringer tests.

3 Results and Discussion

3.1 Effect of Tool Offset on Interface Formation

The welding surfaces at several tool offsets are showed in Fig. 3. It seems that the welding surface is good without crack defects that appeared as using traditional fusion welding. In addition, using the tool offset was not the influence on the joint geometry. The cross-sections of the FSWed T-joints produced by different tool offsets are presented in Fig. 4(a-c). Some tunnel and KB defects were found on the cross-section of joint. As designated in figure, the tunnel defects only occurred at advancing side (AS) whereas the KB defects produced significantly at retreating side (RS). The results could be affected by the materials flow during welding process [2, 10, 16].

The effect of tool offset on the dimension of the KB defects is showed in Fig. 4(d). It is clear that the size of the KBs at the RS is much larger than that at the AS, particularly in distance of 0.8 mm. The lap-joint characteristic is reason for this result, as explained in [9, 10]. It is worthy to note that growing the tool offset led to rising the KBs size at the RS. In contrast, this work is useful for improving the KBs size at the AS. As reported in previous work [10, 15], the empty between die and tool pin played the imperative role in the formation of the KB size.

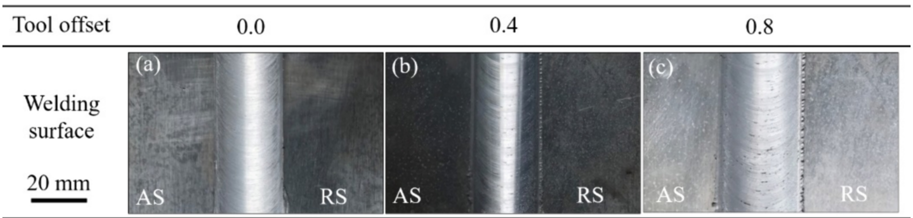

Fig. 3. Welding surface at tool offset of (a) 0.0 mm, (b) 0.4 mm, and (c) 0.8 mm.

3.2 Tensile Strength of Joint

The influence of the welding condition on the joint strengths at both the stringer and skin tests is displays in Fig. 5. In both cases, the joint strengths were decreased corresponding

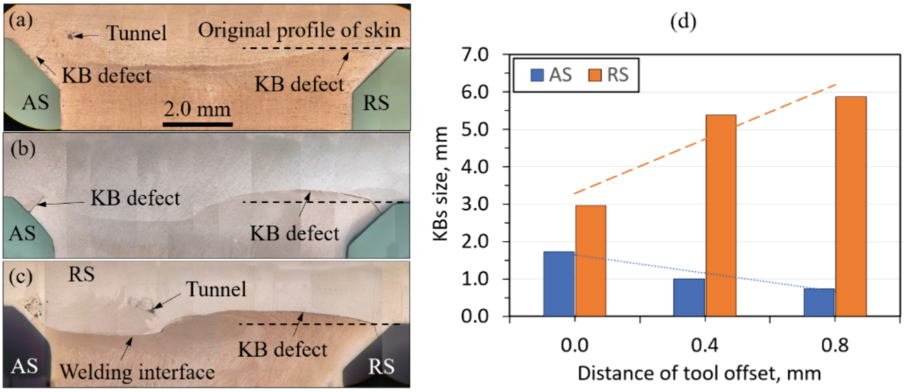

Fig. 4. Welding surface at distance of (a) 0.0 mm, (b) 0.4 mm, (c) 0.8 mm and (d) effect of tool offset on the KBs size.

to increasing the distance of the tool offset. On the other words, the joint strength was susceptible to this variation. It seems that the data point of the joint strength under the stringer test was more dispersed than that under the skin test. As pulling along the stringer part, the welding interface that is perpendicular to loading direction played the imperative part in the fracture behavior of the joints [14, 16]. So, the size and the geometry of the KB defects significantly contributed to the joint strength under the stringer test.

Dissimilar to the stringer test, the effective skin thickness (EST) affected mainly the joint strength induced by the skin test. As observed in Fig. 4(b,c), the upward movement of the KB interface led to decreasing the EST. This phenomenon resulted in degrading the joint strengths by the skin test, as described in earlier works [10, 15].

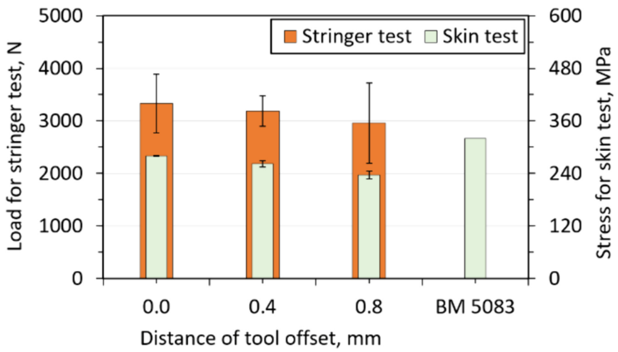

Fig. 5. Impact of tool offset on tensile strength of T-lap joint induced by skin and stringer tests.

The DIC strain maps of the T-lap joints induced by the skin test are shown in Fig. 6. The joint fabricated by the 0.0 mm of tool offset was cracked at the heat affected zone (HAZ) of AA5083 (Fig. 6(a)). As seen in Fig. 4(a), the KBs interface insignificantly impacted the EST of AA5083. The strain focused mainly on the HAZ where had coarser microstructure [12]. In contrast, the KBs interface largely impacted the fracture location

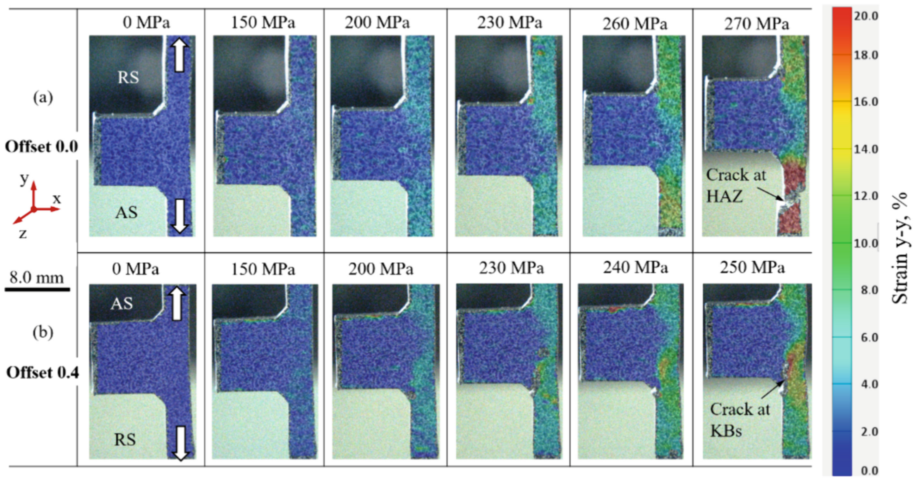

Fig. 6. Impact of the KBs on fracture behavior of T-lap joint induced by skin tests.

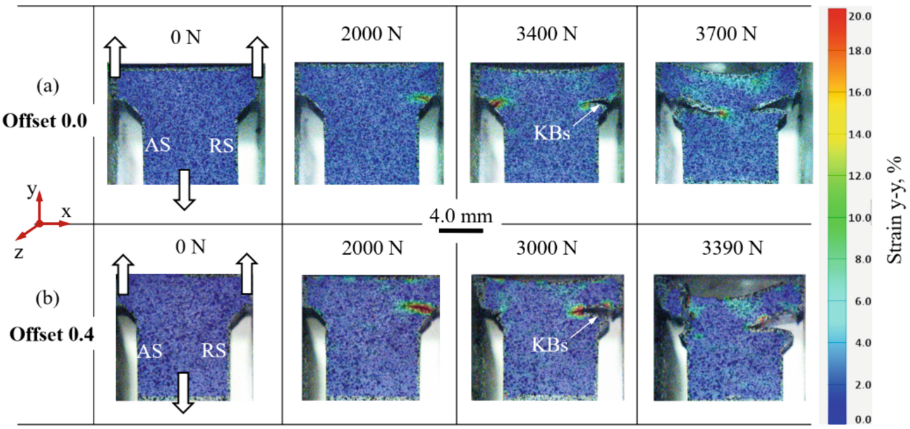

Fig. 7. Impact of the KBs on fracture behavior of T-lap joint induced by stringer tests.

of the joint fabricated by the distance of 0.4 mm (as seen in Fig. 4(b)). Degrading the EST caused by the KBs is reason for the low joint strength that cracked at the KBs (Fig. 6(b)).

Dissimilar to the skin test, the KBs interface strongly affected the fracture behavior of the T-lap joint induced the stringer test in all cases (as seen in Fig. 7). The KBs were easily opened as loading. This phenomenon appeared more clearly at the joint fabricated by the distance of 0.4 mm, which had the longer KBs size (Fig. 7(b)). So, the fracture behavior of the joint induced by the stringer test is more complex than that by the skin test.

4 Conclusions

The dissimilar AA5083 and AA7075 via the T-lap joints was fabricated by FSW technology at different tool offsets. The important conclusions were obtained as followings:

(1) The formation of welding interface of the FSWed T-lap joint is sensitive to the tool offsets. The tunnel defects were detected at the AS whereas the KB defects were observed dominantly at the RS.
(2) Increasing the distance of tool offset decreased the KBs at the AS but increasing the KBs at the RS.
(3) The T-lap joint strength was reduced owing to growing the tool offsets. Nevertheless, the joint efficiency under the skin test is lower than that of AA5083.
(4) The welding interface with the KBs defects remarkably affected the fracture behavior of the joints, especially in the stringer test.

Acknowledgments. Hao Dinh Duong was funded by the Postdoctoral Scholarship Programme of Vingroup Innovation Foundation (VINIF), code VINIF.2023.STS.05.

References

1. Friedrich, H.E.: Challenges of materials technology for low consumption vehicle concepts. Adv. Eng. Mater. **5**, 105–112 (2003)
2. Feistauer, E.E., Bergmann, L.A., dos Santos, J.F.: Effect of reverse material flow on the microstructure and performance of friction stir welded T-joints of an Al-Mg alloy. Mater. Sci. Eng. A **731**, 454–464 (2018)
3. Peng, P., et al.: Effects of interlayer metal on microstructures and mechanical properties of friction stir lap welded dissimilar joints of magnesium and aluminum alloys. J. Mater. Process. Technol. **299**, 117362 (2022)
4. Thomas, W.M., Nicholas, E.D., Needham, J.C., Murch, M.G. Templesmith, P., Dawes, C.J.: G.B. Patent Application No. 9125978.8 (1991)
5. Mishra, R.S., Ma, Z.Y.: Friction stir welding and processing. Mater. Sci. Eng. R **50**, 1–78 (2005)
6. Akinlabi, E.T., Akinlabi, S.A.: Advances in Friction-Stir Welding and Processing: 6-Friction stir welding of dissimilar metals. Elsevier 241–293 (2014)
7. Frank, D., Remes, H., Romanoff, J.: Fatigue assessment of laser stake-welded T-joints. Int. J. Fatigue **33**, 102–114 (2011)
8. Jesus, J.S., Costa, J.M., Loureiro, A., Ferreira, J.M.: Fatigue strength improvement of GMAW T-welds in AA 5083 by friction-stir processing. Int. J. Fatigue **97**, 124–134 (2017)
9. Hao, D.D., Okazaki, M., Tra, T.H.: Effect of welding parameters on mechanical properties of friction stir welded T-lap dissimilar metal joints between 7075 and 5083 aluminum alloys. JSME-Mech. Eng. J. **6** (4) (2019)
10. Hao, D.D., Okazaki, M., Tra, T.H.: Effects of tool offset and reversed metal flow on mechanical properties of dissimilar friction stir welded T-lap joints between AA7075 and AA5083, JSME-Mech. Eng. J. **7** (2020)
11. Cui, L., Yang, X., Zhou, G., Xu, X., Shen, Z.: Characteristics of defects and tensile behaviors on friction stir welded AA6061-T4 T-joints. Mater. Sci. Eng. A **543**, 58–68 (2012)

12. Hao, D.D., Tra, H.T., Xuan-Phuong, D., Dac, D.T., Nam, H.Q.: Microstructure evolution and interfacial bonding properties of dissimilar T-lap joints using friction stir welding parameters. J. Mater. Eng. Perform. **32**, 9428–9439 (2023)
13. Nam, H.Q., Hao, D.D., Tra, H.T.: Impact of tool offset and friction stir welding speed on interface morphology of a dissimilar T-lap joints. Weld. Int. **36**(7), 379–386 (2022)
14. Hao, D.D., Okazaki, M., Tra, T.H.: Influence of probe length on the formation of an interface in friction stir welded T-lap joints. Mat. Manuf. Process. **36**(6), 693–701 (2020)
15. Hao, D.D., Tra, H.T., Okazaki, M., Dac, D.T.: Pin length, pin offset, and reversed metal flow interaction in the improvement of dissimilar friction stir welded T-lap joints. Int. J. Adv. Manuf. Technol. **121**, 4677–4689 (2022)
16. Duong, H.D., Tran, T.H.: Effect of interface morphology on the mechanical properties of friction stir welded T-lap joints of 7075/5083 aluminum alloys. Metall. Mater. Trans. A **52**, 3023–3033 (2021)
17. Hao, D.D., Okazaki, M., Tra, T.H.: Fatigue behavior of dissimilar friction stir welded T-lap joints between AA5083 and AA7075. Int. J. Fatigue **145**, 106090 (2021)

Investigate a Folding Mechanism Using Cylinder for Operation

Thi-Thanh-Nga Nguyen and Anh-Tuan Dang(✉)

Thai Nguyen University of Technology, Thai Nguyen, Vietnam
Anhtuanck@tnut.edu.vn

Abstract. The paper analyzes a popular folding structure that utilizes hydraulic cylinders for operation, developed by the Tenfold firm. Based on the motion of the mechanism, the kinematic characteristics of each link can be determined using fundamental principles of machine and mechanism theories. Consequently, the velocity and acceleration of the elements can also be accurately determined, along with the impact of reactions on revolution joints. This method supports the design process and facilitates the selection of components in the device for manufacturing. The results of the study demonstrate the applicability of simple linkage mechanisms in the design and construction of complex systems in practical applications.

Keywords: Linkage · Folding Mechanism · Kinematic Analysis · Cylinder arrangement

1 Introduction

Linkages are mechanisms using rigid links connected by joints that are designed to transmit forces and motion. These devices play a crucial role in various systems and are widely used in multiple engineering applications. In the field of mechanical engineering, linkage mechanisms, from simple to complex structures, have been extensively studied and analyzed. In a study by Tsai [1], a comprehensive review of different types of mechanisms with detailed applications was conducted. The paper also discusses the fundamental principles of linkages, including the kinematic analysis and synthesis of various configurations. Another research paper by Sy et al. [2] analyzed the operation of a four-bar linkage and proposed an optimization synthesis method to investigate the motion characteristics and performance on different trajectories of the component links. The study provides insights into the behavior of the linkage, enabling engineers to optimize their design to meet the required performance. Moreover, linkage mechanisms can even be utilized to create manipulators for robotics capable of performing complex tasks. A research paper by Schena [3] presents an approach to the modeling of Advanced Robotics and Automated Systems (ARAS) robotic arm using spherical links. A kinematic model and control strategy for the robotic arm were also proposed, enabling precise and efficient manipulation in industrial applications.

D. C. Nguyen et al. (Eds.): ICERA 2023, LNNS 944, pp. 85–95, 2024.
https://doi.org/10.1007/978-3-031-62235-9_11

Developed from simple linkages, folding mechanisms are innovative systems designed to enable compact and efficient folding or unfolding of objects [4–8]. These linkages consist of interconnected components that allow for controlled motion, facilitating the transformation of a structure from an extended or unfolded state to a compact or folded configuration. Applications of these types of linkages can be found in various fields, including engineering, architecture, furniture, and even automotive design. They offer several advantages such as space optimization, portability, ease of storage, and convenience of transportation. By incorporating folding mechanisms into designs, objects can be reduced in size, enabling efficient use of limited space, ease of handling, and enhanced portability. Folding linkages can be classified into many types, with unique configurations and motion patterns. These linkages may utilize hinges, pivots, or other connecting elements to enable smooth and controlled folding motions. The common types include parallel linkages, scissor linkages, pantograph, origami-inspired, and more. Folding linkages require careful design considerations to ensure structural integrity, stability, ease of operation, and durability. Factors such as material selection, load-bearing capacity, locking mechanisms, and ergonomic considerations play a crucial role in the successful implementation of folding mechanisms.

This paper analyzes a folding linkage used for a staircase railing. Based on the motion of the mechanism, the kinematic characteristics of each link can be determined using the fundamental principles of machine and mechanism theories. Consequently, the velocity and acceleration of the elements can also be accurately determined, along with the impact of reactions on revolution joints. This method supports the design process and facilitates the selection of components in the device for manufacturing. The results of the study demonstrate the applicability of simple linkage mechanisms in the design and construction of complex systems in practical applications.

2 Structural Analysis.

The structure of the system is described as shown in Fig. 1, consisting of 9 links: the cylinder (AP) acts as the driving link, extending or retracting to change the shape of the whole mechanism. Through the operation of the cylinder and the revolute joints between intermediate links (AD, BC, CF, DE, PC, and DN), the output link (EF) translates without rotation from the folded to the open state. Observing the operation of the structure indicates that to ensure the translational movement of the output link, the dimensions of each pair of linked components in the system must follow a centrally symmetric principle, meaning AB = EF, AD = CF, BC = DE, CM = DN.

The arrangement of the cylinder also needs to be considered so that during the operation of the mechanism, the cylinder does not protrude outside, affecting the aesthetics and the layout of related linkages. Additionally, to ensure that the mechanism can be fully compacted, the folding and unfolding dimensions of the frames must also be compatible with Eq. (1), as follows:

$$AB - BC = AM - MC \tag{1}$$

By varying the dimension parameters to test the working conditions of the system, a suitable set of dimensions is proposed to analyze the characteristics of the model, as presented in Fig. 2.

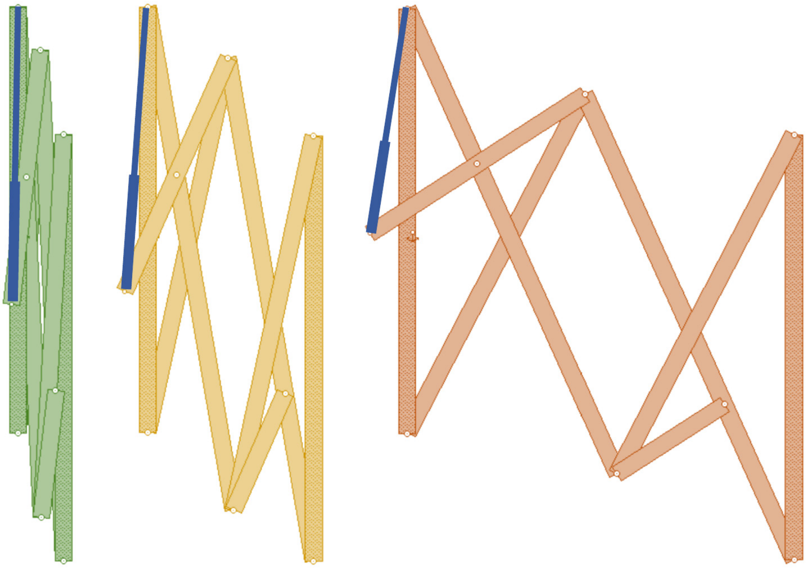

Fig. 1. Structure of the proposed with position of the linkage when cylinder operates

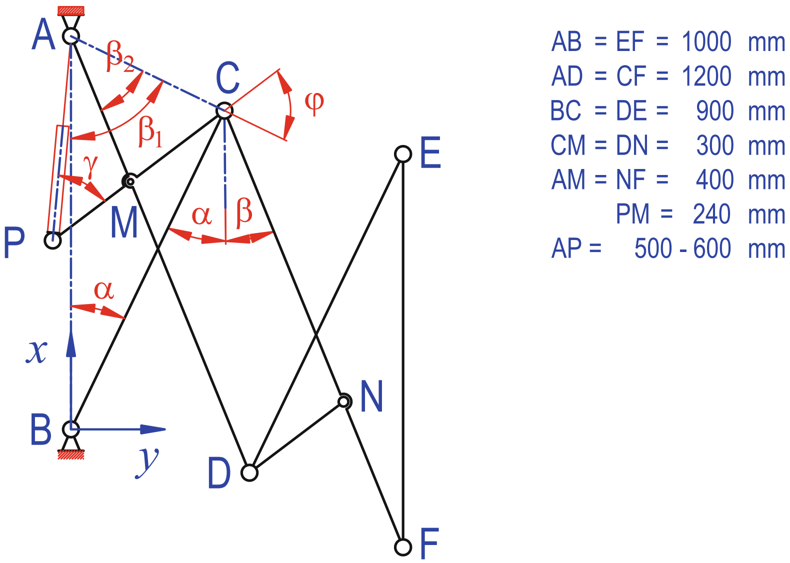

Fig. 2. Kinematic diagram of the structure

Based on the working characteristics of the system, the process of determining the kinematic positions of the components in the mechanism is as follows:

From triangular AMP:

$$\gamma = \arccos\left(\frac{\mathrm{AP}^2 + \mathrm{MP}^2 - \mathrm{AM}^2}{2 \cdot \mathrm{AP} \cdot \mathrm{MP}}\right) \tag{2}$$

From triangular ACP:

$$\mathrm{AC}^2 = \mathrm{AP}^2 + \mathrm{PC}^2 - 2 \cdot \mathrm{AP} \cdot \mathrm{PC} \cdot \cos\gamma = \mathrm{AP}^2 + \mathrm{PC}^2 - \mathrm{PC} \cdot \frac{\mathrm{AP}^2 + \mathrm{MP}^2 - \mathrm{AM}^2}{\mathrm{MP}}$$

$$\mathrm{AC}^2 = \mathrm{PC} \cdot \mathrm{MC} + \mathrm{AM}^2 + \frac{\mathrm{MC} \cdot \left(\mathrm{AM}^2 - \mathrm{AP}^2\right)}{\mathrm{MP}} \tag{3}$$

From triangular ACB:

$$\alpha = \arccos\left(\frac{\mathrm{AB}^2 + \mathrm{BC}^2 - \mathrm{AC}^2}{2 \cdot \mathrm{AB} \cdot \mathrm{BC}}\right)$$

$$\alpha = \arccos\left[\frac{\mathrm{MP}\left(\mathrm{AB}^2 + \mathrm{BC}^2 - \mathrm{MC}^2 - \mathrm{AM}^2 - \mathrm{MC} \cdot \mathrm{MP}\right) + \mathrm{MC}\left(\mathrm{AP}^2 - \mathrm{AM}^2\right)}{2 \cdot \mathrm{AB} \cdot \mathrm{BC} \cdot \mathrm{MP}}\right] \tag{4}$$

And

$$\beta = \beta_1 - \beta_2 = \arcsin\left(\frac{BC \cdot \sin\alpha}{\mathrm{AC}}\right) - \arcsin\left(\frac{\mathrm{MC} \cdot \sin\gamma}{\mathrm{AC}}\right) \tag{5}$$

For the coordinate system with the origin at point B, the coordinates of point F can be determined as a vector with:

$$\overrightarrow{\mathrm{BF}} = \overrightarrow{\mathrm{BC}} + \overrightarrow{\mathrm{CF}} \tag{6}$$

Due to the symmetric characteristic of the structure, the coordinates of point F can be determined as:

$$\begin{cases} x(\mathrm{F}) = \mathrm{BC} \cdot sin\alpha + \mathrm{CF} \cdot sin\beta \\ y(\mathrm{F}) = \mathrm{BC} \cdot \cos\alpha - \mathrm{CF} \cdot \cos\beta \end{cases} \tag{7}$$

Substituting the dimensions of the components link from Fig. 2 into the system (7), the coordinate trajectory of F can be determined based on the motion of the cylinder as shown in the diagram of Fig. 3:

The obtained result in Fig. 3 shows that trajectory of point F can be divided into two phase: the first where the cylinder retracts from L = 640 mm to L = 520 mm, with point F travels a relatively straight segment of Δx = 840 mm in length (Δy = 4.5 mm). And the second phase moves upwards (up to x > -240 mm).

Examining the displacement of the cylinder corresponding to the coordinate of F also reveals that the system's movement is not uniform. In the first 20 mm of retraction of cylinder (from 640 to 620 mm), point F traveled a distance of 345mm, while in the other operation of the cylinder (retraction from 520 to 500 mm), point F only moves only 64 mm.

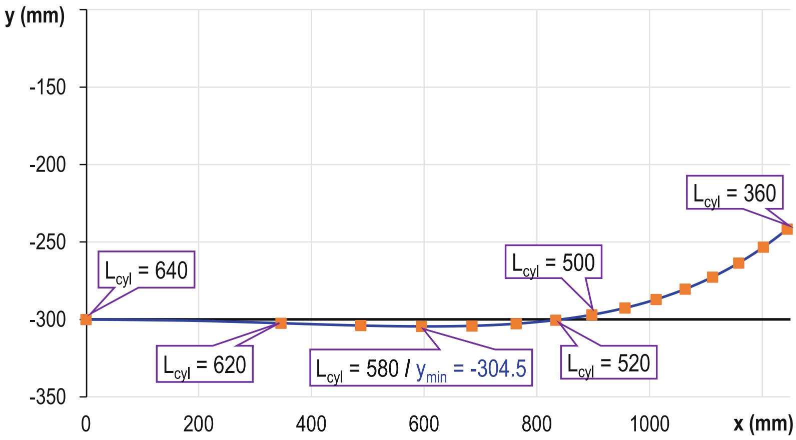

Fig. 3. Locus of point F during the operation of the cylinder

3 Force Analysis

As mentioned from the introduction, the proposed linkage is utilized in the structure of a staircase railing where most of the weight is placed on the post (EF), the spindles (the remaining frames connecting EF to the system), and the stair treads. During the movement of the linkage, the post and spindles play the guiding role in positioning and adjusting the stairs. Once it has reached the desired position, which unfolding the stairs, the post connects to the ground and transfers the whole load of in the mechanism downward, reduce the force on the cylinder. Therefore, the cylinder only operates when the post has not yet reached the desired position (position x specified by operators).

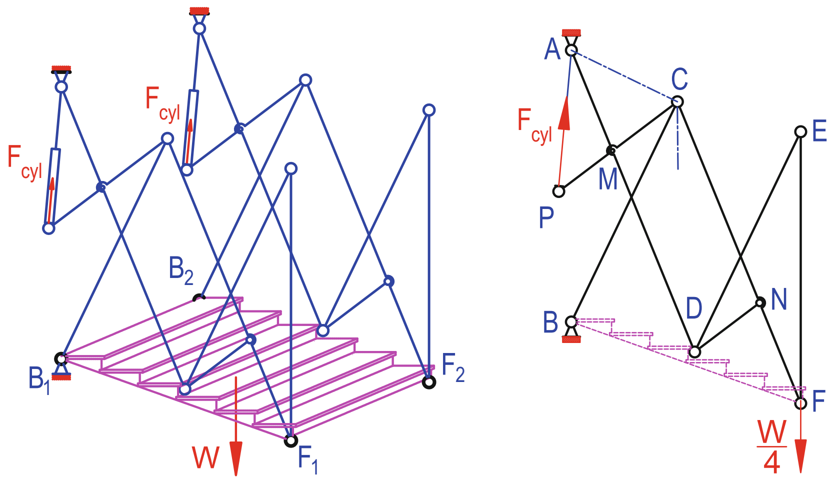

Fig. 4. Position of load P_G during the operation of the system

Assuming that the platform is slowly raised so that the effect of inertia in the system can be neglected, and the weights of component frames are small enough to be ignored, the weight of the stairs is then placed on four pins B_1, B_2, F_1, and F_2, with each pin bearing a load of $\mathbf{P} = \mathbf{W}/4$ (see Fig. 4). In order for the system to work stably, the force on the cylinder must be balanced by the minimum possible component from the stairs, $\mathbf{P} = \mathbf{W}/4$, during the movement of the system.

The process to calculate reactions on the structure can be illustrated in Fig. 5 as follows:

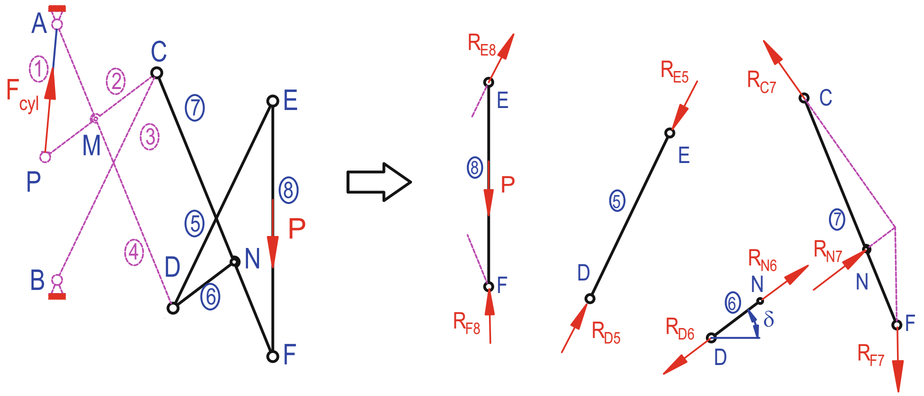

Fig. 5. Separating frames 5, 6, 7, and 8 to calculate reactions

According to Fig. 5, the reactions R_{E5} and R_{D6} at link 5 must lie on a line parallel to DE, which in turn requires that reaction R_{E8} is also parallel to DE. However, this force will generate a moment around point F for link 8 and result in a non-equilibrium state for this frame. Therefore, in order to achieve equilibrium for frame 8, the reaction at point E of this link must be zero, indicating:

$$\mathbf{R}_{E8} = \mathbf{R}_{E5} = \mathbf{R}_{D5} = 0 \tag{8}$$

and

$$\mathbf{R}_{F8} = \mathbf{R}_{F7} = \mathbf{P} \tag{9}$$

which also parallel to EF.

The same case for link 6, because these are two internal forces $\mathbf{R}_{D6}$ and $\mathbf{R}_{N6}$ in the link, these forces lie on a line parallel to DN with an angle $\delta = \varphi - \left(\frac{\pi}{2} - \beta_1\right)$ (see Fig. 2), which make three reactions in link 7 coincident, as presented in**Fig. 5**. Applying the equilibrium equations for the link:

$$\overrightarrow{\mathrm{R}_{\mathbf{N7}}} + \overrightarrow{\mathrm{R}_{\mathbf{F7}}} + \overrightarrow{\mathrm{R}_{\mathbf{C7}}} = 0 \tag{10}$$

and

$$\mathbf{T}_{\mathrm{C}} = CN.\mathbf{R}_{\mathrm{N7}}.\sin\left(\beta + \frac{\pi}{2} - \delta\right) - CF.\mathbf{R}_{F7}.\sin\beta = 0 \tag{11}$$

Solving Eqs. (10), and (11) for different position of link 7 with the load $\mathbf{P} = 500$ N. Result of this step is the magnitude of reactions in the links, corresponding the x-displacement of point F, as presented in Fig. 6.

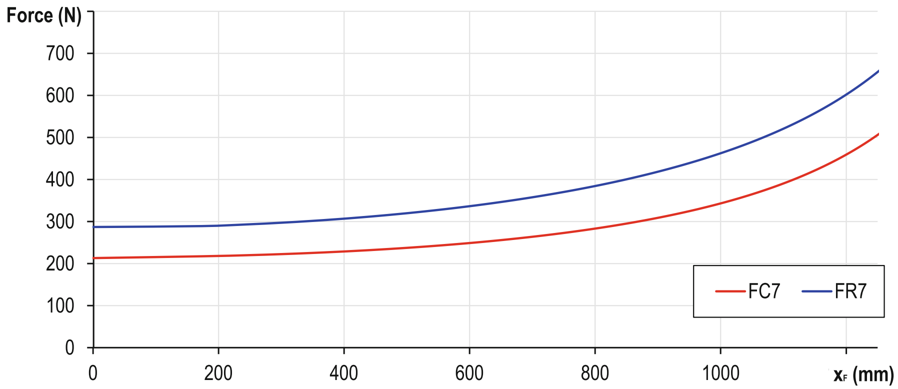

Fig. 6. Reactions on link 7 corresponding the displacement of point F in x-axis

To determine reaction on other links and thrust force in cylinder, the remaining linkage can be separated in two cases for calculate component forces, as illustrated in Fig. 7.

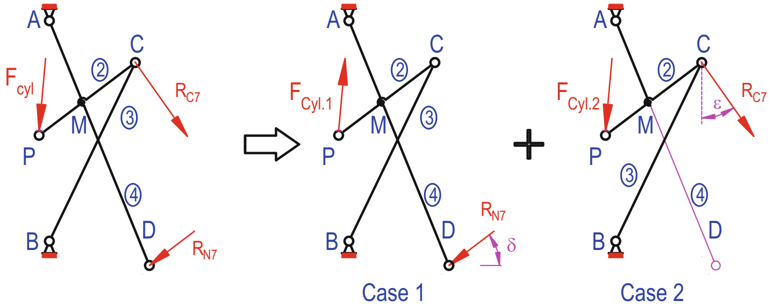

Fig. 7. Divide the mechanism in two cases of single force for cylinder thrust determination

The procedure to determine the component reactions from each case also follows the principle of equilibrium in each link after retracting them from the mechanism (see Fig. 8).

Apply equilibrium for the mechanism in these cases, component thrust force in cylinder can be calculated as:

$$F_{Cyl.1} = \frac{R_{M4} \cdot CM \cdot \sin\theta}{CP \cdot \sin\mu} = R_{N7} \cdot \frac{AD \cdot \sin\left(\frac{\pi}{2} - \delta + \beta\right)}{AM \cdot \sin(\gamma + \theta)} \cdot \frac{CM \cdot \sin\theta}{CP \cdot \sin\mu} \tag{12}$$

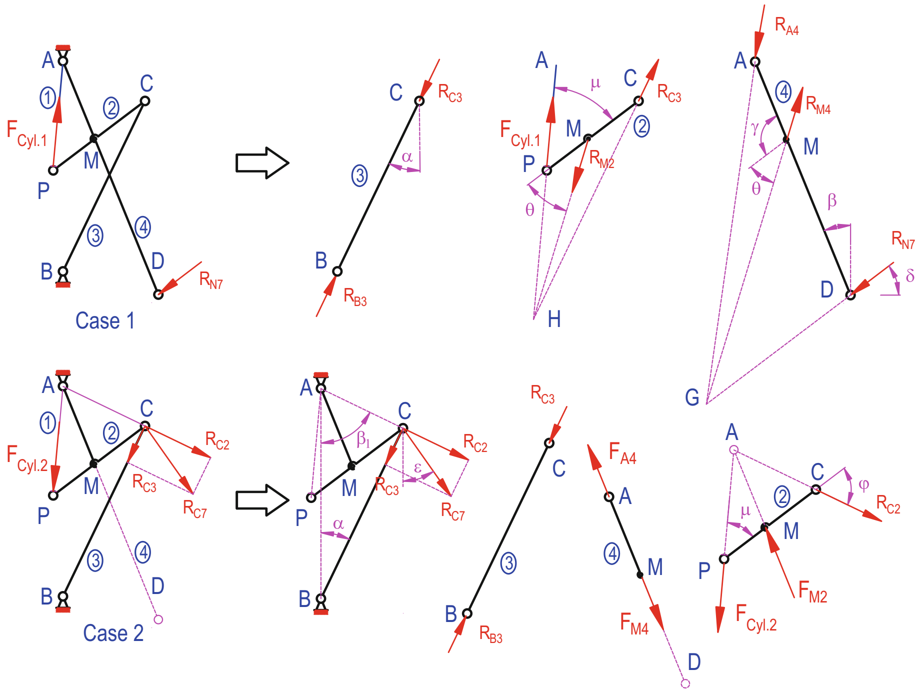

Fig. 8. Determination thrust force in two cases from the singular forces

and

$$F_{Cyl.2} = \frac{R_{C2} \cdot CM \cdot \sin\varphi}{CM \cdot \sin\mu} = \frac{R_{C7} \cdot \sin(\varepsilon + \alpha)}{\sin(\pi - \beta_1 - \alpha)} \cdot \frac{CM \cdot \sin\varphi}{CM \cdot \sin\mu} \tag{13}$$

According to Fig. 7, the total thrust on the cylinder of the whole system is determined from the equation:

$$F_{Cyl} = \left|F_{Cyl.1} - F_{Cyl.2}\right| \tag{14}$$

By assigning different position of the mechanism in Eq. (14), the magnitude of the thrust force during the operation of the cylinder can be determined, as shown in Fig. 9. It can be observed that the cylinder is influenced differently for each different load position. Specifically, while the reaction at point D causes the cylinder to expand ($F_{Cyl.1} < 0$), the reaction at point C tends to compress the cylinder ($F_{Cyl.2} > 0$). The combination of these two forces results in the difference between the two force values ($F_{Cyl.1}$ - $F_{Cyl.2}$).

To verify the accuracy of the calculated equations, a kinematic model with the same dimensions was constructed using the Working Model software. The thrust force on the cylinder was also extracted from the model by inputting the external force P and the cylinder's position, as shown in Fig. 10.

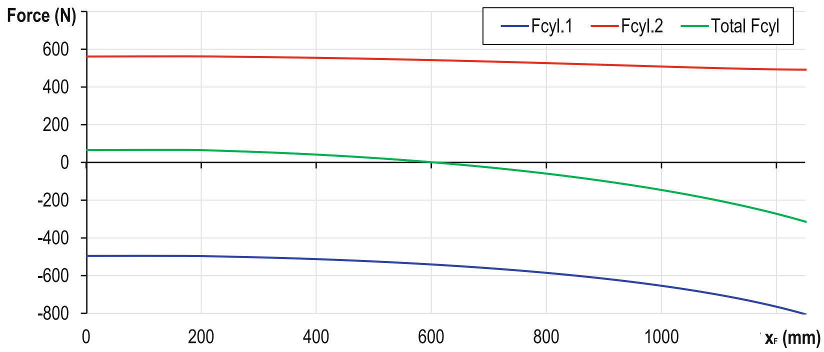

Fig. 9. The change of thrust force during the operation of cylinder.

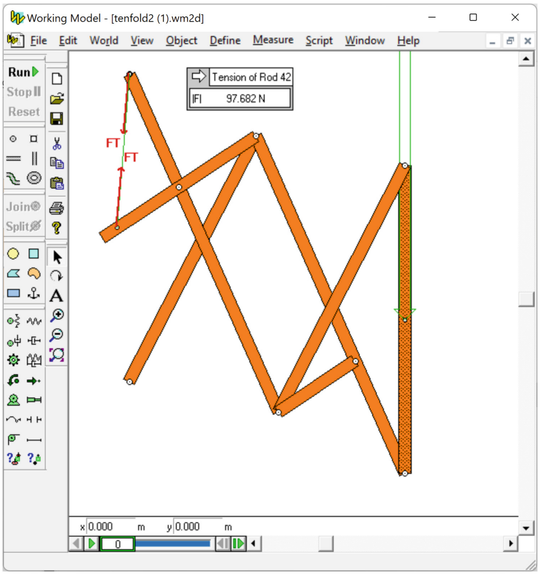

Fig. 10. Construction of a 2D model of the proposed structure in Working Model and extraction of the cylinder's thrust force.

Table 1 presents a comparison of the forces measured in the system using the two methods based on the displacement of the cylinder. The difference of reaction between the obtained results can be expressed as

$$\Delta = \left| \frac{F_1 - F_2}{F_2} \right| \tag{15}$$

in which F_1 is reaction measured from Working Model; F_2 is reaction obtained by the above equations.

It can be seen that with the differences are less than 1.7%, results from the table prove the accuracy of the calculation method in determining the reaction within the

Table 1. Comparing reactions between the calculation method and the simulation model.

		P = 5000 N			P = 1500 N		
		F_1 (N)	F_2 (N)	Δ(%)	F_1 (N)	F_2 (N)	Δ(%)
$L_{cyl} = 360$	F_{Cyl}	3083.54	3083.33	0.01	925.03	925.00	0.00
	F_{N7}	4999.90	5000.00	0.00	1499.96	1500.00	0.00
	F_{C7}	6490.12	6490.73	0.01	1947.75	1947.22	0.03
$L_{cyl} = 480$	F_{Cyl}	1245.45	1243.73	0.14	373.51	373.12	0.10
	F_{N7}	3272.91	3269.06	0.12	981.87	980.72	0.12
	F_{C7}	4419.5	4420.25	0.02	1326.06	1326.08	0.00
$L_{cyl} = 600$	F_{Cyl}	260.45	260.59	0.05	78.09	78.18	0.12
	F_{N7}	2361.26	2361.29	0.00	708.56	708.39	0.02
	F_{C7}	3180.04	3180.07	0.00	953.98	954.02	0.00
$L_{cyl} = 640$	F_{Cyl}	721.43	720.47	0.13	212.48	216.14	1.72
	F_{N7}	2180.96	2147.52	1.53	654.93	644.26	1.63
	F_{C7}	2824.58	2852.49	0.99	846.10	855.75	1.14

mechanism. These errors also suggest the existence of some environmental factors that affect the modeling result (friction, physical contact in joints and even the component link's weight during the simulation).

4 Conclusion

This study proposes a specific structure of a folding linkage operated by a cylinder. By analyzing the relationship between the positions of the component links using geometric methods, the load on the cylinder and the reaction on the component joints can be easily obtained. The results of the proposed model demonstrate the efficiency of applying simple mathematical equations in the design and calculation process. Additionally, this method can guide designers in selecting the appropriate configuration for a specific operational object. From the obtained results, the following conclusions can be drawn:

- By adjusting the dimensions of the component links, the system information such as working distance, cylinder maximum load, and reaction on joints can be accurately calculated. This allows for the selection of components without the need for constructing complex models for inspections or experiments.

- The accuracy of the proposed method is verified using the Working Model software, which further demonstrates the efficiency of using this graphical software in constructing 2D complex structures.

- Overall, the study highlights the effectiveness of the proposed approach in designing and analyzing folding linkages, providing valuable insights for future applications and improvements in this field.

Acknowledgments. The authors wish to thank Thai Nguyen University of Technology for supporting this work.

References

1. Tsai, L.W.: Mechanism design: enumeration of kinematic structures according to function. CRC Press (2000)
2. Nguyen Van, S.Y., et al.: A new study on optimization of four-bar mechanisms based on a hybrid-combined differential evolution and Jaya algorithm. Symmetry **14**(2), 381 (2022)
3. Schena, B.M.: Robotic arm with five-bar spherical linkage. U.S. Patent No. 8,506,556. 13 Aug (2013)
4. Doroftei, I.A., Bujoreanu, C. Doroftei, I.: Modeling and analysis of some planar deployable mechanisms. Part 1: translational bar mechanisms. In: IOP Conference Series: Materials Science and Engineering, vol. 997, no. 1, p. 012073. IOP Publishing (2020)
5. Doroftei, I. A., Bujoreanu, C., Doroftei, I.: Modeling and analysis of some planar deployable mechanisms. Part 2: curvilinear bar mechanisms. In: IOP Conference Series: Materials Science and Engineering, vol. 997, no. 1, p. 012074. IOP Publishing (2020)
6. Alaci, S., Doroftei, I., Ciornei, F.-C., Romanu, I.-C., Doroftei, I.-A., Ciornei, M.-C.: A New RP1PR Type Coupling for Shafts with Crossed Axes. Mathematics **11**(9), 2025 (2023)
7. Doroftei, I., Doroftei, I.A.: Dimensional synthesis and comparative simulation of two planar deployable mechanisms. In IOP Conference Series: Materials Science and Engineering, vol. 1262, no. 1, p. 012043. IOP Publishing (2022).
8. Doroftei, I. A., Bujoreanu, C., I. Doroftei.: Structural and kinematic aspects of some bar mechanisms for deployable structures. In IOP Conference Series: Materials Science and Engineering, vol. 591, no. 1, p. 012077. IOP Publishing (2019)

Investigation of the Particle Velocity of the Amorphous Powder

Vu Duong[1(✉)] and Le Hong Ky[2]

[1] School of Engineering Technology, Duy Tan University, 550000 Da Nang, Vietnam
vuduong@duytan.edu.vn

[2] Vinh Long University of Technology Education, VinhLong, Vietnam

Abstract. The kinetic energy of the particles in the thermal spraying plays an important role in establishing a strong adhesion bond in the collision process with the substrate. Many characteristics of the coatings depend on the particle velocity. The purpose of this research is to look into the effect of some parameters in plasma spraying using ordinary air as the plasma generation gas on velocity behavior. The feedstock material is a Fe-based amorphous alloy, a new competitive group of materials. A brief analysis of the publications on particle velocity in thermal spraying is presented in the introduction paragraph. The methodology paragraph consists of a description of the plasma spray system, the high-speed camera for measurement of the particle velocity, and the data processing for deviation from the regression equation. The series of plasma spraying occurs in the experiment paragraph when all of the main parameters, such as the current, the potential of plasma power, and the flow rate of the air, are changing to investigate the behavior of the particle of powder X-5. The analysis of the variation of parameters helps to evaluate their weight. The findings and discussions in the following paragraph explain the relationships between the process's main parameters. In conclusion, some recommendations for the design of the plasma torch are mentioned, and future solutions to increase particle velocity are proposed.

Keywords: Adhesion bond · High-speed camera · Regression equation · Amorphous alloy · Performance of coating

1 Introduction

In comparison with the common construction of a plasma torch, the inventors in [1] developed a special plasma torch with a mixing two-chamber design, and the particle velocity can be reached up to 500 m/s. It limited the applicability in terms of the analysis of other main parameters, such as plasma power and the flow rate of gas. The study did not mention the principal scheme of measurement using a high-speed camera. The other model, which takes into account all main parameters of supersonic plasma spraying [2], is a significant improvement, but they did not apply the analysis of variation using the regression equation. Anyway, for some predominant plasma torch operating parameters, they presented an empirical formula as follows:

$$V_{max} = 24.3 \text{ x } 10^{-3} \text{x } I^{0.43} \text{x } d^{-1.96} \text{x } G^{0.21} \tag{1}$$

D. C. Nguyen et al. (Eds.): ICERA 2023, LNNS 944, pp. 96–101, 2024.
https://doi.org/10.1007/978-3-031-62235-9_12

Thus, in [3], the research team showed that the higher drag coefficient for the non-spherical particle decreased the velocity, leading to a lower impact on the performance of the coating. The critical value, under which adhesion is not established due to insufficient kinetic energy to create stable physical contact, highlighted the importance of particle velocity in cases of fast and deformable collisions [4]. A very interesting and valuable study in [5] shows that the droplet velocities and droplet diameters may vary by over two orders of magnitude. This variation makes the velocity and the diameter of the particle inadequate. V. I. Bogdanovich's significant progress in [6] involves the establishment of criteria for permissible dispersion of particle diameters, but they unfortunately derive a typical mathematical model without any experiment verification. The importance of the measurement procedure for particle velocity was presented in detail by Uroz Hudomalj et al. [7]. Based on the discussion, the goal of this study was to investigate the influence of the main parameters in plasma spraying of the Fe-based amorphous powder on particle velocity in order to reveal new findings in terms of new materials with specific physical and mechanical properties. A novel empirical formula for predicting particle velocity was presented. The result of the study can be used to make recommendations for the engineering process.

2 Methodology

Atmospheric plasma spraying was utilized in our experiment (SG-100 TAFA-Praxair, USA). Ordinary air serves as the main gas, while nitrogen serves as the carrier gas. [8] describes the chemical composition of X-5 powder. The chemical composition of Fe-base powder (X-5) was analyzed by energy dispersive spectroscopy with the equipment SEM, SM-6510LV, Japan. The coating from powder X-5 had a competitive hardness, especially after heat treatment reaching up to 54–56 HRC [8]. Table 1 shows the chemical composition of powders X–5. The Shimadzu HPV-1 high-speed camera is used to monitor the velocity of spraying particles [9]. The ANOVA method was used to analyze the particle velocity measurement data.

Table 1. Chemical composition of powder X-5

Sample Code	C	Cr	B	Mo	Ni	Mn	Si	Nb	V	W	Fe
X-5	0.73	5.0	0.25	4.20	–	1.25	0.84	0.54	1.20	–	remain

3 Experiment and Result

3.1 Regression Equation and the Analysis of the Variation

Table 2 shows the results of a series of experiments with different input spraying settings and particle velocity measurements.

Table 2. Result of plasma spraying of the powder X-5

no	Plasma curent, I [A]	Potential, U [v]	Flow rate G, [g/s]	Particle velocity, V [m/s]
1	120	140	0.46	15
2	120	160	0.55	23
3	120	170	0.75	31
4	120	180	0.94	39
5	120	195	1.42	56
6	120	205	1.76	67
7	120	215	1.85	71
8	120	225	2.6	89
9	150	145	0.55	20
10	150	155	0.76	29
11	150	200	1.13	53
12	150	210	1.76	72
13	150	240	1.95	84
14	150	250	2.92	107
15	180	145	0.55	22
16	180	155	0.75	32
17	180	170	0.94	42
18	180	200	1.13	56
19	180	210	1.42	67
20	180	220	1.76	79
21	180	240	1.95	90
22	180	250	2.92	117
23	200	145	0.55	28
24	200	160	0.75	39
25	200	170	0.94	48
26	200	200	1.13	63
27	200	205	1.42	73
28	200	210	1.76	84
29	200	240	1.95	98
30	200	250	2.92	117
31	220	145	0.55	31
32	220	160	0.75	42

(*continued*)

Table 2. (*continued*)

no	Plasma curent, I [A]	Potential, U [v]	Flow rate G, [g/s]	Particle velocity, V [m/s]
33	220	170	0.94	51
34	220	180	1.13	60
35	220	195	1.42	73
36	220	207	1.76	86
37	220	225	1.85	95
38	220	240	2.6	117
39	220	250	3.17	132

The experimental results have been processed using Minitab software and have been preliminary analyzed.The result of the first round shown that for two-way interactions between I and G and U and G, p-values are larger than the precision of a = 0.05, namely p-Value$_{I*G}$ = 0.951 and p-Value$_{I*G}$ = 0.668. They can be removed in the regression equation and the second round of analysis helped to ignore the coefficient for the interaction U^2 (p-value for U^2 is 0.835). It is needed to remove this coefficient and continue the next round of the analysis of variation in the regression equation and the analysis of variation (Table 3).

Table 3. Analysis of variation (ANOVA

Source	DF	Adj SS	Adj MS	F-Value	P-Value
Model	6	36488.7	6081.44	4302.16	0.000
Linear	3	27602.7	9200.89	6508.93	0.000
I	1	1642.1	1642.08	1161.65	0.000
U	1	193.5	193.49	136.88	0.000
G	1	736.6	736.61	521.10	0.000
Square	2	113.3	56.63	40.06	0.000
I^2	1	47.4	47.41	33.54	0.000
G^2	1	34.5	34.45	24.37	0.000
2-Way Interaction	1	63.4	63.37	44.83	0.000
IU	1	63.4	63.37	44.83	0.000
Error	32	45.2	1.41		
Total	38	36533.9			

The regression equation in Uncoded Units:

$$V = 3.39 - 0.4498\,I + 0.0992\,U + 32.98\,G + 0.001158\,I^2 - 2.520\,G^2 + 0.001215\,IU \tag{2}$$

3.2 Preliminary Optimization of the Particle Velocity

It is useful to analyze the conditions for the localization of the optimum area for particle velocity because it provides good coating quality, such as density, adhesion, cohesion strength, and so on [10]. Based on the experiment data, the following boundary conditions have been selected according to (2)

$$120 \leq I \leq 220,\ 140 \leq U \leq 250,\ 0.46 \leq G \leq 3.17 \tag{3}$$

The first preliminary localization of the optimum in the planning area: I = 220 A; U = 250V and G = 3.17 g/s.

4 Analysis and Discussion

According to the regression equation, voltage has the largest influence on particle velocity (1). The plasma current is responsible for the second degree of impact. The air flow rate had a positive effect on particle velocity as well. An increase in plasma electric current creates an increase in the number of electrons, which increases ionization and generates more heat. It is vital to remember, however, that the particle velocity is smaller than the plasma jet velocity according to the dynamic phenomenon. The empirical formula can be employed as the dominant answer in the context to bridge the gap between the theoretical prediction and the experiment.

5 Conclusion

The impact of various essential factors, such as plasma jet power, gas flow rate, and particle average size, on particle velocity in atmospheric plasma spraying utilizing ordinary air as the plasma production gas is seen in the case of deposition powder X-5. The increase in plasma power and gas flow rate aid in increasing particle in-flight velocities. The critical velocity is an essential condition for deposition, and its value determines the process's efficiency.The mathematical model using the method of multi-criteria planning and design of experiments is well adapted to the experiment data and can be recommended to find the optimum of the particle velocity when some other related parameters will be involved, and a more complete planning experiment can be designed in a future study.It is useful to make some corrections to the theoretical calculations of the particle velocity, taking into account the morphology of the particles and their size distribution.

References

1. Cliari, F.R., Miranda, F.S., Reis, D.A.P., Filho, G.P., Charakhovski, L.I., Essiptchouk, A.: Plasma torch for supersonic plasma spray at atmospheric pressure. J. Mater. Process. Technol. **237**, 351–360 (2016). https://doi.org/10.1016/j.jmatprotect.2016.06.027
2. Wei, P., Wei, Z., Zhao, G., Bai, Y., Tan, C.: Effect of processing parameters on plasma jet and in-flight particles characters in supersonic plasma spraying. High Temp. Mater. Proc. **35**(8), 775–786 (2016). https://doi.org/10.1515/htmp-2015-0077
3. Mess, J., Anasenzl, M., Ossenbrink, R., Michailov, V.: Influence of particle velocities on adhesion strength of cold spray inner diameter coatings. J. Thermal Spray Technol. **31**(7), 2025–2038 (2022). https://doi.org/10.1007/s11666-022-01439-4
4. Profizi, P.: Development of a Numerical Model of Single Particle Impact with Adhesion for Simulation of the Cold Spray Process, These de Doctorate de L'universite de Lyon, N0 d'ordre NNT :2016LYSE1088. http://theses.insa-lyon.fr/bublication/2016LYSE1088/these.pdf. (2016)
5. Kolakaluri, R., Subramaniam, S., Panchagnula, M.V.:Trends in multiphase modeling and simulation of sprays. Int. J. spray combust. Dyn. **6**(4), 317-356 (2014)
6. Bogdanovich, V.I., Giorbeldze, M.G.: Mathematical modelling of powder material motion and transportation in high-temperature flow core during plasma coatings applications. In: IOP Conference series: Material Science and Engineering, **327**, 022036 (2018). https://doi.org/10.1088/1757-899X/327/2/022036.
7. Hudomalj, U., Fallahi Sichani, E., Weiss, L., Nabavi, M., Wegener, K.: Importance of measurement and evaluation procedure of particle state in atmospheric plasma spraying. J. Therm. Spray Technol. **32**(2), 548–558 (2022). https://doi.org/10.1007/s11666-022-01495-w.
8. Vu, D., Thu, Q.L.: The correlation between main parameters in the air-plasma spraying of fe-based amorphous coatings. In: The Proceedings of the International Conference on Advanced Mechanical Engineering, Automation and Sustainable Development (AMAS 2021), November 04–07,2021, Ha Long city, Vietnam, Lecture Notes in Mechanical Engineering, Springer Publisher, 499–506 (2022). https://doi.org/10.1007/978-3-030-99666-6_72
9. Buchman, N.A., Cierpka, C., Kahler, C.J.: Ultra high speed 3D astigmatic particle tracking velocimetry: application to particle-laden supersonic impinging jets. Exp fluids, **55**, 1842 (2014).https://doi.org/10.1007/s00348-014-1842-1.
10. Antony, J.: Design of Experiments for Engineers and Scientists, Second Edition, Elsevier Publisher, MA 02451, USA (2014)

Investigations on Drilling of Al/CFRP/Ti Stacks Using Micro Grooved Drills

S. Samsudeensadham[1], V. Krishnaraj[1], and R. Zitoune[2,3](✉)

[1] PSG College of Technology, Coimbatore 641004, India
[2] Institut Clément Ader, UMR CNRS 5312, University of Toulouse, Toulouse, France
redouane.zitoune@iut-tlse3.fr
[3] College of Design and Engineering, National University of Singapore, 9 Engineering Drive 1, Singapore 117575, Singapore

Abstract. This paper presents a comprehensive study of the drilling of hybrid Al/CFRP/Ti stacks, which is a critical operation in the assembly of aerospace structures. The intricate amalgamation of aluminum alloy, carbon fiber reinforced polymer (CFRP), and titanium alloy in the stack introduces complex material interactions during drilling. The current work is aimed at evaluating and comparing the surface quality of the Al/CFRP/Ti stack holes drilled by standard and micro-grooved drills under minimum quantity lubrication (MQL) conditions. The experimental investigation is carried out by varying cutting parameters such as cutting speed and feed. In this study the influence of the machining parameters and tool geometry (drilling with micro-grooved and standard drills) on thrust force and torque under MQL conditions have been investigated. Furthermore, the substantial impact of thrust force variations resulting from diverse material stacking on the surface quality (delamination of CFRP, surface roughness) of the holes is highlighted. Circularity characteristics and hole diameter errors are also scrutinized for both drills. The findings offer valuable insights for optimizing the drilling of hybrid Al/CFRP/Ti stacks across industries that demand advanced materials and machining techniques.

Keywords: Drilling · Al/CFRP/Ti · Micro-Groove

1 Introduction

Aircraft play a crucial role in modern society, serving as an essential means of transporting people, goods, and for defence purposes worldwide. These flying machines represent a remarkable achievement for humanity, made possible through the innovative combination of hybrid materials, specifically carbon fiber-reinforced plastics (CFRP) and titanium alloys. These materials are chosen for their exceptional qualities, including stiffness, resistance to corrosion, high specific stiffness, and a favorable weight-to-strength ratio, resulting in reduced fuel consumption. In today's aerospace sector, lightweight metals like titanium alloys are coupled with multi-layer composite structures like CFRP, integrated into the aircraft's fuselage. Additionally, aluminum alloys, known for their

D. C. Nguyen et al. (Eds.): ICERA 2023, LNNS 944, pp. 102–113, 2024.
https://doi.org/10.1007/978-3-031-62235-9_13

ductility, strength, toughness, resistance to fatigue, corrosion resistance, and favorable weight-to-strength ratio, are also incorporated within the CFRP-titanium alloy arrangement. Pioneering aircraft models have already embraced these combinations, using Aluminum, CFRP, and Titanium composites in various components, including wings and tails. Presently, researchers are intensively exploring the potential of applying these three-material composites throughout the entire aircraft fuselage [1, 2]. Apart from their advantages, these materials have demerits such as higher hardness and lower thermal conductivity of Ti alloy [3], abrasive nature of CFRP [4], and ductile nature of aluminium alloy [5] leads to more complications in the drilling process in terms of poor surface integrity and rapid tool wear.

The use of modified drills is pivotal in achieving high-quality holes when drilling hybrid composite-metal stacks. These specialized tools ensure precise and controlled machining, minimizing delamination, burrs, and material damage. Consistent hole quality enhances structural integrity and performance in aerospace applications, ensuring the reliability of composite-metal hybrid components [6, 7]. Several investigations were performed on the drilling of distinct aerospace materials such as Al alloy, Ti alloy, Inconel 718 alloy, and CFRP materials. The researchers investigated the effectiveness of micro-grooved drills during the drilling of Inconel-718 alloy and Ti alloys. The laser surface technology and Wire-EDM techniques were used to fabricate the different patterns of micro grooves on the rake faces of the cutting tools, further, the micro texture imposed by cutting tools effectively minimizes the cutting forces and friction-induced temperatures during machining [8, 9].

Previous research has primarily focused on drilling either CFRP/Ti or Ti/CFRP stacks, however, investigations involving Al/CFRP/Ti hybrid stacks are scarce, and often limited to two materials. This research investigation addresses this gap by evaluating the drilling performance of three-material stacks under micro-textured tools, additionally, the performance of the tool is enhanced by minimum quantity lubrication (MQL) conditions to achieve better surface integrity of drilled CFRP holes.

2 Materials and Methods

2.1 Materials

In this study the hybrid Al/CFRP/Ti stacks are fabricated and fastened at their ends as shown in Fig. 1. The total size of the multi-stack specimen is $300 \times 5 \times 16.25\ mm^3$. Aluminium 7075 alloy with T6 grade of 6 mm was selected and placed as the top layer of the multi stack. Al-7075 alloy has high strength and it also does not have the same level of corrosion resistance or weldability that other common alloys possess. Its resistance to stress and strain makes it highly useful in aerospace applications where it allows for weight savings. In this study T700-M21 grade of CFRP material with 4.25 mm thickness was selected as a middle layer of the multi-stack The CFRP composite was made up of a unidirectional prepreg (T700-M21) and was cured using autoclave. The lay-up sequence of the CFRP laminate was [90/-45/0/45/90/-45/0/45]s. The grade-5 Ti-6Al-4V alloy with 6 mm thickness was selected as the bottom layer of the multi-stack material. Grade 5 Titanium is known as the “workhorse” of titanium alloys. Ti6Al4V is the most commonly used of all titanium alloys. It accounts for 50 percent of total titanium usage the world over.

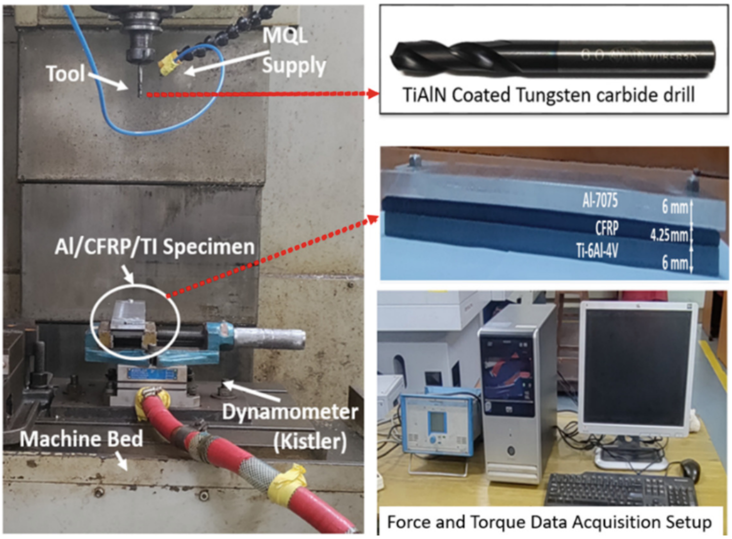

Fig. 1. Experimental setup

In this study, the multi-stacks were drilled by two types of 6 mm tungsten carbide drills such as the standard twist drill and the same drill imposed with laser engraved microgrooves. The parallel pattern of micro-grooves are fabricated on the rake and flank faces of the drill (as shown in Fig. 2) to minimize the friction and store the lubricants during drilling under MQL conditions [10]. In general, the micro-grooves act as micro-pool reservoirs to minimize the heat and friction produced during the drilling process [11]. The flank and rake face micro groove imposed drill is shown in Fig. 2. In this study the micro grooves are fabricated based on the dimensions of diameter as 50 µm, pitch as 100 µm and depth as 40 µm.

2.2 Experimentation

Experiments were carried out with a cutting speed of 20 m/min, to 35 m/min, and a feed rate of 0.03 mm/rev to 0.09 mm/rev. Four levels of speed and feed were considered between these limits. Further, the total number of experiments was designed using Taguchi L16 design of experiments. The Taguchi L16 design of experiments provides 16 different combinations of drilling parameters. Experiments were carried out using the MAKINO S33 machining centre which has a magazine capacity of 20 tools and operates at a maximum speed of 6000 rpm. The Al/CFRP/Ti stacks were clamped on the KISTLER-9257B dynamometer (as shown in Fig. 1) to measure thrust force and torque during drilling. Experiments were performed under MQL conditions. The lubricant oil LRT-30 grade was used and mixed with compressed air to form the minimum quantity

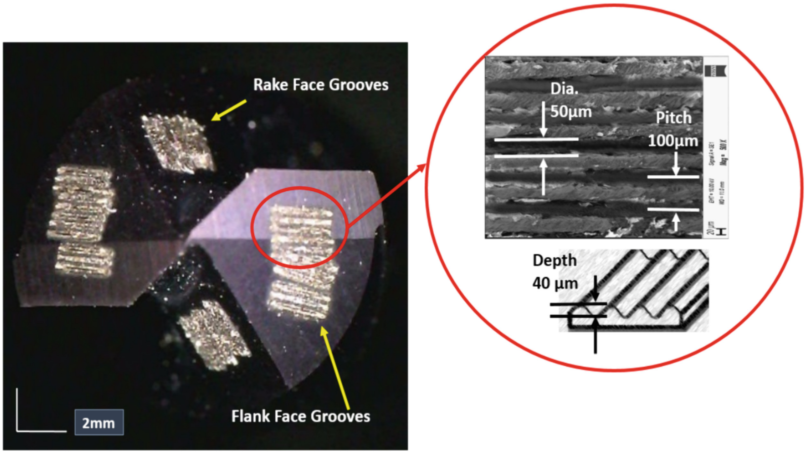

Fig. 2. Micro grooved drill and groove dimensions

of lubrication. Initially, the experiments were conducted with a standard drill and then the micro-grooved drill was used to conduct the same set of experiments. The output parameters such as thrust forces and torque and further, the delamination factor of CFRP, surface roughness and roundness variations of CFRP were studied by dismantling the stacks.

3 Results and Discussions

3.1 Analysis on Thrust Forces

In general thrust forces in the drilling process is produced could be attributed to the drill tool against the work materials to remove the unwanted materials. The thrust force is identified as one of the major parameters to determine the machinability characteristics of different distinct materials and multi-stacks in terms of the surface integrity of drilled holes and the life span of the tool [12]. Figure 3(a-b) shows the variation of thrust forces with respect to standard and grooved drill during the process of drilling Al/CFRP/Ti stacks. Figure 3 (a) provides the thrust force variations Al/CFRP/Ti stacks as three zones during drilling with micro grooved drill. At the initial zone, there is a steep rise of thrust force was observed due to the sudden entry of minor and major cutting edges of the drill into the top layer of the stack (aluminum alloy). Further, a constant level of thrust forces was observed around 100N due to the full engagement of the drill into the aluminum alloy. During the second zone, a sudden drop of thrust forces was observed, where the drill started to enter into the CFRP material, further, it maintained a constant level around 50N. During the third zone, the drill bit started to enter into the titanium alloy, where it reached the maximum level of thrust forces up to 270N. The variation in thrust forces is due to the different mechanical characteristics of distinct materials. However, these variations are pretty high while performing the same experiment with a standard twist drill. Figure 3(b) presents the thrust force variations of drilling Al/CFRP/TI stacks under a grooved drill. In fact, this variation is estimated around 50N of increase in thrust forces was observed concerning Al, CFRP, and Ti as a whole. Based on the observations from Fig. 3(a) it is noted that micro groove plays a major role in decreasing the thrust forces, moreover it acts as a micro pool reservoir to store certain amount of lubricants.

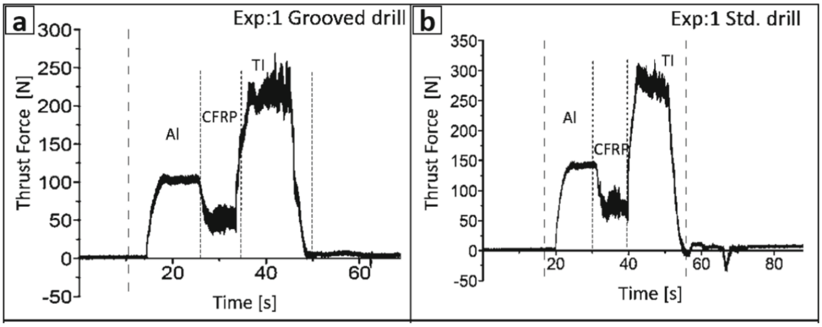

Fig. 3. Variation of thrust forces during the drilling of hybrid Stacks

The experiments were performed with the standard and micro grooved drill for all 16 different experimental runs. The average thrust force data of each material (Al, CFRP, and Ti) is collected separately from the various stages of the combined thrust force plot acquired from the KISTLER dynamometer as shown in Fig. 3. The thrust forces measured from both type of tool is compared and presented in Figs. 4, 5 and 6 such as thrust forces of the Al-7075 phase, CFRP phase, and TI-6Al-4V phase respectively. An increase in feed rate increases the thrust force, due to the chip thickness and higher cutting resistance at higher feed rates. This increasing trend of thrust force is comparatively high in drilling titanium alloy phase due to the higher hardness induced high cutting pressure, furthermore, the increase in feed rate accelerates more removal (MRR) [3]. The increase in thrust concerning increase in feed was followed by Al alloy and CFRP material. Based on the observations from the Figs. 4, 5 and 6 the thrust force produced by micro grooved drill is lower than the un grooved drill.

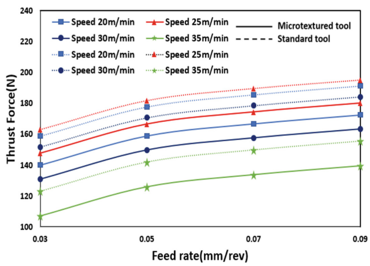

Fig. 4. Effect of Feed on Thrust –Al-7075

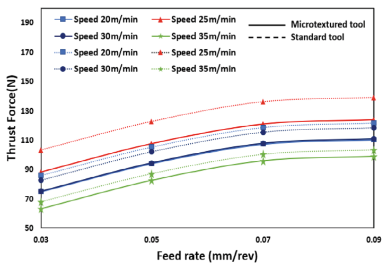

Fig. 5. Effect of Feed on Thrust – CFRP

The performance of both drills tested is better at maximum cutting speeds, especially at 35 m/min minimum thrust force is recorded for both geometries. This reduction in

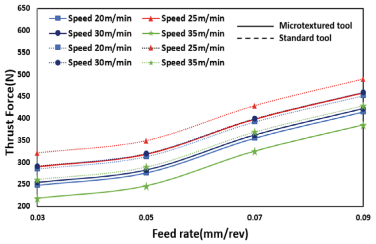

Fig. 6. Effect of Feed on Thrust – Ti-6Al-4V

thrust force could be attributed to the friction between the cutting edges of the drill bit and the workpiece at higher speeds. This friction generates heat, which may lead to the softening of the material being drilled. This softening can reduce the resistance to drilling, resulting in less thrust being required.

3.2 Analysis on Torque

Analyzing torque in the drilling of multi-stacks provides critical insights into machining efficiency, tool wear, and material properties. It aids in optimizing cutting parameters, minimizing energy consumption, and ensuring product quality and reliability in industries such as aerospace, automotive, and manufacturing [13]. The magnitude of toque is acquired from the dynamometer during the drilling of Al/CFRP/Ti stacks and averaged as a single magnitude for each material Figs. 7, 8, and 9 show the variations of torque concerning the various feed and speed conditions. The dotted lines indicate the torque data obtained from the grooved drill, whereas the continuous lines indicate the torque obtained from the standard drill.

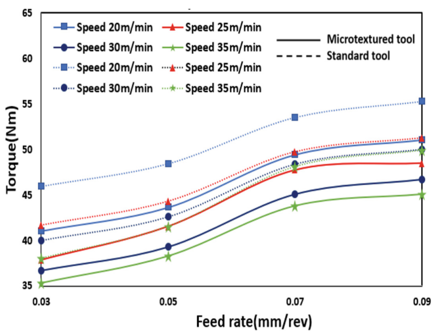

Fig. 7. Effect of Feed on Torque –Al-7075

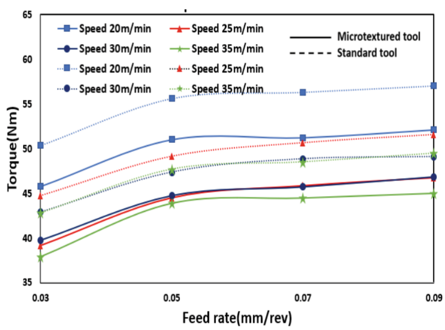

Fig. 8. Effect of Feed on Torque – CFRP

While comparing the increasing trend of Al-Phase torque (ref. Fig. 7) with respect to the remaining two materials (CFRP and Ti) torque, a higher magnitude of increase in torque is observed during the drilling of Al-phase (around 10 Nm) followed by CFRP and Ti alloy. This could be attributed to the formation of buildup edge during the drilling of aluminum alloy results in increased torque values, whereas this increasing trend is

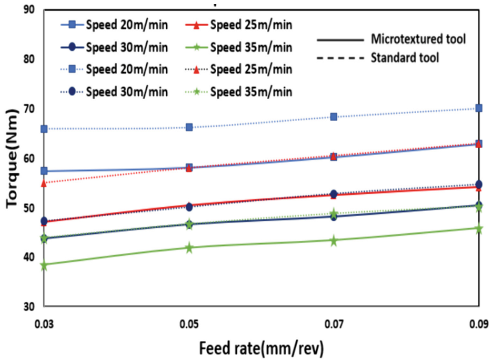

Fig. 9. Effect of Feed on Torque – Ti-6Al-4V

minimized to a certain extent during the interaction of the drill with CFRP because the drill tool enters the CFRP after completing the drilling of Al alloy, also the CFRP fibers act like hard brushes to remove the unnecessary build-up edge materials surrounded on the cutting edges of the drill. Furthermore, the same effect enhances the drilling of the third phase (Ti) of the multi-stack. Also, the torque produced by the micro-grooved drill is comparatively lower than the standard drill this can be attributed to the reduced friction induced by microgrooves [14].

3.3 Analysis on Delamination Factor of CFRP

Measuring the delamination factor of CFRP (Carbon Fiber Reinforced Plastic) during drilling with metallic stacks is crucial for assessing drilling quality, preventing structural defects, and ensuring aerospace component integrity. Measuring the delamination factor of CFRP typically involves non-destructive testing methods like ultrasonic inspection or visual examination, aiming to identify and quantify any internal layer separation or damage [13]. In this study the entry delamination of CFRP was observed by dismantling the multi-stack assembly also, the delamination factor was determined by visual examination using a dinolite digital camera.

Figure 10 compares the occurrence of push-out delamination with two different drills during drilling CFRP via Al alloy. Based on the study it is observed that the occurrence of delamination was higher in the experiments conducted with a grooved drill, especially at lower speed conditions. This phenomenon could be correlated to the lack of chip breakability and delay in the chip removal process at lower speed conditions. Compared to the standard drill, the grooved drill has got almost negligible push-out delamination failure with respect to an increase in speed (eg. Speed 30 and 35 m/min). This could be because of a decrease in thrust force and an increase in chip breakability with a grooved drill compared to a standard drill at higher speeds.

Based on the analysis of delamination, it is more evident that the effectiveness of the grooved drill was observed much better at a higher level of machining parameters, whereas the effectiveness of the standard drill was observed much better at a lower level of drilling parameters. The delamination factor (D_f) was determined by the ratio of the

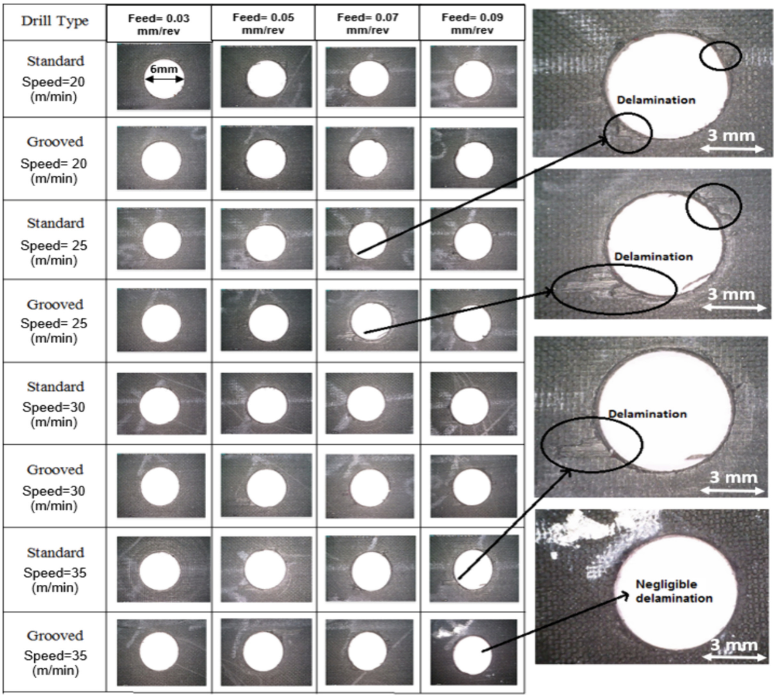

Fig. 10. Effect of groove drill on delamination of CFRP

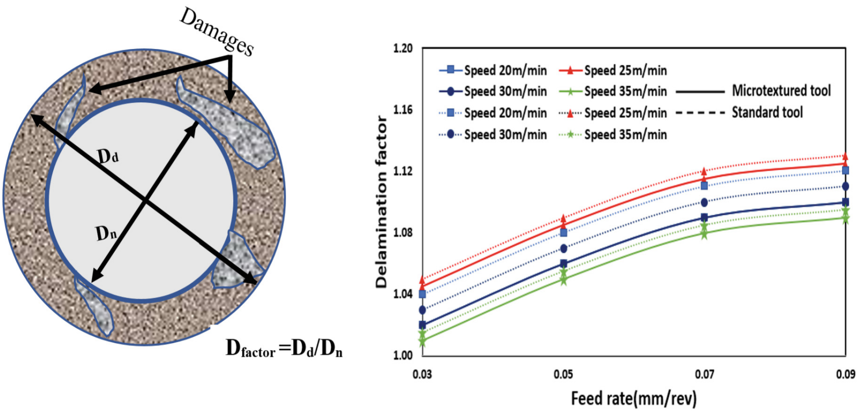

Fig. 11. Delamination factor of CFRP

maximum delaminated diameter (D_d) and the nominal hole diameter (D_n). Figure 11 presents the schematic representation of the measurement of the delamination factor (D_{factor}) and the effect of feed rate on D_{factor}. The delamination factor of the CFRP hole drilled with a grooved drill was lower than the hole drilled with ungrooved drill. The effective breaking of Ti chips by the presence of the grooves at the rake face and reduction in thrust forces minimizes the damages of delaminations at the drill entry zones of CFRP.

3.4 Analysis on Surface Quality Characteristics of CFRP

Measuring the surface integrity of Carbon Fiber Reinforced Plastic (CFRP) takes on heightened significance when compared to the assessment of surface quality in metallic materials, particularly in the context of CFRP's interaction with stacked materials like Al and Ti alloys. CFRP's intricate surface texture plays a pivotal role in its structural integrity and overall performance.

Therefore, precise and meticulous surface quality evaluation becomes paramount in optimizing the mechanical and functional characteristics of CFRP composites, ensuring their reliability in demanding applications [13, 14]. The surface quality investigations of metallic materials were comfortably ignored due to the homogeneous nature and structural stability of th metals such as Al and Ti Alloy, also, these alloys produce a negligible deformations across its hole wall surfaces.

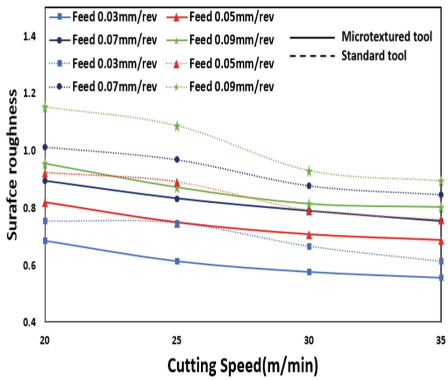

Fig. 12. Effect of speed on roundness –CFRP

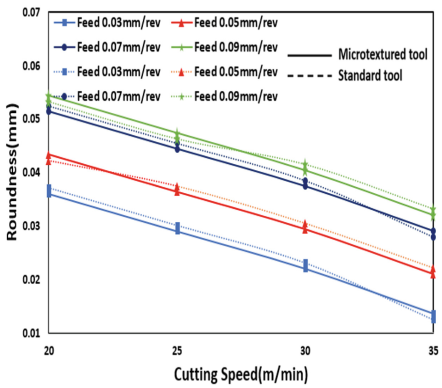

Fig. 13. Effect of speed on roughness – CFRP

Figure 12 presents the effect of cutting speed on the roundness of the CFRP hole wall. As the cutting speed increases there is a decrease in roundness error was observed due to the high speed induced high-temperature results in perfect resin smearing across the CFRP hole wall, especially this phenomenon is highly activated at low feed and high-speed conditions. Further, the negligible effect of microgroove was observed concerning various speed and feed conditions. Similarly, Figs. 13 and 14 provides the variations of surface roughness (μm) and hole diameter error (mm). Increasing the cutting speed during CFRP drilling leads to a notable reduction in surface roughness and diameter errors, especially with metallic stacks like Al/CFRP/Ti. This increased speed minimizes the material deformation, producing cleaner, smoother holes. The dynamic interaction between the drill and composite, coupled with higher velocities enhances the hole quality by continuous wiping action across the hole wall surface of CFRP [17–20]. Further, it decreases the surface irregularities and enhances the overall machining quality. Based

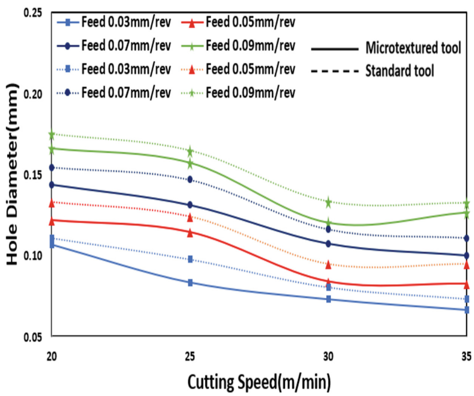

Fig. 14. Effect of speed on hole diameter error– CFRP

on the analysis of the effect of the machining parameters on the machinig quality, it can observed that, the surface quality of CFRP is better at experimental run 13 such as higher speed and lower feed rate combinations (speed-35 m/min and feed-0.03 mm/rev). Furthermore, the experimental run 13 provides the reduced magnitudes of thrust and torque.

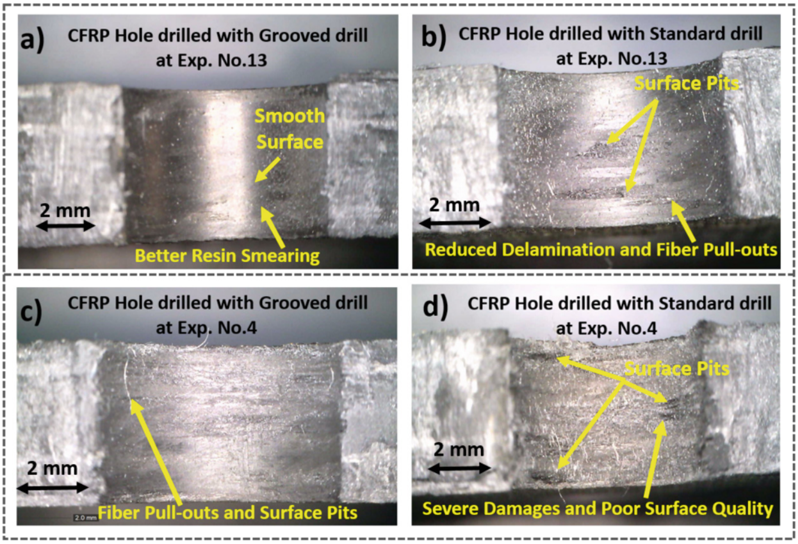

Fig. 15. Effect of maximum and minimum cutting speed on CFRP hole surface quality

Figure 15 shows the captured images of the CFRP hole wall cross-section. Figure 15 (a-b) shows the CFRP holes drilled with high speed-35 m/min and low feed-0.03 mm/rev conditions (Exp. No. 13) concerning grooved and standard drills. It is clear that the grooved drill provides better surface quality compared to the hole drilled with ungrooved drill. Similarly, more fiber pullouts and severe surface pits are observed with un-grooved drill at low speed-20 m/min and high feed-0.09 mm/rev drilling conditions (Exp. No. 4) as shown in Fig. 15 (c-d). This severe damage can be attributed to the high force-induced adhesion of aluminum alloy and serrated Ti alloy chips-induced delamination across the CFRP holes.

4 Conclusions

A comparative analysis on the performance of micro-textured and standard drill tools during drilling of Al-7075/CFRP/Ti-6Al-4V hybrid stacks was performed with the help of advanced minimum quantity lubrication setup. The micro-textures were created with the help of Laser Beam Machining (LBM) technology. Based on this experimental investigation, the following conclusions can be drawn:

- In drilling the reachability of cutting fluids to the machining zone is very well enhanced by the micro-textured tool with the help of MQL setup and thereby detected a reduction of 12 – 17% of the total thrust force when compared with the standard tool (un grooved drill).
- From the drilling study it is observed as maximum thrust force and torque can be reduced by a combination of low feed rate and high cutting speed as 0.03 mm/rev feed rate with a cutting speed of 35 m/min. In this research, the hole number 13 possessed these range of values and provides an extraordinary response in lowering the thrust force and torque.
- The placement of micro-textures nearer to the cutting edges of the drill has been found to reduce the adhesion of chips and thereby reducing the friction between tool and workpiece which in turn enhances the surface integrity of the CFRP phase.

References

1. Alagan, N.T., et al.: Investigation of the quality of Al-CFRP stacks when drilled using innovative approaches. CIRP J. Manuf. Sci. Technol. **1**(43), 260–272 (2023)
2. Samsudeensadham, S., Krishnaraj, V.: Drilling study on CFRP/Ti-6Al-4V stacks using chip breaker grooved drill. Mater. Manuf. Process. **37**, 1511–1525 (2022)
3. Yuan, C.G., Pramanik, A., Basak, A.K., Prakash, C., Shankar, S.: Drilling of Titanium Alloy (Ti6Al4V)–a Review. Mach. Sci. Technol. **25**(4), 637–702 (2021). https://doi.org/10.1080/10910344.2021.1925295
4. Vigneshwaran, S., Uthayakumar, M., Arumugaprabu, V.: Review on machinability of fiber reinforced polymers: a drilling approach. SILICON **10**(5), 2295–2305 (2018). https://doi.org/10.1007/s12633-018-9764-9
5. Pramanik, A., Littlefair, G.: Developments in Machining of Stacked Materials Made of CFRP and Titanium/Aluminum Alloys. Machin. Sci. Technol. An Int. J. **18**(4), 485–508 (2014). https://doi.org/10.1080/10910344.2014.955718
6. Soo, S.L.; Abdelhafeez, A.M.; Li, M., Hood, R., Lim, C.M.: The drilling of carbon fibre composite–aluminium stacks and its effect on hole quality and integrity. Proc. Inst. Mech. Eng. Part B J. Eng. Manuf. **233**(4), 1323–1331 (2019). https://doi.org/10.1177/0954405417728312

7. Ismail, S.O., Dhakal, H.N., Dimla, E., Popov, I.: Recent advances in twist drill design for composite machining: a critical review. Proceedings of the Institution of Mechanical Engineers, Part B: Journal of Engineering Manufacture. **231**(14), 2527–2542 (2017)
8. Pang, K., Wang, D.: Study on the performances of the drilling process of nickel-based superalloy inconel 718 with differently micro-textured drilling tools. Int. J. Mech. Sci. **180**(March), 105658 (2020)
9. Manikandan, N., Arulkirubakaran, D., Palanisamy, D., Raju, R.: Influence of Wire-EDM Textured Conventional Tungsten Carbide Inserts in Machining of Aerospace Materials (Ti–6Al–4V Alloy). Mater. Manuf. Process. **34**(1), 103–111 (2019)
10. Liu, X., Liu, Y., Li, L., Tian, Y.: Performances of Micro-Textured WC-10Ni3Al Cemented Carbides Cutting Tool in Turning of Ti6Al4V. Int. J. Refract. Met. Hard Mater. **84**, 104987 (2019). https://doi.org/10.1016/j.ijrmhm.2019.104987
11. Patel, K., Kaftanoğlu, B., Özel, T.: Micro Textured Cutting Tool Effects on Cutting Forces, Volumetric Wear and Adhesion in Dry Turning of Titanium Alloy. Int. J. Mechatronics Manuf. Syst. **12**(3–4), 180–195 (2019). https://doi.org/10.1504/IJMMS.2019.103482
12. Xu, J., Ji, M., Paulo Davim, J., Chen, M., El Mansori, M., Krishnaraj, V.: Comparative study of minimum quantity lubrication and dry drilling of CFRP/Titanium stacks using TiAlN and diamond coated Drills. Compos. Struct. **2020**(234), 111727 (2019). https://doi.org/10.1016/j.compstruct.2019.111727
13. Kayihan, M., Karaguzel, U., Bakkal, M.: Experimental analysis on drilling of Al/Ti/CFRP hybrid composites. Mater. Manuf. Process. **00**(00), 1–8 (2020). https://doi.org/10.1080/10426914.2020.1819545
14. Selvakumar, J.S., Muthiah Muralidharan, S., Raj, D.S.: Performance Analysis of drills with structured surfaces when drilling CFRP/AA7075 Stack under MQL Condition. J. Manuf. Process.**2023**(89), 194–219 (2022). https://doi.org/10.1016/j.jmapro.2023.01.053
15. Saleem, M., Toubal, L., Zitoune, R., Bougherara, H.: Investigating the effect of machining processes on the mechanical behavior of composite plates with circular holes. Compos. A Appl. Sci. Manuf. **1**(55), 169–177 (2013)
16. Krishnaraj, V., et al.: Optimization of machining parameters at high speed drilling of carbon fiber reinforced plastic (CFRP) laminates. Compos. B Eng. **43**(4), 1791–1799 (2012)
17. Zitoune, R., Krishnaraj, V., Collombet, F.: Study of drilling of composite material and aluminium stack. Compos. Struct. **92**(5), 1246–1255 (2010)
18. Zitoune, R., Krishnaraj, V., Almabouacif, B.S., Collombet, F., Sima, M., Jolin, A.: Influence of machining parameters and new nano-coated tool on drilling performance of CFRP/Aluminium sandwich. Compos. B Eng. **43**(3), 1480–1488 (2012)
19. Zitoune, R., Krishnaraj, V., Collombet, F., Le Roux S.: Experimental and numerical analysis on drilling of carbon fibre reinforced plastic and aluminium stacks. Compos. Struct. **146**, 148–158 (2016)
20. Glaa, N., Mehdi, K., Zitoune R.: Numerical modeling and experimental analysis of thrust cutting force and torque in drilling process of titanium alloy Ti6Al4V. Int. J. Adv. Manuf. Technol. **96**, 2815–2824 (2018)

Kinematic Model and Fast-Terminal Sliding Mode for Four-Mecanum-Wheeled Mobile Robot

Quoc-Dong Hoang[1], Le Dinh Nghiem[1], Le Anh Tuan[1](✉), Pham Duc An[2], and Nguyen Thi Gam[3]

[1] Institute of Mechanical Engineering, Vietnam Maritime University, Hải Phòng, Vietnam
tuanla.ck@vimaru.edu.vn
[2] School of Mechanical Engineering, HUST, Hanoi, Vietnam
[3] School of Electrical and Electronic Engineering, HUST, Hanoi, Vietnam

Abstract. Today's omnidirectional wheeled robot is being widely utilized and developed with different types of omnidirectional wheel versions because of its versatility and multi-tasking mobility. This paper proposes a kinematic model for a robot using four omnidirectional Mecanum wheels with hardware-error compensation and a mathematical model of the motors driving the entire system. On this basis, we develop a nonsingular fast-terminal sliding mode controller with finite-time convergence. Satisfaction of the Lyapunov stability criteria and the finite-time stability ensure that the state variables are forced to their desired values, thereby ensuring the ability of the Mecanum wheels to follow the reference speeds in a short finite-time interval. Finally, the velocity and position of the robot are controlled following the desired trajectories generated.

Keywords: Mecanum wheel · omnidirectional robot · sliding mode control · nonsingular fast terminal sliding mode

1 Introduction

In recent years, robotic systems have witnessed substantial advancements, becoming integral components in various applications ranging from manufacturing to logistics and healthcare. Among these systems, wheeled mobile robots have garnered significant attention due to their versatility and ability to navigate complex environments efficiently. One notable configuration is the Mecanum wheeled robot, characterized by its omnidirectional movement capabilities achieved through four independently driven and steered wheels. The dynamic nature of Mecanum-wheeled robots presents challenges in achieving precise control, trajectory tracking, and stability, particularly in scenarios requiring rapid and accurate maneuvering [1]. To address these challenges, advanced control strategies have been explored to enhance the robots' overall performance. One such promising technique is the nonsingular fast terminal back-stepping control (NFTSCC) [2], a derivative of the well-established back-stepping control methodology. Comparing with other control [3, 4], NFTBSC offers the advantages of rapid convergence, tracking

D. C. Nguyen et al. (Eds.): ICERA 2023, LNNS 944, pp. 114–120, 2024.
https://doi.org/10.1007/978-3-031-62235-9_14

accuracy, and smooth control action, making it well-suited for addressing the intricate control requirements of Mecanum-wheeled robots.

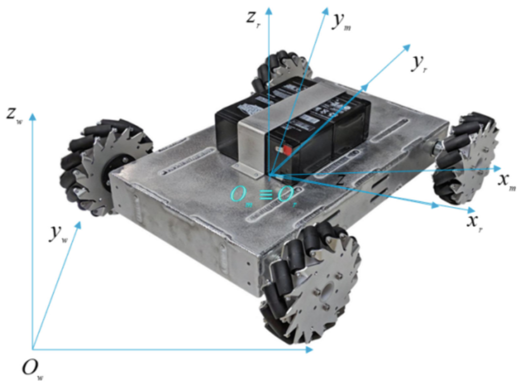

Fig. 1. Coordinate system diagram.

This paper delves into the application of NFTBSC based on kinematic and dynamic models of a Mecanum-wheeled robot with a focus on achieving superior trajectory tracking and finite-time stability. Inheriting the stable and robust characteristics of the traditional sliding mode controller (SMC) [5], which satisfies the Lyapunov stability criteria, the NFTSMC with finite-time convergence promises the possibility of superiority. The intricate kinematics and dynamics of Mecanum-wheeled robots are taken into consideration for the development of the control strategy. The control objective is to ensure precise tracking control while concurrently handling the inherent complexities posed by omnidirectional motion. The simulations are implemented with the results to investigate the controller's effectiveness.

2 Kinematic Model

The coordinate system of the four-Mecanum-wheel robot is illustrated in Fig. 1. The global frame is $R_o(O_0x_oy_oz_o) \equiv R_w(O_wx_wy_wz_w)$. Coordinate frame $R_m(O_mx_my_mz_m)$ is obtained by translating the frame $R_o(O_0x_oy_oz_o)$ with along its x-axis and y-axis. While, $R_r(O_rx_ry_rz_r)$ denotes the local frame of the robot.

The translational position of the wheels is computed by the vector $\boldsymbol{\chi}_w = \left[\chi_{lf}^r\ \chi_{rf}^r\ \chi_{lr}^r\ \chi_{rr}^r\right]^T$, where χ_{lf}^r, χ_{rf}^r, χ_{lr}^r, and χ_{rr}^r are the left-front, right-front, left-rear and right-rear wheels' velocities, respectively.

The relationship between the velocity of the wheels and the pose of robot is given by

$$\delta_W^r = \frac{1}{4}\boldsymbol{J}^r\boldsymbol{\delta}^r + \boldsymbol{\varepsilon}_1(\boldsymbol{\delta}^r), \tag{1}$$

where, $\boldsymbol{\delta}_W^r = \dot{\boldsymbol{\chi}}_W = \left[\, \delta_{lf}^r \ \delta_{rf}^r \ \delta_{lr}^r \ \delta_{rr}^r \,\right]^T$ represents the translational velocity of the robot, and $\boldsymbol{\varepsilon}_1\left(\boldsymbol{\delta}^r\right)$ is the compensator. Additionally, the matrix $\mathbf{J}^r$ is computed by

$$\boldsymbol{J}^r = \begin{bmatrix} j_{11}^r & j_{12}^r & j_{13}^r \\ j_{21}^r & j_{22}^r & j_{23}^r \\ j_{31}^r & j_{32}^r & j_{33}^r \\ j_{41}^r & j_{42}^r & j_{43}^r \end{bmatrix}, \tag{2}$$

where $j_{11}^r = -1, j_{12}^r = -1, j_{13}^r = -(l_a + l_b), j_{21}^r = 1, j_{22}^r = 1, j_{23}^r = -j_{13}^r, j_{31}^r = j_{32}^r = 3$, $j_{33}^r = j_{31}^r$, $-j_{31}^r = j_{42}^r = -1$, $j_{43}^r = -j_{33}^r$

By setting the angular position of the wheel $\boldsymbol{\chi}_W^R = \boldsymbol{\chi}_W^R / r_W = \left[\, \chi_{lf}^r \ \chi_{rf}^r \ \chi_{lr}^r \ \chi_{rr}^r \,\right]^T$, we have the wheels' angular velocity is $\boldsymbol{\delta}_W^R = \boldsymbol{\delta}_W^R / r_W = \dot{\boldsymbol{\chi}}_W^R / r_W = \left[\, \delta_{lf}^r \ \delta_{rf}^r \ \delta_{lr}^r \ \delta_{rr}^r \,\right]^T$, with r_W being the radius of the wheel.

The position of robot in the global frame is $\boldsymbol{\chi}_w = \left[\, \chi_x^w \ \chi_y^w \ \theta_r \,\right]^T$

$$\boldsymbol{\delta}^w = \boldsymbol{J}^w \boldsymbol{\delta}^r, \tag{3}$$

where $\boldsymbol{\delta}^w = \dot{\boldsymbol{\chi}}_w = \left[\, \delta_x^w \ \delta_y^w \ \delta_\omega^w \,\right]^T$ and

$$\boldsymbol{J}^w = 4\left(\left(\boldsymbol{J}^r\right)^T \boldsymbol{J}^r\right)^{-1} \left(\boldsymbol{J}^r\right)^T + \boldsymbol{\varepsilon}_2\left(\boldsymbol{\delta}^r\right), \tag{4}$$

Where $j_{11}^w = \cos(\theta_r), j_{12}^w = \sin(\theta_r), j_{13}^w = j_{23}^w = 0, j_{21}^w = -\sin(\theta_r), j_{33}^w = 1, j_{31}^w = j_{32}^w = 0$, and $\boldsymbol{\varepsilon}_2\left(\boldsymbol{\delta}^r\right)$ is the compensator.

From the constrains given in Fig. 1, we have

$$\left(\delta_x^r \sin\left(\alpha_j + \beta_j\right) - \delta_y^r \cos\left(\alpha_j + \beta_j\right) - l_j \delta_\omega^r \cos\beta_j\right) = r_w \delta_j^r - v_{gj} \cos\gamma_j, \tag{5}$$

$$\left(\delta_x^r \cos\left(\alpha_j + \beta_j\right) + \delta_y^r \sin\left(\alpha_j + \beta_j\right) + l_j \delta_\omega^r \sin\beta_j\right) = -v_{gj} \sin\gamma_j. \tag{6}$$

By eliminate the velocity of roller v_{gj}, we also have

$$\delta_j^r = \boldsymbol{F}_j \boldsymbol{\delta}^r = \left[\, F_{1j} \ F_{2j} \ F_{3j} \,\right] \boldsymbol{\delta}^r, \tag{7}$$

where $F_{1j} = \frac{\cos(\alpha_j + \beta_j + \gamma_j)}{r_w \sin\gamma_j}$, $F_{2j} = \frac{\sin(\alpha_j + \beta_j + \gamma_j)}{r_w \sin\gamma_j}$, $F_{3j} = \frac{l_j \sin(\beta_j + \gamma_j)}{r_w \sin\gamma_j}$. Based on those computation, the compensator function can be obtained.

The entire robot is drove by three motors that have the simple model as

$$L\dot{i}_t^{(j)} = U^{(j)} - R i_t^{(j)} - K_e \delta_j^R, \tag{8}$$

$$J\dot{\delta}_j^R = -B\delta_j^R + K_t i_t^{(j)} - T_L^{(j)}, \tag{9}$$

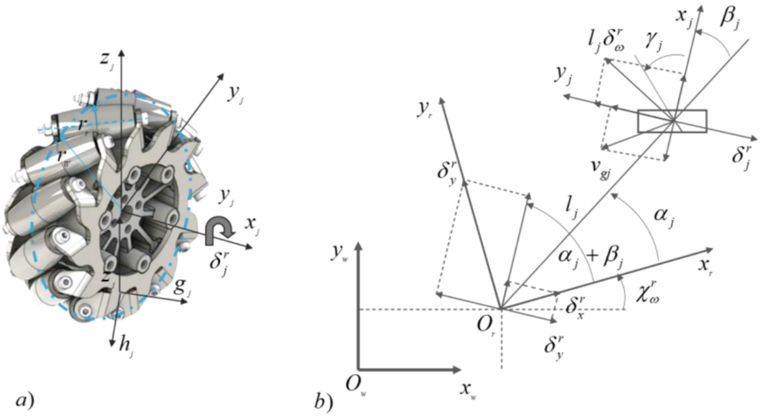

Fig. 2. Constraint diagram: (**a**) structural principle; (**b**) kinematic constraint

where $i_t^{(j)}$ is the armature current, $U^{(j)}$ is the terminal voltage, R is the armature resistance, L is the armature inductance, J is total inertial of motor and wheel, B is the viscous friction, K_t is torque constant K_e is the back emf constant, $T_L^{(j)}$ is the load torque, and the index $j = (1, 2, 3, 4)$ denotes the motor's order (Fig. 2).

By setting the tracking error as $\chi_{1j} = e_j^R = \delta_{jT}^R - \delta_j^R$,

we have

$$\dot{\chi}_{1j} = \dot{e}_j^R = \dot{\delta}_{jT}^R - \dot{\delta}_j^R, \tag{10}$$

and

$$\dot{\chi}_{2j} = \ddot{\delta}_{jT}^R - \ddot{\delta}_j^R. \tag{11}$$

Then, the model of motor can be re-written as

$$\dot{\chi}_{1j} = \chi_{2j}, \dot{\chi}_{2j} = -f_{1j}\chi_{1j} - f_{2j}\chi_{2j} - g_j U^{(j)} + f_j(t). \tag{12}$$

where $f_{1j} = \frac{RJ+BL}{JL}$, $f_{2j} = \frac{RB+K_eK_t}{JL}$, $g_j = \frac{K_t}{JL}$, and $f_j(t) = \ddot{\delta}_{jT}^R + f_{1j}\dot{\delta}_{jT}^R + f_{2j}\delta_{jT}^R - \frac{\dot{T}_L^{(j)}}{J} - \frac{T_L}{JL}$.

3 Controller Design

The control law of the system is proposed as

$$U^{(j)} = \frac{1}{g_j}\begin{bmatrix} -\psi_{1j}^{-1}\lambda_{1j}\zeta_{fj} - \psi_{1j}^{-1}\lambda_{2j}\mathrm{sgn}(\zeta_{fj}) + f_{1j}\chi_{1j} + f_{2j}\chi_{2j} \\ -f_j(t) - \psi_{1j}^{-1}\left(\dot{e}^R\right)\psi_{2j}\left(e_j^R, \dot{e}_j^R\right) \end{bmatrix}, \tag{13}$$

where λ_{1j} and λ_{2j} are the controller parameters, and the function $\zeta_{fj}(t)$, $\psi_{1j}\left(\dot{e}^R\right)$, and $\psi_{2j}\left(e^R, \dot{e}^R\right)$ are

$$\zeta_{fj}(t) = \alpha_{1j}\mathrm{sign}^{\beta_{1j}}\left(\dot{\delta}_{jT}^R - \dot{\delta}_j^R\right) + \alpha_{2j}\mathrm{sign}^{\beta_{2j}}\left(\delta_{jT}^R - \delta_j^R\right) + \left(\delta_{jT}^R - \delta_j^R\right), \tag{14}$$

$$\psi_{1j}\left(\dot{e}_j^R\right) = \alpha_{1j}\beta_{1j}\left|\dot{\delta}_{jT}^R - \dot{\delta}_j^R\right|^{\beta_{1j}-1}, \tag{15}$$

$$\psi_{2j}\left(e_j^R, \dot{e}_j^R\right) = \alpha_{2j}\beta_{2j}\left|\delta_{jT}^R - \delta_j^R\right|^{\beta_{2j}-1}\left(\delta_{jT}^R - \delta_j^R\right) + \dot{e}_j^R, \tag{16}$$

where α_{1j}, α_{2j}, β_{1j}, and β_{2j} satisfy the conditions: $\alpha_{1j} > 0$, $\alpha_{2j} > 0$, $1 < \beta_{1j} < 2$, $\beta_{2j} > \beta_{1j}$. Then, the system is stable and the tracking error $\dot{\chi}_{1j}$ is converged to zero. Finally, the motors' velocity δ_j^R reaches to its reference trajectory δ_{jT}^R and the robot moves with its desired pose. The proof can be basically obtained based on [2, 6, 7].

4 Simulation Implementation

In this section, simulation results are performed for the robot so that it runs around a circle with a radius of 2 m centered at the origin. By applying the NFTSMC algorithm, the robot wheels' velocities can quickly follow the reference trajectory (Figs. 3, 5, 7 and 9). As a result, the position of the wheels can also be shifted to the desired value over time (Figs. 4, 6, 8 and 10). As a result, the robot's spatial coordinate tracking is guaranteed, as shown in Fig. 10 (Fig. 11).

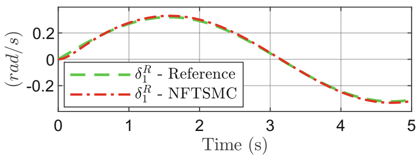

Fig. 3. Angular velocity of the left-front motor

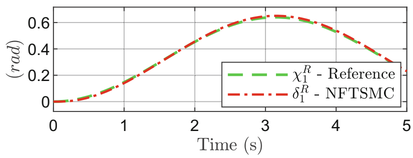

Fig. 4. Angle of the left-front motor

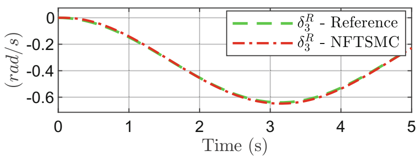

Fig. 5. Angular velocity of the right-front motor

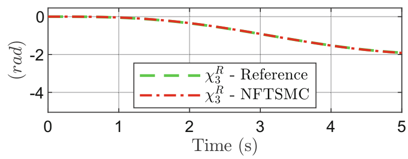

Fig. 6. Angle of the right-front motor

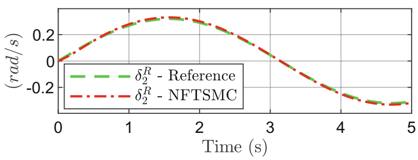

Fig. 7. Angular velocity of the left-rear motor

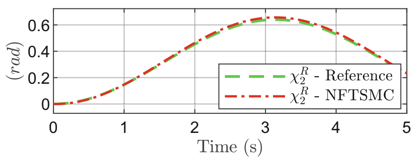

Fig. 8. Angle of the left-rear motor

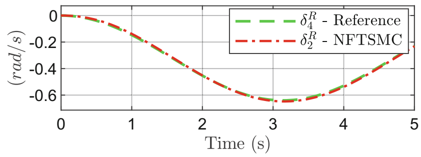

Fig. 9. Angular velocity of the right-rear motor

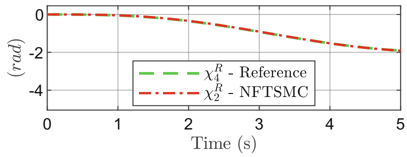

Fig. 10. Angle of the right-rear motor

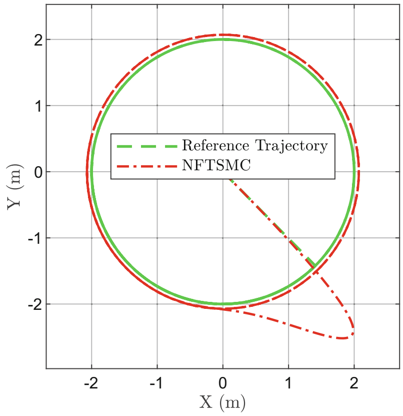

Fig. 11. Control the position of robot in the Oxy plane

5 Conclusion

In summary, this study demonstrated the effectiveness of nonsingular fast terminal backstepping control (NFTSCC) for a Mecanum-wheeled robot. The method's adeptness in trajectory tracking, stability enhancement, and rapid responses was evident from extensive simulations. The successful integration of NFTSMC offers a promising avenue for advancing control capabilities in dynamic Mecanum robot applications, highlighting the potential for broader real-world implementation. This research contributes to the evolving landscape of mobile robotics, showcasing the impact of sophisticated control methodologies on system performance and adaptability.

Acknowledgment. Hoang Quoc Dong was funded by the Postdoctoral Scholarship Programme of Vingroup Innovation Foundation (VINIF), code VINIF.2022.STS.01.

References

1. Watson, M.T., Prescott, T.J.: Collinear mecanum drive: modeling, analysis, partial feedback linearization, and nonlinear control. IEEE Trans. Robot. **37**(2), 642–658 (2021)
2. Xu, B., Ji, W.: Improved non-singular fast terminal sliding mode control with disturbance observer for PMSM drives. IEEE Trans. Transp. Electrif. **7**(4), 2753–2762 (2021)

3. Li, J., et al.: Motion analysis and stability control of four-wheeled omnidirectional mobile robot under limited hardware resource. J. Phys. Conf. Ser. **1487**(1), 12040 (2020)
4. Malayjerdi, E., Malayjerdi, M.: Self-tuning fuzzy PID control of a four-mecanum wheel omnidirectional mobile platform. In: Electr. Eng. (ICEE), Iran. Conf., pp. 816–820 (2018)
5. Wang, Y., et al.: Sliding mode control of fuzzy singularly perturbed systems with application to electric circuit. IEEE Trans. Syst. Man, Cybern. Syst. 1–9 (2017)
6. Solis, C.U., Poznyak, A.S.: Fast terminal sliding-mode control with an integral filter applied to a van der pol oscillator. IEEE Trans. Ind. Electron. **64**(7), 5622–5628 (2017)
7. Van, M., et al.: Self-tuning fuzzy PID-nonsingular fast terminal sliding mode control for robust fault tolerant control of robot manipulators. ISA Trans. **96**, 60–68 (2020)

Mathematical Modeling of the Mechanical Tensile Strength of the Thick Carbon Steel Plates Weld with the Narrow Gap and Variable Chamfer Angles

Minh Hung Ha[1,2,3], Trong Binh Ngo[1], Quy Huy Trieu[2], and Hoang Quan Nguyen[4](✉)

[1] National Research Institute of Mechanical Engineering, Hanoi, Vietnam
[2] Institute for Development of Advanced Technical and Technology, VUSTA, Hanoi, Vietnam
[3] University of Economics – Technology for Industry, Hanoi, Vietnam
[4] VNU University of Engineering and Technology, Hanoi, Vietnam
nhquan@vnu.edu.vn

Abstract. This article presents research results pertaining to the computation, data processing through experimental statistics, and the development of a mathematical model that elucidates the interplay between welding process parameters, specifically welding amperage (I_h), weld speed (v_h), and chamfer angle (α), in the context of narrow gap welding. The primary objective of this study is to establish a goal function capable of predicting the quality of butt weld joints in thick carbon steel plates, specifically SS400. The experimental setup employed in this study encompasses the utilization of LINCOLN's advanced MAG welding machines, specifically the PLEXTEC®500x model, renowned for their industrial manufacturing capabilities. The obtained results reveal that the mechanical tensile strength of the weld material falls within the average range of $\sigma_k = 460.016 \div 540.066$ MPa. These findings substantiate the fulfillment of the technical requirements necessary for welded structures in real-world production scenarios in Vietnam.

Keywords: MAG welding with narrow gap (NG-MAG) · experimental planning · mechanical tensile strength

1 Introduction

The systematic research and development of advanced technologies for application in the industrial production reality in the field of mechanical engineering in many industrialized countries is getting more innovations, especially a lot of types of equipment and technologies including narrow-gap welding equipment used for jointing thick steel plates. With the orientation to make use of many different welding methods (TIG, MIG, MAG) in which the welded structure does not require the chamfering or with a small chamfer angle depending on the weld thickness. In this way, it allows significantly saving the labor in creating a welded workpiece, saving base metal and welding wire, which leads to a decrease in the cost of fabricating welded structures. A number of advanced

D. C. Nguyen et al. (Eds.): ICERA 2023, LNNS 944, pp. 121–131, 2024.
https://doi.org/10.1007/978-3-031-62235-9_15

welding types of equipment and materials originating from the United States have now been imported to Vietnam for a purpose of research, training, and industrial-scale production [1, 2]. However, mastering technology and providing technical solutions, which are suitable for the production reality in Vietnam for researchers and manufacturers is a necessity and topicality.

In order to provide a reliable scientific foundation for the selection of a reasonable welding procedure with optimal process parameters and ensure the potential for application in domestic reality production. Recently, researchers at the Institute of Mechanical Engineering, in collaboration with a number of specialized institutes and universities, have published some experimental results in the application of the MAG process in the protective gas environment of CO2. The experiments had been conducted for welding butt joints of carbon steel plates of SS400 which is equivalent to steel grade CT38 according to Vietnamese standards used in manufacturing with thickness from 25 mm to 150 mm and chamfer angles in the wide range from 5o to 30o (including both sides of the weld chamfer). A proposed solution has been presented in [3] for the design and fabrication of an integrated automatic wire feed welding head assembly. This innovative assembly incorporates the MAG D500 welding machine power supply and welding jigs, and it is specifically developed for research and training purposes at the Institute of Mechanical Engineering. In articles [4, 5], the authors represent experimental results for welding butt joints of thick carbon steel plates of SS400 with the narrow-gaps and variable chamfer angles using PLEXTEC® 500x welding equipment from LINCOLN ELECTRIC (USA), Figs. 2b and 2c). Besides, these authors also reported at the international conferences held at Dang Nang city in April 2022 (ICCRI & ICSTC-2022) [6] and The 5th International Conference on Engineering and Research Applications 2022, ICERA 2022, Thai Nguyen, December 1–2/ 2022, Paper ID: 6295 [7].

The present study provides an result of the experimental mathematical statistics analysis conducted on butt joint welding process for SS400 carbon steel plates, having a thickness of $\delta = 50$ mm, specifically focusing on the narrow-gap configuration with a width of $b_o = 10$ mm and chamfer angles ranging from 5° to 30°. Furthermore, a mathematical model is proposed to forecast the tensile strength of the weld material when subjected to destructive testing in a direction perpendicular to the weld.

2 Research Method

The workpiece material employed in the experiments consisted of SS400 carbon steel plates (Fig. 1a). These plates were prepared in the form of blocks measuring 50 x 100 x 200 mm, specifically tailored to meet the requirements of the welding operations. The chemical composition of test samples is 0.18% C; 0.1 $\div$ 0.2% Si; 0.06% Mn; $\leq$ 0.03% P; $\leq$ 0.04% S, % Fe and mechanical properties at the state of normalized steel is Yield strength $\sigma_s = 206 \div 245$ MPa, Ultimate tensile strength $\sigma_b = 373 \div 481$ MPa, Elongation $\delta = 24 \div 27\%$ and Hardness HB $= 206 \div 245$ [3].

The range of each process parameter was selected based on the trial experiments according to the experimental design, using the orthogonal arrays to organize the factors affecting the process. Using N27 orthogonal array, three parameters are considered as observation factors with three levels (Current, I_h; welding speed, v_h and chamfer angles calculated by both sides of the cross-section of welding direction, α), presented in Table 1. In order to establish the predictive mathematical models for the mechanical tensile strength (σ_k) of welding material, several technical parameters of the welding process were held at predetermined values [4, 5]. The dependent response of the tensile strength was studied in relation to the variables of current, welding speed, and chamfer angles.

The initial gap of the butt joint is defined with a size $b_o = 10$ mm by pre-welding two workpieces plates on a support steel plate. Depending on the selection of chamfer angles on workpiece plates, three groups of experimental samples are classified by $\alpha_1 = 5°$; $\alpha_2 = 10°$and $\alpha_3 = 15°$ respectively.

The experimental setup for narrow gap welding was facilitated by an advanced welding technology transfer enterprise imported from LINCOLN ELECTRIC (USA), providing the necessary equipment and materials. The authenticity of the equipment was verified by a reputable supplier in Vietnam (Figs. 1b and 1c). The schematic diagram illustrating the underlying principles of the narrow gap welding process is depicted in Fig. 2a [4]. The utilization of this specialized equipment, combined with the established technical expertise, ensured the execution of accurate and reliable experiments in the study of narrow gap welding.

(a) (b) (c)

Fig. 1. Experimental workpiece (a); MAG machine and equipments of LINCOLN PLEXTEC® 500x (b); weld line supply GM-70s-6, d = 1,2 mm (c) [4]

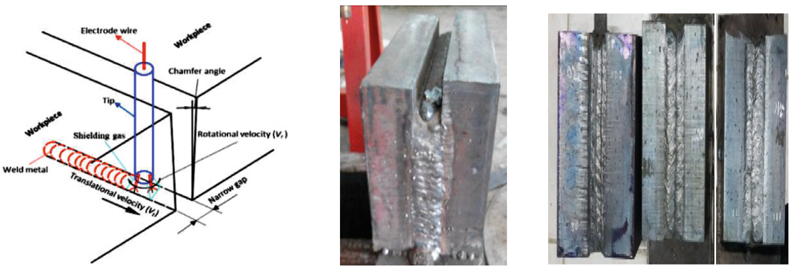

(a) (b) (c)

Fig. 2. The principle schematic of the process in narrow gap welding (a) [4]; front view (b) and top view on welding workpieces (c)

3 Experimental Results

Based on the least squares method, from the tensile test results obtained of the samples designed in the orthogonal array, a mathematical model for the mechanical tensile strength is constructed. The obtained mathematical model is in the form of an orthogonal polynomial model [8]. This approach allows identifying the important factors and their respective contributions to the mechanical tensile strength, facilitating the construction of a robust mathematical model that accurately predicts the behavior.

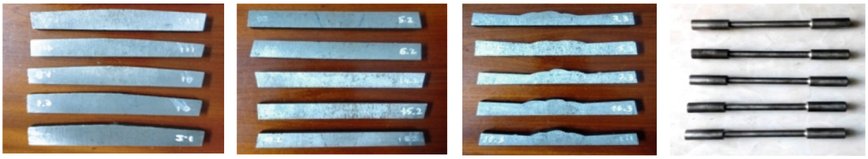

a) 0.25h a) 0.5h a) 0.75h d)

Fig. 3. Workpieces are cut by the ratio with the total height of the weld (h) for machining samples in the destructive tensile test: a) the lower part; b) the middle part; c) the upper part of weld; d) tensile test samples machined according to Standard of Vietnam (TCVN 197:2002).

The experimental setup involves the utilization of an N27 orthogonal array (Table 1) to design and regulate three process parameters (I_h, v_h and α), each with three levels. All welding experiments were conducted under ambient conditions, allowing the cooling process to occur naturally. In order to perform destructive testing, at least two representative positions along the narrow gap welding line were carefully selected on the test samples. These positions were chosen to ensure perpendicularity to the weld, and were typically located at either the starting and middle points or the middle and end points of the welding line. Subsequent to the selection of these positions, the weld material was subjected to cutting tests.

To minimize the distortion of the weld material, the wire cutting method was employed to obtain the workpieces, which were subsequently divided into three sections based on the weld height (Figs. 3a, 3b and 3c). The resulting tensile failure test specimens were machined to meet the specified dimensions, as illustrated in Fig. 3d. The test outcomes are presented in Table 1.

Utilizing the least squares method, the experimental data (Table 1) was analyzed to derive a quadratic polynomial function representing the tensile stress. The obtained function is as follows:

$$\sigma_k = f(I_h, v_h, \alpha) = 391.09 + 1.49872I_h - 25.728v_h + 9.89362\alpha + 0.029908I_h v_h$$

$$-0.201775v_h\alpha - 0,011217I_h\alpha - 0,003627I_h^2 + 1.00204v_h^2 - 0.049273\alpha^2 \quad (1)$$

The Mean sum variance ($S_{t.b}$) is 23.35603/27 equal to 0.865038 and the Mean error ($S^*_{m.h}$) of the model (Eq. 1) in a comparison with the experimental data is 79.88/27 equal to 2.9585%.

The smallest error of the computational model compared to the experimental data: The minimum error of the model is $\min S^{*}_{m.h} = +0.02\%$ (sample 26, code 212). The largest error of the model is $\max S^{*}_{mod} = -2.79\%$ (sample 15, code 121). Therefore, we obtain: $F_{tt} = S^2_{mod} = 37.53/27 = 1.39$. In the case of orthogonal array with N = 33 = 27, referring to the Table 1, we obtain: $F_{tab}(K,m,\alpha) = F_{tab}(26,23,0.95) = 1.78$. According to the Fischer criterion: $F_{tt} = 1.39 < F_{tab}(26,23,0.95) = 1.78$, the model (Eq. 1) is completely suitable when simulating the prediction of tensile strength of NG-MAG weld joint within the investigated region according to standard of experimental planning 2.

Table 1. Experimental results and calculation of the tensile strength of narrow gap weld on carbon steel SS400.

No	Code in Ex	Process parameters			Tensile strength, σ_k, MPa				Variation S^2	Standard Deviation, $\sqrt{S^2}$	Error %
		I_h, A	v_h, m/h	α,°	Ex. 1	Ex. 2	Ex. 3	Mean value			
01	000	160	6	5	476.00	477.50	474.60	476.033	1.40222	1.18415	−1.18
02	010	160	8	5	468.25	469.51	470.82	469.526	1.10095	1.04926	+0.79
03	020	160	10	5	460.20	459.85	460.00	460.016	0.02055	0.14332	+0.44
04	100	190	6	5	491.62	493.22	490.03	491.623	1.69602	1.30231	−0.13
05	110	190	8	5	482.79	481.72	480.63	481.713	0.77762	0.88182	+0.73
06	120	190	10	5	476.78	479.23	478.30	478.103	1.01975	1.00982	+1.24
07	200	220	6	5	494.62	495.72	493.51	494.616	0.81402	0.90223	−0.34
08	210	220	8	5	477.12	475.81	474.53	475.820	1.11806	1.05738	−1.73
09	220	220	10	5	479.32	481.71	480.50	480.510	0.95236	0.97588	+0.15
10	001	160	6	10	520.90	519.67	522.09	520.886	0.97615	0.98800	+1.63
11	011	160	8	10	492.75	491.60	490.55	491.633	0.80722	0.89845	−0.59
12	021	160	10	10	477.34	479.66	478.50	478.500	0.89706	0.94713	−1.29
13	101	190	6	10	525.03	525.75	524.25	525.010	0.37520	0.61253	+0.71
14	111	190	8	10	496.81	497.60	498.42	497.610	0.43206	0.65731	−1.53
15	121	190	10	10	482.55	484.86	483.70	483.703	0.88035	0.93826	−2.79
16	201	220	6	10	528.42	527.94	528.88	528.413	0.14729	0.38378	+0.90
17	211	220	8	10	518.65	519.12	519.55	519.106	0.41530	0.64443	+1.87
18	221	220	10	10	507.53	505.48	506.51	506.506	0.84615	0.91986	+0.67
19	002	160	6	15	531.40	530.39	532.42	531.403	0.68682	0.82874	−1.75
20	012	160	8	15	524.74	523.70	522.67	523.703	0.71415	0.84507	+0.55

(*continued*)

Table 1. (*continued*)

No	Code in Ex	Process parameters			Tensile strength, σ_k, MPa				Variation S^2	Standard Deviation, $\sqrt{S^2}$	Error %
		I_h, A	v_h, m/h	α,°	Ex. 1	Ex. 2	Ex. 3	Mean value			
21	022	160	10	15	516.75	514.66	515.70	515.703	0.72803	0.85324	+1.31
22	102	190	6	15	556.50	555.46	557.54	556.500	0.72106	0.84915	+1.55
23	112	190	8	15	527.38	528.40	529.43	528.403	0.70042	0.83691	−0.27
24	122	190	10	15	521.94	519.86	520.90	520.900	0.72106	0.84915	+0.22
25	202	220	6	15	540.00	539.05	541.15	540.066	0.73722	0.85861	−1.58
26	212	220	8	15	531.15	532.40	533.69	532.413	1.07535	1.03699	+0.02
27	222	220	10	15	522.41	524.62	523.50	523.510	0.81406	0.90225	−0.10

Note: Wire diameter d = 1,2 mm; Weld voltage $U_h = 26 \div 30$ V; Weld speed of head $n_n = 25$ rpm; Nozzle to plate distance $L_{đ.c} = 20$ mm; CO_2 protective air flow rate Q = 20 l/min

In order to visually depict the complex relationship between welding parameters and the resulting tensile strength of welds, the characteristics of pairwise interactions among the input welding technology parameters and their impact on the weld tensile strength are presented in the form of 3D graphs, as depicted in Figs. 4, 5 and 6. The 2D graph obtained by fixing the technological parameters at their average values within the selected survey domain corresponds to the complete adjustment range of the three main parameters, as illustrated in Figs. 6, 7 and 8. The analysis of these graphs aids in understanding the synergistic effects and interdependencies among the input parameters, offering valuable information for optimizing the welding process and achieving desired mechanical properties in the welds.

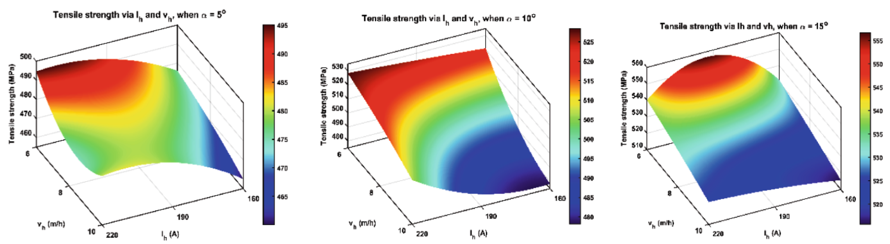

a) σ_k=f(v_h;I_h); α=5° b) σ_k=f(v_h;I_h); α=10° c) σ_k=f(v_h;I_h); α=15°

Fig. 4. Influence of process parameters (I_h, v_h) on the tensile strength (σ_k) when chamfer angle (α) varies

From Figs. 4, 5 and 6, it is possible to depict the variation of the tensile strength with different combinations of process parameters as follows:

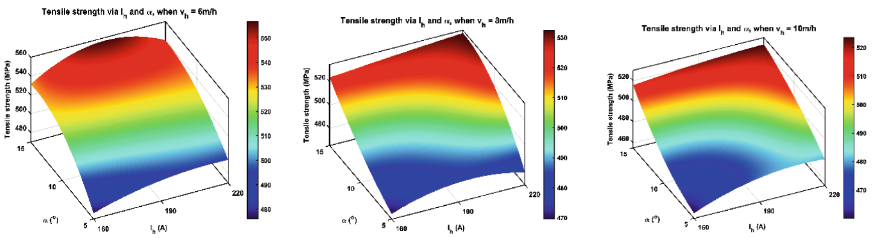

a) σ_k=f(α;I_h); v_h=6 m/h b) σ_k=f(α;I_h); v_h=8 m/h c) σ_k=f(α;I_h); v_h=10 m/h

Fig. 5. Influence of process parameters (I_h, α) on the tensile strength (σ_k) when weld speed (v_h) varies.

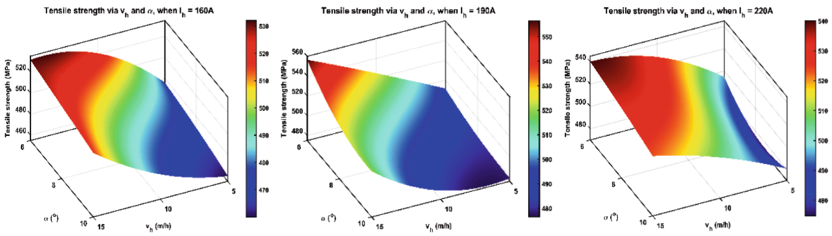

a) σ_k = f(v_h;α); I_h = 160 A b) σ_k=f(v_h;α); I_h=190 A c) σ_k=f(v_h;α); I_h= 220 A

Fig. 6. Influence of process parameters (v_h, α) on the tensile strength (σ_k) when current (I_h) varies.

(i) The influence of current and welding speed (I_h, v_h) on the tensile stress (σ_k) under varying chamfer angles (α) is presented in Fig. 4 as follow:

- With $\alpha = 5°$ and an applied current ranging $I_h = 160$ A to $I_h = 220$ A, the tensile strength σ_k increases proportionally with the rising trend of I_h. This behavior is observed on the nonlinear surface corresponding to the coordinates of v_h and I_h, as shown in Fig. 4a. The experimental results indicate a direct correlation between the applied current and the resulting tensile strength, with higher currents leading to increased tensile strength values. Furthermore, when α was fixed at 5°, it was observed that the tensile strength (σ_k) decreased with an increase in welding speed (v_h) from 6 m/h to 10 m/h. However, it is noteworthy that the nonlinear surface depicting the function of σ_k for welding speed parameters was at a lower level in comparison to the I_h parameters;
- With $\alpha = 10°$ and an applied current increasing from $I_h = 160$ A to $I_h = 220$ A, the tensile strength σ_k increases proportionally with the current I_h and the 3D surface plot is also a nonlinear surface with the coordinate of v_h and I_h. Similar to the case of $\alpha = 5°$ (Fig. 4a), the resulting 3D surface plot of σ_k as a function of v_h and I_h demonstrated a nonlinear surface (Fig. 4b). However, it is worth noting that the magnitude of σ_k was lower compared to the case of $\alpha = 5°$ (Fig. 4a). Moreover, when considering the range of v_h from 6 m/h to 10 m/h, it was observed that the tensile strength (σ_k) exhibited an inverse relationship with v_h, as σ_k decreased with

an increase in v_h. In contrast to the case of $\alpha = 5°$ (Fig. 4a), the 3D surface plot of σ_k as a function of v_h and I_h appeared to approach a flatter shape (Fig. 4b);
- With $\alpha = 15°$, a similar pattern in the change of tensile strength (σ_k) was observed when varying the two parameters, I_h and α, as depicted in Fig. 4c. This behavior closely resembled the case discussed earlier with $\alpha = 5°$ (Fig. 4a). The surface plot illustrating the objective function, σ_k, showcased its dependence on the I_h-v_h pair across the two coordinates of v_h and I_h. This indicates that the combined effect of I_h and v_h contributes significantly to the variation in σ_k, reinforcing the need to carefully consider both parameters in order to achieve desired tensile strength characteristics in the welds.

(i) The influence of welding current and chamfer angle (I_h, α) on the tensile stress (σ_k) under varying weld speed (v_h) is presented in Fig. 5 as follow:

- At a constant welding speed of $v_h = 6$ m/h, the tensile stress was observed to increase proportionally with the corresponding variations in welding current (I_h) ranging from 160 A to 220 A and chamfer angle (α) ranging from 5° to 15°. This relationship between tensile stress and the two parameters, I_h and α, was found to be consistent. Figure 5a provides a visual representation of the objective function, σ, which exhibits a slightly convex nonlinear form when plotted against the coordinates of I_h and α;
- At a constant welding speed of $v_h = 8$ m/h, the investigation revealed a proportional relationship between the tensile stress and the variations in welding current (I_h) ranging from 160 A to 220 A, as well as chamfer angle (α) ranging from 5° to 15°. Notably, in this scenario, the resulting function, σ_k, exhibited a nearly linear pattern when expressed in terms of the coordinates of I_h and α (Fig. 5b). The linearity observed indicates that the tensile stress tends to vary linearly with changes in I_h and α within the given range;
- At a constant welding speed of $v_h = 10$ m/h, an investigation was conducted by varying the welding current (I_h) from 160 A to 220 A and the chamfer angle (α) from 5° to 15°. Remarkably, similar to the previous case of $v_h = 6$ m/h, a comparable trend in the variation of the tensile stress (σ_k) was observed (Fig. 5c).

(iii) The influence of welding speed and chamfer angle (v_h, α) on the tensile stress (σ_k) under varying welding current (I_h) is shown in Fig. 6 as follow:

- At a fixed welding current of $I_h = 160$ A, Fig. 6a demonstrates that as v_h increases from $v_h = 6$ m/h to $v_h = 10$ m/h, σ_k exhibits an inverse relationship, decreasing in the direction of increasing v_h. Additionally, the chamfer angle (α) was found to exert a significant influence on σ_k. When α increases from $\alpha = 5°$ to $\alpha = 15°$, σ_k increases proportionally in the direction of increasing α. The surface plot representing the objective function σ_k exhibits a nonlinear form, albeit with a relatively small degree of curvature, resembling a linear function when observed in the coordinates of v_h and α (Fig. 6a);
- At a fixed welding current of $I_h = 190$ A, Fig. 6b demonstrates that as v_h increases from $v_h = 6$ m/h to $v_h = 10$ m/h, σ_k exhibits an inverse relationship, decreasing in the direction of increasing v_h. Simultaneously, when the chamfer angle (α) increases from $\alpha = 5°$ to $\alpha = 15°$, σ_k increases proportionally in the direction of increasing α,

while maintaining I_h at the level of $I_h = 190$ A. The objective function σ_k illustrated in Fig. 6b, which exhibits a nonlinear form when plotted in the coordinates of v_h and α. Notably, the degree of curvature observed in this case is larger than that observed at $I_h = 160$ A;

- When the current intensity I_h is set at 220 A, an incremental rise in v_h from 6 m/h to 10 m/h results in a corresponding decrease in σ_k, demonstrating an inverse relationship between v_h and σ_k. Similarly, as the angle α progresses from 5° to 15°, σ_k exhibits a proportional increase with respect to α. The graph depicting the objective function σ_k, in the context of both v_h and α coordinates, assumes a non-linear form, as illustrated in Fig. 6c. The degree of curvature observed in this graph is greater than that observed in the case of $I_h = 190$ A, as depicted in Fig. 6b.

In order to elucidate the correlation between the tensile strength of the narrow gap weld (σk) and its input parameters, a comprehensive analysis was conducted. In each scenario, wherein one of the three input parameters remained constant, the objective function to be determined was graphically depicted in a two-dimensional format, as indicated by the aforementioned equations. The resulting graphical representations can be observed in Figs. 7, 8 and 9, presented below.

Based on the 3D surface plots and the 2D plots depicted in Figs. 4, 5, 6, 7, 8 and 9, respectively, it can be deduced that within the confined range of adjustable input process parameters, the objective function exhibits favorable outcomes, thereby ensuring the quality of narrow gap welding process. This finding is particularly noteworthy when comparing it to previously published studies focusing on the microstructural characteristics of weld materials associated with various conventional welding techniques [4–6].

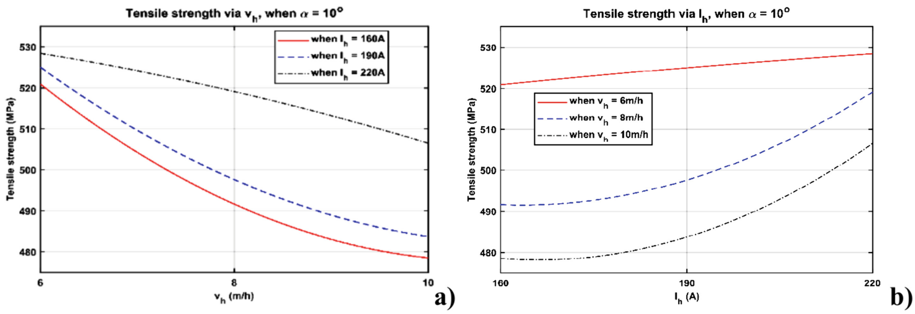

Fig. 7. Influence of process parameters (I_h, v_h) on the tensile strength (σ_k) when chamfer angle $\alpha = 10\ ^0$ and $I_h = 160$ A; 190 A; 220 A (a); $v_h = 6$; 8; 10 m/h (b)

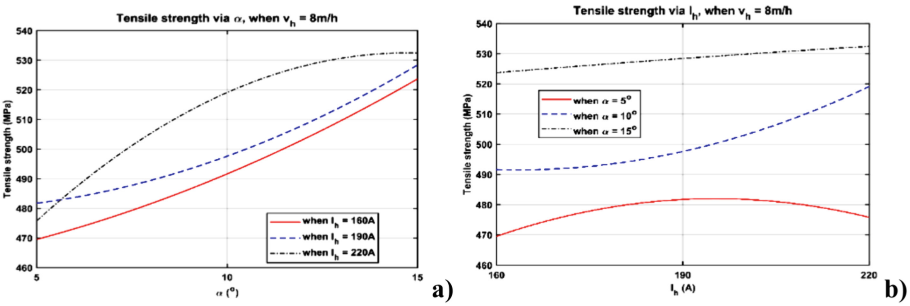

Fig. 8. Influence of process parameters (I_h,α) on the tensile strength (σ_k) when weld speed v_h = 8 m/h and I_h = 160 A; 190 A; 220 A (a); α = 5°; 10°; 15 º (b)

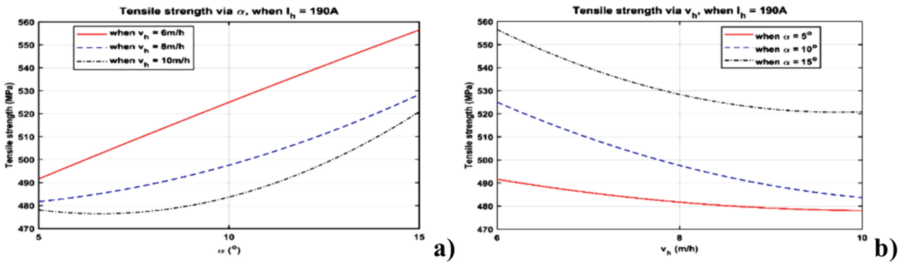

Fig. 9. Influence of process parameters (v_h,α) on the tensile strength (σ_k) when the current I_h = 190 A and v_h = 6; 8; 10 m/h (a); α = 5°; 10°; 15° (b)

4 Conclusion

1) Using the experimental planning method with full orthogonal array N27, this study presents welded workpieces of the butt joint of carbon steel SS400 with a narrow gap (b_0 = 10 mm) with different welding modes. These modes vary based on three levels of input process parameters in the observation range, the current (I_h), weld speed (v_h), and angle chamfer (α).Then, samples for the destructive tensile test are machined and the tensile strength of the weld material in destructively test with the direction perpendicular to the weld are obtained. Experimental result indicates a good weld quality with the mean tensile strength $\sigma_k$in the interval 460.016 ÷ 540.066 MPa for all weld modes selected at 27 points of experimental planning.

2) This study also presents a mathematical mode for predicting the tensile strength of weld material in narrow gap welding carbon steel SS400 (Eq. 1) with a small error around 2.9585% in comparison with the experiment data. Besides, 3D surface plots and 2D plots describe the influence input process parameters (I_h, v_h, and α) on the output of the objective function of the tensile strength of weld material σ_k, then the analysis and evaluation of the research results were discussed. Accordingly, it is possible to select any reasonable parameters set of welding modes in the observation range corresponding to the quality level of the narrow gap welding which is evaluated through the tensile

strength criterion, and this criterion with the corresponding calculated value is suitable for the purpose and requirement of the weld structure to be manufactured.

References

1. Narrow Gap Welding Process Tandem Submerged Arc., LINCOLN Electric Automation
2. www.airliquidewelding.com
3. Ngo, B.T., Le, T.Q., Ngo, V.D., Pham, D.L.: Narrow gap welding in protective gas for thick steel plates with un-chamfered edges. In: Proceeding of the 4th National Conference on Mechanical Science & Technology, Path 1, pp. 121–129. Ho Chi Minh City (2015)
4. Ngo, B.T., Ha, M.H., Dao, D.T., Van, D.N.: Research characteristic butt welding for narrow gap welding with chamfered edges. Vietnam Mechan. Eng. J. **12**, 15–22 (2020)
5. Ha, M.H., Ngo, B.T., Dao, D.T., Van, D.N.: Study on microstructural properties of butt welded material for thick plate carbon steel with narrow gap and small chamfer angles. J. Sci. Technol. Hanoi Industrial University **58**(1), 65–69 (2022)
6. Vu, D., Ha, M.H., Van, D.N., Ngo, B.T.: Study on Mechanical Properties of MAG Welding Joints of Steel Plates with Large Wall Thicness and Small Chamfer Angle. In: The 5th International Conference on Control, Control, Robotics and Informatics, Session 2 – Machinery and Control Technology, RS 005. Danang Vietnam (2022)
7. Ha, M.H., Ngo, T.B., Vu, D.: The experimetal research on mechanical properties and microstructural characteristics of narrow gap welding carbon steel. In: The 5th International Conference on Engineering and Research Applications 2022, ICERA 2022. Thai Nguyen (2022)
8. Ха, М.Х., Орлов, М.И.: Разработка математической модели процесса сварки взрывом Антифрикционных листов сталь+бронзы, сталь+алюминиевые сплавы, Известия Вузов. Изд.“Чёрнаяметаллургия”, МИСиС, Москва, Россия, No. 5, стр. 37–42 (1993)

Multi-objective Optimization for Surface Roughness, Cutting Force, and Material Removal Rate During Turning 4340 Alloy Steel by Using Support Machine Vector and NSGA-III

Van-Hai Nguyen[1](✉), Tien-Thinh Le[1], Nhu-Tung Nguyen[2], Van-Phong Le[1], and Thi-Lien Vu[1]

[1] Faculty of Mechanical Engineering and Mechatronics, PHENIKAA University, Yen Nghia, Ha Dong, Hanoi 12116, Vietnam
hai.nguyenvan1@phenikaa-uni.edu.vn

[2] Faculty of Applied Sciences, International School, Vietnam National University, Hanoi, Vietnam

Abstract. The focus of this research paper is to optimize the process parameters for turning AISI 4340 alloy steel, with the objective functions of achieving a simultaneous minimum of surface roughness (Ra) and cutting force (Fc) and maximum material removal rate (MRR) under the cutting parameter constraints of cutting speed, tool nose radius, feed rate, and depth of cut. In order to achieve this, a combination of Support Vector Machine regression (SVR) algorithms and a Non-Dominated Sorting Genetic Algorithm (NSGA-III) is utilized to determine the optimal solution. First, the SVR model is applied to predict Ra, Fc, and MRR using the GridSearchCV algorithm to search for the best hyperparameters. Then, the NSGA-III is implemented to obtain the optimal solutions, while SVRs are objective functions. Results indicate that Ra ranges between 0.973 and 1.711 µm, while the cutting force ranges between 1.978 and 31.279 kgf, and MRR ranges between 1.679 and 16.192 cm^3/min for the fifty Pareto solutions. Finally, experimental validations are conducted to confirm predictive results.

Keywords: AISI 4340 alloy steel · multi-objective optimization · machine learning · NSGA-III · surface roughness · cutting force · material removal rate

1 Introduction

The AISI 4340 alloy steel is widely used in aircraft and automotive manufacturing industries due to its desirable properties, including high strength, toughness, and wear resistance. However, its classification as a hard-to-cut material presents challenges in machining, particularly in turning operations [1]. The selection of optimal process parameters is crucial to improve the machined quality, productivity, and economics. Cutting parameters, such as cutting speed, feed rate, depth of cut, tool material and geometry, and tool nose radius, significantly affect the machined accuracy and surface quality, which

D. C. Nguyen et al. (Eds.): ICERA 2023, LNNS 944, pp. 132–140, 2024.
https://doi.org/10.1007/978-3-031-62235-9_16

are essential criteria for customer demand [2]. Achieving a good surface finish requires balancing the trade-off between increased cutting speed to reduce machining time and the resulting higher cutting forces and poorer surface quality. Therefore, there is a need to determine the appropriate cutting parameters to enhance machining performance, such as reducing energy consumption and increasing the material removal rate.

Optimization algorithms have been extensively employed to identify the ideal cutting parameters in machining processes. Specifically, evolutionary computing and metaheuristic techniques have been widely used. To consider multiple objectives, multi-objective optimization techniques have been proposed. Support Vector Regression and Artificial Neural Networks have also been investigated as predictive models in recent studies [3]. This amalgamation of techniques has been demonstrated to be effective in optimizing process parameters for enhancing performance characteristics.

Despite the effectiveness of these techniques, there is a lack of studies on multi-objective optimization for performance characteristics during turning AISI 4340. Therefore, this study aims to bridge this gap in the literature by finding the optimal process parameters that concurrently minimize Ra and Fc while maximizing MRR. Current work developed a predictive model for surface roughness, cutting force, and MRR using Support Vector Regression. First, the hyperparameters of this model were tuned using the GridSearchCV algorithm with a criterion of minimum mean squared error. Next, we utilized the NSGA-III algorithm to determine the Pareto Solution.

The results of this study have important implications for sustainable and eco-friendly manufacturing practices. By reducing energy consumption and machining costs and improving product quality, the optimal process parameters identified in this study can contribute to the development of such practices.

2 Materials and Methodologies

2.1 Methodologies

This research presents how to determine optimal Ra, Fc, and MRR solutions regarding the NSGA-III. SVR algorithm plays a role as a predictive model, i.e., objective functions represent Ra, Fc, and MRR. The cutting parameters include cutting speed, cutting nose radius, feed rate, and depth of cut. Figure 1 outlines this study approach, detailing the steps involved in dataset extraction, feature selection, and data normalization, as well as the SVR technique employed to estimate the parameters Ra, Fc, and MRR. The predictive model is developed utilizing SVR, where 80% of the input data is randomly selected for training, and the remaining 20% is used for model validation. GridSearchCV fine-tuning is then utilized to determine the optimal hyperparameters using a low mean squared error criterion. Lastly, the Pareto front determines optimal solutions by setting constraints on the lowest Ra, cutting force, and highest MRR.

2.2 Support Vector Machine Regression (SVR)

The SVM was capable of handling classification and regression problems. Its underlying concept was first introduced by Vapnik et al. [4]. SVM has several advantages. Firstly, it can perform effectively in high-dimensional spaces, making it ideal for problems that involve numerous input variables. Secondly, SVM is memory-efficient because it only utilizes a portion of training data in the decision-making process. Finally, SVM is versatile as various functions can be used in decision-making. In this context, SVR is usually used in mechanical engineering fields [5, 6].

2.3 Multi-objective Optimization Algorithm

NSGA-III algorithm shares a basic framework with the original NSGA-II [5] but significantly changes its selection mechanism. Maintaining variety among population members in NSGA-III is accomplished by supplying and adapting widely distributed reference points. The original NSGA-III algorithm is briefly presented to offer context. The procedure is shown in Algorithm 1.

Algorithm 1 Generation t of NSGA-III procedure

Input: H structured reference points Z^s or supplied aspiration points Z^a, parent population P_t

Output: P_{t+1}

```
S_t = ∅, i = 1
Q_t = Recombination+Mutation(P_t)
R_t = P_t ∪ Q_t
(F_1, F_2, . . .) = Non-dominated-sort(R_t)
repeat
    S_t = S_t ∪ Fi and i = i + 1
until |S_t| ≥ N
Last front to be included: F_l = Fi
if |S_t| = N then
    P_t
else
    P_t+1 = ∪_{j=1}^{l-1} F_j
    Points to be chosen from F_l: K = N − |P_t+1|
    Normalize objectives and create reference set Z^r: Normalize(f^n , S_t, Z^r , Z^s, Z^a)
    Associate each member s of S_t with a reference point: [π(s), d(s)] =Associate(St, Z^r) %π(s): closest reference point, d: distance between s and π(s)
    Compute niche count of reference point j ∈ Z^r: ρ_j = Σ_{s∈S_t/F_l}((π(s)=j) ? 1:0)
    Choose K members one at a time from Fl to construct P_t+1: Niching(K, ρ_j, π, d, Z^r , F_l , P_t+1)
end if
```

3 Data Collection

In this study, the authors conducted experiments on an MTAB MAXTURN CNC lathe, utilizing previously reported data from the literature [1]. The workpiece used in the experiments had specific dimensions and chemical composition, with a length of 100 mm and a diameter of 24 mm, made of AISI 4340 alloy steel. The cutting tool employed in the machining process was a tungsten-coated carbide CCMT-090308 of grade K-10, mounted on the right-hand side of the cutting holder. Sixty experimental runs were carried out with various cutting parameters by factorial design of the experiment, as shown in Table 1. Table 2 summarizes the process parameters and measured results for Ra and cutting force in the 60 experimental runs.

According to the literature [1], Ra was measured using a Mitutoyo SJ-210P handheld instrument, while Fc was determined via Dynoware software connected to the Kistler dynamometer using a magnification unit. MRR is calculated using the following formula:

$$MRR = Vc \times f \times D\left(cm^3/min\right) \tag{1}$$

Table 1. Factors and levels of machining parameters.

Cutting factors	Unit	Level 1	Level 2	Level 3	Level 4	Level 5
Cutting speed, [Vc]	mm/min	75	90			
Feed rate, [f]	mm/rev	0.04	0.06	0.08	0.10	0.12
Depth of cut, [a]	mm	0.5	1.0	1.5		
Tool radius nose, [r]	mm	0.4	0.8			

4 Results and Discussion

4.1 Predictive Performance of SVR

The performance of the SVR model is shown in Fig. 2a-c for regression analysis. The figures indicate the scatter points between experimental and predicted data points for the training and testing parts. The coefficient of correlation R^2 for the prediction of Ra, Fc, and MRR is more than 0.943 regarding the training and testing models. Moreover, the linear fit is also close to the diagonal line, showing the model's good performance. Finally, all data points are distributed almost equally around the linear fit, and there is no concentration zone. This means that the model is not over or under-fitted. Besides, the RMSE values of all models are quite small; this demonstrates that the SVR model exhibits good predictive performance for Ra, Fc, and MRR.

Based on these analyses, the SVR is employed as a prediction function in the next sections.

4.2 Multi-objective Optimization

This study aims to identify optimal turning parameters that minimize surface roughness and cutting force while maximizing MRR. Due to the conflicting nature of these objectives, multi-objective optimization is the most appropriate method to address this problem. As previously discussed, the SVR model has demonstrated strong predictive performance for Ra, cutting force, and MRR. Thus, the multi-objective problem can be formulated as Eq. 1, in which SVR_reg_Ra, SVR_reg_Fc, and SVR_reg_MRR represent models for predicting Ra, cutting force, and MRR, respectively, with distinct hyperparameters (Table 3).

Objectives:

$$Minimize\ Ra = SVR\_reg\_Ra(V_c, r, f, a) \tag{2}$$

$$Minimize\ Fc = SVR\_reg\_Fa(V_c, r, f, a) \tag{3}$$

$$Maxize\ MRR = SVR\_reg\_MRR(V_c, r, f, a) \tag{4}$$

Subject to constraints:

$$50 \le V_c \le 375$$

Table 2. Experimental runs achieve results [1].

No.	Vc	r	f	a	Ra	Fc	MRR	No.	Vc	rt	f	a	Ra	Fc	MRR
1	1	2	1	3	1	22.5	4.50	31	1	1	1	3	1.1	22.6	4.50
2	1	2	1	2	1.1	15.5	3.00	32	1	1	1	2	1.2	15.2	3.00
3	1	2	1	1	1.3	7.67	1.50	33	1	1	1	1	1.5	6.62	1.50
4	1	2	2	3	1.2	33.2	6.75	34	1	1	2	3	1.1	31.4	6.75
5	1	2	2	2	1.3	23.2	4.50	35	1	1	2	2	1.3	21.2	4.50
6	1	2	2	1	1.4	11.7	2.25	36	1	1	2	1	1.6	9.71	2.25
7	1	2	3	3	1.4	39.9	9.00	37	1	1	3	3	1.2	38.8	9.00
8	1	2	3	2	1.5	28.1	6.00	38	1	1	3	2	1.4	27.5	6.00
9	1	2	3	1	1.6	13.6	3.00	39	1	1	3	1	1.9	12.6	3.00
10	1	2	4	3	1.6	45.4	11.25	40	1	1	4	3	1.3	45.6	11.25
11	1	2	4	2	1.6	32.8	7.50	41	1	1	4	2	1.6	31.7	7.50
12	1	2	4	1	1.8	16.9	3.75	42	1	1	4	1	2.1	15.5	3.75
13	1	2	5	3	1.7	52.3	13.50	43	1	1	5	3	1.5	52.8	13.50
14	1	2	5	2	1.8	37.3	9.00	44	1	1	5	2	1.8	37.1	9.00
15	1	2	5	1	1.9	19.2	4.50	45	1	1	5	1	2.3	17.6	4.50
16	2	2	1	3	1.3	20.7	5.40	46	2	1	1	3	2.1	22.8	5.40
17	2	2	1	2	1.4	14.1	3.60	47	2	1	1	2	1.4	14.6	3.60
18	2	2	1	1	1.4	7.81	1.80	48	2	1	1	1	1.8	6.87	1.80
19	2	2	2	3	1.4	31.4	8.10	49	2	1	2	3	2.2	30.8	8.10
20	2	2	2	2	1.5	21.5	5.40	50	2	1	2	2	1.5	20.5	5.40
21	2	2	2	1	1.6	10.7	2.70	51	2	1	2	1	1.9	10.2	2.70
22	2	2	3	3	1.7	39.1	10.80	52	2	1	3	3	2.3	39.8	10.80
23	2	2	3	2	1.7	28.2	7.20	53	2	1	3	2	1.7	27.5	7.20
24	2	2	3	1	1.8	14.7	3.60	54	2	1	3	1	2.2	13.4	3.60
25	2	2	4	3	1.8	44.2	13.50	55	2	1	4	3	2.5	46.2	13.50
26	2	2	4	2	1.8	31.6	9.00	56	2	1	4	2	1.8	31.9	9.00
27	2	2	4	1	1.9	16.5	4.50	57	2	1	4	1	2.3	16.3	4.50
28	2	2	5	3	1.9	50.6	16.20	58	2	1	5	3	2.9	51.1	16.20
29	2	2	5	2	2	36.7	10.80	59	2	1	5	2	2.1	36.6	10.80
30	2	2	5	1	2.2	19.5	5.40	60	2	1	5	1	2.5	18.7	5.40

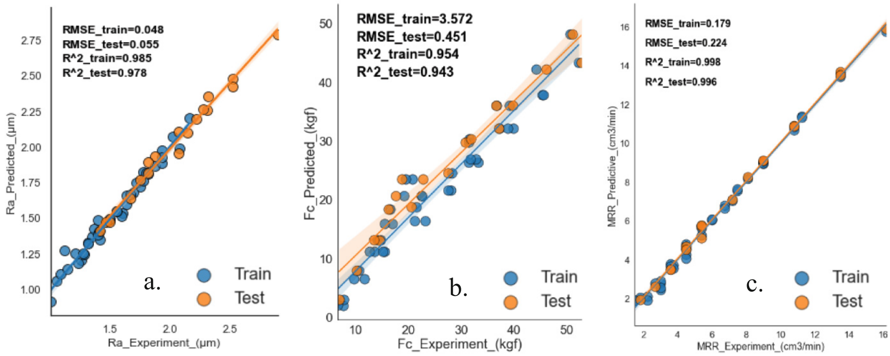

Fig. 1. Relationship between experiment and predictive: a). Ra, b). Fc, c). MRR.

$$0.4 \leq r \leq 0.8$$

$$0.02 \leq f \leq 0.25$$

$$0.1 \leq a \leq 1.5$$

Table 3. Parameters for NSGA-III

Input parameter	Population size	Maximum generations	Crossover rate	Mutation Rate	Selection rate
Value	50	100	0.85	0.25	0.25

The NSGA-III algorithm exhibited successful convergence after 2500 simulation runs, with 50 optimal solutions lying evenly and representatively on the Pareto front, as shown in Fig. 2. These Pareto solutions, marked in red, demonstrate the first performance objective of Ra lying between 0.973 and 1.711 µm, Fc between 1.978 and 31.279 kgf, and MRR between 1.679 and 16.192 cm^3/min. The visualization of predicted and experimental results in Fig. 3 reveals that Ra and Fc converge towards minimizing values for each other. In contrast, MRR is distributed across a wide range of values. The wide range of values for MRR observed among the Pareto solutions indicates that it is more challenging to optimize MRR along with Ra and cutting force simultaneously. This could be because optimizing for one objective could lead to trade-offs with respect to the other objectives.

4.3 Validated Experiment Results

Experimental turning was performed on an FEL-1440GMW MAGNUM-CUT lathe using the Minimum Quantity Lubrication (MQL) technique with Ethylene Glycol as

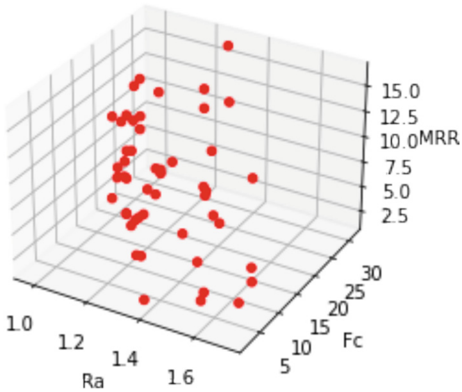

Fig. 2. Performance statistics obtained for 50 Pareto solutions.

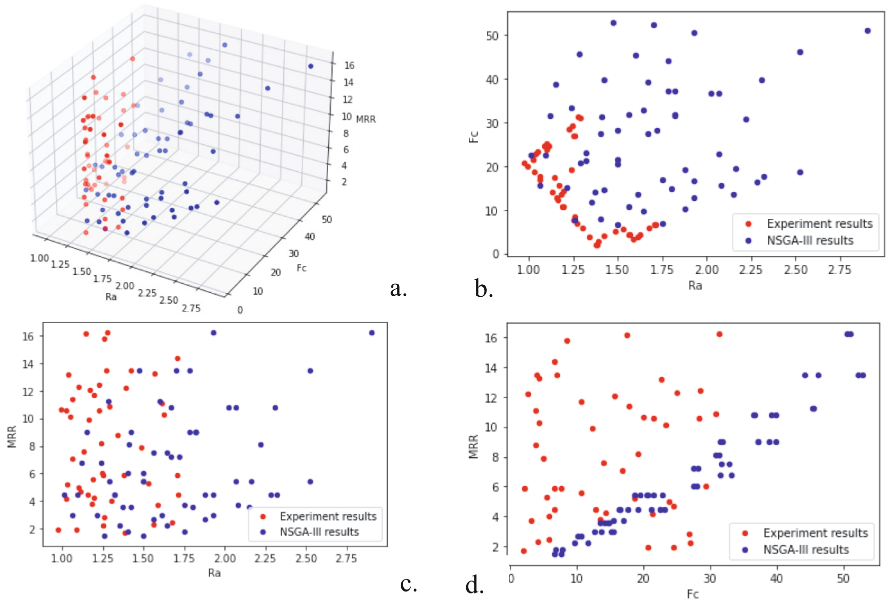

Fig. 3. Visualization of NSGA-III and experimental results.

coolant, delivered at a 140 ml/hr flow rate. The specimens used in the experiments were cylindrical AISI 4340 workpieces with 24 mm diameter and 100 mm length clamped in a self-created fixture. The inserts CCMT-090304 and CCMT-090308 were mounted on grade K10 tool holding. A Kistler Type 9139AA dynamometer was used to measure the cutting force, and the experimental setup is depicted in Fig. 4.

The results in Table 4 demonstrate that the results from NSGA-III are consistent with the test results. The mean absolute percentage errors (MAPE) are 6.97%, 5.28%, and 6.81% for Ra, Fc, and MRR, respectively. The deviation values of Ra, Fc, and MRR

Table 4. Validation of predicted results.

No.	Vc	r	f	a	Optimal results			Experimental results			Absolute percentage error		
					Ra	Fc	MRR	Ra	Fc	MRR	Ra	Fc	MRR
10	87.82	0.8	0.04	0.69	1.68	5.75	2.48	1.442	6.13	2.48	16.5%	6.2%	1.21%
24	88.15	0.4	0.04	0.56	1.09	24.53	1.97	0.126	23.46	1.97	3.2%	4.5%	10.15%
47	75.10	0.8	0.12	1.47	1.57	4.33	13.22	1.489	4.562	13.22	5.4%	5.1%	9.08%
Mean Absolute Percentage Errors											6.97%	5.28%	6.81%

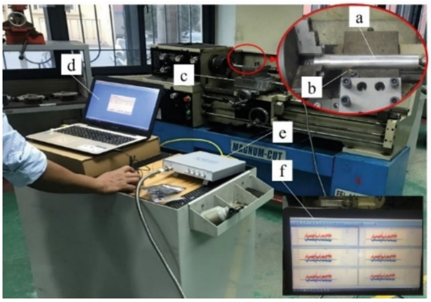

Fig. 4. Experimental procedure: a). Workpiece, b). Cutting insert, c). Dynamometer, d). DynoWare software, e). Data processing box, f). Cutting force results [1].

could be attributed to different machine tools, measurement devices, and other factors. Nonetheless, the test results support the notion that NSGA-III and SVR can be effectively integrated to optimize Ra, Fc, and MRR.

5 Conclusion

This study uses SVR and NSGA-III in multi-objective optimization to minimize Ra and Fc while maximizing MRR in turning AISI 4340 steel. First, SVR is employed to predict output parameters. The NSGA-III algorithm results in Ra lying between 0.973 and 1.711 μm, Fc between 1.978 and 31.279 kgf, and MRR between 1.679 and 16.192 cm^3/min. Experimental results show a MAPE of 6.97% for Ra, 5.28% for Fc, and 6.81 for MRR. Further research is needed to develop an intelligent system incorporating user preferences and to investigate cutting force and other manufacturing cost factors. The study also recommends considering cutting micro tool characteristics and process stability in future research.

References

1. Nguyen, A.-T., Nguyen, V.-H., Le, T.-T., Nguyen, N.-T.: A hybridization of machine learning and NSGA-II for multi-objective optimization of surface roughness and cutting force in AISI 4340 alloy steel turning. J. Machi. Eng. **23**(1), 133–153 (2023)

2. Rao, S.N., Satyanarayana, B., Venkatasubbaiah, K.: Experimental estimation of tool wear and cutting temperatures in MQL using cutting fluids with CNT inclusion. Int. J. Eng. Sci. Technol **3**(4) (2011)
3. Nguyen, V.-H. et al.: Applying bayesian optimization for machine learning models in predicting the surface roughness in single-point diamond turning polycarbonate. Math. Prob. Eng. **2021** (2021)
4. Cortes, C., Vapnik, V.: Support vector machine. Mach. Learn. **20**(3), 273–297 (1995)
5. Nguyen, V.-H., Le, T.-T., Truong, H.-S., Duong, H.T., Le, M.V.: Predicting volumetric error compensation for five-axis machine tool using machine learning. Int. J. Comp. Integr. Manufact. 1–28 (2023)
6. Nguyen, V.-H., Le, T.-T.: Developing geometric error compensation software for five-Axis CNC machine tool on NC program based on artificial neural network. In Advances in Asian Mechanism and Machine Science: Proceedings of IFToMM Asian MMS 2021 6, pp. 541–548. Springer (2022). https://doi.org/10.1007/978-3-030-91892-7_51

Multi-objective Optimization of a Two-Stage Bevel Helical Gearbox to Increase Efficiency and Reduce Gearbox Across Section Area

Dinh Van Thanh[1], Tran Huu Danh[2], Nguyen Van Binh[3], Bui Thanh Danh[4], Hoang Xuan Tu[5], and Nguyen Van Trang[5](✉)

[1] East Asia University of Technology, Ha Noi City, Vietnam
[2] Vinh Long University of Technology Education, Vinh Long, Vietnam
[3] Nguyen Tat Thanh University, Ho Chi Minh City, Vietnam
[4] University of Transport and Communications, Ha Noi, Vietnam
[5] Thai Nguyen University of Technology, Thai Nguyen, Vietnam
nvtrang@tnut.edu.vn

Abstract. The objective of this research is to look at multi-target optimization of two-stage bevel helical gearboxes with the goal of determining the ideal critical design aspects to reduce gearbox across section area (GASA) and boost gearbox efficiency (GE). In two stages, the Taguchi technique and grey relation analysis (GRA) were used to address the problem. First, the single-objective optimization issue was addressed in order to narrow the gap between variable levels, and then the multi-objective optimization problem was handled in order to identify the optimal major design variables. The coefficients of wheel face width (CWFW) of the first and second stages, allowable contact stresses (ACS) of the first and second stages, and the first stage gear ratio were also determined. The study's findings were utilized to identify the best values for five critical design aspects for a two-stage bevel helical gearbox.

Keywords: Bevel helical gearbox · Two-stage gearbox · Multi-objective optimization · Gear ratio · Gearbox efficiency · Gearbox across section area

1 Introduction

The existing literature shows a variety of studies on helical gearbox. [1] conducted a study that explored optimal gear ratios for a two-stage bevel helical gearbox, using cross-sectional area as the objective. In the similar area of interest, [2] determined optimal gear ratios, which affects the size, mass, volume, and cost of a two-stage bevel helical gearbox. This was achieved through getting the minimum gearbox volume. Another study conducted a simulation experiment to assess the impact of input factors like total ratio, face width coefficients, contact stress, and output torque on optimal ratios [3]. [4] looked into gear ratios for three-stage helical gearbox, aiming for minimal volume. Furthermore, [5] investigated gear pitting resistance and movement equilibrium to find explicit formulas for partial ratios for mechanical drive systems with a chain drive and two-step bevel

D. C. Nguyen et al. (Eds.): ICERA 2023, LNNS 944, pp. 141–158, 2024.
https://doi.org/10.1007/978-3-031-62235-9_17

helical gearbox. [6] analyzed ten design factors via a simulation experiment, optimizing partial gear ratios for two-stage bevel helical gearboxes to reduce costs. [7] investigated the use of airborne sound for condition monitoring of multi-stage helical gearboxes. It found that Modulation Signal Bispectrum peaked with baseline normalization enhanced monitoring accuracy and consistency. [8] conducted an experiment using a computer program to assess the effect of different input factors on optimal ratios, proposing models that helped to determine optimal gear ratios accurately. Using simulation to analyze eleven input parameters, [9] aimed to optimize partial gear ratios for three-stage bevel helical gearboxes by minimizing gearbox cost. Moreover, [10] offered effective models for calculating partial ratios of the V-belt and a three-step bevel helical gearbox, giving minimal system height.

The purpose of this research is to explore multi-target optimization learning for a two-stage bevel helical gearbox. Two single aims were targeted in this effort: lowering GASA and optimizing GE. In addition, five major design elements were evaluated: the CWFW for both stages, the ACS for both stages, and the gear ratio for the first stage. Furthermore, by combining the Taguchi technique with the GRA, the multi-objective optimization problem in gearbox design was addressed in two stages. The best values of five critical design variables for developing a two-stage bevel helical gearbox were also proposed.

2 Optimization Problem

2.1 Determining Gearbox Across Section Area

The GASA of a bevel helical gearbox can be determined by (Fig. 1):

$$A_{gb} = L \cdot H \tag{1}$$

where, L and H are the length and the across section area of the gearbox. These elements are found by (Fig. 1):

$$L = 2 \cdot l_0/3 + d_{e21}/2 + d_{w12}/2 + d_{w22} + 2 \cdot k \tag{2}$$

$$H = \max(d_{e21}; d_{w22}) + 8.5 \cdot S_G \tag{3}$$

In (2), $k = 8 \div 12$ [2]; $l_0 = 3 \cdot d_{s1}$ with d_{s1} represents the initial shaft diameter obtained by [2]:

$$d_{s1} = [T_{11}/(0,2 \cdot [\tau])]^{1/3} \tag{4}$$

d_{e21} is the bevel gear's outer pitch diameter (in mm), that can be computed as [12]:

$$d_{e21} = 2 \cdot u_1 \cdot R_e / \left(1 + u_1^2\right)^{1/2} \tag{5}$$

In where, R_e is the cone distance (mm) which can be determined by [12]:

$$R_e = k_R \cdot \sqrt{u_1^2 + 1} \cdot \sqrt[3]{T_{11} \cdot k_{h\beta 1} / \left[(1 - k_{be}) \cdot k_{be} \cdot u_1 \cdot [\sigma_H]^2\right]} \tag{6}$$

wherein, $k_R = 50$ (MPa) is a coefficient [12]; $k_{H\beta 1} = 1.04 \div 1.18$ is the contacting load ratio for pitting resistance [13]; $k_{be} = b/R_e = 0.25 \div 0.3$ is face width coefficient; T_{11} is the torque on pinion (Nmm) and d_{e11} and d_{e21} are the outer pitch diameters of the pinion and the gear of the bevel gear set.

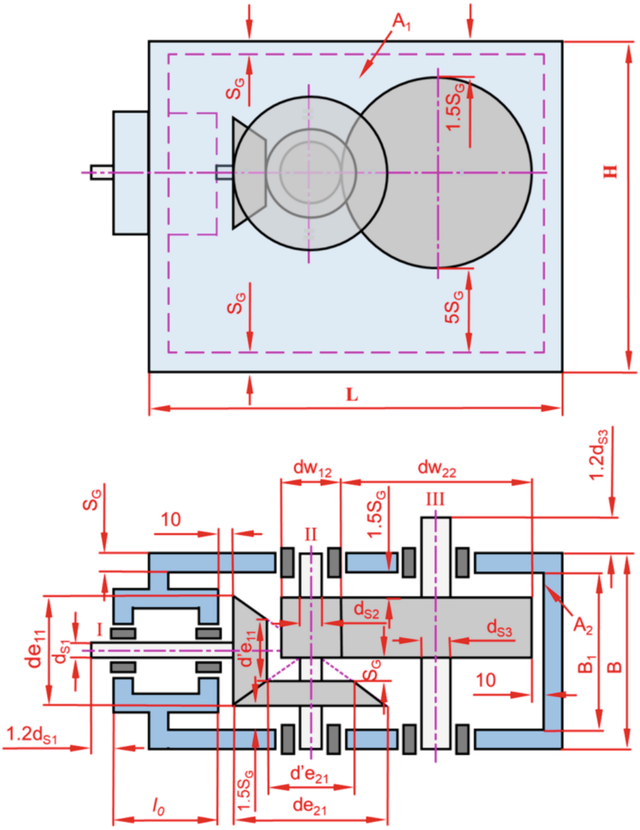

Fig. 1. Calculated schema [11]

In (1), d_{w12} and d_{w22} are the pitch diameters of the pinion and gear of the helical gear set [2]:

$$d_{w12} = 2 \cdot a_w/(u_2 + 1) \tag{7}$$

$$d_{w22} = 2 \cdot a_w \cdot u_2/(u_2 + 1) \tag{8}$$

In which, a_{w2} denotes the center distance of helical gear set which is found by [12]:

$$a_w = k_a \cdot (u_2 + 1) \cdot \sqrt[3]{T_{12} \cdot k_{H\beta 2}/(\mathrm{AS}_2^2 \cdot u_2 \cdot X_{ba})} \tag{9}$$

wherein, $k_{H\beta 2} = 1.05 \div 1.27$ is contacting load ratio for pitting resistance [12]; AS2 is permissible contact stress (MPa); $k_a = 43$ is a coefficient [12]; X_{ba} is the wheel face width of helical gear set; T_{12} are the torque on the pinion of the helical gear set (Nmm):

$$T_{11} = T_{out}/\left(u_g \cdot \eta_{bg} \cdot \eta_{hg} \cdot \eta_b^3\right) \tag{10}$$

$$T_{12} = T_{out}/\left(u_2 \cdot \eta_{hg} \cdot \eta_b^2\right) \tag{11}$$

where, T_{out} is the output torque (N.mm); η_{bg} is the bevel gear efficiency ($\eta_{bg} = 0.95 \div 0.97$; η_{hg} is the helical gear efficiency ($\eta_{hg} = 0.96 \div 0.98$ [12]; η_b is the rolling bearing efficiency ($\eta_b = 0.99 \div 0.995$ [12]).

In (3), S_G is calculated by [14]:

$$S_G = 0.005 \cdot L + 4.5 \tag{12}$$

2.2 Calculating Gearbox Efficiency

A gearbox's efficiency may be calculated in the following manner:

$$\eta_{gb} = \frac{100 \cdot P_l}{P_{in}} \tag{13}$$

In which, P_l represents the total power loss of the gearbox [15]:

$$P_l = P_{lg} + P_{lb} + P_{ls} \tag{14}$$

where, P_{lg} is the total power loss of gears; P_{lb} the power loss of bearings, and P_{ls} the power loss of seals. These elements can be found by:

+) The total power loss of gear:

$$\mathrm{P}_{lg} = \sum_{i=1}^{2} \mathrm{P_{lgi}} \tag{15}$$

In where, P_{lgi} is the gear power losses of i stage which can be calculated by:

$$P_{lgi} = P_{gi} \cdot \left(1 - \eta_{gi}\right) \tag{16}$$

In which,η_{gi} the efficiency of the i step [16]:

$$\eta_{gi} = 1 - \left(\frac{1 + 1/\mathrm{u_i}}{\beta_{\mathrm{ai}} + \beta_{\mathrm{ri}}}\right) \cdot \frac{\mathrm{f_i}}{2} \cdot \left(\beta_{\mathrm{ai}}^2 + \beta_{\mathrm{ri}}^2\right) \tag{17}$$

wherein, u_i is the gear ratio of the i step, f is the friction coefficient; β_{ai} and β_{ri} are the arcs of approach and recess on the i step which are found by [16]:

+) For the bevel gear step:

$$\beta_{\mathrm{ai}} = \frac{\left(\mathrm{R_{eev2}^2} - \mathrm{R_{0v2}^2}\right)^{1/2} - \mathrm{R_{v2}} \cdot \sin\alpha}{\mathrm{R_{01i}}} \tag{18}$$

$$\beta_{\mathrm{ri}} = \frac{\left(\mathrm{R}_{\mathrm{aev1}}^2 - \mathrm{R}_{0\mathrm{v1}}^2\right)^{1/2} - \mathrm{R}_{\mathrm{v1}} \cdot \sin\alpha}{\mathrm{R}_{01\mathrm{i}}} \tag{19}$$

In where R_{aev1} and R_{aev2} are the analogous pinion and gear's outer radiuses, correspondingly; R_{v1} and R_{v2} are the comparable pinion and gear's pitch radiuses, accordingly; R_{0v1} and R_{0v2} are the equivalent pinion and gear's base radiuses, respectively; and is the pressure angle.

$$\mathrm{R}_{\mathrm{v1}} = \mathrm{R}_1/\cos\delta_1 \tag{20}$$

$$\mathrm{R}_{\mathrm{v2}} = \mathrm{R}_2/\cos\delta_2 \tag{21}$$

In where R_1 and R_2 represent the pitch radius of the bevel pinion and the gear at the large end, respectively; and δ_1 and δ_2 indicate the pitch angles of the bevel pinion and gears, correspondingly.

$$\mathrm{R}_{\mathrm{aev1}} = \mathrm{R}_{\mathrm{v1}} + \mathrm{a}_{\mathrm{p}} \tag{22}$$

$$\mathrm{R}_{\mathrm{aev2}} = \mathrm{R}_{\mathrm{v2}} + \mathrm{a}_{\mathrm{g}} \tag{23}$$

+) For the helical gear step:

$$\beta_{\mathrm{ai}} = \frac{\left(\mathrm{R}_{\mathrm{e2i}}^2 - \mathrm{R}_{02\mathrm{i}}^2\right)^{1/2} - \mathrm{R}_{2\mathrm{i}} \cdot \sin\alpha}{\mathrm{R}_{01\mathrm{i}}} \tag{24}$$

$$\beta_{\mathrm{ri}} = \frac{\left(\mathrm{R}_{\mathrm{e1i}}^2 - \mathrm{R}_{01\mathrm{i}}^2\right)^{1/2} - \mathrm{R}_{1\mathrm{i}} \cdot \sin\alpha}{\mathrm{R}_{01\mathrm{i}}} \tag{25}$$

In which, R_{e1i} and R_{e2i} are the outer radiuses of the pinion and gear, separately; R_{1i} and R_{2i} are the pitch radiuses of the pinion and gear, respectively; R_{01i} and R_{02i} are the base-circle radiuses of the pinion and gear, respectively; and α is the pressure angle.

The friction coefficient in (17) is determined by [11]:

- When the sliding velocity $v \le 0.424$ (m/s):

$$f = -0.0877 \cdot v + 0.0525 \tag{26}$$

- When the sliding velocity $v > 0.424$ (m/s):

$$f = 0.0028 \cdot v + 0.0104 \tag{27}$$

+) The power loss of bearings is found by [15]:

$$P_{lb} = \sum_{i=1}^{6} f_b \cdot F_i \cdot v_i \tag{28}$$

where, $f_b = 0.0011$ is the bearing friction coefficient since radical ball bearings with angular contact were used [15]; F is the bearing load (N), v is the peripheral speed, and $i = 1 \div 6$ is the bearing ordinal number.

+) The total power loss in seals is calculated by [15]:

$$P_s = \sum_{i=1}^{2} \mathrm{P}_{si} \tag{29}$$

In which, i = 1 ÷ 2 is the ordinal number of seals; P_{si} is the power loss in a single seal (w), which is determined by:

$$P_{si} = \left[145 - 1.6 \cdot t_{oil} + 350 \cdot log\, log(VG_{40} + 0.8)\right] \cdot d_s^2 \cdot n \cdot 10^{-7} \tag{30}$$

where, VG_{40} is the ISO Viscosity Grade number.

2.3 Objective Function and Constrains

2.3.1 Objectives Functions

In this work, the multi-objective optimization problem has two distinct goals:

Minimizing GASA:

$$\min f_2(X) = A_{\mathrm{gb}} \tag{31}$$

Maximizing GE:

$$\min f_1(X) = \eta_{gb} \tag{32}$$

where X is the vector of design variables indicating variables. Five primary design characteristics were chosen as variables in this study: u_1, k_{be}, X_{ba}, AS_1, and AS_2.

$$X = \{u_1, k_{\mathrm{be}}, X_{\mathrm{ba}}, AS_1, AS_2\} \tag{33}$$

2.3.2 Constrains

The multi-objective function must adhere to the following constraints:

$$1 \le u_1 \le 6 \text{ and } 1 \le u_2 \le 9 \tag{34}$$

$$0.25 \le k_{be} \le 0.3 \text{ and } 0.25 \le X_{ba} \le 0.4 \tag{35}$$

$$350 \le AS_1 \le 420 \text{ and } 350 \le AS_2 \le 420 \tag{36}$$

3 Methodology

Five major design features were chosen for investigation in this research. Table 1 displays the minimum and maximum values for different parameters. To solve the optimization problem, the Taguchi technique and grey relation analysis were applied. The L25 (5^5) design was used to optimize the number of levels for each variable. Among the variables considered, however, u1 has a pretty wide range (u_1 ranges from 1 to 6 - Table 1). Even with five levels, the difference in these attributes' values remained beneficial (in this case, the difference is ((6–1)/4 = 1.5)).

The 2-stage multi-objective optimization problem solution technique [17] (Fig. 2) was used to help narrow the difference between values of a variable spread throughout a wide range. This technique's first stage handles a single-objective optimization problem, while the second stage addresses a multi-objective optimization problem to select the best primary design features.

Table 1. Main design factors and their maximum and lowest restrictions

Factor	Notation	Lower limit	Upper limit
Gear ratio of first stage	u_1	1	6
CWFW of first stage	k_{be}	0.25	0.3
CWFW of second stage	X_{ba}	0.25	0.4
ACS of first stage (MPa)	AS_1	350	420
ACS of second stage (MPa)	AS_2	350	420

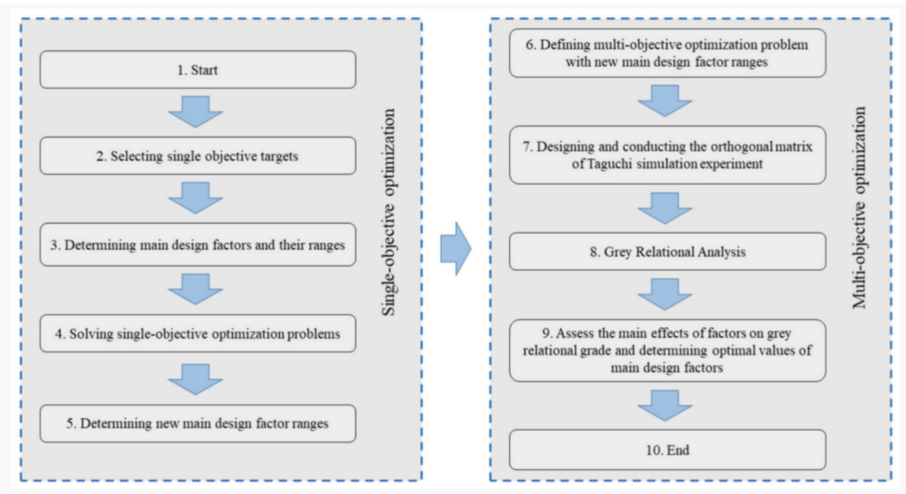

Fig. 2. Method for solving multi-objective problem [11]

4 Single-Objective Optimization

The direct search strategy is used in this work to solve the single-objective optimization issue. A Matlab-based computer program was also created to handle two single-objective problems: reducing GASA and maximizing GE. Figure 4 depicts the relationship between the optimal gear ratio of the first stage u1 and the overall gearbox ratio ut based on the findings of this program. Furthermore, new restrictions for the variable u_1 have been developed, as shown in Table 2 (Fig. 3).

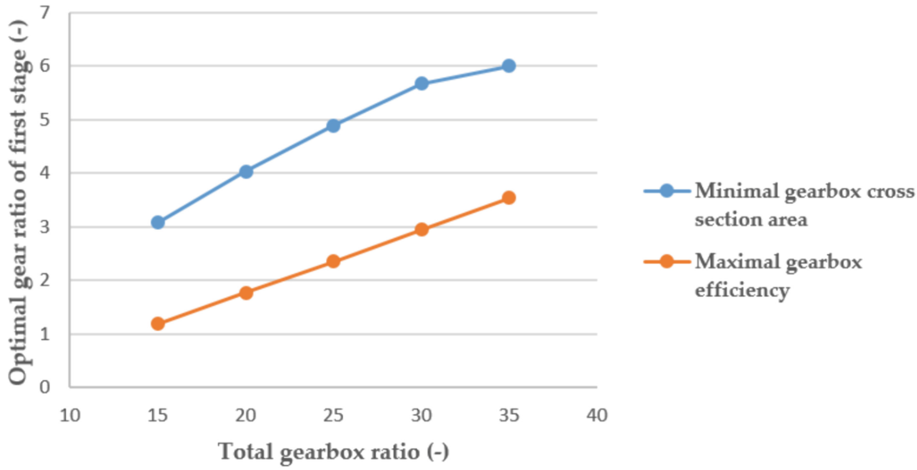

Fig. 3. Optimal first-stage gear ratio in relation to the total gearbox ratio

Table 2. New constraints of u_1

u_t	u_1	
	Lower limit	Upper limit
10	1.17	3.08
15	1.76	4.04
20	2.34	4.89
25	2.93	5.67
30	3.52	6
35	4.1	6

5 Multi-objective Optimization

The purpose of the multi-objective optimization problem for a two-stage bevel helical gearbox in this work is to discover the optimal primary design variables with a given total gearbox ratio that meets two single-objective functions: lowering GASA and optimizing

GE. A computing experiment was constructed for solving the given multi-objective optimization issue. Table 3 displays the key design components and their values for $u_t = 15$. The experimental design was created using the Taguchi technique using L25 (5^5) design, and the data was analyzed using Minitab R18 software. The experimental design and results for $u_t = 15$ are shown in Table 4.

Table 3. Main design factors and their levels for $u_t = 15$.

Factor	Notation	Level				
		1	2	3	4	5
Gear ratio of first stage	u_1	1.76	2.33	2.9	3.47	4.04
CWFW of stage 1	k_{be}	0.25	0.2625	0.275	0.2875	0.3
CWFW of stage 2	X_{ba}	0.25	0.2875	0.325	0.3625	0.4
ACS of stage 1 (MPa)	AS_1	350	367.5	385	402.5	420
ACS of stage 2 (MPa)	AS_2	350	367.5	385	402.5	420

Table 4. Experimental matrix and output findigs for $u_t = 15$

Exp. No.	Input Factors					A_{gb}	η_{gb}
	u_1	k_{be}	X_{ba}	AS_1	AS_2	(cm)	(%)
1	1.76	0.2500	0.2500	350	350	31.412	95.188
2	1.76	0.2625	0.2875	368	368	27.348	95.073
3	1.76	0.2750	0.3250	386	386	24.136	95.043
4	1.76	0.2875	0.3625	404	404	21.538	94.917
5	1.76	0.3000	0.4000	420	420	19.508	94.882
6	2.33	0.2500	0.2875	386	404	21.996	95.018
7	2.33	0.2625	0.3250	404	420	19.669	94.981
8	2.33	0.2750	0.3625	420	350	22.494	94.957
9	2.33	0.2875	0.4000	350	368	20.826	95.006
10	2.33	0.3000	0.2500	368	386	25.324	95.099
11	2.90	0.2500	0.3250	420	368	20.883	94.906
12	2.90	0.2625	0.3625	350	386	19.398	94.944
13	2.90	0.2750	0.4000	368	404	17.483	94.849
14	2.90	0.2875	0.2500	386	420	21.310	94.903
15	2.90	0.3000	0.2875	404	350	23.892	94.971

(*continued*)

Table 4. (*continued*)

Exp. No.	Input Factors					A_{gb}	η_{gb}
	u_1	k_{be}	X_{ba}	AS_1	AS_2	(cm)	(%)
16	3.47	0.2500	0.3625	368	420	16.766	94.894
17	3.47	0.2625	0.4000	386	350	19.068	94.907
18	3.47	0.2750	0.2500	404	368	22.979	94.916
19	3.47	0.2875	0.2875	420	386	20.234	94.833
20	3.47	0.3000	0.3250	350	404	18.841	94.909
21	4.04	0.2500	0.4000	404	386	16.448	94.785
22	4.04	0.2625	0.2500	420	404	19.823	94.871
23	4.04	0.2750	0.2875	350	420	18.502	94.877
24	4.04	0.2875	0.3250	368	350	20.733	94.847
25	4.04	0.3000	0.3625	386	368	18.529	94.463

When dealing with multi-objective optimization issues, the Taguchi and GRA approaches are applied. The key steps of this approach are as follows:

+) Determine the signal-to-noise ratio (S/N) using the following equations:

For shorter the GASA, the better the S/N:

$$SN = -10log_{10}(\frac{1}{n}\sum_{i=1}^{m} y_i^2) \tag{37}$$

The bigger the S/N, the better for the GE goal:

$$SN = -10log_{10}(\frac{1}{n}\sum_{i=1}^{m} \frac{1}{y_i^2}) \tag{38}$$

where y_i is the output result and m is the number of experiment repeats. Since this is a simulation, m = 1 and there are no repetitions necessary. The estimated S/N indices for the two output targets are shown in Table 5.

Table 5. S/N values of each experiment when $u_t = 15$

No.	Input Factors					A_{gb}		η_{gb}	
	u1	Kbe	Xba	AS1	AS2	(cm)	S/N	(%)	S/N
1	1.76	0.2500	0.2500	350	350	31.412	−29.9419	95.188	−3.52183
2	1.76	0.2625	0.2875	368	368	27.348	−28.7385	95.073	−5.79895

(*continued*)

Table 5. (*continued*)

No.	Input Factors					A_{gb}		η_{gb}	
	u1	Kbe	Xba	AS1	AS2	(cm)	S/N	(%)	S/N
3	1.76	0.2750	0.3250	386	386	24.136	−27.6533	95.043	−5.68477
4	1.76	0.2875	0.3625	404	404	21.538	−26.6641	94.917	−6.26687
5	1.76	0.3000	0.4000	420	420	19.508	−25.8043	94.882	−5.58144
6	2.33	0.2500	0.2875	386	404	21.996	−26.8469	95.018	−5.43753
7	2.33	0.2625	0.3250	404	420	19.669	−25.8756	94.981	−4.90152
8	2.33	0.2750	0.3625	420	350	22.494	−27.0413	94.957	−6.24649
9	2.33	0.2875	0.4000	350	368	20.826	−26.3721	95.006	−5.16196
10	2.33	0.3000	0.2500	368	386	25.324	−28.0706	95.099	−5.01744
11	2.90	0.2500	0.3250	420	368	20.883	−26.3959	94.906	−6.08784
12	2.90	0.2625	0.3625	350	386	19.398	−25.7551	94.944	−5.07681
13	2.90	0.2750	0.4000	368	404	17.483	−24.8523	94.849	−4.33496
14	2.90	0.2875	0.2500	386	420	21.310	−26.5717	94.903	−6.28768
15	2.90	0.3000	0.2875	404	350	23.892	−27.5651	94.971	−6.50315
16	3.47	0.2500	0.3625	368	420	16.766	−24.4886	94.894	−3.40806
17	3.47	0.2625	0.4000	386	350	19.068	−25.6061	94.907	−5.15999
18	3.47	0.2750	0.2500	404	368	22.979	−27.2266	94.916	−6.76894
19	3.47	0.2875	0.2875	420	386	20.234	−26.1216	94.833	−6.26946
20	3.47	0.3000	0.3250	350	404	18.841	−25.5021	94.909	−5.00687
21	4.04	0.2500	0.4000	404	386	16.448	−24.3223	94.785	−3.52183
22	4.04	0.2625	0.2500	420	404	19.823	−25.9434	94.871	−5.82424
23	4.04	0.2750	0.2875	350	420	18.502	−25.3444	94.877	−4.98558
24	4.04	0.2875	0.3250	368	350	20.733	−26.3332	94.847	−6.42637
25	4.04	0.3000	0.3625	386	368	18.529	−25.3570	94.798	−5.42056

The data amounts for the two single-objective functions under consideration varied. The data must be normalized, or brought to a consistent scale, to assure comparability. To normalize the data, the normalization value Z_{ij}, which ranges from 0 to 1, is employed. The following formula is used to calculate this value:

$$Z_i = \frac{SN_i - min(SN_i, = 1, 2, ..n)}{\max(SN_i, j = 1, 2, ..n) - min(SN_i, = 1, 2, ..n)} \tag{39}$$

where, n = 25 is the experimental number.

+) The grey relational factor is calculated by:

$$y_i(k) = \frac{\Delta_{min} + \xi.\Delta_{max}(k)}{\Delta_i(k) + \xi.\Delta_{max}(k)} \tag{40}$$

$\Delta_j(k) = \|Z_0(k) - Z_j(k)\|$, where $Z_0(k)$ and $Z_j(k)$ represent the reference and particular comparison sequences, respectively; i = 1,2,…,n; k = 2 is the number of objectives; Δ_{min} and Δ_{max} are the minimum and maximum values of $\Delta_i(k)$, respectively; and $\zeta = 0.5$ is the characteristic factor.

+) Identifying the degree of grey in an interaction: It is calculated by taking the mean of the grey relational coefficients linked with the output objectives:

$$\overline{y_i} = \frac{1}{k}\sum_{j=0}^{k} y_{ij}(k) \tag{41}$$

In where y_{ij} is the grey relation value of the j[th] output aim of the i[th] experiment. Table 6 provides the predicted grey relation number y_i as well as the average grey relation value $\overline{y_i}$ for every experiment.

Table 6. Values of $\Delta_i(k)$ and $\overline{y_i}$

No	S/N		Z_i		Δ_i (k)		Grey relation value yi		$\overline{y_i}$
	A_{gb}	η_{gb}	A_{gb}	η_{gb}					
			Reference values		A_{gb}	η_{gb}	A_{gb}	η_{gb}	
			1.000	1.000					
1	−29.9419	39.5716	0.0000	1.0000	1.000	0.000	0.333	1.000	0.600
2	−28.7385	39.5611	0.2141	0.7151	0.786	0.285	0.389	0.637	0.488
3	−27.6533	39.5584	0.4073	0.6407	0.593	0.359	0.458	0.582	0.507
4	−26.6641	39.5469	0.5833	0.3280	0.417	0.672	0.545	0.427	0.498
5	−25.8043	39.5437	0.7363	0.2411	0.264	0.759	0.655	0.397	0.552
6	−26.8469	39.5561	0.5508	0.5787	0.449	0.421	0.527	0.543	0.533
7	−25.8756	39.5527	0.7236	0.4869	0.276	0.513	0.644	0.494	0.584
8	−27.0413	39.5505	0.5161	0.4273	0.484	0.573	0.508	0.466	0.491
9	−26.3721	39.5550	0.6352	0.5489	0.365	0.451	0.578	0.526	0.557
10	−28.0706	39.5635	0.3330	0.7795	0.667	0.220	0.428	0.694	0.535
11	−26.3959	39.5459	0.6310	0.3007	0.369	0.699	0.575	0.417	0.512
12	−25.7551	39.5494	0.7450	0.3950	0.255	0.605	0.662	0.453	0.578
13	−24.8523	39.5407	0.9057	0.1591	0.094	0.841	0.841	0.373	0.654
14	−26.5717	39.5456	0.5997	0.2932	0.400	0.707	0.555	0.414	0.499
15	−27.5651	39.5518	0.4230	0.4621	0.577	0.538	0.464	0.482	0.471
16	−24.4886	39.5448	0.9704	0.2709	0.030	0.729	0.944	0.407	0.729
17	−25.6061	39.5460	0.7715	0.3032	0.228	0.697	0.686	0.418	0.579

(*continued*)

Table 6. (*continued*)

No	S/N		Z_i		Δ_i (k)		Grey relation value yi		$\overline{y_i}$
	A_{gb}	η_{gb}	A_{gb}	η_{gb}					
			Reference values		A_{gb}	η_{gb}	A_{gb}	η_{gb}	
			1.000	1.000					
18	−27.2266	39.5468	0.4832	0.3255	0.517	0.674	0.492	0.426	0.465
19	−26.1216	39.5392	0.6798	0.1193	0.320	0.881	0.610	0.362	0.511
20	−25.5021	39.5461	0.7901	0.3081	0.210	0.692	0.704	0.420	0.590
21	−24.3223	39.5348	1.0000	0.0000	0.000	1.000	1.000	0.333	0.733
22	−25.9434	39.5427	0.7115	0.2138	0.288	0.786	0.634	0.389	0.536
23	−25.3444	39.5432	0.8181	0.2287	0.182	0.771	0.733	0.393	0.597
24	−26.3332	39.5405	0.6422	0.1541	0.358	0.846	0.583	0.372	0.498
25	−25.3570	39.5360	0.8159	0.0323	0.184	0.968	0.731	0.341	0.575

To increase harmony among the output parameters, a higher average grey relation value is proposed. As a result, the objective function of a multi-objective issue may be reduced to a single-objective optimization problem, providing the mean grey relation value.

The findings of an ANOVA test performed to examine the influence of the primary design aspects on the average grey relation value $\overline{y_i}$ are shown in Table 7. Table 7 shows that k_{be} has the biggest impact on $\overline{y_i}$ (27.02%), followed by X_{ba} (26.10%), AS_2 (15.62%), AS_1 (12.67%), and u_1 (10.54%). Using ANOVA analysis, Table 8 shows the order of the influence of the primary design components on $\overline{y_i}$.

+*) Finding optimum main design parameters:* In principle, the reasonable (or ideal) factor set would consist of core design features with the highest S/N values. As a consequence, the effect of the important design features on the S/N ratio (Fig. 4) was estimated. Furthermore, the optimal set of multi-objective factors (corresponding to the red points) may be simply deduced from the Fig. 4 chart. Table 9 displays the appropriate levels and values for the key design variables of the multi-objective function.

+*) Examining the experimental modeling:* Fig. 5 depicts the findings of the Anderson-Darling technique, which is used to assess the suitability of the proposed model. The data points corresponding to the experimental observations (shown by blue dots in the graph) fall within the 95% standard deviation zone defined by the top and bottom boundaries. Furthermore, the p-value of 0.1 is much greater than the significance threshold of $\alpha = 0.05$. These findings imply that the empirical model employed in this study is appropriate for the purpose of assessment.

Continue in the same manner as with $u_t = 15$, except with the remaining ut values of 10, 20, 25, 30, and 35. Table 10 demonstrates the ideal values of the five main design parameters for each of the five main design parameters at different u_t. The following are the outcomes of this table:

Table 7. Analysis of variance for means

Analysis of Variance for Means							
Source	DF	Seq SS	Adj SS	Adj MS	F	P	C
u1	4	0.012636	0.012636	0.003159	1.31	0.400	10.54
Kbe	4	0.032398	0.032398	0.008100	3.36	0.134	27.02
Xba	4	0.031287	0.031287	0.007822	3.24	0.141	26.10
AS1	4	0.015194	0.015194	0.003798	1.57	0.335	12.67
AS2	4	0.018730	0.018730	0.004683	1.94	0.268	15.62
Residual Error	4	0.009650	0.009650	0.002413			8.05
Total	24	0.119896					
Model Summary							
S		R-Sq		R-Sq(adj)			
0.0491		91.95%		51.71%			

Table 8. Response table for means

Response Table for Means					
Level	u1	Kbe	Xba	AS1	AS2
1	0.5290	0.6215	0.5270	0.5846	0.5280
2	0.5400	0.5530	0.5201	0.5808	0.5195
3	0.5429	0.5430	0.5384	0.5386	0.5729
4	0.5749	0.5126	0.5743	0.5503	0.5623
5	0.5879	0.5445	0.6150	0.5203	0.5922
Delta	0.0589	0.1089	0.0949	0.0643	0.0727
Rank	5	1	2	4	3

Average of grey analysis value: 0.555.

- k_{be} selects the smallest possible value, whereas X_{ba} selects the largest possible value. This is because the average grey relation value $\overline{y_i}$ was maximized using these values.
- Similarly, the ideal AS_1 values are the lowest, while the ideal AS_2 values are the highest. This is because these settings enhanced the average grey relation value $\overline{y_i}$.
- The link between the appropriate first stage gear ratio and the entire gearbox ratio is depicted in Fig. 6. When $u_t > 26.7$, $u_1 = 6$ and when $u_t \leq 26.7$, the following regression formula (with $R^2 = 0.9986$) is supplied to determine the optimal values of u_1:

$$u_1 = 0.1722 \cdot u_t + 1.4063 \tag{42}$$

After determining u_1, the optimal value of u_2 may be calculated using $u_2 = u_t/u_1$.

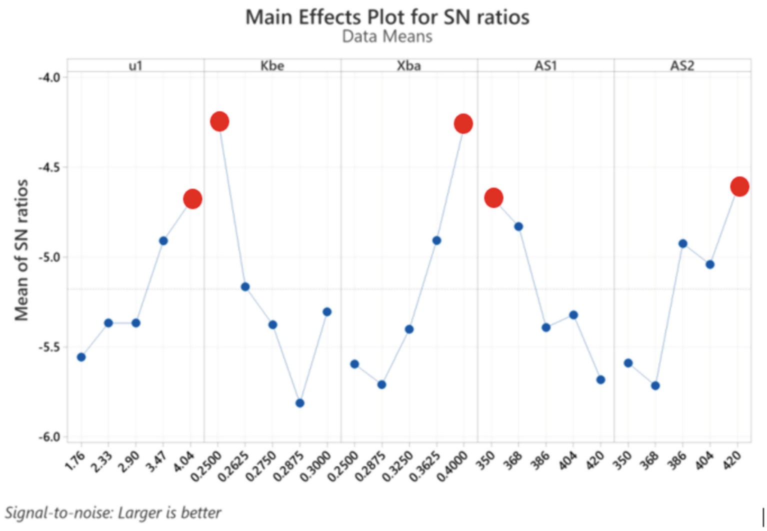

Fig. 4. Main effects plot for S/N ratios

Table 9. Optimum values of main design factors

No.	Input factors	Code	Optimum Level	Optimum Value
1	Gear ratio of first stage	u_1	5	4.04
2	CWFW of stage 1	Xba1	1	0.25
3	CWFW of stage 2	Xba2	5	0.4
4	ACS of stage 1 (MPa)	AS1	1	350
5	ACS of stage 2 (MPa)	AS2	5	420

6 Conclusions

The results of a multi-objective optimization research on improving a two-stage bevel helical gearbox to minimize GASA and increase GE are presented in this paper. This research optimized the first stage's gear ratio, the coefficient of wheel face width for stages 1 and 2, and the permitted contact stress for stages 1 and 2. A simulation experiment based on the Taguchi L25 type was created and carried out to solve this issue. The effect of major design features on the multi-objective goal was also investigated. Furthermore, the best settings for the critical gearbox parameters have been suggested. A regression approach Eq. (42) was also presented for determining the best first stage u_1 gear ratio.

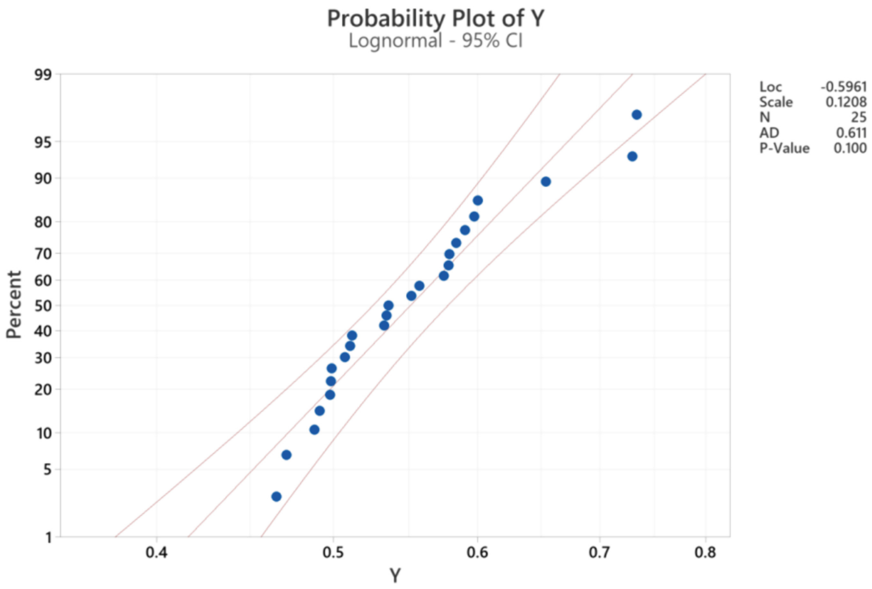

Fig. 5. Probability plot of $\overline{y}$

Table 10. Optimal values of main design factors

No.	u_t					
	10	15	20	26.7	30	35
u_1	3.08	4.04	4.89	5.67	6	6
k_{be}	0.25	0.25	0.25	0.25	0.25	0.25
X_{ba}	0.4	0.4	0.4	0.4	0.4	0.4
AS_1	350	350	350	350	350	350
AS_2	420	420	420	420	420	420

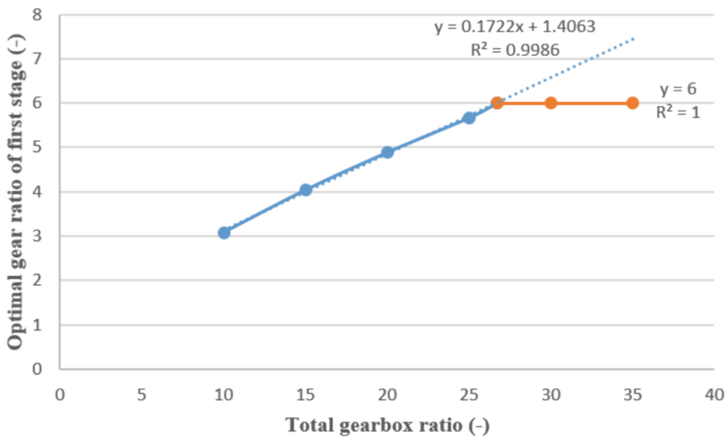

Fig. 6. Optimal gear ratio of bevel gear set versus total gearbox ratio

Acknowledgment. The Thai Nguyen University of Technology provided support for this study.

References

1. Pi, V.N., et al.: Calculation of Optimum Gear Ratios of A Two-Stage Bevel Helical Gearbox. Int. J. Mechan. Eng. Technol. (IJMET) **9**(11), 2126–2133 (2018)
2. Danh, B.T., et al.: Determination of Optimum Gear Ratios of Two-Stage Bevel Helical Gearboxes for Getting Minimum Gearbox Volume. In: International Conference on Engineering Research and Applications. Springer (2021)
3. Hong, T.T., et al.: Calculating optimum gear ratios of two step bevel helical reducer. Int. J. Appl. Eng. Res. **14**(16), 3494–3499 (2019)
4. Tuan, T.K., et al.: Optimization of Gear Ratios for Three-Stage Bevel Helical Gearboxes Based on Gearbox Volume Function. in International Conference on Engineering Research and Applications. Springer (2021)
5. Pi, V.N., Tuan, N.K.: Determining optimum partial transmission ratios of mechanical driven systems using a chain drive and a two-step bevel helical gearbox. Int. J. Mechan. Eng. Robo. Res. **8**(5), 708–712 (2019)
6. Linh, N.H., et al.: Optimization of Transmission Ratios for Two-Stage Bevel Helical Gearboxes Based on Cost Function. In: International Conference on Engineering Research and Applications. Springer (2021)
7. Lu, K., et al.: Acoustics based monitoring and diagnostics for the progressive deterioration of helical gearboxes. Chinese J. Mechan. Eng. **34**, 1–12 (2021)
8. Pi, V.N., et al.: Determination of optimum gear ratios of a three stage bevel helical gearbox. In: IOP Conference Series: Materials Science and Engineering. IOP Publishing (2019)
9. Quang, N.H., et al.: Determination of Optimum Partial Gear Ratios for Three-Stage Bevel Helical Gearboxes for Cost Function. in International Conference on Engineering Research and Applications. Springer (2021)
10. Tuan, N.K., et al.: Optimum calculation of partial transmission ratios of mechanical driven systems using a V-belt and a three-step bevel helical gearbox. In: Advances in Engineering Research and Application: Proceedings of the International Conference, ICERA 2018. Springer (2019)

11. Tran, H.-D., et al.: Application of the taguchi method and grey relational analysis for multi-objective optimization of a two-stage bevel helical gearbox. Machines **11**(7), 716 (2023)
12. Chat, T., Van Uyen, L.: Design and calculation of Mechanical Transmissions Systems, vol. 1. Educational Republishing House, Hanoi (2007)
13. Trinh Chat, L.V.U.: Calculation of mechanical driven systems. Education Publisher (1996)
14. Römhild, I., Linke, H.: Gezielte Auslegung Von Zahnradgetrieben mit minimaler Masse auf der Basis neuer Berechnungsverfahren. Konstruktion **44**(7–8), 229–236 (1992)
15. Jelaska, D.T.: Gears and gear drives. John Wiley & Sons (2012)
16. Buckingham, E.: Analytical mechanics of gears. Courier Corporation (1988)
17. Le, X.-H., Vu, N.-P.: Multi-objective optimization of a two-stage helical gearbox using Taguchi method and grey relational analysis. Appl. Sci. **13**(13), 7601 (2023)

Multi-Objective Optimization of a Two-Stage Bevel Helical Gearbox to Increase Efficiency and Reduce Gearbox Height

Dinh Van Thanh[1], Tran Huu Danh[2], Tran Minh Tan[3], Nguyen Huu Quang[4], Bui Thanh Danh[5], Hoang Xuan Tu[6], and Le Xuan Hung[6](✉)

[1] East Asia University of Technology, Ho Chi Minh City, Vietnam
[2] Vinh Long University of Technology Education, Vinh Long City, Vietnam
[3] Nguyen Tat Thanh University, Ho Chi Minh City, Vietnam
[4] University of Economics – Technology for Industries, Hanoi, Vietnam
[5] University of Transport and Communications, Hanoi, Vietnam
[6] Thai Nguyen University of Technology, Thai Nguyen, Vietnam
lexuanhung@tnut.edu.vn

Abstract. The goal of this research involves investigating into multi-target optimization of two-stage bevel helical gearboxes in order to determine the optimum essential design parameters to reduce gearbox height while enhancing gearbox efficiency. In two stages, the Taguchi method and grey relation analysis (GRA) were used to solve the problem. First, the single-objective optimization problem was dealt with to narrow the gap within variable levels, followed by the multi-objective optimization problem to discover the optimal major design variables. The coefficients of wheel face width (CWFW) of the first and second stages, allowable contact stresses (ACS) of the first and second stages, and the first stage gear ratio were also determined. The study's findings were utilized to identify the best values for five important elements for a two-stage bevel helical gearbox.

Keywords: Bevel helical gearbox · Multi-objective optimization · Gear ratio · Gearbox height · Gearbox efficiency

1 Introduction

Mechanical drive systems are widely utilized in practice due to their simple structure, dependable functioning, and inexpensive cost. The gearbox is the most crucial component of a mechanical drive system. It aids in reducing the speed and torque transmitted from the motor shaft to the working shaft. As a result, several researchers are pursuing the ideal design of the gearbox.

There have been numerous research on the ideal design of a gearbox up to this point. Various types of gearboxes, such as helical gearboxes [1–4], bevel gearboxes [5–9], worm gearboxes [10–12], and so on, have been studied. Furthermore, optimization problems for gearboxes with different stages, such as two-stage gearboxes [1, 2, 6, 10], three-stage gearboxes [7–9, 13], and four-stage gearboxes [3, 4], have been solved.

D. C. Nguyen et al. (Eds.): ICERA 2023, LNNS 944, pp. 159–176, 2024.
https://doi.org/10.1007/978-3-031-62235-9_18

Optimization problems with single objective functions such as minimum gearbox length [14], minimum gearbox across section area [2, 9, 15, 16], minimum gearbox mass [4], minimal gearbox volume [6, 8, 17], minimum gear mass [2], minimum height gearbox [18], and minimal gearbox cost [1, 3, 7, 10] have been created. [19] recently presented a new method for solving multi-objective optimization problems for helical gearboxes using the Taguchi method and gray relation analysis in order to minimize gearbox weight and boost efficiency. [5] also published multi-objective optimization results for a bevel gearbox in order to reduce gearbox volume while increasing efficiency.

The purpose of this research is to investigate multi-target optimization learning for a two-stage bevel helical gearbox. Two single goals were pursued in this effort: reducing gearbox height and maximizing gearbox efficiency. In addition, five major design elements were evaluated: the CWFW for both stages, the ACS for both stages, and the gear ratio for the first stage. Furthermore, by combining the Taguchi approach with the GRA, the multi-objective optimization problem in gearbox design was solved in two stages. The best values of five critical design variables for developing a two-stage bevel helical gearbox were also proposed.

2 Optimization Problem

2.1 Gearbox Height Calculation

The gearbox height H can be calculated by (Fig. 1):

$$H = \max(d_{e21}, d_{w22}) + 8.5 \cdot S_G \tag{1}$$

In which, d_{e21} is the outer pitch diameter of the bevel gear (in mm), which is found by [20]:

$$d_{e21} = 2 \cdot u_1 \cdot R_e / \left(1 + u_1^2\right)^{1/2} \tag{2}$$

where, u_1 is the gear ratio of the bevel gear set; R_e is the cone distance (mm) which is found by [20]:

$$R_e = k_R \bullet \sqrt{u_1^2 + 1} \bullet \sqrt[3]{T_{11} \bullet k_{h\beta 1} / \left[(1 - k_{be}) \bullet k_{be} \bullet u_1 \bullet [\sigma_H]^2\right]} \tag{3}$$

In (3), $k_R = 50$ (MPa) is a factor [20]; $k_{H\beta 1} = 1.04 \div 1.18$ is the contacting load ratio for pitting resistance [21]; $k_{be} = b/R_e = 0.25 \div 0.3$ is face width coefficient; T_{11} is the torque on pinion of the first stage (Nmm) which can be calculated by:

$$T_{11} = T_{out} / \left(u_t \cdot \eta_{bg} \cdot \eta_{hg} \cdot \eta_b^3\right) \tag{4}$$

where, T_{out} is the output torque (N.mm); u_t is the total gearbox ratio; η_{bg} is the bevel gear efficiency ($\eta_{hg} = 0.95 \div 0.97$; η_{hg} is the helical gear efficiency ($\eta_{hg} = 0.96 \div 0.98$ [20]; η_b is the rolling bearing efficiency ($\eta_h = 0.99 \div 0.995$ [20]).

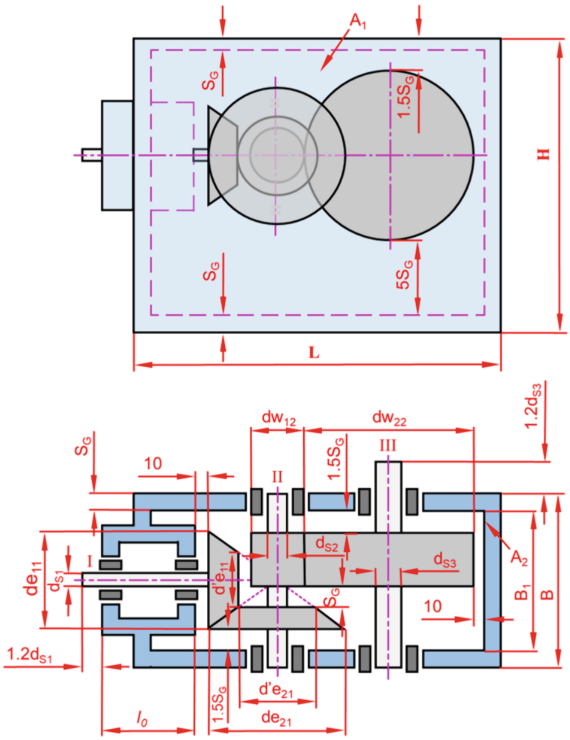

Fig. 1. Calculated schema [5]

+) d_{w22} are the pitch diameters of the gear of the helical gear set which can be determined by [20]:

$$d_{w22} = 2 \bullet a_w \bullet u_2/(u_2 + 1) \tag{5}$$

In where, a_{w2} is the center distances of helical gear set which is found by [20]:

$$a_w = k_a \bullet (u_2 + 1) \bullet \sqrt[3]{T_{12} \bullet k_{H\beta 2}/(\mathrm{AS}_2^2 \bullet u_2 \bullet X_{ba})} \tag{6}$$

In which, $k_{H\beta 2} = 1.05 \div 1.27$ is contacting load ratio for pitting resistance [20]; AS_2 is allowed contact stress (MPa); $k_a = 43$ is the material coefficient [20]; X_{ba} is the wheel face width and T_{12} is the torque on the pinion (Nmm) of helical gear set.

$$T_{12} = T_{out}/\left(u_2 \bullet \eta_{hg} \bullet \eta_{be}^2\right) \tag{7}$$

where, u_2 is the gear ratio of the helical gear set.

3 Gearbox Efficiency Calculation

The gearbox efficiency is determined by:

$$\eta_{gb} = \frac{100 \bullet P_l}{P_{in}} \tag{8}$$

In which, P_l is the entire gearbox power loss [22]:

$$P_l = P_{lg} + P_{lb} + P_{ls} \tag{9}$$

In the above equation, P_{lg} is the total power losses in gears; P_{lb} the power losses in bearings; P_{ls} the power losses in seals. These elements can be calculated as follows:

+) The power losses in gears:

$$\mathrm{P}_{lg} = \sum_{i=1}^{2} \mathrm{P}_{\mathrm{lgi}} \tag{10}$$

In where, P_{lgi} is the gear power los of i stage which can be found by:

$$P_{lgi} = P_{gi} \bullet \left(1 - \eta_{gi}\right) \tag{11}$$

wherein,η_{gi} the efficiency of the gear's i stage which is determined by [23]:

$$\eta_{gi} = 1 - \left(\frac{1 + 1/\mathrm{u_i}}{\beta_{\mathrm{ai}} + \beta_{\mathrm{ri}}}\right) \cdot \frac{\mathrm{f_i}}{2} \cdot \left(\beta_{\mathrm{ai}}^2 + \beta_{\mathrm{ri}}^2\right) \tag{12}$$

In which, $\mathrm{u_i}$ is the gear ratio of i stage; f is the friction coefficient; β_{ai} and β_{ri} are the arcs of approach and recess on the i stage which can be determined by [23]:

+) For the bevel gear set:

$$\beta_{\mathrm{ai}} = \frac{\left(\mathrm{R}_{eev2}^2 - \mathrm{R}_{0v2}^2\right)^{1/2} - \mathrm{R}_{v2} \cdot \sin\alpha}{\mathrm{R}_{01\mathrm{i}}} \tag{13}$$

$$\beta_{\mathrm{ri}} = \frac{\left(\mathrm{R}_{aev1}^2 - \mathrm{R}_{0v1}^2\right)^{1/2} - \mathrm{R}_{v1} \cdot \sin\alpha}{\mathrm{R}_{01\mathrm{i}}} \tag{14}$$

In (13) and (14), $\mathrm{R_{aev1}}$ and $\mathrm{R_{aev2}}$ are the outer radiuses of the equivalent pinion and gear; $\mathrm{R_{v1}}$ and $\mathrm{R_{v2}}$ are the pitch radiuses of the comparable pinion and gear; $\mathrm{R_{0v1}}$ and $\mathrm{R_{0v2}}$ are the base radiuses of the equivalent pinion and gear; and α is pressure angle.

$$\mathrm{R_{v1}} = \mathrm{R_1}/\cos\delta_1 \tag{15}$$

$$\mathrm{R_{v2}} = \mathrm{R_2}/\cos\delta_2 \tag{16}$$

where, $\mathrm{R_1}$ and R2 are the pitch radius of the bevel pinion and the gear at the big end; δ_1 and δ_2 are the pitch angles of the bevel pinion and gears.

$$\mathrm{R_{aev1}} = \mathrm{R_{v1}} + \mathrm{a_p} \tag{17}$$

$$\mathrm{R_{aev2} = R_{v2} + a_g} \tag{18}$$

+) For the helical gear set:

$$\beta_{\mathrm{ai}} = \frac{\left(\mathrm{R_{e2i}^2 - R_{02i}^2}\right)^{1/2} - \mathrm{R_{2i}} \cdot \sin\alpha}{\mathrm{R_{01i}}} \tag{19}$$

$$\beta_{\mathrm{ri}} = \frac{\left(\mathrm{R_{e1i}^2 - R_{01i}^2}\right)^{1/2} - \mathrm{R_{1i}} \cdot \sin\alpha}{\mathrm{R_{01i}}} \tag{20}$$

In which, R_{e1i} and R_{e2i} represent the pinion and gear's outer radius; R_{1i} and R_{2i} represent the pinion and gear's pitch radius; R_{01i} and R_{01i} represent the pinion and gear's base-circle radius, respectively; and α is the pressure angle.

The friction coefficient in eq. (12) is determined by [5]:

– If the sliding velocity v ≤ 0.424 (m/s):

$$f = -0.0877 \cdot v + 0.0525 \tag{21}$$

– If the sliding velocity v > 0.424 (m/s):

$$f = 0.0028 \cdot v + 0.0104 \tag{22}$$

+) The power losses in bearings is found by [22]:

$$P_{lb} = \sum_{i=1}^{6} f_b \cdot F_i \cdot v_i \tag{23}$$

where, f_b is the friction coefficient of bearing; $f_b = 0.0011$ as in this work the radical ball bearings with angular contact were applied [22]; F is the load on the bearing (N); v is the peripheral speed; and i is the bearing ordinal number (i = 1 ÷ 6).

+) The total power losses in seals can be found by [22]:

$$P_{\mathrm{s}} = \sum_{i=1}^{2} \mathrm{P_{si}} \tag{24}$$

In (24), i = 1 ÷ 2 is the seal ordinal number; P_{si} is the power loss caused by a single seal (w), which is determined by:

$$P_{si} = \left[145 - 1.6 \bullet t_{oil} + 350 \bullet loglog(VG_{40} + 0.8)\right] \bullet d_s^2 \bullet n \bullet 10^{-7} \tag{25}$$

In which, VG_{40} is the ISO Viscosity Grade number.

3.1 Objective Function and Constrains

3.1.1 Objectives Functions

The multi-target optimization problem consists of two single objectives:

Minimizing the gearbox height:

$$\min f_2(X) = \mathrm{H} \tag{26}$$

Maximizing the gearbox efficiency:

$$\min f_1(X) = \eta_{gb} \tag{27}$$

where X is the design variable vector indicating variables. In this study, five main design factors were chosen as variables: u_1, Xba_1, Xba_2, AS_1, and AS_2, resulting in:

$$X = \{u_1, Xba_1, Xba_2, AS_1, AS_2\} \tag{28}$$

3.1.2 Constrains

The following constrains must be met by the multi-objective function:

$$1 \leq u_1 \leq 6 \quad \text{and} \quad 1 \leq u_2 \leq 9 \tag{29}$$

$$0.25 \leq k_{be} \leq 0.3 \quad \text{and} \quad 0.25 \leq X_{ba} \leq 0.4 \tag{30}$$

$$350 \leq AS_1 \leq 420 \quad \text{and} \quad 350 \leq AS_2 \leq 420 \tag{31}$$

4 Methodology

Five major design elements were chosen for investigation in this research. Table 1 displays the minimum and maximum values for different parameters. To solve the optimization problem, the Taguchi technique and grey relation analysis were utilized. The L25 (5^5) design was used to optimize the number of levels for each variable. Among the variables considered, however, u_1 has a pretty wide range (u_1 ranges from 1 to 6 – Table 1). Even with five levels, the difference in these attributes' values remained beneficial (in this case, the difference is ((6–1)/4 = 1.5)).

The 2-stage multi-objective optimization problem solution technique [19] was utilized to help narrow the gap between values of a variable spread throughout a wide range. This technique's first stage handles a single-objective optimization problem, while the second stage addresses a multi-objective optimization problem to select the best primary design features (Fig. 2).

Table 1. Main design factors and their maximum and minimum restrictions

Factor	Code	Lower limit	Upper limit
Gear ratio of satge 1	u_1	1	6
CWFW of stage 1	k_{be}	0.25	0.3
CWFW of stage 2	X_{ba}	0.25	0.4
ACS of stage 1 (MPa)	AS_1	350	420
ACS of stage 2 (MPa)	AS_2	350	420

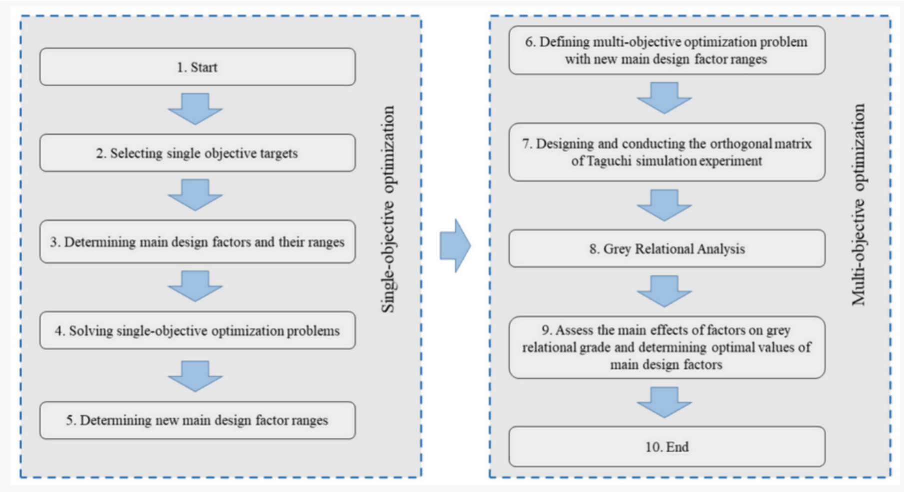

Fig. 2. Method to solve multi-objective problem [5]

5 Single-Objective Optimization

The direct search strategy is used in this work to solve the single-objective optimization issue. A Matlab-based computer program was also created to handle two single-objective problems: reducing gearbox height and maximizing gearbox efficiency (Fig. 3). Figure 4 depicts the relationship between the optimal gear ratio of the first stage u_1 and the overall gearbox ratio u_t based on the findings of this program. Furthermore, new restrictions for the variable u_1 have been developed, as shown in Table 2.

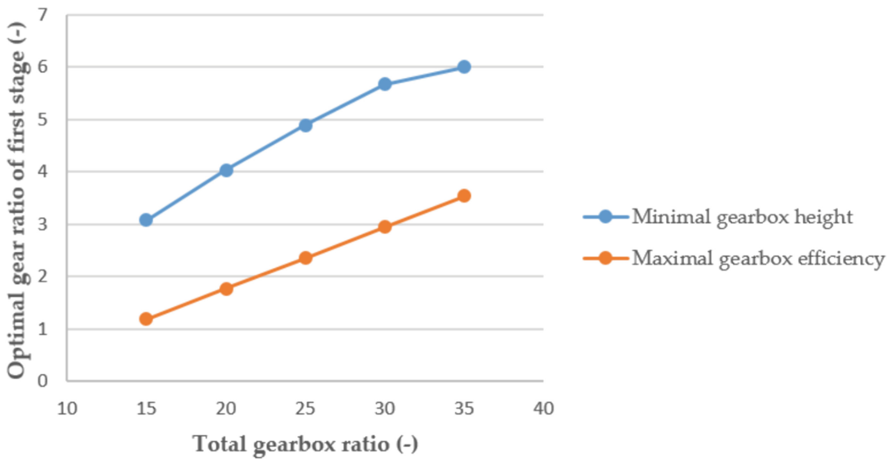

Fig. 3. Optimal gear ratio of bevel gear set versus total gearbox ratio

Table 2. New constraints of u_1

u_t	u_1	
	Lower limit	Upper limit
10	1.17	3.08
15	1.76	4.04
20	2.34	4.89
25	2.93	5.67
30	3.52	6
35	4.1	6

6 Multi-Objective Optimization

The purpose of the multi-objective optimization problem for a two-stage helical gearbox in this work is to discover the optimal primary design variables with a given total gear-box ratio that meets two single-objective functions: lowering gearbox height and maximizing gearbox efficiency. To solve the stated multi-objective optimization problem, a computational experiment was created. Table 3 shows the primary design elements and their respective values for $u_t = 15$. The Taguchi approach with L25 (5^5) design was utilized for the experimental design, and the data was evaluated using Minitab R18 software. Table 4 displays the experimental design and outcomes for $u_t = 15$.

When dealing with multi-objective optimization issues, the Taguchi and GRA approaches are applied. The main steps of this approach are as follows:

+) Determine the signal-to-noise ratio (S/N) using the following equations:

Table 3. Main design factors and their levels for $u_t = 15$.

Factor	Notation	Level				
		1	2	3	4	5
Gear ratio of first stage	u_1	1.76	2.33	2.90	3.47	4.04
CWFW of stage 1	k_{be}	0.25	0.2625	0.275	0.2875	0.3
CWFW of stage 2	X_{ba}	0.25	0.2875	0.325	0.3625	0.4
ACS of stage 1 (MPa)	AS_1	350	368	386	404	420
ACS of stage 2 (MPa)	AS_2	350	368	386	404	420

The shorter the gearbox length, the better the S/N:

$$SN = -10log_{10}(\frac{1}{n}\sum_{i=1}^{m} y_i^2) \tag{32}$$

The bigger the S/N, the better for gearbox efficiency:

$$SN = -10log_{10}(\frac{1}{n}\sum_{i=1}^{m} \frac{1}{y_i^2}) \tag{33}$$

In which, y_i represents the output result and m represents the number of experimental repetitions. Because this is a simulation, m = 1; no repetitions are required. Table 5 shows the estimated S/N indices for the two output goals.

The data amounts for the two single-objective functions under consideration differ. The data must be normalized, or brought to a consistent scale, to assure comparability. To normalize the data, the normalization value Z_{ij}, which ranges from 0 to 1, is employed. The following formula is used to calculate this value:

$$Z_i = \frac{SN_i - min(SN_i, = 1,2,..n)}{max(SN_i, j = 1,2,..n) - min(SN_i, = 1,2,..n)} \tag{34}$$

where, n = 25 is the number of experiments.

+) The grey relational factor is determined by:

$$\mathrm{y_i(k)} = \frac{\Delta_{\min} + \xi.\Delta_{\max}(k)}{\Delta_{\mathrm{i}}(\mathrm{k}) + \xi.\Delta_{\max}(k)} \tag{35}$$

In which, i = 1,2,…,n; k = 2 is the target number; $\Delta_j(k) = \|Z_0(k) - Z_j(k)\|$ with Z0(k) and Zj(k) represent the reference and specific comparison sequences; Δ_{min} and Δ_{max} are the minimum and maximum values of Δi(k); ζ = 0.5 is the characteristic coefficient.

+) Identifying the degree of grey in a relationship: It is calculated using the mean of the grey relational coefficients linked with the output objectives:

$$\overline{y_i} = \frac{1}{k}\sum_{j=0}^{k} y_{ij}(k) \tag{36}$$

Table 4. Experimental plan and output results for $u_t = 15$

Exp.No	Input Factors					H	η_{gb}
	u_1	K_{be}	X_{ba}	AS_1	AS_2	(cm)	(%)
1	1.76	0.2500	0.2500	350	350	48.911	95.188
2	1.76	0.2625	0.2875	368	368	45.381	95.073
3	1.76	0.2750	0.3250	386	386	42.410	95.043
4	1.76	0.2875	0.3625	404	404	39.865	94.917
5	1.76	0.3000	0.4000	420	420	37.764	94.882
6	2.33	0.2500	0.2875	386	404	39.280	95.018
7	2.33	0.2625	0.3250	404	420	36.938	94.981
8	2.33	0.2750	0.3625	420	350	39.951	94.957
9	2.33	0.2875	0.4000	350	368	37.588	95.006
10	2.33	0.3000	0.2500	368	386	42.181	95.099
11	2.90	0.2500	0.3250	420	368	37.462	94.906
12	2.90	0.2625	0.3625	350	386	35.195	94.944
13	2.90	0.2750	0.4000	368	404	33.225	94.849
14	2.90	0.2875	0.2500	386	420	37.441	94.903
15	2.90	0.3000	0.2875	404	350	40.118	94.971
16	3.47	0.2500	0.3625	368	420	31.676	94.894
17	3.47	0.2625	0.4000	386	350	34.332	94.907
18	3.47	0.2750	0.2500	404	368	38.434	94.916
19	3.47	0.2875	0.2875	420	386	35.764	94.833
20	3.47	0.3000	0.3250	350	404	33.518	94.909
21	4.04	0.2500	0.4000	404	386	30.910	94.785
22	4.04	0.2625	0.2500	420	404	34.660	94.871
23	4.04	0.2750	0.2875	350	420	32.455	94.877
24	4.04	0.2875	0.3250	368	350	34.924	94.847
25	4.04	0.3000	0.3625	386	368	32.773	94.798

In which y_{ij} is the grey relation value of the j^{th} output aim of the i^{th} experiment. Table 6 shows the predicted grey relation number y_i as well as the average grey relation value $\overline{y_i}$ for each test.

To increase harmony among the output parameters, a higher average grey relation value is proposed. As a result, the objective function of a multi-objective issue may be reduced to a single-objective optimization problem, providing the mean grey relation value.

The results of an ANOVA test performed to examine the influence of the primary design aspects on the average grey relation value $\overline{y_i}$ are shown in Table 7. AS_1 has the

Table 5. S/N values for each experiment when $u_t = 15$

No	Input Factors					H		η_{gb}	
	u_1	K_{be}	X_{ba}	AS_1	AS_2	(cm)	S/N	(%)	S/N
1	1.76	0.2500	0.2500	350	350	48.911	−33.7881	95.188	39.5716
2	1.76	0.2625	0.2875	368	368	45.381	−33.1375	95.073	39.5611
3	1.76	0.2750	0.3250	386	386	42.410	−32.5494	95.043	39.5584
4	1.76	0.2875	0.3625	404	404	39.865	−32.0118	94.917	39.5469
5	1.76	0.3000	0.4000	420	420	37.764	−31.5416	94.882	39.5437
6	2.33	0.2500	0.2875	386	404	39.280	−31.8834	95.018	39.5561
7	2.33	0.2625	0.3250	404	420	36.938	−31.3495	94.981	39.5527
8	2.33	0.2750	0.3625	420	350	39.951	−32.0306	94.957	39.5505
9	2.33	0.2875	0.4000	350	368	37.588	−31.5010	95.006	39.5550
10	2.33	0.3000	0.2500	368	386	42.181	−32.5023	95.099	39.5635
11	2.90	0.2500	0.3250	420	368	37.462	−31.4718	94.906	39.5459
12	2.90	0.2625	0.3625	350	386	35.195	−30.9296	94.944	39.5494
13	2.90	0.2750	0.4000	368	404	33.225	−30.4293	94.849	39.5407
14	2.90	0.2875	0.2500	386	420	37.441	−31.4669	94.903	39.5456
15	2.90	0.3000	0.2875	404	350	40.118	−32.0668	94.971	39.5518
16	3.47	0.2500	0.3625	368	420	31.676	−30.0146	94.894	39.5448
17	3.47	0.2625	0.4000	386	350	34.332	−30.7140	94.907	39.5460
18	3.47	0.2750	0.2500	404	368	38.434	−31.6943	94.916	39.5468
19	3.47	0.2875	0.2875	420	386	35.764	−31.0689	94.833	39.5392
20	3.47	0.3000	0.3250	350	404	33.518	−30.5056	94.909	39.5461
21	4.04	0.2500	0.4000	404	386	30.910	−29.8020	94.785	39.5348
22	4.04	0.2625	0.2500	420	404	34.660	−30.7966	94.871	39.5427
23	4.04	0.2750	0.2875	350	420	32.455	−30.2256	94.877	39.5432
24	4.04	0.2875	0.3250	368	350	34.924	−30.8625	94.847	39.5405
25	4.04	0.3000	0.3625	386	368	32.773	−30.3103	94.798	39.5360

biggest impact on $\overline{y_i}$ (32.06%), followed by K_{be} (30.07%), u_1 (16.14%), AS_2 (5.5%), and X_{ba} (5.26%), according to Table 7. Using ANOVA analysis, Table 8 shows the order of the influence of the primary design components on $\overline{y_i}$.

+) *Determining optimum main design factors:* In principle, the best factor set would be a collection of key design features with the greatest S/N values. As a consequence, the effect of the important design features on the S/N ratio (Fig. 5) was estimated. Figure 5 and Table 9 were used to estimate the ideal levels and values of the major design parameters for the multi-objective function.

Table 6. Values of $\Delta_i(k)$ and $\overline{y_i}$

No.	S/N		Zi		Δ_i (k)		Grey relation value y_i		$\overline{y_i}$
			H	η_{gb}					
			Reference values		H	η_{gb}	H	η_{gb}	
			1.000	1.000					
1	−33.7881	39.5716	0.0000	1.0000	1.000	0.000	0.333	1.000	0.667
2	−33.1375	39.5611	0.1632	0.7151	0.837	0.285	0.374	0.637	0.506
3	−32.5494	39.5584	0.3108	0.6407	0.689	0.359	0.420	0.582	0.501
4	−32.0118	39.5469	0.4456	0.3280	0.554	0.672	0.474	0.427	0.450
5	−31.5416	39.5437	0.5636	0.2411	0.436	0.759	0.534	0.397	0.466
6	−31.8834	39.5561	0.4778	0.5787	0.522	0.421	0.489	0.543	0.516
7	−31.3495	39.5527	0.6118	0.4869	0.388	0.513	0.563	0.494	0.528
8	−32.0306	39.5505	0.4409	0.4273	0.559	0.573	0.472	0.466	0.469
9	−31.5010	39.5550	0.5738	0.5489	0.426	0.451	0.540	0.526	0.533
10	−32.5023	39.5635	0.3226	0.7795	0.677	0.220	0.425	0.694	0.559
11	−31.4718	39.5459	0.5811	0.3007	0.419	0.699	0.544	0.417	0.481
12	−30.9296	39.5494	0.7171	0.3950	0.283	0.605	0.639	0.453	0.546
13	−30.4293	39.5407	0.8426	0.1591	0.157	0.841	0.761	0.373	0.567
14	−31.4669	39.5456	0.5823	0.2932	0.418	0.707	0.545	0.414	0.480
15	−32.0668	39.5518	0.4318	0.4621	0.568	0.538	0.468	0.482	0.475
16	−30.0146	39.5448	0.9467	0.2709	0.053	0.729	0.904	0.407	0.655
17	−30.7140	39.5460	0.7712	0.3032	0.229	0.697	0.686	0.418	0.552
18	−31.6943	39.5468	0.5253	0.3255	0.475	0.674	0.513	0.426	0.469
19	−31.0689	39.5392	0.6822	0.1193	0.318	0.881	0.611	0.362	0.487
20	−30.5056	39.5461	0.8235	0.3081	0.177	0.692	0.739	0.420	0.579
21	−29.8020	39.5348	1.0000	0.0000	0.000	1.000	1.000	0.333	0.667
22	−30.7966	39.5427	0.7505	0.2138	0.250	0.786	0.667	0.389	0.528
23	−30.2256	39.5432	0.8937	0.2287	0.106	0.771	0.825	0.393	0.609
24	−30.8625	39.5405	0.7340	0.1541	0.266	0.846	0.653	0.372	0.512
25	−30.3103	39.5360	0.8725	0.0323	0.128	0.968	0.797	0.341	0.569

+) *Investigating the experimental modeling:* Fig. 6 depicts the findings of the Anderson-Darling technique, which is used to assess the suitability of the proposed model. The data points corresponding to the experimental observations (shown by blue dots in the graph) fall within the 95% standard deviation zone defined by the top and

Table 7. Analysis of variance for means

Analysis of Variance for Means							
Source	DF	Seq SS	Adj SS	Adj MS	F	P	C (%)
u1	4	0.015378	0.015378	0.003845	1.56	0.339	16.14
Kbe	4	0.029230	0.029230	0.007308	2.96	0.159	30.67
Xba	4	0.005015	0.005015	0.001254	0.51	0.736	5.26
AS1	4	0.030557	0.030557	0.007639	3.09	0.150	32.06
AS2	4	0.005240	0.005240	0.001310	0.53	0.723	5.50
Residual Error	4	0.009879	0.009879	0.002470			10.37
Total	24	0.095300					
Model Summary							
S	R-Sq	R-Sq(adj)					
0.0497	89.63%	37.80%					

bottom boundaries. Furthermore, the p-value of 0.068 is much greater than the significance threshold of $\alpha = 0.05$. These findings imply that the empirical model employed in this study is appropriate for the purpose of assessment.

Table 8. Response table for means

Level	u1	Kbe	Xba	AS1	AS2
1	0.5179	0.597	0.5406	0.5867	0.5349
2	0.5211	0.5318	0.5184	0.5598	0.5114
3	0.5095	0.5231	0.5203	0.5235	0.5519
4	0.5485	0.4923	0.5378	0.5179	0.5281
5	0.5769	0.5296	0.5567	0.486	0.5475
Delta	0.0674	0.1047	0.0383	0.1007	0.0405
Rank	3	1	5	2	4
Average of grey analysis value: 0.535					

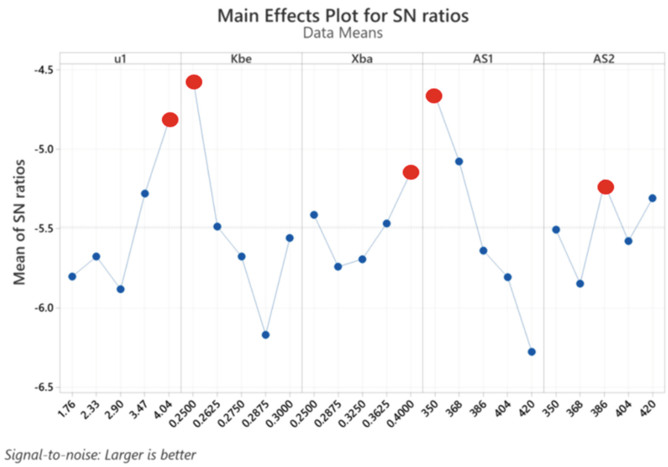

Fig. 4. Main effects plot for S/N ratios

Table 9. Optimum values of main design factors

No.	Input Parameters	Code	Optimum Level	Optimum Value
1	Gear ratio of stage 1	u_1	5	4.04
2	CWFW of stage 1	Xba1	1	0.25
3	CWFW of stage 2	Xba2	5	0.4
4	ACS of stage 1 (MPa)	AS1	1	350
5	ACS of stage 2 (MPa)	AS2	3	386

Continue in the same manner as with $u_t = 15$, but with the remaining u_t values of 10, 20, 25, 30, and 35. Table 10 shows the best values for each of the five key design parameters at various u_t. The following are the outcomes of this table:

- k_{be} takes the smallest possible value, whereas X_{ba} selects the largest possible value. This is because the average grey relation value $\overline{y_i}$ was maximized using these values.

- The optimum AS_1 levels are the lowest, while most optimal AS_2 values are the highest. This is because these settings enhanced the average grey relation value $\overline{y_i}$.

- The relation between the appropriate first stage gear ratio and the entire gearbox ratio is depicted in Fig. 7. When ut is more than 27.59, u_1 equals 6, and when $u_t \leq 27.59$, the following regression formula (with $R^2 = 0.9964$) is used to calculate the ideal values of u1:

$$u_1 = 0.1662 \cdot u_t + 1.4928 \tag{37}$$

After having u_1, the gear ratio of the helical gear set u_2 is found by $u_2 = u_t/u_1$.

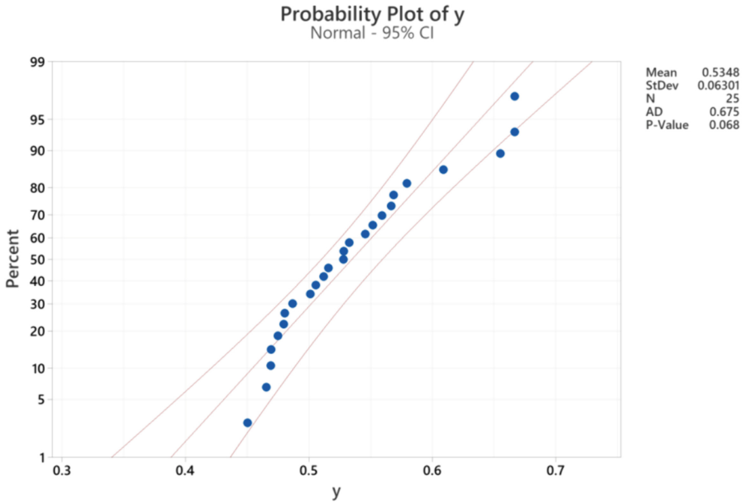

Fig. 5. Probability plot of $\overline{y}$

Table 10. Optimal values of main design parameters

No.	u_t					
	10	15	20	25	30	35
u_1	3.08	4.04	4.89	5.67	6	6
k_{be}	0.25	0.25	0.25	0.25	0.25	0.25
X_{ba}	0.4	0.4	0.4	0.4	0.4	0.4
AS_1	350	350	350	350	350	350
AS_2	350	386	420	420	420	420

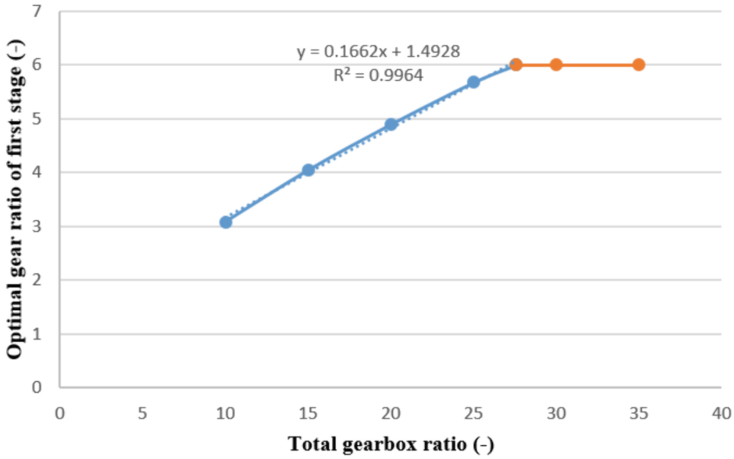

Fig. 6. Optimal first-stage gear ratio versus total gearbox ratio

7 Conclusions

The results of a multi-objective optimization research on optimizing a two-stage bevel helical gearbox to reduce gearbox height and enhance gearbox efficiency are presented in this paper. This research optimized the first stage's gear ratio, the coefficient of wheel face width for stages 1 and 2, and the permitted contact stress for stages 1 and 2. A simulation experiment based on the Taguchi L25 type was created and carried out to solve this issue. The effect of major design features on the multi-objective goal was also investigated. AS_1 has the greatest influence on $\overline{y_i}$ (32.06%), followed by K_{be} (30.07%), u_1 (16.14%), AS_2 (5.5%), and X_{ba} (5.26%). Furthermore, the best settings for the critical gearbox parameters have been suggested. A regression approach (Eq. (37) was also presented for determining the best first stage u_1 gear ratio.

Acknowledgment. Thai Nguyen University of Technology provided support for this research.

References

1. Danh, T.H., et al.: Determining partial gear ratios of a two-stage helical gearbox with first stage double gear sets for minimizing total gearbox Cost. In: Nguyen, D.C., Vu, N.P., Long, B.T., Puta, H., Sattler, K.-U. (eds.) Advances in Engineering Research and Application: Proceedings of the International Conference on Engineering Research and Applications, ICERA 2022, pp. 376–388. Springer International Publishing, Cham (2023). https://doi.org/10.1007/978-3-031-22200-9_41
2. Tuan, N.K., et al.: Determining optimal gear ratios of a two-stage helical reducer for getting minimal acreage of cross section. MATEC Web Conf. **213**, 01008 (2018). https://doi.org/10.1051/matecconf/201821301008

3. Quang, N.H., et al.: Determining optimum gear ratios for a four-stage helical gearbox for getting minimum gearbox cost. In: Nguyen, D.C., Vu, N.P., Long, B.T., Puta, H., Sattler, K.U. (eds.) Advances in Engineering Research and Application: Proceedings of the International Conference on Engineering Research and Applications, ICERA 2021, pp. 350–364. Springer International Publishing, Cham (2022). https://doi.org/10.1007/978-3-030-92574-1_36
4. Tuan, T.K., et al.: Calculating Optimum Gear Ratios for a Four-stage Helical Gearbox for Gearbox Mass Target
5. Tran, H.-D., et al.: Application of the taguchi method and grey relational analysis for multi-objective optimization of a two-stage bevel helical gearbox. Machines **11**(7), 716 (2023)
6. Danh, B.T., et al.: Determination of optimum gear ratios of two-stage bevel helical gearboxes for getting minimum gearbox volume. In: Nguyen, D.C., Vu, N.P., Long, B.T., Puta, H., Sattler, K.-U. (eds.) Advances in Engineering Research and Application: Proceedings of the International Conference on Engineering Research and Applications, ICERA 2021, pp. 302–311. Springer International Publishing, Cham (2022). https://doi.org/10.1007/978-3-030-92574-1_32
7. Quang, N.H., et al.: Determination of optimum partial gear ratios for three-stage bevel helical gearboxes for cost function. In: Nguyen, D.C., Vu, N.P., Long, B.T., Puta, H., Sattler, K.-U. (eds.) Advances in Engineering Research and Application: Proceedings of the International Conference on Engineering Research and Applications, ICERA 2021, pp. 312–327. Springer International Publishing, Cham (2022). https://doi.org/10.1007/978-3-030-92574-1_33
8. Tuan, T.K., et al.: Optimization of gear ratios for three-stage bevel helical gearboxes based on gearbox volume function. In: Nguyen, D.C., Vu, N.P., Long, B.T., Puta, H., Sattler, K.-U. (eds.) Advances in Engineering Research and Application: Proceedings of the International Conference on Engineering Research and Applications, ICERA 2021, pp. 708–720. Springer International Publishing, Cham (2022). https://doi.org/10.1007/978-3-030-92574-1_73
9. Thao, T.T.P., et al.: Determining optimum gear ratios of mechanical driven systems using three stage bevel helical gearbox and chain drive. In: Sattler, K.-U., Nguyen, D.C., Vu, N.P., Long, B.T., Puta, H. (eds.) ICERA 2019. LNNS, vol. 104, pp. 249–261. Springer, Cham (2020). https://doi.org/10.1007/978-3-030-37497-6_29
10. Quang, N.H., et al.: Optimizing the partial gear ratios of the two-stage worm gearbox for minimizing total gearbox cost. Eastern-Eur. J. Enterprise Technol. **1**(1), 115 (2022)
11. Tung, L.A., et al.: A study on determination of optimum gear ratios of a two-stage worm gearbox. In: Sattler, K.-U., Nguyen, D.C., Vu, N.P., Tien Long, B., Puta, H. (eds.) ICERA 2019. LNNS, vol. 104, pp. 76–84. Springer, Cham (2020). https://doi.org/10.1007/978-3-030-37497-6_8
12. Cuong, N.M., et al.: Calculation of optimum gear ratios of two-step worm gearbox. In: Advances in Engineering Research and Application: Proceedings of the International Conference on Engineering Research and Applications, ICERA 2019. Springer (2020)
13. Hong, T.: A study on calculation of optimum gear ratios for three stage bevel helical gearboxes. ARPN J. Eng. Appl. Sci. **14**, 2592–2598 (2019)
14. Cam, N.T.H., et al.: Calculating optimum gear ratios of mechanical drive systems using two-stage helical gearbox with second-stage double gear sets and chain drive for minimum gearbox length. In: Advances in Engineering Research and Application: Proceedings of the International Conference on Engineering Research and Applications, ICERA 2019. Springer (2020)
15. Tuan, N.K., et al.: A study on determining optimum gear ratios of mechanical driven systems using two-step helical gearbox with first step double gear sets and chain drive. In: Advances in Engineering Research and Application: Proceedings of the International Conference on Engineering Research and Applications, ICERA 2019. Springer (2020)

16. Tu, N.T., et al.: Determining optimal gear ratios of mechanical drive systems using two-stage helical gearbox with second-stage double gear sets and chain drive for minimal system cross section area. In: Sattler, K.-U., Nguyen, D.C., Vu, N.P., Long, B.T., Puta, H. (eds.) Advances in Engineering Research and Application: Proceedings of the International Conference on Engineering Research and Applications, ICERA 2019, pp. 238–248. Springer International Publishing, Cham (2020). https://doi.org/10.1007/978-3-030-37497-6_28
17. Quang, H., et al.: Determination of optimum gear ratios for minimum gearbox volume of two-stage helical gearbox with second-stage double gear sets. IOP Conf. Ser.: Mater. Sci. Eng. **635**, 012012 (2019)
18. Ky, L.H., et al.: Calculation of optimum gear ratios of mechanical driven systems using worm-helical gearbox and chain drive. In: Sattler, K.-U., Nguyen, D.C., Vu, N.P., Long, B.T., Puta, H. (eds.) Advances in Engineering Research and Application: Proceedings of the International Conference on Engineering Research and Applications, ICERA 2019, pp. 66–75. Springer International Publishing, Cham (2020). https://doi.org/10.1007/978-3-030-37497-6_7
19. Le, X.-H., Vu, N.-P.: Multi-objective optimization of a two-stage helical gearbox using taguchi method and grey relational analysis. Appl. Sci. **13**(13), 7601 (2023)
20. Chat, T., Van Uyen, L.: Design and calculation of Mechanical Transmissions Systems, vol. 1. Educational Republishing House, Hanoi (2007)
21. Trinh Chat, L.V.U.: Calculation of mechanical driven systems. Education Publisher (1996)
22. Jelaska, D.: Gears and gear drives. Wiley (2012). https://doi.org/10.1002/9781118392393
23. Buckingham, E.: Analytical mechanics of gears. Courier Corporation (1988)

Check for updates

Multi-Objective Optimization of a Two-Stage Helical Gearbox to Increase Efficiency and Reduce Bottom Area

Dinh Van Thanh[1], Tran Huu Danh[2], Nguyen Van Chien Thang[3], Bui Thanh Danh[4], Hoang Xuan Tu[5], and Nguyen Thi Quoc Dung[5](✉)

[1] East Asia University of Technology, Ho Chi Minh City, Vietnam
[2] Vinh Long University of Technology Education, Vinh Long City, Vietnam
[3] Nguyen Tat Thanh University, Ho Chi Minh City, Vietnam
[4] University of Transport and Communications, Hanoi, Vietnam
[5] Thai Nguyen University of Technology, Thai Nguyen, Vietnam
quocdung@tnut.edu.vn

Abstract. This paper presents the outcomes of a study on multi-objective optimization of a two-stage helical gearbox in establishing the ideal key design variables to decrease gearbox bottom area and gearbox efficiency. The Taguchi method and grey relation analysis (GRA) were used to solve the problem in two steps: first, a single-objective optimization problem was solved to close the gap within variable levels, and then a multi-objective optimization problem was solved to determine the optimal main design factors. The coefficients of wheel face width (CWFW) of the first and second stages, the allowed contact stresses (ACS) of the first and second stages, and the first stage's gear ratio were also chosen. The study's findings were used to determine the best values for five important design factors while designing a two-stage helical gearbox.

Keywords: Helical Gearbox · Multi-objective optimization · Gear ratio · Bottom area · gearbox efficiency

1 Introduction

The gearbox is the most important component of any mechanical drive system. It is often employed to reduce the speed of the motor shaft while increasing the torque transferred to the machine shaft. As a result, optimizing gearbox design is a continuous concern.

There have been several papers on optimum partial gear ratio computation up to this point. A gearbox's gear ratios have been determined using three major methods: the graphical technique, the "practice method," and the model method. A graph is used to find the partial gear ratios in the graph technique. Figure 1 shows how to calculate the gear ratio u1 of a two-speed helical gearbox. This approach enables for rapid and easy gear ratio measurement, although the gear ratio values are frequently not ideal. G. Milou and his colleagues' "practical method" is based on manufacturer statistics on gearbox data. The mass of a two-stage helical gearbox is reduced using this approach

D. C. Nguyen et al. (Eds.): ICERA 2023, LNNS 944, pp. 177–194, 2024.
https://doi.org/10.1007/978-3-031-62235-9_19

if the ratio of the center distances of the second stage to the first stage, aw2/aw1, is between 1.4 and 1.6 [1]. Using the data from the lookup table, the ideal partial gear ratios will be computed. The modeling approach is the most often utilized. The best gear ratios are computed using explicit formulae in this technique, making the computation exceedingly straightforward and convenient. These algorithms are designed to achieve certain goals, such as minimizing gear box length [2–4], minimizing gear mass [5, 6], minimum gearbox cross-section area [7, 8], or minimal gearbox cost [9–12].

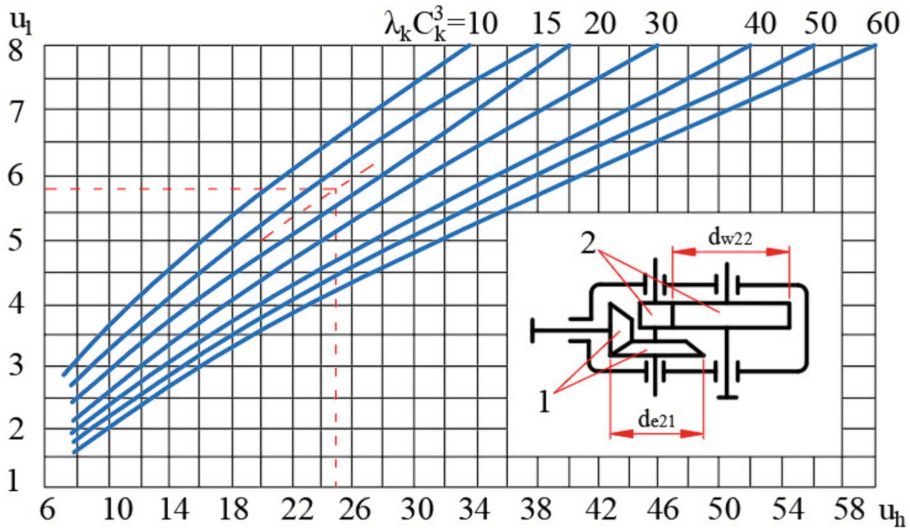

Fig. 1. Relation between gear ratio of stage 1 and total gear ratio [13]

Optimal gear ratio studies have been conducted for helical gear gearboxes [8, 14], bevel gear boxes [11, 15–18], worm gearboxes [9, 19, 20] etc. Furthermore, research was conducted on two-stage [8–10, 16], three-stage [11, 17, 18, 21], and four-stage gearboxes [12, 22]. [23] has introduced a novel technique for addressing multi-objective optimization issues for helical gearboxes utilizing the Taguchi method and gray connection analysis, with the goal of reducing gearbox weight and increasing efficiency. [15] also released the findings of multi-objective optimization for a bevel gearbox in order to minimize gearbox volume while enhancing efficiency.

This article discusses a multi-objective optimization research for a two-stage helical gearbox with two single objectives in mind: optimizing gearbox efficiency and minimizing gearbox bottom area. The identification of five ideal major design elements for the two-stage helical gearbox is a crucial signal of this research. These variables include the CWFW for both stages, the ACS for both stages, and the first stage gear ratio. Furthermore, the multi-objective optimization issue in gearbox design was addressed in two stages by integrating the Taguchi approach with the GRA. The research findings were also utilized to identify the best values for five important design factors while creating a two-stage helical gearbox.

2 Optimization Problem

2.1 Gearbox Bottom Area Calculation

For the gearbox, the bottom area A_b is determined by (Fig. 1):

$$A_{gb} = L \cdot B_1 \tag{1}$$

In which, L, and B_1 can be calculated by (Fig. 2):

$$L = \frac{d_{w11}}{2} + a_{w1} + a_{w2} + \frac{d_{w22}}{2} + 20 \tag{2}$$

$$B_1 = b_{w1} + 4 \cdot S_G \tag{3}$$

$$S_G = 0.005 \cdot L' + 4.5 \quad [24] \tag{4}$$

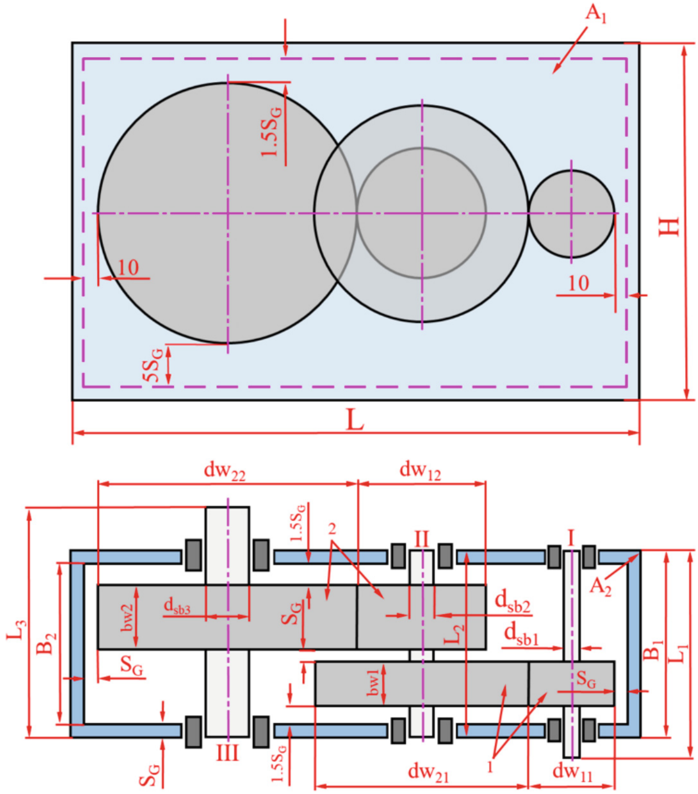

Fig. 2. Calculated schema

In the preceding formulas, bw_1 is the first stage's gear width; dw_{12}, dw_{21}, and dw_{22} are the pitch diameters of the pinion and gear sets, as estimated by [25]:

$$d_{w21} = 2 \cdot a_{w1} \cdot u_1/(u_1 + 1) \tag{5}$$

$$d_{w12} = 2 \cdot a_{w2}/(u_2 + 1) \tag{6}$$

$$d_{w22} = 2 \cdot a_{w2} \cdot u_2/(u_2 + 1) \tag{7}$$

$$b_{w1} = X_{ba1} \cdot a_{w1} \tag{8}$$

In Eqs. (5), (6), (7) and (8), u_1 and u_2 are partial gear ratios; $u_2 = u_t/u_1$; where u_t is the total gearbox ratio; and a_{w1} and a_{w2} are the first and second stage center distances, which may be found by [25]:

$$a_{w1} = k_a \cdot (u_1 + 1) \cdot \sqrt[3]{T_{11} \cdot k_{H\beta}/(\mathrm{AS}_1^2 \cdot u_1 \cdot X_{ba})} \tag{9}$$

$$a_{w2} = k_a \cdot (u_2 + 1) \cdot \sqrt[3]{T_{12} \cdot k_{H\beta 2}/(\mathrm{AS}_2^2 \cdot u_2 \cdot X_{ba2})} \tag{10}$$

where, $k_{H\beta}$ is the contacting load ratio for pitting resistance; $k_{H\beta} = 1.05 \div 1.27$ [25] and it can be chosen as $k_{H\beta} = 1.16$; AS1 and AS2 is the allowable contact stress of stages 1 and 2 (MPa); k_a is the material coefficient; $k_a = 43$ [25]; X_{ba1} and X_{ba2} are the coefficients of the wheel face width of stages 1 and 2; T_{11} and T_{12} are the torques on the pinions of stages 1 and 2 (Nmm):

$$T_{11} = T_{out}/\left(u_t \cdot \eta_{hg}^2 \cdot \eta_b^3\right) \tag{11}$$

$$T_{12} = T_{out}/\left(u_2 \cdot \eta_{hg} \cdot \eta_{be}^2\right) \tag{12}$$

In which, T_{out} is the output torque (N.mm); η_{hg} is the helical gear efficiency ($\eta_{hg} = 0.96 \div 0.98$ [25]; η_b is the efficiency of a rolling bearing pair ($\eta_h = 0.99 \div 0.995$ [25]).

2.2 Gearbox Efficiency Calculation

The efficiency of the gearbox can be determined by:

$$\eta_{gb} = \frac{100 \cdot P_l}{P_{in}} \tag{13}$$

where, P_l is the overall gearbox power loss [26]:

$$P_l = P_{lg} + P_{lb} + P_{ls} \tag{14}$$

In which, P_{lg} is total gear power loss, P_{lb} is bearing power loss, and P_{ls} is seal power loss. Those parts can be found by:

+) The gear power loss:

$$P_{lg} = \sum_{i=1}^{2} P_{lgi} \tag{15}$$

P_{lgi} is the gear power losses of i stage which is found by:

$$P_{lgi} = P_{gi} \cdot (1 - \eta_{gi}) \tag{16}$$

where,η_{gi} is the expected efficiency of stage i [27]:

$$\eta_{gi} = 1 - \left(\frac{1 + 1/u_i}{\beta_{ai} + \beta_{ri}}\right) \cdot \frac{f_i}{2} \cdot \left(\beta_{ai}^2 + \beta_{ri}^2\right) \tag{17}$$

In (17), u_i is the gear ratio of i stage; β_{ai} and β_{ri} are the arcs of approach and retreat on the i step which can be calculated by [27]:

$$\beta_{ai} = \frac{\left(R_{e2i}^2 - R_{02i}^2\right)^{1/2} - R_{2i} \cdot \sin\alpha}{R_{01i}} \tag{18}$$

$$\beta_{ri} = \frac{\left(R_{e1i}^2 - R_{01i}^2\right)^{1/2} - R_{1i} \cdot \sin\alpha}{R_{01i}} \tag{19}$$

where, R_{e1i} and R_{e2i} are the pinion and gear's outer radiuses; R_{1i} and R_{2i} are the pinion and gear's pitch radiuses; R_{01i} and R_{01i} are the pinion and gear's base-circle radiuses; α and is the pressure angle.

The friction coefficient f in (12) can be found by [15]:

– In the case of sliding velocity v ≤ 0.424 (m/s):

$$f = -0.0877 \cdot v + 0.0525 \tag{20}$$

– In the case of sliding velocity v > 0.424 (m/s):

$$f = 0.0028 \cdot v + 0.0104 \tag{21}$$

+) The bearing power loss can be determined by [26]:

$$P_{lb} = \sum_{i=1}^{6} f_b \cdot F_i \cdot v_i \tag{22}$$

In which, f_b is the bearing friction coefficient; in this work, radical ball bearings with angular contact were selected and $f_b = 0.0011$ [26]; F is the bearing load (N), v is the peripheral speed, and i is the bearing ordinal number (i = 1 ÷ 6).

+) The overall seal power loss can be found by [26]:

$$P_s = \sum_{i=1}^{2} P_{si} \tag{23}$$

where P_{si} is the power loss in a single seal (w):

$$P_{si} = \left[145 - 1.6 \cdot t_{oil} + 350 \cdot loglog(VG_{40} + 0.8)\right] \cdot d_s^2 \cdot n \cdot 10^{-7} \tag{24}$$

With VG_{40} is the ISO Viscosity Grade number.

2.3 Objective Function and Constrains

2.3.1 Objectives Functions

The multi-objective optimization problem in this study has two single objectives:

Minimizing the gearbox bottom area:

$$\min f_2(X) = \mathrm{A_{gb}} \tag{25}$$

Minimizing the gearbox mass:

$$\min f_1(X) = \mathrm{m}_{gb} \tag{26}$$

In which, X is the design variable vector. In this study, five main design parameters, including u_1, Xba_1, Xba_2, AS_1, and AS_2 have been selected as variables, and we get:

$$X = \{u_1, Xba_1, Xba_2, AS_1, AS_2\} \tag{27}$$

2.3.2 Constrains

For a helical gear set, the maximum value of the gear ratio is 9 [25]. Furthermore, the CWFW of both gear stages of a two-stage helical gearbox ranges between 0.25 and 0.4 [25]. Furthermore, the gear materials employed in this study are steel refinement 40, 45, 40X, and 35XM, with surface teeth hardness of 350 HB (the most often used gear materials in gearboxes). According to the computed results, the allowed contact stresses for the first and second stages are 350 to 420 (MPa). As a result of these observations, the following restrictions emerged:

$$1 \le u_1 \le 9 \quad \text{and} \quad 1 \le u_2 \le 9 \tag{28}$$

$$0.25 \le Xba_1 \le 0.4 \quad \text{and} \quad 0.25 \le Xba_2 \le 0.4 \tag{29}$$

$$350 \le AS_1 \le 420 \quad \text{and} \quad 350 \le AS_2 \le 420 \tag{30}$$

3 Methodology

In this study, five key design aspects were chosen for consideration. Table 1 shows the minimum and maximum values for several parameters. The Taguchi technique and grey relation analysis were used to address the optimization problem. To optimize the number of levels for each variable, the L25 (5^5) design was employed. The gear ratio of the first stage u_1, on the other hand, has a wide range (from 1 to 9 – see Table 1). Even with five levels, the values of these qualities varied significantly (in this case, the difference is ((9–1)/4 = 2).

The 2-stage multi-objective optimization problem solution technique [23] was used to help narrow the gap between variable values scattered throughout a wide range. The

Table 1. Input factors and their maximum and lowest limits

Factor	Notation	Lowest limit	Maximum limit
Gearbox ratio of stage 1	u_1	1	9
CWFW of stage 1	Xba1	0.25	0.4
CWFW of stage 2	Xba2	0.25	0.4
ACS of stage 1 (MPa)	AS_1	350	420
ACS of stage 2 (MPa)	AS_2	350	420

first step of this approach handles a single-objective optimization problem, while the second stage addresses a multi-objective optimization problem in order to discover the best key design characteristics (Fig. 3).

In this work, the direct search approach is employed to solve the single-objective optimization problem. In addition, a computer program written in Matlab was developed to address two single-objective problems: decreasing the gearbox bottom area and increasing gearbox efficiency. Based on the program's results, Fig. 4 depicts the link between the ideal value of the first stage gear ratio u1 and the whole gearbox ratio ut. Table 2 shows that new constraints for the variable u1 have been identified.

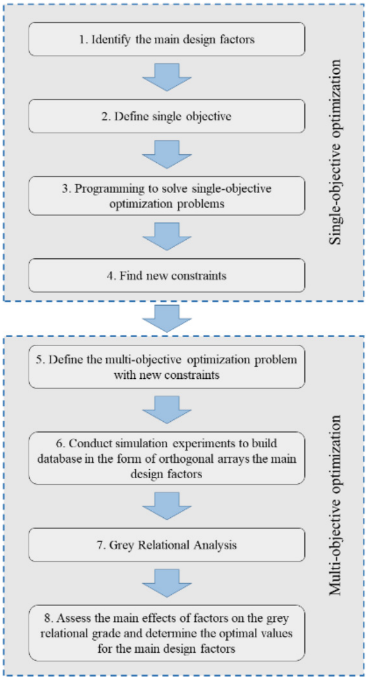

Fig. 3. Method for solving the multi-objective problem [23]

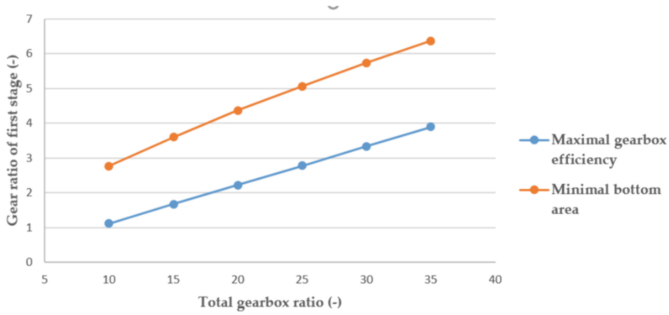

Fig. 4. Optimal gear ratio of the first stage versus total gearbox ratio

Table 2. New constraints of u_1

u_t	u_1	
	Lower Bound	Upper Bound
10	1	2.86
15	1.57	3.7
20	2.12	4.46
25	2.68	5.16
30	3.23	5.83
35	3.79	6.46

4 Multi-Objective Optimization

The purpose of this work's multi-objective optimization issue of a two-stage helical gearbox is to determine the ideal major design variables with a certain total gear-box ratio that meets two single-objective functions: decreasing gearbox bottom area and optimizing gearbox efficiency. To solve this issue, a simulation experiment was carried out. Table 3 displays the key design components and their values for $u_t = 15$. The experimental design was created using the Taguchi technique using L25 (55) design, and the data was analyzed using Minitab R18 software. The experimental design and results for $u_t = 15$ are shown in Table 4.

When dealing with the multi-optimization optimization problem, the Taguchi and GRA approaches are used. The major phases in this method are as follows:

+) Calculating the signal-to-noise ratio (S/N) using the following formulae in order to reduce gearbox bottom area and increase gearbox efficiency.

The bigger the S/N, the better for gearbox efficiency:

$$SN = -10log_{10}(\frac{1}{n}\sum_{i=1}^{m}\frac{1}{y_i^2}) \tag{31}$$

Table 3. Main design factors and their levels for $u_t = 15$.

Factor	Notation	Level				
		1	2	3	4	5
Gear ratio of stage 1	u_1	1.57	2.1025	2.635	3.1675	3.70
CWFW of stage 1	X_{ba1}	0.25	0.2875	0.325	0.3625	0.4
CWFW of stage 2	X_{ba2}	0.25	0.2875	0.325	0.3625	0.4
ACS of stage 1 (MPa)	AS_1	350	367.5	385	402.5	420
ACS of stage 2 (MPa)	AS_2	350	367.5	385	402.5	420

The lesser the S/N, the better for the gearbox bottom area goal:

$$SN = -10log_{10}(\frac{1}{n}\sum_{i=1}^{m} y_i^2) \tag{32}$$

In which, y_i is the output result, and m is the number of experimental repetitions. Because this is a simulation, m = 1; there is no need for repetition. Table 5 displays the estimated S/N indices for the two output objectives.

In actuality, the data of the two single-objective functions under consideration have distinct dimensions. To assure similarity, the data must be normalized, or brought to a consistent scale. The normalization value Z_{ij}, which ranges from 0 to 1, is used to normalize the data. This value is calculated using the formula:

$$Z_i = \frac{SN_i - min(SN_i, = 1,2, ..n)}{max(SN_i, j = 1,2, ..n) - min(SN_i, = 1,2, ..n)} \tag{33}$$

With n = 25 is the experimental amount.

+) The grey relational coefficient can be found by:

$$y_i(k) = \frac{\Delta_{min} + \xi.\Delta_{max}(k)}{\Delta_i(k) + \xi.\Delta_{max}(k)} \tag{34}$$

In which, i = 1,2,…,n. k = 2 is the objective number; $\Delta_j(k)$ is the absolute value, $\Delta_j(k) = \|Z_0(k) - Z_j(k)\|$ with Z0(k) and Zj(k) are the reference and specific comparison sequences; Δ_{min} and Δ_{max} are the min and max values of Δi(k); ζ is the characteristic coefficient, $0 \leq \zeta \leq 1$. In this case, ζ = 0.5.

+) Determining the degree of grey relation by the following equation:

$$\overline{y_i} = \frac{1}{k}\sum_{j=0}^{k} y_{ij}(k) \tag{35}$$

Table 4. Experimental plan and output results for $u_t = 15$.

No	Input Factors					η_{gb}	A_b
	u_1	X_{ba1}	X_{ba2}	AS_1	AS_2	(%)	(dm)
1	1.5700	0.2500	0.2500	350.0	350.0	98.154	8.223
2	1.5700	0.2875	0.2875	367.5	367.5	98.189	7.970
3	1.5700	0.3250	0.3250	385.0	385.0	98.168	7.727
4	1.5700	0.3625	0.3625	402.5	402.5	98.123	7.494
5	1.5700	0.4000	0.4000	420.0	420.0	98.129	7.273
6	2.1025	0.2500	0.2875	385.0	402.5	97.946	6.845
7	2.1025	0.2875	0.3250	402.5	420.0	97.910	6.663
8	2.1025	0.3250	0.3625	420.0	350.0	98.000	7.852
9	2.1025	0.3625	0.4000	350.0	367.5	97.960	7.585
10	2.1025	0.4000	0.2500	367.5	385.0	97.986	7.481
11	2.6350	0.2500	0.3250	420.0	367.5	97.786	6.929
12	2.6350	0.2875	0.3625	350.0	385.0	97.876	7.261
13	2.6350	0.3250	0.4000	367.5	402.5	97.862	7.033
14	2.6350	0.3625	0.2500	385.0	420.0	97.756	6.479
15	2.6350	0.4000	0.2875	402.5	350.0	97.818	7.544
16	3.1675	0.2500	0.3625	367.5	420.0	97.712	6.502
17	3.1675	0.2875	0.4000	385.0	350.0	97.762	7.569
18	3.1675	0.3250	0.2500	402.5	367.5	97.630	6.900
19	3.1675	0.3625	0.2875	420.0	385.0	97.616	6.695
20	3.1675	0.4000	0.3250	350.0	402.5	97.743	7.093
21	3.7000	0.2500	0.4000	402.5	385.0	97.606	6.793
22	3.7000	0.2875	0.2500	420.0	402.5	97.472	6.220
23	3.7000	0.3250	0.2875	350.0	420.0	97.601	6.650
24	3.7000	0.3625	0.3250	367.5	350.0	97.547	7.652
25	3.7000	0.4000	0.3625	385.0	367.5	97.617	7.388

In which y_{ij} is the grey relation value of the jth output goal of the ith experiment. The predicted grey relation value y_i and average grey relation value $\overline{y_i}$ for all test runs are shown in Table 6.

Table 5. S/N results with ut = 15

No.	Input Factors					η_{gb}		Ab	
	u_1	X_{ba1}	X_{ba2}	AS_1	AS_2	(%)	S/N	(dm)	S/N
1	1.5700	0.2500	0.2500	350.0	350.0	98.154	39.8382	8.223	−18.3006
2	1.5700	0.2875	0.2875	367.5	367.5	98.189	39.8413	7.970	−18.0292
3	1.5700	0.3250	0.3250	385.0	385.0	98.168	39.8394	7.727	−17.7602
4	1.5700	0.3625	0.3625	402.5	402.5	98.123	39.8354	7.494	−17.4943
5	1.5700	0.4000	0.4000	420.0	420.0	98.129	39.8359	7.273	−17.2343
6	2.1025	0.2500	0.2875	385.0	402.5	97.946	39.8197	6.845	−16.7075
7	2.1025	0.2875	0.3250	402.5	420.0	97.910	39.8165	6.663	−16.4734
8	2.1025	0.3250	0.3625	420.0	350.0	98.000	39.8245	7.852	−17.8996
9	2.1025	0.3625	0.4000	350.0	367.5	97.960	39.8210	7.585	−17.5991
10	2.1025	0.4000	0.2500	367.5	385.0	97.986	39.8233	7.481	−17.4792
11	2.6350	0.2500	0.3250	420.0	367.5	97.786	39.8055	6.929	−16.8134
12	2.6350	0.2875	0.3625	350.0	385.0	97.876	39.8135	7.261	−17.2199
13	2.6350	0.3250	0.4000	367.5	402.5	97.862	39.8123	7.033	−16.9428
14	2.6350	0.3625	0.2500	385.0	420.0	97.756	39.8029	6.479	−16.2302
15	2.6350	0.4000	0.2875	402.5	350.0	97.818	39.8084	7.544	−17.5520
16	3.1675	0.2500	0.3625	367.5	420.0	97.712	39.7990	6.502	−16.2609
17	3.1675	0.2875	0.4000	385.0	350.0	97.762	39.8034	7.569	−17.5808
18	3.1675	0.3250	0.2500	402.5	367.5	97.630	39.7917	6.900	−16.7770
19	3.1675	0.3625	0.2875	420.0	385.0	97.616	39.7904	6.695	−16.5150
20	3.1675	0.4000	0.3250	350.0	402.5	97.743	39.8017	7.093	−17.0166
21	3.7000	0.2500	0.4000	402.5	385.0	97.606	39.7895	6.793	−16.6412
22	3.7000	0.2875	0.2500	420.0	402.5	97.472	39.7776	6.220	−15.8758
23	3.7000	0.3250	0.2875	350.0	420.0	97.601	39.7891	6.650	−16.4564
24	3.7000	0.3625	0.3250	367.5	350.0	97.547	39.7843	7.652	−17.6755
25	3.7000	0.4000	0.3625	385.0	367.5	97.617	39.7905	7.388	−17.3705

To ensure harmony among the output parameters, a higher average grey relation value is preferred. As a result, the objective function of a multi-objective problem can be reduced to a single-objective optimization problem, with the mean grey relation value as the output.

Table 6. Values of $\Delta_i(k)$ and $\overline{y_i}$

No.	S/N		Zi		Δ_i (k)		Grey Relation Value yi		$\overline{y_i}$
	η_{gb}	Ab	η_{gb}	Ab					
			Reference Value		η_{gb}	**Ab**	η_{gb}	**Ab**	
			1.000	1.000					
1	39.8382	−18.3006	0.9514	0.0000	0.049	1.000	0.911	0.333	0.622
2	39.8413	−18.0292	1.0000	0.1119	0.000	0.888	1.000	0.360	0.680
3	39.8394	−17.7602	0.9708	0.2229	0.029	0.777	0.945	0.391	0.668
4	39.8354	−17.4943	0.9083	0.3325	0.092	0.667	0.845	0.428	0.637
5	39.8359	−17.2343	0.9166	0.4398	0.083	0.560	0.857	0.472	0.664
6	39.8197	−16.7075	0.6619	0.6570	0.338	0.343	0.597	0.593	0.595
7	39.8165	−16.4734	0.6117	0.7536	0.388	0.246	0.563	0.670	0.616
8	39.8245	−17.8996	0.7371	0.1654	0.263	0.835	0.655	0.375	0.515
9	39.8210	−17.5991	0.6814	0.2893	0.319	0.711	0.611	0.413	0.512
10	39.8233	−17.4792	0.7176	0.3388	0.282	0.661	0.639	0.431	0.535
11	39.8055	−16.8134	0.4388	0.6133	0.561	0.387	0.471	0.564	0.518
12	39.8135	−17.2199	0.5644	0.4457	0.436	0.554	0.534	0.474	0.504
13	39.8123	−16.9428	0.5448	0.5600	0.455	0.440	0.523	0.532	0.528
14	39.8029	−16.2302	0.3970	0.8539	0.603	0.146	0.453	0.774	0.614
15	39.8084	−17.5520	0.4835	0.3087	0.517	0.691	0.492	0.420	0.456
16	39.7990	−16.2609	0.3355	0.8412	0.664	0.159	0.429	0.759	0.594
17	39.8034	−17.5808	0.4053	0.2969	0.595	0.703	0.457	0.416	0.436
18	39.7917	−16.7770	0.2210	0.6284	0.779	0.372	0.391	0.574	0.482
19	39.7904	−16.5150	0.2014	0.7364	0.799	0.264	0.385	0.655	0.520
20	39.8017	−17.0166	0.3788	0.5295	0.621	0.470	0.446	0.515	0.481
21	39.7895	−16.6412	0.1874	0.6843	0.813	0.316	0.381	0.613	0.497
22	39.7776	−15.8758	0.0000	1.0000	1.000	0.000	0.333	1.000	0.667
23	39.7891	−16.4564	0.1805	0.7605	0.820	0.239	0.379	0.676	0.528
24	39.7843	−17.6755	0.1049	0.2578	0.895	0.742	0.358	0.403	0.380
25	39.7905	−17.3705	0.2028	0.3836	0.797	0.616	0.385	0.448	0.417

Table 7 shows the results of an ANOVA test used to examine the impact of the main design variables on the average grey relation value $\overline{y_i}$. Table 7 shows that u_1 has the most influence on $\overline{y_i}$ (48.31%), followed by AS_2 (26.93%), X_{ba1} (8.84%), X_{ba2} (6.48%), and AS_1 (3.79%). Using ANOVA analysis, Table 8 shows the order of influence of the main design factors on $\overline{y_i}$.

Table 7. Analysis of variance for means

Analysis of Variance for Means							
Source	DF	Seq SS	Adj SS	Adj MS	F	P	C (%)
u1	4	0.082579	0.082579	0.020645	8.53	0.031	48.31
Xba1	4	0.015113	0.015113	0.003778	1.56	0.338	8.84
Xba2	4	0.011073	0.011073	0.002768	1.14	0.450	6.48
AS1	4	0.006475	0.006475	0.001619	0.67	0.647	3.79
AS2	4	0.046038	0.046038	0.011509	4.76	0.080	26.93
Residual Error	4	0.009675	0.009675	0.002419			5.66
Total	24	0.170953					

Model Summary		
S	R-Sq	R-Sq(adj)
0.0492	94.34%	66.04%

+) *Finding the best main design factors:* In principle, the reasonable (or ideal) factor set would be a collection of primary design variables with the highest S/N values. As a consequence, the influence of the primary design elements on the S/N ratio (Fig. 5) was estimated. Figure 5 and Table 9 were used to estimate the ideal levels (the red circles) and values of the primary design parameters for multi-objective function.

Table 8. Response table for means

Level	u1	Xba1	Xba2	AS1	AS2
1	0.6543	0.5652	0.5839	0.5293	0.4820
2	0.5546	0.5807	0.5556	0.5434	0.5217
3	0.5238	0.5441	0.5326	0.5459	0.5448
4	0.5026	0.5325	0.5334	0.5376	0.5813
5	0.4977	0.5104	0.5274	0.5767	0.6032
Delta	0.1567	0.0703	0.0565	0.0474	0.1212
Rank	1	3	4	5	2
Average of grey analysis value: 0.547					

+) *Examining the experimental model:* The Anderson-Darling technique is used to assess the sufficiency of the proposed model, and the results are shown in Fig. 6. As seen in the graph, the data points corresponding to the experimental observations (represented by blue dots) fall within the zone defined by the top and lower bounds with a 95% standard deviation. Furthermore, the p-value of 0.213 considerably surpasses the significance level of $\alpha = 0.05$. These findings indicate that the empirical model utilized in this study is appropriate and appropriate for the analysis.

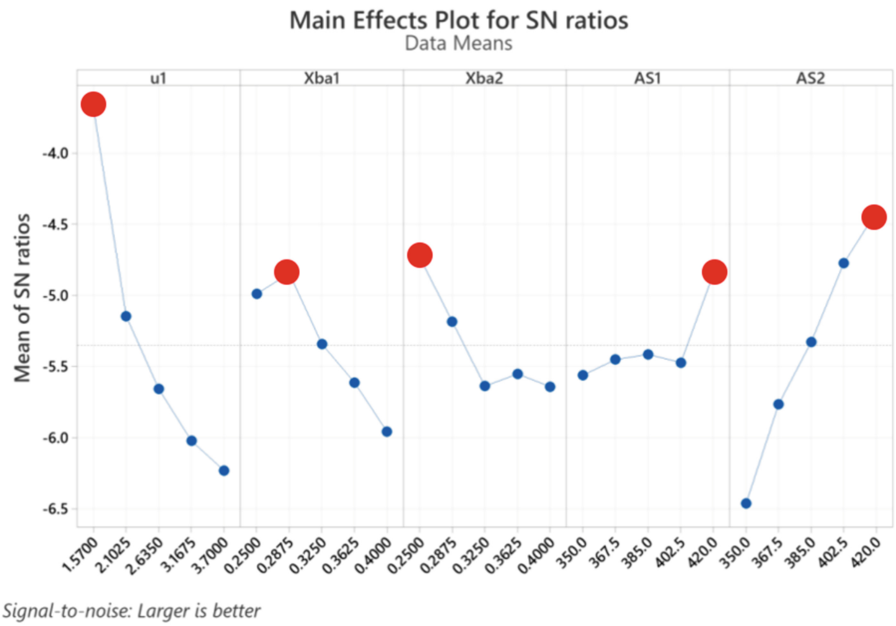

Fig. 5. Main effects plot for S/N ratios

Table 9. Optimum values of main design factors

No.	Input Parameters	Code	Optimum Level	Optimum Value
1	Gear ratio of stage 1	u_1	5	1.57
2	CWFW of stage 1	Xba1	5	0.2875
3	CWFW of stage 2	Xba2	5	0.25
4	ACS of stage 1 (MPa)	AS1	5	420
5	ACS of stage 2 (MPa)	AS2	5	420

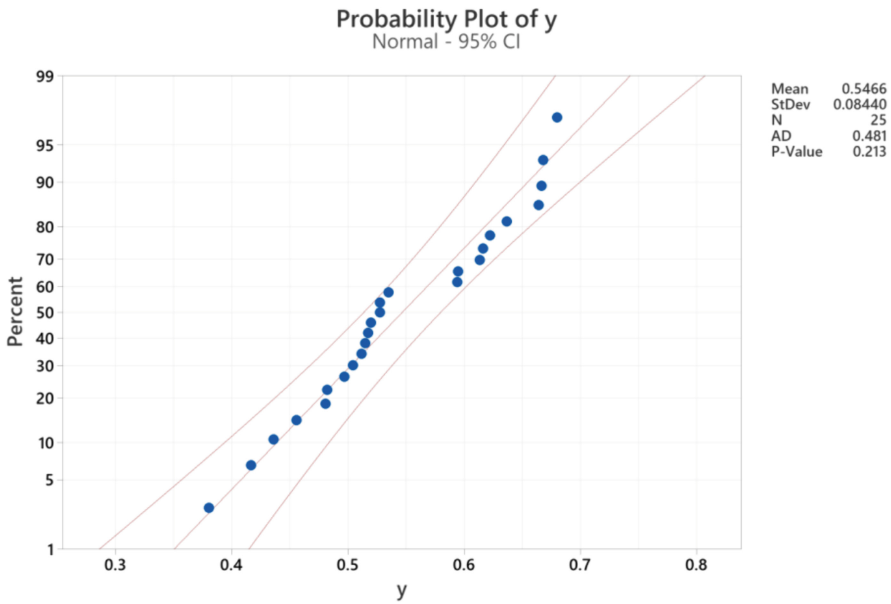

Fig. 6. Probability plot of $\overline{y}$

Continue in the same manner as with $u_t = 15$, but with the remaining u_t values of 10, 20, 25, 30, and 35. Table 10 shows the optimal values for each of the five key design parameters at different u_t. Figure 6 depicts the relationship between the proper first stage gear ratio and the total gearbox ratio. To determine the optimal values of u_1, use the regression formula below (with $R^2 = 1$).

$$u_1 = 0.1114 \cdot u_t - 0.1075 \tag{36}$$

After calculating u_1, the optimum value of u_2 is found using $u_2 = u_t/u_1$ (Fig. 7).

Table 10. Optimal values of main design factors

No	u_t					
	10	15	20	25	30	35
u_1	1	1.57	2.12	2.68	3.23	3.79
X_{ba1}	0.2875	0.2875	0.2875	0.25	0.25	0.25
X_{ba2}	0.25	0.25	0.25	0.25	0.25	0.25
AS_1	350	420	420	420	420	420
AS_2	420	420	420	420	420	420

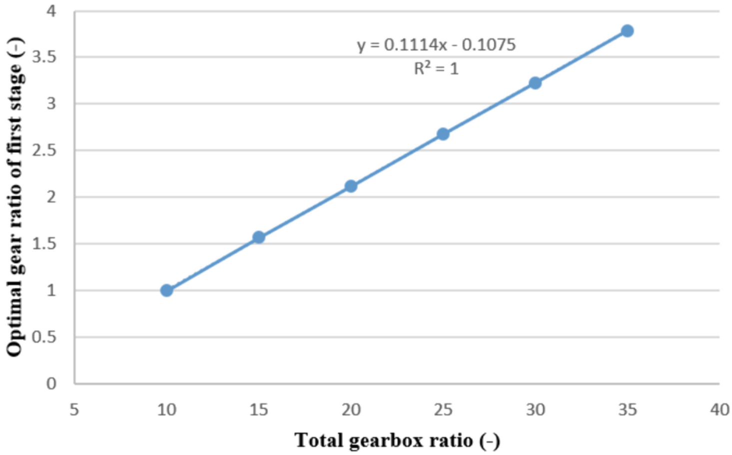

Fig. 7. Optimal gear ratio of the stage 1 versus total gearbox ratio

5 Conclusions

The findings of a multi-objective optimization research on optimizing a two-stage helical gearbox to decrease gearbox bottom area and maximize gearbox efficiency are presented in this work. This study improved the first stage's gear ratio, the coefficient of wheel face width of stages 1 and 2, and the permitted contact stress of stages 1 and 2. To address this issue, a simulation experiment using Taguchi L25 type was devised and executed. The effect of major design elements on the multi-objective aim was also investigated. It was reported that that u_1 has the most influence on $\overline{y_i}$ (48.31%), followed by AS_2 (26.93%), X_{ba1} (8.84%), X_{ba2} (6.48%), and AS_1 (3.79%). In addition, the ideal settings for the key gearbox parameters have been suggested. A regression approach for identifying the appropriate first stage u1 gear ratio was also suggested (Eq. (36)).

Acknowledgment. The Thai Nguyen University of Technology supported for this work.

References

1. Milou, G., et al.: Optimal design of two step gear units, regarding the main parameters. VDI Berichte **1230**, 227 (1996)
2. Pi, V.N.: Optimal calculation of partial transmission ratios for four-step helical gearboxes with first and third-step double gear-sets for minimal gearbox length. In: American Conference on Applied Mathematics (MATH 2008), Harvard, Massachusetts, USA (2008)
3. Pi, V.N., et al.: Determination of optimum gear ratios of a two-stage helical gearbox with second stage double gear sets. IOP Conf. Ser.: Mater. Sci. Eng. **635**(1), 012012 (2019). https://doi.org/10.1088/1757-899X/635/1/012012
4. van Cuong, N., Le Hong, K., Tran, T.H.: Splitting total gear ratio of two-stage helical reducer with first-stage double gearsets for minimal reducer length. Int. J. Mech. Product. Eng. Res. Dev. **9**(6), 595–608 (2019)

5. Cam, N.T.H., et al.: A study on determination of optimum partial transmission ratios of mechanical driven systems using a chain drive and a three-step helical reducer. In: Fujita, H., Nguyen, D.C., Vu, N.P., Banh, T.L., Puta, H.H. (eds.) Advances in Engineering Research and Application: Proceedings of the International Conference, ICERA 2018, pp. 91–99. Springer International Publishing, Cham (2019). https://doi.org/10.1007/978-3-030-04792-4_14
6. Pi, V.N., et al.: Cost optimization study of two-step helical gearboxes with first stage double gear sets. Int. J. Mech. Product. Eng. Res. Dev. **10**, 573–584 (2020)
7. Pi, V.N., et al.: Determining optimum gear ratios of a worm—helical gearbox for minimum acreage of the cross section. In: Advances in Material Sciences and Engineering, pp. 89–96. Springer (2020)
8. Tuan, N.K., et al.: Determining optimal gear ratios of a two-stage helical reducer for getting minimal acreage of cross section. MATEC Web Conf. **213**, 01008 (2018). https://doi.org/10.1051/matecconf/201821301008
9. Quang, N.H., et al.: Optimizing the partial gear ratios of the two-stage worm gearbox for minimizing total gearbox cost. Eastern-European J. Enterprise Technol. **1**(1), 115 (2022)
10. Danh, T.H., et al.: Determining partial gear ratios of a two-stage helical gearbox with first stage double gear sets for minimizing total gearbox cost. In: Nguyen, D.C., Vu, N.P., Long, B.T., Puta, H., Sattler, K.-U. (eds.) Advances in Engineering Research and Application: Proceedings of the International Conference on Engineering Research and Applications, ICERA 2022, pp. 376–388. Springer International Publishing, Cham (2023). https://doi.org/10.1007/978-3-031-22200-9_41
11. Quang, N.H., et al.: Determination of optimum partial gear ratios for three-stage bevel helical gearboxes for cost function. In: Nguyen, D.C., Vu, N.P., Long, B.T., Puta, H., Sattler, K.-U. (eds.) Advances in Engineering Research and Application: Proceedings of the International Conference on Engineering Research and Applications, ICERA 2021, pp. 312–327. Springer International Publishing, Cham (2022). https://doi.org/10.1007/978-3-030-92574-1_33
12. Quang, N.H., et al.: Determining optimum gear ratios for a four-stage helical gearbox for getting minimum gearbox cost. In: Nguyen, D.C., Vu, N.P., Long, B.T., Puta, H., Sattler, K.-U. (eds.) Advances in Engineering Research and Application: Proceedings of the International Conference on Engineering Research and Applications, ICERA 2021, pp. 350–364. Springer International Publishing, Cham (2022). https://doi.org/10.1007/978-3-030-92574-1_36
13. Kudreavtev, V.N.G., I.A.; Glukharev, E.G.: Design and Calculus of Gearboxes. 1971: Mashinostroenie Publishing: Moscow, Russia, 1971. (In Russian)
14. Pi, V.N., et al.: A new study on determination of optimum gear ratios of a two-stage helical gearbox. In: Advances in Material Sciences and Engineering, pp. 107–115. Springer (2020)
15. Tran, H.-D., et al.: Application of the Taguchi method and grey relational analysis for multi-objective optimization of a two-stage bevel helical gearbox. Machines **11**(7), 716 (2023)
16. Danh, B.T., et al.: Determination of optimum gear ratios of two-stage bevel helical gearboxes for getting minimum gearbox volume. In: Nguyen, D.C., Vu, N.P., Long, B.T., Puta, H., Sattler, K.-U. (eds.) ICERA 2021. LNNS, vol. 366, pp. 302–311. Springer, Cham (2022). https://doi.org/10.1007/978-3-030-92574-1_32
17. Tuan, T.K., et al.: Optimization of gear ratios for three-stage bevel helical gearboxes based on gearbox volume function. In: Nguyen, D.C., Vu, N.P., Long, B.T., Puta, H., Sattler, K.-U. (eds.) ICERA 2021. LNNS, vol. 366, pp. 708–720. Springer, Cham (2022). https://doi.org/10.1007/978-3-030-92574-1_73
18. Thao, T.T.P., et al.: Determining optimum gear ratios of mechanical driven systems using three stage bevel helical gearbox and chain drive. In: Sattler, K.-U., Nguyen, D.C., Vu, N.P., Tien Long, B., Puta, H. (eds.) ICERA 2019. LNNS, vol. 104, pp. 249–261. Springer, Cham (2020). https://doi.org/10.1007/978-3-030-37497-6_29

19. Tung, L.A., et al.: A study on determination of optimum gear ratios of a two-stage worm gearbox. In: Sattler, K.-U., Nguyen, D.C., Vu, N.P., Tien Long, B., Puta, H. (eds.) ICERA 2019. LNNS, vol. 104, pp. 76–84. Springer, Cham (2020). https://doi.org/10.1007/978-3-030-37497-6_8
20. Cuong, N.M., et al.: Calculation of optimum gear ratios of two-step worm gearbox. In: Sattler, K.-U., Nguyen, D.C., Vu, N.P., Tien Long, B., Puta, H. (eds.) ICERA 2019. LNNS, vol. 104, pp. 179–188. Springer, Cham (2020). https://doi.org/10.1007/978-3-030-37497-6_21
21. Hong, T.: A study on calculation of optimum gear ratios for three stage bevel helical gearboxes. ARPN J. Eng. Appl. Sci. **14**, 2592–2598 (2019)
22. Tuan, T.K., et al.: Calculating Optimum Gear Ratios for a Four-stage Helical Gearbox for Gearbox Mass Target
23. Le, X.-H., Vu, N.-P.: Multi-objective optimization of a two-stage helical gearbox using taguchi method and grey relational analysis. Appl. Sci. **13**(13), 7601 (2023)
24. Römhild, I., Linke, H.: Gezielte Auslegung Von Zahnradgetrieben mit minimaler Masse auf der Basis neuer Berechnungsverfahren. Konstruktion **44**(7–8), 229–236 (1992)
25. Chat, T., Van Uyen, L.: Design and calculation of Mechanical Transmissions Systems, vol. 1. Educational Republishing House, Hanoi (2007)
26. Jelaska, D.: Gears and Gear Drives. Wiley (2012). https://doi.org/10.1002/9781118392393
27. Buckingham, E.: Analytical mechanics of gears. 1988: Courier Corporation

Multi-objective Optimization of a Two-Stage Helical Gearbox to Increase Gearbox Efficiency and Decrease Gearbox Length

Dinh Van Thanh[1], Bui Thanh Danh[2], Vi Le The Anh[3], Tran Huu Danh[4], Hoang Xuan Tu[5], and Nguyen Manh Cuong[5](✉)

[1] East Asia University of Technology, Ho Chi Minh City, Vietnam
[2] University of Transport and Communications, Hanoi, Vietnam
[3] Nguyen Tat Thanh University, Ho Chi Minh City, Vietnam
[4] Vinh Long University of Technology Education, Vinh Long City, Vietnam
[5] Thai Nguyen University of Technology, Thai Nguyen, Vietnam
nmcuong@tnut.edu.vn

Abstract. The purpose of this study is to examine multi-target optimization of a two-stage helical gearbox in order to identify the optimum critical design factors for reducing gearbox length and increasing gearbox efficiency. The Taguchi approach and grey relation analysis (GRA) were employed in two stages to solve the problem. The single-objective optimization problem was solved first in order to decrease the gap among variable levels, and then the multi-objective optimization problem was performed in order to find the best primary design variables. The first and second stage coefficients of wheel face width (CWFW), permissible contact stresses (ACS), and first stage gear ratio were also computed. The outcomes of the study were used to determine the optimal values for five essential design features of a two-stage helical gearbox.

Keywords: Helical gearbox · Multi-objective optimization · Gear ratio · Gearbox length · Gearbox efficiency

1 Introduction

A mechanical drive system's major component is the gearbox. It is employed to reduce motor speed and boost torque to meet the needs of the working machines. As a result, the optimal design of the gearbox has been, is, and will continue to be a hot topic.

A number of studies have confirmed that finding the correct gear ratio is a critical issue when developing a gearbox. Because the gear ratio is a criterion that has a significant impact on the size, volume, mass, and cost of the gearbox. As a result, numerous research is done to determine the ideal gear ratios.

There have been numerous studies on identifying the best gear ratio. Various types of gearboxes have been studied, including helical gear gearboxes [1–6], bevel gearboxes [7–11], worm gearboxes [3, 12], and planetary gearboxes [17]. Gearboxes with varied gear stages, such as two stages [6, 9, 13, 14], three stages [7, 8, 10], or four stages

D. C. Nguyen et al. (Eds.): ICERA 2023, LNNS 944, pp. 195–211, 2024.
https://doi.org/10.1007/978-3-031-62235-9_20

[15], are also studied. In addition, many different objective functions have been studied in this optimization problem, such as minimum gear mass [16], minimum gearbox length [4, 17, 18], minimum gearbox cross-section [14], reasonable gearbox structure [3, 12], or minimum gearbox expenses [10, 15, 19, 20]. Several studies have recently been published on determining the main design parameters of gearboxes when constructing multi-objective optimization [21, 22]. The sole goal function chosen in the aforementioned studies was either maximal gearbox efficiency and minimal gearbox volume [22] or maximal gearbox efficiency and minimal gearbox mass [21].

According to the previously mentioned research, there have been numerous studies on the optimal design of gearboxes. However, no research has been conducted on multi-objective optimization for a two-stage helical gearbox with the single objective functions of greatest gearbox efficiency and shortest gearbox length.

The goal of this study is to investigate multi-target optimization techniques for a two-stage helical gearbox. In this effort, two single goals were pursued: lowering gear-box length and optimizing gearbox efficiency. In addition, the CWFW for both stages, the ACS for both stages, and the gear ratio for the first stage were also analyzed. Furthermore, the multi-objective optimization issue in gearbox design was addressed in two phases by integrating the Taguchi approach with the GRA. The optimal values for five essential design factors were also offered for creating a two-stage helical gearbox.

2 Optimization Problem

2.1 Gearbox Length Calculation

The length L of a two-stage helical gearbox is determined by (Fig. 1):

$$L = d_{w11}/2 + a_{w1} + a_{w2} + d_{w22}/2 + 2 \cdot k \tag{1}$$

In (1), $k = 8 \div 12$ [23]; d_{w11}, d_{w22} are pitch diameters of the first and second stages which can be calculated by [23]:

$$d_{w11} = 2a_{w1}/(u_1 + 1) \tag{2}$$

$$d_{w22} = 2a_{w2}u_2/(u_2 + 1) \tag{3}$$

where, a_{w1} and a_{w2} are the center distances of the first and the second stages which are found by [23]:

$$a_{w1} = k_a(u_1 + 1)\sqrt[3]{T_{11}k_{H\beta1}/([\sigma_{H1}]^2 u_1 X_{ba1})} \tag{4}$$

$$a_{w2} = k_a(u_2 + 1)\sqrt[3]{T_{12}k_{H\beta2}/([\sigma_{H2}]^2 u_2 X_{ba2})} \tag{5}$$

In the above equations, k_a is the material coefficient; $k_{H\beta1}$ and $k_{H\beta2}$ are the contacting load ratio for pitting resistance of the first and second stages [23]. $[\sigma_{H1}]$ and $[\sigma_{H2}]$ are ACS of the first and second stages (MPa), respectively; u1 and u2 are the gear ratios of the first and second stages. X_{ba1} and X_{ba2} are CWFW of the first and second stages. T_{11} and T_{12} are the torque on the first and second stage's pinion (Nmm):

$$T_{11} = T_{out}/\left(u_g \cdot \eta_{hg}^2 \cdot \eta_b^3\right) \tag{6}$$

$$T_{12} = T_{out}/\left(u_2 \cdot \eta_{hg} \cdot \eta_{be}^2\right) \tag{7}$$

In which, T_{out} is the output torque (N.mm); η_{hg} is the helical gear efficiency ($\eta_{hg} = 0.96 \div 0.98$); η_b is the rolling bearing efficiency ($\eta_h = 0.99 \div 0.995$) [23].

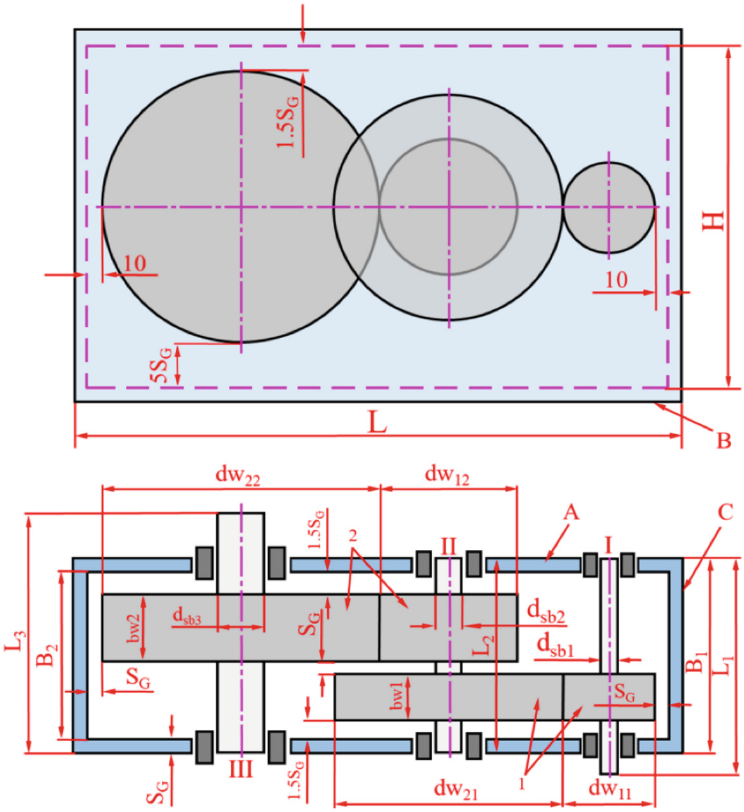

Fig. 1. Calculated schema [21]

2.2 Gearbox Efficiency Calculation

The efficiency of the gearbox can be determined by:

$$\eta_{gb} = \frac{100 \cdot P_l}{P_{in}} \tag{8}$$

where, P_l is the total gearbox power loss [24]:

$$P_l = P_{lg} + P_{lb} + P_{ls} \tag{9}$$

In (9), P_{lg} is total gear power loss, P_{lb} is power loss in bearings, and P_{ls} is power loss in seals. These elements can be found by:

+) The power loss in gears:

$$\mathrm{P}_{lg} = \sum\nolimits_{i=1}^{2} \mathrm{P_{lgi}} \tag{10}$$

P_{lgi} is the gear power losses of i stage which is found by:

$$P_{lgi} = P_{gi} \cdot \left(1 - \eta_{gi}\right) \tag{11}$$

where,η_{gi} is the expected efficiency of i gear's stage [25]:

$$\eta_{gi} = 1 - \left(\frac{1 + 1/\mathrm{u_i}}{\beta_{\mathrm{ai}} + \beta_{\mathrm{ri}}}\right) . \frac{\mathrm{f_i}}{2} . \left(\beta_{\mathrm{ai}}^2 + \beta_{\mathrm{ri}}^2\right) \tag{12}$$

W he r e, $\mathrm{u_i}$ is the gear ratio of i stage; β_{ai} and β_{ri} are the arcs of approach and retreat on the i stage which can be determined by [25]:

$$\beta_{\mathrm{ai}} = \frac{\left(\mathrm{R_{e2i}^2} - \mathrm{R_{02i}^2}\right)^{1/2} - \mathrm{R_{2i}} \cdot \sin\alpha}{\mathrm{R_{01i}}} \tag{13}$$

$$\beta_{\mathrm{ri}} = \frac{\left(\mathrm{R_{e1i}^2} - \mathrm{R_{01i}^2}\right)^{1/2} - \mathrm{R_{1i}} \cdot \sin\alpha}{\mathrm{R_{01i}}} \tag{14}$$

In where, R_{e1i} and R_{e2i} are the pinion and gear's outer radiuses, respectively; R_{1i} and R_{2i} are the pinion and gear's pitch radiuses, respectively; R_{01i} and R_{01i} are the pinion and gear's base-circle radiuses, respectively; and α is the pressure angle.

The friction coefficient f in (12) can be found by [22]:

– When the sliding velocity $v \le 0.424$ (m/s):

$$f = -0.0877 \cdot v + 0.0525 \tag{15}$$

– When the sliding velocity $v > 0.424$ (m/s):

$$f = 0.0028 \cdot v + 0.0104 \tag{16}$$

+) The power loss in bearings can be determined by [24]:

$$P_{lb} = \sum\nolimits_{i=1}^{6} f_b \cdot F_i \cdot v_i \tag{17}$$

In which, f is the friction coefficient of a bearing; as radical ball bearings with angular contact were selected $f_b = 0.0011$ [24]; F is the bearing load (N), v is the peripheral speed, and i is the bearing ordinal number ($i = 1 \div 6$).

+) The overall power loss in seals can be found by [24]:

$$P_{\mathrm{s}} = \sum\nolimits_{i=1}^{2} \mathrm{P_{si}} \tag{18}$$

P_{si} is the power loss in a single seal (w), which is determined by:

$$P_{si} = \left[145 - 1.6 \cdot t_{oil} + 350 \cdot loglog(VG_{40} + 0.8)\right] \cdot d_s^2 \cdot n \cdot 10^{-7} \tag{19}$$

wherein, VG_{40} is the ISO Viscosity Grade number.

2.3 Objective Function and Constrains

2.3.1 Objectives Functions

In this work, the multi-objective optimization problem consists of two single targets:

Minimizing the gearbox length:

$$\min f_2(X) = \mathrm{L} \tag{20}$$

Maximizing the gearbox efficiency:

$$\min f_1(X) = \eta_{gb} \tag{21}$$

In which X is the design variable vector denoting variables. In this study, five key design elements were chosen as factors: u_1, Xba_1, Xba_2, AS_1, and AS_2, resulting in:

$$X = \{u_1, Xba_1, Xba_2, AS_1, AS_2\} \tag{22}$$

2.3.2 Constrains

The following restrictions must be met by the multi-objective function:

$$1 \le u_1 \le 9 \quad \text{and} \quad 1 \le u_2 \le 9 \tag{23}$$

$$0.25 \le k_{be} \le 0.3 \quad \text{and} \quad 0.25 \le X_{ba} \le 0.4 \tag{24}$$

$$350 \le AS_1 \le 420 \quad \text{and} \quad 350 \le AS_2 \le 420 \tag{25}$$

3 Methodology

In this study, five major design characteristics were chosen for investigation. The minimum and maximum values for various variables are shown in Table 1. The Taguchi technique and grey relation analysis were used to tackle the optimization problem. To optimize the number of levels for each variable, the L25 (5^5) design was employed. However, among the variables evaluated, u1 has a fairly broad range (u_1 ranges from 1 to 9 – Table 1). Even with five levels, the difference in the values of these qualities remained significant (in this case, the difference is ((9–1)/4 = 2).

The 2-stage multi-objective optimization problem solution technique [21] was used to help close the gap between variable values scattered throughout a wide range. The first step of this technique deals with a single-objective optimization problem, while the second stage deals with a multi-objective optimization problem to identify the best primary design elements (Figs. 2 and 3).

Table 1. Main design factors and their maximum and minimum constraints

Factor	Notation	Lower limit	Upper limit
Gear ratio of stage 1	u_1	1	9
CWFW of stage 1	X_{ba1}	0.25	0.4
CWFW of stage 2	X_{ba2}	0.25	0.4
ACS of stage 1 (MPa)	AS_1	350	420
ACS of stage 2 (MPa)	AS_2	350	420

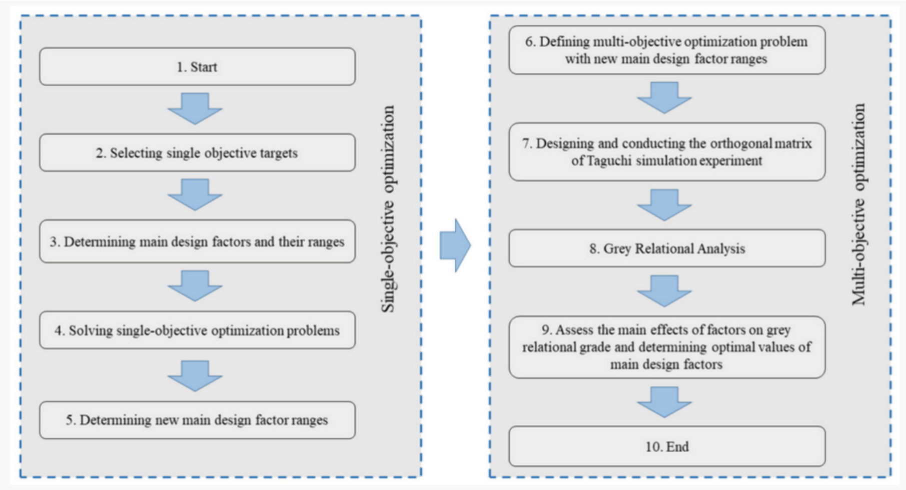

Fig. 2. Method of solving multi-objective problem [22]

4 Single-Objective Optimization

In this investigation, the direct search approach is employed to solve the single-objective optimization issue. A computer program based on Matlab was also developed to tackle two single-objective problems: lowering gearbox length and maximizing gearbox efficiency. Based on the program's findings, Fig. 4 displays the relationship between the optimal gear ratio of the first stage u_1 and the overall gearbox ratio u_t. In addition, new constraints for the variable u1 have been devised, as indicated in Table 2.

5 Multi-objective Optimization

The goal of this work's multi-objective optimization issue for a two-stage helical gearbox is to find the best main design factors with a given total gear-box ratio that satisfies two single-objective functions: reducing gearbox length and maximizing gearbox efficiency. To accomplish this, a computational experiment was carried out. The Taguchi approach

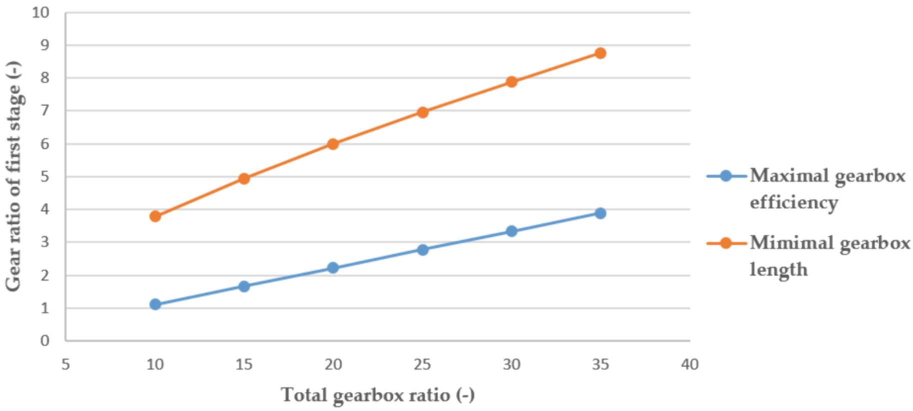

Fig. 3. Optimal first-stage gear ratio versus total gearbox ratio

Table 2. New constraints of u_1

u_t	u_1	
	Lower limit	Upper limit
10	1	3.89
15	1.57	5.04
20	2.12	6.09
25	2.68	7.06
30	3.23	7.98
35	3.79	8.86

with L25 (5^5) design was used to build the experimental design, and the data was analyzed using the Minitab R18 program. Table 3 outlines the survey input parameters and levels chosen for inclusion when $u_t = 15$. Table 4 shows the experimental matrix as well as the results of the gearbox efficiency and gearbox length calculations.

The Taguchi and GRA approaches are used for dealing with multi-objective optimization problems. The following are the major steps in this approach:

+) Calculate the signal-to-noise ratio (S/N) using the following formulas:

The better the S/N, the shorter the gearbox length:

$$SN = -10log_{10}(\frac{1}{n}\sum\nolimits_{i=1}^{m} y_i^2) \tag{26}$$

The higher the S/N, the more efficient the gearbox:

$$SN = -10log_{10}(\frac{1}{n}\sum\nolimits_{i=1}^{m} \frac{1}{y_i^2}) \tag{27}$$

Table 3. Main design factors and their levels for $u_t = 15$

Factor	Notation	Level				
		1	2	3	4	5
Gear ratio of first stage	u_1	1.57	2.4375	3.305	4.1725	5.04
CWFW of stage 1	X_{ba1}	0.25	0.2875	0.325	0.3625	0.4
CWFW of stage 2	X_{ba2}	0.25	0.2875	0.325	0.3625	0.4
ACS of stage 1 (MPa)	AS_1	350	367.5	385	402.5	420
ACS of stage 2 (MPa)	AS_2	350	367.5	385	402.5	420

Table 4. Experimental plan and output results for $u_t = 15$

Exp. No.	Input Factors					η_{gb}	L
	u_1	X_{ba1}	X_{ba2}	AS_1	AS_2	(%)	(m)
1	1.5700	0.2500	0.2500	350.0	350.0	98.001	0.785
2	1.5700	0.2875	0.2875	367.5	367.5	98.032	0.726
3	1.5700	0.3250	0.3250	385.0	385.0	97.969	0.677
4	1.5700	0.3625	0.3625	402.5	402.5	97.905	0.635
5	1.5700	0.4000	0.4000	420.0	420.0	97.915	0.599
6	2.4375	0.2500	0.2875	385.0	402.5	97.796	0.632
7	2.4375	0.2875	0.3250	402.5	420.0	97.771	0.590
8	2.4375	0.3250	0.3625	420.0	350.0	97.812	0.624
9	2.4375	0.3625	0.4000	350.0	367.5	97.759	0.586
10	2.4375	0.4000	0.2500	367.5	385.0	97.728	0.658
11	3.3050	0.2500	0.3250	420.0	367.5	97.586	0.597
12	3.3050	0.2875	0.3625	350.0	385.0	97.618	0.576
13	3.3050	0.3250	0.4000	367.5	402.5	97.575	0.541
14	3.3050	0.3625	0.2500	385.0	420.0	97.539	0.589
15	3.3050	0.4000	0.2875	402.5	350.0	97.596	0.619
16	4.1725	0.2500	0.3625	367.5	420.0	97.371	0.536
17	4.1725	0.2875	0.4000	385.0	350.0	97.391	0.562
18	4.1725	0.3250	0.2500	402.5	367.5	97.391	0.609
19	4.1725	0.3625	0.2875	420.0	385.0	97.364	0.566

(*continued*)

Table 4. (*continued*)

Exp. No.	Input Factors					η_{gb}	L
	u_1	X_{ba1}	X_{ba2}	AS_1	AS_2	(%)	(m)
20	4.1725	0.4000	0.3250	350.0	402.5	97.397	0.546
21	5.0400	0.2500	0.4000	402.5	385.0	97.294	0.528
22	5.0400	0.2875	0.2500	420.0	402.5	97.145	0.568
23	5.0400	0.3250	0.2875	350.0	420.0	97.195	0.548
24	5.0400	0.3625	0.3250	367.5	350.0	97.213	0.572
25	5.0400	0.4000	0.3625	385.0	367.5	97.183	0.536

where y_i is the output result and m is the number of experiment is repeated. Since this is a simulation, $m = 1$ and there are no repetitions expected. The estimated S/N indices for the two output targets are shown in Table 5.

Table 5. S/N values for every experiment when $u_t = 15$

Exp. No.	Input Factors					η_{gb}		L	
	u_1	X_{ba1}	X_{ba2}	AS_1	AS_2	(%)	S/N	(m)	S/N
1	1.5700	0.2500	0.2500	350.0	350.0	98.001	39.8246	0.785	2.10261
2	1.5700	0.2875	0.2875	367.5	367.5	98.032	39.8274	0.726	2.78127
3	1.5700	0.3250	0.3250	385.0	385.0	97.969	39.8218	0.677	3.38823
4	1.5700	0.3625	0.3625	402.5	402.5	97.905	39.8161	0.635	3.94453
5	1.5700	0.4000	0.4000	420.0	420.0	97.915	39.8170	0.599	4.45146
6	2.4375	0.2500	0.2875	385.0	402.5	97.796	39.8064	0.632	3.98566
7	2.4375	0.2875	0.3250	402.5	420.0	97.771	39.8042	0.590	4.58296
8	2.4375	0.3250	0.3625	420.0	350.0	97.812	39.8078	0.624	4.09631
9	2.4375	0.3625	0.4000	350.0	367.5	97.759	39.8031	0.586	4.64205
10	2.4375	0.4000	0.2500	367.5	385.0	97.728	39.8004	0.658	3.63548
11	3.3050	0.2500	0.3250	420.0	367.5	97.586	39.7878	0.597	4.48051
12	3.3050	0.2875	0.3625	350.0	385.0	97.618	39.7906	0.576	4.79155
13	3.3050	0.3250	0.4000	367.5	402.5	97.575	39.7868	0.541	5.33605
14	3.3050	0.3625	0.2500	385.0	420.0	97.539	39.7836	0.589	4.59769
15	3.3050	0.4000	0.2875	402.5	350.0	97.596	39.7886	0.619	4.16619
16	4.1725	0.2500	0.3625	367.5	420.0	97.371	39.7686	0.536	5.41670
17	4.1725	0.2875	0.4000	385.0	350.0	97.391	39.7704	0.562	5.00527

(*continued*)

Table 5. (*continued*)

Exp. No.	Input Factors					η_{gb}		L	
	u_1	X_{ba1}	X_{ba2}	AS_1	AS_2	(%)	S/N	(m)	S/N
18	4.1725	0.3250	0.2500	402.5	367.5	97.391	39.7704	0.609	4.30765
19	4.1725	0.3625	0.2875	420.0	385.0	97.364	39.7680	0.566	4.94367
20	4.1725	0.4000	0.3250	350.0	402.5	97.397	39.7709	0.546	5.25615
21	5.0400	0.2500	0.4000	402.5	385.0	97.294	39.7617	0.528	5.54732
22	5.0400	0.2875	0.2500	420.0	402.5	97.145	39.7484	0.568	4.91303
23	5.0400	0.3250	0.2875	350.0	420.0	97.195	39.7529	0.548	5.22439
24	5.0400	0.3625	0.3250	367.5	350.0	97.213	39.7545	0.572	4.85208
25	5.0400	0.4000	0.3625	385.0	367.5	97.183	39.7518	0.536	5.41670

The data quantities for the two single-objective functions are different. To ensure comparability, the data must be normalized, or converted to a standard scale. The normalization value Z_{ij}, which ranges from 0 to 1, is used to normalize the data. This value is obtained using the following formula:

$$Z_i = \frac{SN_i - min(SN_i, = 1,2,..n)}{max(SN_i, j = 1,2,..n) - min(SN_i, = 1,2,..n)} \tag{28}$$

n is experimental number (n = 25).

+) The grey relational factor can be found by:

$$\mathrm{y_i(k)} = \frac{\Delta_{\min} + \xi.\Delta_{\max}(k)}{\Delta_{\mathrm{i}}(\mathrm{k}) + \xi.\Delta_{\max}(k)} \tag{29}$$

wherein, i = 1,2,…,n; k = 2 is the number of objectives; $\Delta_j(k) = \|Z_0(k) - Z_j(k)\|$ with Z0(k) and Zj(k) symbolize the reference and particular comparison sequences, respectively; Δ_{min} and Δ_{max} are the minimum and maximum values of i(k), respectively; and $\zeta = 0.5$ is the characteristic coefficient.

+) Identifying the degree of grey in a relationship: It is calculated by averaging the grey relational coefficients associated with the output goals:

$$\overline{y_i} = \frac{1}{k}\sum\nolimits_{j=0}^{k} y_{ij}(k) \tag{30}$$

where y_{ij} is the grey relation value of the j^{th} output aim of the i^{th} experiment. For each test, Table 6 displays the projected grey relation number yi as well as the average grey relation value $\overline{y_i}$.

Table 6. Values of $\Delta_i(k)$ and $\overline{y_i}$

Exp. No.	S/N		Zi		Δ_i (k)		Grey relation value yi		$\overline{y_i}$
	η_{gb}	L	η_{gb}	L	η_{gb}	L	η_{gb}	L	
			Reference values						
			1.000	1.000					
1	39.8246	2.1026	0.9652	0.0000	0.035	1.000	0.935	0.333	0.634
2	39.8274	2.7813	1.0000	0.1970	0.000	0.803	1.000	0.384	0.692
3	39.8218	3.3882	0.9293	0.3732	0.071	0.627	0.876	0.444	0.660
4	39.8161	3.9445	0.8574	0.5347	0.143	0.465	0.778	0.518	0.648
5	39.8170	4.4515	0.8686	0.6819	0.131	0.318	0.792	0.611	0.702
6	39.8064	3.9857	0.7348	0.5466	0.265	0.453	0.653	0.524	0.589
7	39.8042	4.5830	0.7067	0.7200	0.293	0.280	0.630	0.641	0.636
8	39.8078	4.0963	0.7528	0.5788	0.247	0.421	0.669	0.543	0.606
9	39.8031	4.6420	0.6932	0.7372	0.307	0.263	0.620	0.655	0.638
10	39.8004	3.6355	0.6583	0.4450	0.342	0.555	0.594	0.474	0.534
11	39.7878	4.4805	0.4983	0.6903	0.502	0.310	0.499	0.618	0.558
12	39.7906	4.7916	0.5344	0.7806	0.466	0.219	0.518	0.695	0.606
13	39.7868	5.3361	0.4859	0.9387	0.514	0.061	0.493	0.891	0.692
14	39.7836	4.5977	0.4453	0.7243	0.555	0.276	0.474	0.645	0.559
15	39.7886	4.1662	0.5096	0.5991	0.490	0.401	0.505	0.555	0.530
16	39.7686	5.4167	0.2557	0.9621	0.744	0.038	0.402	0.930	0.666
17	39.7704	5.0053	0.2783	0.8426	0.722	0.157	0.409	0.761	0.585
18	39.7704	4.3077	0.2783	0.6401	0.722	0.360	0.409	0.581	0.495
19	39.7680	4.9437	0.2477	0.8248	0.752	0.175	0.399	0.740	0.570
20	39.7709	5.2561	0.2850	0.9155	0.715	0.085	0.412	0.855	0.633
21	39.7617	5.5473	0.1686	1.0000	0.831	0.000	0.376	1.000	0.688
22	39.7484	4.9130	0.0000	0.8159	1.000	0.184	0.333	0.731	0.532
23	39.7529	5.2244	0.0566	0.9063	0.943	0.094	0.346	0.842	0.594
24	39.7545	4.8521	0.0770	0.7982	0.923	0.202	0.351	0.712	0.532
25	39.7518	5.4167	0.0430	0.9621	0.957	0.038	0.343	0.930	0.636

A greater average grey relation value is advised to promote harmony among the output elements. As a result, a multi-objective problem's objective function can be reduced to a single-objective optimization problem, yielding the mean grey relation value.

Table 7 displays the results of an ANOVA test run to assess the influence of the main design factors on the average grey relation value $\overline{y_i}$. According to Table 7, Xba2 has the greatest influence on $\overline{y_i}$ (40.69%), followed by u_1 (26.04%), AS_2 (9.71%), Xba1 (4.26%), and AS_1 (4.1%). Table 8 demonstrates the order of the influence of the key design components on $\overline{y_i}$ using ANOVA analysis.

Table 7. Analysis of variance for means

Analysis of Variance for Means							
Source	DF	Seq SS	Adj SS	Adj MS	F	P	C (%)
u1	4	0.021817	0.021817	0.005454	1.71	0.307	26.04
Xba1	4	0.003570	0.003570	0.000893	0.28	0.877	4.26
Xba2	4	0.034089	0.034089	0.008522	2.68	0.181	40.69
AS1	4	0.003432	0.003432	0.000858	0.27	0.884	4.10
AS2	4	0.008136	0.008136	0.002034	0.64	0.662	9.71
Residual Error	4	0.012725	0.012725	0.003181			15.19
Total	24	0.083768					

Model Summary		
S	R-Sq	R-Sq(adj)
0.0564	84.81%	8.85%

+) *Identifying the best major design factors:* In theory, the best main design factors would be those with the highest S/N values. As a result, the effect of the key design aspects on the S/N ratio (Fig. 4) was calculated. Furthermore, the optimal set of multi-objective parameters (corresponding to the red points) may be simply deduced from the Fig. 4 chart. Table 9 displays the proper levels and values for the key design variables of the multi-objective function.

+) *Evaluating the experimental modeling:* Figure 5 displays the Anderson-Darling approach findings, which are used to examine the adequacy of the suggested model. The data points corresponding to the experimental observations (shown in the graph as blue dots) are within the 95% standard deviation zone specified by the top and bottom limits. Furthermore, the p-value of 0.436 is much higher than the significance level of $\alpha = 0.05$. These findings show that the empirical model used in this work is suitable for assessment.

Continuing in the same approach as with ut = 15, using the remaining ut values of 10, 20, 25, 30, and 35. Table 10 displays the ideal values of the five main design parameters for each of the five main design parameters for different ut. This table provided the following results in:

- Xba1 takes the minimum value when ut is less than 20 and the highest value when ut is greater than 20. Furthermore, Xba2 always takes the maximum value. This is because these variables were used to optimize the average grey relation value $\overline{y_i}$.

Table 8. Response table for means

Level	u1	Xba1	Xba2	AS1	AS2
1	0.6671	0.627	0.551	0.6212	0.5774
2	0.6004	0.6102	0.595	0.6231	0.6039
3	0.5892	0.6095	0.6039	0.6059	0.6116
4	0.5899	0.5893	0.6325	0.5993	0.6189
5	0.5965	0.607	0.6607	0.5936	0.6313
Delta	0.0779	0.0376	0.1098	0.0295	0.0539
Rank	2	4	1	5	3
Average of grey analysis value: 0.609					

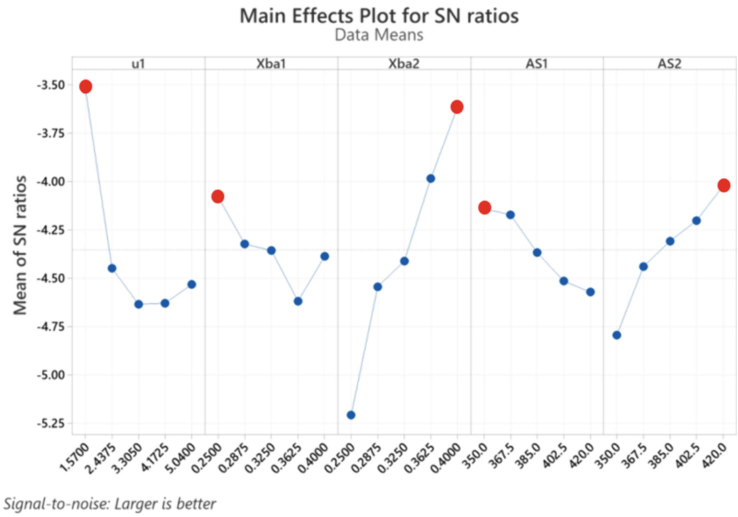

Fig. 4. Main effects plot for S/N ratios

– Ideal AS1 values are the lowest, while ideal AS2 values are the highest. This is due to the fact that these modifications increased the average grey relation value $\overline{y_i}$.
– Figure 6 depicts the relationship between the suitable first stage gear ratio and the overall gearbox ratio. To calculate the optimal values of u1, the following regression formula (with R2 = 1) is presented.

$$u_1 = 0.1114 \cdot u_t - 0.1075 \tag{31}$$

Once u_1 has been determined, the ideal value of u_2 can be computed using $u_2 = u_t/u_1$.

Table 9. Optimum values of key design parameters

No.	Input Parameters	Code	Optimum Level	Optimum Value
1	Gear ratio of first stage	u_1	1	1.57
2	CWFW of stage 1	Xba1	1	0.25
3	CWFW of stage 2	Xba2	5	0.4
4	ACS of stage 1 (MPa)	AS1	1	350
5	ACS of stage 2 (MPa)	AS2	5	420

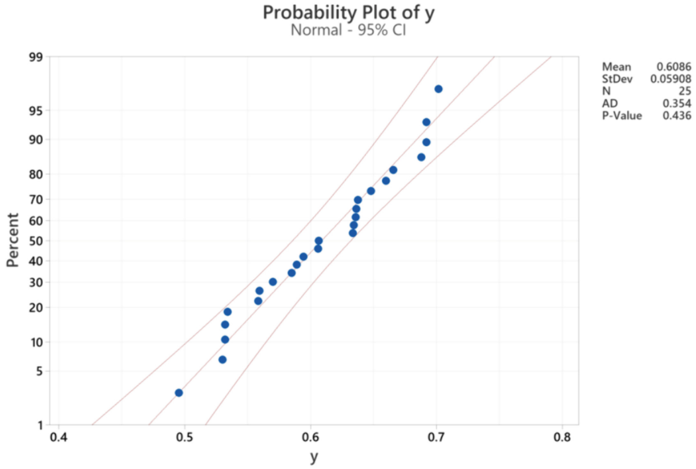

Fig. 5. Probability plot of $\overline{y}$

Table 10. Optimal values of main design parameters

No.	u_t					
	10	15	20	25	30	35
u_1	1	1.57	2.12	2.68	3.23	3.79
X_{ba1}	0.25	0.25	0.25	0.4	0.4	0.4
X_{ba2}	0.4	0.4	0.4	0.4	0.4	0.4
AS_1	350	350	367.5	367.5	367.5	350
AS_2	420	420	420	420	420	420

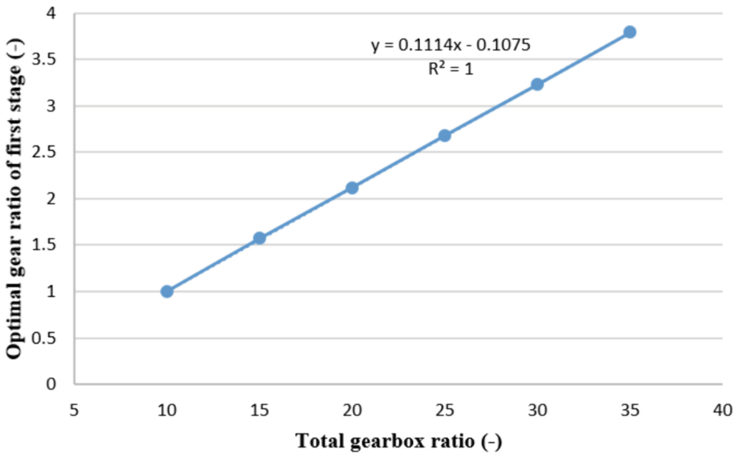

Fig. 6. Optimal first-stage gear ratio versus total gearbox ratio

6 Conclusions

This paper presents the outcomes of a multi-objective optimization study on upgrading a two-stage helical gearbox to minimize gearbox length and enhance gearbox efficiency. This study optimized the gear ratio of the first stage, the efficiency of wheel face width in stages 1 and 2, and the allowable contact stress in stages 1 and 2. To address this issue, a simulation experiment based on the Taguchi L25 type was developed and carried out. The impact of significant design elements on the multi-objective goal was also studied. Additionally, the ideal settings for the essential gearbox parameters have been recommended. For identifying the appropriate first stage u_1 gear ratio, a regression approach Eq. (31) was also proposed.

Acknowledgment. Thai Nguyen University of Technology supported for this research.

References

1. Pi, V.N., et al.: A new study on determination of optimum gear ratios of a two-stage helical gearbox. In: Awang, M., Emamian, S.S., Yusof, F. (eds.) Advances in Material Sciences and Engineering. LNME, pp. 107–115. Springer, Singapore (2020). https://doi.org/10.1007/978-981-13-8297-0_14
2. Tuan, N.K., et al.: A study on determining optimum gear ratios of mechanical driven systems using two-step helical gearbox with first step double gear sets and chain drive. In: Advances in Engineering Research and Application: Proceedings of the International Conference on Engineering Research and Applications, ICERA 2019. Springer (2020). https://doi.org/10.1007/978-3-030-37497-6_9
3. Tung, L.A., et al.: A study on determination of optimum gear ratios of a two-stage worm gearbox. In: Sattler, K.-U., Nguyen, D.C., Vu, N.P., Tien Long, B., Puta, H. (eds.) ICERA 2019. LNNS, vol. 104, pp. 76–84. Springer, Cham (2020). https://doi.org/10.1007/978-3-030-37497-6_8

4. Hung, L.X., et al.: Calculation of optimum gear ratios of mechanical driven systems using two-stage helical gearbox with first stage double gear sets and chain drive. In: Sattler, K.-U., Nguyen, D.C., Vu, N.P., Tien Long, B., Puta, H. (eds.) ICERA 2019. LNNS, vol. 104, pp. 170–178. Springer, Cham (2020). https://doi.org/10.1007/978-3-030-37497-6_20
5. Hung, L.X., et al.: Calculation of optimum gear ratios of mechanical driven systems using two-stage helical gearbox with first stage double gear sets and chain drive. In: Sattler, K.-U., Nguyen, D.C., Vu, N.P., Tien Long, B., Puta, H. (eds.) ICERA 2019. LNNS, vol. 104, pp. 170–178. Springer, Cham (2020). https://doi.org/10.1007/978-3-030-37497-6_20
6. Khai, D.Q., et al. Determination of Optimum Main Design Parameters of a Two-Stage Helical Gearbox for Minimum Gearbox Cross-Section Area. in Advances in Engineering Research and Application: Proceedings of the International Conference on Engineering Research and Applications, ICERA 2022. 2022. Springer
7. Thao, T.T.P., et al.: Determining optimum gear ratios of mechanical driven systems using three stage bevel helical gearbox and chain drive. In: Sattler, K.-U., Nguyen, D.C., Vu, N.P., Tien Long, B., Puta, H. (eds.) ICERA 2019. LNNS, vol. 104, pp. 249–261. Springer, Cham (2020). https://doi.org/10.1007/978-3-030-37497-6_29
8. Pi, V.N., et al. Determination of optimum gear ratios of a three stage bevel helical gearbox. in IOP Conference Series: Materials Science and Engineering. 2019. IOP Publishing
9. Danh, B.T., et al.: Determination of optimum gear ratios of two-stage bevel helical gearboxes for getting minimum gearbox volume. In: Nguyen, D.C., Vu, N.P., Long, B.T., Puta, H., Sattler, K.-U. (eds.) ICERA 2021. LNNS, vol. 366, pp. 302–311. Springer, Cham (2022). https://doi.org/10.1007/978-3-030-92574-1_32
10. Quang, N.H., et al.: Determination of optimum partial gear ratios for three-stage bevel helical gearboxes for cost function. In: Nguyen, D.C., Vu, N.P., Long, B.T., Puta, H., Sattler, K.-U. (eds.) ICERA 2021. LNNS, vol. 366, pp. 312–327. Springer, Cham (2022). https://doi.org/10.1007/978-3-030-92574-1_33
11. Pi, V.N., Tuan, N.K.: Determining optimum partial transmission ratios of mechanical driven systems using a chain drive and a two-step bevel helical gearbox. Int. J. Mech. Eng. Robot. Res. **8**(5), 708–712 (2019)
12. Cuong, N.M., et al.: Calculation of optimum gear ratios of two-step worm gearbox. In: Sattler, K.-U., Nguyen, D.C., Vu, N.P., Long, B.T., Puta, H. (eds.) Advances in Engineering Research and Application: Proceedings of the International Conference on Engineering Research and Applications, ICERA 2019, pp. 179–188. Springer International Publishing, Cham (2020). https://doi.org/10.1007/978-3-030-37497-6_21
13. Pi, V.N., et al.: Determination of optimum gear ratios of a two-stage helical gearbox with second stage double gear sets. IOP Conf. Ser.: Mater. Sci. Eng. **635**(1), 012012 (2019). https://doi.org/10.1088/1757-899X/635/1/012012
14. Tuan, N.K., et al.: Determining optimal gear ratios of a two-stage helical reducer for getting minimal acreage of cross section. MATEC Web Conf. **213**, 01008 (2018)
15. Quang, N.H., et al.: Determining optimum gear ratios for a four-stage helical gearbox for getting minimum gearbox cost. In: Nguyen, D.C., Ngoc Pi, V., Long, B.T., Puta, H., Sattler, K.-U. (eds.) ICERA 2021. LNNS, vol. 366, pp. 350–364. Springer, Cham (2022). https://doi.org/10.1007/978-3-030-92574-1_36
16. Pi, V.N., Tuan, N.K.: Optimum determination of partial transmission ratios of three-step helical gearboxes for getting minimum cross section dimension. J. Env Sci. Eng. A **5**(11), 570–573 (2016). https://doi.org/10.17265/2162-5298/2016.11.004
17. Van Cuong, N., K. Le Hong, T. Tran: Splitting total gear ratio of two-stage helical reducer with first-stage double gearsets for minimal reducer length. Int. J. Mech. Prod. Eng. Res. Dev. (IJMPERD) **9**(6), 595–608 (2019)
18. Pi, V.N.: Optimum determination of partial transmission ratios of three-step helical gearboxes. WSEAS Trans. Appl. Theor. Mech. **3**(2), 43–52 (2008)

19. Quang, N.H., et al.: Determining optimum gear ratios for a four-stage helical gearbox for getting minimum gearbox cost. In: Nguyen, D.C., Vu, N.P., Long, B.T., Puta, H., Sattler, K.-U. (eds.) Advances in Engineering Research and Application: Proceedings of the International Conference on Engineering Research and Applications, ICERA 2021, pp. 350–364. Springer International Publishing, Cham (2022). https://doi.org/10.1007/978-3-030-92574-1_36
20. Danh, T.H., et al.: Determining partial gear ratios of a two-stage helical gearbox with first stage double gear sets for minimizing total gearbox cost. In: Nguyen, D.C., Ngoc Pi, V., Long, B.T., Puta, H., Sattler, K.-U. (eds.) Advances in Engineering Research and Application: Proceedings of the International Conference on Engineering Research and Applications, ICERA 2022, pp. 376–388. Springer International Publishing, Cham (2023). https://doi.org/10.1007/978-3-031-22200-9_41
21. Le, X.-H., Vu, N.-P.: Multi-objective optimization of a two-stage helical gearbox using taguchi method and grey relational analysis. Appl. Sci. **13**(13), 7601 (2023)
22. Tran, H.-D., et al.: Application of the taguchi method and grey relational analysis for multi-objective optimization of a two-stage bevel helical gearbox. Machines **11**(7), 716 (2023)
23. Chat, T., Van Uyen, L.: Design and calculation of Mechanical Transmissions Systems, vol. 1. Educational Republishing House, Hanoi (2007)
24. Jelaska, D.: Gears and Gear Drives. Wiley (2012). https://doi.org/10.1002/9781118392393
25. Buckingham, E.: Analytical mechanics of gears. Courier Corporation (1988)

Multi-objective Optimization of a Two-Stage Helical Gearbox with Second Stage Double Gear Sets to Decrease Gearbox Height and Increase Gearbox Efficiency

Dinh Van Thanh[1], Tran Huu Danh[2], Nguyen Van Binh[3], Bui Thanh Danh[4], Nguyen Anh Tuan[5], Hoang Xuan Tu[6], and Bui Thanh Hien[6](✉)

[1] East Asia University of Technology, Ho Chi Minh City, Vietnam
[2] Vinh Long University of Technology Education, Vinh Long City, Vietnam
[3] Nguyen Tat Thanh University, Ho Chi Minh City, Vietnam
[4] University of Transport and Communications, Hanoi, Vietnam
[5] University of Economics – Technology for Industries, Hanoi, Vietnam
[6] Thai Nguyen University of Technology, Thai Nguyen, Vietnam
buithanhhienkc@tnut.edu.vn

Abstract. The aim of this study is to investigate multi-target optimization of a two-stage helical gearbox with second stage double gear sets (SSDGS) in order to discover the optimal major design factors for reducing gearbox height and increasing gearbox efficiency. The Taguchi approach and grey relation analysis (GRA) were employed to solve the problem in two steps. The single-objective optimization problem was handled first in order to decrease the difference among variable levels, and then the multi-objective optimization problem was dealt with in order to identify the best primary design variables. The first and second stage coefficients of wheel face width (CWFW), permissible contact stresses (ACS), and first stage gear ratio were also computed. The outcomes of the study were used to determine the optimal values for five essential characteristics of a two-stage helical gearbox with SSDGS.

Keywords: Helical gearbox · Double gear sets · Multi-objective optimization · Gear ratio · Gearbox height · Gearbox efficiency

1 Introduction

In actuality, several types of drive systems exist, such as mechanical drive, electric drive, pneumatic drive, hydraulic drive, and so on. The mechanical drive system is the most commonly utilized due of its simple form, dependable functioning, and inexpensive cost. A mechanical drive system is made up of a motor, a gearbox, and two couplings, or a coupling and a V-belt or chain drive. The most significant component is the gearbox, which functions to lower the speed and torque from the shaft of the motor to the operating shaft. As a result, many academics are pursuing the optimal design of the mechanical drive system and the most suitable design of the gearbox.

D. C. Nguyen et al. (Eds.): ICERA 2023, LNNS 944, pp. 212–228, 2024.
https://doi.org/10.1007/978-3-031-62235-9_21

Until now, numerous scientific investigations have been conducted concerning optimal design of helical gearboxes. [1] presents a study on optimizing partial transmission ratios in mechanical drive systems using a chain and a two-stage helical reducer. [2] analyzes eleven input parameters' impacts on second and third stage ratios to minimize the cost of a three-stage helical gearbox. [3] designed an optimized 3-stage gearbox for industrial applications like conveyer belts, extruders, cranes, and crushing machines, emphasizing safety, durability, and efficiency improvement. Using a simulation experiment, [4] focuses on minimizing the volume of a two-stage helical gearbox. Within a similar field of interest, [5] puts forth models that determines optimal partial ratios in mechanical drive systems using a V-belt drive and a two-stage helical reducer. [6] proposes the best parameter values to identify optimal main design parameters for a two-stage helical gearbox to minimize its mass. [7] introduces a regression formula to calculate the optimal partial ratio for a two-stage helical gearbox with second-stage double gear-sets. Furthermore, [8] explores optimal gear ratios for a four-speed helical gearbox using cost optimization. [9] recommended ideal gear ratios for mechanically driven systems using a two-stage helical gearbox with double gear sets in the first stage and a chain drive to achieve the shortest system length. [10] discusses optimal gear ratios for system using a two-stage helical gearbox with double gear sets in the first step. After solving an optimization problem, the study confirmed models that provide highly accurate optimum ratios.

The goal of this study is to explore multi-target optimization learning for a two-stage helical gearbox using SSDGS. This investigation had two distinct goals: lowering gearbox height and increasing gearbox efficiency. Furthermore, the CWFW for both stages, the ACS for both stages, and the gear ratio for the first stage were also analyzed. Furthermore, the multi-objective optimization issue in gearbox design was tackled in two phases by integrating the Taguchi approach with the GRA. The optimal values for five essential design factors were also offered for creating a two-stage helical gearbox with SSDGS.

2 Optimization Problem

2.1 Gearbox Height Determination

The gearbox height is determined by (Fig. 1):

$$H = \max(d_{w21}, d_{w22}) + 8.5 \cdot S_G \tag{1}$$

In (1), d_{w21}, d_{w22} are the pitch diameters of the first and second stage gears, as computed by [11]:

$$d_{w21} = 2 \cdot a_{w1} \cdot u_1/(u_1 + 1) \tag{2}$$

$$d_{w22} = 2 \cdot a_{w2} \cdot u_2/(u_2 + 1) \tag{3}$$

where, a_{w1} and a_{w2} are the center distances of stages 1 and 2 which are found by [11]:

$$a_{w1} = k_a(u_1 + 1)\sqrt[3]{T_{11}k_{H\beta 1}/([\sigma_{H1}]^2 u_1 X_{ba1})} \tag{4}$$

$$a_{w2} = k_a(u_2 + 1)\sqrt[3]{T_{12}k_{H\beta 2}/([\sigma_{H2}]^2 u_2 X_{ba2})} \tag{5}$$

In (4) and (5), k_a is the material coefficient; $k_{H\beta 1}$ and $k_{H\beta 2}$ are the contacting load ratio for pitting resistance of the first and second stages [11]; $[\sigma_{H1}]$ and $[\sigma_{H2}]$ are ACS of the first and second stages (MPa), respectively; u_1 and u_2 are the gear ratios of stages 1 and 2. X_{ba1} and X_{ba2} are CWFW of stages 1 and 2. T_{11} and T_{12} are the torque on the first shaft of stage 1 and 2 (Nmm):

$$T_{11} = T_{out}/\left(u_g \cdot \eta_{hg}^2 \cdot \eta_b^3\right) \tag{6}$$

$$T_{12} = T_{out}/\left(2 \cdot u_2 \cdot \eta_{hg} \cdot \eta_{be}^2\right) \tag{7}$$

In which, T_{out} is the output torque (N.mm); η_{hg} is the helical gear efficiency ($\eta_{hg} = 0.96 \div 0.98$); η_b is the rolling bearing efficiency ($\eta_h = 0.99 \div 0.995$) [11].

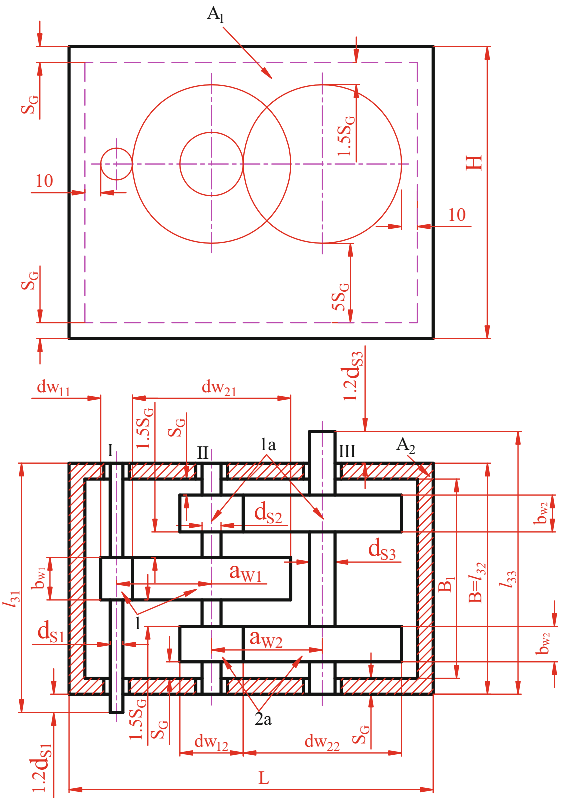

Fig. 1. Calculated schema

2.2 Gearbox Efficiency Determination

The efficiency of the gearbox can be found by:

$$\eta_{gb} = \frac{100 \cdot P_l}{P_{in}} \tag{8}$$

where, P_l is the overall gearbox power loss [12]:

$$P_l = P_{lg} + P_{lb} + P_{ls} \tag{9}$$

In which, P_{lg} is power loss in gears, P_{lb} is the power loss in bearings; P_{ls} is the power loss in seals. These elements can be determined by:

+) The power loss in gears:

$$\mathrm{P}_{lg} = \sum\nolimits_{i=1}^{2} \mathrm{P_{lgi}} \tag{10}$$

P_{lgi} is the gear power loss of i stage which is found by:

$$P_{lgi} = P_{gi} \cdot \left(1 - \eta_{gi}\right) \tag{11}$$

In which, η_{gi} is the anticipated efficiency of the gearbox's i stage which can be determined by [13]:

$$\eta_{gi} = 1 - \left(\frac{1 + 1/\mathrm{u_i}}{\beta_{\mathrm{ai}} + \beta_{\mathrm{ri}}}\right) \cdot \frac{\mathrm{f_i}}{2} \cdot \left(\beta_{\mathrm{ai}}^2 + \beta_{\mathrm{ri}}^2\right) \tag{12}$$

wherein, $\mathrm{u_i}$ is the i stage's gear ratio; f is the friction coefficient; β_{ai} and β_{ri} are the arcs of approach and retreat on the i stage which can be found by [13]:

$$\beta_{\mathrm{ai}} = \frac{\left(\mathrm{R_{e2i}^2} - \mathrm{R_{02i}^2}\right)^{1/2} - \mathrm{R_{2i}} \cdot \mathrm{sin}\alpha}{\mathrm{R_{01i}}} \tag{13}$$

$$\beta_{\mathrm{ri}} = \frac{\left(\mathrm{R_{e1i}^2} - \mathrm{R_{01i}^2}\right)^{1/2} - \mathrm{R_{1i}} \cdot \mathrm{sin}\alpha}{\mathrm{R_{01i}}} \tag{14}$$

In which, R_{e1i} and R_{e2i} are the outer radiuses of the pinion and gear; R_{1i} and R_{2i} are the pitch radiuses of the pinion and gear; R_{01i} and R_{01i} are the base-circle radiuses of the pinion and gear; α is the pressure angle.

The friction coefficient f in (12) can be found by [14]:

– If the sliding velocity $v \le 0.424$ (m/s):

$$f = -0.0877 \cdot v + 0.0525 \tag{15}$$

– If the sliding velocity $v > 0.424$ (m/s):

$$f = 0.0028 \cdot v + 0.0104 \tag{16}$$

+) The power loss in bearings can be determined by [12]:

$$P_{lb} = \sum\nolimits_{i=1}^{6} f_b \cdot F_i \cdot v_i \tag{17}$$

In where, $f_b = 0.0011$ is the bearing friction coefficient (for radical ball bearings with angular contact) [12]; F is the bearing load (N); v is the peripheral speed; i is bearing ordinal number (i = 1 ÷ 6).

+) The total power losses in seals can be found by [12]:

$$P_s = \sum\nolimits_{i=1}^{2} \mathrm{P_{si}} \tag{18}$$

P_{si} is the power loss for a single seal (w) which is determined by:

$$P_{si} = \left[145 - 1.6 \cdot t_{oil} + 350 \cdot loglog(VG_{40} + 0.8)\right] \cdot d_s^2 \cdot n \cdot 10^{-7} \tag{19}$$

In (19), VG_{40} is the ISO Viscosity Grade number.

2.3 Objective Function and Constrains

2.3.1 Objectives Functions

In this work, the multi-target optimization problem has two following objectives:

Minimizing the gearbox height:

$$\min f_2(X) = \mathrm{H} \tag{20}$$

Maximizing the gearbox efficiency:

$$\min f_1(X) = \eta_{gb} \tag{21}$$

where X is the design variable vector. In this study, five primary design characteristics including u_1, Xba_1, Xba_2, AS_1, and AS_2 were chosen as variables leading in:

$$X = \{u_1, Xba_1, Xba_2, AS_1, AS_2\} \tag{22}$$

2.3.2 Constrains

The following constraints apply to the multi-objective function:

$$1 \le u_1 \le 9 \quad \text{and} \quad 1 \le u_2 \le 9 \tag{23}$$

$$0.25 \le k_{be} \le 0.3 \quad \text{and} \quad 0.25 \le X_{ba} \le 0.4 \tag{24}$$

$$350 \le AS_1 \le 420 \quad \text{and} \quad 350 \le AS_2 \le 420 \tag{25}$$

3 Methodology

In this study, five main design characteristics were chosen for analysis. The lowest and maximum values for various variables are shown in Table 1. The Taguchi approach and grey relation analysis were used to tackle the op-timization problem. To optimize the number of levels for each variable, the L25 (5^5) design was employed. However, among the variables evaluated, u_1 has a rather broad range (u_1 runs from 1 to 9 – Table 1). Even with five levels, the difference in the values of these qualities remained significant (in this case, the difference is ((9–1)/4 = 2).

The 2-stage multi-objective optimization problem solution approach [15] was used to help close the distance between variable values scattered throughout a large range. The first step of this approach deals with a single-objective optimization issue, while the second stage deals with a multi-objective optimization problem to identify the best key design elements (Figs. 2 and 3).

Table 1. Main design factors and their maximum and lowest values

Factor	Notation	Lower limit	Upper limit
Gear ratio of stage 1	u_1	1	9
CWFW of stage 1	X_{ba1}	0.25	0.3
CWFW of stage 2	X_{ba2}	0.25	0.4
ACS of stage 1 (MPa)	AS_1	350	420
ACS of stage 2 (MPa)	AS_2	350	420

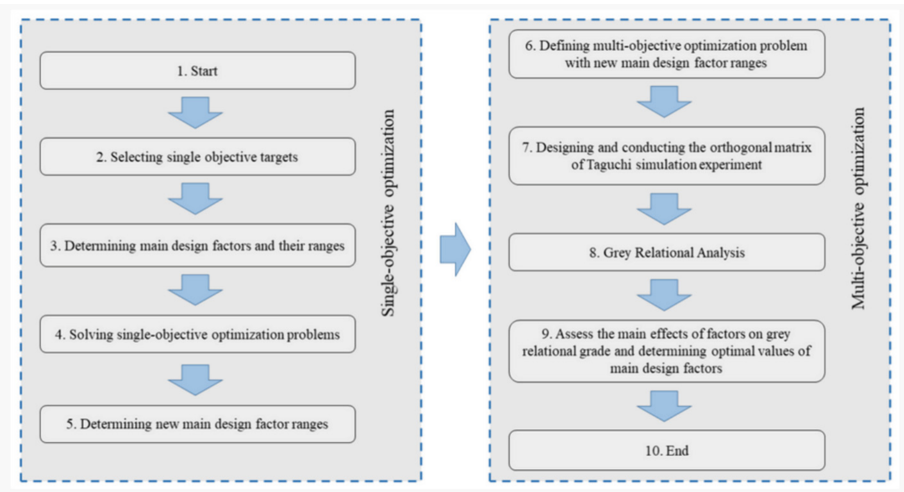

Fig. 2. Method to solve multi-objective problem [14]

4 Single-objective Optimization

In this study, the direct search approach is employed to solve the single-objective optimization problem. A computer program based on Matlab was also developed for solving two single-objective problems: reducing gearbox height and enhancing gearbox efficiency. Based on the program's findings, Fig. 4 displays the link between the ideal gear ratio of the first stage u_1 and the total gearbox ratio u_t. In addition, additional constraints for the variable u_1 have been devised, as indicated in Table 2.

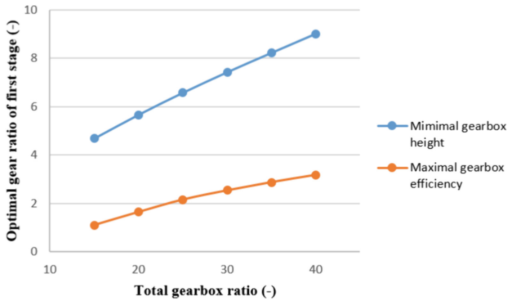

Fig. 3. Optimal gear ratio of stage 1 versus total gearbox ratio

Table 2. New constraints of u_1

u_t	u_1	
	Lower limit	Upper limit
10	1.09	4.68
15	1.63	5.66
20	2.14	6.57
25	2.52	7.42
30	2.86	8.22
35	3.16	9.00

5 Multi-objective Optimization

The goal of this work's multi-objective optimization problem for a two-stage helical gearbox with SSDGS is to find the best primary design variables for a given total gearbox ratio while meeting two single-objective functions: minimizing gearbox height and maximizing gearbox efficiency. To accomplish this, a computer experiment was carried out. The Taguchi technique with L25 (5^5) design was implemented to build the experimental design, and the data was analyzed using the Minitab R18 application. Table 3 outlines the survey input elements and levels that were chosen for inclusion when $u_t = 20$. Table 4 details the experimental strategy as well as the gearbox efficiency and gearbox height estimations.

Table 3. Main design factors and their levels for $u_t = 20$

Factor	Notation	Level				
		1	2	3	4	5
Gear ratio of stage 1	u_1	1.63	2.6375	3.645	4.6525	5.66
CWFW of stage 1	X_{ba1}	0.25	0.2675	0.275	0.2875	0.3
CWFW of stage 2	X_{ba2}	0.25	0.2875	0.325	0.3625	0.4
ACS of stage 1 (MPa)	AS_1	350	368	386	404	420
ACS of stage 2 (MPa)	AS_2	350	368	386	404	420

Table 4. Experimental plan and output results for $u_t = 20$

Exp. No	Input Factors					H	η_{gb}
	u_1	X_{ba1}	X_{ba2}	AS_1	AS_2	(cm)	(%)
1	1.6300	0.2500	0.2500	350	350	44.733	95.572
2	1.6300	0.2625	0.2875	368	368	41.520	95.540
3	1.6300	0.2750	0.3250	386	386	38.815	95.534
4	1.6300	0.2875	0.3625	404	404	36.497	95.500
5	1.6300	0.3000	0.4000	420	420	34.584	95.498
6	2.6375	0.2500	0.2875	386	404	33.831	95.224
7	2.6375	0.2625	0.3250	404	420	31.837	95.217
8	2.6375	0.2750	0.3625	420	350	34.400	95.275
9	2.6375	0.2875	0.4000	350	368	32.390	95.235
10	2.6375	0.3000	0.2500	368	386	36.299	95.251
11	3.6450	0.2500	0.3250	420	368	31.279	95.016
12	3.6450	0.2625	0.3625	350	386	29.417	95.015
13	3.6450	0.2750	0.4000	368	404	27.796	94.997
14	3.6450	0.2875	0.2500	386	420	31.260	95.035
15	3.6450	0.3000	0.2875	404	350	33.460	95.041
16	4.6525	0.2500	0.3625	368	420	26.418	94.756
17	4.6525	0.2625	0.4000	386	350	28.158	94.794
18	4.6525	0.2750	0.2500	404	368	31.458	94.838

(*continued*)

Table 4. (*continued*)

Exp. No	Input Factors					H	η_{gb}
	u_1	X_{ba1}	X_{ba2}	AS_1	AS_2	(cm)	(%)
19	4.6525	0.2875	0.2875	420	386	29.308	94.839
20	4.6525	0.3000	0.3250	350	404	27.503	94.785
21	5.6600	0.2500	0.4000	404	386	28.071	94.578
22	5.6600	0.2625	0.2500	420	404	28.053	94.614
23	5.6600	0.2750	0.2875	350	420	29.729	94.585
24	5.6600	0.2875	0.3250	368	350	28.478	94.621
25	5.6600	0.3000	0.3625	386	368	27.327	94.607

The Taguchi and GRA approaches serve as tools for dealing with multi-objective optimization problems. The following are the major steps in this approach:

+) Using the following equations, calculate the signal-to-noise ratio (S/N):

The higher the S/N, the lower the gearbox height:

$$SN = -10log_{10}(\frac{1}{n}\sum\nolimits_{i=1}^{m} y_i^2) \tag{26}$$

The higher the S/N, the more efficient the gearbox:

$$SN = -10log_{10}(\frac{1}{n}\sum\nolimits_{i=1}^{m} \frac{1}{y_i^2}) \tag{27}$$

In which y_i is the output result and m is the number of trial repeats. Because this is a simulation, m = 1 and there are no repetitions necessary. The estimated S/N indices for the two output targets are shown in Table 5.

Table 5. S/N values for each experiment when $u_t = 20$

No.	Input Factors					H		η_{gb}	
	u_1	X_{ba1}	X_{ba2}	AS_1	AS_2	(cm)	S/N	(%)	S/N
1	1.6300	0.2500	0.2500	350	350	44.733	−33.0126	95.572	39.6066
2	1.6300	0.2625	0.2875	368	368	41.520	−32.3651	95.540	39.6037
3	1.6300	0.2750	0.3250	386	386	38.815	−31.7800	95.534	39.6032
4	1.6300	0.2875	0.3625	404	404	36.497	−31.2451	95.500	39.6001
5	1.6300	0.3000	0.4000	420	420	34.584	−30.7775	95.498	39.5999
6	2.6375	0.2500	0.2875	386	404	33.831	−30.5863	95.224	39.5749

(*continued*)

Table 5. (*continued*)

No.	Input Factors					H		η_{gb}	
	u_1	X_{ba1}	X_{ba2}	AS_1	AS_2	(cm)	S/N	(%)	S/N
7	2.6375	0.2625	0.3250	404	420	31.837	−30.0586	95.217	39.5743
8	2.6375	0.2750	0.3625	420	350	34.400	−30.7312	95.275	39.5796
9	2.6375	0.2875	0.4000	350	368	32.390	−30.2082	95.235	39.5759
10	2.6375	0.3000	0.2500	368	386	36.299	−31.1979	95.251	39.5774
11	3.6450	0.2500	0.3250	420	368	31.279	−29.9051	95.016	39.5559
12	3.6450	0.2625	0.3625	350	386	29.417	−29.3720	95.015	39.5558
13	3.6450	0.2750	0.4000	368	404	27.796	−28.8796	94.997	39.5542
14	3.6450	0.2875	0.2500	386	420	31.260	−29.8998	95.035	39.5577
15	3.6450	0.3000	0.2875	404	350	33.460	−30.4905	95.041	39.5582
16	4.6525	0.2500	0.3625	368	420	26.418	−28.4380	94.756	39.5321
17	4.6525	0.2625	0.4000	386	350	28.158	−28.9920	94.794	39.5356
18	4.6525	0.2750	0.2500	404	368	31.458	−29.9546	94.838	39.5396
19	4.6525	0.2875	0.2875	420	386	29.308	−29.3397	94.839	39.5397
20	4.6525	0.3000	0.3250	350	404	27.503	−28.7876	94.785	39.5348
21	5.6600	0.2500	0.4000	404	386	28.071	−28.9652	94.578	39.5158
22	5.6600	0.2625	0.2500	420	404	28.053	−28.9596	94.614	39.5191
23	5.6600	0.2750	0.2875	350	420	29.729	−29.4636	94.585	39.5164
24	5.6600	0.2875	0.3250	368	350	28.478	−29.0902	94.621	39.5198
25	5.6600	0.3000	0.3625	386	368	27.327	−28.7318	94.607	39.5185

The data quantities for the two single-objective functions are different. To ensure comparability, the data must be normalized, or brought to a standard scale. The normalization value Z_{ij}, which ranges from 0 to 1, is used to normalize the data. This value is calculated using the following formula:

$$Z_i = \frac{SN_i - min(SN_i, = 1,2, ..n)}{max(SN_i, j = 1,2, ..n) - min(SN_i, = 1,2, ..n)} \tag{28}$$

where, n = 25 is the experimental number.

+) The grey relational factor can be found by:

$$y_i(k) = \frac{\Delta_{min} + \xi.\Delta_{max}(k)}{\Delta_i(k) + \xi.\Delta_{max}(k)} \tag{29}$$

where, i = 1,2,…,n; k = 2 is the objective number; $\Delta_j(k) = \|Z_0(k) - Z_j(k)\|$ with Z0(k) and Zj(k) are the reference and particular comparison sequences; Δ_{min} and Δ_{max} are the minimal and maximal values of i(k); $\zeta = 0.5$ is the characteristic coefficient.

+) Determining the grey relationship degree: It can be found by taking the mean of the grey relational coefficients associated with the output objectives:

$$\overline{y_i} = \frac{1}{k}\sum\nolimits_{j=0}^{k} y_{ij}(k) \tag{30}$$

where y_{ij} is the grey relation value of the i^{th} experiment's j^{th} output target. For each test, Table 6 displays the estimated grey relation number y_i as well as the average grey relation value $\overline{y_i}$.

Table 6. Values of Δ_i(k) and $\overline{y_i}$

Exp. No.	S/N		Z_i		Δ_i (k)		Grey relation value yi		$\overline{y_i}$
	H	η_{gb}	H	η_{gb}					
			Reference values		H	η_{gb}	H	η_{gb}	
			1.000	1.000					
1	−33.0126	39.6066	0.0000	1.0000	1.000	0.000	0.333	1.000	0.667
2	−32.3651	39.6037	0.1415	0.9680	0.858	0.032	0.368	0.940	0.654
3	−31.7800	39.6032	0.2694	0.9620	0.731	0.038	0.406	0.929	0.668
4	−31.2451	39.6001	0.3864	0.9279	0.614	0.072	0.449	0.874	0.661
5	−30.7775	39.5999	0.4886	0.9259	0.511	0.074	0.494	0.871	0.683
6	−30.5863	39.5749	0.5304	0.6511	0.470	0.349	0.516	0.589	0.552
7	−30.0586	39.5743	0.6457	0.6441	0.354	0.356	0.585	0.584	0.585
8	−30.7312	39.5796	0.4987	0.7023	0.501	0.298	0.499	0.627	0.563
9	−30.2082	39.5759	0.6130	0.6621	0.387	0.338	0.564	0.597	0.580
10	−31.1979	39.5774	0.3967	0.6782	0.603	0.322	0.453	0.608	0.531
11	−29.9051	39.5559	0.6793	0.4419	0.321	0.558	0.609	0.473	0.541
12	−29.3720	39.5558	0.7958	0.4409	0.204	0.559	0.710	0.472	0.591
13	−28.8796	39.5542	0.9035	0.4228	0.097	0.577	0.838	0.464	0.651
14	−29.8998	39.5577	0.6805	0.4611	0.320	0.539	0.610	0.481	0.546
15	−30.4905	39.5582	0.5513	0.4671	0.449	0.533	0.527	0.484	0.506
16	−28.4380	39.5321	1.0000	0.1798	0.000	0.820	1.000	0.379	0.689
17	−28.9920	39.5356	0.8789	0.2182	0.121	0.782	0.805	0.390	0.598
18	−29.9546	39.5396	0.6685	0.2626	0.332	0.737	0.601	0.404	0.503
19	−29.3397	39.5397	0.8029	0.2636	0.197	0.736	0.717	0.404	0.561
20	−28.7876	39.5348	0.9236	0.2091	0.076	0.791	0.867	0.387	0.627
21	−28.9652	39.5158	0.8848	0.0000	0.115	1.000	0.813	0.333	0.573

(*continued*)

Table 6. (*continued*)

Exp. No.	S/N		Z_i		Δ_i (k)		Grey relation value yi		$\overline{y_i}$
	H	η_{gb}	H	η_{gb}					
			Reference values		H	η_{gb}	H	η_{gb}	
			1.000	1.000					
22	−28.9596	39.5191	0.8860	0.0364	0.114	0.964	0.814	0.342	0.578
23	−29.4636	39.5164	0.7758	0.0071	0.224	0.993	0.690	0.335	0.513
24	−29.0902	39.5198	0.8574	0.0435	0.143	0.957	0.778	0.343	0.561
25	−28.7318	39.5185	0.9358	0.0293	0.064	0.971	0.886	0.340	0.613

A greater average grey relation value is advised to promote harmony among the output factors. As a consequence, a multi-objective problem's objective function may be converted to a single-objective optimization problem, generating the mean grey relation value.

Table 7 displays the results of an ANOVA test run to assess the effect of the main design variables on the average grey relation value $\overline{y_i}$. According to Table 7, u_1 has the greatest influence on $\overline{y_i}$. . (49.08%), followed by X_{ba2} (23.01%), AS_1 (9.00%), AS_2 (6.57%), and X_{ba1} (3.18%). Table 8 demonstrates the order of the effect of the key design components on $\overline{y_i}$. Using ANOVA analysis.

Table 7. Analysis of variance for means

Analysis of Variance for Means							
Source	DF	Seq SS	Adj SS	Adj MS	F	P	C (%)
u1	4	0.038411	0.038411	0.009603	5.36	0.066	49.08
Xba1	4	0.002489	0.002489	0.000622	0.35	0.835	3.18
Xba2	4	0.018009	0.018009	0.004502	2.51	0.197	23.01
AS1	4	0.007043	0.007043	0.001761	0.98	0.507	9.00
AS2	4	0.005146	0.005146	0.001286	0.72	0.622	6.57
Residual Error	4	0.007169	0.007169	0.001792			9.16
Total	24	0.078267					

Model Summary		
S	R-Sq	R-Sq(adj)
0.0423	90.84%	45.04%

+) *Determining optimum main design factors:* The reasonable (or ideal) factor set would, in theory, consist of essential design characteristics with the highest S/N values. As a result, the influence of the key design aspects on the S/N ratio (Fig. 4) was calculated. Furthermore, the optimal set of multi-objective parameters (corresponding to the red points) may be simply deduced from the Fig. 4 chart. Table 9 displays the proper levels and values for the key design variables of the multi-objective function.

+) *Examining the experimental modeling:* The outcomes of the Anderson-Darling approach, which is used to test the adequacy of the suggested model, are depicted in Fig. 5. The data points corresponding to the experimental observations (shown in the graph as blue dots) are within the 95% standard deviation zone specified by the top and bottom limits. Furthermore, the p-value of 0.230 is much higher than the significance level of $\alpha = 0.05$. These findings show that the empirical model used in this work is suitable for evaluation.

Table 8. Response table for means

Level	u1	Xba1	Xba2	AS1	AS2
1	0.6665	0.6045	0.5648	0.5956	0.5787
2	0.5622	0.601	0.5571	0.6172	0.5782
3	0.5669	0.5795	0.5963	0.5953	0.5847
4	0.5956	0.5818	0.6236	0.5655	0.6141
5	0.5675	0.5919	0.6169	0.5851	0.603
Delta	0.1043	0.025	0.0666	0.0517	0.0359
Rank	1	5	2	3	4
Average of grey analysis value: 0.592					

Continue in the same manner as with ut = 20, but with the ut values 15, 25, 30, 35, and 40. Table 10 shows the optimal values for each of the five major design parameters for different u_t. Figure 6 depicts the relationship between the suitable first stage gear ratio u_1 and the overall gearbox ratio u_t. To calculate the ideal values of u_1, the following regression formula (with $R^2 = 0.999$) is provided.

$$u_1 = 2.1241 \cdot \ln(u_t) - 4.694 \tag{31}$$

After having u_1, the optimal value of u_2 can be found by $u_2 = u_t/u_1$.

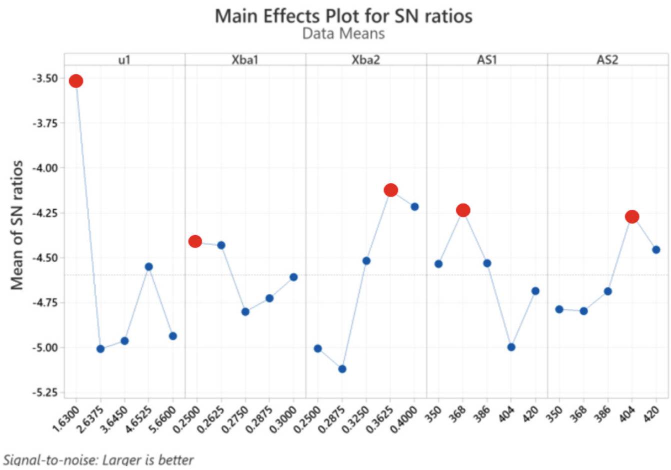

Fig. 4. Main effects plot for S/N ratios

Table 9. Optimum values of main design factors

No.	Input Parameters	Code	Optimum Level	Optimum Value
1	Gear ratio of stage 1	u_1	1	1.63
2	CWFW of stage 1	Xba1	1	0.25
3	CWFW of stage 2	Xba2	4	0.3625
4	ACS of stage 1 (MPa)	AS1	2	368
5	ACS of stage 2 (MPa)	AS2	4	404

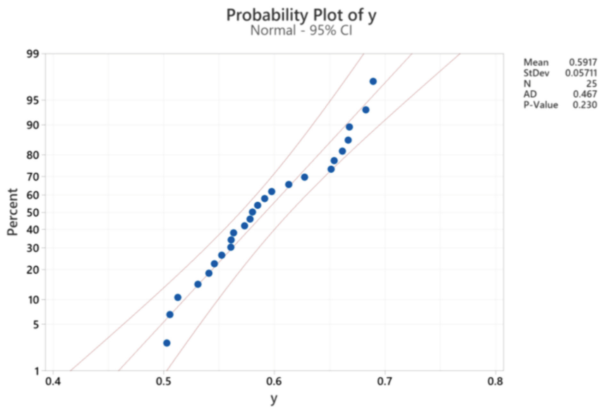

Fig. 5. Probability plot of $\overline{y}$

Table 10. Optimal values of main design factors

No.	u_t					
	15	20	25	30	35	40
u_1	1.09	1.63	2.14	2.52	2.86	3.16
X_{ba1}	0.25	0.25	0.2625	0.2625	0.2625	0.2625
X_{ba2}	0.3625	0.3625	0.3625	0.3625	0.3625	0.3625
AS_1	368	368	368	368	368	368
AS_2	404	404	404	404	404	404

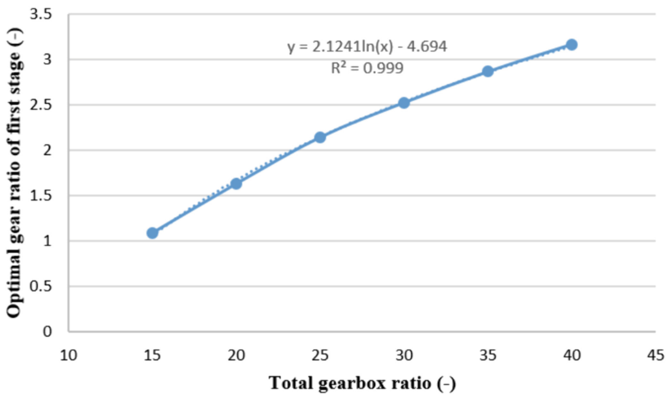

Fig. 6. Optimal first-stage gear ratio versus total gearbox ratio

6 Conclusions

This article discusses the results of a multi-objective optimization study on optimizing a two-stage helical gearbox with SSDGS to decrease gearbox height and enhance gearbox efficiency. This research improved the gear ratio in the first stage, the efficiency of wheel face width in stages 1 and 2, and the allowable contact stress in stages 1 and 2. To address this issue, a simulation experiment based on the Taguchi L25 type was developed and carried out. The impact of significant design elements on the multi-objective aim was also studied. It was found that u1 has the greatest influence on $\overline{y_i}$. . (49.08%), followed by X_{ba2} (23.01%), AS_1 (9.00%), AS_2 (6.57%), and X_{ba1} (3.18%). Additionally, the ideal settings for the essential gearbox parameters have been recommended. For identifying the appropriate first stage u1 gear ratio, a regression technique (Eq. (31)) was also presented.

Acknowledgment. This work was supported by Thai Nguyen University of Technology.

References

1. Pi, V.N., Tuan, N.K., Hung, L.X.: A new study on calculation of optimum partial transmission ratios of mechanical driven systems using a chain drive and a two-stage helical reducer. In: Awang, M., Emamian, S., Yusof, F. (eds.) Advances in Material Sciences and Engineering. LNME, pp. 97–105. Springer, Singapore (2020). https://doi.org/10.1007/978-981-13-8297-0_13
2. Vu, N.-P., et al.: The influence of main design parameters on the overall cost of a gearbox. Appl. Sci. **10**(7), 2365 (2020)
3. Patil, S.S., et al.: Design and optimization of a 3-stage industrial gearbox. In: Dikshit, M.K., Soni, A., Davim, J.P. (eds.) Advances in Manufacturing Engineering: Select Proceedings of ICFAMMT 2022, pp. 297–315. Springer Nature Singapore, Singapore (2023). https://doi.org/10.1007/978-981-19-4208-2_21
4. Danh, T.H., et al.: Optimization of main design parameters for a two-stage helical gearbox based on gearbox volume function. In: Nguyen, D.C., Vu, N.P., Long, B.T., Puta, H., Sattler, K.-U. (eds.) Advances in Engineering Research and Application: Proceedings of the International Conference on Engineering Research and Applications, ICERA 2022, pp. 771–779. Springer International Publishing, Cham (2023). https://doi.org/10.1007/978-3-031-22200-9_81
5. Pi, V.N., Hong, T.T., Hung, L.X.: Determining optimal partial transmission ratios of mechanical driven systems using a V-belt drive and a two-stage helical reducer. IOP Conf. Ser.: Mater. Sci. Eng. **635**(1), 012011 (2019). https://doi.org/10.1088/1757-899X/635/1/012011
6. Khai, D.Q., et al.: Calculating optimum main design factors of a two-stage helical gearboxes for minimum gearbox mass. In: Nguyen, D.C., Vu, N.P., Long, B.T., Puta, H., Sattler, K.-U. (eds.) Advances in Engineering Research and Application: Proceedings of the International Conference on Engineering Research and Applications, ICERA 2022, pp. 314–325. Springer International Publishing, Cham (2023). https://doi.org/10.1007/978-3-031-22200-9_34
7. Linh, N.H., et al.: Cost optimization study for two-stage helical gearbox with second stage double gear sets. In: Nguyen, D.C., Ngoc Pi, V., Long, B.T., Puta, H., Sattler, K.-U. (eds.) Advances in Engineering Research and Application: Proceedings of the International Conference on Engineering Research and Applications, ICERA 2022, pp. 1–12. Springer International Publishing, Cham (2023). https://doi.org/10.1007/978-3-031-22200-9_1
8. Quang, N.H., et al.: Determining optimum gear ratios for a four-stage helical gearbox for getting minimum gearbox cost. In: Nguyen, D.C., Vu, N.P., Long, B.T., Puta, H., Sattler, K.-U. (eds.) Advances in Engineering Research and Application: Proceedings of the International Conference on Engineering Research and Applications, ICERA 2021, pp. 350–364. Springer International Publishing, Cham (2022). https://doi.org/10.1007/978-3-030-92574-1_36
9. Hung, L.X., et al.: Calculation of optimum gear ratios of mechanical driven systems using two-stage helical gearbox with first stage double gear sets and chain drive. In: Sattler, K.-U., Nguyen, D.C., Vu, N.P., Long, B.T., Puta, H. (eds.) Advances in Engineering Research and Application: Proceedings of the International Conference on Engineering Research and Applications, ICERA 2019, pp. 170–178. Springer International Publishing, Cham (2020). https://doi.org/10.1007/978-3-030-37497-6_20

10. Tuan, N.K., et al.: A study on determining optimum gear ratios of mechanical driven systems using two-step helical gearbox with first step double gear sets and chain drive. In: Sattler, K.-U., Nguyen, D.C., Vu, N.P., Long, B.T., Puta, H. (eds.) Advances in Engineering Research and Application: Proceedings of the International Conference on Engineering Research and Applications, ICERA 2019, pp. 85–93. Springer International Publishing, Cham (2020). https://doi.org/10.1007/978-3-030-37497-6_9
11. Chat, T., Van Uyen, L.: Design and Calculation of Mechanical Transmissions Systems, vol. 1. Educational Republishing House, Hanoi (2007)
12. Jelaska, D.: Gears and Gear Drives. Wiley (2012). https://doi.org/10.1002/9781118392393
13. Buckingham, E.: Analytical Mechanics of Gears. Courier Corporation (1988)
14. Tran, H.-D., et al.: Application of the taguchi method and grey relational analysis for multi-objective optimization of a two-stage bevel helical gearbox. Machines **11**(7), 716 (2023)
15. Le, X.-H., Vu, N.-P.: Multi-objective optimization of a two-stage helical gearbox using taguchi method and grey relational analysis. Appl. Sci. **13**(13), 7601 (2023)

Multi-objective Optimization of a Two-Stage Helical Gearbox with Second Stage Double Gear Sets to Reduce Gearbox Length and Increase Gearbox Efficiency

Dinh Van Thanh[1], Bui Thanh Danh[2], Nguyen Van Chien Thang[3], Tran Huu Danh[4], Nguyen Van Trang[5], and Hoang Xuan Tu[5](✉)

[1] East Asia University of Technology, Hanoi, Vietnam
[2] University of Transport and Communications, Hanoi, Vietnam
[3] Nguyen Tat Thanh University, Ho Chi Minh City, Vietnam
[4] Vinh Long University of Technology Education, Vinh Long City, Vietnam
[5] Thai Nguyen University of Technology, Thai Nguyen, Vietnam
hxt_dhktcn@tnut.edu.vn

Abstract. The goal of this research is to look at multi-target optimization of a two-stage helical gearbox with second stage double gear sets (SSDGS) in order to find the best key design aspects to reduce gearbox length and enhance gearbox efficiency. In two stages, the Taguchi technique and grey relation analysis (GRA) were used to address the problem. First, the single-objective optimization issue was addressed in order to narrow the gap within variable levels, and then the multi-objective optimization problem was solved in order to discover the optimal major design variables. The coefficients of wheel face width (CWFW) of the first and second stages, allowed contact stresses (ACS) of the first and second stages, and the first stage gear ratio were also determined. The study's findings were utilized to identify the best values for five critical design aspects for a two-stage helical gearbox with SSDGS.

Keywords: Helical gearbox · Double gear sets · Multi-objective optimization · Gear ratio · Gearbox length · Gearbox efficiency

1 Introduction

In the existing literature, there are numerous studies that focus on helical gearbox. [1] answered to the rising demand and popularity of all-terrain vehicle (ATV) and investigated theoretical design, calculation, and analysis of a gearbox for BAJA SAE applications. [2] explored optimal partial transmission ratios in mechanical drive systems with a chain drive and a three-step helical reducer. In addition, [3] focused on designing hybrid composite gears for a two-stage constant mesh helical gearbox. It found that by replacing EN36 steer gears with EN36/Carbon Fibre Composite material, weight and inertia of the helical gear were reduced, which also increase the safety of gearbox application. [4] introduced a novel investigation using optimization and regression techniques

D. C. Nguyen et al. (Eds.): ICERA 2023, LNNS 944, pp. 229–244, 2024.
https://doi.org/10.1007/978-3-031-62235-9_22

to predict optimal partial ratios of the three-step helical gearboxes with second-step double gear-sets, in which explicit models for calculating partial ratios were proposed. Understanding the importance of minimizing gearbox cost in both design and manufacturing, [5] calculated cost using components' mass for two-stage helical gearboxes with second-stage double gear-sets. Within the same area of interest, [6] proposed two models for determining optimal gear ratios to minimize helical reducer's cross-sectional area. [7] filled in the research gap by tackling the design of a two-step helical gearbox with second stage double gear sets. [8] aimed to minimize gear mass by determining optimal partial transmission ratios for four-step helical gearboxes with double gear-sets. Furthermore, [9] conducted a simulation experiment to explore the connection between partial gear ratios and input parameters, from which models for dividing the total gear ratio of a two-step helical reducer were established. In addition, [10] investigated the use of airborne sound for condition monitoring of a multi-stage helical gearbox.

The purpose of this research is exploring multi-target optimization learning for a two-stage helical gearbox with SSDGS. Two single aims were pursued in this effort: reducing gear-box length and optimizing gearbox efficiency. In addition, five major design elements were evaluated: the CWFW for both stages, the ACS for both stages, and the gear ratio for the first stage. Furthermore, by combining the Taguchi technique with the GRA, the multi-objective optimization problem in gearbox design was addressed in two stages. The best values of five critical design variables for building a two-stage helical gearbox with SSDGS were also provided.

2 Optimization Problem

2.1 Calculating Gearbox Length

The gearbox length L can be calculated by (Fig. 1):

$$L = d_{w11}/2 + a_{w1} + a_{w2} + d_{w22}/2 + 2 \cdot k \tag{1}$$

In (1), $k = 8 \div 12$ [11]; d_{w11}, d_{w22} are gear pitch diameters of the first and second stages which are found by [11]:

$$d_{w11} = 2a_{w1}/(u_1 + 1) \tag{2}$$

$$d_{w22} = 2a_{w2}u_2/(u_2 + 1) \tag{3}$$

In the above equations, a_{w1} and a_{w2} are the center distances of the first and the second stages which can be determined by [11]:

$$a_{w1} = k_a(u_1 + 1)\sqrt[3]{T_{11}k_{H\beta1}/([\sigma_{H1}]^2 u_1 X_{ba1})} \tag{4}$$

$$a_{w2} = k_a(u_2 + 1)\sqrt[3]{T_{12}k_{H\beta2}/([\sigma_{H2}]^2 u_2 X_{ba2})} \tag{5}$$

In (4) and (5), $k_a = 43$ is the material coefficient [11]; $k_{H\beta1}$ and $k_{H\beta2}$ are the contacting load ratio for pitting resistance of the first and second stages; $k_{H\beta1} = 1.0 \div 1.06$

and $k_{H\beta 2} = 1.02 \div 1.28$ [11]. $[\sigma_{H1}]$ and $[\sigma_{H2}]$ are ACS of the first and second stages (MPa), respectively; u_1 and u_2 are the gear ratios of the first and second stages. X_{ba1} and X_{ba2} are CWFW of the first and second stages. T_{11} and T_{12} are the torque on the first and second stage's pinion (Nmm):

$$T_{11} = T_{out} / \left(u_g \cdot \eta_{hg}^2 \cdot \eta_b^3 \right) \tag{6}$$

$$T_{12} = T_{out} / \left(2 \cdot u_2 \cdot \eta_{hg} \cdot \eta_{be}^2 \right) \tag{7}$$

where, T_{out} is the output torque (N.mm); η_{hg} is the helical gear efficiency (($\eta_{hg} = 0.96 \div 0.98$); η_b is the rolling bearing efficiency ($\eta_h = 0.99 \div 0.995$) [11].

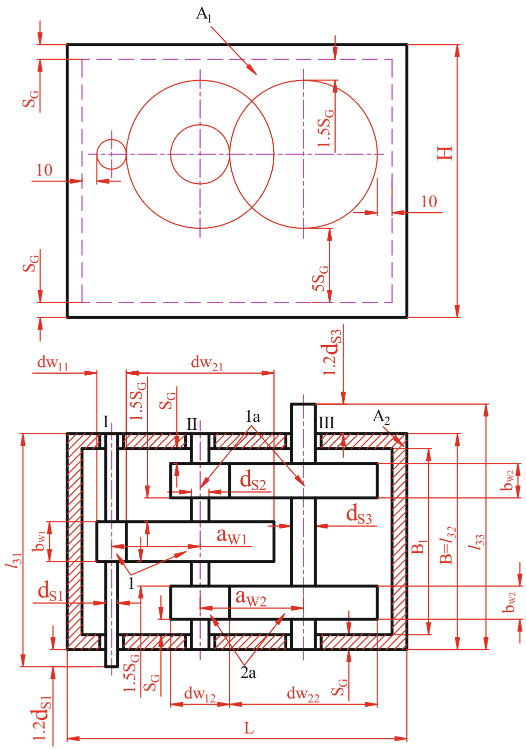

Fig. 1. Calculated schema

2.2 Calculating Gearbox Efficiency

The gearbox's efficiency is calculated as follows:

$$\eta_{gb} = \frac{100 \cdot P_l}{P_{in}} \tag{8}$$

In which, P_l is the total gearbox power loss [12]:

$$P_l = P_{lg} + P_{lb} + P_{ls} \tag{9}$$

In where, P_{lg} represents overall gear power loss, P_{lb} provides bearing power loss, and P_{ls} indicates seal power loss. These parts are as follows:

+) The power loss in gears:

$$P_{lg} = \sum_{i=1}^{2} P_{lgi} \tag{10}$$

P_{lgi} signifies the gear power losses of i stage as calculated by:

$$P_{lgi} = P_{gi} \cdot \left(1 - \eta_{gi}\right) \tag{11}$$

where, η_{gi} is the anticipated efficiency of the gearbox's i stage from [13]:

$$\eta_{gi} = 1 - \left(\frac{1 + 1/u_i}{\beta_{ai} + \beta_{ri}}\right) \cdot \frac{f_i}{2} \cdot \left(\beta_{ai}^2 + \beta_{ri}^2\right) \tag{12}$$

where, u_i is the i stage's gear ratio, f is the friction coefficient, and β_{ai} and β_{ri} are the arcs of approach and retreat on the i stage, as calculated [13]:

$$\beta_{ai} = \frac{\left(R_{e2i}^2 - R_{02i}^2\right)^{1/2} - R_{2i} \cdot \sin\alpha}{R_{01i}} \tag{13}$$

$$\beta_{ri} = \frac{\left(R_{e1i}^2 - R_{01i}^2\right)^{1/2} - R_{1i} \cdot \sin\alpha}{R_{01i}} \tag{14}$$

where, R_{e1i} and R_{e2i} are the outer radiuses of the pinion and gear, respectively; R_{1i} and R_{2i} are the pitch radiuses of the pinion and gear, respectively; R_{01i} and R_{01i} are the base-circle radiuses of the pinion and gear, respectively; and α is the pressure angle.

The friction coefficient f in (12) is determined by [14]:

– When the sliding velocity $v \leq 0.424$ (m/s):

$$f = -0.0877 \cdot v + 0.0525 \tag{15}$$

– When the sliding velocity v >0.424 (m/s):

$$f = 0.0028 \cdot v + 0.0104 \tag{16}$$

+) The power loss in bearings is found by [12]:

$$P_{lb} = \sum_{i=1}^{6} f_b \cdot F_i \cdot v_i \tag{17}$$

where, $f_b = 0.0011$ is the bearing friction coefficient since radical ball bearings with angular contact were chosen [12], F is the bearing load (N), v is the peripheral speed, and i is the bearing ordinal number ($i = 1 \div 6$).

+) The overall power loss in seals is calculated by [12]:

$$P_s = \sum_{i=1}^{2} \mathrm{P_{si}} \tag{18}$$

P_{si} is the power loss caused by sealing for a single seal (w), which may be calculated as follows:

$$P_{si} = \left[145 - 1.6 \cdot t_{oil} + 350 \cdot loglog(VG_{40} + 0.8)\right] \cdot d_s^2 \cdot n \cdot 10^{-7} \tag{19}$$

In which, VG_{40} is the ISO Viscosity Grade number.

2.3 Objective Function and Constrains

2.3.1 Objectives Functions

This paper's multi-target optimization problem has two distinct goals:

Minimizing the gearbox length:

$$\min f_2(X) = \mathrm{L} \tag{20}$$

Maximizing the gearbox efficiency:

$$\min f_1(X) = \eta_{gb} \tag{21}$$

where X is the vector of design variables indicating variables. Five primary design characteristics were chosen as variables in this study: u_1, Xba_1, Xba_2, AS_1, and AS_2, leading in:

$$X = \{u_1, Xba_1, Xba_2, AS_1, AS_2\} \tag{22}$$

2.3.2 Constrains

The multi-objective function must adhere to the following constraints:

$$1 \le u_1 \le 9 \text{ and } 1 \le u_2 \le 9 \tag{23}$$

$$0.25 \le k_{be} \le 0.3 \text{ and } 0.25 \le X_{ba} \le 0.4 \tag{24}$$

$$350 \le \mathrm{AS}_1 \le 420 \text{ and } 350 \le \mathrm{AS}_2 \le 420 \tag{25}$$

3 Methodology

Five major design features were chosen for investigation in this research. Table 1 displays the minimum and maximum values for various variables. To solve the optimization problem, the Taguchi technique and grey relation analysis were applied. The L25 (5^5) design was used to optimize the number of levels for each variable. Among the variables considered, however, u1 has a pretty wide range (u_1 ranges from 1 to 9 – Table 1). Even with five levels, the difference in these attributes' values remained relevant (in this case, the difference is ((9–1)/4 = 2)).

The 2-stage multi-objective optimization problem solution technique [15] was utilized to help narrow the gap between values of a variable spread throughout a wide range. This technique's first stage handles a single-objective optimization problem, while the second stage addresses a multi-objective optimization problem to select the best primary design features (Fig. 2).

Table 1. Main design factors and their maximum and minimum restrictions

Factor	Notation	Lower limit	Upper limit
Gear ratio of stage 1	u_1	1	9
CWFW of stage 1	X_{ba1}	0.25	0.3
CWFW of stage 2	X_{ba2}	0.25	0.4
ACS of stage 1 (MPa)	AS_1	350	420
ACS of stage 2 (MPa)	AS_2	350	420

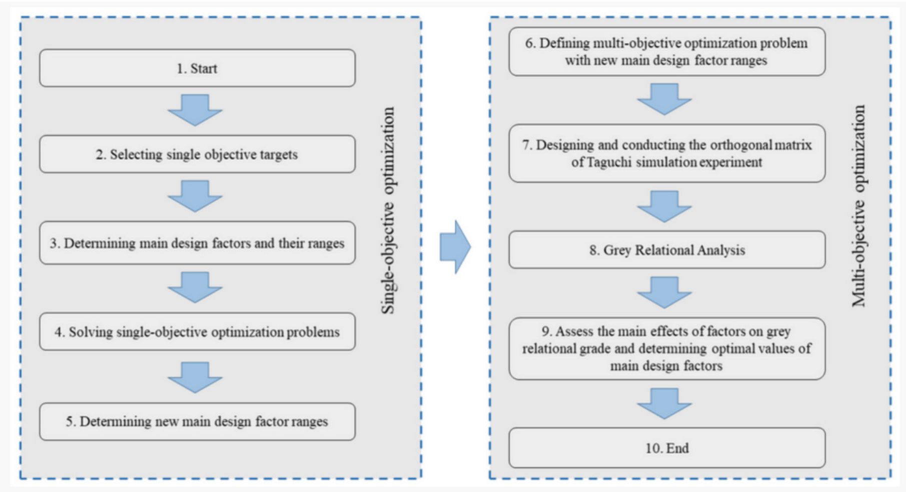

Fig. 2. Method to solve multi-objective problem [14]

4 Single-Objective Optimization

The direct search strategy is used in this work to solve the single-objective optimization issue. A Matlab-based computer program was also created to handle two single-objective problems: reducing gearbox length and maximizing gearbox efficiency. Figure 3 depicts the relationship between the optimal gear ratio of the first stage u_1 and the overall gearbox ratio ut based on the findings of this program. Furthermore, new restrictions for the variable u_1 have been developed, as shown in Table 2.

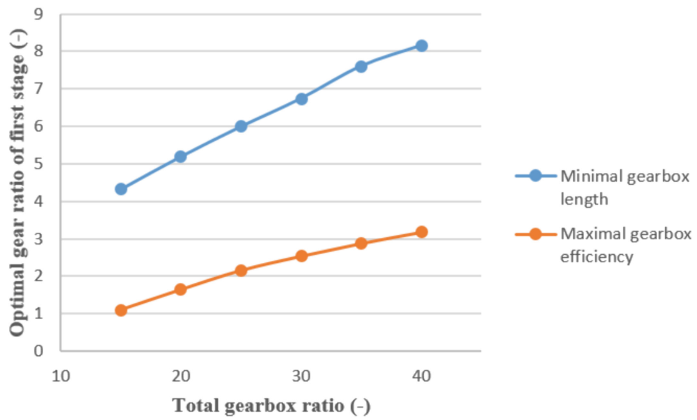

Fig. 3. Optimal first-stage gear ratio versus total gearbox ratio for single-objective

Table 2. New constraints of u_1

u_t	u_1	
	Lower limit	Upper limit
10	1.09	4.33
15	1.63	5.20
20	2.14	6.00
25	2.52	6.75
30	2.86	7.61
35	3.16	8.16

5 Multi-objective Optimization

The purpose of the multi-objective optimization problem for a two-stage helical gearbox with SSDGS in this work is to discover the optimal primary design variables with a given total gear-box ratio that meets two single-objective functions: lowering gearbox length and maximizing gearbox efficiency. A computational experiment was carried out to accomplish this. The experimental design was created using the Taguchi approach with L25 (5^5) design, and the data was analyzed using the Minitab R18 program (Table 3, Table 4).

Table 3. Main design parameters and their levels for $u_t = 20$

Factor	Notation	Level				
		1	2	3	4	5
Gear ratio of first stage	u_1	1.76	2.0	2.24	2.48	2.72
CWFW of stage 1	X_{ba1}	0.25	0.2675	0.275	0.2875	0.3
CWFW of stage 2	X_{ba2}	0.25	0.2875	0.325	0.3625	0.4
ACS of stage 1 (MPa)	AS_1	350	368	386	404	420
ACS of stage 2 (MPa)	AS_2	350	368	386	404	420

When dealing with multi-objective optimization issues, the Taguchi and GRA approaches are applied. The key steps of this approach are as follows:

+) Determine the signal-to-noise ratio (S/N) using the following equations:

The shorter the gearbox length, the better the S/N:

$$SN = -10log_{10}(\frac{1}{n}\sum_{i=1}^{m} y_i^2) \tag{26}$$

The bigger the S/N, the better for gearbox efficiency:

$$SN = -10log_{10}(\frac{1}{n}\sum_{i=1}^{m} \frac{1}{y_i^2}) \tag{27}$$

where, y_i represents the output result and m indicates the number of experimental repetitions. Because this is a simulation, m = 1; no repetitions are required. Table 5 shows the estimated S/N indices for the two output goals.

The data amounts for the two single-objective functions under consideration differ. The data must be normalized, or brought to a consistent scale, to assure comparability. To normalize the data, the normalization value Z_{ij}, which ranges from 0 to 1, is employed. The following formula is used to calculate this value:

$$Z_i = \frac{SN_i - min(SN_i, = 1,2, ..n)}{max(SN_i, j = 1,2, ..n) - min(SN_i, = 1,2, ..n)} \tag{28}$$

The experimental number is n = 25 in this case.

+) The grey relational factor is calculated by:

$$y_i(k) = \frac{\Delta_{min} + \xi.\Delta_{max}(k)}{\Delta_i(k) + \xi.\Delta_{max}(k)} \tag{29}$$

Table 4. Experimental matrix and output results for $u_t = 20$

Exp. No.	Input Factors					L	η_{gb}
	u_1	X_{ba1}	X_{ba2}	AS_1	AS_2	(cm)	(%)
1	1.6300	0.2500	0.2500	350	350	58.673	95.572
2	1.6300	0.2625	0.2875	368	368	54.694	95.540
3	1.6300	0.2750	0.3250	386	386	51.303	95.534
4	1.6300	0.2875	0.3625	404	404	48.365	95.500
5	1.6300	0.3000	0.4000	420	420	45.927	95.498
6	2.5225	0.2500	0.2875	386	404	48.658	95.252
7	2.5225	0.2625	0.3250	404	420	45.901	95.242
8	2.5225	0.2750	0.3625	420	350	48.138	95.301
9	2.5225	0.2875	0.4000	350	368	47.362	95.244
10	2.5225	0.3000	0.2500	368	386	50.928	95.277
11	3.4150	0.2500	0.3250	420	368	47.074	95.065
12	3.4150	0.2625	0.3625	350	386	46.542	95.062
13	3.4150	0.2750	0.4000	368	404	44.020	95.043
14	3.4150	0.2875	0.2500	386	420	47.187	95.061
15	3.4150	0.3000	0.2875	404	350	49.014	95.086
16	4.3075	0.2500	0.3625	368	420	44.326	94.825
17	4.3075	0.2625	0.4000	386	350	45.985	94.897
18	4.3075	0.2750	0.2500	404	368	49.029	94.905
19	4.3075	0.2875	0.2875	420	386	46.007	94.908
20	4.3075	0.3000	0.3250	350	404	45.565	94.887
21	5.2000	0.2500	0.4000	404	386	43.946	94.667
22	5.2000	0.2625	0.2500	420	404	46.715	94.697
23	5.2000	0.2750	0.2875	350	420	46.440	94.676
24	5.2000	0.2875	0.3250	368	350	47.887	94.706
25	5.2000	0.3000	0.3625	386	368	45.165	94.691

In which, i = 1,2,…,n; k = 2 is the number of targets; $\Delta_j(k) = \|Z_0(k) - Z_j(k)\|$ with Z0(k) and Zj(k) represent the reference and particular comparison sequences, respectively; Δ_{min} and Δ_{max} are the minimum and maximum values of i(k), respectively; and $\zeta = 0.5$ is the characteristic coefficient.

Table 5. S/N values for each experiment when $u_t = 20$

Exp. No.	Input Factors					L		η_{gb}	
	u_1	X_{ba1}	X_{ba2}	AS_1	AS_2	(cm)	S/N	(%)	S/N
1	1.6300	0.2500	0.2500	350	350	58.673	–35.3688	95.572	39.6066
2	1.6300	0.2625	0.2875	368	368	54.694	–34.7588	95.540	39.6037
3	1.6300	0.2750	0.3250	386	386	51.303	–34.2029	95.534	39.6032
4	1.6300	0.2875	0.3625	404	404	48.365	–33.6906	95.500	39.6001
5	1.6300	0.3000	0.4000	420	420	45.927	–33.2414	95.498	39.5999
6	2.5225	0.2500	0.2875	386	404	48.658	–33.7431	95.252	39.5775
7	2.5225	0.2625	0.3250	404	420	45.901	–33.2364	95.242	39.5766
8	2.5225	0.2750	0.3625	420	350	48.138	–33.6498	95.301	39.5819
9	2.5225	0.2875	0.4000	350	368	47.362	–33.5086	95.244	39.5768
10	2.5225	0.3000	0.2500	368	386	50.928	–34.1391	95.277	39.5798
11	3.4150	0.2500	0.3250	420	368	47.074	–33.4556	95.065	39.5604
12	3.4150	0.2625	0.3625	350	386	46.542	–33.3569	95.062	39.5601
13	3.4150	0.2750	0.4000	368	404	44.020	–32.8730	95.043	39.5584
14	3.4150	0.2875	0.2500	386	420	47.187	–33.4764	95.061	39.5600
15	3.4150	0.3000	0.2875	404	350	49.014	–33.8064	95.086	39.5623
16	4.3075	0.2500	0.3625	368	420	44.326	–32.9332	94.825	39.5385
17	4.3075	0.2625	0.4000	386	350	45.985	–33.2523	94.897	39.5450
18	4.3075	0.2750	0.2500	404	368	49.029	–33.8091	94.905	39.5458
19	4.3075	0.2875	0.2875	420	386	46.007	–33.2565	94.908	39.5461
20	4.3075	0.3000	0.3250	350	404	45.565	–33.1726	94.887	39.5441
21	5.2000	0.2500	0.4000	404	386	43.946	–32.8584	94.667	39.5240
22	5.2000	0.2625	0.2500	420	404	46.715	–33.3891	94.697	39.5267
23	5.2000	0.2750	0.2875	350	420	46.440	–33.3378	94.676	39.5248
24	5.2000	0.2875	0.3250	368	350	47.887	–33.6044	94.706	39.5275
25	5.2000	0.3000	0.3625	386	368	45.165	–33.0960	94.691	39.5262

+) Finding the degree of grey relationship: It is calculated by taking the mean of the grey relational coefficients linked with the output goals:

$$\overline{y_i} = \frac{1}{k}\sum_{j=0}^{k} y_{ij}(k) \tag{30}$$

In which y_{ij} is the grey relation value of the j^{th} output aim of the i^{th} experiment. Table 6 shows the predicted grey relation number y_i as well as the average grey relation value $\overline{y_i}$ for each test.

Table 6. Values of $\Delta_i(k)$ and $\overline{y_i}$

No.	S/N		Zi		Δ_i (k)		Grey relation value yi		$\overline{y_i}$
	L	η_{gb}	Lgb	η_{gb}					
			Reference values		L	η_{gb}	L	η_{gb}	
			1.000	1.000					
1	–35.3688	39.6066	0.0000	1.0000	1.000	0.000	0.333	1.000	0.667
2	–34.7588	39.6037	0.2430	0.9648	0.757	0.035	0.398	0.934	0.666
3	–34.2029	39.6032	0.4644	0.9582	0.536	0.042	0.483	0.923	0.703
4	–33.6906	39.6001	0.6685	0.9208	0.332	0.079	0.601	0.863	0.732
5	–33.2414	39.5999	0.8474	0.9186	0.153	0.081	0.766	0.860	0.813
6	–33.7431	39.5775	0.6476	0.6475	0.352	0.353	0.587	0.587	0.587
7	–33.2364	39.5766	0.8494	0.6365	0.151	0.364	0.769	0.579	0.674
8	–33.6498	39.5819	0.6848	0.7015	0.315	0.298	0.613	0.626	0.620
9	–33.5086	39.5768	0.7410	0.6387	0.259	0.361	0.659	0.580	0.620
10	–34.1391	39.5798	0.4898	0.6751	0.510	0.325	0.495	0.606	0.551
11	–33.4556	39.5604	0.7621	0.4410	0.238	0.559	0.678	0.472	0.575
12	–33.3569	39.5601	0.8014	0.4376	0.199	0.562	0.716	0.471	0.593
13	–32.8730	39.5584	0.9942	0.4166	0.006	0.583	0.988	0.462	0.725
14	–33.4764	39.5600	0.7538	0.4365	0.246	0.563	0.670	0.470	0.570
15	–33.8064	39.5623	0.6224	0.4642	0.378	0.536	0.570	0.483	0.526
16	–32.9332	39.5385	0.9702	0.1753	0.030	0.825	0.944	0.377	0.661
17	–33.2523	39.5450	0.8431	0.2550	0.157	0.745	0.761	0.402	0.581
18	–33.8091	39.5458	0.6213	0.2639	0.379	0.736	0.569	0.405	0.487
19	–33.2565	39.5461	0.8414	0.2672	0.159	0.733	0.759	0.406	0.582
20	–33.1726	39.5441	0.8748	0.2440	0.125	0.756	0.800	0.398	0.599
21	–32.8584	39.5240	1.0000	0.0000	0.000	1.000	1.000	0.333	0.667
22	–33.3891	39.5267	0.7886	0.0333	0.211	0.967	0.703	0.341	0.522
23	–33.3378	39.5248	0.8090	0.0100	0.191	0.990	0.724	0.336	0.530
24	–33.6044	39.5275	0.7028	0.0433	0.297	0.957	0.627	0.343	0.485
25	–33.0960	39.5262	0.9053	0.0266	0.095	0.973	0.841	0.339	0.590

To increase harmony among the output factors, a higher average grey relation value is proposed. As a result, the objective function of a multi-objective issue may be reduced to a single-objective optimization problem, providing the mean grey relation value.

The findings of an ANOVA test performed to examine the influence of the primary design aspects on the average grey relation value $\overline{y_i}$ are shown in Table 7. Table 7 shows that u1 has the highest impact on $\overline{y_i}$ (47.56%), followed by X_{ba2} (30.47%), AS_2 (12.2%), X_{ba1} (1.91%), and AS_1 (0.97%). Using ANOVA analysis, Table 8 shows the order of the influence of the primary design components on $\overline{y_i}$.

Table 7. Analysis of variance for means

Analysis of Variance of Means							
Source	DF	Seq SS	Adj SS	Adj MS	F	P	C (%)
u1	4	0.073965	0.073965	0.018491	6.90	0.044	47.56
Xba1	4	0.002972	0.002972	0.000743	0.28	0.879	1.91
Xba2	4	0.047378	0.047378	0.011844	4.42	0.089	30.47
AS1	4	0.001509	0.001509	0.000377	0.14	0.958	0.97
AS2	4	0.018970	0.018970	0.004742	1.77	0.297	12.20
Residual Error	4	0.010712	0.010712	0.002678			6.89
Total	24	0.155505					
Model summary							
S	R-Sq	R-Sq(adj)					
0.0517	93.11%	58.67%					

+*) Finding optimum main design factors:* In principle, the reasonable (or ideal) factor set would consist of core design features with the highest S/N values. As a consequence, the effect of the important design features on the S/N ratio (Fig. 4) was estimated. Furthermore, the ideal set of multi-objective parameters (corresponding to the red points) may be easily determined from the chart in Fig. 4. Table 9 shows the appropriate levels and values for the multi-objective function's primary design variables.

+*) Examining the experimental modeling:* Fig. 5 depicts the findings of the Anderson-Darling technique, which is used to assess the suitability of the proposed model. The data points corresponding to the experimental observations (shown by blue dots in the graph) fall within the 95% standard deviation zone defined by the top and bottom boundaries. Furthermore, the p-value of 0.507 is much greater than the significance threshold of $\alpha = 0.05$. These findings imply that the empirical model employed in this study is appropriate for the purpose of assessment.

Proceed in the same method as with $u_t = 15$, but with the following ut values of 10, 20, 25, 30, and 35. Table 10 indicates the ideal values of the five main design parameters for each of the five main design parameters for various u_t. The following are the outcomes of this table:

- X_{ba1} selects the smallest feasible value, whereas X_{ba2} selects the largest possible value. This is because the average grey relation value $\overline{y_i}$ was maximized using these values.
- Similarly, the ideal AS_1 values are the lowest, while the ideal AS_2 values are the highest. This is because these settings enhanced the average grey relation value $\overline{y_i}$.

Table 8. Response table for means.

Level	u1	Xba1	Xba2	AS1	AS2
1	0.7162	0.6311	0.5592	0.6016	0.5758
2	0.61	0.6072	0.5781	0.6175	0.5875
3	0.5979	0.6128	0.6071	0.6062	0.6191
4	0.582	0.5979	0.6392	0.6171	0.6329
5	0.5587	0.6158	0.6812	0.6224	0.6494
Delta	0.1575	0.0331	0.122	0.0208	0.0736
Rank	1	4	2	5	3
Average of grey analysis value: 0.613					

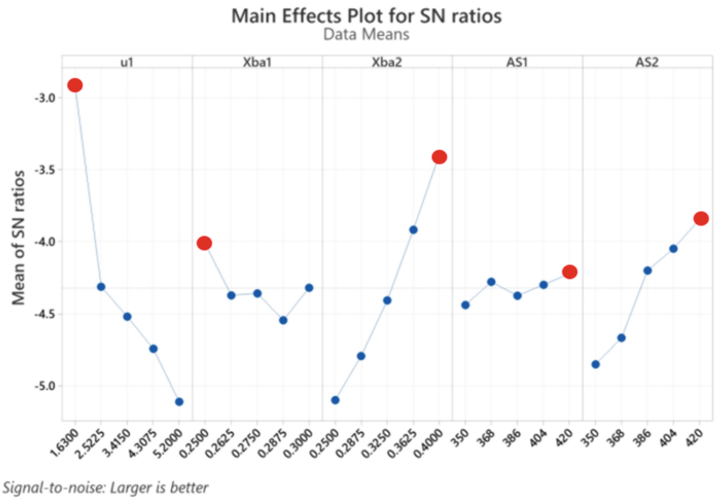

Fig. 4. Main effects plot for S/N ratios

Table 9. Optimum values of main design factors

No.	Input Parameters	Code	Optimum Level	Optimum Value
1	Gear ratio of first stage	u_1	1	1.63
2	CWFW of stage 1	Xba1	1	0.25
3	CWFW of stage 2	Xba2	5	0.4
4	ACS of stage 1 (MPa)	AS1	5	420
5	ACS of stage 2 (MPa)	AS2	5	420

– The link between the appropriate first stage gear ratio and the entire gearbox ratio is depicted in Fig. 6. The following regression formula (with $R^2 = 0.999$) is presented to determine the optimal values of u_1.

$$u_1 = 2.1241 \cdot \ln(u_t) - 4.694 \tag{31}$$

After determining u_1, the optimal value of u_2 may be calculated using $u_2 = u_t/u_1$.

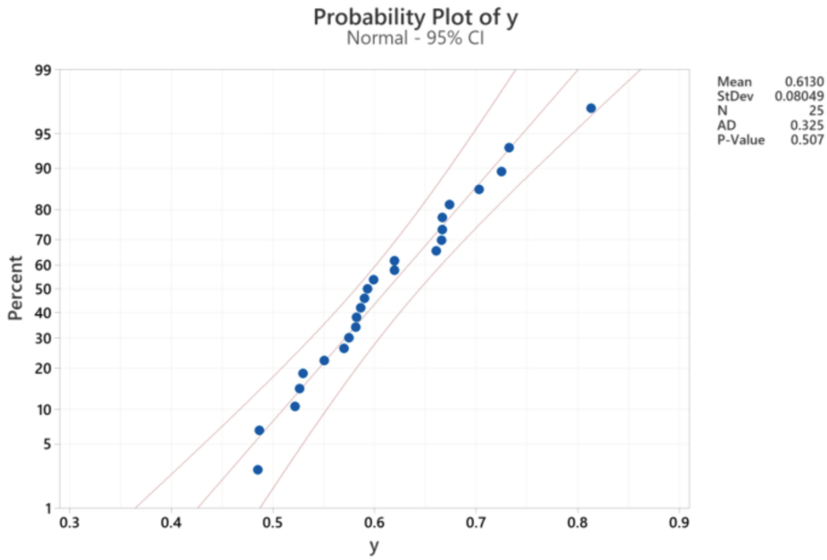

Fig. 5. Probability plot of $\overline{y}$

Table 10. Optimal values of main design parameters

No.	u_t					
	15	20	25	30	35	40
u_1	1.09	1.63	2.14	2.52	2.86	3.16
X_{ba1}	0.25	0.25	0.25	0.25	0.25	0.25
X_{ba2}	0.4	0.4	0.4	0.4	0.4	0.4
AS_1	420	420	420	420	420	420
AS_2	420	420	420	420	420	420

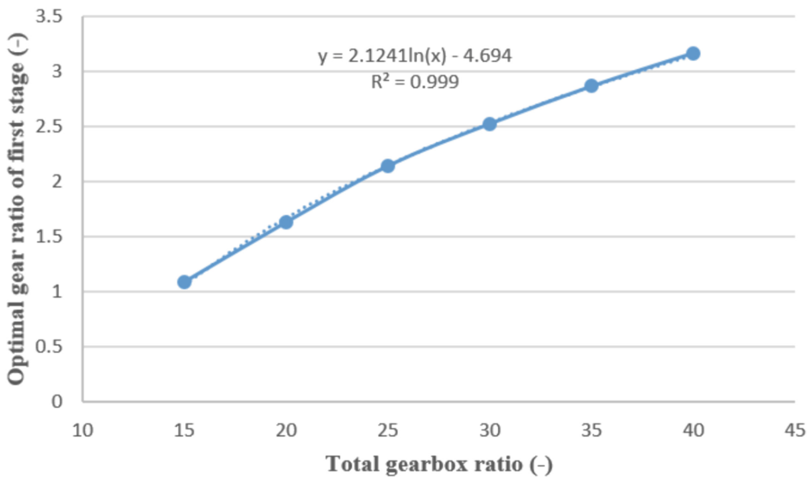

Fig. 6. Optimal first-stage gear ratio versus total gearbox ratio for multi-objective

6 Conclusions

The results of a multi-objective optimization research on improving a two-stage helical gearbox with SSDGS to minimize gearbox length and maximize gearbox efficiency are discussed in this paper. This study optimized the first stage's gear ratio, the efficiency of wheel face width in stages 1 and 2, and the permitted contact stress in stages 1 and 2. A simulation experiment based on the Taguchi L25 type was created and carried out to solve this issue. The effect of major design features on the multi-objective goal was also investigated. Furthermore, the best settings for the critical gearbox parameters have been suggested. A regression approach (Eq. (31)) was also proposed for determining the best first stage u_1 gear ratio.

Acknowledgment. Thai Nguyen University of Technology provided support for this research.

References

1. Reddy, B.S., Mahato, K.K.: Calculation, design and analysis of two stage single speed gearbox for all terrain vehicle for Baja Sae. Mater. Today: Proc. **46**, 7187–7203 (2021)
2. Cam, N.T.H., et al.: A study on determination of optimum partial transmission ratios of mechanical driven systems using a chain drive and a three-step helical reducer. In: Advances in Engineering Research and Application: Proceedings of the International Conference, ICERA 2018. Springer (2019)
3. Joshi, S., et al.: Design of helical gear with carbon reinforced EN36 steel for two stage constant mesh gearbox weight reduction. Mater. Today: Proc. **46**, 626–633 (2021)
4. Pi, V.N.: A new study on the optimal prediction of partial transmission ratios of three-step helical gearboxes with second-step double gear-sets. WSEAS Trans. Appl. Theor. Mech **2**(11), 156–163 (2007)

5. Anh, L.H., et al.: Cost optimization of two-stage helical gearboxes with second stage double gear-sets. EUREKA: Phys. Eng. (6), 89–101 2021)
6. Tuan, N.K., et al.: Determining optimal gear ratios of a two-stage helical reducer for getting minimal acreage of cross section. In: MATEC Web of Conferences. EDP Sciences (2018)
7. Linh, N.H., et al.: Cost Optimization Study for Two-Stage Helical Gearbox with Second Stage Double Gear Sets. In: International Conference on Engineering Research and Applications. Springer (2022)
8. Pi, V.N.: Optimal determination of partial transmission ratios for four-step helical gearboxes with first and third step double gear-sets for minimal mass of gears. In: Proceedings of the WSEAS International Conference on Applied Computing Conference (2008)
9. Van Cuong, N., Le Hong, K., Tran, T.: Splitting total gear ratio of two-stage helical reducer with first-stage double gearsets for minimal reducer length. Int. J. Mech. Prod. Eng. Res. Dev.(IJMPERD) **9**(6), 595–608 (2019)
10. Lu, K., et al.: Acoustics based monitoring and diagnostics for the progressive deterioration of helical gearboxes. Chinese J. Mech. Eng. **34**, 1–12 (2021)
11. Chat, T., Van Uyen, L.: Design and calculation of Mechanical Transmissions Systems, vol. 1. Educational Republishing House, Hanoi (2007)
12. Jelaska, D.T.: Gears and gear drives. John Wiley & Sons (2012)
13. Buckingham, E.: Analytical mechanics of gears. Courier Corporation (1988)
14. Tran, H.-D., et al.: Application of the Taguchi method and grey relational analysis for multi-objective optimization of a two-stage bevel helical gearbox. Machines **11**(7), 716 (2023)
15. Le, X.-H., Vu, N.-P.: Multi-objective optimization of a two-stage helical gearbox using Taguchi method and grey relational analysis. Appl. Sci. **13**(13), 7601 (2023)

Multi-objective Optimization of Dressing Process in Surface Grinding Hardox 500 to Reduce Surface Roughness and Increase Wheel Life

Dinh Van Thanh[1], Tran Huu Danh[2], Nguyen Duc Anh[3], Do Duc Dung[4], Nguyen Van Me[4], Nguyen Xuan Cuong[4], Nguyen Van Trang[5], and Luu Anh Tung[5](✉)

[1] East Asia University of Technology, Hanoi, Vietnam
[2] Vinh Long University of Technology Education, Vinh Long, Vietnam
[3] Nguyen Tat Thanh University, Ho Chi Minh City, Vietnam
[4] Bac Ninh Industrial College, Bac Ninh City, Vietnam
[5] Thai Nguyen University of Technology, Thai Nguyen, Vietnam
luuanhtung@tnut.edu.vn

Abstract. This paper presents the results of a multi-objective optimization study on the dressing process in surface grinding Hardox 500. For this effort, two single objectives were chosen: minimal surface roughness (SR) and maximum wheel life (WL). Furthermore, the following dressing parameters were investigated: rough dressing depth Tr, rough dressing times Nr, fine dressing depth Tf, fine dressing times Nf, and non-feeding dressing Nnon. The influence of these elements on the objective of the grinding process was evaluated. Furthermore, an ideal dressing mode for increasing MRR while decreasing SR was proposed. The suggested model has been reported to be useful.

Keywords: Surface grinding · Optimal dressing parameters · Multi-Objective Optimization · Wheel life · Surface roughness · Hardox 500

1 Introduction

Dressing the wheel involves removing the present abrasive coating from the work surface, revealing a fresh and sharp surface. It contributes to increased grinding accuracy and decreased machining time.

So far, much study has been conducted on wheel dressing. Various forms of grinding have been examined, including external grinding, surface grinding, and inter-nal grinding. Many studies on the best dressing mode have been undertaken. [1] explains the Taguchi approach for optimizing dressing settings to maximize wheel life in sur-face grinding of hardened SKD 11 steel. [2] illustrates how dressing parameters affect wheel lifetime while external grinding SKD11 steel. This study looked at the effect of dressing parameters including coarse dressing depth, number of coarse dressing, fine dressing depth, number of fine dressing, non-feeding dressing, and dressing feed speed on surface texture. When external grinding SKD11, optimal dressing parameters for maximum

D. C. Nguyen et al. (Eds.): ICERA 2023, LNNS 944, pp. 245–254, 2024.
https://doi.org/10.1007/978-3-031-62235-9_23

wheel life expectancy [2], maximum MRR [3], and lowest roundness tolerance [4] were identified. When machining SKD11, the influence of dressing parameters on SR [5], MRR, and WL was described for internal grinding. The effects of dressing parameters while surface grinding SKD11 on flatness tolerance [6], wheel life [1], and normal cutting force [7] were studied. For surface grinding [8–10] and internal grinding [11, 12], the multi-objective optimization issue of the wheel dressing process has been solved.

As previously stated, despite several studies on improving the dressing process, a multi-objective optimization study to determine the best dressing mode for surface grinding Hardox 500 to minimize SR and enhance WL remains unavailable. This study looks into how dressing parameters affect SR and WL in the Hardox 500 surface grinding process. In addition, the optimal dressing method was advised to improve WL and decrease SR.

2 Experimental Work

Fig. 1. Experimental setup

An experiment was carried out to investigate the effect of dressing parameters on SR and MRR when processing Hardox 500. The Minitab R19 program was used to create this experiment, which had an L16 ($4^4 \times 2^1$) design and 16 experimental runs. The input components and their levels are shown in Table 1. Figure 1 depicts the experimental setup. The setup includes a surface machine, PSG-CL3060AH (Taiwan), a grinding wheel, Cn60MV1G V1 350 × 40 × 127 35 (m/s), a dressing tool, 3908-0088C type 2 (Russia), and a piezoelectric dynamometer, Kistler 9257BA (Germany). The experiment was carried out as follows: Each experiment was repeated three times. The wheel life is determined by the time between starting to grind after dressing and utilizing the standard Py spike. SR was calculated using an SJ201 surface roughness meter. Table 2 shows the experimental matrix and outcomes (SR and WL).

Table 1. Input parameters and their levels

No.	Parameters	Symbol	Level			
			1	2	3	4
1	Rough dressing depth (mm)	a_r	0.015	0.02	0.025	0.03
2	Rough dressing times	nr	1	2	3	4
3	Fine dressing depth (mm)	a_f	0.005	0.01	-	-
4	Fine dressing times	n_f	0	1	2	3
5	Non-feeding dressing	nnon	0	1	2	3

Table 2. Experimental matrix and output results

No.	a_r	n_r	n_f	n_{non}	a_f	SR (μm)			WL (min.)		
						Trial 1	Trial 2	Trial 3	Trial 1	Trial 2	Trial 3
1	0.015	1	0	0	0.005	0.642	0.735	0.645	23.10	22.3	23.8
2	0.015	2	1	1	0.005	0.573	0.653	0.545	33.60	34.6	31.4
3	0.015	3	2	2	0.010	0.698	0.554	0.53	5.05	5.3	4.8
4	0.015	4	3	3	0.010	0.631	0.692	0.618	1.90	1.7	2.1
5	0.020	1	1	2	0.010	0.476	0.409	0.423	19.40	19.8	20.5
6	0.020	2	0	3	0.010	0.469	0.476	0.495	41.60	39.8	42.2
7	0.020	3	3	0	0.005	0.647	0.607	0.598	44.30	44.8	42.9
8	0.020	4	2	1	0.005	0.708	0.81	0.837	23.70	22.9	24.6
9	0.025	1	2	3	0.005	0.44	0.465	0.451	5.20	4.8	5.7
10	0.025	2	3	2	0.005	0.813	0.819	0.805	36.80	35.2	38.0
11	0.025	3	0	1	0.010	1.276	1.122	1.25	28.80	27.4	27.9
12	0.025	4	1	0	0.010	0.862	0.882	0.88	35.70	35.9	40.2
13	0.030	1	3	1	0.010	0.989	0.938	0.902	26.50	25.7	27.2
14	0.030	2	2	0	0.010	0.733	0.681	0.666	35.50	34.8	35.2
15	0.030	3	1	3	0.005	1.399	1.452	1.301	41.70	42.2	41.4
16	0.030	4	0	2	0.005	0.762	0.8	0.759	16.90	17.6	16.4

3 Multi-objective Optimization

Using Gray Relational Analysis (GRA), the following procedures may be utilized to solve the multi-objective optimization problem for S/N ratio:

Step 1: Determine S/N ratio:

– Since "smaller is better" is the desired outcome for surface roughness, the ratio is as follows:

$$S/N = -10\log_{10}(\frac{1}{n}\sum_{i=1}^{n} y_1^2) \tag{1}$$

– The desire is "bigger is better" with WL, and the ratio is:

$$S/N = -10log_{10}(\frac{1}{n}\sum_{i=1}^{n}\frac{1}{y_i^2}) \tag{2}$$

In which y_i is the observed data and n is experimental number.

Step 2: A high S/N ratio provides more reliable and noise-resistant results. To avoid the influence of differing units, this ratio is normalized to Z_{ij} ($0 \leq Z_{ij} \leq 1$) using the following equation:

$$Z_{ij} = \frac{SN_{ij} - \min(SN_{ij}, j = 1, 2, ..k)}{\max\left(SN_{ij}, j = 1, 2, ..n\right) - \min(SN_{ij}, j = 1, 2, ..n)} \tag{3}$$

In which j = 16 is the trial number.

Table 3 shows the S/N ratio as well as the normalized value Z for each output objective.

Step 3: Calculate the interaction coefficient for the normalized SN ratios in the fuzzy relationship:

$$\gamma(k) = \frac{\Delta min + \zeta\,\Delta max}{\Delta_j(k) + \zeta\,\Delta max} \tag{4}$$

In which, j = 1, 2,…n; k = 1, 2, ….m; n = 16 is the number of trials, k = 2 is the number of objectives; Δ_{0j} is the deviation sequence; $\Delta_{0j} = Z_0(k) - Z_j(k)$ is the absolute value of the difference between Z0(k) (reference value) and Zj(k) (Z value of the j^{th} experiment of the k^{th} objective). Δ min $= \underset{\forall j\in i}{\min}\underset{\forall k}{\min}\left\| Z_0(k) - Z_j(k)\right\|$ is the minimum value of Δ_{0j}; $\Delta max = \underset{\forall j\in i}{\max}\underset{\forall k}{\max}\left\| Z_0(k) - Z_j(k)\right\|$ is the maximum value of Δ_{0j}; ζ k is the discriminant coefficient, defined in the range $0 \leq K \leq 1$; in this study, ζ = 0.5.

Step 4: Determine the degree of gray association using the following formula:

$$\overline{\gamma_j} = \frac{1}{k}\sum_{i=1}^{m}\gamma_{ij} \tag{5}$$

This is the mean of the gray related interactions computed in step 3. The number of objectives to be optimized is k. The gray relationship values linked with the objectives, as well as the average gray relation values, are shown in Table 4.

Step 5: Calculate the optimal level of dressing factors:

A higher gray relation value suggests higher product quality. As a result, depending on the degree of gray connectivity, the influence and optimality of each dressing parameter may be determined. The gray relation values and interactive gray relation values for

Table 3. Values of S/N, Zij and $\Delta_j(k)$

No.	S/N		Z_{ij}		$\Delta_j(k)$	
	Ra	WL	Ra	WL	Ra	WL
			Reference values			
			1.000	1.000		
1	3.409	27.25	0.623	0.795	0.377	0.205
2	4.552	30.40	0.737	0.910	0.263	0.090
3	4.457	14.04	0.727	0.313	0.273	0.687
4	3.771	5.48	0.659	0.000	0.341	1.000
5	7.191	25.97	1.000	0.748	0.000	0.252
6	6.373	32.29	0.918	0.979	0.082	0.021
7	4.184	32.86	0.700	1.000	0.300	0.000
8	2.081	27.50	0.490	0.804	0.510	0.196
9	6.895	14.31	0.970	0.322	0.030	0.678
10	1.805	31.27	0.463	0.942	0.537	0.058
11	–1.712	28.95	0.112	0.857	0.888	0.143
12	1.163	31.39	0.399	0.946	0.601	0.054
13	0.504	28.45	0.333	0.839	0.667	0.161
14	3.174	30.92	0.599	0.929	0.401	0.071
15	–2.832	32.42	0.000	0.984	1.000	0.016
16	2.226	24.58	0.505	0.698	0.495	0.302

each trial are shown in Table 5. As a result, experiment 6 has the highest interaction gray relation value (0.91) since it rough dressed twice with a depth of 0.02 (mm), without fine dressing, and three times with a feed rate of 1.2 (m/min). It suggests that, among the 16 trials, experiment 6 has a matching SN ratio that is near to the normalized SN ratio and has a number of favorable characteristics. This, however, is not the optimum mix of factors. Taguchi's technique necessitates calculating the average gray relation value for each element at different levels. Table 5 and Fig. 2 show the average value of the gray association at each component level (the study was done using Minitab 19 software).

Each factor's gray relation value at its greatest level will be its ideal level. According to Table 6 and Fig. 2, the best dressing mode for decreasing SR while increasing WL is $a_r2/n_r2/n_f2/n_{non}1/a_f1$. Thus, the optimal dressing variables are fine dressing twice at 0.02 mm depth, rough dressing once at 0.005 mm depth, and no non-feeding dressing at a feed rate of $S = 1.2$ (m/min).

Step 6: ANOVA is used to find the important factors: The application of statistical tools to identify the influence of each element on the process's aim is known as regression analysis of variance. The ANOVA contribution ratio will compensate for the Taguchi

Table 4. Grey relational coefficient and grey grade values

No	Grey relational co-efficient γi		$\overline{\gamma}$
	Ra	WL	
1	0.570	0.709	0.640
2	0.655	0.848	0.751
3	0.647	0.421	0.534
4	0.594	0.333	0.464
5	1.000	0.665	0.833
6	0.860	0.960	0.910
7	0.625	1.000	0.812
8	0.495	0.719	0.607
9	0.944	0.425	0.684
10	0.482	0.896	0.689
11	0.360	0.778	0.569
12	0.454	0.903	0.678
13	0.428	0.756	0.592
14	0.555	0.876	0.715
15	0.333	0.969	0.651
16	0.502	0.623	0.563

Table 5. Response table for means

Response Table for Means					
Level	a_r	n_r	n_f	n_{non}	a_f
1	0.5971	0.6871	0.6703	0.7115	0.6747
2	0.7905	0.7665	0.7284	0.6299	0.6619
3	0.6552	0.6416	0.6352	0.6545	
4	0.6302	0.5779	0.6392	0.6772	
Delta	0.1934	0.1886	0.0931	0.0816	0.0128
Rank	1	2	3	4	5
$\overline{\gamma} = 0,668$					

method's failure to investigate the influence of the factors on the overall process. The results of the regression analysis of variance are shown in Table 6.

According to the ANOVA results (Table 6), the rough dressing depth a_r has the greatest influence on the overall aim (41.6%), followed by the number of rough dressing

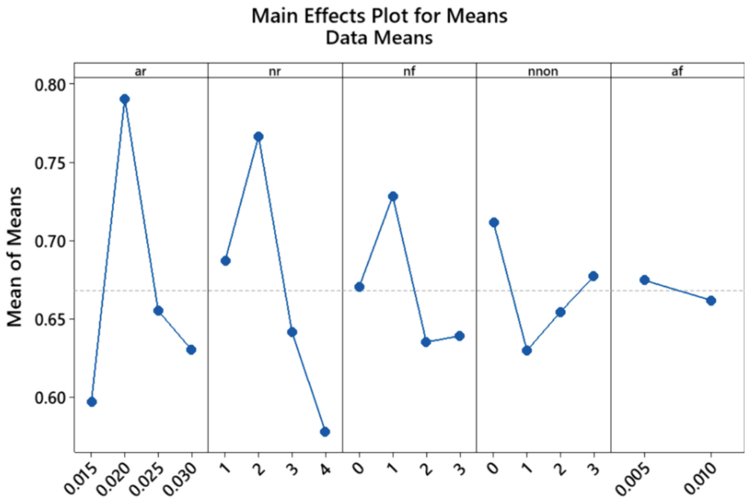

Fig. 2. Main effects plot for means

Table 6. Results of ANOVA on grey grade

Analysis of Variance for Means							
Source	DF	Seq SS	Adj SS	Adj MS	F	P	C%
a_r	3	0.086467	0.086467	0.028822	6.75	0.132	41.60
n_r	3	0.075543	0.075543	0.025181	5.89	0.148	36.34
n_f	3	0.022196	0.022196	0.007399	1.73	0.386	10.68
n_{non}	3	0.014453	0.014453	0.004818	1.13	0.502	6.95
a_f	1	0.000657	0.000657	0.000657	0.15	0.733	0.32
Residual Error	2	0.008545	0.008545	0.004272			4.11
Total	15	0.207861					100.00

depth n_r (36.34%), the number of times fine dressing n_{non} (18.17%), the number of times fine dressing n_f (10.68%), and lastly the fine dressing depth a_f (0.32%).

Step 7: Calculate and validate the optimization outcomes.

The optimal fuzzy relationship value is calculated as follows:

$$\overline{\gamma_{op}} = \eta_m + \sum_{i=1}^{5}(\overline{\eta} - \eta_m) = \overline{T}_{r2} + \overline{N}_{r1} + \overline{N}_{f3} + \overline{N}_{non3} + \overline{T}_{f1} - 4*\overline{\gamma} \quad (6)$$

In which: $\overline{\gamma}$ is the average gray relation value $\overline{\gamma} = 0.668$; the values a_{r2}, n_{r2}, n_{f2}, n_{non1}, a_{f1} are the gray relation values of the parameters corresponding to the optimal level taken from Table 6. Accordingly, $\overline{\gamma_{op}} = 0.9996$. The CI confidence interval is calculated as follows:

$$CI = \pm\sqrt{F_{\alpha}(1.f_e).V_e.\left(\frac{1}{N_e} + \frac{1}{R}\right)} = \pm 0, 17 \tag{7}$$

where fe = 2 is the degrees of freedom of error, Ve = 0.004272 is the mean error of error; $F_{\propto}(1, f_e) = 8.5263$ is the coefficient of table lookup with 90% significance level; Ne is the effective number of iterations, and R is the number of experiment repeats.

$$\begin{aligned} N_e &= \frac{\text{Total number of experiments}}{1 + \text{Averaging the degrees of freedom of all parameters}} \\ &= \frac{48}{1+3+3+3+1} = 4.364 \end{aligned} \tag{8}$$

Substituting numbers gets:

$$CI = \pm\sqrt{F_{\alpha}(1.f_e).V_e.\left(\frac{1}{N_e} + \frac{1}{R}\right)} = \pm 0.17 \tag{9}$$

Therefore, with the significance level α = 90%, the gray relation value is predicted with the reasonable level of the input parameters $T_{rd}1/N_{rd}2/N_{non}4/N_{fd}1/T_{fd}2/S1$ as follows:

$$(0.9996 - 0.15) \leq \overline{\gamma}_{op} \leq 1 \tag{10}$$

The optimal value of the outputs RS and WL is obtained by the following formula, based on the optimal level of input parameters:

$$(Ra,\ \text{WL})_{op} = \overline{a}_{r2} + \overline{n}_{r2} + \overline{n}_{f2} + \overline{n}_{non1} + \overline{a}_{f1} - 4 * \overline{T} \tag{11}$$

where,

$(Ra, \text{Tw})_{op}$ is optimal SR or WL; $\overline{a_{r2}}$ is average SR or WL when rough dressing depth in level 2; $\overline{n_{r2}}$ is average SR or WL when rough dressing times at level 2; $\overline{n_{f2}}$ is average SR or WL when fine dressing times in level 2; $\overline{n_{non1}}$ is average SR or WL when non-dressing times in level 1; $\overline{a_{f1}}$ is average SR of WL when fine dressing depth in leven 1; $\overline{T}$ is average SR or WL of the entire experiment.

Accordingly, we have:

$$(Ra)_{op} = 0.491(\mu\text{m}) \tag{12}$$

$$(\text{WL})_{op} = 59.88(\text{min}) \tag{13}$$

To validate the aforementioned optimal set of parameters, an experiment was carried out with three iterations using the following parameters: ar = 0.05 mm; nr = 1 times; nf = 2 times; $a_f = 0.02$ mm; $n_{non} = 0$; and S = 1.2 m/min. Table 7 compares the experimental findings with the optimum computation results. The greatest discrepancy between experimental and calculated findings is 3.86% for SR, according to this data. This suggests that the computational technique can predict both SR and WL simultaneously.

Table 7. Comparative results between calculation and experiment

Machining characteristics	Optimal values		
	Calculation	Experiment	% difference
	$a_{r2}/n_{r2}/n_{f2}/n_{non1}/a_{f1}$	$a_{r2}/n_{r2}/n_{f2}/n_{non1}/a_{f1}$	
SR (μm)	0.491	0.472	3.86
WL (min)	59.88	58.83	1.75

4 Conclusions

This paper presents the findings of a multi-objective optimization research on the dressing process in surface grinding Hardox 500. Two separate objectives were investigated in the study: lowest SR and maximum WL. Furthermore, the rough dressing depth ar, rough dressing times nr, fine dressing depth nf, fine dressing times nf, and non-feeding dressing nnon were examined. The effect of these variables on the grinding process's objective was assessed. It was reported that the rough dressing depth a_r has the greatest influence on the overall aim (41.6%), followed by the number of rough dressing depth n_r (36.34%), the number of times fine dressing n_{non} (18.17%), the number of times fine dressing n_f (10.68%), and lastly the fine dressing depth a_f (0.32%). Furthermore, the following optimal dressing mode was recommended to increase WL while lowering SR: $a_r = 0.05$ (mm), $n_r = 1$ (times), $n_f = 2$ (times), $a_f = 0.02$ (mm), $n_{non} = 0$ and $S = 1.2$ (m/min). Furthermore, the proposed model is said to be useful.

Acknowledgment. This work was supported by Thai Nguyen University of Technology.

References

1. Tran, T.H., et al.: Improvement of wheel life by optimization of dressing parameters in surface grinding of SKD11 steel. In: Materials Science Forum. Trans Tech Publ (2021)
2. Le, H.A., et al. Impacts of dressing conditions on wheel lifetime when external grinding of SKD11 steel. in International Conference on Engineering Research and Applications. 2021. Springer
3. Tran, T.H., et al. Effect of Dressing Parameters on Material Removal Rate when Surface Grinding SKD11 Tool Steel. in Materials Science Forum. 2021. Trans Tech Publ
4. Nguyen, T.T., et al.: Influence of dressing parameters on roundness tolerance in cylindrical external grinding SKD11 tool steel. In: Materials Science Forum. Trans Tech Publ (2021)
5. Hung, L.X., et al.: Determining the optimum set of dressing parameters satisfying minimum surface roughness when conducting the internal grinding of hardened SKD11 steel. Solid State Phenom. **324**, 58–65 (2021)
6. Tran, T.H., et al.: Optimizing dressing conditions for minimum flatness tolerance when grinding SKD11 tool steel. In: Materials Science Forum. Trans Tech Publ (2021)
7. Hong, T.T., et al.: Optimization of dressing parameters in surface grinding SKD11 tool steel by using Taguchi method. In: Advances in Engineering Research and Application: Proceedings of the International Conference on Engineering Research and Applications, ICERA 2020. Springer (2021)

8. Hong, T.T., et al.: Multi response optimization of dressing conditions for surface grinding SKD11 steel by HaiDuong grinding wheel using grey relational analysis in Taguchi method. In: Advances in Engineering Research and Application: Proceedings of the International Conference on Engineering Research and Applications, ICERA 2020. Springer (2021)
9. Hong, T.T., et al.: Multi-criteria optimization of dressing parameters for surface grinding 90CrSi tool steel using Taguchi method and grey relational analysis. In: Materials Science Forum. Trans Tech Publ (2020)
10. Krishna, A.G., Rao, K.M.: Multi-objective optimisation of surface grinding operations using scatter search approach. Int. J. Adv. Manuf. Technol. **29**, 475–480 (2006)
11. Hung, L.X., et al.: Multi-objective optimization of dressing parameters of internal cylindrical grinding for 9CrSi Alloy steel using Taguchi method and grey relational analysis. Mater. Today: Proc. **18**, 2257–2264 (2019)
12. Tuan, N.A., et al.: Optimization of dressing parameters for minimum surface roughness and maximum material removal rate in internal grinding of SKD11 tool steel. In: E3S Web of Conferences. EDP Sciences (2021)

Observing and Stabilizing Control for an Eccentric Inverted Pendulum

Hao Nguyen Dang[1](✉) and Dinh Gia Thi[2]

[1] Thai Nguyen University of Technology, Thai Nguyen, Vietnam
nguyendanghao@tnut.edu.vn
[2] Thai Nguyen University of Information and Communication Technology, Thai Nguyen, Vietnam

Abstract. Cart-pole is an underactuated system meaning that it has only one actuator to control two degree of freedom. It is more difficult to govern when adding an eccentric mass to the pendulum because the new system has center of mass that the direction from it to pivot is not matching with the direction of the measured tilt angle. This paper focuses on designing control for an eccentric inverted pendulum to stabilize at the vertical position by using the direct Lyapunov and backsteping methods. The simulation illustrates the performance of the designed controllers.

Keywords: Inverted pendulum · Underactuated Control · High gain observers

1 Introduction

An inverted pendulum system (IPen) has the center of mass above the pivot point and is unstable without external control forces. IPen is usually a nonlinear, under-actuated system in which only one actuator governs two degree of freedom. To stabilize the pendulum at the inverted position, external forces acting on the system can be oscillated rapidly up and down or in the same direction of the carrier's pendulum. There has been a variety of research on stabilizing, tracking a pendulum at the vertical position. The Kapitza's model [1] stabilizes the pendulum at the inverted equilibrium when forcing the pivot to oscillate rapidly up and down. The cart and pole model keeps the pole stable at equilibrium point with horizontally controlling forces. The other kinds can be named as the rotary inverted pendulum [2], two-wheeled mobile robot [3], Dean Kamen's iBot [4] for people with a disability; BallBot [5] balancing with only one ball; and other locomotion with legs like BigDog [6], Humanoid robot [7], published articles about controlling the inverted pendulum system can be divided into two groups: 1) Stabilize and 2) Swing-up the pendulum stable at the vertical position. The designed controls for cart-pole use linear and nonlinear control techniques like PID, LQR [8], adaptive control [9], intelligent control [10], these models employ a symmetric pendulum with the same direction with the tilt angle. It can be seen that if an eccentric mass is added to the inverted pendulum system, the direction going through the new center of mass does not match with the direction of the measured tilt angle. Moreover, if only the displacement x and the tilt angle θ can be measured, designing control for eccentric inverted pendulum system becomes more complicated.

D. C. Nguyen et al. (Eds.): ICERA 2023, LNNS 944, pp. 255–260, 2024.
https://doi.org/10.1007/978-3-031-62235-9_24

This paper introduces a new controller designed to stabilize the eccentric inverted pendulum system at the vertical position. The simulation is illustrated to show the performance of the designed controller.

2 Mathematical Model

An inverted pendulum system model with an added eccentric mass and its parameters are shown in the Fig. 1 and Table 1. The equations of motion of IPen are constructed in two cases: the IPen without and with an added eccentric mass. In addition, point B and point C are the center of mass of the rigid body of the pendulum and the added eccentric mass comparing with the pivot point A, respectively.

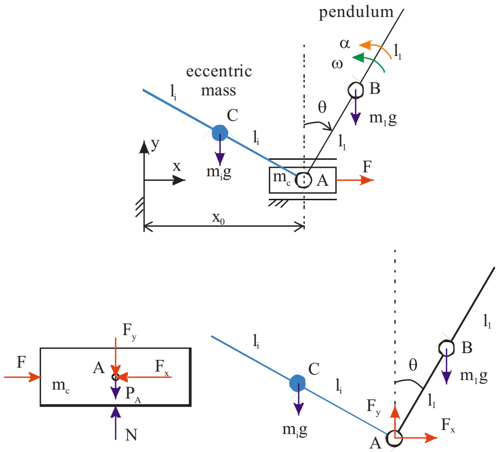

Fig. 1. Inverted pendulum system and its parameters.

Without and with the eccentric mass C, the equation of motion of the IPen can be written as in Eqs. (1) and (2) respectively.

$$\begin{aligned} &(m_c + m_1)\ddot{x} + m_1 l_1 \ddot{\theta}\cos\theta - m_1 l_1 \dot{\theta}^2 \sin\theta = F \\ &m_1 l_1 \ddot{x}\cos\theta + \left(I_1 + m_1 l_1^2\right)\ddot{\theta} = m_1 l_1 g \sin\theta \end{aligned} \tag{1}$$

$$\begin{aligned} &(m_c + m_n)\ddot{x} + m_n l_n \ddot{\theta}\cos(\theta + \Delta\theta) - m_n l_n \dot{\theta}^2 \sin(\theta + \Delta\theta) = F \\ &m_n l_n \ddot{x}\cos(\theta + \Delta\theta) + \left(I_n + m_n l_n^2\right)\ddot{\theta} = m_n l_n g \sin(\theta + \Delta\theta) \end{aligned} \tag{2}$$

where the new center of mass after adding eccentric mass to the pendulum is shown as in Eq. (3).

$$m_n = \sum m_i;\ l_n = \sum m_i l_i / m_n;\ I_n = \sum I_i \tag{3}$$

Table 1. Inverted pendulum parameters and variables.

Parameters	Description
F	The control force
m_c	The mass of the cart
m_1	The mass of the pendulum
m_i	The eccentric mass (i) putting on the pendulum
θ	The angle between the vertical and the pendulum; it is positive in the clock-wise direction
$\Delta\theta$	The angle between the new center of mass and the pendulum
$\omega,\ \dot{\theta}$	The angular velocity of the pendulum
$\alpha,\ \ddot{\theta}$	The angular acceleration of the pendulum
x	Displacement of the cart along the x-axis
g	The acceleration of gravity
$l_1,\ l_i$	The distance from the pivot point to the center of gravity of the pendulum and eccentric mass
$I_1,\ I_i$	The moment of inertia respect to pendulum and eccentric mass
$m_n,\ l_n,\ I_n$	The mass and moment of inertia respect to the added eccentric mass pendulum

3 Control Objective and Design

Assuming that only the tilt angle θ and the displacement x can be measured, and at the initial time t_0, the inverted pendulum is strictly in the upper half plan, there exists a positive constant c_0 such that $|\theta(t_0)| \le c_0$. The control objective is to design a control law F that forces the inverted pendulum to be stable at the equilibrium position while tracking desired trajectories or serial positions.

The second equation of (1) can be rewritten as

$$F_x \cos\theta + (4m_1 l_1/3 + m_1 l_1)\ddot{\theta} = m_1 g \sin\theta \tag{4}$$

where $F_x = m_1\ddot{x}$; $I_1 = 4m_1 l_1^2/3$.

From the Eq. (4), designing control force F so that the pendulum is stabilized at the vertical position and the angular velocity of the pendulum can be controlled. Choose the virtual control and control force $\ddot{\theta}$ and F_x for IPen and IPen with the added eccentric mass as in the Eq. (5)

$$\begin{aligned} &(4m_1 l_1/3 + m_1 l_1)\ddot{\hat{\theta}} = -k_1\dot{\hat{\theta}}, \\ &F_x = \sigma\left(k_1\dot{\hat{\theta}}/\cos\theta - m_1 g \tan\theta\right) \end{aligned} \tag{5}$$

$$\begin{aligned} &(4m_n l_n/3 + m_n l_n)\ddot{\hat{\theta}} = -k_1\dot{\hat{\theta}}, \\ &F_x = \sigma\left(k_1\dot{\hat{\theta}}/\cos\theta - m_n g \tan\theta\right) \end{aligned} \tag{6}$$

where $\sigma(\cdot)$ is a smooth saturation and p-times function. Choose $\sigma(\cdot) = x\left(3a^2 - x^2\right)/\left(2a^3\right)$, where a is maximum value depending on the limited force generated by the actuator of the IPen.

To track desired trajectories or serial points, the virtual control and control force can be chosen as in (7)

$$\begin{aligned} \alpha_2 &= -k_2 x_{1e} \\ F &= -k_3 x_{2e} - x_{1e} - F_x \end{aligned} \tag{7}$$

$$\text{where} \quad \begin{aligned} x_{1e} &= x_1 - x_{1d} \\ x_{2e} &= \hat{x}_2 - \alpha_2 \\ (m_c + m_n)\ddot{x} &= F + g\left(\theta, \dot{\hat{\theta}}, m_n, l_n\right) \end{aligned} \tag{8}$$

The observer is chosen as in (9)

$$\begin{aligned} \dot{\hat{x}}_1 &= \hat{x}_2 + h_1(x_1 - \hat{x}_1) \\ \dot{\hat{x}}_2 &= F + h_2(x_1 - \hat{x}_1) \\ \dot{\hat{\theta}}_1 &= \hat{\theta}_2 + h_1\left(\theta_1 - \hat{\theta}_1\right) \\ \dot{\hat{\theta}}_2 &= -k_1\hat{\theta}_2 + h_2\left(\theta_1 - \hat{\theta}_1\right) \end{aligned} \tag{9}$$

4 Simulation

To illustrate the effectiveness of the proposed controllers, the parameters for simulating are chosen as following: $m_c = 3.5$ [kg], $g = 9.8\,[m/s^2]$, $m_1 = 1\,[kg]$, $m_2 = 1\,[kg]$, $l_1 = 0.5\,[m]$, $l_2 = 0.5\,[m]$, $I_1 = 0.333\,[kg.m^2]$, $I_2 = 0.333\,[kg.m^2]$.

The initial conditions are taken as $x(0) = -1\,[m]$, $\dot{x}(0) = 0\,[m/s]$, $\theta(0) = 1\,[rad]$, and $\dot{\theta} = 0.2\,[rad/s]$; $\hat{x}(0) = 0\,[m]$, $\dot{x}(0) = 0\,[m/s]$, $\hat{\theta}(0) = 0\,[rad]$, $\dot{\hat{\theta}} = 0\,[rad/s]$. The gain controls are chosen as $k_1 = 3$, $k_2 = 3$, $k_3 = 15$, $h_1 = 1$ and $h_2 = 100$.

To demonstrate the performance of the designed controllers, two cases for simulating are taken: stabilizing the IPen and the IPen with added eccentric mass at a position. The references are chosen as $x_d = 0.5\,[m]$ and $\dot{x}_d = 0\,[m/s]$.

Case 1: Stabilizing the IPen. It can be seen from the Fig. 2.a that the IPen's pendulum is stable at the vertical position or the tilt angle θ is converged to zero.

Case 2: Stabilizing the IPen with added eccentric mass m_2 in which it has the same pivot point A and is perpendicular with the pendulum. To demonstrate the effectiveness of the designed control laws, $m_1 = m_2$, $l_1 = l_2$ are chosen. With these choices, the new pendulum are going to balance at the tilt angle $\theta = 45^0$. The simulation results from Fig. 2b show that the pendulum is stabilized at the vertical position on upper-haft plan with the tilt angle $\theta = 45^0$ matching with the calculated value.

The displacement x_{1e} of both cases are converged to zero while keeping the pendulum stabilizing around the equilibrium point. All the observer values also converge to the system states.

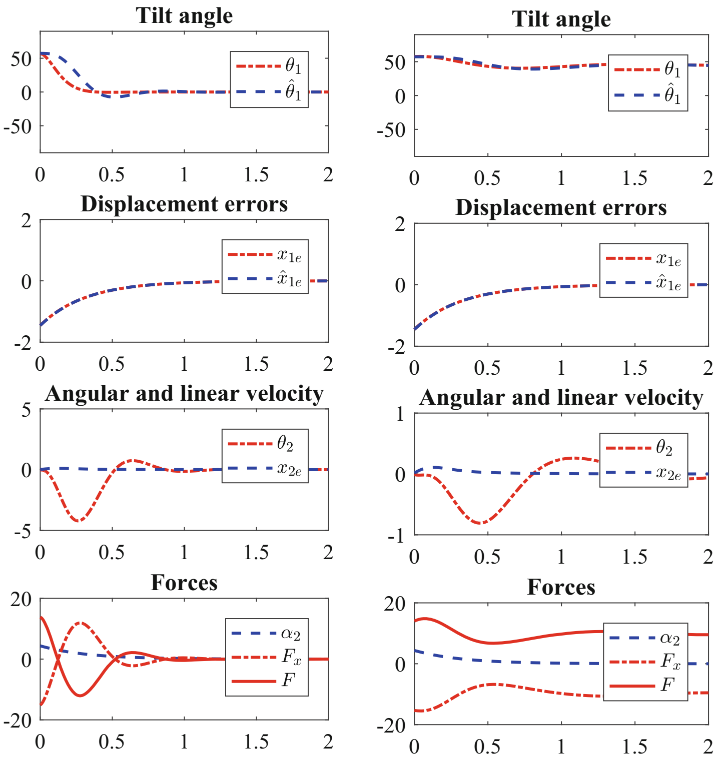

(a) (b)

Fig. 2. Simulation results for the IPen and the eccentric IPen.

5 Conclusion

The control laws, designed for the eccentric inverted pendulum system, are presented and simulated. It can be seen that the designed control laws can stabilize the pendulum at the inverted equilibrium point with/without the added eccentric mass. All the observer values converge to the system states. The parameters of the added eccentric mass m_2 are chosen as equivalent to the pendulum for easier calculating and checking the designed controller. In the real application, the added eccentric mass can be attached to any location on the pendulum.

Acknowledgments. Special thanks to Thai Nguyen University of Technology for funding this research.

References

1. Kapitza, P.L.: Dynamic stability of a pendulum when its point of suspension vibrates. Soviet Phys. JETP. **21**, 588–597 (1951)

2. Hamza, M.F., Yap, H.J., Choudhury, I.A., Isa, A.I., Zimit, A.Y., Kumbasar, T.: Current development on using Rotary Inverted Pendulum as a benchmark for testing linear and nonlinear control algorithms. Mech. Syst. Signal Process. **116**, 347–369 (2019). https://doi.org/10.1016/j.ymssp.2018.06.054
3. Ha, Y.-S., Yuta, S.: Trajectory Tracking Control for Navigation of the Inverse Pendulum Type Self-Contained Mobile Robot. Elsevier Science (1995)
4. Panomruttanarug, B., Chotikunnan, P.: Self-balancing iBOT-like wheelchair based on type-1 and interval type-2 fuzzy control. In: 2014 11th International Conference on Electrical Engineering/Electronics, Computer, Telecommunications and Information Technology (ECTI-CON), Nakhon Ratchasima, Thailand, pp. 1–6. IEEE (2014)
5. Lauwers, T., Kantor, G., Hollis, R.: One is enough! Robotics Research Oct (2005)
6. Tripathy, S., Gaur, S.: Rough terrain quadruped robot- BigDog. Mater. Todays Proc. **81**(2), 481–485 (2023)
7. Masato, H., Kenichi, O.: Honda humanoid robots development. Phil. Trans. R. Soc. A. **365**, 11–19 (2007)
8. Prasad, L.B., Tyagi, B., Gupta, H.O.: Optimal control of nonlinear inverted pendulum system using PID controller and LQR: performance Analysis without and with disturbance input. Int. J. Autom. Comput. **11**, 661–670 (2014)
9. Jmel, I., Dimassi, H., Hadj-Said, S., M'Sahli, F.: An adaptive sliding mode observer for inverted pendulum under mass variation and disturbances with experimental validation. ISA Trans. **102**, 264–279 (2020)
10. Gao, H., Li, X., Gao, C., Wu, J.: Neural network supervision control strategy for inverted pendulum tracking control. Discrete Dyn. Nat. Soc. 1–14 (2021)

Obtaining High-Strength Aluminum Sheets from Powder by Friction-Assisted Lateral Extrusion

Viet Q. Vu[1](✉), Abhishek Pariyar[2], Laszlo S. Toth[3,4,5], and Satish V. Kailas[6]

[1] Mechanical and Materials Engineering Division - International Training Faculty, Thai Nguyen University of Technology (TNUT), Thai Nguyen, Vietnam
vqviet@tnut.edu.vn

[2] Department of Mechanical Engineering, University of Southampton, Southampton, UK

[3] Laboratory of Excellence on Design of Alloy Metals for Low-Mass Structure (Labex-DAMAS), Université de Lorraine, Nancy, France

[4] Laboratoire d'Etude des Microstructures et de Mécanique Des Matériaux (LEM3), Université de Lorraine, Nancy, France

[5] Institute of Physical Metallurgy, Metal-Forming and Nanotechnology, University of Miskolc, Miskolc, Hungary

[6] Department of Mechanical Engineering, Indian Institute of Science, Bangalore, Bangalore, India

Abstract. Consolidating powder to obtain high strength materials with a dense structure is challenging due to the lack of bonding between the powder particles. This study aims to overcome this challenge by using an effective and efficient processing called Friction-Assisted Lateral Extrusion. In this work, both Al1050-bulk and Al1050-powder were processed by the FALEP process at room temperature in a single-step deformation. The microstructure and texture transformations and the improvement in mechanical properties of the Al1050-bulk and Al1050-powder samples were investigated. The results showed that the Al1050-powder sample was successfully consolidated at room temperature with a high density and high efficiency. Although the microstructure of the bulk processed sample was significantly refined, its grain size was still larger than that of the powder-consolidated samples. The smaller grain size and the presence of the oxide particles in the consolidated samples, acting as obstacles hindering dislocation motion, could have resulted in their superior mechanical strength compared with that of the bulk processed sample.

Keywords: powder consolidation · Friction-Assisted Lateral Extrusion · mechanical strength

1 Introduction

Via the assembly of individual particles, powder metallurgy (PM) is an effective means to produce near-net-shape products with a specifically designed composition. It can also avoid coarse and segregated microstructures that are typically formed by casting

D. C. Nguyen et al. (Eds.): ICERA 2023, LNNS 944, pp. 261–270, 2024.
https://doi.org/10.1007/978-3-031-62235-9_25

processes. However, the disadvantage of PM is that it requires a hot isostatic pressing or sintering treatment after the compacting step to reduce porosities formed in the compacted sample in order to reach a full densification. This treatment, on the other hand, causes unfavorable grain growth or even phase changes in the material, which deteriorates the microstructure of the processed sample [1]. In addition, this high temperature treatment needs to be carried out in inert atmosphere, which adds an increase in the manufacturing cost. Recently, severe plastic deformation (SPD) processing has been employed to address these problems. Using SPD methods allows to decrease the temperatures required for consolidating metallic powders, and therefore can avoid grain growth and phase changes [2]. SPD can be even applied at room temperature for consolidating metallic powders, which gives significant grain refinement along with good densification [3]. The most used SPD techniques for consolidating powders are High Pressure Torsion (HPT) [4–7], equal channel angular pressing (ECAP) [8–12]. These SPD techniques impose a very large shear strain and high hydrostatic pressure on the processed sample which is effective to consolidate powders at low or room temperatures. These techniques, however, exhibit some limitations. ECAP can only offer a limited amount of shear strain (less than two depending on the configuration) in one processing pass, and might therefore require several processing passes to accumulate a large plastic strain in case a significant grain refinement is required. HPT can impose an extremely high shear strain but the sample shape is limited to the form of a disk with its diameter usually not more than about 20 mm and its thickness usually restricted to about 1 mm [6, 13].

Recently, a new SPD process called friction-assisted lateral extrusion (FALEP) has been proposed to address these limitations [14]. FALEP is able to produce a relatively large sample with a significant imposed shear strain. In the study [14], FALEP was used to deformed bulk Al-1050 to produce sheets with an imposed shear strain of 20. The microstructure was refined to 0.6 μm in grain size and the produced texture is simple shear texture with a shear plane nearly parallel to the plane of the sheet that enhances Lankford value which was measured at 1.28. The yield strength increased by about 10 times, and the ultimate strength increased by three times after the processing. These advantages of the FALEP process were obtained from the development of the Plastic Flow Machining (PFM) process by the same author [15–18]. In the present study, FALEP is used to produce Al-1050 sheets from a bulk sample and also from powders via a consolidating process at room temperature. The results obtained from these two cases (initial bulk sample and initial powders) will be compared. The differences will reveal the effects of the oxide layers covering the surface of Al powder particles on microstructure, texture and mechanical properties of the processed sample.

2 Experimental Procedures

Commercial aluminum Al-1050 powders with an average grain size of 50 μm and an Al-1050 billet with an initial grain size of 100 μm were used as the starting materials in the present work. The powders were poured into the FALEP die and consolidated at room temperature. The billet was inserted into the die and processed in the same conditions as the powders. The processing is illustrated in the Fig. 1 below.

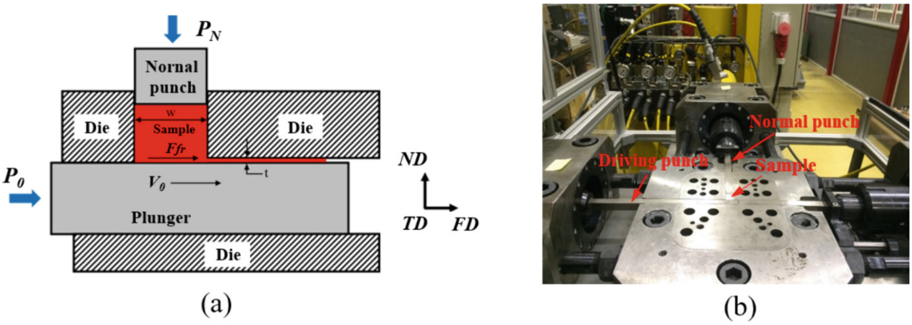

Fig. 1. Schematic and experimental setup of FALEP processing

During processing, under the normal force caused by the normal punch and the friction force between the sample and the driving punch, the material flows out laterally throughout the outlet between the die and the driving punch (Fig. 1a). This principle seems to be like in a normal extrusion process; however, the noticeable difference is that by moving the driving punch, the friction force Ffr is applied on the bottom of the sample in the direction of its extrusion, thus assisting the material to flow into the gap. Therefore, in this process, the friction has a positive role as a driving force for the extrusion. Note that in other SPD processes, the friction force has a negative role because it acts opposite to the material flow, hindering the process.

The experiments were conducted in an ECAP machine in which the normal punch and driving punch are controlled by a hydraulic piston-cylinder system with the maximum force capacity of each hydraulic punch was 72 tons (Fig. 1b). The vertical channel was in a square shape of 20 mm × 20 mm while that of the horizontal channel was set at a thickness of 1.5 mm for the bulk and powder samples. In addition, another thickness of 0.5 mm was also set for the powder sample to examine the effect of shear strain. The microstructure of the fin produced from the bulk sample was examined by EBSD using a JEOL JSM-6500F field-emission gun-scanning electron microscope. For the case of the powder sample, Focused Ion Beam-scanning electron microscopy (FIB-SEM). For EBSD analyses, ATEX software [19] was used. To examine mechanical properties, tensile tests were performed at room temperature. Tensile direction was set parallel to the longitudinal direction of the fin, and the strain rate was 0.001 s^{-1}.

3 Results and Discussions

3.1 Microstructure Transformation by FALEP

The FIB-SEM micrograph of the Al1050-powder consolidated specimen obtained after FALEP is shown in Fig. 2. The specimen was well consolidated with a good surface finish. The density value of the sample was defined at 2.69 ± 0.01 g/cm^3 using the Archimede's principle. It can be seen that there is the presence of porosities, which indicates the consolidation process took place effectively. Moreover, particles with higher atomic contrast can be spotted on the rest microstructure of the Al1050-powder consolidated sample. These particles can be attributed to aluminum oxide layers fragmented at the boundary area of Al powder particles [20, 21].

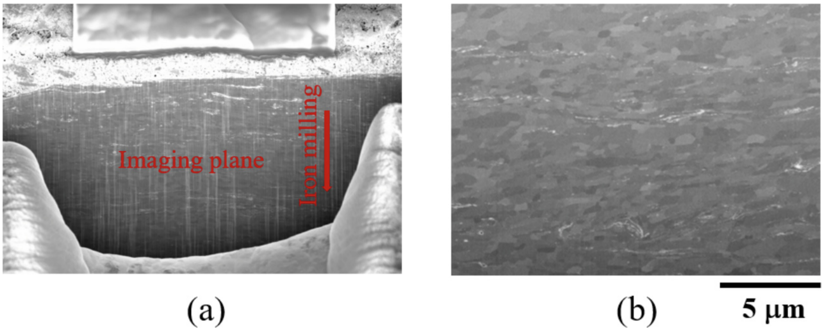

Fig. 2. FIB-SEM microstructure of the Al-powder consolidated specimens produced by FALEP.

The microstructures of the Al1050-powder consolidated samples and the Al1050-bulk sample that were produced by FALEP were obtained and then compared by using the EBSD measurements. Figure 3 shows the inverse pole figure (IPF) maps of these samples on the ND-FD plane.

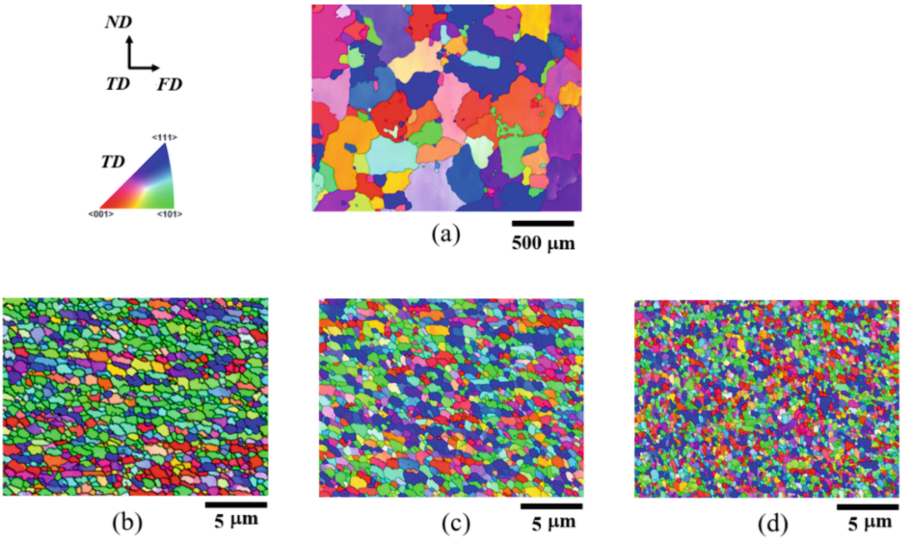

Fig. 3. EBSD microstructures of (a) and (b): initial bulk and bulk processed samples with 1.5mm thickness; (c) and (d): powder-consolidated processed samples with 1.5 mm thickness and 0.5 mm thickness, respectively.

The average grain size of the initial Al1050 bulk sample was 100 µm which decreased to 600 nm after the FALEP processing with the sheet thickness t = 1.5 mm (Fig. 1a).

Meanwhile, the average grain sizes of the Al-power-consolidated processed samples were defined at 500 nm and 390 nm, respectively. These results show the significant grain refinement effect of the FALEP processing that contributes to the significant improvement in mechanical strength of Aluminum (will be discussed in the later section). The grain refinement effect induced by severe plastic deformation is quite well documented [22]. The grain refinement process starts with the formation of geometrically necessary dislocations (GNDs) [23]. These dislocations are necessary to accommodate the strain heterogeneity which is caused by plastic deformation, mostly at grain boundaries. GNDs are same-signed dislocations grouped together to form geometrically necessary boundaries (GNBs) GND or dense walls [23, 24]. The next stage of the grain refinement process is the transformation of GNDs into high angle grain boundaries (HAGBs). This transformation is due the increase in the misorientations between sub-grains, leading to the formation of new grains surrounded HAGBs. The process of with the forming and transforming GNBs under high strain helps the microstructure continued to be refined with smaller grain sizes. In FALEP processing, the initial grain size of 100 μm of the Al1050 bulk samples was refined to 600 nm after the process (Figs. 3a–b). Under high strain, the 50 μm Al1050 powder particles were consolidated to form samples with small grain sizes of 500 nm (for the 1.5 mm thickness sample) and 390 nm (for the 0.5 mm thickness sample), respectively (Figs. 3c–d). The smaller grain size obtained in the 0.5 mm thickness sample is due to the higher strain imposed in this sample compared to the 1.5 mm thickness sample. This grain refinement in the powder consolidated samples after the FALEP processing indicates that room temperature recrystallization took place in the samples thanks to high strain. This process is commonly called continuous dynamic recrystallization (CDRX) process that characterized by the continuous grain refinement process with the formation of GNBs and their transformation into HAGBs [22].

3.2 Micro-Texture Transformation by FALEP

Texture refers to orientation distribution of grains in orientation space and is represented by pole figures (PF) and orientation distribution functions (ODFs). A PF is a stereographic projection of crystallographic directions on the sample reference [25], while the ODF shows the distribution of crystal orientations in Euler space. Each orientation is defined by three Euler angles (φ1, Φ, φ2). If the orientation is represented by the vector g(φ1, Φ, φ2), the ODF can be defined as [25]:

$$f(g)\Delta g = \frac{\Delta V}{V} \text{ with } \Delta g \to 0 \tag{1}$$

where, $f(g)$ is the function of orientation density, V is the volume of the sample, ΔV is the grain orientation volume within the Δg is orientation interval [25].

The PFs can be recalculated from the ODF to display the texture in a more effective way with respect to the sample reference system. The PF results obtained for the bulk and powder consolidated samples before and after the FALEP processing are shown in Fig. 4. Figure 4a shows the initial texture of the bulk sample which is more or less random and the textures produced by the FALEP processing of the bulk and consolidated samples are shown in Figs. 4c–e. As can be seen, the strain mode imposed by the FALEP processing is defined as the simple shear deformation mode. The identification of the simple shear texture is confirmed by the ideal orientations of FCC materials deformed by simple shear plastic deformation (Fig. 4b).

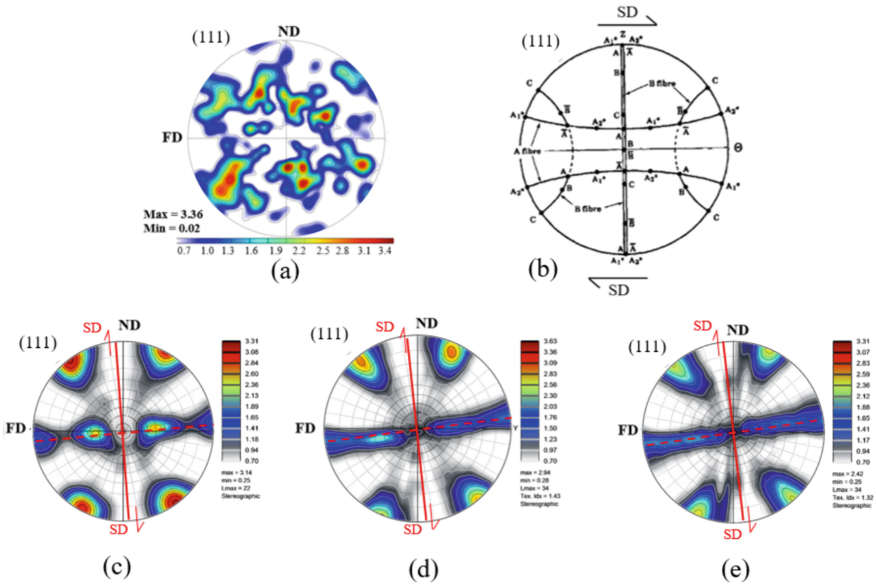

Fig. 4. (111) PFs showing the texture transformation by FALEP. (a): initial bulk sample, (b) ideal texture orientations of simple shear FCC metals, (c) initial bulk and bulk processed samples with 1.5mm thickness; (d) and (e): powder-consolidated processed samples with 1.5 mm thickness and 0.5 mm thickness, respectively.

In Figs. 4c–e, the C texture components appear to have strong intensities. This is a typical characteristic of simple shear textures of aluminum [26, 27] in which high stacking fault energy metals like Aluminum are recorded to develop strong B fiber including the C texture component during severe plastic deformation [16–18]. It also can be seen that the powder-consolidated samples have more continuous and uniform B fibers than the bulk processed sample (Figs. 4c–e). This is probably due to the fact that the initial bulk sample had some cube texture components retained from rolling while the initial texture of the powder samples was random. The development of the cube component in the initial bulk sample would result in the stronger concentration of the grain orientations towards the C texture orientations, causing the less uniform B fiber of the bulk sample texture compared with that of the powder-consolidated ones. Lastly, the texture intensity of the powder-consolidated sample with 1.5 mm thickness (Max 2.94) is observed to be greater than that of the sample with 0.5 mm thickness (Max 2.42). This can be attributed to the higher shear strain produced in the later sample. At higher shear strains, grain boundary sliding (GBS) can cause the weakening of the texture [28].

3.3 Mechanical Property Improvement by FALEP

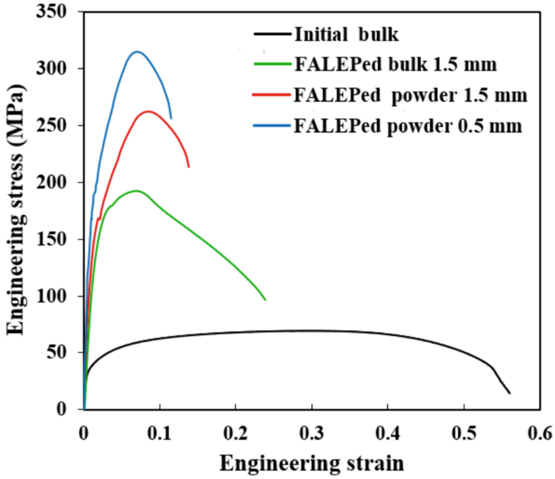

Fig. 5. Mechanical properties of Al1050-bulk and Al1050-powder consolidated processed at room temperature by FALEP.

Tensile tests were performed for the Al1050-bulk and Al1050-powder consolidated processed samples a strain rate of 0.001 s^{-1} and the results are shown in Fig. 5. As can be seen, both bulk and powder-consolidated Aluminum samples exhibit significant improvements in yield strengths and ultimate strengths compared with the initial bulk sample. Specifically, the ultimate yield strengths were measured at 320 MPa for the powder-consolidated sample with 0.5 mm thickness, 260 MPa for the powder-consolidated sample with 1.5 mm thickness, and 190 MPa for the bulk sample with 1.5 mm thickness, respectively. Whereas, the initial bulk sample had a far small ultimate strength of 70 MPa. This shows a great advantage FALEP processing in improving material strength. Ductility, on the other hand, declined, as a result of the increase in strength. This is a typical characteristic of the severe plastic deformation and cold working. The enhancement of the mechanical strength during FALEP processing is associated with the well-known Hall-Petch relation:

$$\sigma_y = \sigma_0 + \frac{k}{\sqrt{d}} \tag{2}$$

where σy is the yield strength, k is a material constant, and d is the average grain size of the material.

Since grain refinement by FALEP in this study takes place at room temperature, grain growth is hindered. As a result, ultrafine grained microstructures with small grain sizes (d) are obtained (390 ÷ 600 nm), which in turn enhance the mechanical strength according to the Eq. 2. This level of grain refinement is greatly significant that conventional thermo-mechanical processing is not capable of [14]. Moreover, FALEP showed higher efficiency because only one deformation pass was needed for obtaining this superior enhancement in mechanical strength; the other severe plastic deformation processes, on the other hand, require several passes to reach similar mechanical properties [14]. It is also observed from Fig. 5 that the powder-consolidated sample exhibited higher strength than the bulk processed sample with the same thickness of 1.5 mm. This can be attributed to the presence of oxide particles that can strengthen a material [29–32]. These particles were visible in the FIB-SEM images (Fig. 2). They serve a role as obstacles impeding dislocation motion, which in turn, can significantly increase the mechanical strength of the powder-consolidated sample.

4 Conclusions

In this work, both Al1050-bulk and Al1050-powder were processed by the FALEP process at room temperature in a single-step deformation with high efficiency. The microstructure and texture transformations and the improvement in mechanical properties of the Al1050-bulk and Al1050-powder samples were examined and studied. Some conclusions can be drawn from the obtained results as follows.

- The Al1050-powder sample was successfully consolidated at room temperature with a high density that mostly reached the value of the bulk sample.
- The powder-consolidated sample with 0.5 mm thickness had the average grain size of 390 nm, smaller than that of the powder-consolidated sample with 1.5 mm thickness with 500 nm. The smaller grain size of the former can be attributed to the higher shear strain imposed during FALEP processing. Meanwhile, the bulk processed sample had the biggest average size of 600 nm.
- Texture measurements of both powder-consolidated and bulk processed samples confirmed the simple shear deformation mode of the FALEP processing. Texture measurements also exhibited the dominance of the C component and B fiber which is a typical characteristic of simple shear texture in Aluminum.
- FALEP process significantly improved mechanical strengths of materials. The ultimate strengths of the powder-consolidated samples were 320 and 260 MPa for the 0.5 mm and 1.5 mm thickness samples, respectively. Whereas, that of the bulk processed sample was lower, at 190 MPa. This can be attributed to the presence of the oxide particles in the powder-consolidated samples, serving as obstacles restricting dislocation motion.

Acknowledgments. The authors would like to thank Thai Nguyen University of Technology (TNUT), Vietnam for the support.

References

1. Carter, C.B., Norton, M.G.: Sintering and grain growth. In: Carter, C.B., Norton, M.G. (eds.) Ceramic Materials: Science and Engineering, pp. 427–443. Springer, New York (2007). https://doi.org/10.1007/978-0-387-46271-4_24
2. Valiev, R., Islamgaliev, R., Alexandrov, I.V.: Bulk nanostructured materials from severe plastic deformation. Prog. Mater. Sci. **45**, 103–189 (2000)

3. Zhao, Y., Massion, R., Thierry, G., Toth, L.: Contribution of shear deformation to grain refinement and densification of iron powder consolidated by high pressure torsion. IOP Conf. Ser. Mater. Sci. Eng. **63**, 012032 (2014)
4. Botta, W., Fogagnolo, J., Rodrigues, C., Kiminami, C., Bolfarini, C., Yavari, A.: Consolidation of partially amorphous aluminium-alloy powders by severe plastic deformation. Mater. Sci. Eng. A **375**, 936–941 (2004)
5. Khajouei-Nezhad, M., Paydar, M.H., Ebrahimi, R., Jenei, P., Nagy, P., Gubicza, J.: Microstructure and mechanical properties of ultrafine-grained aluminum consolidated by high-pressure torsion. Mater. Sci. Eng. A **682**, 501–508 (2017)
6. Panda, S., Toth, L.S., Zou, J., Grosdidier, T.: Effect of strain heterogeneities on microstructure, texture, hardness, and H-activation of high-pressure torsion mg consolidated from different powders. Materials **11**(8), 1335 (2018)
7. Stolyarov, V., Zhu, Y., Lowe, T., Islamgaliev, R.K., Valiev, R.: Processing nanocrystalline Ti and its nanocomposites from micrometer-sized Ti powder using high pressure torsion. Mater. Sci. Eng. A **282**, 78–85 (2000)
8. Derakhshandeh. H, R., Jenabali Jahromi, A.: An investigation on the capability of equal channel angular pressing for consolidation of aluminum and aluminum composite powder. Mater. Des. **32**(6), 3377–3388 (2011)
9. Haouaoui, M., Karaman, I., Harwig, K.T., Maier, H.J.: Microstructure evolution and mechanical behavior of bulk copper obtained by consolidation of micro- and nanopowders using equal-channel angular extrusion. Metall. Mater. Trans. A **35**(9), 2935–2949 (2004)
10. Lapovok, R., Tomus, D., Bettles, C.: Shear deformation with imposed hydrostatic pressure for enhanced compaction of powder. Scripta Mater. **58**(10), 898–901 (2008)
11. Matsuki, K., Aida, T., Takeuchi, T., Kusui, J., Yokoe, K.: Microstructural characteristics and superplastic-like behavior in aluminum powder alloy consolidated by equal-channel angular pressing. Acta Mater. **48**(10), 2625–2632 (2000)
12. Senkov, O., Senkova, S., Scott, J., Miracle, D.: Compaction of amorphous aluminum alloy powder by direct extrusion and equal channel angular extrusion. Mater. Sci. Eng. A **393**, 12–21 (2005)
13. Panda, S.: New processing routes by high-pressure torsion of different nature of magnesium based powders for improved hydrogen storage applications. Université de Lorraine (2018)
14. Vu, V.Q., Toth, L.S., Beygelzimer, Y., Zhao, Y.: Microstructure, texture and mechanical properties in aluminum produced by friction-assisted lateral extrusion. Materials **14**(9), 2465 (2021)
15. Vu, V.Q., Beygelzimer, Y., Kulagin, R., Toth, L.S.: Mechanical modelling of the plastic flow machining process. Materials **11**(7), 1218 (2018)
16. Vu, V.Q., Beygelzimer, Y., Kulagin, R., Toth, L.S.: The new plastic flow machining process for producing thin sheets. Adv. Mater. Sci. Eng. **2018**, 8747960 (2018)
17. Vu, V.Q., Beygelzimer, Y., Toth, L.S., Fundenberger, J.-J., Kulagin, R., Chen, C.: The plastic flow machining: a new SPD process for producing metal sheets with gradient structures. Mater. Charact. **138**, 208–214 (2018)
18. Vu, V.Q., Toth, L.S., Beygelzimer, Y., Kulagin, R., Kobaissy, A.H.: Modeling of crystallographic texture in plastic flow machining. Adv. Eng. Mater. **22**(1), 1900661 (2020)
19. Beausir, B., Fundenberger, J.-J.: ATEX-software, Analysis Tools for Electron and X-ray diffraction. Université de Lorraine - Metz (2017). www.atex-software.eu
20. Hasani, S., Panjepour, M., Shamanian, M.: The oxidation mechanism of pure aluminum powder particles. Oxid. Met. **78**, 179–195 (2012)
21. Zhang, S., Dreizin, E.L.: Reaction interface for heterogeneous oxidation of aluminum powders. J. Phys. Chem. C **117**(27), 14025–14031 (2013)
22. Vu, V.Q., Pariyar, A.: Recrystallization in metals and continuous dynamic recrystallization via severe plastic deformation. In: Nucleation and Growth in Applied Materials (2023)

23. Hughes, D.A., Hansen, N., Bammann, D.J.: Geometrically necessary boundaries, incidental dislocation boundaries and geometrically necessary dislocations. Scripta Mater. **48**(2), 147–153 (2003)
24. Hughes, D.A., Hansen, N.: High angle boundaries formed by grain subdivision mechanisms. Acta Mater. **45**(9), 3871–3886 (1997)
25. Kocks, F., Tomé, C., Wenk, H.R.: Texture and Anisotropy. Preferred Orientations in Polycrystals and Their Effect on Material Properties (2000)
26. Liu, R., Wang, W., Chen, H., Tan, M., Zhang, Y.: Microstructure evolution and mechanical properties of micro-/nano-bimodal size B4C particles reinforced aluminum matrix composites prepared by SPS followed by HER. Vacuum **151**, 39–50 (2018)
27. Naghdy, S., Kestens, L., Hertelé, S., Verleysen, P.: Evolution of microstructure and texture in commercial pure aluminum subjected to high pressure torsion processing. Mater Charact **120**, 285–294 (2016)
28. Skrotzki, W., et al.: New experimental insight into the mechanisms of nanoplasticity. Acta Mater. **61**(19), 7271–7284 (2013)
29. Bachmaier, A., Pippan, R.: Effect of oxide particles on the stabilization and final microstructure in aluminium. Mater. Sci. Eng. A **528**(25), 7589–7595 (2011)
30. Wang, C., et al.: Strengthening mechanism and effect of Al2O3 particle on high-temperature tensile properties and microstructure evolution of W-Al2O3 alloys. Mater. Sci. Eng. A **835**, 142678 (2022)
31. Asgharzadeh, H., Simchi, A., Kim, H.: Microstructure and mechanical properties of oxide-dispersion strengthened Al6063 alloy with ultra-fine grain structure. Metall. Mater. Trans. A **428**, 16–824 (2011)
32. Saka, N., Suh, N.: Delamination wear of dispersion-hardened alloys (1977)

Optimal Design Using BCMO Algorithm of Fuzzy Controllers for Active Suspension Systems

Hai-Le Bui(✉)

Hanoi University of Science and Technology, Hanoi, Vietnam
le.buihai@hust.edu.vn

Abstract. This report presents the optimal design problem of fuzzy controllers in vibration control of active suspension systems. In fuzzy controllers, the control rule base, the reference range of variables, and the distribution of membership functions of variables in the fuzzification step are often determined based on experts' experience. Therefore, the parameters to set up the above components can be considered as design variables to optimize fuzzy controllers in the present work. The investigated model is the active suspension of a quarter car model. The Balancing Composite Motion Optimization (BCMO), a recently introduced swarm-based algorithm, is used as the tool when optimizing the controllers. Simulation results indicate that the proposed controllers have a high efficiency compared to the one in a published study with the same maximum control force. With a large number of design variables, it is possible to consider that the optimal approach to the controllers in this paper is overall.

Keywords: Active Suspension · Fuzzy Control · Optimization

1 Introduction

Active suspension systems are increasingly attractive in research and increasingly popular in the vehicle industry. Modern and intelligent control algorithms are often used for these systems [1–3].

Controllers based on fuzzy set theory (FCs) play an important role and are increasingly common in research as well as practical applications because of their outstanding advantages [4–6]. However, the empirical determination of many parameters of fuzzy controllers is their disadvantage.

A recently novel optimal algorithm, Balancing Composite Motion Optimization (BCMO), has been validated and applied effectively in various studies [7–10].

For the above reasons, the optimization problem using BCMO of fuzzy controllers in control of active suspension systems is proposed in this study. The optimal approach is overall with a large number of design variables, including parameters: the range of the variables, the distribution of membership functions of the variables, and the weights of the rules in the control rule base. Thus, these parameters are optimized based on different objective functions instead of being determined based on experience. As a result, optimized fuzzy controllers provide high efficiency in simulations.

D. C. Nguyen et al. (Eds.): ICERA 2023, LNNS 944, pp. 271–276, 2024.
https://doi.org/10.1007/978-3-031-62235-9_26

2 Investigated Model

Consider the active suspension of a quarter-car model in Fig. 1 [1]. The model's parameters include the body and wheel masses (m_1, m_2), the suspension and tyre damping coefficients (c_1, c_2), and the suspension and tire stiffnesses (k_1, k_2). The control force u is applied between two masses m_1 and m_2. The vertical displacements of the car body and the wheel are x_1 and x_2, respectively. The bump road profile x_r, as shown in Fig. 1, corresponds to the height and length of the bump being 0.08 and 5 m, respectively, and the vehicle's speed is 45 km/h (12.5 m/s). The system's state equations are [1, 2]:

$$\begin{bmatrix} m_1 & 0 \\ 0 & m_2 \end{bmatrix}\begin{Bmatrix} \ddot{x}_1 \\ \ddot{x}_2 \end{Bmatrix} + \begin{bmatrix} c_1 & -c_1 \\ -c_1 & c_1 + c_2 \end{bmatrix}\begin{Bmatrix} \dot{x}_1 \\ \dot{x}_2 \end{Bmatrix} + \begin{bmatrix} k_1 & -k_1 \\ -k_1 & k_1 + k_2 \end{bmatrix}\begin{Bmatrix} x_1 \\ x_2 \end{Bmatrix} = \begin{Bmatrix} 0 \\ c_2\dot{x}_r + k_2 x_r \end{Bmatrix} + \begin{Bmatrix} u \\ -u \end{Bmatrix} \quad (1)$$

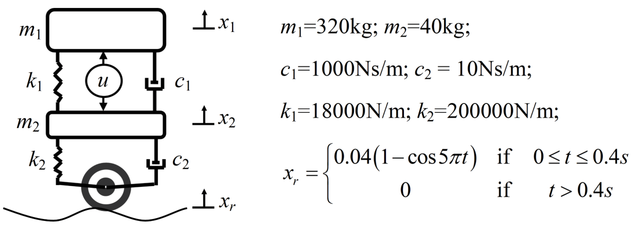

Fig. 1. Investigated model.

For this model, parameters that need to be minimized include the maximum body acceleration ($\ddot{x}_{1\,max}$), the suspension deflection (x_1 - x_2), the road holding or the relative tire force $k_2(x_2 - x_r)/(g(m_1 - m_2))$ (this parameter must be less than 1, and g is the gravity acceleration), the tyre deflection ($x_2 - x_r$), and the car body displacement x_1.

3 Control Design

The system's control diagram is shown in Fig. 2. In which the "And method" is min, the Implication is min, the Aggregation is max, and the De-fuzzification is the centroid.

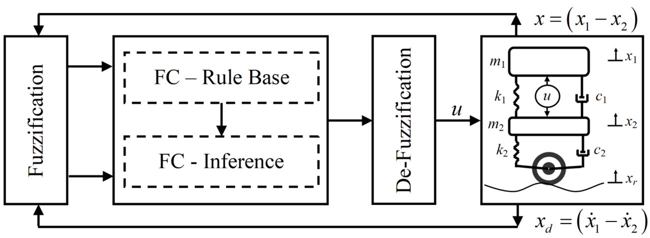

Fig. 2. System's control diagram.

The fuzzification of variables uses triangulation functions, see Fig. 3. The variable x includes five linguistic values: Very Negative (VN), Negative (N), Zero (Z), Positive (P), and Very Positive (VP). The variable x_d includes three linguistic values: N, Z, and P. Finally, the variable u contains seven linguistic values: Very VN (VVN), VN, N, Z, P, VP, and Very VP (VVP). The control rule base consists of 15 rules arranged in Table 1, in which the numbers in parentheses represent the order of the corresponding rules.

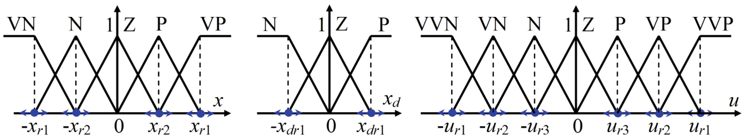

Fig. 3. Fuzzification of variables x, x_d, and u.

Table 1. Control rule base

x_d	x				
	VN	N	Z	P	VP
N	VVP (1)	VP (4)	P (7)	Z (10)	N (13)
Z	VP(2)	P (5)	Z (8)	N (11)	VN (14)
P	P (3)	Z (6)	N (9)	VN (12)	VVN (15)

Next, the optimal problem of fuzzy controllers is performed. The objective functions include minimizing maximum body acceleration and suspension deflection:

$$\ddot{x}_{1\,\max} \rightarrow \min \tag{2}$$

$$(x_1 - x_2) \rightarrow \min \tag{3}$$

Note that by minimizing the maximum body acceleration and/or suspension deflection, the relevant quantities, as described in Sect. 2, will also be reduced. The fuzzy controllers optimized based on Eqs. 2 and 3 are denoted FC_A and FC_SD, respectively. Design variables include:

* Fuzzification parameters of variables: x_{r1}, x_{r2}, x_{dr1}, u_{r1}, u_{r2}, and u_{r3} (see Fig. 3).

* Weights $w_i \in [0, 1]$ of control rules, $i = 1$–15.

Constraints involve:

* $k_2(x_2 - x_r)/(g(m_1 - m_2)) < 1$. This constraint ensures the vehicle's road holding.

* $|u_{\max}| \leq 50\text{N}$, $|\ddot{x}_{1\,\max}| \leq 0.1\text{m/s}^2$ in a period of 1.5 to 3s (end time of simulations). This constraint quickly eliminates the vehicle's vibration.

* $|u_{\max}| \leq 918\text{N}$, this constraint facilitates the comparison of results with the controller in [1].

* $x_{r1} > x_{r2}$; $u_{r1} > u_{r2} > u_{r3}$. These constraints provide the appropriate placement of the membership functions.

The fuzzy controllers are optimized using the BCMO algorithm.

4 Numerical Simulations

This section presents the numerical simulation results for the FC_A and FC_SD controllers. In addition, the robustness controller (denoted by Hinf) in [1] is also included for comparison. Hinf's formula for determining the control force u is [1]:

$$u = 10^4[1.0098\ \ 4.9655\ \ -0.1896\, 0.0909][x_1 - x_2\ x_2 - x_r\ \dot{x}_1\ \dot{x}_2]^{\mathrm{T}} \tag{4}$$

The optimal fuzzification diagram for variables of the controllers FC_A and FC_SD is shown in Fig. 4. The rules' optimal weights w_i are plotted in Fig. 5. Figure 6 shows the time response of the body acceleration, the suspension deformation, the control force, the relative tyre force, the tyre deflection, and the body displacement. The results in Fig. 4 show that the fuzzification diagrams of FC_A are relatively well-balanced. The distribution of membership functions of x tends to be slightly clustered towards Z. In contrast to FC_SD, there is a significant disproportion in the fuzzification diagrams of x and u. The distribution of membership functions of x is very close to Z, while the distribution of membership functions of u is far from Z.

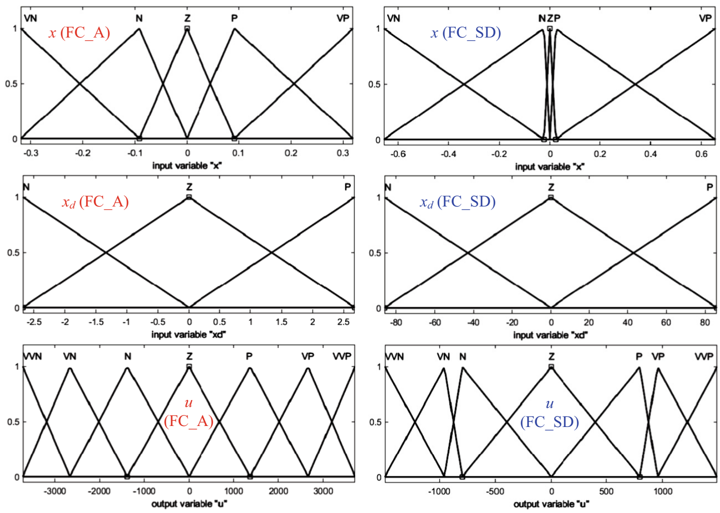

Fig. 4. Optimal fuzzification diagram of variables x, x_d, and u.

The optimal values of the weights w_i, $i = 1$–15, in Fig. 5 show the importance of each rule in each controller. The time response in Fig. 6 indicates that the controller FC_A has remarkable control efficiency for most parameters. Specifically, for the crucial criterion (body acceleration) in Fig. 6a, FC_A, FC_SD, and Hinf reduce it by 61%, 41%, and 27%, respectively, compared with the open loop case (denoted OL). In addition, the settling time for this criterion of FC_A and Hinf is equivalent. It is noted that the maximum control force of FC_A and Hinf is also approximately equal (~918N), while this value of FC_SD is only 585N, see Fig. 6c. Another important parameter is the suspension deflection in Fig. 6b. It can be seen that FC_SD and Hinf are equally effective for this

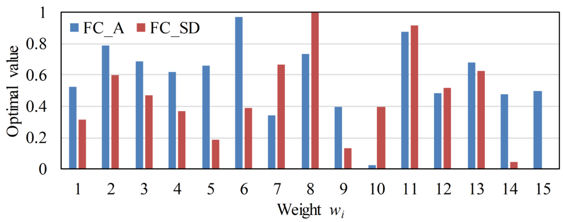

Fig. 5. Optimal value of w_i.

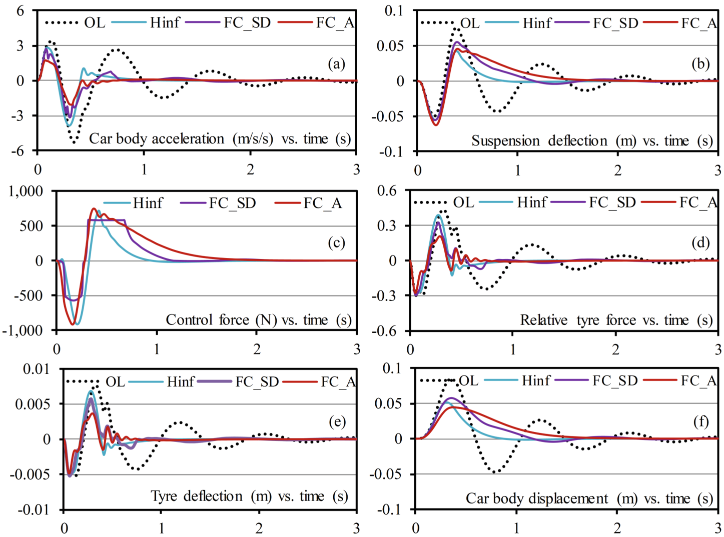

Fig. 6. Time responses of the system: (a) Car body acceleration; (b) Suspension deflection; (c) Control force; (d) Relative tyre force; (e) Tyre deflection; (f) Car body displacement

parameter, reducing about 27% compared to the OL case. However, FC_A only reduces the suspension deflection by 18%. For the criteria relative tyre force and tyre deflection in Figs. 6d and 6e, the order of efficiency of the controllers is FC_A, FC_SD, and Hinf, reductions of 37%, 25%, and 10%, respectively. In which the settling time of all three controllers is equivalent. In addition, FC_A also gives the highest control efficiency for car body displacement, as shown in Fig. 6f.

5 Conclusions

This paper presents the problem of the optimal design of fuzzy controllers for active suspension systems of the quarter car model. The optimization problem is established based on these variables with suitable objective functions and constraints for the investigated model by giving the parameters determined empirically by a fuzzy set theory-based controller. This optimal approach is simple, explicit, and overall. The simulation results show that the proposed optimal fuzzy controllers, FC_A and FC_SD, are more efficient than the Hinf controller. Applying this approach to more complex active suspension models will be the essential development of this study.

Acknowledgment. This research is funded by Hanoi University of Science and Technology (HUST) under project number T2023-PC-007.

References

1. Sun, W., Gao, H., Shi, P.: Advanced Control for Vehicle Active Suspension Systems. Springer, Cham (2020). https://doi.org/10.1007/978-3-030-15785-2
2. Bui, H.-L.: Multi-objective optimization of hedge-algebra-based controllers for quarter-car active suspension models. In: Khang, N.V., Hoang, N.Q., Ceccarelli, M. (eds.) ASIAN MMS 2021 IFToMM. Springer, pp. 876–85 (2021). https://doi.org/10.1007/978-3-030-91892-7_84
3. Mac, T.-T., Nguyen, T.-D., Bui, H.-L., Tran, N.-A.: Optimal design of hedge-algebras–based controller for vibration control of vehicle suspension systems. In: Proceedings of the Institution of Mechanical Engineers, Part I: Journal of Systems and Control Engineering (2023). https://doi.org/10.1177/09596518231196900
4. Bui, H.-L., Tran, Q.-C.: A new approach for tuning control rule based on hedge algebras theory and application in structural vibration control. J. Vib. Control **27**(23–24), 2686–2700 (2021)
5. Bui, H.-L., Pham, M.-N., Nguyen, T.-T.-H.: Swing-up control of an inverted pendulum cart system using the approach of Hedge-algebras theory. Soft. Comput. **26**(10), 4613–4627 (2022)
6. Nguyen, T.-D., Bui, H.-L.: General optimization procedure of the Hedge-algebras controller for controlling dynamic systems. Artif. Intell. Rev. **56**, 2749–2784 (2022). https://doi.org/10.1007/s10462-022-10242-0
7. Bui, H.-L., Tran, N.-A.: Multi-objective optimal design of TMDs for increasing critical flutter wind speed of bridges. J. Wind Eng. Ind. Aerodyn. **225**, 104992 (2022)
8. Bui, H.-L., Tran, N.-A., Cao, Q.-H.: Active control based on hedge-algebras theory of seismic-excited buildings with upgraded tuned liquid column damper. J. Eng. Mech. **149**(1), 04022091 (2022). https://doi.org/10.1061/JENMDT/EMENG-6821
9. Bui, H.-L.: An approach for optimizing the hedge-algebras-based controller and application in structural vibration control. In: Nguyen, D.C., Vu, N.P., Long, B.T., Puta, H., Sattler, KU. (eds.) ICERA 2022. LNCS, vol. 602, pp. 157–165. Springer, Cham (2022). https://doi.org/10.1007/978-3-031-22200-9_17
10. Bui, V.-B., Mac, T.-T., Bui, H.-L.: Design optimization considering the stability constraint of the Hedge-algebras-based controller for building structures subjected to seismic excitations. Proc. Inst. Mech. Eng. Part I: J. Syst. Control Eng. (2023). https://doi.org/10.1177/09596518231171960

Optimal Fuzzy Control of Building Models Under Seismic Excitations

Van-Bao Hoang[1], Hong-Son Nguyen[2], Van-Tuan Nguyen[3], Thi-Thoa Mac[1], Dinh-Ba Bui[1], and Xuan-Thuan Nguyen[1](✉)

[1] Hanoi University of Science and Technology, Hanoi, Vietnam
thuan.nguyenxuan@hust.edu.vn
[2] Hanoi University of Industry, Hanoi, Vietnam
[3] PHENIKAA University, Hanoi, Vietnam

Abstract. Structures' vibration active control problem has always been of interest in research and industrial applications. This study presents the optimization of a controller based on fuzzy set theory (FC) to control building models subjected to seismic load. Optimization aims to minimize the system's peak relative displacement and absolute acceleration. The design variables include the partitioning parameters of the membership functions, the reference range of the variables, the choice of the linguistic value of the control variable in the control rule base, and the weights of the rules. The appropriate constraints are also considered in the optimization process. The optimization tool is the Balancing composite motion optimization (BCMO) algorithm. Calculation results of a robust controller from a published study are also included to validate the performance of the proposed optimal controllers. The simulation results in this study show that the optimized fuzzy controllers have high control efficiency for different earthquake excitations.

Keywords: Building model · Seismic · Fuzzy control · Optimization · BCMO

1 Introduction

Fuzzy logic provides a helpful tool for modeling the linguistic values of linguistic variables. Therefore, controllers based on fuzzy set theory can use qualitative control rule bases represented as relational propositions of linguistic values between input and output variables. These fuzzy control rule bases are usually established based on experts' observations and experience [1].

Fuzzy controllers have been widely applied in industry in general and the mechanical field in particular because of their outstanding advantages compared to other controllers [2, 3]. However, the components as well as the rule base of a fuzzy controller, are often designed based on designers' experience or trial and error. Therefore, optimizing the controller parameters is necessary for the fuzzy controller to be highly effective for a particular controlled model. In this study, the fuzzy controller optimization problem for a building model under earthquake load is performed. The optimization tool is BCMO, a modern algorithm that is simple and highly efficient [4, 5].

D. C. Nguyen et al. (Eds.): ICERA 2023, LNNS 944, pp. 277–282, 2024.
https://doi.org/10.1007/978-3-031-62235-9_27

2 The Controlled Model

Figure 1a shows a 3-story building model with the control force u on the 1st floor. The structure's masses m_i, dampings c_i, and stiffnesses k_i are also shown in this figure [6].

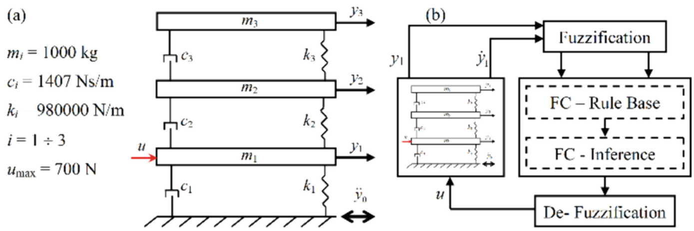

Fig. 1. The controlled model

The system's motion equations are as follows [6, 7]:

$$\begin{aligned} &[M]\{\ddot{y}\} + [C]\{\dot{y}\} + [K]\{y\} = \{F\}; \{y\} = \begin{bmatrix} y_1 & y_2 & y_3 \end{bmatrix}^T \\ &\{F\} = \begin{bmatrix} u - m_1\ddot{y}_0 - m_2\ddot{y}_0 - m_3\ddot{x}_0 \end{bmatrix}^T \end{aligned} \quad (1)$$

The control force u will be calculated from optimal fuzzy controllers, as represented in Sect. 3.

3 Optimal Design of Fuzzy Controllers

In the BCMO method (Balancing Composite Motion Optimization), the solution space is formally referred to as the Cartesian space. In this space, the individuals of the population are ranked according to their objective function values. These individuals then engage in interactive movements within the solution space, with the ultimate goal of identifying the global optimum outcome. An individual is attracted by an upper-ranked one and a perceived "instant global optimization point". In this method, the dynamic between the lower-ranked individual and the higher-ranked individual is seen as a localized search, while the remaining one is characterized as engaging in a global search.

The control diagram of FC with two input state variables (y and $\dot{y}$) is shown in Fig. 1b for the earthquake-loaded building model. In which the controller uses Mamdani's inference and the centroid defuzzification method. The fuzzy controller's components and rule base of FC are shown in Fig. 2.

Where N, Z, P, and V stand for Negative, Zero, Positive, and Very. The data in Fig. 2 shows that FC can be optimized based on the following design variables:

- The parameters of the membership functions: var(1–4).
- Reference ranges of state and control variables: var(5–7).
- The choice of the control variable's linguistic values in the rule base: var(8–32).

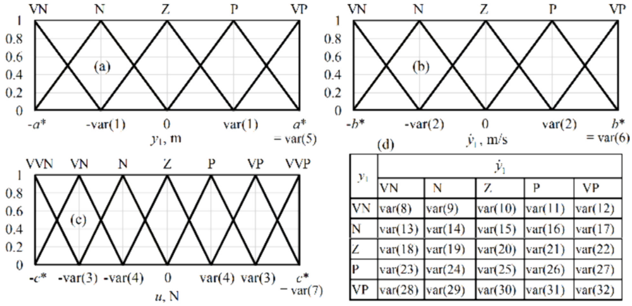

y_1 \ $\dot{y}_1$	VN	N	Z	P	VP
VN	var(8)	var(9)	var(10)	var(11)	var(12)
N	var(13)	var(14)	var(15)	var(16)	var(17)
Z	var(18)	var(19)	var(20)	var(21)	var(22)
P	var(23)	var(24)	var(25)	var(26)	var(27)
VP	var(28)	var(29)	var(30)	var(31)	var(32)

Fig. 2. FC's fuzzification and rule base

The weight of the rules is also considered as the design variable: var(33–57).

The objective functions include:

$$OF_d \rightarrow \min \tag{2a}$$

$$OF_a \rightarrow \min \tag{2b}$$

OF_d and OF_a are the ratio of the system's peak relative displacement and absolute acceleration between the controlled and uncontrolled systems (OL), respectively.

Constraints include:

- $0 < \text{var}(1) < \text{var}(5)$; $0 < \text{var}(2) < \text{var}(6)$; $0 < \text{var}(4) < \text{var}(3) < \text{var}(7)$.
- $1 \leq \text{var}(8–32) \leq 7$, and var(8–32) are integers. The values 1 to 7 of var(8–32) correspond to the linguistic values VVN, VN, N, Z, P, VP, and VVP, as shown in Fig. 2c.
- $0 \leq \text{var}(33–57) \leq 1$.

The population size and number of generations of BCMO are given as 200.

4 Numerical Simulations

Training data during optimization using 1940 El Centro earthquake data with peak acceleration scaled to 0.112g. The optimal fuzzy controllers corresponding to objectives (2a) and (2b) are denoted FCd and FCa. The parameters of FCd include:

- var(1) = 0.405var(5); var(2) = 0.457var(6); var(3) = 0.552var(7); var(4) = 0.182var(7).
- var(5) = 5.316m; var(6) = 0.294 m/s; var(7) = 4780 N.
- var(8–32) = 2, 2, 7, 2, 4, 3, 3, 5, 5, 4, 6, 1, 4, 6, 1, 7, 7, 6, 2, 5, 2, 4, 2, 3, 4.
- var(33–57) = 0.722, 0.471, 0.807, 0.289, 0.320, 0.383, 0.241, 0.590, 0.750, 0.485, 0.175, 0.761, 0.323, 0.488, 0.563, 0.480, 0.356, 0.052, 0.329, 0.046, 0.397, 0.709, 0.327, 0.283, 0.879.

The parameters of FCa include the following:

- var(1) = 0.324var(5); var(2) = 0.112var(6); var(3) = 0.754var(7); var(4) = 0.506var(7).
- var(5) = 0.039 m; var(6) = 0.701 m/s; var(7) = 4176 N.
- var(8–32) = 4, 4, 4, 5, 2, 3, 4, 2, 4, 6, 3, 3, 4, 6, 5, 5, 7, 4, 3, 2, 6, 3, 4, 3, 5.
- var(33–57) = 0.041, 0.774, 0.821, 0.793, 0.604, 0.895, 0.253, 0.499, 0.365, 0.596, 0.371, 0.448, 0.084, 0.529, 0.255, 0.818, 0.773, 0.792, 0.125, 0.141, 0.849, 0.359, 0.343, 0.426, 0.603.

The optimal control rule surfaces of FCd and FCa are plotted in Fig. 3. The criteria OFd and OFa are listed in Table 1. The calculation results of the robustness controller (denoted by Hinf) in [6] are also included for comparison. The formula to determine the control force u of Hinf depends on the system's six state variables as follows [6]:

$$u = 10^5[0.7829 \ -3.6796 \ 2.4813 \ -0.5351 \ -0.0472 \ 0.0427]\begin{Bmatrix} y \\ \dot{y} \end{Bmatrix} \tag{3}$$

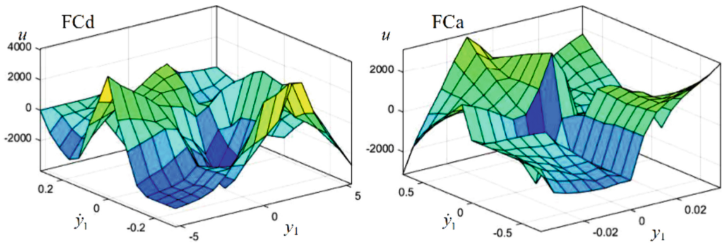

Fig. 3. Optimal rule surfaces of FCd and FCa

Table 1. Criteria OF_d and OF_a, El Centro earthquake

Controller	Hinf [6]	FCd	FCa
OF_d	0.41	0.40	0.43
OF_a	0.53	0.54	0.42
Mean value	0.470	0.470	0.425

The maximum relative displacement (RD) and absolute acceleration (AA) of the floors are shown in Fig. 4. The system's time responses are plotted in Fig. 5. Verification of the optimal fuzzy controllers' performance with the 1994 Northridge, 1999 Chi Chi, and 1999 Duzce earthquakes is shown in Fig. 6.

The results in Table 1 and Fig. 4 show that the proposed optimal fuzzy controllers have high control efficiency for all different earthquakes. Figures 5 and 6 indicate that in the case of the system subjected to the El Centro earthquake, the time response of the control force u of the three controllers is not much different. This phenomenon implies that the control energies of the three controllers Hinf, FCd, and FCa are equivalent. The controller FCa has the highest efficiency and should be preferred for the model under investigation.

In addition, fuzzy controllers use only two state variables, while Hinf uses all state variables (six variables) to calculate the control force. Therefore, FCd and FCa are simpler to use because they require less sensor information than Hinf.

Furthermore, the optimal rule surfaces in Fig. 3 show that the control rule base may not be as monotonous as common experience or observation [7–10].

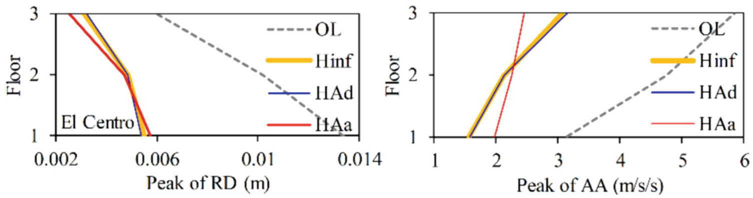

Fig. 4. The peak of floors' RD and AA, El Centro earthquake

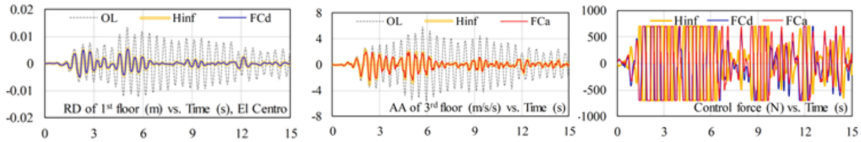

Fig. 5. The system's time responses, El Centro earthquake

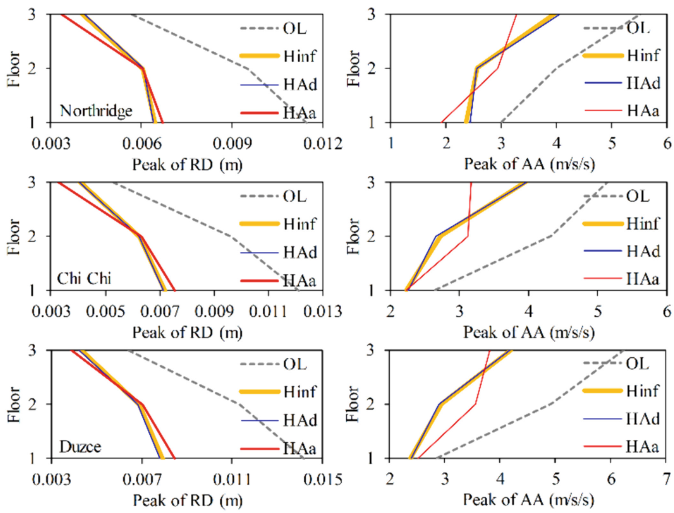

Fig. 6. The peak of floors' RD and AA, three testing earthquakes

5 Conclusions

This study presents the optimization problem of a controller based on fuzzy set theory using the BCMO algorithm to reduce vibrations for building structures subjected to earthquake loads. With many design variables, optimal fuzzy controllers have high control efficiency. In addition, the small number of state variables needed to calculate the control force is also an advantage of the controller. This approach can be extended to control the vibration and motion of different mechanical models.

Acknowledgment. This research is funded by Hanoi University of Science and Technology (HUST) under project number T2023-PC-013.

References

1. Mac, T.-T., Nguyen, T.-D., Bui, H.-L., Tran, N.-A.: Optimal design of hedge-algebras–based controller for vibration control of vehicle suspension systems. Proc. Inst. Mech. Eng. Part I J. Syst. Control Eng. (2023). https://doi.org/10.1177/09596518231196900
2. Precup, R.-E., Hellendoorn, H.: A survey on industrial applications of fuzzy control. Comput. Ind. **62**(3), 213–226 (2011)
3. Bui, H.-L., Pham, M.-N., Nguyen, T.-T.-H.: Swing-up control of an inverted pendulum cart system using the approach of Hedge-algebras theory. Soft. Comput. **26**(10), 4613–4627 (2022)
4. Bui, H.-L., Tran, N.-A.: Multi-objective optimal design of TMDs for increasing critical flutter wind speed of bridges. J. Wind Eng. Ind. Aerodyn. **225**, 104992 (2022)
5. Bui, H.L.: Multi-objective optimization of hedge-algebra-based controllers for quarter-car active suspension models. In: Khang, N.V., Hoang, N.Q., Ceccarelli, M. (eds.) ASIAN MMS 2021. MMS, vol. 113, pp. 876–885. Springer, Cham (2022). https://doi.org/10.1007/978-3-030-91892-7_84
6. Du, H., Zhang, N., Naghdy, F.: Actuator saturation control of uncertain structures with input time delay. J. Sound Vib. **330**(18–19), 4399–4412 (2011)
7. Nguyen, T.-D., Bui, H.-L.: General optimization procedure of the Hedge-algebras controller for controlling dynamic systems. Artif. Intell. Rev. **56**(3), 2749–2784 (2023)
8. Bui, H.L.: An approach for optimizing the hedge-algebras-based controller and application in structural vibration control. In: Nguyen, D.C., Vu, N.P., Long, B.T., Puta, H., Sattler, K.U. (eds) ICERA 2022. LNNS, vol. 602, pp. 157–165. Springer, Cham (2023). https://doi.org/10.1007/978-3-031-22200-9_17
9. Bui, H.-L., Tran, N.-A., Cao, H.Q.: Active control based on hedge-algebras theory of seismic-excited buildings with upgraded tuned liquid column damper. J. Eng. Mech. **149**(1), 04022091 (2023)
10. Bui, V.-B., Mac, T.-T., Bui, H.-L.: Design optimization considering the stability constraint of the Hedge-algebras-based controller for building structures subjected to seismic excitations. Proc. Inst. Mech. Eng. Part I J. Syst. Control Eng. (2023). https://doi.org/10.1177/09596518231171960

Optimal Motion Planning Motivated by Differential Flatness and Lyapunov-Based Model Predictive Control for 5-DOF Tower Cranes

Thi Hue Luu[2], Van Chung Nguyen[1], Tung Lam Nguyen[1](✉), Danh Huy Nguyen[1], and Duc Chuyen Tran[3]

[1] Hanoi University of Science and Technology, Hanoi, Vietnam
lam.nguyentung@hust.edu.vn
[2] Electric Power University, Hanoi, Vietnam
[3] University of Economics - Technology for Industries, Hanoi, Vietnam

Abstract. The paper proposes a method to solve the time optimal problem, thereby building the time optimal trajectory, as input for Lyapunov-based model predictive control (LMPC) for the three-dimensional tower crane (3DTC) system. The 3DTC system is a flatness system, and the time optimal trajectory of the payload is determined by solving the time optimization problem. The states of the system and the reference control signal are calculated based on the flatness theory. The optimal trajectory and reference control signal are fed to the Lyapunov-based model predictive control. The LMPC takes advantage of the second-order sliding mode control stable conditions as a strict constraint to ensure the closed-loop system's global stability. Finally, simulation results based on the semi-physical model are given to confirm the effectiveness and sustainability of the proposed method the proposed method.

Keywords: Motion Planning · Differential Flatness · Model predictive control · Lyapunov-based model predictive control

1 Introduction

Three-dimensional tower crane (3DTC) is widely used in factories and construction sites to transport goods to replace human labor in the workspace. Trans-porting a payload requires the simultaneous coordination of all movements at high speeds to reduce time traveling. However, moving at high speed increases the swing angle of the payload, which can be dangerous to people and surrounding structures. On the contrary, slow operation can have a small swing angle but prolong the time traveling, which reduces the performance of the 3DTC system. To solve the performance problem for the 3DTC system, building an optimal time reference trajectory plays an important role. Some studies for the system with constant cable length, such as [1] have proposed a motion planning for the double pendulum tower crane system. With the 3DTC system in the

D. C. Nguyen et al. (Eds.): ICERA 2023, LNNS 944, pp. 283–292, 2024.
https://doi.org/10.1007/978-3-031-62235-9_28

process of raising/lowering the cable length payload changes over time to complete the task, in [2], a real-time trajectory planning method is presented. The optimal trajectory can be obtained by the optimization model or the adaptive control method based on the motion planning presented in [3, 4]. In addition, motion planning is done by separating into time different motion intervals: acceleration interval, constant speed interval, and deceleration interval [5]. In [6–8], construct the optimal time trajectory by minimizing the cost function and obeying strict constraints. However, the above motion planning methods have numerous computations and are difficult to implement in practice. To solve this problem, a method based on flatness theory, which can consider the motion planning of the 3DTC system to be a motion planning problem for the payload satisfying the constraints, since the state variables and the control signal can be represented by the position of the payload and its derivatives. The problem based on flatness theory has reduced the computational volume significantly, creating favorable conditions for practical implementation.

Most control techniques for 3DTC systems are built on the assumption that the controller needs as much force/torque as the motor provides. But in reality, the movements are provided within a certain limit, the nonlinear model predictive controller has been developed in [9, 10] for tower crane system, taking into the kinematic conditions during controller design. The model predictive control [11–13] with all state, input, and output constraints controls the payload movement effectively. However, this algorithm does not guarantee a stable system in a closed loop. Inspired by the article [14], this paper proposes a Lyapunov-based model predictive control with tight stability conditions based on the stability condition of the second-order sliding mode controller. The controller not only controls payload effectively but also ensures global stability in closed-loop systems. The main contributions of the paper are summarized as follows:

- The time-optimal path planning of the payload motion is designed by bidirectional mapping between the input and output of the system through its flatness, and taking into the kinematic constraints of the system in the design process.
- The Lyapunov-based model predictive control for the trajectory tracking control problem and payload anti-swing is developed. The LMPC controller ensures closed-loop system stability, which proves theoretically.

2 Dynamics of the Tower Crane

The model of the three-dimensional tower crane (3DTC) is illustrated in Fig. 1, where m is the payload mass; M_t is the trolley mass; J_0 is the equivalent rotational mass; Vector $\mathbf{F} = [\tau_\gamma, f_x, f_l, 0, 0]^T$ is the force acting on the system; γ, x, and l are turntable rotation angle, trolley position, and cable rope length; ϕ, θ are the swing angles of the payload. Set $\mathbf{q} = [\gamma, x, l, \phi, \theta]^T$ is the position vector of the system; b_γ, b_x, b_l, b_ϕ, b_θ is the coefficient of friction of the tower crane when moving along the axes; (x_l, y_l, z_l) is the position of the payload. Following the Lagrange equation, the dynamic of the 3DTC can be written as in [15] in the matrix form as follows:

$$\mathbf{M}(\mathbf{q})\ddot{\mathbf{q}} + \mathbf{C}(\mathbf{q}, \dot{\mathbf{q}})\dot{\mathbf{q}} + \mathbf{G}(\mathbf{q}) + \mathbf{D} + \mathbf{B}\dot{\mathbf{q}} = \mathbf{F} \tag{1}$$

where $\mathbf{M}(\mathbf{q}) \in \Re^{5\times5}$ is the symmetric mass matrix; $\mathbf{C}(\mathbf{q}, \dot{\mathbf{q}}) \in \Re^{5\times5}$ is the Coriolis and centrifugal; $B \in \Re^{5\times5}$ is the damping coefficient matrix, with $\mathbf{B} = \mathrm{diag}([b_\gamma, b_x, b_l, b_\phi, b_\theta])$; $\mathbf{G}(\mathbf{q}) \in \Re^{5\times1}$ is gravitational vector, and $\mathbf{D} \in \Re^{5\times1}$ denotes disturbance vector.

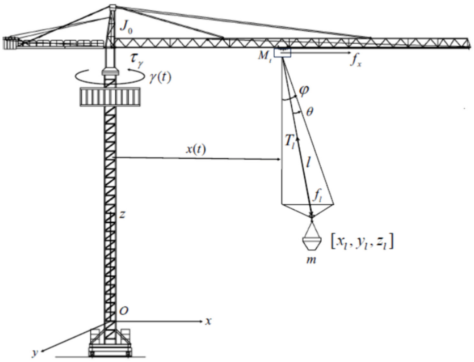

Fig. 1. Model of a three dimensions tower crane.

3 Time Optimal Problem Based on Differential Flatness

The position of the payload (x_l, y_l, z_l) is controlled indirectly through the position control of the trolley and the turntable in the 3DTC system. The tower crane is a flat system, the control signal $[\tau_\gamma, f_x, f_l]^{\mathrm{T}}$ and response $[\gamma, x, l, \phi, \theta]^{\mathrm{T}}$ can be represented via flat output.

Theorem 1: *Assuming the payload is the point mass at* (x_l, y_l, z_l), *the flat output is* $y_o = (x_l, y_l, z_l)$. *The 3DTC system is a flat system satisfying the following conditions:*

1. *Flat output is a function of state variables, control signal, and some of its derivatives* $y_o = \Psi(\mathbf{q}, \mathbf{F}_a, \dot{\mathbf{F}}_a, \ldots, \mathbf{F}_\mathbf{a}^{(\mathbf{n})})$. *So, the reference state variables and the control signals can be determined through* y_0 *and its derivative:* $\mathbf{q} = f_q(y_o, \dot{y}, \dot{y}_0)$; $\mathbf{F}_\mathbf{a} = f_f(y_o, \dot{y}_0, \dot{y}_0, y_o^{(3)}, y_o^{(4)})$
2. y_0 *and its derivatives are independent and satisfy no differential equations of the form:* $\phi(y_o, \dot{y}_0, \ldots, y_o^{(n)}) = 0$.

Proof: The payload position is determined:

$$\begin{cases} x_l = x\cos(\gamma) + l\sin(\phi)\cos(\theta) \\ y_l = x\sin(\gamma) + l\sin(\theta) \\ z_l = h - l\cos(\phi)\cos(\theta) \end{cases} \tag{2}$$

where h is the crane height.

According to Newton's 2^{nd} law, the crane equation of motion in Fig. 1 will be determined. From there, calculate the swing angle:

$$\begin{cases} \phi = \arctan(-\frac{\ddot{x}_l}{\ddot{z}_l+g}) \\ \theta = \arctan(\frac{\ddot{y}_l}{\sqrt{\ddot{x}_l^2+(g+\ddot{z}_l)^2}}) \end{cases} \tag{3}$$

Substituting Eq. (3) into Eq. (2), x, l, γ can be calculated as follows:

$$\begin{cases} \gamma = \gamma(x_l, y_l, z_l, \ddot{x}_l, \ddot{y}_l, \ddot{z}_l) \\ x = x(x_l, y_l, z_l, \ddot{x}_l, \ddot{y}_l, \ddot{z}_l) \\ l = \sqrt{\frac{\ddot{x}_l^2}{(g+\ddot{z}_l)^2} + 1}(h - zl)\sqrt{\frac{\ddot{y}_l^2}{(g+\ddot{z}_l)^2+\ddot{x}_l^2} + 1} \end{cases} \tag{4}$$

From Eqs. (4) and (3), it can be seen that $\mathbf{q} = f_{q1}(y_o, \dot{y}_o, \ddot{y}_o)$, then $\dot{q} = f_{q2}(y_o, \dot{y}_o, \ddot{y}_o, y_o^{(3)})$ and $\ddot{\mathbf{q}} = f_{q3}(y_o, \dot{y}_o, \ddot{y}_o, y_o^{(3)}, y_o^{(4)})$. Therefore, the force acting on the 3DTC system is described: $\mathbf{F_a} = f_f(y_o, \dot{y}_0, \ddot{y}_0, y_o^{(3)}, y_o^{(4)})$. The flat output is the payload position $y_0 = (x_l, y_l, z_l)$, which is differentially independent and does not satisfy any differential equation of the form $\phi(y_o, \dot{y_o}, ..., y_o^{(n)}) = 0$. So, Theorem 1 is proved.

Limit swing angles ϕ, θ to solve the problem of vibrating payload:

$$\begin{aligned} &\phi_{min} \le \arctan(-\frac{\ddot{x}_l}{\ddot{z}_l+g}) \le \phi_{max}; \\ &\theta_{min} \le \arctan(\frac{\ddot{y}_l}{\sqrt{\ddot{x}_l^2+(g+\ddot{z}_l)^2}}) \le \theta_{max} \end{aligned} \tag{5}$$

In this paper, the objective of the control is to move the payload to the desired position $y_{or} = [x_{lr}, y_{lr}, z_{lr}]^T$ in the shortest time and ensure system constraints. Or set the planning motion trajectory of the payload $\boldsymbol{\xi} = [x_l, y_l, z_l]^T$ with optimal time, then the payload velocity: $\dot{\xi} = [\dot{x}_l, \dot{y}_l, \dot{z}_l]^T$ and control signal $u(\boldsymbol{\xi}) = [\ddot{x}_l, \ddot{y}_l, \ddot{z}_l]^T$. The payload swing angles for the optimization problem is represented by $\ddot{x}_l$, $\ddot{y}_l$, and $\ddot{z}_l$ with $u(\boldsymbol{\xi}) = [\ddot{x}_l, \ddot{y}_l, \ddot{z}_l]^T$, $f(u(\boldsymbol{\xi})) = arctan(-\frac{u(1)}{u(3)+g})$ and $g(u(\boldsymbol{\xi})) = arctan(\frac{u(2)}{\sqrt{u^2(1)+(g+u(3))^2}})$. The optimal time based on differential flatness with kinematic constraints and swing angle constraints becomes an optimization problem as follows:

$$\text{minimize} \quad J = t_f \tag{6}$$

$$\begin{aligned} &\text{subject to: } \boldsymbol{\xi}(t_f) = y_{or} = [x_{lr}, y_{lr}, z_{lr}]^T \\ &\dot{\xi}(t_f) = 0 \\ &\ddot{\xi}(t) = f(\dot{\xi}(t), u(\boldsymbol{\xi}(t))) \\ &\dot{\xi}_{\min} \leqslant \dot{\xi}(t) \leqslant \dot{\xi}_{\max} \\ &\phi_{min} \le f(u(\boldsymbol{\xi}(t))) \le \phi_{max} \\ &\theta_{min} \le g(u(\boldsymbol{\xi}(t))) \le \theta_{max} \end{aligned} \tag{7}$$

t_f is the optimal time to move the 3DTC system to the desired position, which must satisfy the constraints (7).

The optimal trajectory for the payload $\boldsymbol{\xi}_r(t)$ is achieved through (6). The desired trajectory and the control input for the 3DTC can be determined through the payload position and its derivative: $\mathbf{q_r} = f_{y_1}(x_r(t), \dot{\xi}_r(t), \ddot{\xi}_r(t))$ and control signal reference $\mathbf{F_r} = f_f(x_\mathbf{r}(\mathbf{t}), \dot{\xi}_\mathbf{r}(\mathbf{t}), \ddot{\xi}_\mathbf{r}(\mathbf{t}), x_\mathbf{r}^{(\mathbf{3})}(\mathbf{t}), x_\mathbf{r}^{(\mathbf{4})}(\mathbf{t}))$, which are used as input for the next sections.

4 Control Law

4.1 Second-Order Sliding Mode Control

The 3DTC system is un-actuated, in order to facilitate the control of 3DTC progress, the dynamics equation of the system (1) can be rewritten into two equations as follows:

$$\mathbf{F_a} = \mathbf{M_{a1}}(\mathbf{q})\ddot{\mathbf{q}}_a + \mathbf{M_{u1}}(\mathbf{q})\ddot{\mathbf{q}}_u + \mathbf{C_{a1}}(\mathbf{q}, \dot{\mathbf{q}})\dot{\mathbf{q}}_a + \mathbf{C_{u1}}(\mathbf{q}, \dot{\mathbf{q}})\dot{\mathbf{q}}_u + \mathbf{G_1}(\mathbf{q}) + \mathbf{D_{a1}} \tag{8}$$

$$\mathbf{0} = \mathbf{M_{a2}}(\mathbf{q})\ddot{\mathbf{q}}_a + \mathbf{M_{u2}}(\mathbf{q})\ddot{\mathbf{q}}_u + \mathbf{C_{a2}}(\mathbf{q}, \dot{\mathbf{q}})\dot{\mathbf{q}}_a + \mathbf{C_{u2}}(\mathbf{q}, \dot{\mathbf{q}})\dot{\mathbf{q}}_u + \mathbf{G_2}(\mathbf{q}) + \mathbf{D_{u1}} \tag{9}$$

where: $\mathbf{q}_a = [\gamma, x, l]^T$; $\mathbf{q}_u = [\phi, \theta]^T$; $\mathbf{M_{a1}}(\mathbf{q}), \mathbf{C_{a1}}(\mathbf{q}, \dot{\mathbf{q}}) \in \Re^{3\times3}$; $\mathbf{M_{u1}}(\mathbf{q})$, $\mathbf{C_{u1}}(\mathbf{q}, \dot{\mathbf{q}}) \in \Re^{3\times2}$; $\mathbf{G_1}(\mathbf{q}), \mathbf{D_{a1}}(\mathbf{q}) \in \Re^{3\times1}$; $\mathbf{M_{a2}}(\mathbf{q}), \mathbf{C_{a2}}(\mathbf{q}, \dot{\mathbf{q}}) \in \Re^{2\times3}$; $\mathbf{M_{u2}}(\mathbf{q})$, $\mathbf{C_{u2}}(\mathbf{q}, \dot{\mathbf{q}}) \in \Re^{2\times2}$; $\mathbf{G_2}(\mathbf{q}), \mathbf{D_{u1}}(\mathbf{q}) \in \Re^{2\times1}$;

Substituting (9) into (8), the actuated dynamics equation is as follows:

$$\mathbf{F_a} = \overline{\mathbf{M}}(\mathbf{q})\ddot{\mathbf{q}}_a + \overline{\mathbf{C_1}}(\mathbf{q}, \dot{\mathbf{q}})\dot{\mathbf{q}}_a + \overline{\mathbf{C_2}}(\mathbf{q}, \dot{\mathbf{q}})\dot{\mathbf{q}}_u + \overline{\mathbf{G}}(\mathbf{q}) + \overline{\mathbf{D_a}} \tag{10}$$

where: $\overline{\mathbf{M}}(\mathbf{q}) = \mathbf{M_{a1}}(\mathbf{q}) - \mathbf{M_{u1}}(\mathbf{q})\mathbf{M_{u2}^{-1}}(\mathbf{q})\mathbf{M_{a2}}(\mathbf{q})$;
$\overline{\mathbf{C}}_1(\mathbf{q}, \dot{\mathbf{q}}) = \mathbf{C_{a1}}(\mathbf{q}, \dot{\mathbf{q}}) - \mathbf{M_{u1}}(\mathbf{q})\mathbf{M_{u2}^{-1}}(\mathbf{q})\mathbf{C_{a2}}(\mathbf{q}, \dot{\mathbf{q}})$;
$\overline{\mathbf{C}}_2(\mathbf{q}, \dot{\mathbf{q}}) = \mathbf{C_{u1}}(\mathbf{q}, \dot{\mathbf{q}}) - \mathbf{M_{u1}}(\mathbf{q})\mathbf{M_{u2}^{-1}}(\mathbf{q})\mathbf{C_{u2}}(\mathbf{q}, \dot{\mathbf{q}})$;
$\overline{\mathbf{G}}(\mathbf{q}) = \mathbf{G_1}(\mathbf{q}) - \mathbf{M_{u1}}(\mathbf{q})\mathbf{M_{u2}^{-1}}(\mathbf{q})\mathbf{G_2}(\mathbf{q})$; $\overline{\mathbf{D}}_\mathbf{a} = \mathbf{D_{a1}} - \mathbf{M_{u1}}(\mathbf{q})\mathbf{M_{u2}^{-1}}(\mathbf{q})\mathbf{D_{u1}}$;

The sliding surface of the system is defined as follows:

$$\mathbf{s_0} = \dot{\mathbf{e}}_{qa} + \boldsymbol{\lambda}\mathbf{e}_{qa} + \boldsymbol{\delta}\mathbf{e}_{qu} \tag{11}$$

where $\mathbf{e}_{qa} = \mathbf{q}_a - \mathbf{q}_{ar}$ and $\mathbf{e}_{qu} = \mathbf{q}_u - \mathbf{q}_{ur}$ are error vectors with $\mathbf{q}_{ar} = [\gamma_r, x_r, l_r]^T$ and $\mathbf{q}_{ar} = [\gamma_r, x_r, l_r]^T$ are desired positions and desired swing angle. $\boldsymbol{\lambda} = \mathrm{diag}(\lambda_1, \lambda_2, \lambda_3)$ and $\boldsymbol{\delta} = \begin{bmatrix} \delta_1 & 0 & 0 \\ 0 & \delta_2 & 0 \end{bmatrix}^T$ are positive parameters. The second-order sliding mode control for the 3DTC system is proposed as follows:

$$\begin{aligned} \mathbf{F_a} = &-\overline{\mathbf{M}}(\mathbf{q})\Big(2\boldsymbol{\lambda}(\dot{\mathbf{q}}_a - \dot{\mathbf{q}}_{ar}) - \ddot{\mathbf{q}}_{ar} + \boldsymbol{\lambda}^T\boldsymbol{\lambda}(\mathbf{q}_a - \mathbf{q_{ar}}) + \boldsymbol{\delta}(\dot{\mathbf{q}}_u - \dot{\mathbf{q}}_{ur}) + \boldsymbol{\lambda}\boldsymbol{\delta}(\mathbf{q}_u - \mathbf{q_{ur}})\Big) \\ &-\mathbf{Ksign}(\mathbf{s_0}) + \overline{\mathbf{C_1}}(\mathbf{q}, \dot{\mathbf{q}})\dot{\mathbf{q}}_a + \overline{\mathbf{C_2}}(\mathbf{q}, \dot{\mathbf{q}})\dot{\mathbf{q}}_\mathbf{u} + \overline{\mathbf{G}}(\mathbf{q}) \end{aligned} \tag{12}$$

where $\mathbf{K} \in \Re^{\mathbf{3}\times\mathbf{3}}$ is a positive definite diagonal coefficient matrix.

The Lyapunov candidate function is proposed as follows:

$$V_{SMC} = \frac{1}{2}\mathbf{s_0}^T\mathbf{s_0} \tag{13}$$

With some calculation, its derivative can be illustrated by:

$$\begin{aligned}\dot{V}_{SMC} = {\mathbf{s}_0}^T[&-\boldsymbol{\lambda}(\dot{\mathbf{q}}_a - \dot{\mathbf{q}}_{ar}) - \boldsymbol{\lambda}^T\boldsymbol{\lambda}(\mathbf{q}_\mathbf{a} - \mathbf{q}_{ar}) - \boldsymbol{\lambda}\boldsymbol{\delta}(\mathbf{q}_u - \mathbf{q}_{ur}) \\ &- \overline{\mathbf{M}}^{-1}(\mathbf{q})\left(\mathbf{Ksign}(\mathbf{s}_0) + \overline{\mathbf{D}}_\mathbf{a}\right)]\end{aligned} \tag{14}$$

Assumption 1: *The disturbance* $\overline{\mathbf{D}}_\mathbf{a}$ *is continuous and bounded. Therefore, there exist positive vector* $\boldsymbol{\varepsilon}$ *such that:* $|\bar{\mathbf{D}}_\mathbf{a}| < \varepsilon$

Since the matrix $\overline{\mathbf{M}}(\mathbf{q})$ is the positive inertia matrix. According to Eq. (11), Assumption 1 and choosing the coefficient $\mathbf{K}$ such that: $\mathrm{diag}(\mathbf{K}) > \varepsilon$, then Eq. (14) becomes as:

$$\dot{V}_{SMC} \leqslant -{\mathbf{s}_0}^T\boldsymbol{\lambda}\mathbf{s}_0 - {\mathbf{s}_0}^T\mathbf{M}^{-1}(\mathbf{q})\left(\mathrm{diag}(\mathbf{K}) - \boldsymbol{\varepsilon}\right) \leqslant \mathbf{0} \tag{15}$$

From (13) and (15), the sliding surface $\mathbf{s}_0$ converges to zero. Therefore, applying Barlalat's lemma [16], the sliding surface is asymptotically stable. Under the gravity influence ϕ, θ will approach zero, that mean $\mathbf{e}_{qu} \to 0$. So $\dot{\mathbf{e}}_{qa} + \lambda\mathbf{e}_{qa} \to 0$, solve the first-order differential equation then $\mathbf{e}_{qa} \to 0$. Thus, the 3DTC system works stably with the control law (12).

4.2 Lyapunov-Based Model Predictive Control

The limitation of the SO-SMC is that the kinematic and the control signal constraints $\mathbf{F} = [\tau_\gamma, f_x, f_l, 0, 0]^T$ of the system have been not considered. The MPC controller solves this problem, which takes the previous states and the desired trajectory to predict the next behavior while maintaining the states and controlling signal constraints.

Set $\mathbf{x_1} = \mathbf{q}$; $\mathbf{x_2} = \dot{\mathbf{q}}$, the model for MPC controller based on (1) by:

$$\begin{cases}\dot{\mathbf{x}}_1 = \mathbf{x_2} \\ \mathbf{x}_2 = \mathbf{M^{-1}}(\mathbf{x_1})(-\mathbf{C}(\mathbf{x_1}, \mathbf{x_2})\mathbf{x_2} - \mathbf{G}(\mathbf{x_1}) - \mathbf{D}) + \mathbf{M^{-1}}(\mathbf{x_1})\mathbf{F}\end{cases} \tag{16}$$

Assumption 2: *The desired trajectory and its derivatives are continuous and bounded that mean* $\|\mathbf{q_r}\|_\infty \leq \overline{\mathbf{q}}_r$; $\|\dot{\mathbf{q}}_\mathbf{r}\|_\infty \leq \overline{\mathbf{q}}_{r1}$; $\|\ddot{\mathbf{q}}_\mathbf{r}\|_\infty \leq \overline{\mathbf{q}}_{r2}$*; where* $\overline{\mathbf{q}}_r$, $\overline{\mathbf{q}}_{r1}$, $\overline{\mathbf{q}}_{r2}$ *are positive numbers.*

Fixed time prediction horizon $T_p = NT_s$ with N is the prediction horizon and T_s is the sampling time. The cost function and constraints for the LMPC controller are formulated as follows:

$$J = \int_{t_k}^{t_k+T_p} \left(\|\widetilde{\mathbf{x}}(t)\|_Q^2 + \left\|\widetilde{\mathbf{F}}(t)\right\|_R^2\right) dt \tag{17}$$

Subject to:

$$\begin{aligned}&\dot{\mathbf{x}}_2 = \mathbf{M^{-1}}(\mathbf{x_1})(-\mathbf{C}(\mathbf{x_1}, \mathbf{x_2})\mathbf{x_2} - \mathbf{G}(\mathbf{x_1}) - \mathbf{D}) + \mathbf{M^{-1}}(\mathbf{x_1})\mathbf{F} \\ &\mathbf{x}_{\min} \leqslant \mathbf{x}(t) \leqslant \mathbf{x}_{\max} \\ &\mathbf{F}_{\min} \leqslant \mathbf{F}(t) \leqslant \mathbf{F}_{\max} \\ &\dot{V}(\mathbf{x}(t), \mathbf{F}(t)) \leqslant \dot{V}_{smc}(\mathbf{x}(t), h(\mathbf{x}(t)))\end{aligned} \tag{18}$$

where $\tilde{\mathbf{x}}(t) = \mathbf{x_1}(t) - \mathbf{q_r}(t)$ is the error of output states of the system and reference; $\widetilde{\mathbf{F}}(t) = \mathbf{F}(t) - \mathbf{F_r}(t)$ is the error between the control signal at time t and the actual control signal from the flatness theory. The control objective can be achieved by minimizing the cost function J. Q, R are positive matrices. $h(.)$ is the Lyapunov-based nonlinear controller and $V(.)$ represent respectively the Lyapunov function. The LMPC controller will provide the control signal to track the desired orbital trajectory. The constraints (18) ensure that the LMPC guarantees stable properties regardless of the length of the prediction horizon.

The sliding surface is defined is defined as follows:

$$\mathbf{s_1} = (\dot{\mathbf{x}}_{1a} - \dot{\mathbf{q}}_{ar}) + \boldsymbol{\lambda}(\mathbf{x}_{1a} - \mathbf{x}_{ar}) + \boldsymbol{\delta}(\mathbf{x}_{1u} - \mathbf{q}_{ur}) \tag{19}$$

The auxiliary controller h($\mathbf{x(t)}$) the dependent Lyapunov-based as:

$$\begin{aligned} h(\mathbf{x}(t)) = &-\overline{\mathbf{M}}(\mathbf{x}_1)(2\boldsymbol{\lambda}(\mathbf{x}_{2a} - \dot{\mathbf{q}}_{ar}) - \ddot{\mathbf{q}}_{ar} + \boldsymbol{\lambda}^T\boldsymbol{\lambda}(\mathbf{x}_{1a} - \mathbf{q_{ar}}) + \boldsymbol{\delta}(\mathbf{x}_{2u} - \dot{\mathbf{q}}_{ur}) \\ &+ \boldsymbol{\lambda\delta}(\mathbf{x}_{1u} - \mathbf{q_{ur}})) - \mathbf{Ksign(s_1)} + \overline{\mathbf{C_1}}(\mathbf{x}_1, \mathbf{x}_2)\mathbf{x}_{2a} + \overline{\mathbf{C_2}}(\mathbf{x}_1, \mathbf{x}_2)\mathbf{x}_{2u} + \overline{\mathbf{G}}(\mathbf{x_1}) \end{aligned} \tag{20}$$

The proposed candidate function V_{LMPC} is as follows:

$$V_{LMPC} = \frac{1}{2}\mathbf{s}_1^T\mathbf{s}_1 \tag{21}$$

The derivative of Eq. (21) to get the result of $\dot{V}_{LMPC}$, then the constraint condition (18) is written briefly as follows:

$$\begin{aligned} \dot{V}_{LMPC} = \mathbf{s}_1^T \{&\overline{\mathbf{M}}^{-1}(\mathbf{x}_1)\mathbf{F_a} - \overline{\mathbf{M}}^{-1}(\mathbf{x}_1)\,[\,\overline{\mathbf{C_1}}(\mathbf{x}_1, \mathbf{x}_2)\mathbf{x}_{2a} + \overline{\mathbf{C_2}}(\mathbf{x}_1, \mathbf{x}_2)\mathbf{x}_{2u} \\ &+ \overline{\mathbf{G}}(\mathbf{x}_1) + \overline{\mathbf{D}}_\mathbf{a}] - \ddot{\mathbf{q}}_\mathbf{ar} + \boldsymbol{\lambda}(\mathbf{x_{2a}} - \dot{\mathbf{q}}_\mathbf{ar}) + \boldsymbol{\delta}(\mathbf{x_{2u}} - \dot{\mathbf{q}}_\mathbf{ur})\} \\ &\leq -\mathbf{s_1}^\mathbf{T}\boldsymbol{\lambda}\mathbf{s_1} - \mathbf{s_1}^\mathbf{T}\mathbf{M}^{-1}(\mathbf{q})(\mathrm{diag}(\mathbf{K}) - \boldsymbol{\varepsilon}) \leqslant \mathbf{0}, \forall \mathbf{t} \in [\mathbf{t_k}, \mathbf{t_k} + \mathbf{T_p}] \end{aligned} \tag{22}$$

Therefore, the closed-loop system with the LMPC algorithm will be asymptotically stable and the 3DTC's trajectory will track the desired trajectory.

5 Simulation Results

In this section, simulation results are provided to show the effectiveness and feasibility of the proposed control strategy. The comparison with SO-SMC is also provided to highlight the advances of the LMPC control method. System's parameter and controller's parameter as chosen as in Table 1.

Table 1. Parameter of the 3DTC system, the observer and the controller

System parameter	Control and observer parameters
$m = 500\,\text{kg}$, $h = 48\,\text{m}$ $J_0 = 10215\,\text{kg.m}^2$ $M_t = 1140.75\,\text{kg}$ $b_\gamma = 40\,\text{Nm/s}$, $b_x = 50\,\text{Nm/s}$ $b_l = 30\,\text{Nm/s}$, $b_\theta = 15\,\text{Nm/s}$, $g = 9.81\,\text{m/s}^2$	$\boldsymbol{\lambda} = \text{diag}\,(2.2, 2.6, 2)$, $\delta_1 = 0.4$, $\delta_2 = 0.4$, $T_s = 0.25\,\text{s}$, $T_p = 2{,}5\,\text{s}$ $\mathbf{K} = \text{diag}\,(0.1, 0.1, 0.1)$, $\text{R} = \text{diag}\,(0.05, 0.2, 0.1)$, $N = 10$, $\text{Q} = \text{diag}$ $(15000, 400, 500, 12000, 12000)$, $\mathbf{x}_{\min} = -[\infty, 0, 0, 0.05, 0.05, 0.05, 0.125, 0.225, 0.1, 0.1]$ $\mathbf{x}_{\max} = [\infty, 35, 45, 0.05, 0.05, 0.05, 0.125, 0.225, 0.1, 0.1]$ $\mathbf{F}_{\max} = -\mathbf{F}_{\min} = [1000, 200, 7500]$ (Nm, N, N)

The optimization dilemma grounded in flatness theory incorporates the following parameter selections: $\phi_{min} = \theta_{min} = -0.05$ radians, $\phi_{max} = \theta_{max} = 0.05$ radians, $\dot{\xi}_{\min} = -[0.125; 0.125; 0.215]$ m/s, $\ddot{\xi}_{\max} = [0.125; 0.125; 0.215]$ m/s. The formulation of the optimization problem was carried out using Matlab/Simulink 2022a on a computer equipped with an Intel Core i7-11800H at 2.3 GHz and 16 GB RAM. The Casadi program was supplemented with the open-source Interior Point Optimize (IPOPT) package to analyze cost function gradients and optimization problem constraints based on flatness theory. The solution's sampling time was set at 5 ms, and all constraints were aligned with those listed in Table 1. The initial state of the load was defined as $[x_l(0), y_l(0), z_l(0)] = [0, 0, 3]$ meters. The ultimate target for the load was established as $[x_l(t_f), y_l(t_f), z_l(t_f)] = [3.1, 17.75, 33]$ meters. Given this hardware configuration, the optimization problem was solved in approximately 31 s, revealing the optimal time as $t_f = 140.61$ seconds. The tracking performance of 3DTC is shown in Fig. 2 – Fig. 3 and the control input is shown in Fig. 4. The swing angles of the LMPC method are stable in the range of [−0.025–0.025] (rad) while the swing angles of the LMPC method are in the range of [−0.05–0.05] (rad). Moreover, the control forces of the LMPC are stable and do not have a saturation phenomenon like the SO-SMC, also verifying the effectiveness of the control method.

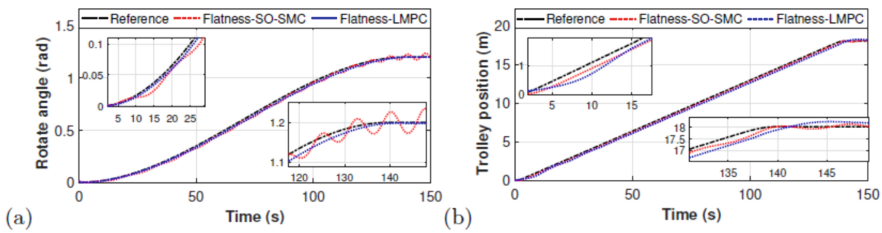

Fig. 2. Tracking performances of rotate angle γ (rad) and trolley position x (m).

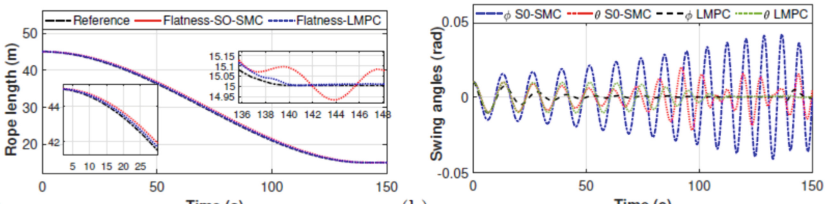

(a) (b)

Fig. 3. Rope length$l$(m) and the swing angles ϕ, θ (rad).

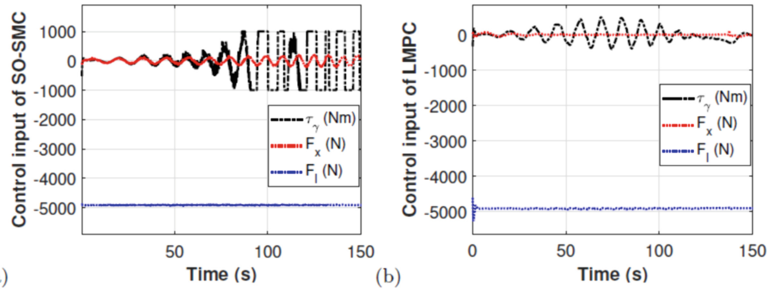

(a) (b)

Fig. 4. Control inputs

6 Conclusion

In this paper, a Lyapunov-based model predictive control motivated by Flatness theory is designed to control a 3DTC system. Thanks to differential flatness, an optimal motion plan is created by considering all system constraints. The proposed controller - the LMPC has solved the backlog problems of controlling the 3DTC - antivibration control and ensuring actuator capacity. The stability of the 3DTC also is guaranteed based on the auxiliary controller of the dependent Lyapunov-based. Finally, simulation results in Matlab/Simulink verified the quality of the proposed closed-loop control strategy. In the near future, trials will be conducted on the experimental model to validate the accuracy and real-world suitability of the controller.

Acknowledgements. This research is funded by the Hanoi University of Science and Technology (HUST) under project number T2023-TĐ-002.

References

1. Ouyang, H., Tian, Z., Yu, L., Zhang, G.: Motion planning approach for payload swing reduction in tower cranes with double-pendulum effect. J. Franklin Inst. **357**(13), 8299–8320 (2020)
2. Tian, Z., Yu, L., Ouyang, H., Zhang, G.: Swing suppression control in tower cranes with time-varying rope length using real-time modified trajectory planning. Autom. Constr. **132**, 103954 (2021)

3. Wu, Z., Xia, X.: Optimal motion planning for overhead cranes. IET Control Theory Appl. **8**(17), 1833–1842 (2014)
4. Fang, Y., Ma, B., Wang, P., Zhang, X.: A motion planning-based adaptive control method for an underactuated crane system. IEEE Trans. Control Syst. Technol. **20**(1), 241–248 (2011)
5. Lee, H.-H.: Motion planning for three-dimensional overhead cranes with high-speed load hoisting. Int. J. Control **78**(12), 875–886 (2005)
6. Kaserer, D., Gattringer, H., Müller, A.: Time optimal motion planning and admittance control for cooperative grasping. IEEE Robot. Autom. Lett. **5**(2), 2216–2223 (2020)
7. Verschueren, R., van Duijkeren, N., Swevers, J., Diehl, M.: Time-optimal motion planning for n-DOF robot manipulators using a path-parametric system reformulation. In: 2016 American Control Conference (ACC), pp. 2092–2097. IEEE (2016)
8. Liang, X., Fang, Y., Sun, N., Lin, H.: Dynamics analysis and time-optimal motion planning for unmanned quadrotor transportation systems. Mechatronics **50**, 16–29 (2018)
9. Ileš, Š, Matuško, J., Kolonić, F.: Sequential distributed predictive control of a 3D tower crane. Control Eng. Pract. **79**, 22–35 (2018)
10. Bariša, T., Bartulović, M., Žužić, G., Ileš, Š, Matuško, J., Kolonić, F.: Nonlinear predictive control of a tower crane using reference shaping approach. In: 2014 16th International Power Electronics and Motion Control Conference and Exposition, pp. 872–876. IEEE (2014)
11. Böck, M., Kugi, A.: Real-time nonlinear model predictive path-following control of a laboratory tower crane. IEEE Trans. Control Syst. Technol. **22**(4), 1461–1473 (2013)
12. Arnold, E., Sawodny, O., Neupert, J., Schneider, K.: Anti-sway system for boom cranes based on a model predictive control approach. In: IEEE International Conference Mechatronics and Automation, vol. 3, pp. 1533–1538. IEEE (2005)
13. Tysse, G.O., Cibicik, A., Tingelstad, L., Egeland, O.: Lyapunov-based damping controller with nonlinear MPC control of payload position for a knuckle boom crane. Automatica **140**, 110219 (2022)
14. Cao, Y., Li, T., Hao, L.-Y.: Lyapunov-based model predictive control for shipboard boom cranes under input saturation. IEEE Trans. Autom. Sci. Eng. (2022)
15. Zhang, M., Zhang, Y., Ji, B., Ma, C., Cheng, X.: Modeling and energy-based sway reduction control for tower crane systems with double-pendulum and spherical pendulum effects. Meas. Control **53**(1–2), 141–150 (2020)
16. Slotine, J.-J. E., Li, W., et al.: Applied Nonlinear Control, vol. 199. Prentice Hall, Englewood Cliffs (1991)

Optimization of Multi-TMD Using BCMO Algorithm for Building Models Subjected to Earthquake

Ngoc-An Tran[1,2], Van-Binh Bui[3], and Hai-Le Bui[4](✉)

[1] PHENIKAA University, Hanoi, Vietnam
[2] PHENIKAA Research and Technology Institute (PRATI), Hanoi, Vietnam
[3] Electric Power University, Hanoi, Vietnam
[4] Hanoi University of Science and Technology, Hanoi, Vietnam
le.buihai@hust.edu.vn

Abstract. Tuned Mass Dampers (TMDs) have been investigated in many studies to reduce the vibration of high-rise buildings under seismic loads. This paper presents a passive control method to install multi-TMD on the building model's floors. The high-rise building system studied is the shear frame building model. The system's motion equation is established by the Lagrange method. The parameters of multi-TMD are optimized using the Balancing composite motion optimization (BCMO) algorithm. The optimal objectives are to minimize the model's peak relative displacement and absolute acceleration. The design variables are the parameters of TMDs. The constraint when optimizing is that the total mass of the TMDs is not more than 2% of the total mass of the building structure. The numerical simulation results for a 5-story building model show the effectiveness of installed multi-TMD. The calculation results in this paper can be extended to the active control problem with different damping devices.

Keywords: Multi-TMD · Building model · Earthquake · BCMO

1 Introduction

High-rise buildings are being built more and more in Vietnam as well as in the world. Due to their slender structure, high-rise buildings are very sensitive to the effects of dynamic loads such as wind or earthquake loads.

Tuned Mass Dampers (TMDs) have been studied in many publications to reduce vibrations of high-rise buildings subjected to seismic loads in both directions, including active and passive control [1]. In addition, upgraded forms of TMDs have also been developed to improve their vibration reduction efficiency [2, 3]. This work presents a new approach to arranging TMDs on the building's floors. The parameters of TMDs are optimized to minimize the system's relative displacement and absolute acceleration. BCMO, a modern and swarm-based optimization algorithm, is used as the optimization tool. The advantages of this algorithm have been demonstrated in various studies [4–6]. The simulation results are performed with a 5-story building model subjected to different earthquakes.

D. C. Nguyen et al. (Eds.): ICERA 2023, LNNS 944, pp. 293–298, 2024.
https://doi.org/10.1007/978-3-031-62235-9_29

2 Investigated Model

Considering the n-degree of freedom (DOF) shear frame building model with massless columns, as shown in Fig. 1. TMDs are installed on the floors. In which m_i, c_i, and k_i are the equivalent mass, damping, and stiffness of the i^{th} floor. The TMD's mass, damping, and stiffness attached to the i^{th} floor are m_{ci}, c_{ci}, and k_{ci}.

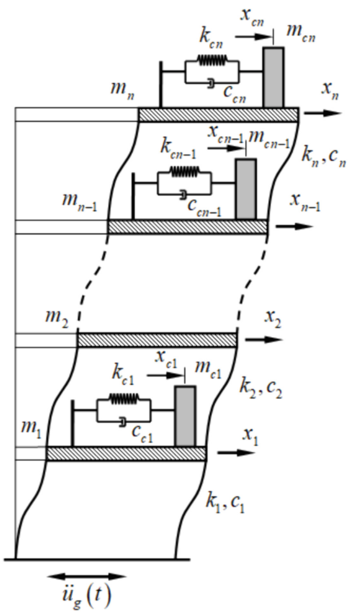

Fig. 1. Investigated model

Hence, the generalized coordinates have the form including absolute displacements of masses $\mathbf{q} = [x_1, x_2, ..., x_n, x_{c1}, x_{c2}, ..., x_{cn}]^T$. Using the Lagrange method, the system's motion equations are

$$
\begin{aligned}
& m_1\ddot{x}_1 + (k_1 + k_{c1} + k_2)x_1 - k_{c1}x_{c1} - k_2x_2 + (c_1 + c_{c1} + c_2)\dot{x}_1 - c_{c1}\dot{x}_{c1} - c_2\dot{x}_2 = f_1 \\
& m_i\ddot{x}_i - k_ix_{i-1} + (k_i + k_{ci} + k_{i+1})x_i - k_{ci}x_{ci} - k_{i+1}x_{i+1} - c_i\dot{x}_{i-1} \\
& + (c_i + c_{ci} + c_{i+1})\dot{x}_i - c_{ci}\dot{x}_{ci} - c_{i+1}\dot{x}_{i+1} = f \\
& m_n\ddot{x}_n - k_nx_{n-1} + (k_n + k_{cn})x_n - k_{cn}x_{cn} - c_n\dot{x}_{n-1} + (c_n + c_{cn})\dot{x}_n - c_{cn}\dot{x}_{cn} = f_n \\
& m_{cj}\ddot{x}_{cj} - k_{cj}x_j + k_{cj}x_{cj} - c_{cj}\dot{x}_j + c_{cj}\dot{x}_{cj} = f_{j+n} \\
& f_i = -m_i\ddot{u}_g(t); \quad f_{j+n} = -m_{cj}\ddot{u}_g(t); \quad i = 2 \div n-1; j = 1 \div n;
\end{aligned}
\tag{1}
$$

Equation (1) represents the motion equations of the n-DOF building with n-TMD on the floors. In this study, TMDs can be distributed on different floors, and $n = 5$.

3 Optimal Design of Multi-TMD

First of all, the initial designs included the following, where m_{c_tol}, c_{c_tol}, and k_{c_tol}, respectively, are the total mass, damping, and stiffness of the installed TMDs:

- One TMD is installed on the top floor, $m_{c5} = m_{c\_tol}$, $c_{c5} = c_{c\_tol}$, and $k_{c5} = k_{c\_tol}$, denoted by TMD5.
- Two TMDs are set up on the 4th and 5th floors, $m_{c4} = m_{c5} = m_{c\_tol}/2$, $c_{c4} = c_{c5} = c_{c\_tol}/2$, and $k_{c4} = k_{c5} = k_{c\_tol}/2$, denoted by TMD45.
- Three TMDs are put on the 3rd, 4th, and 5th floors, $m_{c3} = m_{c4} = m_{c5} = m_{c\_tol}/3$, $c_{c3} = c_{c4} = c_{c5} = c_{c\_tol}/3$, and $k_{c3} = k_{c4} = k_{c5} = k_{c\_tol}/3$, denoted by TMD35.
- Four TMDs are installed on the 2nd, 3rd, 4th, and 5th floors, $m_{c2} = m_{c3} = m_{c4} = m_{c5} = m_{c\_tol}/4$, $c_{c2} = c_{c3} = c_{c4} = c_{c5} = c_{c\_tol}/4$, and $k_{c2} = k_{c3} = k_{c4} = k_{c5} = k_{c\_tol}/4$, denoted by TMD25.
- Five TMDs are installed on each floor, $m_{ci} = m_{c\_tol}/5$, $c_{ci} = c_{c\_tol}/5$, and $k_{ci} = k_{c\_tol}/5$, denoted by mTMD.

The optimization objectives include the following, where $D_{\max}$, $D_{\max UC}$, $A_{\max}$, and $A_{\max UC}$, respectively, are the system's maximum relative displacement and absolute acceleration when the system is equipped with TMDs and when the system without TMDs (denoted by UC):

$$O_D = D_{\max}/D_{\max UC} \rightarrow \min \tag{2}$$

$$O_A = A_{\max}/A_{\max UC} \rightarrow \min \tag{3}$$

The design variables, when optimizing, include the parameters of TMDs (m_{ci}, c_{ci}, and k_{ci}). The constraint of the optimization problem is that the total mass of TMDs $m_{c\_tol} \leq 2\%$ of the total mass of the structure.

4 Numerical Simulations

Considering the TMDs-building model having following parameters: $m_i = 6000$ kg, $c_i = 3000$ Ns/m, $k_i = 1.5 \times 10^7$ N/m, $m_{c\_tol} = 600$ kg, $c_{c\_tol} = 340$ Ns/m, and $k_{c\_tol} = 1.215 \times 10^5$ N/m ($i = 1$ to n). When optimizing, the 1940 El Centro earthquake's data [7, 8] with the peak acceleration scaled to 0.4g are used as training data. The population size and maximum generation when using the BCMO algorithm are both given as 300.

The TMDs' optimal configurations of their installation distribution cases, as shown in Sect. 3, follow the objectives in Eqs. (2–3) are denoted by TMD5d, TMD5a, TMD45d, TMD45a, TMD35d, TMD35a, TMD25d, TMD25a, mTMDd, and mTMDa, respectively.

Variations (%) of TMDs' optimal parameters compared to their initial designs are arranged in Table 1. The maximum relative displacement (RD) and maximum absolute acceleration (AA) of the floors in the case of the system subjected to the excitation of the El Centro earthquake are plotted in Fig. 2.

The results in Table 1 show that the optimal parameters of TMDs changed significantly compared to the initial designs in all cases of installing TMDs. These changes are unpredictable, so the optimization problem proposed in this study is necessary.

Table 1. Variations (%) of optimal parameters compared to initial designs

	TMD5d	TMD5a	TMD45d	TMD45a	TMD35d	TMD35a	TMD25d	TMD25a	mTMDd	mTMDa
m_{c1}									−79.1	−55.1
m_{c2}							−36.7	−79.4	−50.9	−53.6
m_{c3}					−36.2	−54.5	−39.6	−46.3	−71.2	18.2
m_{c4}			−76.4	−74.1	−79.9	−67.8	−78.5	−80.0	171.9	86.9
m_{c5}	0	0	75.4	71.4	102.2	119.4	85.3	183.6	22.7	−16.3
c_{c1}									30.0	144.6
c_{c2}							−66.3	262.3	−60.5	−49.4
c_{c3}					−77.2	−18.8	−70.4	−80.0	118.4	−27.1
c_{c4}			372.3	−69.5	395.5	201.8	315.3	216.8	−28.1	−13.5
c_{c5}	400.0	71.9	201.1	362.9	275.3	267.9	223.1	400.0	−32.6	−59.8
k_{c1}									26.9	339.3
k_{c2}							392.9	137.3	290.9	379.2
k_{c3}					399.8	309.0	383.8	400.0	−77.6	−22.4
k_{c4}			399.8	398.2	399.4	−76.7	364.3	−80.0	48.6	67.4
k_{c5}	−32.6	−21.6	48.7	43.3	68.4	79.0	51.4	131.2	6.3	−35.8

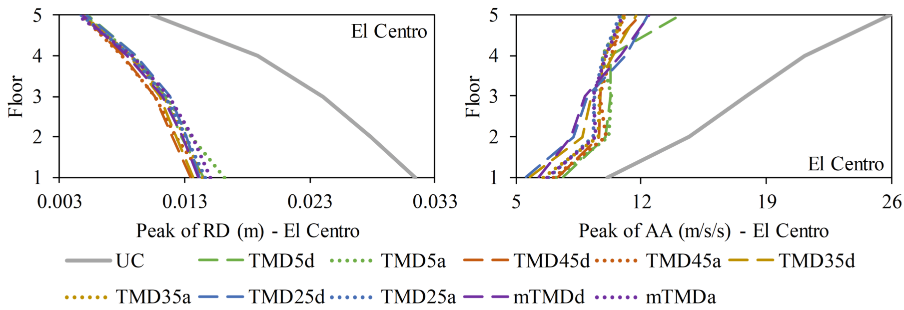

Fig. 2. The system's peak of RD and AA, El Centro.

All optimal configurations and different distributions of TMDs significantly reduce the dynamic responses of the system, as shown in Fig. 2. In which TMD45d and TMD25a have the highest efficiency, reducing RD and AA parameters by nearly 60%. The time response of the first floor's RD and the top floor's AA for these configurations is shown in Fig. 3.

The optimal configurations of TMDs are designed based on the El Centro earthquake. Therefore, these configurations must be validated for their effectiveness with different earthquakes. Figure 4 shows simulation results for the 1952 Kern County, 1979 Imperial Valley, 1986 Chalfant Valley, 1995 Kobe, and 1999 Kocaeli earthquakes.

It can be seen from Fig. 4 that all optimal configurations and distribution cases of TMDs are highly effective in reducing vibrations of the investigated structure. Therefore, these configurations can be selected for the practical application of this structure.

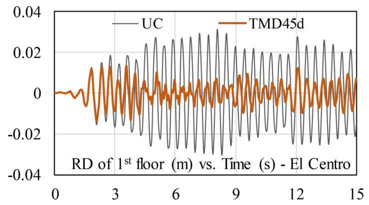

Fig. 3. Time response of RD of the first floor and AA of the top floor, El Centro.

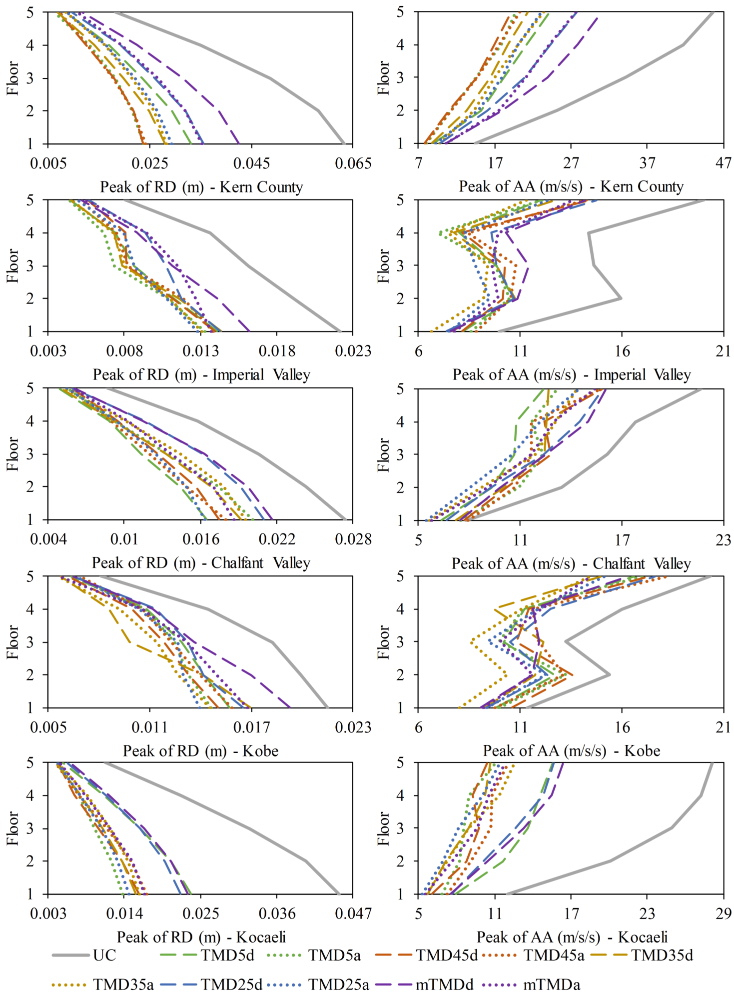

Fig. 4. Simulation results for the testing earthquakes.

5 Conclusions

This paper presents the optimal problem of multi-TMD installed on a building model using the BCMO algorithm. The simulation results show high efficiency in reducing the structure's vibration for all optimal configurations and different distribution cases of TMDs. In addition, these cases also offer the same effect when tested with other earthquakes. Extending this research to different dynamic damping devices, such as pendulums or tuned liquid column dampers, will be necessary research in the future.

Acknowledgment. This research is funded by Hanoi University of Science and Technology (HUST) under project number T2023-PC-007.

References

1. Yang, F., Sedaghati, R., Esmailzadeh, E.: Vibration suppression of structures using tuned mass damper technology: a state-of-the-art review. J. Vib. Control **28**(7–8), 812–836 (2022)
2. Bui, H.-L., Tran, N.-A., Cao, Q.-H.: Active control based on hedge-algebras theory of seismic-excited buildings with upgraded tuned liquid column damper. J. Eng. Mech. **149**(1), 04022091 (2022). https://doi.org/10.1061/JENMDT/EMENG-6821
3. Bui, H.-L., Tran, N.-A.: Multi-objective optimal design of TMDs for increasing critical flutter wind speed of bridges. J. Wind Eng. Ind. Aerodyn. **225**, 104992 (2022)
4. Bui, H.L.: An approach for optimizing the hedge-algebras-based controller and application in structural vibration control. In: Nguyen, D.C., Vu, N.P., Long, B.T., Puta, H., Sattler, K.U. (eds) ICERA 2022. LNNS, vol. 602, pp. 157–165. Springer, Cham (2023). https://doi.org/10.1007/978-3-031-22200-9_17
5. Bui, H.L.: Multi-objective optimization of hedge-algebra-based controllers for quarter-car active suspension models. In: Khang, N.V., Hoang, N.Q., Ceccarelli, M. (eds.) ASIAN MMS 2021. MMS, vol. 113, pp. 876–885. Springer, Cham (2022). https://doi.org/10.1007/978-3-030-91892-7_84
6. Mac, T.-T., Nguyen, T.-D., Bui, H.-L., Tran, N.-A.: Optimal design of hedge-algebras–based controller for vibration control of vehicle suspension systems. Proc. Inst. Mech. Eng. Part I J. Syst. Control Eng. (2023). https://doi.org/10.1177/09596518231196900
7. Nguyen, T.-D., Bui, H.-L.: General optimization procedure of the Hedge-algebras controller for controlling dynamic systems. Artif. Intell. Rev.Intell. Rev. **56**(3), 2749–2784 (2023)
8. Bui, V.-B., Mac, T.-T., Bui, H.-L.: Design optimization considering the stability constraint of the Hedge-algebras-based controller for building structures subjected to seismic excitations. Proc. Inst. Mech. Eng. Part I J. Syst. Control Eng. (2023). https://doi.org/10.1177/09596518231171960

Optimization of NURBS Fitting for Non-symmetric Acetabulum Bone Surface with Bending Energy

Vu Thi Lien(✉)

Faculty of Mechanical Engineering and Mechatronics, Phenikaa University, Hanoi, Vietnam
lien.vuthi@phenikaa-uni.edu.vn

Abstract. This paper presents a proposed method of fitting NURBS (Non- Uniform Rational B-Spline) surfaces for freeform surfaces to obtain both accuracy and smoothness. This proposed method has been applied to reconstruct human acetabulum surfaces from given grid of data points ($m \times n$) that are obtained from the opened bone layer contours. Three parameters of the NURBS surface, namely weights, control points and knot vectors are optimized to minimize fitting error. In order to obtain smoothness surfaces, the bending energy that related to surface curvature is used as a constraint of this optimization problem. In the simulation result, the smooth acetabulum model is obtained with an acceptable fitting error from a given bone data of dimension 43 × 50 × 39 mm. This result shows that this proposed method can be applied to reconstruct freeform surfaces.

Keywords: Acetabulum · NURBS · Fitting · Bending Energy · Simulated Annealing

1 Introduction

Nowadays, the development of biomedical technology allows bio-engineers not only to observe but also to reconstruct the 3-D human anatomical organs [1–3]. 3-D geometric representation of human bone surfaces is a process that contains three main steps [2, 3]. First, Computed Tomography (CT) digital processing techniques are used to filter original data (2-D photographic images) for 3-D reconstruction. After this step, planar contours in each Computed Tomography (CT) data slice are obtained. Then, segmentation technique is used to isolate the desired bones from the tissues. Second, from these contours are reconstructed to become a 3-D model. Finally, the data of the model is stored in the STL or IGES format, which can be imported into an engineering CAD software or rapid prototyping machine [2, 3].

Almost researches are focused on creating an automatic process to reconstruct the bone models form the CT images to medical rapid prototyping models [1–3]. Not many topics were done to improve both accuracy and smoothness of the reconstructed models. This research is focused on the second step of 3D geometric representation of human bone surfaces to improve these two criteria of bone model surfaces.

D. C. Nguyen et al. (Eds.): ICERA 2023, LNNS 944, pp. 299–305, 2024.
https://doi.org/10.1007/978-3-031-62235-9_30

The acetabulum, research object, is the socket of the ball-and-socket hip joint whose functions are support and mobility in all directions. Thus, the acetabulum is a natural and non-symmetric freeform surface. Therefore, a flexible method is needed to be developed to reconstruct it with accuracy and smoothness.

NURBS is a great flexible parameter surface for handling freeform shapes [4–6]. It can be applied to reconstruct non-symmetric surfaces such as acetabulum. In general, almost researches are concentrated to optimize or modify weights, control points and knot vectors of NURBS surface to obtain these criteria [5, 6]. To optimize these parameters, two concepts that are fitting error and bending energy should be reminded. The fitting error (distance error) is the distance between a data point and its corresponding point on the NURBS surface. If the sum of these error distances is minimized, the surface should follow the shape of the data polygon closely. So that, the least squares fitting problem relates to the accurate of the reconstructed surface. In computer-aided design, the curvature concepts are used to determine or visualize the fairness or smoothness of surfaces [5]. A surface is said to be smooth if its bending energy is minimal [7]. The bending energy has relation with Gaussian and means curvatures of the surface. Therefore, knot, weights and control points can be optimized by the least squares fitting error or energy minimization.

This study presents a constrained optimization problem in which three parameters of NURBS surface are optimized to minimize fitting error subjected to the bending energy functions by using Simulated Annealing algorithm [8, 9].

2 NURBS Surface

2.1 NURBS Surface Definition

NURBS is a very flexible form of mathematical function and commonly used in CAD applications. The NURBS surface of degree (p, q) is defined [4–6]:

$$S(u, v) = \frac{\sum_{i=1}^{h}\sum_{j=1}^{t} N_{i,p}(u)N_{j,q}(v)w_{i,j}P_{i,j}}{\sum_{i=1}^{h}\sum_{j=1}^{t} N_{i,p}(u)N_{j,q}(v)w_{i,j}}; (0 \leq u, v \leq 1) \tag{1}$$

where $\{P_{i,j} = (x_{i,j}, y_{i,j}, z_{i,j})\}$ are control points, the $\{w_{i,j}\}$ are the weights; $\{N_{i,p}(u)\}$ and $\{N_{j,q}(v)\}$ are the i-th and j-th B-spline basis functions of degree p and q in the bi-parametric u and v directions, respectively. Two knot vectors U, V are:

$$U = \left\{\underbrace{0, \ldots, 0}_{p+1}, u_{p+2}, \ldots, u_{h+1}, \underbrace{1, \ldots, 1}_{p+1}\right\}; \quad V = \left\{\underbrace{0, \ldots, 0}_{q+1}, v_{q+2}, \ldots, v_{t+1}, \underbrace{1, \ldots, 1}_{q+1}\right\}, \tag{2}$$

$N_{i,p}(u)$ and $N_{j,q}(v)$ are defined as follows:

$$\begin{cases} N_{i,0}(u) = \begin{cases} 1 \, \textit{if} \; u_i \le u \le u_{i+1} \\ 0 \, \textit{otherwise} \end{cases} \\ N_{i,p}(u) = \dfrac{u - u_i}{u_{i+p} - u_i} N_{i,p-1}(u) + \dfrac{u_{i+p+1} - u}{u_{i+p+1} - u_{i+1}} N_{i+1,p-1}(u) \end{cases} \tag{3}$$

and

$$\begin{cases} N_{j,0}(v) = \begin{cases} 1 \, \textit{if} \; v_j \le v \le v_{j+1} \\ 0 \, \textit{otherwise} \end{cases} \\ N_{j,q}(v) = \dfrac{v - v_j}{v_{j+p} - v_j} N_{j,q-1}(v) + \dfrac{v_{j+q+1} - v}{v_{j+q+1} - v_{j+1}} N_{j+1,q-1}(v) \end{cases} \tag{4}$$

Using rational basis functions:

$$R_{i,j}(u, v) = \frac{N_{i,p}(u) N_{j,q}(v) w_{i,j}}{\sum_{i=1}^{h} \sum_{j=1}^{t} N_{i,p}(u) N_{j,q}(v) w_{i,j}} \tag{5}$$

NURBS surface can be written as:

$$S(u, v) = \sum_{i=1}^{h} \sum_{j=1}^{t} R_{i,j}(u, v) P_{i,j} \tag{6}$$

Three main parameters including weights, control points and knot vectors are unknowns and needed to be determined in fitting process.

2.2 Gaussian and Mean Curvatures of NURBS Surface

The smoothness of a bi-parametric NURBS surface can be expressed through Gaussian curvature (K) and mean curvature (H). The Gaussian curvature determines whether a surface is locally convex or locally saddle-shaped while mean curvature is related to variation of surface area. Theses curvatures are given by [4, 6]:

$$K = \frac{A|S_v|^2 - 2BS_u S_v + C|S_u|^2}{2|S_v \times S_v|^3} \quad \text{and} \quad H = \frac{AC - B^2}{|S_v \times S_v|^4} \tag{7}$$

where,

$$(A \, B \, C) \; = \; [S_u \times S_v].[S_{uu} S_{uv} S_{vv}] \tag{8}$$

and,

$$S_u = \frac{\partial S(u, v)}{\partial u}; \; S_v = \frac{\partial S(u, v)}{\partial v}; S_{uu} = \frac{\partial S^2(u, v)}{\partial u^2}; S_{vv} = \frac{\partial S^2(u, v)}{\partial v^2}; S_{uv} = \frac{\partial S^2(u, v)}{\partial u \partial v} \tag{9}$$

The parametric derivatives of NURBS are obtained by formally differentiating Eq. (1).

2.3 Constrained Optimization Problem

Two types of fitting are distinguished interpolation and approximation [4–6]. In interpolation, a NURBS surface passes all data points in the given order. Thus, the distance between a data point and its corresponding point on the curve is zero. Since the parametric surface has to pass through all data points, it may wiggle through all data points. To overcome this problem, approximation method is used in this research. Except for the first and last data points, the NURBS curve may not need to contain other points.

Suppose there are m rows and n columns of data points ($m \times n$) $\overline{\mathrm{D}_{\mathrm{k,l}}}$ ($1 \le k \le m$, $1 \le l \le n$) and wish to find a NURBS surface of degree (p, q) that approximates all of them. A NURBS surface must be satisfied two criteria, which are accuracy and smoothness. Because the surface does not need to pass through all data points, to measure how accurate a surface can approximate the given data polygon, the concept of fitting error is used. The fitting error is the distance between a data point $\overline{\mathrm{D}_{\mathrm{k,l}}}$ and its corresponding point ($\mathrm{D}_{k,l}$) on the NURBS surface. Thus, the square root of the mean of the square of all of these errors is minimized, the surface should follow the shape of the data polygon closely.

Therefore, the objective function is:

$$\text{Minimize } f = \sqrt{\frac{1}{m.n}\sum_{k=1}^{m}\sum_{l=1}^{n}\left(\left|\left(\sum_{i=1}^{h}\sum_{j=1}^{t}R_{i,j}(u,v)P_{i,j}\right)_{k,l} - \overline{D_{k,l}}\right|^2\right)} \tag{10}$$

$$\text{Subject to } w_{i,j} > 0$$

For an unknown surface such as a bone surface, the curvatures at a data points are not given, it is very difficult to compare the curvatures of NURBS surface with these of original surface. A method to evaluate smoothness of the constructed surface has been introduced in [5, 7]. In order to satisfy a smoothness criterion for the second derivatives of the NURBS surface [7], bending energy E is minimized:

$$E = \int_0^1\int_0^1 (k_1^2 + k_2^2)dudv \tag{11}$$

where k_1 and k_2 are two principle curvatures at point (u, v). The Gaussian curvature K is the product of the principal curvatures and defined as $K = k_1k_2$. The mean curvature is defined as $H = (k_1 + k_2)/2$. Rewrite Eq. (11):

$$E = \int_0^1\int_0^1 [4H^2 - 2K]dudv \tag{12}$$

Furthermore, for computational efficiency, Eq. (12) is proposed to approximate as:

$$K_{RMS} = \sqrt{\frac{1}{mn}\sum_{i=1}^{m}\sum_{j=1}^{n}(4H_{i,j}^2 - 2K_{i,j})^2} \tag{13}$$

and,

$$K_{RS} = (4H_{i,j}^2 - 2K_{i,j})^{1/2} \tag{14}$$

K_{RS} is defined as root square curvature to measure the surface flatness in neighborhood of a point (u,v) on the fitting surface. This positive definite quantity is equal to zero only when both principle curvatures are zero. Conversely, if the surface has ripples resulting, the magnitude of K_{RS} will increase rapidly as a function of amplitude and frequency of the ripples. The value $K_{RMS,}$ root mean square curvature, is a global measure of the variation of K_{RS} over the entire surface. Therefore, to obtain smooth surfaces, K_{RMS} should be small values. The K_{RMS} is used as the constraint function of this optimization problem. The constrained optimization problem in this study is presented as follow:

$$\begin{aligned} &\text{Minimize} f(w_{i,j}, P_{i,j}, U, V) \\ &\text{Subject to} w_{i,j} > 0 \end{aligned} \tag{15}$$

$K_{RMS} \leq \varepsilon$, where ε is an expected value.

In this study, weights, control points and knot vectors are optimized by supporting of Simulated Annealing algorithm [8, 9].

3 Results and Discussions

In order to verify the proposed method, NURBS surface is used fit a Monkey saddle surface, $z = x^2–3xy^2$ (Fig. 1a) with 16 × 16 data points (Fig. 1b). Since Monkey saddle is a known surface, the original K_{RMS} can be calculated as 1.037. This number is used aa a reference number to choose the expected value of the root mean square in the optimization process. The cubic NURBS surface is shown in Fig. 1c with 10 × 10 control points and a small fitting error of 0.0029 mm. As observed in Fig. 2, the K_{RMS} maps of Monkey saddle and NURBS surface are similar. Thus, this proposed method has provided the accuracy and smoothness for the reconstructed surface.

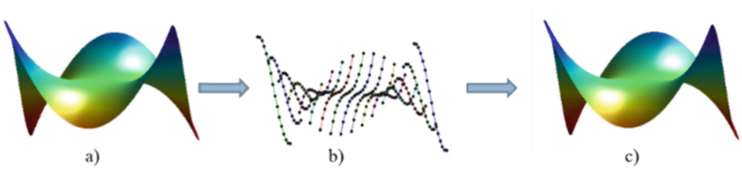

Fig. 1. a) The Monkey saddle surface; b) 16 × 16 data point; c) NURBS surface.

After that, the proposed method is applied to fit an acetabulum model, shown in Fig. 3a. The dimension of the given acetabulum is around 43 × 50 × 39 mm with 39 × 13 data points. To demonstrate the ability of the proposed method, two NURBS fitting cases have been performed. In the first case, a cubic NURBS surface with 12 × 7 control points is optimized to fit the data points without the constraint of bending energy, shown in Fig. 3b. Using the same control points, the proposed method is applied to fit these

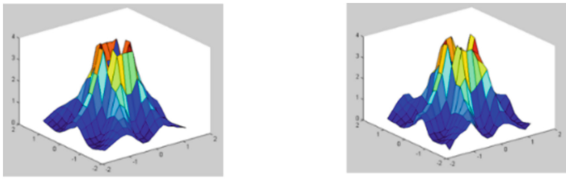

Fig. 2. K_{RMS} maps of: a) Original surface; b) NURBS surface.

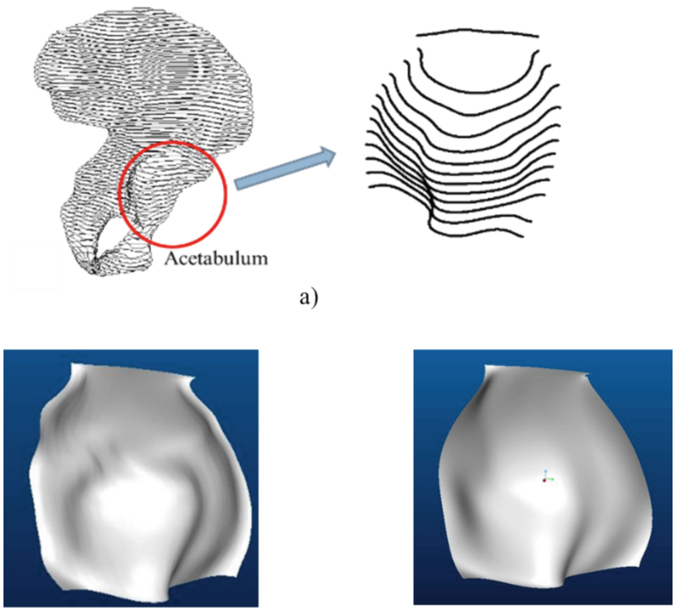

Fig. 3. a) A hip bone with an acetabulum having 39 × 13 data points, b) NURBS surface fitting without constraint of the bending energy, c) NURBS surface fitting using the proposed method.

data points in Fig. 3c and the accepted fitting error after optimization is 0.2105 mm. Since, the acetabulum is an unknown surface, the root mean square curvature (K_{RMS}) of NURBS cannot compare with that of the original surface. However, by observation, it can be seen that the NURBS surface fitting using the proposed method is smoother than the NURBS that optimized without the constraint. Thus the proposed method can be applied to reconstructed the freeform surfaces.

4 Conclusions

This paper has developed a method for fitting non-symmetric objects i.e. bone surfaces using NURBS surface. Three parameters of NURBS surface, namely weight, control points and knot vectors are optimized to obtain both accuracy and smoothness of the reconstructed surface. This is a constrained optimization problem in which the objective function is to minimize the fitting error and the constraint function is bending energy. For both known and unknown surfaces, the proposed method has provided the accuracy and smoothness NURBS surface. These results show that the proposed method can be applied to reconstruct freeform surfaces.

References

1. Gupta, N., Mishra, B., Crandall, D.M: A new workflow of X-ray CT image processing and data analysis of structural features in rock using open-source software. Mining, Metall. Explor. **39**, 2011–2024 (2022)
2. Kerem Ün, M., Avşar, E., Akçalı, İ.D.: An analytical method to create patient-specific deformed bone models using X-ray images and a healthy bone model. Comput. Biol. Med. **104**, 43–51 (2019)
3. Majeed, A., Piah, A.R.M., Rafique, M., Abdullah, J.Y., Rajion, Z.A.: NURBS curves with the application of multiple bones fracture reconstruction. Appl. Math. Comput. **315**, 70–84 (2017)
4. Jane Jiang, X., Scott, P.J.: Chapter 4 - Geometrical fitting of free-form surfaces, Advanced Metrology. Academic Press, pp.65–92 (2020)
5. Hashemian, A., Hosseini, S.F.: An integrated fitting and fairing approach for object reconstruction using smooth NURBS curves and surfaces. Comput. Math. Appl. **76**(7), 1555–1575 (2018)
6. Piegl, L.A., Tiller, W.: The NURBS Book. Springer (1997)
7. Wang, X., Cheng, F., Barsky, B.A.: Energy and B-spline interpolation. Comput. Aid. Design **29**, 458–496 (1997)
8. Ueda, E.K., et al.: Piecewise Bézier curve fitting by multiobjective simulated annealing. IFAC-PapersOnLine **49**(31), 49–54 (2016)
9. Lee, Y.S., Graham, E., Jackson, G., Galindo, A., Adjiman, C.S.: A comparison of the performance of multi-objective optimization methodologies for solvent design. Comput. Aid. Chem. Eng. **46**, 37–42 (2019)

Optimization of Minimum Quantity Lubricant Conditions in Hard Turning of 9CrSi Steel - An Application of Taguchi Method

Thanh-Dat Phan[1](✉), Thi-Nguyen Nguyen[1], The-Vinh Do[1], and Nguyen-Anh-Vu Le[2]

[1] Thai Nguyen University of Technology, Thai Nguyen, Vietnam
leophanvn@tnut.edu.vn

[2] Nha Trang University, Khanh Hoa, Nha Trang, Vietnam

Abstract. Minimum Quantity Lubrication (MQL) is an advanced cooling and lubrication method that replaces traditional cooling and lubrication methods in metal cutting processes, offering several advantages. In this study, the parameters of MQL conditions were optimized during hard turning of the 9CrSi steel to achieve the minimum surface roughness. The Taguchi method was applied due to its numerous benefits, especially its high efficiency and low implementation cost. The three parameters of MQL conditions are nozzle-to-workpiece distance, fluid flow, and compressed air pressure. Each factor was investigated at three levels. Thus, the L9 array was employed for experimental design. Using Analysis of Variance (ANOVA), the research findings revealed that the compressed air pressure has the most significant impact on surface roughness compared to the other two factors, which are fluid flow and nozzle-to-workpiece distance. The compressed air pressure factor contributed over 47% of the total influence. The remaining factors, including fluid flow and nozzle-to-workpiece distance, contributed 31.07% and 9.24% respectively to the total influence on surface roughness. Furthermore, the optimal MQL conditions for achieving the best surface roughness were determined to be a nozzle-to-workpiece distance of 10 mm, a fluid flow of 50 ml/h, and a compressed air pressure supplied to the nozzle of 5 kg/cm2. A first-order regression equation was developed to predict surface roughness based on the three input parameters, yielding a determination coefficient (R-squared) of 88.08%. The research outcomes serve as a valuable reference for further studies in metal cutting processes with MQL applications.

Keywords: Minimum Quantity Lubrication · Hard turning · 9CrSi Steel · Taguchi Method · Optimization · Analysis of Variance

1 Introduction

The Taguchi method finds extensive application due to its simplicity and robustness in optimizing process parameters, leading to significant reductions in both cost and processing time [1, 2]. Within the experimental design, the Taguchi method employs orthogonal arrays to yield optimal outcomes while minimizing the number of required experiments.

D. C. Nguyen et al. (Eds.): ICERA 2023, LNNS 944, pp. 306–313, 2024.
https://doi.org/10.1007/978-3-031-62235-9_31

An indicator called signal-to-noise (S/N) ratio quantifies performance characteristics and facilitates the computation of each process parameter's percentage contribution through analysis of variance.

The S/N ratio gauges the extent of variation present in the quality characteristic, wherein 'S' signifies the mean value of the output characteristic, and 'N' represents the undesired value of the output characteristic. The analysis of the S/N ratio falls into three categories: 'the-bigger-is-the-better', 'the-smaller-is-the-better', and 'the-nominal-is-the-better' [3]. Consequently, the suitable category is chosen based on the specifics of each individual case.

The widespread adoption of hard machining in mechanical processing is attributed to its numerous inherent advantages. These advantages encompass enhanced geometric precision, elevated quality of finished surfaces, lowered labor expenses [4], decreased burr formation, improved chip disposal, heightened stability, streamlined tooling [5], and adaptable process design [6, 7]. Nevertheless, it is imperative to acknowledge the drawbacks associated with hard machining, which comprise a high rate of tool wear, a decrease in tool longevity due to the impact of the workpiece material's elevated hardness and cutting temperatures [7–10]. Despite its benefits, the application of flood coolant in hard milling has faced limitations, particularly concerning environmental and health-related concerns for workers.

MQL stands as a successful remedy within the realm of hard machining, proving its efficacy and eco-friendly nature through widespread integration across various machining operations such as turning [11–13], drilling [14, 15], and milling [16, 17]. As defined by numerous scholars [2, 18, 19], MQL machining involves the judicious application of a minute quantity of lubricant, typically at a flow rate below 250 ml/h, which is mixed with compressed air and subsequently sprayed onto the cutting zone. The manifold benefits of MQL encompass enhancements in surface finish quality, elongated tool lifespan, attenuation of tool wear, reduction in cutting temperature, and diminished lubrication costs [18–20].

In the application of MQL, there are multiple parameters that require careful consideration due to their influence on the effectiveness of the machining process when utilizing MQL. The parameters of MQL encompass various factors such as the compressed air pressure supplied to the nozzle, the flow rate of the liquid stream, the type of fluid used, the distance and the angle of the nozzle… The process of selecting an optimal MQL condition with the best parameters to achieve maximum efficiency in the machining process is an intriguing endeavor for researchers.

In this study, the Taguchi method was employed to investigate the influence of three parameters of MQL conditions, including the nozzle-to-workpiece distance, fluid flow, and compressed air pressure, on the output factor, which is the surface roughness. The hard turning process of 9CrSi steel with a hardness of 50HRC was carried out on an EMCO Maxxturn 45 CNC lathe. An optimal MQL condition was determined to achieve the lowest surface roughness. Furthermore, a first-order regression equation was developed to predict surface roughness based on the input parameters.

2 Materials and Experiment Setup

The workpieces utilized were cylindrical 9CrSi alloy steel blocks with an initial diameter of 35mm, which underwent heat treatment to achieve a hardness of 50HRC. The chemical components of 9CrSi steel is shown in Table 1.

Table 1. The chemical components of 9CRSi steel

C	Si	Mn	S	P	Cr	Ni	Cu
0.85 ~ 0.95	1.20 ~ 1.60	0.30 ~ 0.60	≤ 0.03	≤ 0.03	0.95 ~ 1.25	≤ 0.25	≤ 0.30

An EMCO Maxxturn 45 CNC lathe machine was deployed to carry out experiments following the Taguchi method. Workpieces were securely clamped onto a three-jaw chuck as show in Fig. 1. The MQL nozzle was attached within the working area and was adjusted to point directly at the tip of the CBN insert of the cutting tool. The distance of the nozzle to workpiece was maintained as introduced in Table 2. This parameter is symbolized by letter (d) while the fluid flow of coconut oil and the air pressure are (f) and (p) respectively. After each experiment performed with a set of the three parameters, the surface roughness of the workpiece was collected with the help of the Mitutoyo SJ-401 roughness measuring instrument. Due to the scope of this study was to optimize the factors related to the MQL setup, other parameters applied during the turning process such as the depth of cut, cutting speed and feed rate were kept as shown in Table 3.

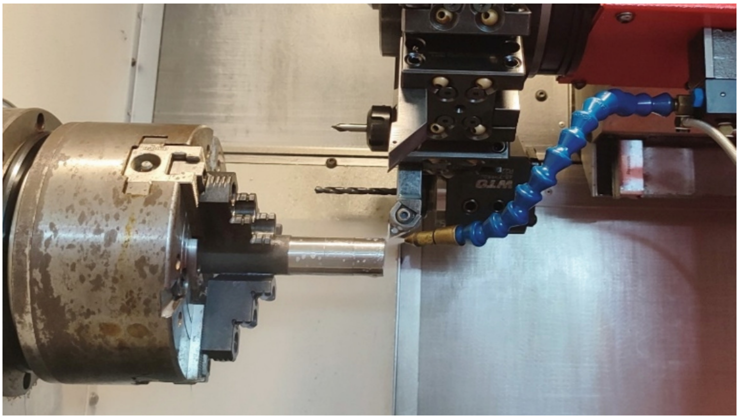

Fig. 1. Experimental setup.

Table 2. MQL parameters with their three levels

Parameters	Unit	Symbol	Levels		
			1	2	3
Distance of nozzle	mm	D	10	20	30
Fluid flow	ml/h	F	10	30	50
Air pressure	kg/cm2	P	3	4	5

Table 3. Cutting parameters

Cutting parameters	Values
Feed-rate (mm/rev)	0.15
Cutting speed (m/min)	80
Depth of cut (mm)	0.2

3 Result and Discussion

The result of L9 array experiments following Taguchi method is shown in Table 4. The surface roughness Ra values were reasonable comparing to other studies [21]. Nevertheless, this output value was obtained only to evaluate the MQL parameters that effected the cutting quality. According to nine experiment results, it could be clearly observed that the higher the air pressure value (p), the better the surface roughness value we could get.

Table 4. Experimental results

No	*d*	*f*	*p*	*Ra*	*S/N*
1	10	10	3	1.117	-0.96106
2	10	30	4	0.988	0.10486
3	10	50	5	0.948	0.46383
4	20	10	4	1.085	-0.70859
5	20	30	5	0.962	0.33650
6	20	50	3	1.021	-0.18051
7	30	10	5	1.044	-0.37401
8	30	30	3	1.157	-1.26667
9	30	50	4	1.002	-0.01735

Further analyzed with the Signal to noise ratio drew deeper analysis of the role of each MQL parameter as shown in Table 5. The rank value indicated that the air pressure had the most effect to the cutting result, following by the fluid flow (f) and the nozzle distance (d) accordingly. A mean of S/N ratios plot is presented in Fig. 2 in order to visualize the effects of the studied parameters. As shown in Fig. 2, the optimal MQL conditions for achieving the best surface roughness were determined to be a nozzle-to-workpiece distance of 10mm, a fluid flow of 50ml/h, and a compressed air pressure supplied to the nozzle of 5kg/cm2.

Table 5. S/N Analysis

Level	d	f	p
1	-0.13079	-0.68122	-0.80275
2	-0.18420	-0.27510	-0.20703
3	-0.55268	0.08865	0.14211
Delta	0.42189	0.76988	0.94486
Rank	3	2	1

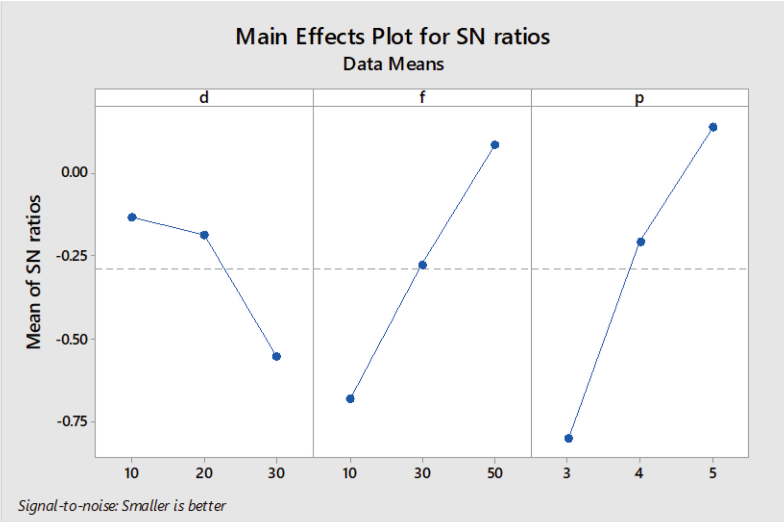

Fig. 2. Mean of S/N ratios plot

From the experiment results, a regression model of the Ra value was built to help with further prediction of the proposed method and future applying parameters (1).

$$Ra = 1.2821 + 0.00250\,d - 0.002292\,f - 0.0568\,p \quad (1)$$

Another common method in evaluating the accurate of a research result, the ANOVA table, was conducted to determine the accuracy of the model mentioned above (Table 6). The significance of (p) and (f) value were confirmed as the P-value of them were smaller than 0.05. The R-sq value of 88.08% was a promising indicator for the model reliance.

Table 6. ANOVA table

Source	DF	Adj-SS	Adj-MS	F-Value	P-Value	PC%
Regression	3	0.035734	0.011911	12.31	0.010	88.08
d	1	0.003750	0.003750	3.88	0.106	9.24
f	1	0.012604	0.012604	13.03	0.015	31.07
p	1	0.019380	0.019380	20.03	0.007	47.77
Error	5	0.004838	0.000968	–	–	–
Total	8	0.040572	–	–	–	–
R-sq = 88.08%						

4 Conclusion

Recent researches in the state of the art showed variety interests in the field of hard turning integrated MQL process. These researches tried to improve the cutting quality regarding main factors of turning process such as: cutting parameters, new technologies in turning or different nano particles mixed in the coolant lubricant. This study, on the other hand, implemented with a simple and straight forward approach as looking at the less impact factors including the air pressure, the fluid flow of the MQL system together with the distance between the nozzle and the workpiece. The result of the research is believed to have a good contribution to the cutting quality as the following conclusion:

– The pressure applied to the lubricant plays a significance role in the MQL system
– The distance between the nozzle and the workpiece should be considered only for the convenience of the experimental setup because it has rather small effect to the experimental design overall.
– The best surface roughness was found to be achievable under the following optimal conditions for Minimum Quantity Lubrication: a 10mm distance between the nozzle and workpiece, a fluid flow of 50ml/h, and a nozzle-supplied compressed air pressure of 5kg/cm^2.
– A mathematical model regarding the three studied parameters was built with the confident of 88.08%. This model should help further study in our investigation or other authors with the MQL parameters.

Acknowledgements. The authors wish to thank Thai Nguyen University of Technology. This work was supported by Thai Nguyen University of Technology.

References

1. Phadke, M.S.: Quality engineering using design of experiments. Qual. Control Robust Des. Taguchi Method, 31–50 (1989)
2. Do, T.-V., Hsu, Q.-C.: Optimization of minimum quantity lubricant conditions and cutting parameters in hard milling of AISI H13 steel. Appl. Sci. **6**(3), 83 (2016)

3. Fratila, D., Caizar, C.: Application of Taguchi method to selection of optimal lubrication and cutting conditions in face milling of AlMg3. J. Clean. Prod. **19**(6–7), 640–645 (2011)
4. Lobanov, A.A.: Technological advantages of hard milling. Russ. Eng. Res. **27**(6), 396–397 (2007)
5. Schulz, H., Moriwaki, T.: High-speed machining. CIRP Ann. **41**(2), 637–643 (1992)
6. An, Q., Wang, C., Xu, J., Liu, P., Chen, M.: Experimental investigation on hard milling of high strength steel using PVD-AlTiN coated cemented carbide tool. Int. J. Refract. Met. Hard Mater. **43**, 94–101 (2014)
7. Denkena, B., Köhler, J., Bergmann, B.: Development of cutting edge geometries for hard milling operations. CIRP J. Manuf. Sci. Technol. **8**, 43–52 (2015)
8. Do, T.V.: Empirical model for surface roughness in hard milling of AISI H13 steel under nanofluid-MQL condition based on analysis of cutting parameters. J. Mech. Eng. Res. Dev. **43**(2), 89–94 (2020)
9. Nguyen, Q.-M. Do, T-V.: Optimal approaches for hard milling of SKD11 steel under MQL conditions using SIO 2 nanoparticles. Adv. Mater. Sci. Eng., 2022 (2022)
10. Do, T.-V., Le, N.-A.-V.: Optimization of surface roughness and cutting force in MQL hard-milling of AISI H13 steel. In: Advances in Engineering Research and Application: Proceedings of the International Conference, ICERA 2018, pp. 448–454. Springer (2019). https://doi.org/10.1007/978-3-030-04792-4_58
11. Hadad, M., Sadeghi, B.: Minimum quantity lubrication-MQL turning of AISI 4140 steel alloy. J. Clean. Prod. **54**, 332–343 (2013)
12. Ekinovic, S., Prcanovic, H., Begovic, E.: Investigation of influence of MQL machining parameters on cutting forces during MQL turning of carbon steel St52-3. Procedia Eng. **132**, 608–614 (2015)
13. Masoudi, S., Vafadar, A., Hadad, M., Jafarian, F.: Experimental investigation into the effects of nozzle position, workpiece hardness, and tool type in MQL turning of AISI 1045 steel. Mater. Manuf. Process. **33**(9), 1011–1019 (2018)
14. Le Coz, G., Marinescu, M., Devillez, A., Dudzinski, D., Velnom, L.: Measuring temperature of rotating cutting tools: application to MQL drilling and dry milling of aerospace alloys. Appl. Therm. Eng. **36**, 434–441 (2012)
15. Heinemann, R., Hinduja, S., Barrow, G., Petuelli, G.: Effect of MQL on the tool life of small twist drills in deep-hole drilling. Int. J. Mach. Tools Manuf **46**(1), 1–6 (2006)
16. Do, T.-V.: A case study of minimizing cutting force in hard milling JIS SKD61 steel under nanofluid-MQL condition. In: Advances in Engineering Research and Application: Proceedings of the International Conference on Engineering Research and Applications, ICERA 2021, pp. 12–18. Springer (2022). https://doi.org/10.1007/978-3-030-92574-1_2
17. Nguyen, Q.-M., Nguyen, H.-T., Le, N.-A.-V., Nguyen, T.-N., Dang, T.-H.-T., Do, T.-V.: Investigation on the effect of nanofluid-MQL parameters on surface roughness during milling of hardened 9CrSi steel. In: Proceedings of the 2nd Annual International Conference on Material, Machines and Methods for Sustainable Development (MMMS2020), pp. 311–316. Springer (2021). https://doi.org/10.1007/978-3-030-69610-8_43
18. Dhar, N.R., Kamruzzaman, M., Ahmed, M.: Effect of minimum quantity lubrication (MQL) on tool wear and surface roughness in turning AISI-4340 steel. J. Mater. Process. Technol. **172**(2), 299–304 (2006)
19. Phafat, N.G., Deshmukh, R., Deshmukh, S.D.: Study of cutting parameters effects in MQL-employed hard-milling process for AISI H13 for tool life. Appl. Mech. Mater. Trans Tech. Publ., 240–245 (2013)

20. Do, T.V., Phan, T.D.: Multi-objective optimization of surface roughness and MRR in milling of hardened SKD 11 steel under nanofluid MQL condition. Int. J. Mech. Eng. Robot. Res. **10**, 357–362 (2021)
21. Le, T.-S., Tran, M.-D., Nguyen, D.-B., Nguyen, V.-C.: An investigation on effect of characteristics of the peanut oil MQL on tool life in hard turning 9CrSi steel. Int. J. Mach. Mach. Mater. **13**(4), 428–438 (2013)

Optimization of Parameters Affecting the Hammer Rapping Force to Ensure the Durability of the Discharge Electrode Frame, Dust Removal Acceleration and Durability of the Collecting Electrode Plate in the Electrostatic Precipitator

Nguyen Anh Tung, Phan Dang Phong, Hoang Van Got(✉), and Hoang Trung Kien

National Research Institute of Mechanical Engineering, Hanoi, Vietnam
gotnarime@yahoo.com.vn

Abstract. The scientific purpose of this study is to optimize 3 main parameters: hammer mass (m), hammer drop height (h) and filter chamber inlet dust concentration (η) of the Electrostatic precipitator, to meet the dust removal acceleration (a) and the hammer rapping force (F), ensure the working life span of the discharge electrode frames and the collecting electrode plates. This issue is evaluated as a multi-objective problem. The cyclic impact force (F) not only creates an acceleration (a) to remove the dust from the discharge frame but also causes fatigue damage to important parts of the dust filter chamber such as the discharge frames and collecting plates. To solve the scientific problem mentioned above, the article has applied the standard [2], the theoretical basis of empirical study of the author's [1, 10], experimental results on the static and actual models of the filter chamber, and the theory of fatigue curve construction based on experiments [5, 6].

Keywords: Dust filter chambers · Hammer rapping system · Discharge electrode

1 Introduction

Currently, in Vietnamese coal-fired power plants and cement factories, advanced horizontal electrostatic precipitators imported from Germany, France are being popularly utilized [3, 4, 7, 8]. The most important components of the dust filter chamber in ESP are the discharge and collecting electrodes. In which, the collecting electrode plates act as the negative pole and the discharge electrodes in the form of discharge frames fitting with spiked discharge rods act as the positive pole, together ionizing the dust particles passing through the filter chamber [3]. The objective is to gain control of the technology and design of the filter chamber. The study applied empirical study to determine the relationship between the main contributing parameters [1, 3, 4, 7–9] including: hammer rapping force (F), creating dust removal acceleration (a) on the basis of optimizing some technological parameters such as hammer mass (m), drop height of the hammer (h) and

D. C. Nguyen et al. (Eds.): ICERA 2023, LNNS 944, pp. 314–331, 2024.
https://doi.org/10.1007/978-3-031-62235-9_32

the dust concentration of the inlet flue gas (η) in the filter chamber to ensure the durability of the discharge electrode frame and the collecting plate in the filter chamber of the ESP.

According to the Ministry of Construction, nationwide there are currently 29 coal-fired power plants in operation with a total of 58 units, capacity vary from 200 MW to 600 MW, and about 120 coal-fired boilers that emit a large volume of flue gas into the environment. The dust concentration of the flue gas emitted from the boiler is approximately from 250 to 350 mg/Nm^3 and allowable discharge into the environment (depending on specific location of the plant) must be reduced to 50 mg/Nm^3 – 100 mg/Nm^3 [3, 4]. Electrostatic precipitator is the capable equipment to meet the above requirements. The electrodes are supplied with high D.C. voltage ranging from tens to several hundred (kV) [1, 4] to form a high intensity electric field. The flue gas stream passes through the filter chamber is ionized by discharge electrode system (positive charged) and microscopic dust particles are attracted to the surface of the collecting plates (negative charged). One of the most important component in the ESP filter chamber is discharge electrodes with frame-discharge rod structure [3, 4]. In Vietnam the past decades, ESP equipment has always been imported as synchronous system from abroad. However, recently, the Research Institute of Mechanical Engineering has designed the ESP on the basis of cooperation with foreign suppliers and has manufactured and commissioned the ESPs successfully at Vung Ang 1, Thai Binh 2 and Nghi Son 2 Thermal power plants.

When a discharge electrode frame is damaged, it will lead to stoppage of the plant operation for repair, causing great damage to the power industry. While there are hundreds of active ESPs in the whole country, it is a matter of concern for local scientific researches. Therefore, the research for a scientific solution to determine the appropriate durability of the discharge electrode frame sustaining periodic rapping force (F) that meet the dust removal acceleration (a), and at the same time ensure the durability of the collecting plates [5, 6] is currently an urgent issue in Vietnam.

2 Experiment Design

The relationship equation between dust removal acceleration (a), rapping force (F) and influencing parameters (m), (h) and (η) is established by experiment.

2.1 Influence of Factors

The factors that influence the durability of the discharge electrode frame and the collecting electrode plates include:

- The impact force F(N) of the hammer on the lower beam anvil of the discharge frame every 15 min to remove dust is influenced by the hammer mass (m) and the hammer drop height of the hammer (h);

- The dust concentration (η) of flue gas entering the filter chamber ranges from 250 mg/Nm^3 to 350 mg/Nm^3 after the boiler. According to environmental standard requirements for coal-fired power plants in Vietnam is 50 mg/Nm^3. For one boiler unit capacity of 300 MW, the average amount of dust collected in a 15-min cycle is approximately 200 kg.

Practically, for imported ESPs from foreign countries, the parameters of hammer mass (m), hammer drop height (h) and dust accumulated on the frame (η) are selected and optimized to achieve the appropriate operation hammer rapping force (F). Therefore, in this study, three parameters were selected to study are: (m), (h) and (η) to establish the relationship between rapping force (F) of the hammer, hammer mass (m) and drop height (h) and the relationship between dust removal acceleration (a) with 3 parameters: (m); (h) and (η). On the other hand, the rapping force (F) must ensure the dust removal acceleration (a), at the same time satisfying the service life of the discharge frame and the durability of the collecting plate, which is target to be studied (Fig. 1).

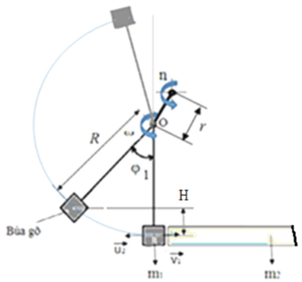

Fig. 1. Impact model of hammer and discharge frame.

2.2 Screening Design

Depending on the number of variables to be investigated and the cost and time requirements for the experiment, select the L9 type experiment design for screening design plan. In order to improve the reliability of the experiments, repeat some selected experiments one more time if necessary. Thus, the L9 type exploratory experiment design was selected, in which includes 3 central experiments. From the experimental results, the below matrix is documented (Tables 1 and 3).

In Fig. 2, three effect graphs of 3 variables are plotted in independent plots. The upper left corner of the graph shows the influence of the mass variable of the hammer (m), observed on the graph, when m changes from 6 kg to 8 kg, the graph (a) is steepest among the factors, the objective function varies from 2920 (m/s^2) to 3275 (m/s^2). The slope of this graph is (3275–2920)/2 = 177.5. By qualitative comparison shows that the slope of the influence graph of (m) is the largest; next is the graph of (h) with slope (3210–2970)/2 = 120 and finally η has slope (3110–3090)/2 = 10. The greater the slope of the graph, the greater the influence of the variable plotted on that graph to the objective function. Thus, the variable (m) has the strongest influence on the objective function; and variable (η) has the weakest effect.

Another way to evaluate the main effects is to look at the standardized effects graph or the Pareto effects graph.

On the graph in Fig. 3, Minitab uses the significance level value α to indicate the limit line (with coordinates 2.776 on the graph) of the reversed null hypothesis area.

Table 1. Exploratory matrix for 3 factors

m (kg)	h (m)	η (mg/Nm^3)	a_{tt} (m/s^2)	F_{tn} (N)
6	0.53	350	2908	492.53
6	0.53	250	2877	481.81
6	0.49	250	2831	472.32
9	0.53	350	3455	549.77
9	0.49	250	3239	535.25
9	0.49	350	3258	541.49
6	0.49	350	2803	469.32
9	0.53	250	3417	542.08

Table 2. Input parameters

Parameter	Symbol	Unit	Value level		
			1	2	3
Hammer mass	m	Kg	6	7	8
Drop height between hammer center and impact point	h	M	0.49	0.53	0.57
Dust concentration	η	(mg/Nm^3)	250	300	350

Table 3. Experimental matrix and result for dust removal acceleration

No	m (kg)	h (m)	η (mg/Nm^3)	Dust removal acceleration a (m/s^2)
1	6	0.49	250.00	2831.00
2	6	0.53	300.00	2905.77
3	6	0.57	350.00	3064.95
4	7	0.49	300.00	2888.66
5	7	0.53	350.00	3203.55
6	7	0.57	250.00	3121.00
7	8	0.49	350.00	3201.75
8	8	0.53	250.00	3239.00
9	8	0.57	300.00	3270.26
10	8	0.57	350.20	3510.00
11	8	0.57	349.15	3495.00
12	8	0.57	350.15	3505.00

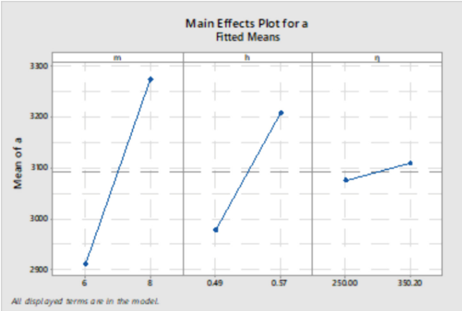

Fig. 2. Main factor affecting the dust removal acceleration plot

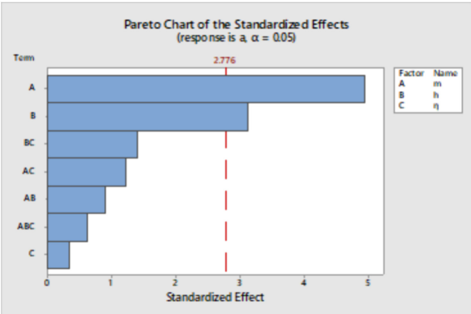

Fig. 3. Pareto chart for the factors affecting the dust removal acceleration (a)

The influence values (standardized) are presented as horizontal bars. The factors corresponding to the bar represented to the right of the limit line are values with significant influence. The factors represented to the left of the limit line are weakly influential.

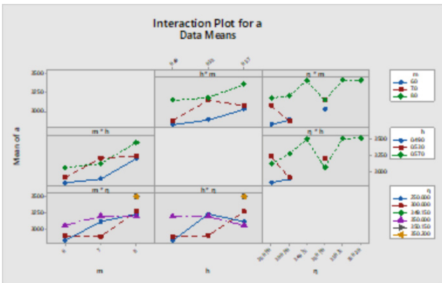

Fig. 4. Pareto chart for the factors affecting the dust removal acceleration (a)

The graph shows that the factors: A (variable m), B (variable h) have values beyond the limit line. Interaction effects will be analyzed in more detail in the next section. Thus, two experimental variables m and h have a great influence on the objective function. This is consistent with the conclusions drawn from the graph analysis of the main influencing factors (Fig. 4).

From the graph it is shown that:

- Consider the second cell in the first row: it can be seen that when rapping with a hammer mass m = 6 kg, the value of the objective function (a) increases when (h) increases from 0.49 m to 0.53 m and increases sharply if (h) increases from 0.53 m to 0.57 m; but if rapping with a 7 kg hammer, the objective function value increases when (h) increases from 0.49 m to 0.53 m, however (a) will decrease if it continues to increase from 0.53 m to 0.57 m. On the graph, the dashed line is steeper than the solid line. This means, whether (m) is large or small, it will affect the effect of the variable (h) on the objective function (a). In other words, (m) has a significant interaction effect and then the effect of (h).
- The same procedure was conducted to the remaining effect (Fig. 5).

ANOVA for Regression

Table 4. Experimental matrix and result for dust removal acceleration

Source	DF	Adj SS	Adj MS	F-Value	P-Value
Model	7	602327	86047	15.51	0.009
Linear	3	238883	79628	14.35	0.013
m	1	135467	135467	24.41	0.008
h	1	54044	54044	9.74	0.036
η	1	650	650	0.12	0.749
2-Way Interactions	3	16676	5559	1.00	0.478
m*h	1	4522	4522	0.81	0.418
m*η	1	8223	8223	1.48	0.290
h*η	1	10764	10764	1.94	0.236
3-Way Interactions	1	2133	2133	0.38	0.569
m*h*η	1	2133	2133	0.38	0.569
Error	4	22198	5549		
Total	11	624525			

Table 5. Model Summary

S	R-sq	R-sq (adj)	R-sq (pred)
74.4944	96.45%	90.23%	0.00%

Firstly, by observing the regression model, it is shown that the coefficients of the variables (m) and (h) have very small (p) values. That proves the presence of these two variables in the regression equation is significant. The other variables and interactions all have p-values much larger than the significance level $\alpha = 0.05$, so they can be removed from the regression equation. The analysis of variance shows that the probability (p) value corresponding to the main effects is small (0.013). Therefore, the effects of the variables are significant. Two-way interactions (2-way Interactions) have a p-value of 0.478 and 3-way interactions (3-way Interactions) have a p-value of 0.569 which is much larger than the level α (0.05). Therefore, it can be asserted that the variables have a relatively small interaction effect (Tables 2, 4, 5).

2.3 Experiment Planning $3^2 + 3$

a) Design the 3^2 matrix: After the exploration step, it can be confirmed that the 3 main factors affecting the dust removal acceleration are hammer mass (m), hammer drop height (h), and dust concentration (η). On the other hand, on the basis of experimental results with hammer weight ranges from 6 kg to 9 kg, the maximum tensile stress σ_{max} at the dangerous point of the frame has been calculated, showing that when m = 9kg, σ_{max} is larger than the allowable stress of the material CT3 steel of the discharge frame: $\sigma_{max} \leq [\sigma] = 240$ MPa. Therefore, for the experimental matrix planning, the hammer mass is limited from 6 to 8 kg. Exploratory empirical matrix with 3 factors allows the establishment of an exploratory matrix (Table 6).

Table 6. Empirical matrix $3^2 + 3$

No	Variable			Coded variable			Average acceleration (m/s^2)
	m (kg)	h (kg)	η (mg/Nm^3)	X_1	X_2	X_3	a
1	6	0.49	250	− 1	− 1	− 1	2831
2	6	0.49	300	− 1	− 1	0	2888
3	6	0.49	350	− 1	− 1	1	2803
4	6	0.53	250	− 1	0	− 1	2877
5	6	0.53	300	− 1	0	0	2906
6	6	0.53	350	− 1	0	1	2908
7	6	0.57	250	− 1	1	− 1	2919
8	6	0.57	300	− 1	1	0	2890
9	6	0.57	350	− 1	1	1	3065
10	7	0.49	250	0	− 1	− 1	2978
11	7	0.49	300	0	− 1	0	2889
12	7	0.49	350	0	− 1	1	2859
13	7	0.53	250	0	0	− 1	3051

(*continued*)

Table 6. (*continued*)

No	Variable			Coded variable			Average acceleration (m/s^2)
	m (kg)	h (kg)	η (mg/Nm^3)	X_1	X_2	X_3	a
14	7	0.53	300	0	0	0	3020
15	7	0.53	350	0	0	1	3204
16	7	0.57	250	0	1	− 1	3121
17	7	0.57	300	0	1	0	3177
18	7	0.57	350	0	1	1	3207
19	8	0.49	250	1	− 1	− 1	3105
20	8	0.49	300	1	− 1	0	3160
21	8	0.49	350	1	− 1	1	3202
22	8	0.53	250	1	0	− 1	3239
23	8	0.53	300	1	0	0	3304
24	8	0.53	350	1	0	1	3327
25	8	0.57	250	1	1	− 1	3337
26	8	0.57	300	1	1	0	3270
27	8	0.57	350	1	1	1	3404

– Analysis of Variance and Regression Equation:

The values of the regression coefficients are denoted as constants in the Term column of the table. The values of the coefficients are listed in the "Coef" column. Column T represents the t-distribution value of the considering variables; column P lists the probability (p) (p-value) when testing the statistical hypothesis about the possibility that the coefficients equal zero. A (p) value greater than the significance level $\alpha = 0.05$ indicates that the existence of the corresponding coefficient is not statistically significant. The independent variables that have a very strong influence are (m), (h). The (p) value for these variables is less than 0.001, so Minitab displays the value 0.000. The variable (η) with p-value equal to 0.048 has a weaker influence than the above two variables on the objective function (a). In the two-level and three-level interaction factors, both p-values greater than 0.05 are weak effects. The table displays the regression model evaluation parameters. The decision coefficients r^2 (denoted as R-Sq) and r^2_{adj} (denoted as R-sq (adj)) are 92.41% and 89% respectively, which are greater than 90%, proving that the model is appropriate with the data.

Regression Equation in Uncoded Units:

$$a = 18762 - 2112\,m - 31647\,h - 55.7\,\eta + 4229\,m \times h + 6.94\,m \times \eta + 103.9\,h \times \eta - 12.8\,m \times h \times \eta \quad (1)$$

Table 7. Analysis of Variance

Source	DF	Adj SS	Adj MS	F-Value	P-Value
Model	7	781533	111648	33.06	0.000
Linear	3	762189	254063	75.23	0.000
M	1	591042	591042	175.02	0.000
H	1	156116	156116	46.23	0.000
H	1	15031	15031	4.45	0.048
2-Way Interactions	3	14128	4709	1.39	0.275
m*h	1	3058	3058	0.91	0.353
m*η	1	878	878	0.26	0.616
h*η	1	10193	10193	3.02	0.099
3-Way Interactions	1	5216	5216	1.54	0.229
m*h*η	1	5216	5216	1.54	0.229
Error	19	64164	3377		
Total	26	845697			

Table 8. Model Summary

S	R-sq	R-sq (adj)	R-sq (pred)
58.1122	92.41%	89.62%	87.24%

Table 9. Analysis of Variance

Term	Effect	Coef	SE Coef	T-Value	P-Value	VIF
Constant		3071.8	11.2	274.67	0.000	
m	362.4	181.2	13.7	13.23	0.000	1.00
h	186.3	93.1	13.7	6.80	0.000	1.00
η	57.8	28.9	13.7	2.11	0.048	1.00
m*h	31.9	16.0	16.8	0.95	0.353	1.00
m*η	17.1	8.6	16.8	0.51	0.616	1.00
h*η	58.3	29.1	16.8	1.74	0.099	1.00
m*h*η	− 51.1	− 25.5	20.5	− 1.24	0.229	1.00

2.4 Experiment Analysis for Factors Affecting Rapping Force (F)

Screening Design: According to the number of variables to be investigated and the cost and time requirements for the experiment, the L9 type of experiment design is selected as experimental plan for the screening experiment. In order to improve the reliability of the experiments, repeat some selected experiments one more time if necessary. Thus, the total number of experiments to be carried out is 12 experiments. The statistical analysis technique will allow evaluation of the influence of the variables considered on the output function as well as the interaction effect between them. Multivariate regression technique is used to determine the relationship between variables and the objective function.

Table 10. Input parameters

Parameter	Symbol	Unit	Value level		
			1	2	3
Hammer mass	M	Kg	6	7	8
Drop height between hammer center and impact point	H	M	0.49	0.53	0.57
Dust concentration	H	(mg/Nm^3)	250	300	350

2.5 The Effect of the Main Factors on Rapping Force

Experimental Matrix and Result for Rapping Force

Table 11. Experimental matrix and result for rapping force

No	m (kg)	h (m)	η (mg/Nm^3)	Rapping force F (N)
1	6	0.49	250.00	472.317
2	6	0.53	300.00	462.541
3	6	0.57	350.00	519.022
4	7	0.49	300.00	481.322
5	7	0.53	350.00	517.601
6	7	0.57	250.00	511.483
7	8	0.49	350.00	532.196
8	8	0.53	250.00	511.377
9	8	0.57	300.00	551.140
10	8	0.57	350.20	549.200
11	8	0.57	349.15	516.200
12	8	0.57	350.15	597.200

The Effect of the Main Factors on Rapping Force (F) Plot

On the chart in Fig. 6, Minitab uses the significance level value α to draw the limit line (with coordinate 4.303 on the graph) of the reversed null hypothesis area. The factors

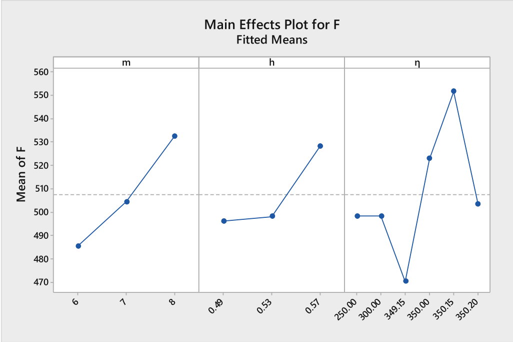

Fig. 5. The effect of the main factors on rapping force (F) plot

corresponding to the bar that exceed the right of the limit line are values that have a significant effect. The influence values (standardized) are presented as horizontal bars. The factors corresponding to the bar represented to the right of the limit line are values with significant influence. The factors represented to the left of the limit line are weakly influential. The graph shows that all factors have a negligible influence on F. Specifically, independent parameter (m) has the greatest influence on the rapping force F followed by (h) and then (m) (Tables 7, 8, 9, 10 and 11).

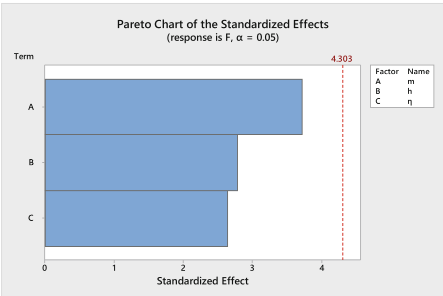

Fig. 6. Main factor affecting the rapping force (F) plot

ANOVA for Regression

The analysis of variance shows that the probability (p) value corresponding to the Main effects is 0.158. Therefore, the effects of the variables are insignificant. Two-way interactions (2-way Interactions) is with a p-value of 0.928 and 3-way interactions (3-way Interactions) is with a p-value of 0.449 which is much larger than the α level (0.05). Therefore, it can be asserted that the variables have a relatively small interaction effect.

2.6 Experiment Planning 3^3

After the exploration step, it can be confirmed that the two main factors affecting the rapping force (F) are the hammer mass (m), the hammer dropping height (h). Experiment design L27 is applied.

Table 12. Analysis of Variance

Source	DF	Adj SS	Adj MS	F-Value	P-Value
Model	7	11653.3	1664.76	1.91	0.278
Linear	3	7860.9	2620.30	3.00	0.158
M	1	3320.3	3320.28	3.81	0.123
H	1	1897.1	1897.08	2.18	0.214
H	1	273.8	273.81	0.31	0.605
2-Way Interactions	3	380.2	126.74	0.15	0.928
m*h	1	11.2	11.16	0.01	0.915
m*η	1	51.8	51.82	0.06	0.819
h*η	1	31.0	31.03	0.04	0.860
3-Way Interactions	1	611.7	611.67	0.70	0.449
m*h*η	1	611.7	611.67	0.70	0.449
Error	4	3488.7	872.19		
Total	11	15142.0			

On the basis of the experimental matrix L27, utilize Minitap software to set up the function F = f (m,h) and graph (Fig. 7).

2.7 Analyzing the Influence of Factors to F

From the experimental results, the Pareto chart was established (Fig. 7).

On the graph in Fig. 7, Minitab uses the significance level value α to indicate the limit line (with coordinates 2.068 on the graph) of the reversed null hypothesis area. The influence values (standardized) are presented as horizontal bars. The factors corresponding to the bar that exceed the right of the limit line, (m) and (h), have a great influence on (F), The factor represented to the left of the limit line has no significant effect (Tables 12, 13, 14, 15 and 16).

Analysis of Variance and Regression Equation

The values of the regression coefficients are denoted as constants in the "Term" column of the table. The values of the coefficients are listed in the "Coef" column. Column T represents the t-distribution value of the quantity in question; column P lists the probability p (p-value) when testing the statistical hypothesis about the possibility that the coefficients equal zero. A (p) value greater than the significance level $\alpha = 0.05$ indicates that the existence of the corresponding coefficient is not statistically significant. The independent variables that have very strong influence are (m), (h). The (p) value for these variables is less than 0.001, so Minitab displays the value 0.000. In the two-level interaction factors, p-values greater than 0.05 are all weak effects.

Regression Equation in Uncoded Units:

$$F = 14 + 31.7\,m + 678\,h + 24\,m \times h \tag{2}$$

Table 13. Experimental matrix L27 and measuring results of force F

No	Variable		Coded variable		Average acceleration
	m (kg)	h (m)	X_1	X_2	a (m/s^2)
1	6	0.49	− 1	− 1	472.32
2	6	0.49	− 1	− 1	453.42
3	6	0.49	− 1	− 1	469.32
4	6	0.53	− 1	0	481.81
5	6	0.53	− 1	0	462.54
6	6	0.53	− 1	0	492.54
7	6	0.57	− 1	1	511.79
8	6	0.57	− 1	1	517.02
9	6	0.57	− 1	1	519.02
10	7	0.49	0	− 1	486.18
11	7	0.49	0	− 1	481.32
12	7	0.49	0	− 1	500.77
13	7	0.53	0	0	492.95
14	7	0.53	0	0	497.88
15	7	0.53	0	0	517.60
16	7	0.57	0	1	511.48
17	7	0.57	0	1	501.25
18	7	0.57	0	1	526.83
19	8	0.49	1	− 1	506.85
20	8	0.49	1	− 1	491.65
21	8	0.49	1	− 1	532.20
22	8	0.53	1	0	511.38
23	8	0.53	1	0	485.81
24	8	0.53	1	0	517.60
25	8	0.57	1	1	558.14
26	8	0.57	1	1	551.14
27	8	0.57	1	1	562.47

From the experimental regression equation shows:

Independent parameters (h) and (m) have the greatest influence on the rapping force (F) followed by the interaction between (h) and (m).

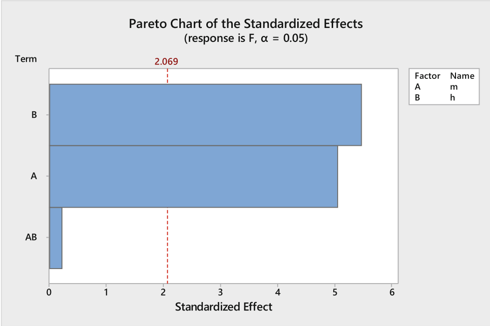

Fig. 7. Pareto chart of the influence of factors on F

Table 14. Analysis of Variance

Source	DF	Adj SS	Adj MS	F-Value	P-Value
Model	3	13743.6	4581.21	18.53	0.000
Linear	2	13732.2	6866.08	27.77	0.000
M	1	6326.2	6326.16	25.58	0.000
H	1	7406.0	7406.01	29.95	0.000
2-Way Interactions	1	11.5	11.46	0.05	0.831
m*h	1	11.5	11.46	0.05	0.831
Error	23	5687.4	247.28		
Lack-of-Fit	5	2642.3	528.45	3.12	0.033
Pure Error	18	3045.1	169.17		
Total	26	19431.0			

Table 15. Coded Coefficients

Term	Effect	Coef	SE Coef	T-Value	P-Value	VIF
Constant		504.20	3.03	166.61	0.000	
M	37.49	18.75	3.71	5.06	0.000	1.00
H	40.57	20.28	3.71	5.47	0.000	1.00
m*h	– 1.95	– 0.98	4.54	– 0.22	0.831	1.00

3 Experiment Results

Construction of Tensile and Fatigue Curves for Discharge Electrode Frames

Tensile strength test with specimen conforms to TCVN 8185:2009 "Metal material – Fatigue test – controllable axial force application method". Tensile test graph of CT3 steel discharge frame (Fig. 8), Experimental fatigue curve of discharge frame (Fig. 9):

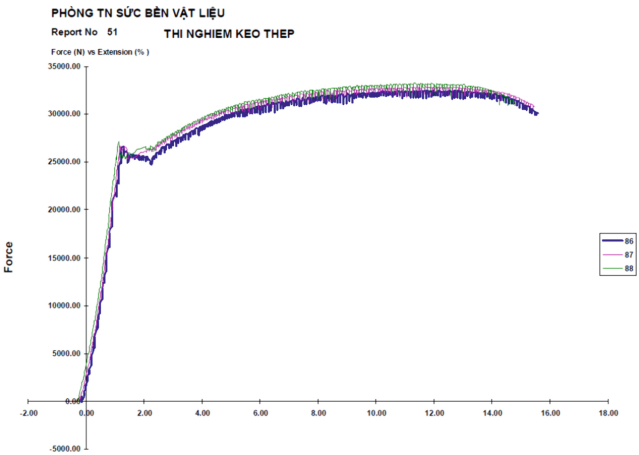

Fig. 8. Tensile test result for CT3 steel

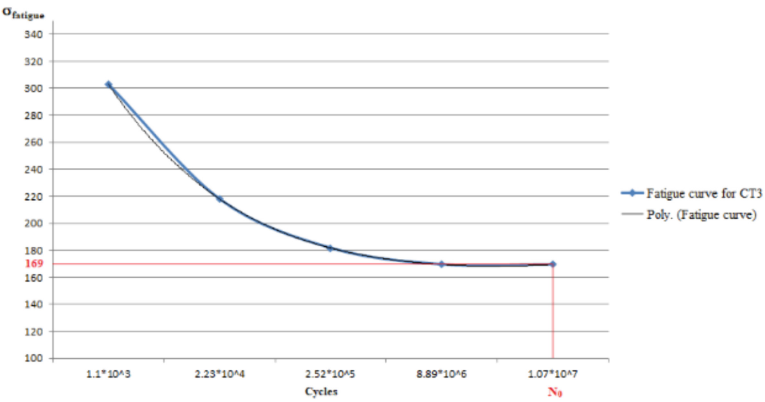

Fig. 9. CT3 steel discharge frame fatigue curve – test on standard test piece

From the above theoretical bases, a set of fatigue stress parameters can be calculated to establish a fatigue curve for the discharge frame. By calculation, the similarity factor is constant, i.e. 1.27476. Fatigue stress parameters for the discharge frame was developed according to Table 17.

From Table 17, the fatigue curve of the discharge frame was established (Fig. 10).

Table 16. Fatigue test result for CT3 steel

Test no	Test wt. (kg)	Moment of inertia	No. of cycles	No. of cycles	Fatigue stress of test piece (kg/cm^2)	Fatigue stress of test piece (MPa)
1	25	0.0396263	1100	1.1x10^3	3028.295301	302.8295301
2	18	0.0396263	22300	2.23x10^4	2180.372616	218.0372616
3	15	0.0396263	252000	2.52x10^5	1816.97718	181.697718
4	14	0.0396263	8890000	8.89x10^6	1695.845368	169.5845368
5	14	0.0396263	10700000	1.07x10^7	1695.845368	169.5845368

Table 17. Parameters for experimental fatigue curves for discharge frames

Fatigue stress of test piece (MPa)	Similarity ratio	Fatigue stress of frame (MPa)
302.8295301	1.27476	386.0349717
218.0372616	1.27476	277.9451797
181.697718	1.27476	231.620983
169.5845368	1.27476	216.1795842
169.5845368	1.27476	216.1795842

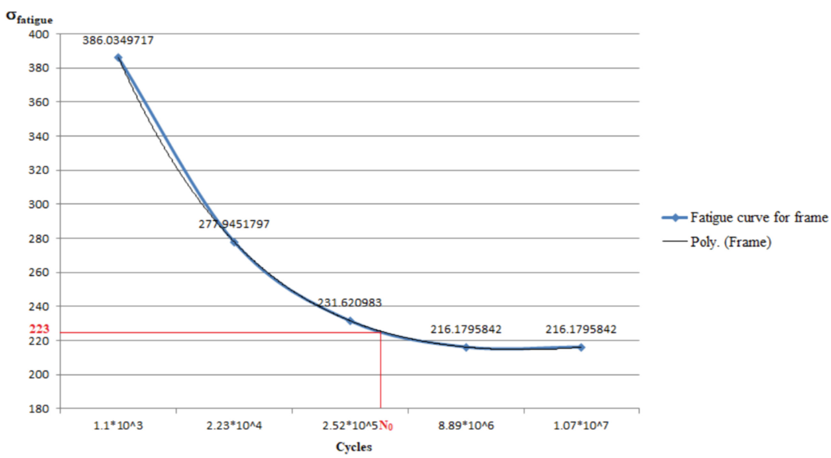

Fig. 10. Experimental fatigue curve for the discharge frame

A 3D model of the discharge electrode frame was developed to perform finite element simulation. Applying the measured rapping force for the worst case scenario, the maximum stress location and value $\sigma_{max} = 222.945$ MPa (~223 MPa) was calculated. By reflecting the maximum stress on the fatigue curve in Fig. 10 can determine the expected life N_0 of the discharge electrode, by taking the lower nearest horizontal axis coordinate for safety expectation. The corresponding N_0 shown 2.52×10^5 cycles.

4 Scientific Discussion of the Achieved Results

The experiments the following discussion have been achieved:

- Applying simulation software on the experimental curve have found the maximum stress on the discharge electrode frame: $\sigma_{max} = 222.945$ MPa (223 MPa);
- Determined the expected life of the discharge frame based on the number of rapping cycles is $N_0 \sim 2.52 \text{x} 10^5$ cycles (equivalent to minimum of ~ 8.75 years of operation);
- Compared to the allowable tensile stress of the discharge frame made of CT3, the tested tensile stress of CT3 steel $[\sigma_{ch\_CT3}] = 328.17$ MPa and meeting the allowable stress for the collecting plates made of CT0 steel with $[\sigma_{ch\_CT0}] = 304.23$ MPa (according to standard GOST – 3SP/PS 380/94). This means that the rapping force (F) meets the durability of the discharge frame while creates the required dust removal acceleration (a) and at the same time is suitable with the allowable stress of the collecting electrode plates.

5 Conclusion

On the basis of experimental results, a matrix $3^3 = 27$ has been established with 3 input parameters: hammer mass (m), hammer drop height (h) and inlet dust concentration (η), satisfying the output criteria are the dust removal acceleration (a) and the appropriate rapping force (F) of the hammer. From which, two important empirical regression equations have been established, meeting the objectives:

$$\begin{aligned} \mathrm{a} = {} & 18762{-}2112\ \mathrm{m}{-}31647\ \mathrm{h} - 55.7\ \eta + 4229\ \mathrm{m} \times \mathrm{h} \\ & + 6.94\ \mathrm{m} \times \eta + 103.9\ \mathrm{h} \times \eta - 12.8\ \mathrm{m} \times \mathrm{h} \times \eta \end{aligned}$$

$$\mathrm{F} = 14 + 31.7\,\mathrm{m} + 678\,\mathrm{h} + 24\,\mathrm{m} \times \mathrm{h}$$

The experiment results show that, compared with the ultimate tensile stress of the CT3 steel discharge frame, the tensile stress $[\sigma_{max}] = 222.945$ MPa due to the impact of rapping force F = 558.14 N with a hammer mass of 8 kg and a drop height of h = 0.57 m, meets the allowable strength of the discharge frame CT3 steel $\sigma_{ch\_CT3} = 328.17$ MPa, creates the dust removal acceleration and satisfies the allowable tensile strength of the collecting plate CT0 Steel $\sigma_{ch\_CT0} = 304.23$ MPa (GOST – 3SP/PS 380/94).

Thus, by comparison, the obtained results satisfy the multi-objective requirements of the research which, with the rapping force (F) to meet the durability of the discharge frame, creating the dust removal acceleration (a), and at the same time ensuring the durability of the collecting plate.

References

1. Yamamoto, T., Velkoff, H.R.: Electrohydrodynamics in an electrostatic precipitator. J. Fluid Mech. **108**, 1–18 (1981)
2. TCVN 8185:2009: Metal material – Fatigue test – controllable axial force application method
3. Sy, N.T.: Study on the influence of some technical parameters of electrostatic precipitator rapping system on dust removal ability, PhD Thesis (2020)
4. Tung, N.A., Got, H.V., Sy, N.T., Toan, N.D.: Empirical study on the relationship between cyclic rapping force and the lifespan of discharge electrode frames in dust filter chambers. Eur. Chem. Bull., ISSN 2063-5346, 2146-2157 (2023)
5. Писаренко, Г.С.: Справочник по сопротивлению матералов. In: НАУКОВА ДУМКА (1976)
6. Серенсен, С.В., Когаев, В.П.: Несущая способность и Расчёты деталей машин на прочность. In: Москва “машиностроение” (1975)
7. Kim, S.H., Lee, K.W.: Experimental study of electrostatic precipitator performance and comparison with existing theoretical prediction models. J. Electr. **48**(1), 3–25 (1999)
8. Song, Y., Zhang, Y.: Study on the influence of electrodes on the collection efficiency during the treatment of welding fume in electrostatic precipitators. J. Electr. **123**, 103808 (2023)
9. Lima, F.A., Guerra, V.G.: Influence of wire spacing and plate spacing on electrostatic precipitation of nanoparticles: An approach involving electrostatic shielding and diffusion charging. Particuology **80**, 127–139 (2023)
10. Cuong, N.V., Khanh, N.L.: Parameter selection to ensure multi-criteria optimization of the Taguchi method combined with the data envelopment analysis-based ranking method when milling SCM440 steel. Eng. Technol. Appl. Sci. Res. **11**(5), 7551–7557 (2021)

Ride Performance Analysis of a Semi-active Hydraulic Engine Mounting System of a Passenger Car

Hoang Anh Tan[1], Pham Van Thoan[2], Nguyen Dinh Tan[3], Vu Thi Hien[1], and Le Van Quynh[1](✉)

[1] Faculty of Vehicle and Energy Engineering, Thai Nguyen University of Technology, Thai Nguyen 250000, Vietnam
lequynh@tnut.edu.vn

[2] School of Mechanical and Automotive Engineering, Hanoi University of Industry, Hanoi 100000, Vietnam

[3] Faculty of Mechanical Engineering, East Asia University of Technology, Bac Ninh 220000, Vietnam

Abstract. To enhance a passenger car ride comfort, a semi-active hydraulic engine mounts (HEMs) is offered to analyze the ride comfort performance of its compared to passive hydraulic engine mounts (HEMs). A FLC (Fuzzy Logic Controller) is set up a damping coefficient control of a semi-active HEMs. The obtained results show that the peak amplitude acceleration response values of vehicle body with semi-active HEMs respectively reduce compared to passive HEMs under the survey conditions. Especially, the root mean square (r.m.s) acceleration response values of vehicle body (a_{wb}, a_{wphi} and a_{wteta}) with semi-active HEMs respectively reduce by 14.7%, 8.40% and 8.81% respectively compared to passive HEMs when the vehicle operates under survey conditions.

Keywords: Passenger car · hydraulic engine mounting system (HEMs) · dynamic model · ride comfort

1 Introduction

The internal combustion engine (ICE)is a main source of propulsion for traditional passenger car, however, it is also one of the causes of environmental pollution as well as the source of vibrations from ICE that are also transmitted to passengers. ICE vibration not only has a great impact on the vehicle noises but also has a great impact on the vehicle ride comfort under the excitation sources of ICE at low-frequency vibration. A solution to enhance vehicle ride comfort using additional values of the damping coefficient for a rubber mounting system of an ICE was recommended to evaluate the ride comfort effectiveness of a passenger car using additional values of the damping coefficient for a rubber mounting system with a 10-DOF full-vehicle dynamic model with two combined excitation sources between road surface roughness and ICE excitations [1]. A

D. C. Nguyen et al. (Eds.): ICERA 2023, LNNS 944, pp. 332–340, 2024.
https://doi.org/10.1007/978-3-031-62235-9_33

mounting system of an ICE including rubber elements and hydraulic shock absorbers was proposed to evaluate its ride effectiveness based on a method of measuring and analyzing vehicle vibration data [2]. The ride performance of a passenger car was investigated and compared between the hydraulic ICE mounts and rubber ICE mounts via a full dynamic model with ICE dynamic model with two combined excitation sources between road surface roughness and ICE excitations [3]. A mounting engine system of an ICE was proposed to be optimally designed to reduce vehicle noise and improve vehicle ride comfort [4]. HEMs via the glycol-based magnetorheological (MR) fluids was proposed to investigate the effectiveness of their properties [5]. A control strategy of a semi-active HEMs with magnetorheological (MR) fluid of auxiliary chamber was proposed for development in reference [6]. An electronically controllable ER mount of an ICE was then combined with a dynamic model of whole vehicle to analyze the ride performance of driver's seat [7]. Three different types of ICE mounts including rubber engine mounts (REMs), HEMs and semi-active HEMs were proposed to evaluate the ride comfort effectiveness between them under different survey conditions [8]. A 14-DOF full-vehicle dynamic model was proposed to analyze the effect of HEMs on vehicle ride comfort under different survey conditions [9]. However, most of the proposed dynamic models of vehicles and construction machines for research do not consider ICE vibration excitation that affects the vehicle ride comfort [10–14, 21, 22]. Therefore, the main purpose of this paper is to analyze and compare the ride comfort performance between the semi-active HEMs and the passive HEMs based on the control model development for passive HEMs in reference literature [3]. A FLC is set up for control change in damping coefficient value for the semi-active HEMs and A controller-simulation strategy for two types of the semi-active HEMs and the passive HEMs is set up via Matlab/simulink software. Finally, the ride comfort performance of semi-active HEMs is analyzed and compared to the passive HEMs with different road surface quality.

2 Vehicle Dynamic Model

In order to analyze the ride performance of a passenger car with a semi-active HEMs and passive HEMs with different road surface quality, a 10-DOF full-vehicle dynamic model of a passenger car with passive HEMs is selected and developed to control the change in danping coefficient through an actuator of semi-active HEMs based on reference [3], as shown in Fig. 1. Explanation of parameters and symbols in Fig. 1, m_e, m_b, as well as m_s are respectively the masses of engine body, vehicle body as well as axles; z_e, z_b, and z_s are respectively the vertical displacements at the center of gravity of objects such as m_e, m_b, and m_s; φ_e, θ_e and φ_b, θ_b are respectively the angular displacements at the center of gravity of objects such as m_e and m_b; I_{ex}, I_{ey} and I_{bx}, I_{by} are respectively the inertia moments of object masses such as m_e and m_b; k_{ern}, c_{ern}; k_s, c_s; and k_{ts}, c_{ts} are respectively the stiffness and damping coefficients of vehicle suspensions, passive HEMs as well as tires; a, b, l_s, x_{bn}, y_{bn}, x_{en} and y_{en} are respectively the distances; and q_n are respectively the road surface excitations ($s = 1 \div 4$, $n = 1 \div 3$).

Lumped parameter system model of passive HEMs and semi-active HEMs is denoted in Fig. 2. Explanation of parameters and symbols in Fig. 2, Explanation of parameters and symbols, c_{ehn} and $c_{semi\text{-}n}$ are respectively the damping coefficients of the passive HEMs and the semi-active HEMs.

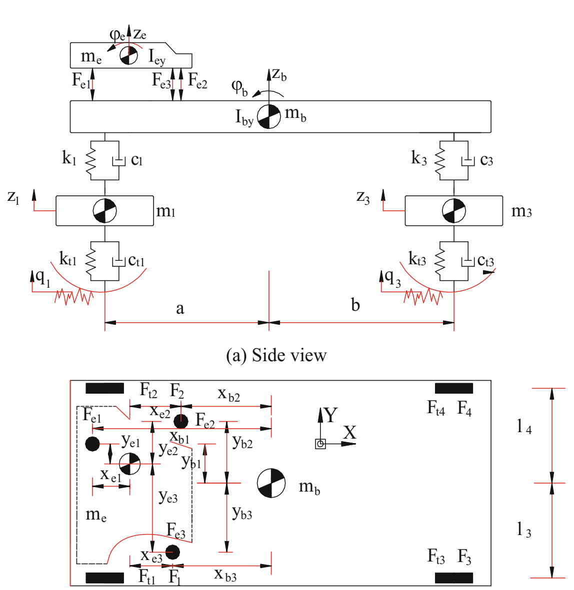

Fig. 1. A 10-DOF full-vehicle dynamic model of a passenger car

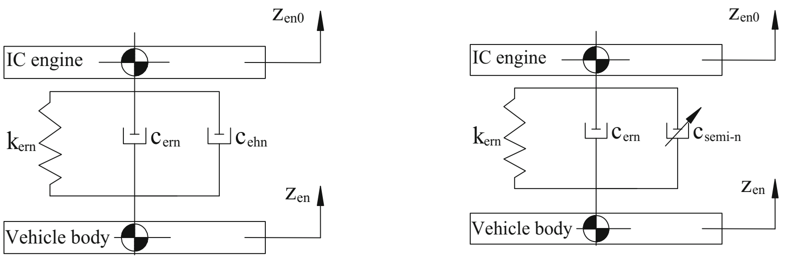

(a) Diagram of passive HEMs (b) Diagram of semi-active HEMs

Fig. 2. Lumped parameter system model of passive and semi-active HEMs

The equations of motion of objects in Fig. 1 could be written by a combined method of the multi-body system theory and D'Alembert's principle as follows.

The equations of vehicle axle motions are determined according to Eq. (1).

$$m_s\ddot{z}_s = \sum_{s=1}^{s=4} F_s - \sum_{s=1}^{s=4} F_{ts} \tag{1}$$

where, $F_{ts} = k_{ts}(z_s - q_s) + c_{ts}(\dot{z}_s - \dot{q}_s)$

The equations of vehicle body motions are determined according to Eq. (2).

$$\begin{cases} m_b\ddot{z}_b = \sum_{n=1}^{n=3} F_{en} - \sum_{s=1}^{s=4} F_s \\ I_{bx}\ddot{\varphi}_b = \sum_{s=1}^{s=2} F_s l_1 - \sum_{s=3}^{s=4} F_s l_2 - F_{e1}x_{b1} - F_{e2}x_{b2} - F_{e3}x_{b3} \\ I_b\ddot{\theta}_b = \sum_{s=2}^{s=4} F_s l_3 - (F_1 + F_3)l_4 - F_{e1}y_{b1} - F_{e2}y_{b2} - F_{e3}x_{b3} \end{cases} \tag{2}$$

where, $F_s = k_s(z_{bs} - z_s) + c_s(\dot{z}_{bs} - \dot{z}_s)$

$$z_{b1} = z_b - a\varphi_b + l_1\theta_b, z_{b2} = z_b - a\varphi_b - l_2\theta_b, z_{b3} = z_b + b\varphi_b \\ +l_3\theta_b, z_{b4} = z_b + b\varphi_b - l_4\theta_b.$$

The equations of engine body motion are determined according to Eq. (3).

$$\begin{cases} m_e\ddot{z}_e = F_{ez} - \sum_{n=1}^{n=3} F_{h1n} \\ I_{ey}\ddot{\varphi}_e = M_{ey} + F_{e1}x_{e1} - F_{e2}x_{e2} - F_{e3}x_{e3} \\ I_{ex}\ddot{\theta}_e = M_{ex} + F_{e1}y_{e1} + F_{e2}y_{e2} - F_{e3}y_{e3} \end{cases} \tag{3}$$

where,

$$F_{en} = k_{ern}(z_{e0n} - z_{b0n}) + c_{ern}(\dot{z}_{e0n} - \dot{z}_{b0n}) + c_{en}(\dot{z}_{e0n} - \dot{z}_{b0n}),$$

$$c_{en} = \begin{cases} c_{ehn} & Passive\text{HEMs} \\ c_{semi-n} & Semi-active\text{HEMs} \end{cases}$$

n = 1 ÷ 3, $z_{e01} = z_e - x_{e1}\varphi_e - y_{e1}\theta_e$,$z_{e02} = z_e + x_{e2}\varphi_e - y_{e2}\theta_e$,$z_{e03} = z_e + x_{e3}\varphi_e + y_{e3}\theta_e \cdot z_{b01} = z_b - x_{b1}\varphi_b - y_{b1}\theta_b$,$z_{b02} = z_b - x_{b2}\varphi_b - y_{b2}\theta_b$,$z_{b03} = z_b - x_{b3}\varphi_b + y_{b3}\theta_b$

Road Surface Excitation [15–17]: Vehicle discomfort is mainly caused by low frequency excitation sources, the road surface roughness often produce low frequency and high amplitude vibrations. In this paper, the excitation function of road surface is written according to ISO 8608 (2016) [19] which is determined by Eq. (4).

$$q(t) = \sum_{i=1}^{N} \sqrt{\frac{2vn_0^2 G_q(n_0)}{f_{mid,i}^2}\Delta f} . \cos(2\pi f_{mid,i}t + \varphi_i) \tag{4}$$

where, $G_q(n_0)$ is the coefficient of road surface roughness which is defined for typical road surface classes from class A to class H, n_0 is a reference spatial frequency; v is vehicle speed; φ_i is an uniform probabilistic distribution within the 0-2π range; $f_{mid,i}$ is the the road roughness temporal frequencies.

ICE Excitations: Many research results on vehicle ride-friendly dynamic model often ignore the influence of ICE excitation [24–28]. In this paper, the vibrational ICE excitations transmitted from the engine to the vehicle body are referenced from the literatures [1, 3, 8], which are determined by the formulas below

$$F_{ez} = 4m_c r\lambda\omega_0^2 \cos(2\omega_0 t) \tag{5}$$

$$M_{ex} = M_e[1 + 1.3\sin(2\omega_0 t)] \tag{6}$$

$$M_{ey} = 4m_c r\lambda\omega_0^2 l \cos(2\omega_0 t). \tag{7}$$

where, m_c is a piston reciprocating mass, r is the crank radius, λ is the ratio of the crank radius (r) to the shaft length, ω_0 is the crank rotational frequency, l is the distance between the center of gravity and the centre-line of the second/third cylinders, M_e is mean torque value.

3 Design of FLC

In order to analyze the ride performance of a passenger car with the semi-active HEMs and passive HEMs with different road surface quality, a fuzzy logic controller (FLC) is design to adjust the change in $c_{semi\text{-}n}$ of HEMs. To adjust $c_{semi\text{-}n}$ value of the semi-active HEMs, a FLC is is set up with two input variables such the relative displacement (e) of HEMs and the relative velocity (ce) of HEMs as well as an output control variable $c_{semi\text{-}n}$ of the semi-active HEMs. Five triangular fuzzy sets are selected for input and output variables such as NB, NS, ZE, PS, PB, as shown in Table 1. The membership functionshape values are between 0 and 1. The control law system is set up in Table 2.

Table 1. Linguistic labels definitions as fuzzy sets.

NB	NS	ZE	PS	PB
Negative Big	Negative Small	Zero	Positive Small	Positive Big

Table 2. Rule base of FLC

$c_{semi\text{-}n}$		e				
		NB	NS	ZE	PS	PB
ec	PB	PB	PB	PB	PB	ZE
	PB	PB	PB	PS	ZE	NS
	PB	PB	PS	ZE	NS	NS
	PS	PS	ZE	NS	NS	NB
	ZE	ZE	NB	NB	NB	NB

4 Results and Discussion

In order to solve the motion equations in Sect. 2 and set up FLC for the effective analysis of the semi-active HEMs compared to the passive HEMs, Matlab /Simulink environment software is used to simulate and control according to a set of reference data from the literature [3]. The obtained results of the time domain vertical acceleration response (a_b), pitch angle acceleration response (a_{phi}) as well as roll angle acceleration response (a_{teta}) at the center of gravity of the vehicle body with semi-active HEMs compared to passive HEMs are exposed in Fig. 3 when the vehicle moves at the vehicle speed of 60km/h on ISO class B surfaces road and full load. The obtained results of Fig. 3 show that the peak amplitude values of a_b, a_{phi} and a_{teta} at the center of gravity of the vehicle body with the semi-active HEMs respectively decreased compared to the passive HEMs.

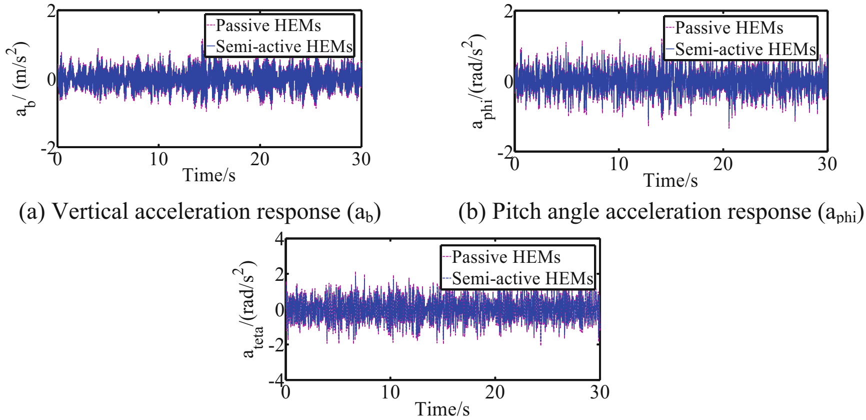

(a) Vertical acceleration response (a_b) (b) Pitch angle acceleration response (a_{phi})

(c) Roll angle acceleration response (a_{teta})

Fig. 3. Time domain acceleration responses at the center of gravity of the vehicle body with the semi-active HEMs in comparison with the passive HEMs

From the obtained results of Fig. 3, the values of the r.m.s vertical acceleration response (a_{wb}), pitch angle acceleration response (a_{wphi}) and roll angle acceleration response (a_{wteta}) at the center of gravity of the vehicle body are determined through Eq. (8) based on the ISO 2631:1997(E) standard [20, 23]. The a_{wb}, a_{wphi} and a_{wteta} values are respectively are 0.2537 m/s^2, 0.2417 rad/s^2 and 0.3384 rad/s^2 with semi-active HEMs, and are 0.2916 m/s^2, 0.2627 rad/s^2 and 0.3845 rad/s^2 with passive HEMs. The a_{wb}, a_{wphi} and a_{wteta} values with semi-active HEMs respectively decrease by 14.7%, 8.40% and 8.81% compared to passive HEMs. The vehicle ride comfort effectiveness with the semi-active HEMs is significantly enhanced compared to passive HEMs.

$$a_w = \left[\frac{1}{T} \int_0^T a^2(t)dt \right]^{\frac{1}{2}} \tag{5}$$

where, a(t) is the measured-simulated translational and rotational accelerations as the functions of time, m/s^2 or rad/s^2; T is the measurement duration or the simulation time.

In order to verify the vehicle ride comfort effectiveness with semi-active HEMs compared to passive HEMs with changes in road surface quality from very good to very poor, the a_{wb}, a_{wphi} and a_{wteta} values with changes in road surface quality at vehicle speed of 60km/h are presented in Fig. 4. The achieved results in Fig. 4 indicate that the a_{wb}, a_{wphi} and a_{wteta} values with semi-active HEMs respectively decrease compared to passive HEMs with changes in road surface quality. That achieved values indicate that vehicle ride comfort with semi-active HEMs for ICE engine are significantly enhanced compared to passive HEMs for ICE engine. In addition, the a_{wb}, a_{wphi} and a_{wteta} values escalate quickly when road surface quality becomes bad.

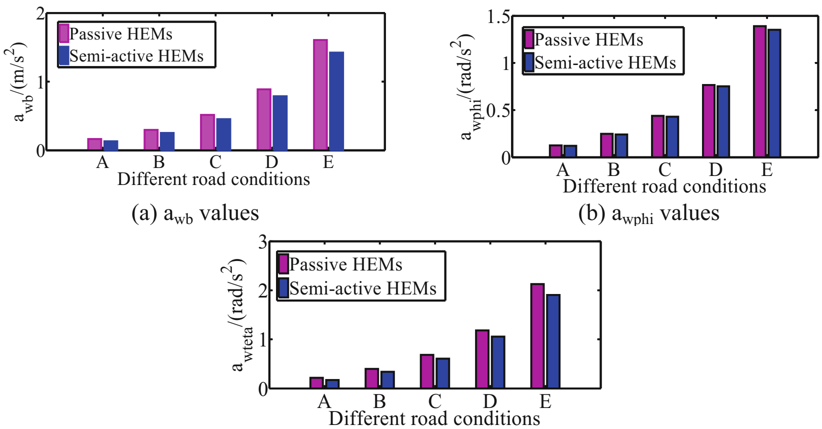

(a) a_{wb} values (b) a_{wphi} values (c) a_{wteta} values

Fig. 4. a_{wb}, a_{wphi} and a_{wteta} values with changes in road surface quality

5 Conclusions

In this study, a FLC is set up for control c_{semi-n} value of the semi-active HEMs via a 10-DOF full-vehicle dynamic model to analyze the ride performance of a passenger car with the semi- active HEMs compared to the passive HEMs with changes in road surface quality from very good to very poor. The obtained results indicate that the peak amplitude values of a_b, a_{phi} and a_{teta} at the center of gravity of the vehicle body with the semi-active HEMs respectively decreased compared to the passive HEMs and the a_{wb}, a_{wphi} and a_{wteta} values with semi-active HEMs respectively decrease by 14.7%, 8.40% and 8.81% compared to passive HEMs when the vehicle moves at the vehicle speed of 60km/h on ISO class B surfaces road and full load. That indicates that the semi-active HEMs has significantly improved passenger car ride comfort. Additionally, the passenger car ride comfort with semi-active HEMs is significantly are significantly enhanced compared to passive HEMs with changes in road surface quality at vehicle speed of 60 km/h.

Acknowledgment. The authors wish to thank the Thai Nguyen University of Technology for supporting this work.

References

1. Tan, H.A., Quynh, L.V., Liem, N.V., Cuong, B.V., Long, L.X., Truyen, V.T.: Influence of damping coefficient into engine rubber mounting system on vehicle ride comfort. Vibroengineering Procedia **29**, 112–117 (2019)
2. Mrad, F.L., Machado, D.M.L., Horta, G.J.C., Sad, A.U.: Optimization of the vibrational comfort of passenger vehicles through improvement of suspension and engine rubber mounting setups. Shock Vib. **2018,** 9861052 (2018)
3. Hung, T.T., Quynh, L.V., Ha, D.V., Cuong, B.V., Tan, H.A.: A comparison of vehicle ride comfort performance of hydraulic engine mount system with rubber engine mount system. ARPN J. Eng. Appl. Sci. **16**(23), 2610–2619 (2021)
4. Zhou, H., Liu, H., Gao, P., et al.: Optimization design and performance analysis of vehicle powertrain mounting system. Chin. J. Mech. Eng **31**, 31 (2018)
5. Barber, D.E., Carlson, J.D.: Performance characteristics of prototype MR engine mounts containing LORD glycol MR fluids. In: Proceedings of the 11th International Conference on Electrorheological Fluids and Magnetorheological Suspensions, Dresden, Germany (2009)
6. Mansour, H., Arzanpour, S., Golnaraghi, M.F., Parameswaran, A.M.: Semi-active engine mount design using auxiliary magneto-rheological fluid compliance chamber. Veh. Syst. Dyn. **49**(3), 449–462 (2021)
7. Choi, S.-B.S., Song, H.-J.H.: Vibration control of a passenger vehicle utilizing a semi-active ER engine mount. Veh. Syst. Dyn. **37**(3), 193–216 (2022)
8. Tan, H.A., Quynh, L.V., Liem, N.V., Cuong, B.V., Long, L.X., Quyet, T.V.: Ride comfort analysis of engine mounting systems using full vehicle dynamic model. Int. J. Adv. Res. Eng. Technol. (IJARET) **12**(1) , 448–456 (2021)
9. Guo, R., Gao, J., Wei, X., Wu, Z. et al.: Full vehicle dynamic modeling for engine shake with hydraulic engine mount. SAE Technical Paper 1–11 (2017)
10. Long, L.X., Quynh, L.V., Cuong, B.V.: Study on the influence of bus suspension parameters on ride comfort. Vibroengineering Procedia **21**, 77–82 (2018)
11. Quynh, L.V.: Ride comfort analysis of vibratory roller via numerical simulation and experiment. DEStech Trans. Eng. Technol. Res. ID 264213167 (2017)
12. Q,L.V., Zhang, J. R., et al.: Ride comfort evaluation of vibratory roller under different soil ground. Tran. Chinese Soc. Agric. Eng. **29**, 39–47 (2013)
13. Quynh, L.V., Jianrun, Z., et al.: Experimental modal analysis and optimal design of cab's isolation system for a single drum vibratory roller. Vibr. Procedia **31**, 52–56 (2020)
14. Quynh, L.V., Nguyen, K.T.: Optimal design parameters of cab's isolation system for vibratory roller using a multi-objective genetic algorithm. Appl. Mech. Mater. **875**, 105–112 (2018)
15. Huan, C.C., Ha, D.V., Vu, L.A., Thoan, T.V., Quynh, L.V.: Ride comfort evaluation for a wheel loader with cab's hydraulic isolation system. In: Lecture Notes in Networks and Systems vol. 602, pp. 846–854 (2022)
16. Van Quynh, L., Van Cuong, B., et al.: Effects of suspension design parameters of a semi-trailer truck on vehicle ride comfort and road surface friendliness. In: Lecture Notes in Networks and Systems, vol. 104, pp. 281–289 (2020)
17. Van Cuong, B., Van Quynh, et al.: Influence of heavy truck operating condition on dynamic load coefficient. In: Lecture Notes in Networks and Systems, vol. 63, pp. 372–379 (2019)
18. Dodds, C.J., Robson, J.D.: The description of road surface roughness. J. Sound Vib. **31**(2), 175–183 (1973)

19. ISO 8608, Mechanical Vibration-Road Surface Profiles-Reporting of Measured Data. ISO (2016)
20. ISO 2631–1. Mechanical Vibration and Shock-Evaluation of Human Exposure to Whole-Body Vibration, Part I: General Requirements. Int. Organ. Stand. (1997)
21. Ha, D.V., Van Quynh, L., Long, L.X.: Performance analysis of a mining dump truck ride comfort with a hydro-pneumatic suspension system under different operating conditions. In: Lecture Notes in Networks and Systems vol. 602, pp. 790–797 (2023)
22. Van Cuong, B., Huan, C.C., Van Quynh, L., Binh, D.T.: Effects of design parameters of cab's suspension system on an agricultural tractor ride comfort. In: Lecture Notes in Networks and Systems, vol. 602, pp. 881–886 (2023)
23. Quynh, L.V., Cuong, B.V., Tan, H.A., Huan, C.C.: Modified skyhook control for semi-active electric vehicle suspension. In: Lecture Notes in Networks and Systems, vol. 602, pp. 839–845 (2023)
24. Quynh, L.V., Thao, V.T.P., et al.: Optimal design parameters of drum's isolation system for a double-drum vibratory roller. Vibroengineering Procedia **31**, 74–79 (2020)
25. Tuan, N.V., et al: Optimal design parameters of air suspension systems for semi-trailer truck. Part 1: modeling and algorithm. Vibroengineering Procedia **33**, 72–77 (2020)
26. Long, L.X., , et al.: A comparison of ride performance of hydro-pneumatic suspension system with those of rubber and leaf suspension systems. IOP Conf. Ser. Mater. Sci. Eng. **914**, 012037 (2020)
27. Jiao, R., et al.: Ride comfort performance of hydro pneumatic isolation for soil compactors cab in low frequency region. J. Vibroengineering **22**(5), 1174–1186 (2020)
28. Duy, N.T., et al.: Ride comfort evaluation for a double-drum vibratory roller with semi-active hydraulic cab mount system. In: E3S Web of Conferences, vol. 304, pp. 01008 (2021)

Preliminary Results for Optimal Design of the Horn with Complex Welding Profiles in Ultrasonic Welding

Khoa Ngo-Nhu, Chec Nguyen-Van, Bich Ngoc Nguyen-Thi, Ngoc Nguyen-Dinh, and Nguyen-Thi Hue(✉)

Thai Nguyen University of Technology, Thai Nguyen, Vietnam
nguyenthihue@tnut.edu.vn

Abstract. In the ultrasonic welding system, the horn is a very important part, its working mode determines the quality of the weld. It is for this reason that the horn design is constantly being improved by researchers to increase productivity. There have been design studies on welding horns with different profiles, but with complex welding profile, such as the profile of welding turn signals on cars, there have been few studies published. In this paper, the design and simulation of welding horns with complex welding profiles used in auto-turn signal welding will be presented. There are two design steps that are of interest, the initial design, without the slots, and the advanced design – with the slots. The results show that the performance of the advanced design is better than that of the initial design at three criteria such as amplitude uniformity, small stress generation, and resonance frequency separation. The research results in this paper open up a development direction to study complex welding profiles for industrial use.

Keywords: Ultrasonic welding · complex welding profiles · longitudinal mode · amplitude uniformity

1 Introduction

In recent decades, engineering plastics has been used widely. In order to join the plastics components, the suitable operations are always needed. Ultrasonic welding (UW) process can be run with fast and efficient when the welding time is smaller than 1 s. For this reason, UW has been significantly utilized in various industries like aerospace, food, automotive, electronics, medical [1–5]. Typically, a UW system includes four components such as generator, transducer, amplifier or booster, and horn or sonotrode [1, 2, 6]. The mechanical vibration with a small amplitude from transducer could be amplified by booster to get the required amplitude at the tip face where the welding process is happened. In this context the horn plays an important role in the UW process. The working performance of the horn is typically evaluated by three conditions including the vibration amplitude uniformity at the transmitting surface, high amplitude of the operating mode, and the isolation of the nominal operating frequency from nearby non-tuned modes. The letter means that the longitudinal mode frequency has to be isolated from other nearby

D. C. Nguyen et al. (Eds.): ICERA 2023, LNNS 944, pp. 341–353, 2024.
https://doi.org/10.1007/978-3-031-62235-9_34

modes which can cause the mode switching to appear during operation. The isolation between longitudinal mode frequency and other non-tuned mode frequencies should be at least 1 kHz [7]. The isolation of the longitudinal mode frequency from other non-tuned mode and uniformity of amplitude at the transmission face of the horn can be overcome by inserting the slots machined through the horn thickness. The direction of these slots is along to the horn length. Among various method, Finite element analysis (FEA) has been attractively used by researchers for designing UW [8–10]. M. Lucas et el. [11] applied FEA to predict the horn modal behavior and experiment to validate the results. This combination can be considered as a good indicator for redesign of ultrasonic block horn. Moreover, it is also shown that the horn thickness has no influence on the longitudinal mode frequency, while flexural and torsional mode frequency increase when the horn thickness increase. The enhance of vibration performance of ultrasonic block horn was concerned in the study of A. Cardoni et al. [7]. The results showed that the block horn without slots exhibits the non-uniformity of amplitude because of Poisson effect in the longitudinal mode and a 0.64 kHz isolation of frequency is received. In order to increase the amplitude uniformity at the transmission face, the standard slots were also machined along the length of the block horn. The results showed that a high horn amplitude uniformity and good frequency separation were observed. To improve the high amplitude, six fine slots were additionally added in the block horn. This shows that the addition of fine slots to a slotted block horn is illustrated to suggest a practical design solution, and increase the amplitude at the transmission surface without appearance of modal coupling. Although adding slots in the block horn can generate the benefits as previously mentioned, this creates several problems dealing with the weakness of the columns due to the slotting. For this reason, it is necessary to have more studies for optimizing the utilize of slots in the block ultrasonic horns. Optimization processes of the dimensions and relative positions of slots have been conducted in the studies of earlier authors [12–14]. In these studies, the design of experiment technique was applied to find the optimum set of the slot dimensions which can reduce the modal coupling, achieve the high amplitude uniformity at the transmission face of the horn. Moreover, from the experimental results it was observed that the amplitude is crucially affected by the design variables and the interaction between these variables. Z. Abdullah et al. [15] presented the process to find the optimum position of two diagonal slots in the block horn of ultrasonic plastic welding by using FEA, Response surface methodology, and Genetic algorithm. The optimal slot dimension can lead to an increase in the block horn amplification. Moreover, the predicted values of stress induced in the optimal design are smaller than the ultimate strength and within the safe range of design. Based on the above analysis, it is noticed that the available research work dealing with the design of the block horn of the UW system has been most considered with simple profiles of transmission surface. There have been no studies concerning the design of block horns with complex welding profiles (CWP).

Therefore, in order to overcome the lack of literatures, preliminary results for optimal design of the horn with CWP in ultrasonic welding will be conducted. The complicated geometry horns are considered both with and without standard slots along the horn high. The slot additions can improve the amplitude uniformity at the transmission surface.

Two types of dynamics analysis including modal and harmonic are carried out. The FEA models are performed by using Abaqus software.

2 Design of the Complicated Geometry Horn

The welded part studied is a kind of the turn signals made of thermoplastics, which is currently applied in cars as shown in Fig. 1. The dimension of the block horn is chosen to be suitable with this product. The basic dimensions of the horn include the length, width and thickness. The width and thickness are decided by the corresponding dimension of the welded product, while the length is dependent on the mechanical properties of horn materials such as density and Young's modulus as Eq. (1).

$$\lambda = \frac{c}{f} = \frac{1}{f}\sqrt{\frac{E}{\rho}} = 2l \tag{1}$$

where

λ – Wavelength (μm)
c – Speed of sound (m/s)
f – Operating frequency (Hz)
E – Young's modulus of the horn materials (GPa)
ρ – Density of the horn materials (kg/m^3)
l - The horn length (mm)

Fig. 1. Products for welding of car turn signals (a) lower half, (b) upper half

The shape of block horn will be considered to design. Two steps of designing are carried out, namely the initial and advance designs. At the initial design, the performance of the block horn without slots inserted along the horn length is analyzed. While, the horn being machined two slots through the horn thickness is concerned in the advance step. For both design steps, the modal and harmonic analyses are utilized to evaluate the design quality. The working frequency is close to the resonant frequency or the default frequency of the welder is 20 kHz.

2.1 Initial Design

2.1.1 Modal Analysis

The boundary condition in the modal analysis is chosen as follows: at the bolt position on the top face of the horn, the imposed horizontal displacement is zero, while others displacements are fixed (Fig. 2).

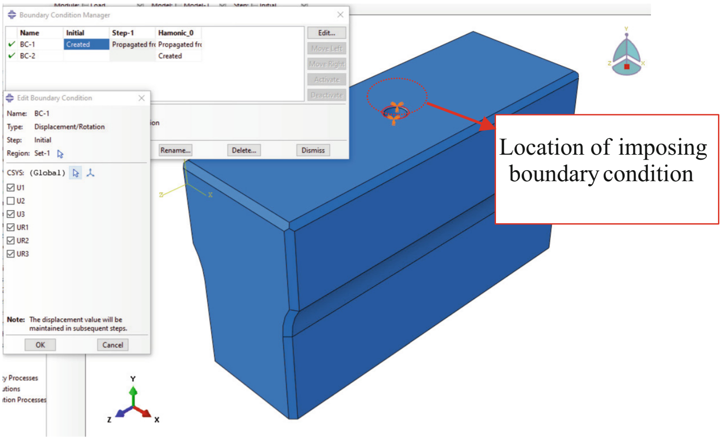

Fig. 2. Description of boundary conditions for modal analysis

The results of modal analysis show that the natural frequency in longitudinal mode is 18568 Hz (Fig. 3). This value differs from the machine default frequency of 20000 Hz which is 7.6%. Other modes of vibration such as bending have a frequency of 18972 Hz, while torsion has a frequency of 17362 Hz (Fig. 4). It is noticed that the frequency separation between the modes is not ensured at least 1 kHz. For ultrasonic welding applications, the longitudinal vibration mode is necessary to achieve the welding effect, but the natural frequency is not the closest value to the machine default frequency value (20000 Hz).

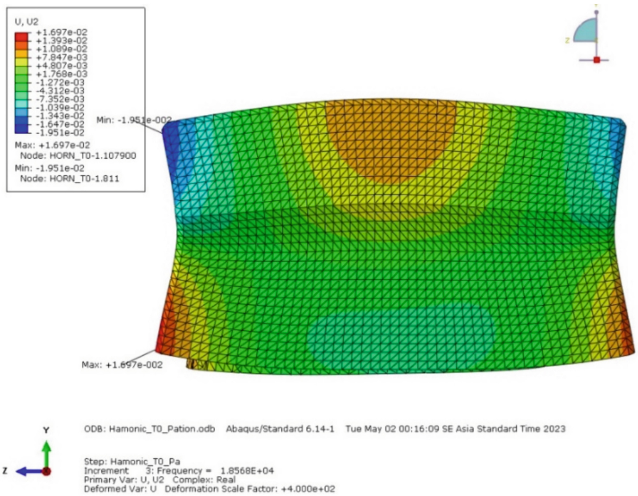

Fig. 3. Longitudinal mode of the initial design

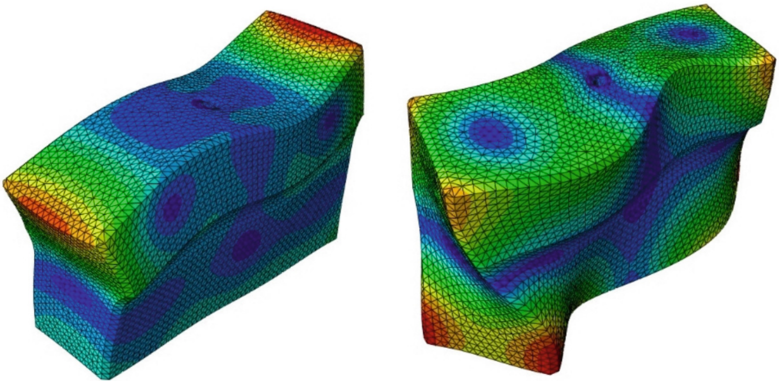

Fig. 4. Bending (a) and torsional (b) mode of the initial design

2.1.2 Harmonic Analysis

In harmonic analysis, boundary conditions are applied at the bolt position similar to that in the case of modal analysis. A displacement value of 10 μm is applied to this position. This is the given displacement value assumed to be amplified from the transducer of the welder by booster. The natural frequency of 18568 Hz belonging to the longitudinal mode is applied to determine the stress and the displacements in the working surface of the block horn.

The results reveal that regarding to the algebraic value, the largest displacement of 16.66 μm is obtained at the points on the left side and lower right edge of the block horn, while the smallest displacement of −19.18 μm also belongs to the upper points of the welding horn, the left and right sides (Fig. 5). In addition, from the color chart, it is seen that the displacements of the points at the working surface profile are significantly different. This can be explained by the influence of the Poisson effect, in addition to longitudinal vibration, the block horn also vibrates in the transverse direction. As a result, the amplitudes on the working surface profile is not uniform. The displacement unevenness on the welding surface profile (α) which is defined as the absolute value of different between the maximum and minimum displacements of the block horn. The formula for determining the displacement unevenness as follows:

$$\alpha = |u_{max} - u_{min}| \tag{2}$$

The larger the absolute value of the difference between the largest displacement and the smallest displacement, the higher the unevenness. In order to qualitatively observe the displacement patent, the displacements of points on the weld tip profile as described in Fig. 6 are developed horizontally. These values are shown as shown in Fig. 7. The above results show that the maximum displacement on the working surface profile is 10.23 μm, while the minimum displacement is −4.63 μm.

Hence, the displacement unevenness is found to be as follows:

$$\alpha = |10.23 - (-4.63)| = 14.86\,\mu\text{m}$$

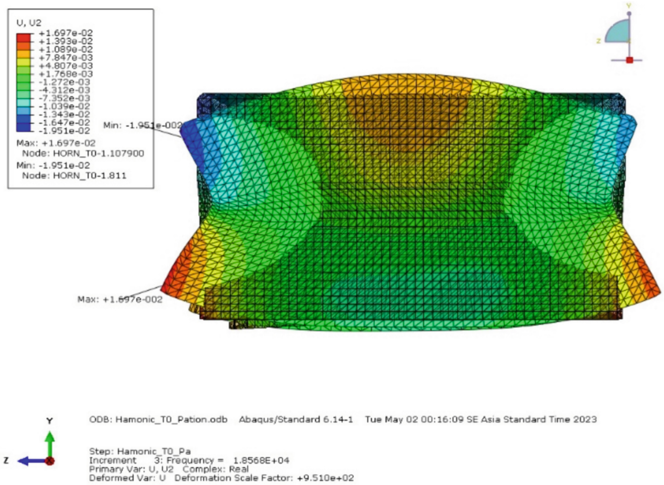

Fig. 5. Displacement analysis of the longitudinal vibration mode of the Initial design

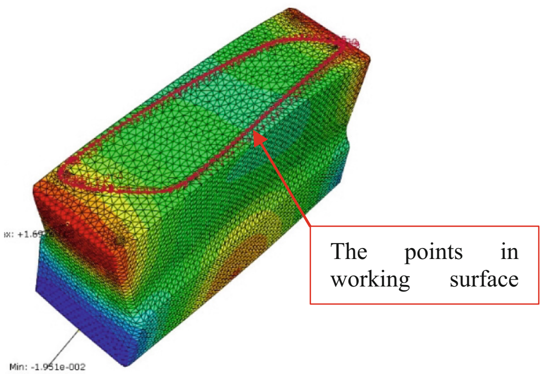

Fig. 6. Points on the working surface profile

The dynamic stress generated inside the horn is observed as shown in Fig. 8. The maximum and minimum stress referring to be tensile and compressive respectively are concentrated along the mid-transition position upper and lower parts. The compressive stress is due to the points on the side bulge, causing the center position to be compressive. From a design point of view, it can be said that the above stress distribution is not beneficial because the durability is not achieved. In addition, on the working surface profile the stress is not the minimum value. The structure may be destroyed in the process of welding when the working face comes into contact with the welded parts.

From the results of the modal analysis and the harmonic analysis for the initial design, it can be seen that the Poisson effect has a great influence on the design of the turn signal car, welded parts. To reduce this effect due to the interaction between the desired and undesirable modes as mentioned above, the slots should be created along

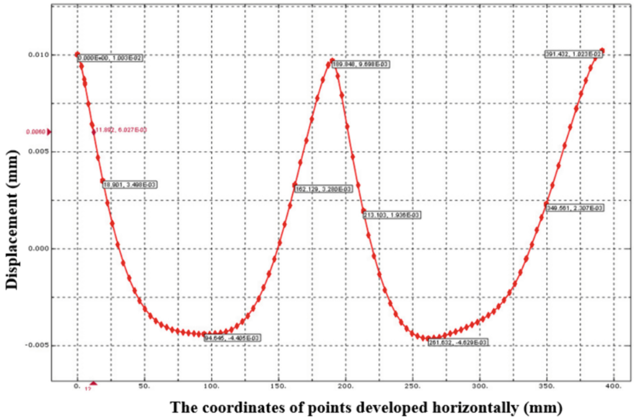

Fig. 7. Displacement of points on the working profile deploying in the horizontal direction

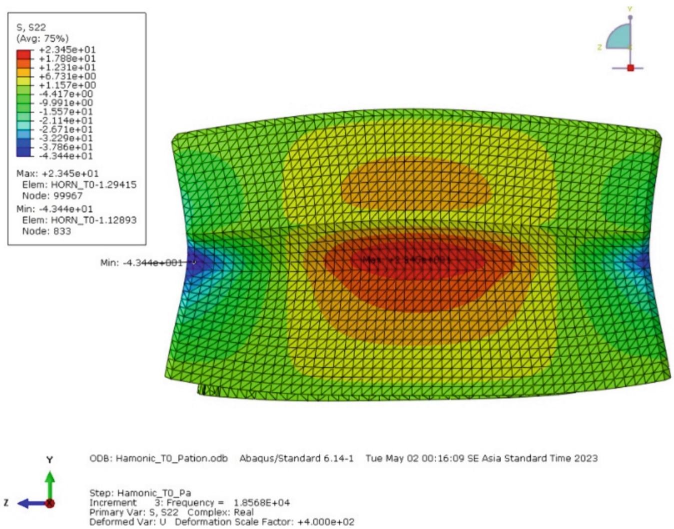

Fig. 8. Stress analysis of the longitudinal vibration mode of the Initial design

the horn length. In next section, the slotted welding horn design is called the advanced design, the second step as above mentioned.

2.2 Advanced Design

In this design step, two slots machined along the length horn with the dimensional detail given in Table 1 are shown in Fig. 9. The boundary conditions for both modal and harmonic analysis are similarly applied to the initial design.

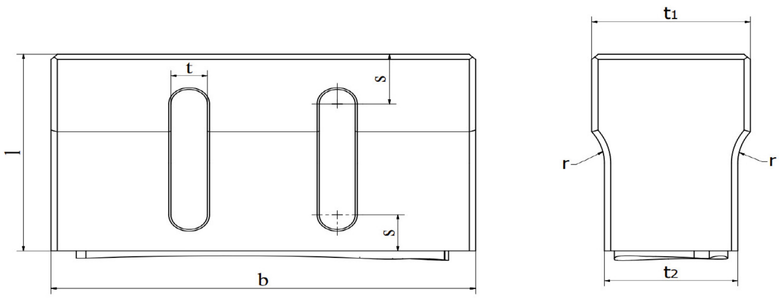

Fig. 9. Basic dimensions of the horn with complex welding profile

Table 1. Design geometrical parameters of inserted slots

t (mm)	s (mm)	l_1 (mm)	Length slot, l_2 (mm)
17	29	57	65

2.2.1 Modal Analysis

The results of the modal analysis for the advanced design are shown in Fig. 10. In this form of longitudinal vibration mode, the natural frequency found is 20042 Hz. It can be seen that, this predicted value is close to the operating frequency value of the ultrasonic welding machine (20000 Hz). The error between the prediction and the actual operating frequency is 0.16%. Whereas in the bending and torsional modes, the natural frequencies are 19005 Hz and 20494 Hz, respectively (Fig. 11). The deviation of the natural frequency of these modes with the actual operating frequency of the machine is 4.7% and 3.7%.

2.2.2 Harmonic Analysis

Figure 12 describes the displacement diagram of the points on the working surface of the horn based on the natural frequency found in the model analysis process. This value is 20042 Hz. Considering the algebraic value, the maximum displacement in the upward direction is 11.35 μm, the values with the greatest stress are on the upper face of the block horn. The minimum value belongs to the points on the working surface profile with a value of -12 μm.

In this analysis step, the displacement uniformity on the working profile surface is crucially considered, because this result affects the quality of the weld. From the color chart, it can be seen that the absolute displacement of the points on the working surface profile is relatively even. This result is due to the presence of slots along the length of the block horn, which has the function of reducing the Poisson effect, helping the deformation of the welding profile surface more uniform. The displacements of points on the working surface profile as shown in Fig. 13 are developed horizontally. The above

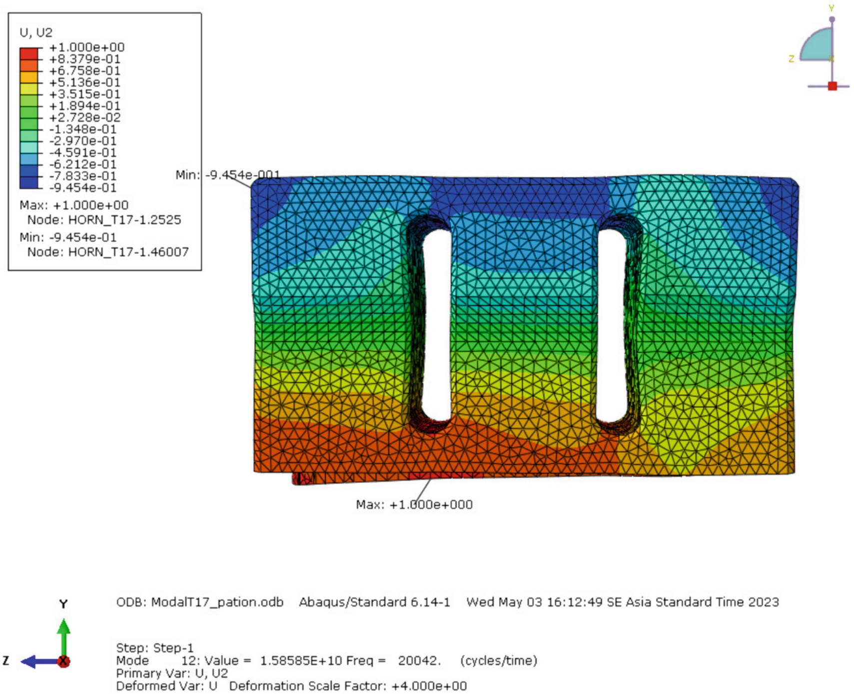

Fig. 10. Longitudinal mode of the advanced design

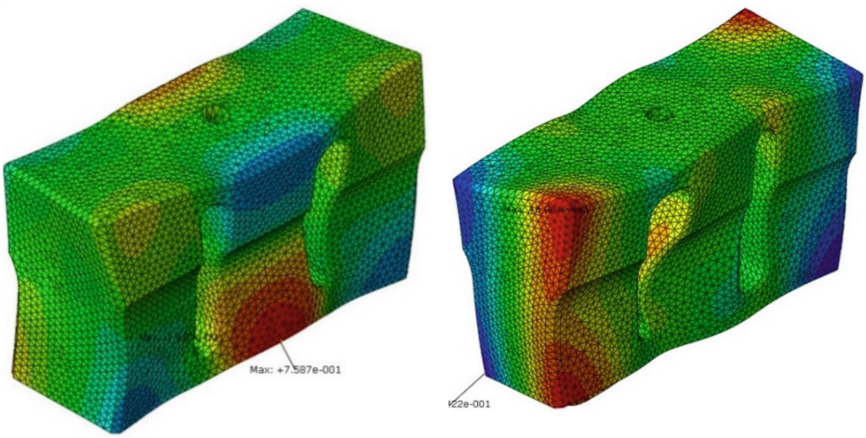

Fig. 11. Bending (a) and tortional modes (b) of the advanced design

results show that the maximum displacement value on the working surfaces profile is −8,096 μm, while the minimum displacement value is −10.7 μm. The unevenness of amplitude is as follows:

$$\alpha = |-8.096 - (-10.7)| = 2.604\,\mu\text{m}$$

This value indicates that the unevenness is low, or the displacement uniformity on the working profile surface is high. Compared with the unevenness result of the initial design (value α = 14.33 μm), it can be seen that in the advanced design, the displacement uniformity of the working surface profile is better.

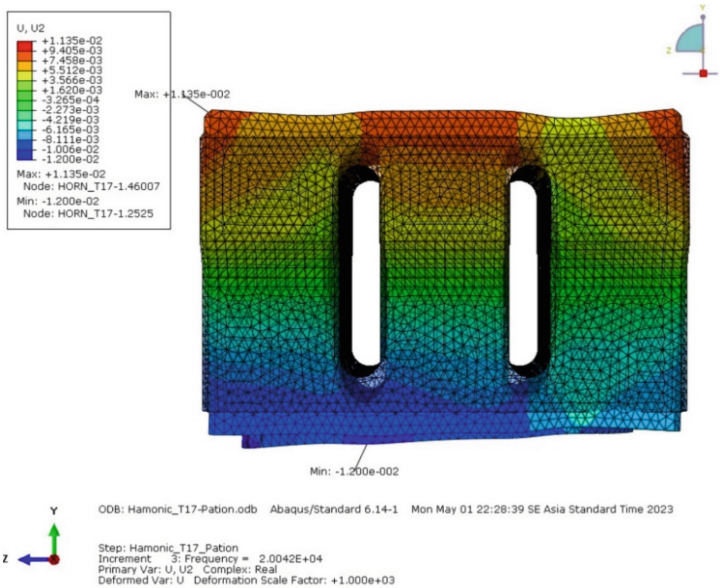

Fig. 12. Displacement analysis of longitudinal vibration mode of advanced design

The maximum stress is concentrated in the connection part between the upper and the lower body of the block horn due to the change in cross-section causing stress concentration (Fig. 14). The stresses at points on the working surface profile extracted from the ABAQUS results have an absolute value close to zero. This is beneficial to the design, because during operation the contact between the tip profile and the weld is not destructive at these points. The stress distribution as shown in this figure ensures uniform strength in the weld end structure.

Based on the modal and harmonic analysis of both the initial and the advanced designs, it can be concluded that the advanced design is more reasonable than the initial one due to the following three criteria:

– At the longitudinal mode, the natural frequency predicted is more close the operating frequency of the welder machine

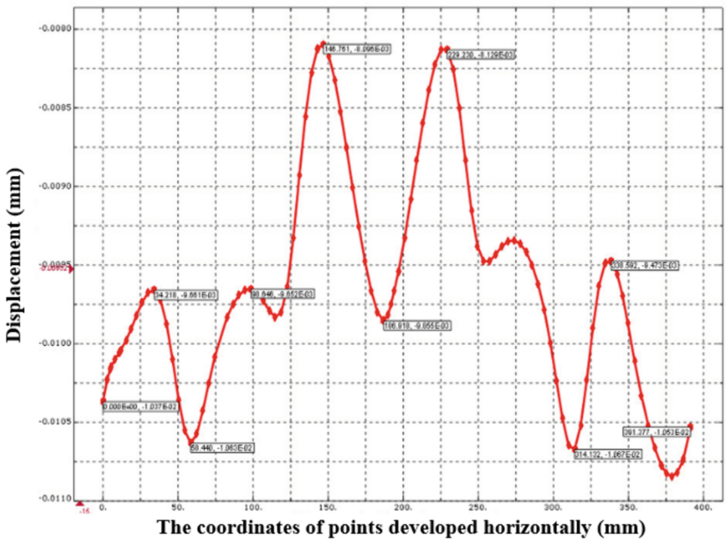

Fig. 13. Displacement of points on the working profile surface

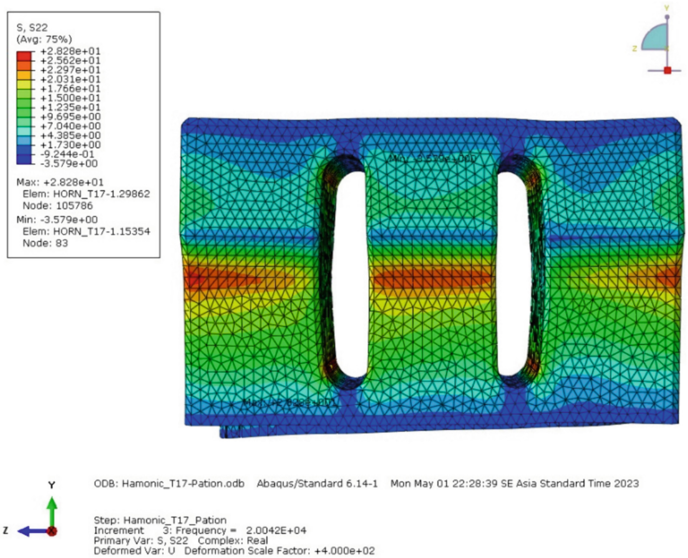

Fig. 14. Stress analysis of longitudinal vibration mode of advanced design

– Displacements of the points in the working surface profile of the advanced design is more uniform than those given in the initial design;
– The stress distribution in the block horn of the advanced design is more suitable.

Although the advanced design has represented a better design when the appearance of the slots along the horn length. However, more detailed evaluations are needed to achieve optimal design of ultrasonic horn with complex profiles. In the future work, the advanced design as described above will be studied in more depth. In which the influence of the slot width on such criteria as the separation of natural vibration frequencies in the longitudinal mode (how close to the operating frequency of the welding machine), displacement uniformity in the welding profile, and reasonableness in the stress distribution.

3 Conclusion

In this study, a type of ultraonic horn with complex profiles used for plastic material turn signal welding has been designed and simulated. The finite element method is used to analyze and simulate designs. Initial design and advanced design for this type of welding head has been carried out. From the research results of the article, some conclusions can be drawn as follows:

– The analysis results of the initial design show that in longitudinal vibration mode, the predicted natural oscillation frequency of the welding head is far from the default value of operating frequency of the welder. The harmonic analysis shows that the displacements of the points on the working profile surface are not uniform. In addition, the stress on the working profile surface has a relatively large magnitude. This design is not safe to ensure basic engineering.
– In the advanced design, the modal analysis shows that in longitudinal vibration mode, the natural vibration frequency is closest to the working frequency of the welder machine. The displacement unevenness of the points on the working profile surface is quite small. In addition, the stress distribution on the working profile surface also shows that the points on the working profile surface have zero stress absolute value. This result ensures that when in contact with the welded parts during work, the horn structure is not destroyed at the contact points.
– The advanced design is more reasonable than the initial design, and is expressed through three output parameters that show the quality of the design. These parameters include the separation of natural vibration frequencies, the uniformity of displacement on the working profile surface and finally the distribution of stresses generated within the structure.

Acknowledgements. This research was funded by the Vietnam Ministry of Education and Training, grant number B2023-TNA-18.

References

1. Roopa Rani, M., Rudramoorthy, R.: Computational modeling and experimental studies of the dynamic performance of ultrasonic horn profiles used in plastic welding. Ultrasonics **53**(3), 763–72 (2013)
2. Nguyen, T.H., et al.: Investigation the amplitude uniformity on the surface of the wide-blade ultrasonic plastic welding horn. IOP Conf. Ser Mater Sci Eng **241**(1), 012023 (2017)

3. Lin, J., Lin, S.: Study on a Large-Scale Three-Dimensional Ultrasonic Plastic Welding Vibration System Based on a Quasi-Periodic Phononic Crystal Structure. Crystals **10**(1), 21 (2020)
4. Afshari Mehran, A.B.: Optimal design and experimental validation of ultrasonic wide blade horn. Appl. Acoust.ics **182**, 108254 (2021)
5. Hahn, M., et al.: Optimal Design and Experimental Verification of Ultrasonic Cutting Horn for Ceramic Composite Material. Appl. Sci. **11**(4), 1954 (2021)
6. Roopa Rani, M., Prakasan, K., Rudramoorthy, R.: Studies on thermo-elastic heating of horns used in ultrasonic plastic welding. Ultrasonics **55**, 123–32 (2015)
7. Andrea Cardoni, M.L.: Enhanced vibration performance of ultrasonic block horns. Ultrasonics **40**(1−2), 365–369 (2002)
8. Behera, B.C., S.K.S., Patra, L.N., Rout, M.P., Kanaujia, K.K.: Finite element analysis of ultrasonic stepped Horn. 5th Int. Conf. Adv.Mech. Eng. **8** (2011)
9. Wang, D.A., et al.: Design of a Bezier-profile horn for high displacement amplification. Ultrasonics **51**(2), 148–156 (2011)
10. Kothuru, V.V.L., et al.: Design and numerical analysis of rectangular sonotrode for ultrasonic welding. Trends Sci. **19**(11), 4215 (2022)
11. Lucas, M., A.C.S.: Redesign of ultrasonic block horns for improved vibration performance. ASME. J. Vib. Acoust. **119**(3), 410–414 (1997)
12. Dipin Kumar, R., Elangovan, S.: Block horn design and analysis for ultrasonic plastic welding. J. Manufact. Eng. **9**(2), 082–087 (2014)
13. Al Sarraf, Z.S., Saeed, M.M.: Design and analysis of slotted block horn used for ultrasonic power applications. J. Southwest Jiaotong Univ. **54**(5) (2019)
14. Kumarasamy, A., Sooriyamoorthy, E.: Design and optimization of slotted block horn utilized in ultrasonic insertion process through RSM-FEA-GA integration technique (2021)
15. Al Sarraf, Z.S., Abdullah, Z.T.: Design optimization of two diagonal slotted block horn for ultrasonic plastic welding. Int. J. Adv. Res. Eng. Innovation, 2023

Radio Path Circuitry of a Novel Transceiver Module of a Promising VHF Digital AESA

I. Yu. Malevich[1,3], P. V. Zayats[2,3], and Minh T. Nguyen[2,3(✉)]

[1] Belarusian State University of Informatics and Radioelectronics, Minsk, Belarus
[2] LLC, Analog Systems, Minsk, Belarus
[3] Thai Nguyen University of Technology, Thai Nguyen City, Vietnam
nguyentuanminh@tnut.edu.vn

Abstract. As is known, the use of digital active electronically scanned array (AESA) in the development of radio equipment with electronic beam scanning makes it possible to realize a high speed of space-time signal processing. It helps to increase the amount of information received about the distribution of radiation or reflection sources in the environment, improve resolution, speed, bandwidth, range, noise immunity and other parameters and characteristics of radio engineering systems for various purposes. The transceiver module (TRM) is a key link in the AESA and primarily determines the technical characteristics of the complete system. Therefore, the development of TRM is a key stage in the design of AESA based radio system, which guarantees the success of its implementation. The article discusses the technical solutions of the main components of the TRM, designed to work as part of the promising very high frequency (VHF) AESA.

Keywords: Very high frequency (VHF) · Active electronically scanned array (AESA) · Transceiver module (TRM)

1 Introduction

For many years, the revolving or sector-scanning antenna served as an immediate indicator of a radar's presence. However, electronic scanned antennas that provide almost immediate beam steering are rapidly replacing conventional mechanically scanned antennas. These occur in passive and active varieties, and the terms PESA (passive electronically scanned array) and AESA (actively electronically scanned array) are used to build the resulting arrays [1, 2].

Active electronically scanned arrays (AESA) which perform space-distributed radiation, reception and processing of signals are currently one of the priority areas for the development of VHF radio electronic systems [3–7]. Radars and 5G are two of the primary use for AESA. To boost throughput and deliver the necessary high data rates, 5G incorporates beam guiding technology that uses AESA technology. With Rada, the adoption of AESA technology extends the lifespan of radars and reduces maintenance expenses because AESA radars do not require mechanical steering and have fewer moving parts. Along with the physical advantages, AESA-based radars are more resistant

D. C. Nguyen et al. (Eds.): ICERA 2023, LNNS 944, pp. 354–360, 2024.
https://doi.org/10.1007/978-3-031-62235-9_35

to electronic jamming. In other applications, such as using unmanned aerial vehicles (UAVs) for remote sensing [8–10], communication with UAVs is made better by using airborne vehicle-based antenna arrays [11].

In accordance with the principles of AESA construction, each channel of the array includes a digital transceiver module (TRM) with a dedicated antenna element. Independent control of the amplitude and phase of the transmitted and received signals for each channel is carried out by digital codes [12]. These antenna elements, often referred to as transmit/receive (T/R) modules, use digitally controlled elements for phase and gain in addition to high-power amplifiers (HPA) for broadcasting and low-noise amplifiers (LNA) for receiving. High efficiency, low noise figure, consistent and accurate control of signal amplitude and phase, and T/R modules are required. An antenna with dynamic beam steering and very minimal sidelobes can be made by digitally controlling the timing and gain of the individual modules.

Obviously, TRM is a key element of AESA and largely determines the characteristics of the complete system. Therefore, the development of the circuitry of TRM subsystems is a key stage in the design of the AESA [13], which guarantees the success of its implementation.

In this work, a promising VHF digital AESA's transceiver module's structure and operation are proposed. We build a structure of a TRM working with VHF utilizing the SDR platform. We operate the system, including sub-systems, and consider noise immunity of the systems. Simulation results are provided to clarify our problems.

The rest of this paper is organized as follows. The structure and operation of the transceiver module are presented in Sect. 2. Section 3 discusses the TRM subsystems that provide a gain of noise immunity. Finally, conclusions and future work are provided in Sect. 4.

2 Structure and Operation of the Transceiver Module

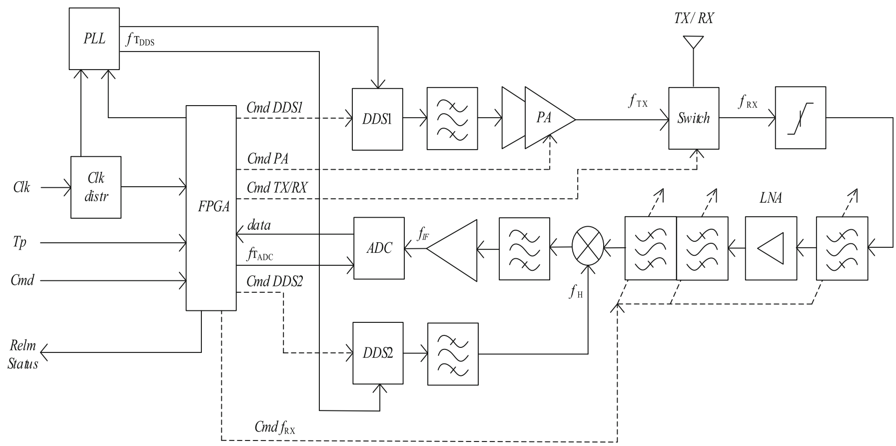

Fig. 1. Block diagram of the VHF TRM

As is known [12–14], TRM is a digital-analog device that provides the synthesis of a probing signal (PS), its amplification and feeding to the antenna element as well as echo signal (ES) reception with subsequent amplification, filtering, digitization and decomposition into quadrature components Re and Im.

Figure 1 shows the TRM structure that implements the VHF signal processing steps described above using the SDR platform.

The reference clock signal (Clk) is fed to the distributor, one of the outputs of which is intended for clocking the FPGA, the second is used as a reference signal for a phase-locked loop synthesizer (PLL), which generates a low jitter clock signal for digital synthesizers DDS1 and DDS2.

FPGA receives Clk signal and control commands (Cmd) from the digital synthesis and information processing module (DSIP). DSIP controls the operating mode, type of PS, its frequency, amplitude and phase; generates synchronization signal (Tp); ensures the coordinated operation of TRM devices. DDS1 generates a low-power PS, and DDS2 synthesizes a local oscillator signal.

PS from the output of DDS1 is fed through a bandpass filter to a broadband power amplifier (PA). The amplified PS is fed to the antenna element through a solid-state Rx/Tx switch (Switch).

In the receive mode, the ES is fed through Switch to the receiving channel, where it undergoes low-noise amplification, conversion to an intermediate frequency and filtering.

Digital samples of the received ES obtained in the ADC are transferred to the FPGA, where decomposition into quadrature components Re/Im and phase detection is performed followed by decimation. The data synchronized with the Tp is transmitted to the DSIP.

3 The Main TRM Subsystems Providing an Increase in Its Noise Immunity

The VHF AESA operates in a dense electromagnetic environment (EME) [15]. In this case, effective suppression of external interference due to spatial antenna selectivity is virtually excluded, since the reception and digital-to-analogue conversion of the received signal are carried out by each of individual TRMs of the antenna array.

Under the influence of intense interference, including deliberate ones created by electronic warfare, the radio receiving path of each TRM of the AESA is exposed to a large amount of intense out-of-band interference, which can lead to its non-linear operation. As a result, a number of undesirable effects may occur. The decorrelation of signals received by different elements of the AESA leads to degradation of the antenna pattern, cross modulation. This reduces the noise suppression efficiency of the AESA, as well as the appearance of interference components in the received signal due to intermodulation and insufficient suppression of out-of-band interferers. These interference components can lead to a significant deterioration of TRM parameters and thus degrade overall AESA performance. In this regard, the issue of improving the noise immunity of TRM is of particular importance.

Among the promising approaches to improve the noise immunity of VHF TRM, at the present stage of development of technology, two approaches are of particular interest: the use of a non-stationary operation mode, characterized by a fast pseudo-random synchronous change in signal parameters, including frequency, modulation, polarization, and the implementation of a large (up to 60…65 dB) instantaneous dynamic range.

A fast tunable narrowband preselector (TP) can significantly increase the noise immunity of the receiving path in a harsh EME. As a rule, the VHF preselector with amplification represents a structure with distributed selectivity, consisting of one-stage and two-stage connected by a low-noise amplifier (DA1), which is necessary to compensate for the losses that occur in narrow-band filter circuits (Fig. 2). In this case, all chains of the structure are synchronously tuned in a given frequency range (Fig. 3).

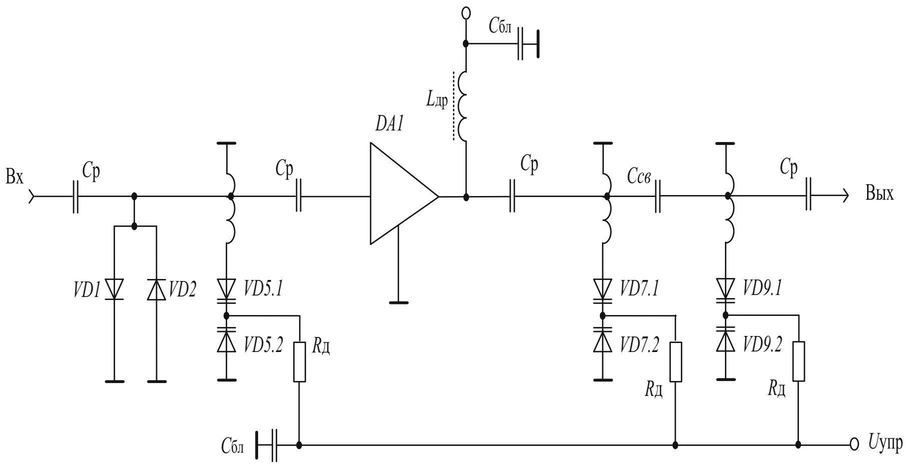

Fig. 2. Narrowband electronic tunable preselector of the VHF TRM

As can be seen, TP in the frequency band of 140… 250 MHz has a gain of 17… 19 dB, a −3 dB bandwidth is less than 8 MHz, selectivity with an offset of ± 10% is 20… 24 dB. The VSWR of the input and output of the TP in a 50-Ω system in the passband does not exceed 1.8.

Because of the limited selectivity of the first frequency-selective circuit of the considered TP, the problem of realizing a high dynamic range of DA1 becomes important. So, for example, the required dynamic range of a broadband LNA, included in the VHF TP, operating in the industrial area of a large city, should be at least 80… 100 dB (1 MHz BW) [15]. At the same time, the LNA noise figure in a still EME should usually not exceed 3… 4 dB.

Obviously, a rational option for implementation DA1 will be an adaptive circuit, which in a still EME will provide maximum sensitivity, and with a dense EME - the maximum dynamic range. Such adaptation is possible, for example, in DA1 (Fig. 4) proposed in [16].

In a still EME, the switches SW1 and SW2 are open and the gain of the adaptive LNA is at its maximum value (approx. 22… 23 dB). With the complication of the EME, leading to an overload of the LNA, the SW2 switches are closed activating feedback via

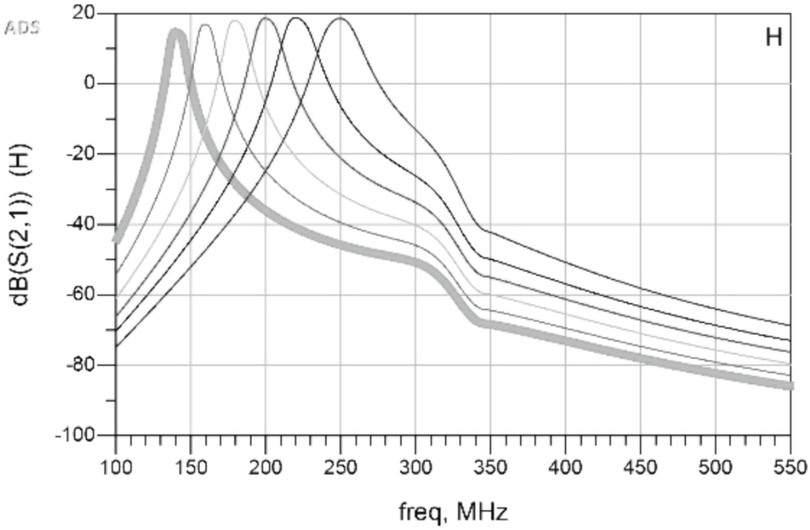

Fig. 3. VHF preselector amplitude vs. frequency plots

transformers. So, the structure is switched to the reduced gain mode. For example, for m = 4, the adaptive LNA gain in the matched path is 14 dB.

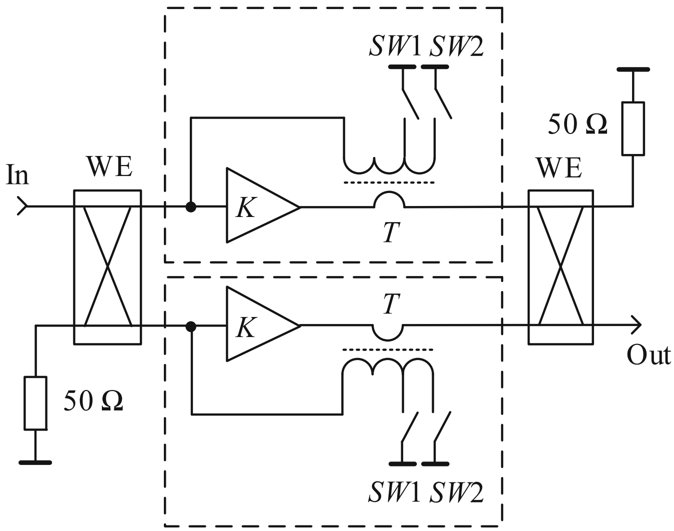

Fig. 4. Adaptive VHF LNA

In this case, the overload threshold will increase by 8 dB, and the noise figure remains almost unchanged. In the case of further EME complication, the switches SW1 are closed (SW2 are opened at the same time). The feedback increases and the adaptive LNA gain decreases. This provides further increase in the overload threshold of the TRM receiving channel.

4 Conclusions

The transceiver module (TRM), a crucial component of the AESA, is what largely determines the technical specifications of the entire system. As a result, a crucial step in the design of an AESA-based radio system that ensures the implementation's success is the development of TRM. The key TRM components, intended to function as a component of the prospective very high frequency (VHF) AESA, are discussed in detail in this article's technical discussion. We examined the structure and operation of the transceiver module of a promising VHF digital AESA. The issues of improving the noise immunity of the VHF transceiver module and the circuitry of its main components were discussed. The results show promising points for practical fields.

Acknowledgments. The authors would like to thank Thai Nguyen University of Technology (TNUT), Viet Nam for the support.

References

1. Richardson, D.: AESA radar technology. Armada Int. **39**(3), 24–30 (2015)
2. Lakshmaiah, A., Prasad, N.N.S.S.R.K., Ray, K.P.: Investigations on monolithic radome interactions with active electronically scanned array on fighter platform. Defence Sci. J. **71**(5) (2021)
3. [Airborne antenna arrays and their elements]. Ed. D.I. Voskresensky. Moscow: Radiotekhnika, 2013. (In Russ)
4. Grigoriev, L.N.: Digital beamforming in phased array antennas. Radiotekhnika, Moscow (2011). (In Russ.)
5. [Active phased antenna arrays]. Ed. V.L. Gostyukhin. Moscow: Radiotekhnika, 2011. (In Russ.)
6. Indenbom M.V. [Antenna arrays of mobile surveillance radars. Theory, calculation, designs]. Moscow: Radiotekhnika (2015) (In Russ)
7. Dobychina, E.M., Koltsov, Y.: Digital Antenna Arrays in Airborne Radar Systems. Publishing house MAI, Moscow (2013). (In Russ.)
8. Nguyen, M.T., Truong, L.H., Le, T.T.H.: Video surveillance processing algorithms utilizing artificial intelligent (AI) for unmanned autonomous vehicles (UAVs). MethodsX **8**, 101472 (2021). https://doi.org/10.1016/j.mex.2021.101472
9. Nguyen, M.T., et al.: UAV-assisted data collection in wireless sensor networks: a comprehensive survey. Electronics **10**(21), 2603 (2021)
10. Nguyen, H.T.T., Nguyen, M.T., Do, H.T., Hua, H.T., Nguyen, C.V.: DRL-based intelligent resource allocation for diverse QoS in 5G and toward 6G vehicular networks: a comprehensive survey. Wireless Commun. Mob. Comput. **2021**, 1–21 (2021). https://doi.org/10.1155/2021/5051328
11. Inata, H., Say, S., Ando, T., Liu, J., Shimamoto, S: Unmanned aerial vehicle based missing people detection system employing phased array antenna. In: 2016 IEEE Wireless Communications and Networking Conference, pp. 1–6. IEEE (2016)

12. Dobychina, E.M., Malakhov, R.: Digital transceiver module of the active phased antenna array. Sci. Bull. MSTU GA **209**, 117–123 (2014). (In Russ.)
13. Malevich, I., Zayats, P.V.: Substantiation of the structure of the transceiver module of the digital antenna array of the VHF radar. Sci. mil. Secur. No. **2**(56), 24–30 (2018). (In Russ.)
14. Malevich, I., Bobkov, Y.Y., Zayats, P.V., Ivanov, S.G.: Transceiver module for VHF digital antenna array with switchable orthogonal polarization. Doklady BGUIR No. **7**(19), 58–64 (2021). (In Russ.)
15. Malevich, I.Y., Nguyen, M.T., Zayats, P.V., Nguyen, T.T., Le, Q.C.: Problematic issues of improving the quality of reception in VHF SDR. In: Nguyen, D.C., Vu, N.P., Long, B.T., Puta, H., Sattler, KU. (eds.) Advances in Engineering Research and Application. ICERA 2022. Lecture Notes in Networks and Systems, vol. 602. Springer, Cham (2023). https://doi.org/10.1007/978-3-031-22200-9_84
16. Malevich I.Y., Zayats P.V. [High dynamic range adaptive VHF LNA]. Digest of scientific articles of the VI international scientific and practical conference. Actual probl. Prospects Dev. Radio Eng. Infocommunication Syst. Moscow 374–377 (2022)

Development of AFPID Based Stanley Controller to Control the Steering Wheel Angle of Vehicle on Tire Blowout

J. Thiyagarajan and T. Muthurmalingam(✉)

Department of Mechatronics Engineering, SRM Institute of Science and Technology, Kattankulathur, Tamilnadu 603203, India
muthurat@srmist.edu.in

Abstract. A tire blowout is an exceptionally rare scenario, which when occurs causes heavy damage not only in terms of damage to the vehicle but also, the surroundings as well. In the context of tire blowout, there are multiple variables that affect the stability of the vehicle, our work involves taking these exhaustive lists of variables into consideration and studying these variables to provide optimum control. Some of the variables taken into study are the Slip, Lateral and Longitudinal forces, Steering angles, Payload, Normal force and Moment along these forces. The basic necessity of implementing this project in the current scenario is due to unavailability of tubeless tires for commercial vehicles in the Indian market. The vehicle model is created along with the dynamic equations under a nominal scenario and all the aforementioned variables are studied. The Simulink model yielded the dynamic slip values, lateral and longitudinal forces and the rest of the aforementioned variables in the form of a time varying graph. This software provides the user with various tire models that are compatible with the Simulink model. With the given controller design in Simulink, the given dynamics are incorporated and as per user requirement, the CarMaker software yields results. The ultimate aim of running the simulation is to use the results to provide countermeasures. The contingency implemented here is that of lane keeping mechanism and gradual braking to then bring the vehicle to a halt.

Keywords: AFPID · Controller · Steering · blowout

1 Introduction

1.1 Tire Model Implementation

The majority of traffic accidents are caused by tire blowout. According to the statistics from the Ministry of Public Security, tire blowout is responsible for almost 70% of major highway traffic accidents and this proportion has reached up to 80% in the United States [1]. In India traffic accidents in highways and major expressways are caused due to the bursting of tires due to either overloading or poor condition of roads, leading to loss of life [2]. When puncture occurs, serious damage could happen to the vehicles and

D. C. Nguyen et al. (Eds.): ICERA 2023, LNNS 944, pp. 361–367, 2024.
https://doi.org/10.1007/978-3-031-62235-9_36

drivers if correct measures are not taken. Puncture is a process during which the tire loses pressure due to rupture in a fraction of a second (generally less than 0.1 s). Due to the suddenness, short duration, and unpredictability, the vehicle tends to yaw if no measure is taken under the condition that one side of the vehicle has a flat tire. Majority drivers are unable to cope with such a sudden situation due to the suddenness of the situation [3]. This leads to a catastrophic situation which causes not only loss of life but also loss to personal and public property.

The Magic Tire model is a mathematical formula that incorporates all the variables such as Slip, Lateral Force, and Longitudinal Force. This Magic Tire formula will give the other two variables, when one variable is defined completely. Because of the available heavy documentation regarding the Magic Tire model it makes result validation much more cemented and therefore, this work too implements the Magic Tire Formula [4]. The initial approach to design the vehicular model started by the implementation of the bicycle model. The bicycle model is a 2-wheel symmetry-oriented model that partially incorporates the dynamics of the vehicle. Moving forward, the approach was that of a full car body with four wheels wherein each wheel could not be controlled independently but would provide a more accurate result due to the presence of the 4 wheeled and a more closely mimicked vehicle model. In the final implementation, using the MATLAB & SIMULINK software, independent blocks were used in this methodology, one block for each tire with independent dynamics linked to another cascade of blocks.

1.2 Tire Blowout Generation

There are multiple inputs that can be fed into the blocks such as vehicle velocity, steering angle and tire pressure which are our integral variables to control the tire blowout system. Apart from the tire, a comparative study is done by changing the nature of the suspension. The two suspensions used in this case are the MacPherson suspension and the double wishbone suspension system. The most integral part of the entire work was to be able to design the system and make it mimic the tire blowout. To realize this on the software the values of different blocks have been manipulated and the necessary condition has been generated.

For a tire blowout, the first essential aspect that takes place is the sudden loss of pressure in the tire. For this a given user defined time period is selected, wherein the tire pressure suddenly changes. It is imperative to understand that the vehicle needs to be in absolute motion while this sudden change in pressure takes place. This is replicated through an impulse signal, which indicates the tire blowout has taken place.

Once the tire blowout occurs, it is important to study the various factors such as the yaw rate, yaw angle, side slip angle, lateral offset, lateral acceleration and the steering angle. These graphs provide conclusive evidence that the tire blowout has been successfully implemented.

2 Methodology

2.1 Dynamic Equation

The static friction and air resistance have been taken into consideration too because they have a direct impact on the way the entire vehicle is interacting as a whole with respect to the external surroundings. The factors related to engine dynamics and breaking are incorporated within the model itself but they are not manipulated as such to create a significant change in the case of the tire blowout.

Dynamic Equation:

1. Magic Tire Formula – Y = Dsin(C Arctan{Bx-E(Bx- arctan(Bx))})

On differentiation, for initial slip angle that is x = 0, the value of the slope is BCD

2.

$$(t) = (\varphi(t) - \varphi ss(t)) + arctan\frac{ke(t)}{ksoft(t) + v(t)} + Kdyaw\left(R_{\text{means}} - R_{\text{traj}}\right)$$
$$+ Kdstee(\delta measu(i)) - (\delta meaus(i + 1))$$

where,

Ψ ss(t) = Steady state Yaw relative to constant curvature of path; Ψ(t) = Yaw angle with respect to the trajectory (current heading of vehicle); δ(i) = Discrete time measurement of steering angle; e(t) = Cross track error; v(t) = Speed of the vehicle

2. $e(t) = v(t)\sin(\varphi(t) - \delta(t))$ …. Cross Track Error Derivative

3. $\varphi\prime(t) = (t) = \mathrm{v(t)sin}\delta(t)$ …. $\frac{\text{Derivative}}{\text{a+b}}$ of Yaw angle, Yaw rate.

Where a,b = Distance from center of gravity from the front and rear axle respectively.

To compensate for the error in the steering angle due to a delay in the response time another equation is implemented

$$\mathrm{T}^{-1}[(\delta_{\mathrm{c}}(t) - \delta(\mathrm{t}))]$$

where,

δ_c(t) – current angle of wheel with respect to vehicle axis; δ(t) – desired angle of wheels with respect to vehicle axis; T – Time constant of first order differential equation

$$\delta(\mathrm{t}) = \varphi(t) + arc\tan\frac{ke(t)}{v(t)}$$

ke(t) – Gain value cross track error

Ψ (t) – Yaw angle with respect to the trajectory (current heading of vehicle).

These dynamic equations form the basis for the Stanley Controller that is used for the corrective action. The Stanley controller directly incorporates these equations that provide a set of points for 14 trajectory generation throughout the process. The usage of Stanley Controller is slightly different in this case, but the base equations are unchanged.

2.2 Controller Design

There are multiple inputs that can be fed into the blocks such as vehicle velocity, steering angle and tire pressure which are our integral variables to control the tire blowout system.

The most basic controller for a second order system control is the PID controller. Once the tire blowout was successfully implemented, a corrective action needed to be provided to bring the vehicle back to a given trajectory. It takes the deviation between the actual quantity and the expected quantity as inputs and tracks the expected value through the linear combination of proportion (K_p), integration (K_i), and differentiation (K_d).

The Stanley Controller would prove beneficial in this application because of the fact that the path is predefined and the only 16 manipulated variables is the steering angle. Stanley Controllers are most prevalent in driverless cars that need to make sharp maneuvers.

A fuzzy logic controller comprises of a rule base. These set of rules are defined to make the error tend to zero. The fuzzification process first takes place that convert the crisp input values into 17 fuzzy values making it complaint with the rule base. The triangular membership function is implemented and for each of the parameters namely small positive and small negative. Delta K_p, Delta K_i and Delta K_d values are to be found out for the error rates.

For the given tire blowout scenario, as the final corrective action a combination of the fuzzy PID and the Stanley Lateral Controller have been implemented. The main idea behind this implementation is to bring about a novel approach to the given problem statement. The inputs fed into each of the respective blocks is the same the collective

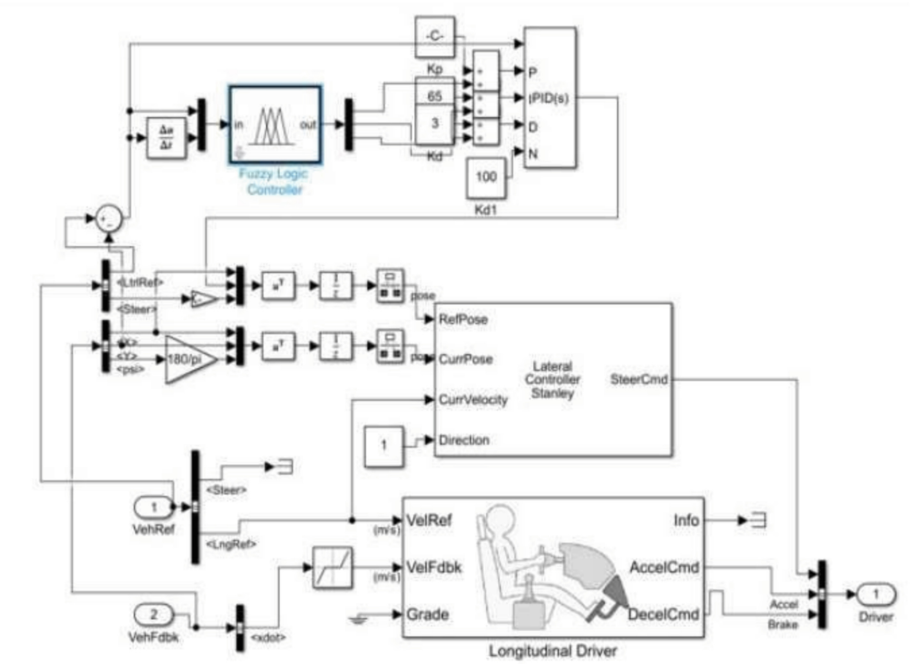

Fig. 1. 7*7 Rule base Used in the Fuzzy Logic Controller

error rectification is fed into the controller loop and a streamlined output is generated as shown in Fig. 1

3 Results and Discussion

The simulation has been carried out for an exhaustive speed, these are 40 km/h, 50 km/h, 80 km/h and 120 km/h. The objective of including various values of speeds made it bolster the validity of the controller. The error would be spread out across a range of speeds and troubleshooting would become more specific and enhanced the entire working of the controller as shown in Fig. 2.

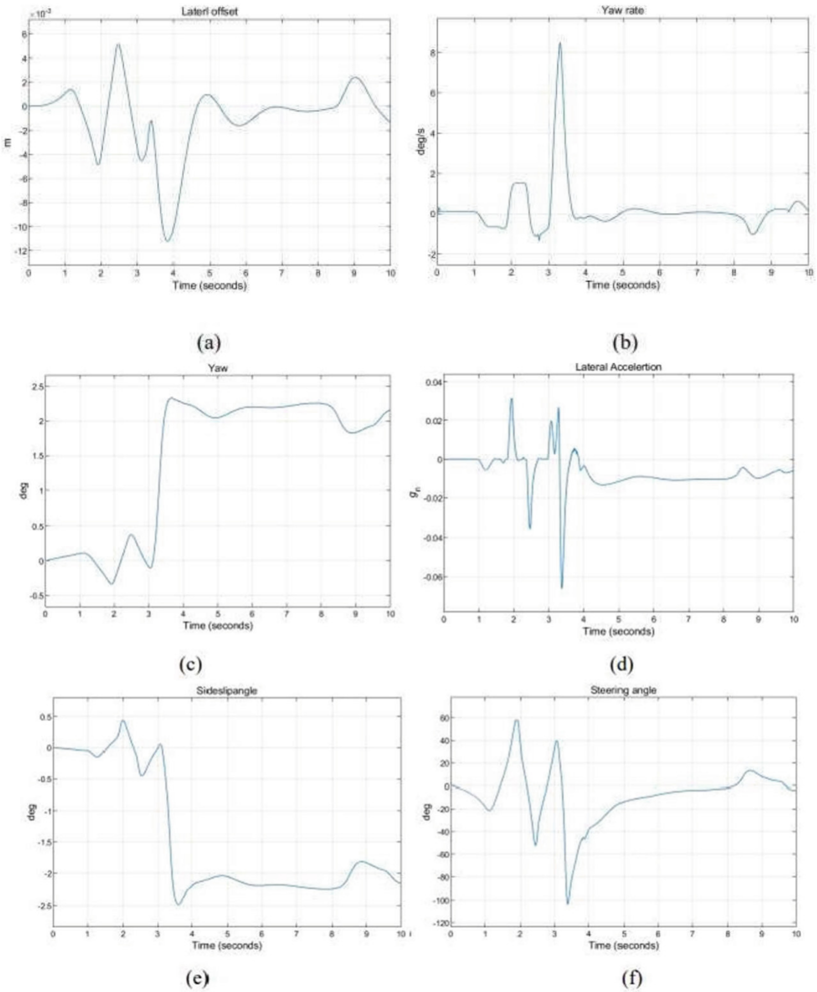

Fig. 2. Stabilizing curves obtained from simulation after application of FPID + Stanley Controller at a constant velocity of 120 kmph

It can be inferred from simulation there's a linear increase in lateral offset when the tire blowout occurs, which is then stabilized using the FPID + Stanley controller at different velocities as seen in the damped oscillatory curves obtained from the simulation. The abrupt change in yaw rate can be observed in the non-stabilized system due to the absence of a restoring force, which when is provided by the controller, yaw rate oscillates near to its initial value. The change in yaw whilst the vehicle is in a non-stable condition is due to the constant unbalanced force due to tire blowout, which is later on stabilized by a restoring variable input from the controller dependent on error input as can be seen from the results obtained. Steering angle is modified by the controller in accordance of the error value obtained, positive and negative variation of which can be observed due to constant unbalancing force. The overshoot in the side slip angle is due to the sudden slippage during tire blowout, compensation from the controller for the constant lateral force provides with a maximum constant value of side slip angle [5, 6]. The side slip will always have a damped oscillation because there is always going to be a relative heading because of the Lateral Component of force present. Variation seen in the magnitude is due to the constant application of lateral force which is stabilized by the controller. There is always a lateral acceleration persisting because of the fact that there is a component of lateral force always present in the given condition after the tire blowout.

4 Conclusions

In this work, the AFPID + Stanley controller is developed to control the steering wheel angle of the vehicle on tire blowout. It assists the driver and determines the direction and yaw of the vehicles, which prevents the driver from incorrectly operating the steering wheel and improves driving safety. It was easily observed that car follow the trajectory more closely and try to remain on the trajectory path much earlier. Overshoot observed in the FPID + Stanley controller is also very less compared to previous controllers. The only problem with the use of Stanley controller is that it provides oscillatory motions. Though Oscillations are very less and are minimized with the help of FPID but they are still present. A future research is needed to minimize these oscillations. For further research we can also look into active hydraulic cylinder braking for active deceleration of vehicle.

References

1. Chen, Q., Li, X., Guo, L., He, R.: Research on estimated calculation model of additional yaw torque after vehicle tire blowout. China Mech. Eng. **25**, 422–425 (2014)
2. Li, S., Guo, K., Chou, T.: Stability control of vehicle with active front steering under extreme conditions. Automot. Eng. **42**, 191–198 (2020)
3. Liu, P., Sun, L., Yang, M., Yuan, F.: Research on ideal vehicle reference model for yaw stability control. J. Chongqing Univ. Technol. Nat. Sci. **34**, 17–24 (2020)
4. Chen, L., Xie, Y., Cai, Y., Sun, X., Teng, C., Zhou, K.: Stable tracking control of autonomous vehicles at extreme conditions. Automot. Eng. **42**, 1016–1026 (2020)

5. Thiyagarajan, J., Muthuramalingam, T.: Standalone and interconnected analysis of an independent accumulator pressure compressibility hydro-pneumatic suspension for the four-axle heavy truck. Actuators **12**, 347 (2023)
6. Thiyagarajan, J., Sathishkumar, P., Muthuramalingam, T.: Hydraulic control valve integrated novel semi active roll resistant interconnected suspension with vertical and roll coordinated control scheme. P. I. Mech. Eng. D-J Aut. **237**, 98–111 (2023)

Research on Simulation and Optimization of the Self-driving Minibus Frame Design

Tien Thanh Do[1,2], Anh Son Le[1,2](✉), Xuan Nang Ho[1,2], and Duy Vinh Nguyen[1]

[1] Phenikaa University, Yen Nghia, Ha Dong, Hanoi, Vietnam
son.leanh@phenikaa-university.edu.vn
[2] Phenikaa-X Joint Stock Company, Yen Nghia, Ha Dong, Hanoi, Vietnam

Abstract. Vehicle frame plays a crucial role in ensuring the safety and performance of vehicles including autonomous vehicles. The frame needs sufficient rigidity to withstand the loads from various components and external forces during operation. Moreover, the frame is required to have minimize the weight to optimize the acceleration and energy consumption of the vehicle. In order to fabricate an optimal frame that ensures the requirements of durability and weight for autonomous vehicle, two frames (called XBUS 1.0 and XBUS 1.1) were proposed. Steel plates made XBUS 1.0, while XBUS 1.1 comprises steel plates and steel boxes. This study focuses on evaluating the durability of the two frames using the Finite Element Method (FEM). Static durability analysis and dynamic analysis were conducted in this research. The static analysis result shows that XBUS 1.1 indicates a 29% reduction in the maximum stress value, while the safety factor increases to 2.48 compared to XBUS 1.0. Dynamic analysis shows that at 14,726 Hz, the strongest oscillation will occur. In summary, the research has demonstrated that incorporating additional steel boxes and reducing the components' thickness can reduce vehicle weight while still maintaining the durability of the frame, contributing to the development and production of energy-efficient and environmentally friendly minibus vehicles in the future.

Keywords: Numerical simulation · optimization process · finite element method · meshing

1 Introduction

In recent decades, green vehicles that utilize environmentally friendly energy sources such as electricity, hydrogen, or hybrid vehicleshave been increasing popular over traditional gasoline vehicles [1, 2]. Electric vehicles (EVs) have been extensively researched and developed recently, compared to the other green vehicles [3]. EVs can address severe air pollution issues in large urban areas by producing no tailpipe emissions during operation [1, 2]. Moreover, the use of electricity enables favorable conditions for integrating advanced driver assistance systems or fully autonomous driving systems powered directly by the vehicle's electric-electronic devices. However, the use of electric vehicles still face several issues. Due to limitations in storage technology, EVs often

D. C. Nguyen et al. (Eds.): ICERA 2023, LNNS 944, pp. 368–377, 2024.
https://doi.org/10.1007/978-3-031-62235-9_37

have shorter travel ranges compared to gasoline-powered vehicles and require significantly more time for charging. Additionally, the weight of the battery pack is usually substantial, limiting the useful payload capacity of the vehicle and increasing energy consumption during transportation [4]. Safety and the risk of battery fires or explosions are also crucial concerns for vehicle developers.

Vehicle weight minimization is one of the primary solutions to save energy. This can be achieved by using new materials with lower specific gravity or optimizing the vehicle's structure [5–7]. However, the vehicle's structure must still meet durability, rigidity, and longevity requirements throughout its operational life. Additionally, the structure needs to have the ability to absorb energy during collisions and ensure absolute safety for passengers and the vehicle's battery pack [8].

Currently, tasks related to testing, simulation, and optimization of automotive structures are greatly supported by numerical simulation software, which helps save a considerable amount of time and development costs, thereby swiftly bringing these products into production and commerce. For structural problems, the Finite Element Method (FEM) is predominantly used by most simulation software, with the most significant market share held by software like Ansys, Abaqus, LS-DYNA, HyperWorks, and others.

With the approach of reducing weight by using new materials, several types of materials have been investigated by scientists. Lyu et al. conducted a static strength analysis of a car frame using ANSYS Static Structure solver and compared the behavior of the frame when applying one of three types of materials: steel, aluminum, and magnesium alloy [9]. Idreesa et al. performed behavior surveys of an automobile frame made from AL-7075T6 aluminum material in a collision scenario. The AL-7075T6 aluminum material has a relatively high strength-to-weight ratio, which can help save fuel consumption. The research's objective was to evaluate the AL-7075T6 aluminum frame's ability to protect occupants during a frontal collision. Using the ANSYS Explicit solver, collision experiments of the frame were conducted at different speeds and obstacles, and the results indicated that the frame's displacements remained within allowable limits that would not adversely affect passengers [10]. Apart from metal materials, in recent years, composite materials have become increasingly popular not only in the aviation industry but also in the automotive industry. Many studies have evaluated and compared the behavior and performance of composite materials with traditional metal materials in static and dynamic problems of vehicle structures [11–14].

In addition to weight reduction, over the past years, researchers have also focused on optimizing the torsional stiffness of automobile body frames. Many frame designs of various types of vehicles such as buses, trucks, personal cars, and Formula SAE race cars, have been studied [15–18]. Besides torsional loading, primary loading cases during car design simulations, and secondary loading cases involving vertical bending and lateral bending must also be considered. Denny et al. evaluated the overall structure of a solar-powered vehicle's monocoque frame. The frame model was simulated to determine the most suitable shape and materials that meet the requirements for torsional stiffness. Additionally, the frame was subjected to stress tests when experiencing concentrated loads applied to the suspension mounting points [19].

Therefore, the application of the FEM for testing behavior and optimizing frame designs has demonstrated feasibility and high efficiency in the development of new automotive products. The XBUS autonomous vehicle prototype is a completely new vehicle developed by Phenikaa-X company, and the company's team of engineers quickly grasped the technology and implemented numerical simulation into the development process of this product. The construction process and results of the structural strength analysis of the Phenikaa-X XBUS autonomous vehicle frame using ANSYS Mechanical 2022R2 software will be presented in this paper.

2 Methods and Materials

2.1 General Requirement for Vehicle Frame Design

Loads Type on the Vehicle Frame

The frame and chassis of a vehicle always endure various types of loads during operation. Bending and torsional loads often occur when the vehicle is driven on rough roads or when performing different types of movements (acceleration, deceleration, braking, turning).

The types of loads that the vehicle frame must bear include bending load, torsional load, bending-torsional load, horizontal load, and vertical load. The bending and torsional loads play the most crucial roles when considering the load-bearing capacity of the structure. Cases of horizontal and vertical loads are of greater concern when designing the vehicle's shock absorber system, but they are not as critical when considering the overall structure of the vehicle, as shown in Fig. 1 [20]. In this paper, the bending load case will be considered since the XBUS autonomous vehicle mainly operates at a constant speed of 10 km/h on flat roads.

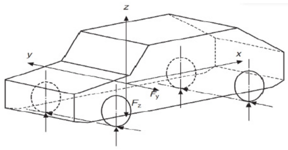

Fig. 1. The coordinate system attached to the vehicle [20].

Safety Requirements

In static analysis, alongside the two main parameters of displacement and stress, we can evaluate the structural strength through the safety factor. David Ulman's safety factor is determined using Eq. (1) as follows [21].

$$FS = \frac{S_{al}}{\sigma_{ap}} \quad (1)$$

where FS is the safety factor, S_{al} is the allowable strength, which may limit the yield strength, σ_{ap} is the stress calculated by the designer. The safety factor indicates the structural failure threshold, and if this factor is equal to or less than one, the structure may fail. For ductile materials like aluminum or steel, the applied stress is the maximum equivalent stress σmax, and the allowable strength is taken as the yield stress Sy. The structure is considered safe when the maximum equivalent stress does not exceed the yield limit, which means the safety factor is greater than one [22].

2.2 Autonomous Vehicle Frames

During the calculation and selection process, two versions of the autonomous vehicle (XBUS) frame, version 1.0 (called XBUS 1.0) and version 1.1 (called XBUS 1.1), are proposed for transporting four people with a load of 350 kg. The frame is a crucial component in the vehicle's structure, responsible for providing mounting positions for various components and bearing the load from passengers while transmitting it to the chassis.

The vehicle frame is constructed using steel material to ensure strength, rigidity, and cost-effectiveness. The frame design includes a combination of plate elements and beam-like structures, such as box sections, to maximize efficiency. To optimize computational resources, details are simplified into plate forms, and solid blocks are transformed into mid-surfaces. Fillets and chamfers are also simplified for better computational efficiency. Figure 2 illustrates the frame model, designed with a combination of plate elements and beam-like structures, such as box sections.

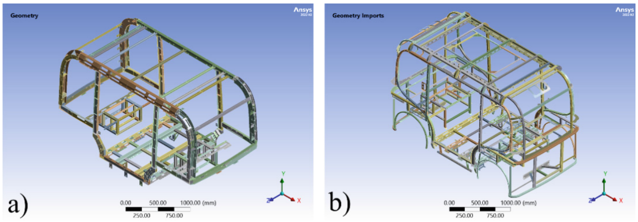

Fig. 2. The geometric models of XBUS 1.0 frame (a) and XBUS 1.1 frame (b).

The frame of XBUS 1.0 is entirely made of SPHC steel plate components. As for XBUS 1.1, the material parameters are selected based on the certificates provided by the material supplier, with a density of 7800 kg/m^3, Young's modulus of 2×10^{11} Pa, and Poisson's ratio of 0.29.

2.3 Evaluations of the Proposed Autonomous Vehicle Frames Using FEM

General Conditions

Mesh Model

The meshes of both XBUS 1.0 and XBUS 1.1 frame models are created using Ansys Meshing. All components are divided into quad elements (4 nodes). Large components use a 5 mm element size, while small surfaces or bolted connections use a 4mm element size. Circular features are meshed with 12 nodes.

Load and Boundary Conditions

In this paper, the loads acting on the frame include the weight of the vehicle body, the weight of electrical-electronic devices, and the weight of passengers. The vehicle body's weight is determined either directly through actual measurements or estimated based on an assumed density of 1000 kg/m^3.

Similarly, electrical-electronic devices weighing less than 2 kg will be neglected and not considered in the computational model. To reduce the setup time for loads, the details of the vehicle body and electrical-electronic devices will be combined, and their masses will be represented as point masses attached to the frame. The point masses will be described by their mass, coordinates, and constraints as shown in Fig. 3

The chassis is assumed to be absolutely rigid with tightly bolted connection points, thus preventing any displacement. Consequently, fixed boundary conditions are applied to all six degrees of freedom. Some contact surfaces between the frame and the chassis, without bolted connections, will have displacement limitations, allowing only movements perpendicular to the contact surfaces.

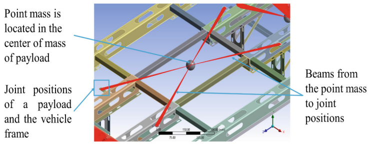

Fig. 3. Modeling the clustered vehicle body components into a lumped mass point.

Dynamic Durability Analysis

The following conditions will be applied for the computation of the Xbus 1.1 frame structure. The rationale for selecting these conditions for computation is explained in the conclusion section below.

Free Vibration Analysis

Free vibration analysis involves determining the natural frequencies and mode shapes of a structure. These characteristics depend on the mass, stiffness, and damping coefficient of the structure itself. The free vibration analysis does not require any external loads or forces acting on the system to be solved; it only needs to define the boundary conditions and material properties.

The frame is subjected to load, leading to stress on its components, resulting in changes to the frame's stiffness matrix. As mentioned above, the natural frequencies in the free vibration problem of the frame depend on the stiffness of the structure. Therefore, the stress state of the frame will also be an input for calculating the natural frequencies of the vehicle frame.

Random Vibration Analysis

The input of the random vibration analysis is represented in the form of the Power Spectral Density (PSD) function, which shows the intensity of vibrations with respect to frequency. Time-domain vibrations are unique and unpredictable in their trends. Therefore, converting time-domain vibrations into frequency-domain vibrations using statistical methods is necessary.

Since there is a lack of experimental data on random vibration surveys in practice, the input PSD for the problem is taken following the ISO 16750-3 standard [23] (Fig. 4).

According to ANSYS recommendations, the input for random vibration should have a maximum frequency that is less than 1.5 times the highest natural frequency obtained

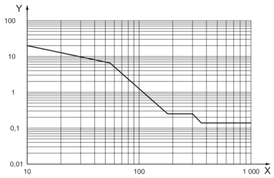

Fig. 4. PSD of acceleration versus frequency [23]

from the free vibration analysis. Therefore, the synthesized input PSD for the random vibration problem will consist of input excitations along the Z-axis with specific values as listed in the table below.

Table 1. Table of PSD values by frequency in the free vibration test for the body (sprung masses)

Frequency (Hz)	PSD $(m/s^2)^2/Hz$
10	20
23,452	11,402

3 Results and Discussions

3.1 Static Stability Analysis

For the static strength verification problem, three main criteria are used to evaluate the structure: displacement, stress, and safety factor. When comparing the two frame models, the XBUS 1.1 frame has a lighter weight of 137.162 kg compared to the 189.54 kg of version 1.0. As shown in Fig. 5, significant displacements in both frame versions occur in components located in the nosecone assembly, which bears the direct load from the additional 12 kg mass of the sensor block placed on top. However, the XBUS 1.1 exhibits the largest displacement on a larger glass component compared to version 1.0. In the simulation model, this component is subjected to a load due to its connection with the composite shell, resulting in a significant concentrated displacement.

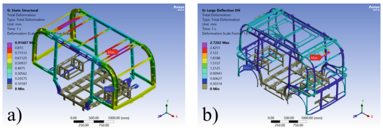

Fig. 5. Displacement of frame XBUS 1.0 (a) and frame XBUS 1.1 (b).

Regarding stress, the XBUS 1.1 frame has shown significant improvement, with the maximum stress reaching only 110 MPa compared to the value of 143 MPa for the XBUS 1.0 frame. This is clearly demonstrated in Fig. 6.

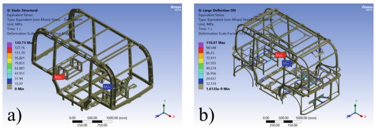

Fig. 6. Stress of frame XBUS 1.0 (a) and frame XBUS 1.1 (b).

The figure below shows that reducing the maximum stress has resulted in an increase in the safety factor. Additionally, the properties of the steel used in manufacturing the XBUS 1.1 frame are significantly improved compared to version 1.0, especially in terms of yield strength. Even though the minimum safety factor has significantly increased from 1.45 in version 1.0 to 2.48 in version 1.1, it still does not meet the minimum safety factor requirement in the case of static loads, which should be greater than 3.75–4.5 according to Julian Happian-Smith's recommendation (2002) to provide a safety margin when the vehicle is subjected to dynamic loads [20] (Fig. 7).

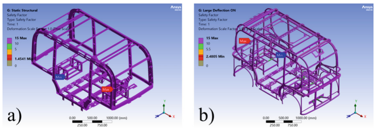

Fig. 7. Safety factor of frame XBUS 1.0 (a) and frame XBUS 1.1 (b).

3.2 Dynamic Durability Analysis

In this study, the paper will investigate random vibrations to determine the natural frequencies of the XBUS 1.1 frame. Subsequently, random vibration simulation will be performed based on the conditions mentioned above to identify the resonance frequencies of the XBUS 1.1 frame.

The reason for conducting the study only on version 1.1 is that the frame's mass has been reduced by 52 kg compared to version 1.0 in the total frame mass. Additionally, the simulation results indicate that the maximum stress value in version 1.1 has decreased by 29%, while the safety factor has increased to 2.48 compared to the initial version.

Free Vibration Analysis

The model is quite large, and the number of natural frequencies will depend on the model's degrees of freedom. Hence, the model will have a considerable number of natural frequencies. Therefore, it is unnecessary to find all the natural frequencies. The problem will focus on identifying the dominant natural frequencies of the model, where most of the structural components will undergo significant oscillations at those frequencies.

To assess which natural frequencies are considered important, we will use two quantities: participation factor and total effective mass ratio, both of which have values ranging from 0 to 1. The closer the total effective mass ratio is to 1, the more significant the corresponding natural frequency is, indicating a higher presence of structural components oscillating at that frequency. The table below lists the important natural frequencies (Table 2).

Table 2. The important natural frequencies of the XBUS 1.1 frame model.

Mode	Frequency (Hz)	Degree of Freedom	Mode	Frequency (Hz)	Degree of Freedom
1	5,4867	Z, ROTX	6	14,726	Z, ROTX
2	7,7384	X	7	14,776	Z
4	12,209	X	13	20,872	Y, ROTX
5	12,378	X	18	26,218	Y

According to the recommendations of ANSYS, the total effective mass ratio to the total corresponding mass should be greater than 0.9. However, this value may vary depending on the computational model, so 0.8 is chosen as the total effective mass ratio to the total mass corresponding to the first 30 natural frequencies.

Random Vibration Analysis

In the random vibration problem, the output quantities include stress-strain, displacement directions, and reactions. The results of the random vibration problem will all be statistically analyzed according to the 1-σ standard in the Gaussian distribution. Figure 8 shows the displacement results for each X, Y, Z direction of the two XBUS frame models following the 1-σ standard. For example, the XBUS frame for the new chassis will have a 68.269% probability of having displacements in the Z direction within the range of 0 to 9.4945 mm.

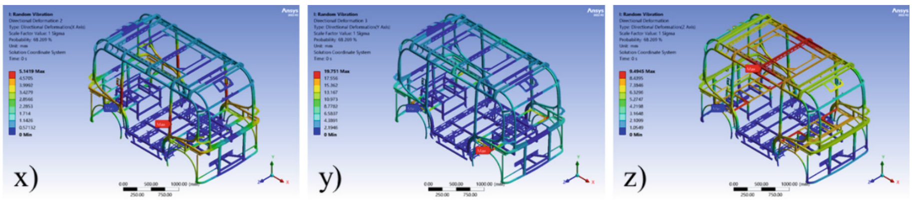

Fig. 8. The displacements in different directions in the random vibration of oscillation.

The Response Power Spectral Density (PSD) is the output response of the structure in the form of a PSD function with respect to frequency. The PSD response graph will indicate the frequency at which oscillations occur most strongly or where the intensity of the oscillations is highest. This frequency value is often close to the resonance frequencies. With the input PSD from Table 1, the XBUS 1.1 will have resonant oscillations at a frequency of 14.726 Hz equivalent to mode 6 of the free vibration analysis. Figure 9 below illustrates the result of this oscillation. At this resonant frequency, the XBUS 1.1 frame will experience its strongest oscillations at the front-end and seat cluster with displacements of 9.5 mm and 19.7 mm, respectively.

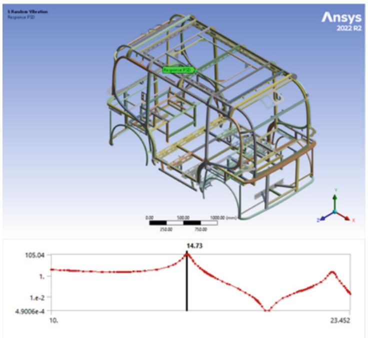

Fig. 9. The resonant oscillation frequency at mode 6.

The problem still has some remaining issues. Although the safety factor has improved in version 1.1, it is still not sufficient to meet the minimum safety factor requirement according to the standard. Moreover, for the random vibration analysis, we are unable to calculate the structural fatigue life under the excitation of input PSD. Additionally, the input PSD standard applied is intended for electrical and electronic devices. Therefore, besides improving the safety factor and calculating the structural fatigue, further research is required to understand and study the input PSD according to international standards applicable to the frame or conduct experimental measurements to obtain these values.

4 Conclusion

The autonomous vehicle XBUS is a new design and production by the engineering team at Phenikaa-X Company. Analyzing, researching, and simulating to find the optimal solution for the XBUS frame is essential. The design of the XBUS 1.1 frame has seen significant improvements in geometry and manufacturing materials. This has helped reduce the XBUS 1.1 frame's total weight by 52 kg compared to version 1.0. The frame designs were modeled and simulated using Ansys Mechanical software to evaluate the structural behavior under maximum static loads equivalent to operating with four passengers. The simulation results showed that the maximum stress value for version 1.1 decreased by 29%, while the safety factor increased to 2.48 compared to the initial version. Furthermore, at the frequency of 14.726 Hz, the frame structure will experience the most intense oscillation, reaching up to 19.751 mm of displacement. However, the design of the XBUS autonomous vehicle frame will still require further improvement and optimization, with continued in-depth evaluations when the vehicle experiences dynamic loads and vibrations to enhance reliability and safety.

References

1. Peng, L., Liu, F., Zhou, M., Li, M., Zhang, Q., Mauzerall, D.L.: Alternative-energy-vehicles deployment delivers climate, air quality, and health co-benefits when coupled with decarbonizing power generation in China. One Earth **4**, 1127–1140 (2021)

2. Bielaczyc, P., Woodburn, J., Szczotka, A.: An assessment of regulated emissions and CO2 emissions from a European light-duty CNG-fueled vehicle in the context of Euro 6 emissions regulations. Appl. Energy **117**, 134–141 (2014)
3. Kittner, N., Tsiropoulos, I., Tarvydas, D., Schmidt, O., Staffell, I., Kammen, D.M.: Chapter 9 - Electric vehicles. In: Louwen, A., Junginger, M. (ed.) 1st Technological Learning in the Transition to a Low-Carbon Energy System - Conceptual Issues, Empirical Findings, and Use in Energy Modeling. s.l. Academic Press (2020)
4. Abo-Khalil, A.G., et al.: Electric vehicle impact on energy industry, policy, technical barriers, and power systems. Int. J. Thermofluids **13**, 100–134 (2022)
5. Pan, F., Zhu, P., Zhang, Y.: Metamodel-based lightweight design of B-pillar with TWB structure via support vector regression. Comput. Struct. **88**, 36–44 (2010)
6. Yang, Z., Deng, B., Deng, M., Sun, G.: A study on finite element analysis of electric bus frame for lightweight design. In: 2018 International Forum on Construction, Aviation and Environmental Engineering-Internet of Things (2018)
7. Joost, W.: Reducing vehicle weight and improving U.S. energy efficiency using integrated computational materials engineering. JOM **64**(9), 1032–1038 (2012)
8. Zhang, H., Huang, G., Yu, D.: Numerical modeling for the frame structure of light van-type electric truck. Sci. Prog. **103**, 1–27 (2020)
9. Lyu, R., Jiang, X., Minoru, O., Ju, D.Y.: Lightweight design of automobile frame based on magnesium alloy. In: 2018 International Conference on Material Strength and Applied Mechanics (2018)
10. Idrees, U., et al.: Finite element analysis of car frame frontal crash using lightweight materials. J. Eng. Res. **11**(1), 100007 (2023)
11. Prucz, J.C., Shoukry, S.N., William, G.W., Shoukry, M.S.: Lightweight Composite Materials for Heavy Duty Vehicles. West Virginia University, Morgantown (2013)
12. Wu, J., Badu, O.A., Tai, Y., George, A.R.: Design, analysis, and simulation of an automotive carbon fiber monocoque chassis. SAE Int. J. Passeng. Veh. Syst. **7**, 838–861 (2014)
13. Garud, R.Y., Tamboli, S.C., Pandey, A.: Structural analysis of automotive chassis, design modification and optimization. Int. J. Appl. Eng. Res. **13**(11), 9887–9892 (2018)
14. Pravilonis, T., Sokolovskij, E., Kilikevičius, A., Matijošius, J., Kilikevičienė, K.: The usage of alternative materials to optimize bus frame structure. Symmetry **12**(6), 1010 (2020)
15. Tebby, S., Esmailzadeh, E., Barari, A.: Methods to determine torsion stiffness in an automotive chassis. Comput.-Aided Des. Appl. 67–75 (2011)
16. Gauchia, A., Diaz, V., Boada, M.J.L., Boada, B.L.: Torsional stiffness and weight optimization of a real bus structure. Int. J. Automot. Technol. **11**, 41–47 (2010)
17. Kurdi, O., Rahman, R.A., Samin, P.M.: Optimization of heavy duty truck chassis design by considering torsional stiffness and mass of the structure. Appl. Mech. Mater. **554**, 459–463 (2014)
18. Krzikalla, D., Slíva, A., Měsíček, J., Petrů, J.: On modelling of simulation model for racing car frame torsional stiffness analysis. Alexandria Eng. J. **59**, 5123–5133 (2020)
19. Denny, J., Veale, K., Adali, S., Leverone, F.: Conceptual design and numerical validation of a composite monocoque solar passenger vehicle chassis. Eng. Sci. Technol. Int. J. **21**, 1067–10777 (2018)
20. Happian-Smith, J.: An Introduction to Modern Vehicle Design. Elsevier, Oxford (2022)
21. Ullman, D.G.: The Mechanical Design Process. McGraw-Hill, New York (2003)
22. ANSYS, Inc. Maximum Equivalent Stress Safety Tool. ANSYS help. https://ansyshelp.ansys.com/account/secured?returnurl=/Views/Secured/corp/v231/en/wb_sim/ds_MaxEquiSST.html. Cited 20 May 2023
23. ISO 16750-3, Road vehicles Environmental conditions and testing for electrical and electronic equipment, vol. 3, p. 10 (2007)

Research on Using Non-circular Gears in Designing an Uninterrupted Two-Speed Gearbox for Electric Vehicles

Phung Van Thom[1], Nguyen Thanh Trung[2], Bui Van Tram[3], Phung Cong Dzung[3], and Nguyen Hong Thai[1(✉)]

[1] School of Mechanical Engineering, Hanoi University of Science and Technology, Hanoi, Vietnam
thai.nguyenhong@hust.edu.vn
[2] National Research Institute of Mechanical Engineering, Hanoi, Vietnam
[3] Faculty of Mechanical Engineering, University of Transport Technology, Hanoi, Vietnam

Abstract. In the powertrain system of electric vehicles (EVs), using a standalone electric motor or combining it with a single-speed gearbox does not guarantee maximum performance across different speed ranges and operating modes. The multi-speed gearboxes (MSGs) are considered a viable alternative, providing suitable operating modes for the electric motor, aiming to improve dynamic performance and energy consumption economy. However, MSGs have some limitations, including torque interruption during gear shifting, which causes energy loss, and jerking affecting passenger comfort. In addition, they have a more complex structure, increase vehicle weight and higher manufacturing costs. Therefore, a two-speed transmission is one of the solutions to balance the transmission performance and the system's costs of EVs. To solve the problem of interrupted torque during the gear shifting of a two-speed gearbox, in this study, the authors used a non-circular gear pair combined with a suitable shifting strategy. The centrodes of non-circular gears are determined from the appropriate gear ratio function for the shifting between speed levels. Then, the design parameters of the tooth profile are also selected to avoid undercutting. Finally, a design calculation program was written on Matlab software to verify the theory. The results show that the design method is completely feasible to overcome the torque interruption issue of the two-speed gearbox for EVs, which is an important approach in studying MSGs for EVs.

Keywords: Non-circular Gear · Two-speed Gearbox · Uninterrupted · Electric Vehicles

1 Introduction

Electric vehicles (EVs) with the advantage of emitting no emissions and being able to draw electricity from a variety of renewable energy sources have become an important means of alleviating the problems of environmental pollution and the limited supply

D. C. Nguyen et al. (Eds.): ICERA 2023, LNNS 944, pp. 378–389, 2024.
https://doi.org/10.1007/978-3-031-62235-9_38

of fossil energy. In the EVs market today, most EVs are equipped with single-speed gearboxes such as Tesla-S, Tesla Y, Audi E-TRON, VFe34, BYD e5, etc. due to their simple mechanical structure, which minimizes transmission losses and production costs economy [1, 2]. However, under different operating conditions, the powertrain transmission using a single-speed gearbox cannot provide suitable modes for the electric motor to operate at high efficiency.

Along with the expansion of the EV market, broader segments of EVs require higher acceleration capabilities and higher maximum speeds, posing significant challenges in the research and design of high-performance electric motors and batteries. Researchers and manufacturers have demonstrated the effectiveness of multi-speed gearboxes (MSGs) in the design of EV powertrains to utilize the high-efficiency operating range of the electric motor to improve overall EV performance, meeting requirements for load capacity and different terrains [3–5]. Nevertheless, MSGs also have limitations, such as *(1)* Increasing the number of gears in the transmission results in higher production costs and require advanced shifting strategies and control techniques [6]; *(2)* Torque interruption during gear shifting causes localized energy losses and jerking [7]. To this day, the use of a two-speed transmission is deemed appropriate to strike a balance between production costs and dynamic performance [8, 9]. The performance of the gearboxes for EVs is typically evaluated based on three main criteria: dynamic performance, energy consumption, and passenger comfort [10, 11]. The greatest challenge among these is how to ensure passenger comfort while still achieving energy efficiency during gear shifting.

Almost all MSGs used for internal combustion engine vehicles have been considered for EVs, among which automated manual transmissions (AMT) are evaluated to have higher efficiency compared to other types of transmissions such as automatic transmission (AT), dual-clutch (DCT), and continuously variable transmissions (CVT) [12–14]. Researchers have made initial advancements in improving two-speed AMT into more suitable variants for EVs, focusing on optimizing gear ratios and overcoming torque interruption. Gao et al. [15] proposed a novel two-speed inverse automated manual transmission (I-AMT) with a dry clutch mechanism placed behind the gearbox, which eliminates the torque interruption issue of conventional AMT, resulting in better acceleration performance. However, the losses caused by clutch friction significantly affect the energy efficiency of the EV, along with the requirement for a specialized clutch design to prevent surface overheating friction face. Continuing in this direction, Fang et al. [16] employed a fuzzy logic controller using signals of the EV's speed and accelerator pedal position, combined with an optimization control method, which resulted in a significant improvement in dynamic power transmission efficiency and enhanced comfort compared to an optimized AMT with the same gear ratio. Some studies propose the use of Clutch-less Automated Manual Transmission (CLAMT) as a simpler, smaller, lighter, and cost-effective solution. Liang et al. [17] combined a two-speed CLAMT with a supplementary motor used to compensate for the required torque during gear shifting, employing a control strategy to maintain constant output torque. Although not eliminate torque interruption, experimental results have demonstrated a significant improvement in shift quality. This design helps to enhance both drivability and driving comfort, but it requires advanced gearshift and engine control strategies to achieve fast and precise responsiveness. Zhang et al. [18] continued to develop the CLAMT drive-train system with an elastic load friction ring synchronizer combined with a Fuzzy-PID control method to reduce most of the shift shock.

The variants of the AMT are considered very potential for EVs, but previous studies are focused on changing the mechanical structure and developing advanced controllers with appropriate shifting strategies or compensating for loss and torque losses at the output of the system. The powertrain is designed to overcome the interruption of torque at the wheel shaft, limit jerks, and enhance comfort. Nonetheless, the issue of torque and speed variation at the drive motor has not been taken care of during gear shifting, while the drive motor is the main energy-consuming component. Therefore, the problem of optimizing the operating mode of the electric motor in the highest efficiency region has not been solved. If the task of creating a constant torque and speed variation function to meet the shifting requirements is performed by another mechanical part, it will help to minimize torque and speed variation of the motor during gear shifting. This is the key to achieving the dual goals of overcoming torque discontinuity and saving energy.

Non-circular gears (NCGs) have the advantage of generating gear ratio function and torque continuously variable with compact size and simple mechanical structure [19–21], which are a potential design alternative to overcome the disadvantages of MSGs during gear shifting. The idea of using NCG in gearbox was first used by Kerr [22] for CVT of internal combustion engine vehicles, and then further developed in studies by Ferguson [23], Dooner [24, 25], and perfected by the research group of Hebbale [26] and Kang [27]. However, these designs have not been applied in EV gearboxes because they have not considered the requirements of the gear ratio function from the problem of uninterrupted gear shifting and the magnitude of the gear ratio is also limited. The types of profiles commonly used today also need to be considered, evaluated, and selected appropriately, such as involute profile [28–30], novikov profile [31], cycloid profiles [32, 33], and improved cycloid profiles [34–37].

Based on the analyses above, in this study, we applied NCGs in the design of an uninterrupted two-speed transmission, aiming to mitigate jerks and reduce variations in motor torque and speed during gear shifting. The remaining parts of the paper are organized as follows: Sect. 2 discusses the selection of fixed gear ratios for each gear pair and determines the gear ratio function during shifting based on relevant studies. Section 3 presents the design of the NCGs centrodes according to the gear ratio function. In Sect. 4, the involute tooth profile of NCGs is generated considering the conditions to avoid tooth undercutting. Finally, the main conclusions and directions for future research are provided in Sect. 5.

2 Gear Ratios Selection and Determination of the Gear Ratio Function During Gear Shifting

2.1 Gear Ratio Optimization

Once the parameters of the electric motor and battery have been determined, different gear ratio combinations will directly affect the dynamic performance and energy economy of the EVs. From an optimization perspective, the gear ratio selection can be considered a multi-objective optimization problem, requiring the use of suitable optimization methods. After analyzing relevant literature, Table 1 presents the main optimization methods that have been employed and the resulting achieved gear ratios.

Table 1. Main methods of gear ratio optimization for two-speed gearboxes of EVs.

Researchers	Optimization method	Objective Function	Gear ratios result
Walker et al. [38]	Genetic algorithm	The mean motor efficiency and driving range	$i_1 = 11.47{:}1$; $i_2 = 4.64{:}1$
Tang et al. [39]	Genetic algorithm	The minimum vehicle energy consumption	$i_1 = 8.174{:}1$; $i_2 = 4.544{:}1$
Yin et al. [40]	Genetic algorithm	The energy consumption economy	$i_1 = 9.80{:}1$; $i_2 = 3.56{:}1$
Zhou et al. [41]	Auto-Search Method	Driving range	$i_1 = 9.3986{:}1$; $i_2 = 4.8304{:}1$
Gao et al. [15]	Dynamic programming	The energy consumption	$i_1 = 10.608{:}1$; $i_2 = 5.122{:}1$

From Table 1, it can be seen that each optimization method and objective function yield different results in terms of gear ratios. The genetic algorithm is the most widely used method for optimizing the gear ratios of the two-speed gearboxes. To select an appropriate gear ratio for designing the gear shift function between the two-speed stages, in this study, we employ the optimized results from Walker et al. when considering motor efficiency and driving range. The optimized gear ratios obtained are $i_1 = 11.47{:}1$ and $i_2 = 4.64{:}1$, respectively.

In order to reduce the size of the gearbox and facilitate the design of the NCG pair in Sect. 3, the auxiliary gear ratio is chosen $i_a = 3.5$, along with the two main gear ratios $i_1 = 3.277{:}1$ and $i_2 = 1.326{:}1$. The schematic of the two-speed gearbox is illustrated in Fig. 1, where the NCG pair 1–2 functions to achieve the desired gear ratio i_{12} during

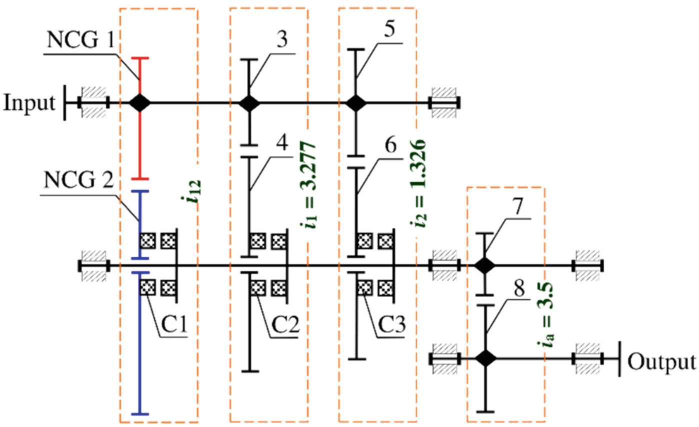

Fig. 1. Schematic diagram of two-speed gearbox using NCGs for EVs.

shifting. The circular gear pairs 3–4, 5–6, and 7–8 provide the respective gear ratios i_1, i_2, and i_a. The clutch mechanisms from C1 to C3 allow the disengagement or engagement of the motion between the gear pairs and the output shaft of the gearbox.

2.2 Determine the Gear Ratio Function During Gear Shifting

The phenomenon of jerkiness and shocks occurs when there is a sudden change in speed and torque at the output shaft of the gearbox during shifting. A seamless shift curve from 1st to 2nd gear has been proven to eliminate jerkiness and shocks [8]. The combination of motor control and gear shifting control can generate the desired shift curve, but the large variations in motor torque and speed inevitably lead to energy losses. To reduce the variations in motor torque and speed while still achieving a seamless shift curve, we propose a NCG pair that functions to create the desired gear ratio as described in Fig. 2. With the gear ratio function in each stage presented in Table 2.

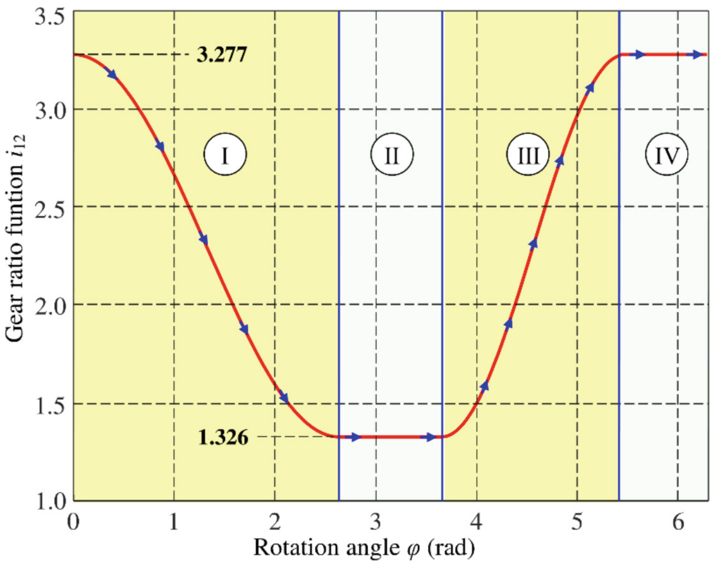

Fig. 2. Gear ratio function during gear shifting.

Specifically, when the gear ratio is at the first level ($i_1 = 3.277$), the 3–4 gear pair is working (clutch C2 is active). During acceleration (in stage I), clutch C1 is activated, while clutches C2 and C3 are disengaged. The NCG pair 1–2 meshes, creating a gear ratio function that continuously decreases until reaching the value of the second level gear ratio ($i_2 = 1.326$). At stage II, clutch C1 is still active so that the NCG pair performs the gear ratio phase is constant ($i_{12} = i_2$), and at the same time, clutch C3 starts to be activated. Until the end of stage 2, clutch C1 is disengaged, gear pair 5–6 working, and the end acceleration phase. During the deceleration phase, at this time clutch C3 is being activated, the synchronization process will occur to engage clutch C1 and simultaneously disengage clutch C3. The NCG pair 1–2 meshes to create the gear ratio function during

Table 2. The corresponding gear ratio function in the stages.

Stages	Gear ratio function i_{12}	Rotation angle of NCG 1 (rad)
I	$i_{12} = \frac{1611}{700} - \frac{683}{700}\cos\left(\frac{3600}{3019}\varphi + \pi\right)$	$\left[0 \div \frac{3019}{3600}\pi\right]$
II	$i_{12} = 1.326$	$\left[\frac{3019}{3600}\pi \div \frac{7}{6}\pi\right]$
III	$i_{12} = \frac{1611}{700} + \frac{683}{700}\cos\left(\frac{31}{18}\varphi + \pi\right)$	$\left[\frac{7}{6}\pi \div \frac{31}{18}\pi\right]$
IV	$i_{12} = 3.277$	$\left[\frac{31}{18}\pi \div 0\right]$

the deceleration phase (stage III). During the deceleration phase, at this time clutch C3 is being activated. The synchronization process will occur to engage clutch C1 and simultaneously disengage clutch C3. The NCG pair 1–2 meshes to create the gear ratio function during the deceleration phase (stage III). Afterward, the NCG pair 1–2 continues to perform the constant gear ratio phase (phase IV) to provide a favorable timing for engaging clutch C2 while disengaging clutch C1. The deceleration process concludes with the working of the 3–4 gear pair.

The gear ratio function of the NCG pair is designed for seamless shifting capability throughout both the acceleration phase (stage I) and the deceleration phase (stage III). Additionally, the constant gear ratio phases (stages II and IV) provide favorable conditions for coordinating the engagement and disengagement of the clutch mechanisms. Thus, during the shifting process, the torque and speed of the motor remain stable within the high-efficiency operating range, resulting in energy savings, while still achieving smooth gear shifting. This is a significant advantage of employing NCGs in the design of an uninterrupted two-speed gearbox compared to other design options.

3 Design Centrodes of the Non-circular Gear Pair

Let $\rho_1(\varphi_1)$, $\varphi_1 \in [0 \div 2\pi]$ are the pole radius and pole angle of centrode Σ_1 of NCG 1, respectively, and $\rho_2(\varphi_2)$, φ_2 are the pole radius and pole angle of centrode Σ_2 of NCG 2, respectively. With the gear ratio function $i_{12}(\varphi_1)$ defined in Sect. 2.2 and a given shaft distance A_{12}, the parameters $\rho_1(\varphi_1)$, $\rho_2(\varphi_2)$, $\varphi_2(\varphi_1)$ as described in the Fig. 3 is defined as follows:

From Fig. 3, we have the shaft distance A_{12}:

$$\rho_1(\varphi_1) + \rho_2(\varphi_2(\varphi_1)) = A_{12} \tag{1}$$

And gear ratio function $i_{12}(\varphi_1)$ of NCG pair is given by:

$$i_{12}(\varphi_1) = \frac{\omega_1}{\omega_2} = \frac{d\varphi_1}{d\varphi_2} = \frac{\rho_2(\varphi_2(\varphi_1))}{\rho_1(\varphi_1)} \tag{2}$$

From Eqs. (1) and (2), after transformations and simplification, we obtain the mathematical equation for the centrode Σ_1 as follows:

$$\rho_1(\varphi_1) = \frac{A_{12}}{i_{12}(\varphi_1) + 1} \tag{3}$$

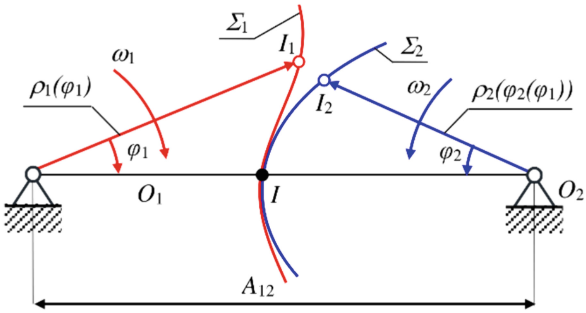

Fig. 3. Determine the centrodes of a NCG pair according to the gear ratio function.

From (1), (2) and (3), the mathematical model of centrode Σ_2 is determined by the equations:

$$\begin{cases} \rho_2(\varphi_2(\varphi_1)) = \frac{A_{12} i_{12}(\varphi_1)}{i_{12}(\varphi_1)+1} \\ \varphi_2(\varphi_1) = \int\limits_0^{\varphi_1} \frac{d\varphi_1}{i_{12}(\varphi_1)} \end{cases} \tag{4}$$

Based on the developed theory, with the designed gear ratio function shown in Fig. 2 and Table 2, after performing calculations and designing using software written by the authors in Matlab, the centrode of the NCG pair is described in Fig. 4. In which, the shaft distance $A_{12} = 200$ mm is chosen, and the circumferential ratio of centrode Σ_1 to centrode Σ_2 is $n = 2$. On the other hand, it can be seen that the centrode of the NCG

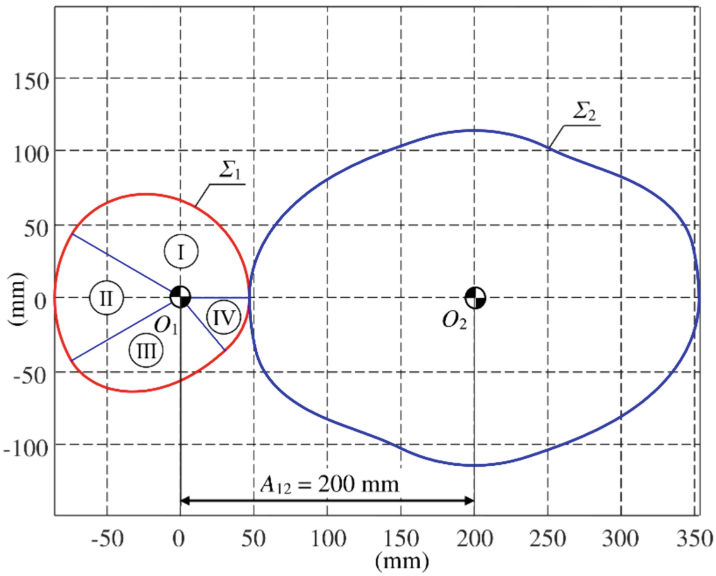

Fig. 4. The centrode of NCG pair.

pair 1–2 consists of non-circular arcs and circular arcs with radii corresponding to the radii of the circular gear pairs. Therefore, when adding the NCG pair to the gearbox, it will not cause any size changes in the radial direction of the transmission.

4 Shaping the Tooth Profile of the Non-circular Gear Pair

In this study, the commonly involute profile will be used as the tooth profile for the NCG pair 1–2. To ensure that there is no undercutting phenomenon, module m_c of the rack cutter must satisfy [30]:

$$m_c \leq \varsigma_{\min} \sin^2 \alpha_c \tag{5}$$

where α_c is the pressure angle of the rack cutter, $\varsigma_{\min}$ is the minimum radius of curvature of the centrode Σ and determined by the following equation [42]:

$$\varsigma(\varphi) = \frac{\sqrt{\left(\rho(\varphi)^2 + \left(\frac{d\rho(\varphi)}{d\varphi}\right)^2\right)^3}}{\rho(\varphi)^2 + 2\left(\frac{d\rho(\varphi)}{d\varphi}\right)^2 - \rho(\varphi)\frac{d^2\rho(\varphi)}{d\varphi^2}} \tag{6}$$

On the other hand, to the number of teeth z of the NCGs is a positive integer, the module m of the NCGs must be equal to the module m_c of the rack cutter, which must ensure the distribution of the number of teeth on the centrode:

$$m = m_c = \frac{C_{\sum}}{z\pi} \tag{7}$$

Here $C_{\sum} = \int\limits_0^{\varphi} \sqrt{(\rho(\varphi))^2 + \left(\frac{d\rho(\varphi)}{d\varphi}\right)^2} d\varphi$ is the circumference of the centrode.

With the centrode of the NCG pair designed in Sect. 3 and the pressure angle $\alpha_c = 20°$, from Eq. (6) the minimum curvature radius of the centrodes (Σ_1, Σ_2) is $\varsigma_{\min} = 38.40$ mm. Then, the module of the rack cutter must satisfy $m_c \leq 4.49$ mm. Basis on the shaping method presented in the article [28], the tooth profile design parameters of the NCG pair after calculation are given in Table 3 and the shaped NCG pair is presented in Fig. 5.

Based on Table 3 and the resulting tooth profile generation shown in Fig. 5, it can be seen that the tooth profiles on different working stages of the NCG pair with the same design parameters, thus reducing differences in the geometric shape and size of teeth, leading to the transition process between the working stages (I, II, III, IV) are smoother.

Table 3. Design parameters of NCG pair.

Parameter	Notation	NCG 1	NCG 2
Module (mm)	m	3.35	3.35
Pressure angle (^{o})	a	20.00	20.00
Circumference coefficient	n	2.00	–
Number of teeth	z	40.00	80.00
Tooth pitch (mm)	p	10.53	10.53
Tooth thickness (mm)	s	5.265	5.265
Width of space (mm)	w	5.265	5.265
Whole depth (mm)	h	6.70	6.70
Tooth addendum (mm)	h_a	3.35	3.35
Tooth dedendum (mm)	h_f	3.35	3.35

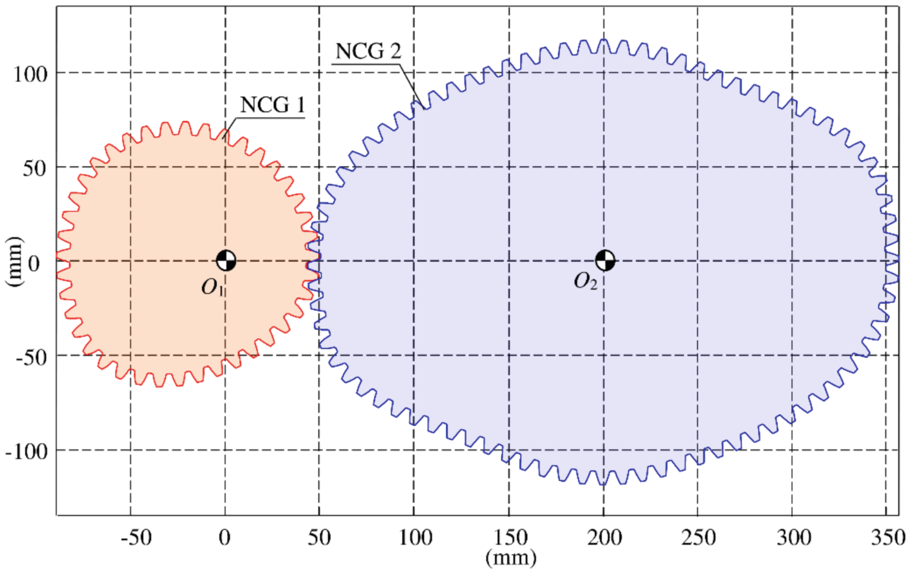

Fig. 5. A NCG pair has been designed.

5 Conclusion

The paper has investigated applying NCG in the design of an uninterrupted two-speed gearbox for EVs. The NCG pair was designed to provide continuous and seamless gear shifting. Based on the theoretical research and experimental design, the main conclusions can be expressed as follow:

(i) During the gear shifting, the NCG pair provides continuous torque, meeting the smooth shifting requirements without altering the speed torque of the motor. This enables the motor to operate efficiently in the high-performance range, ensuring passenger comfort and energy economy.
(ii) The new design allows for flexible gear shifting through the coordinated movement of the NCG pair and the clutch mechanism, without increasing the radial size of the original gearbox.
(iii) The transition process between different working stages of the NCG pair is smooth due to the tooth profiles the same design parameters.

The research results have provided the theoretical basis and demonstrate the potential application of NCG in the design of an uninterrupted multi-speed gearboxes for EVs. However, related aspects such as optimizing the gear ratio function during shifting, power transmission capability, and performance of the NCG transmission, etc., still require further investigation. Thus, it will be considered part of our future research goals.

References

1. Spanoudakis, P., Tsourveloudis, N.C., Doitsidis, L., Karapidakis, E.S.: Experimental research of transmissions on electric vehicles' energy consumption. Energies **12**(3), 388 (2019)
2. Momen, F., Rahman, K.M., Son, Y., Savagian, P.: Electric motor design of general motors' Chevrolet Bolt electric vehicle. SAE Int. J. Altern. Powertrains **5**(2), 286–293 (2016)
3. Kwon, K., Lee, J.H., Lim, S.K.: Optimization of multi-speed transmission for electric vehicles based on electrical and mechanical efficiency analysis. Appl. Energy **342**, 121203 (2023)
4. Ahssan, M.R., Ektesabi, M.M., Gorji, S.A.: Electric vehicle with multi-speed transmission: a review on performances and complexities. SAE Int. J. Altern. Powertrains **7**(2), 169–182 (2018)
5. Xu, X., Dong, P., Liu, Y., Zhang, H.: Progress in automotive transmission technology. Automot. Innov. **1**, 187–210 (2018)
6. Zhu, B., et al.: Gear shift schedule design for multi-speed pure electric vehicles. Proc. Inst. Mech. Eng. Part D J. Automobile Eng. **229**(1), 70–82 (2015)
7. Beaudoin, M.A., Boulet, B.: Fundamental limitations to no-jerk gearshifts of multi-speed transmission architectures in electric vehicles. Mech. Mach. Theory **160**, 104290 (2021)
8. Gao, B., et al.: Topology optimization and the evolution trends of two-speed transmission of EVs. Renew. Sustain. Energy Rev. **161**, 112390 (2022)
9. He, B., Chen, Y., Wei, Q., Wang, C., Wei, C., Li, X.: Performance comparison of pure electric vehicles with two-speed transmission and adaptive gear shifting strategy design. Energies **16**(7), 3007 (2023)
10. More, P., Deshmane, S., Gurav, O.: Gear shift quality parameters optimization for critical to quality dimensions. SAE Int. J. Engines **11**(3), 265–276 (2018)
11. Machado, F.A., Kollmeyer, P.J., Barroso, D.G., Emadi, A.: Multi-speed gearboxes for battery electric vehicles: current status and future trends. IEEE Open J. Veh. Technol. **2**, 419–435 (2021)
12. Huang, C., Du, C.: An integrated control approach for shifting process of single-axis parallel hybrid electric vehicle with a multi-speed AMT gearbox. Processes **11**(9), 2710 (2023)
13. Park, K., Lim, S.K., Kwon, K.: Multi-speed transmission optimization of electric vehicles based on shifting pattern considering dynamic inertia efficiency. IEEE Access **11** (2023)

14. Liu, Y., et al.: Study on the design and speed ratio control strategy of continuously variable transmission for electric vehicle. IEEE Access **11**, 107880–107891 (2023)
15. Gao, B., Liang, Q., Xiang, Y., Guo, L., Chen, H.: Gear ratio optimization and shift control of 2-speed I-AMT in electric vehicle. Mech. Syst. Signal Process. **50**, 615–631 (2015)
16. Fang, S., Song, J., Song, H., Tai, Y., Li, F., Nguyen, T.S.: Design and control of a novel two-speed uninterrupted mechanical transmission for electric vehicles. Mech. Syst. Signal Process. **75**, 473–493 (2016)
17. Liang, J., Yang, H., Wu, J., Zhang, N., Walker, P.D.: Power-on shifting in dual input clutchless power-shifting transmission for electric vehicles. Mech. Mach. Theory **121**, 487–501 (2018)
18. Zhang, L., Yang, H., Peng, Y., Li, S.: A novel synchronizer for clutchless automated manual transmissions applied in electric vehicles. Mech. Mach. Theory **170**, 104688 (2022)
19. Thai, N.H., Ly, T.T.K., Trung, N.T.: Research design and experimental manufacturing of compound non-circular gear train with an improved cycloid profile of the ellipse. In: Nguyen, D.C., Vu, N.P., Long, B.T., Puta, H., Sattler, K.-U. (eds.) ICERA 2021. LNNS, vol. 366, pp. 813–825. Springer, Cham (2022). https://doi.org/10.1007/978-3-030-92574-1_83
20. Thai, N.H., Trung, N.T.: A novel curve for the generation of the non-circular gear tooth profile. Int. J. Eng. **35**(5), 1024–1036 (2022)
21. Trung, N.T., Thom, P.V.: Influence of the fixed angle of the non-circular gears on the intermediate shaft on the gear ratio function characteristics. JST: Eng. Technol. Sustain. Dev. **33**(2), 52–59 (2023)
22. Kerr, J.H.: Variable output transmission, US Pat. 3919895 (1975)
23. Ferguson, D., Kerr, J.H., Daws, L.F.: The design of a stepless transmission using non-circular gears. Mech. Mach. Theory **10**, 467–478 (1975)
24. Dooner, D., Seireg, A.: Synthesis of non-circular gears for a continuously variable transmission. Proc. Int. Congr. Gear Transm. 38–45 (1996)
25. Dooner, D., Yoon, H.D., Seireg, A.: Kinematic considerations for reducing the circulating power effects in gear-type continuously variable transmission. Proc. Inst. Mech. Eng. Part D J. Automobile Eng. **212**(6), 463–478 (1998)
26. Hebbale, K., et al.: Study of a non-circular gear infinitely variable transmission. In: Dynamic Systems and Control Conference, vol. 46209. American Society of Mechanical Engineers (2014)
27. Kang, J., Komori, M., Zhang, S., Sugiyama, K.: Control method for output speed during velocity ratio change under high rotational speed using an uninterrupted transmission system. J. Adv. Mech. Des. Syst. Manuf. **6**(7), 1281–1297 (2012)
28. Hong Thai, N., Van Thom, P.: Research on the characteristics of tooth shape and size of the oval gear drive with an involute profile. In: Le, A.T., Pham, V.S., Le, M.Q., Pham, H.L. (eds.) The AUN/SEED-Net Joint Regional Conference in Transportation, Energy, and Mechanical Manufacturing Engineering. RCTEMME 2021. LNME. Springer, Singapore (2021). https://doi.org/10.1007/978-981-19-1968-8_14
29. Thai, N.H., Thom, P.V., Lam, D.B.: Effects of pressure angle on uneven wear of a tooth profile of an elliptical gear generated by ellipse involute. Sci. Tech. Dev. J. **24**(3), 2031–2043 (2021)
30. Thai, N.H.: Shaping the tooth profile of elliptical gear with the involute ellipse curve. Sci. Technol. Dev. J.-Eng. Technol. **4**(3), 1048–1056 (2021)
31. Batsch, M.: Mathematical model and tooth contact analysis of convexo-concave helical bevel Novikov gear mesh. Mech. Mach. Theory **149**, 103842 (2020)
32. Thai, N.H., Trung, N.T., Nghia, L.X., Duong, N.T.: Synthesis of the external non-circular gear-train with cycloid profile. J. Sci. Technol. Tech. Univ. **145**, 033–039 (2020)
33. Thai, N.H., Trung, N.T., Nghia, L.X., Duong, N.T.: Profile sliding phenomenon in the external non-circular gear-train with cycloidal profile. Eng. Technol. Sustain. Dev. **31**(2), 053–057 (2021)

34. Thai, N.H., Thom, P.V., Trung, N.T.: Influence of centrodes coefficient on the characteristic of gear ratio function of the compound non-circular gear train with improved cycloid tooth profile. In: Khang, N.V., Hoang, N.Q., Ceccarelli, M. (eds.) ASIAN MMS 2021. MMS, vol. 113, pp. 204–214. Springer, Cham (2022). https://doi.org/10.1007/978-3-030-91892-7_19
35. Thai, N.H., Thom, P.V., Trung, N.T.: Experimental design and manufacture a pair of the internal non-circular gears with an improved cycloid profile. In: Le, A.T., Pham, V.S., Le, M.Q., Pham, H.L. (eds.) The AUN/SEED-Net Joint Regional Conference in Transportation, Energy, and Mechanical Manufacturing Engineering. RCTEMME 2021. LNME, pp. 118–134. Springer, Singapore (2021). https://doi.org/10.1007/978-981-19-1968-8_11
36. Trung, N.T., Thom, P.V., Thai, N.H.: The design of the compound non-circular gear train has an internal gears pair with an improved cycloid tooth profile. In: Nguyen, D.C., Vu, N.P., Long, B.T., Puta, H., Sattler, K.U. (eds.) Advances in Engineering Research and Application. ICERA 2022. LNNS, vol. 602, pp. 910–923. Springer, Cham (2023). https://doi.org/10.1007/978-3-031-22200-9_97
37. Thai, N.H., Thom, P.V.: Replacing the involute profile with an improved cycloid profile to improve the bearing capacity for the elliptical gear drives. Vietnam J. Sci. Technol. **62**(3), 588–600 (2023)
38. Walker, P.D., Abdul Rahman, S., Zhu, B., Zhang, N.: Modelling, simulations, and optimisation of electric vehicles for analysis of transmission ratio selection. Adv. Mech. Eng. **5**, 340435 (2013)
39. Tang, Z.Q., Ma, D.P., Gong, X.W.: Transmission ratio optimization of two-speed pure electric vehicle. Appl. Mech. Mater. **722**, 271–275 (2015)
40. Yin, Q., Wu, Z., Rui, X.: Parameter design and optimization of electric vehicle. In: 2014 IEEE Conference and Expo Transportation Electrification Asia-Pacific (ITEC Asia-Pacific), pp. 1–7. IEEE (2014)
41. Zhou, X., Walker, P., Zhang, N., Zhu, B.: Performance improvement of a two speed EV through combined gear ratio and shift schedule optimization. SAE Tech. Paper (2013)
42. Litvin, F.L., Alfonso, F.-A., Ignacio, G.-P., Kenichi, H.: Noncircular Gears Design and Generation. Cambridge University Press, New York (2009)

Research on Simulation of Thermal Stability and Optimization of Drum Brakes on Toyota Innova

Vu Hai Quan[1], Nguyen Anh Ngoc[1](✉), Nguyen Minh Tien[1], Le Van Quynh[2], and To Hoang Hai[1]

[1] School of Mechanics and Automotive Engineering, Hanoi University of Industry, Hanoi, Vietnam
ngocnguyencnoto@haui.edu.vn
[2] Thai Nguyen University of Technology, Thai Nguyen, Vietnam

Abstract. The brake system in a car is an important system that helps control speed and ensures safety while driving. The main function of the brake system is to slow down and stop the vehicle when necessary, ensuring the safety of the driver and other road users. In particular, the drum brake mechanism is a commonly used braking system for vehicles, in addition to competing with the disc brake mechanism. The kinetic energy of the rotating wheels is converted into frictional heat by the action of the brakes, causing the wheels to stop spinning. In this study, NX Siemens software is used to design brake drum and brake pad models, while the Ansys software is applied for detailed analysis using the finite element method. Initial simulation results provide important parameters such as temperature distribution, total heat flow, heat flow distribution, total strain, pressure, etc. Through these parameters, stress and displacement can be evaluated, forming the basis from which to infer the safety and durability of the components. Based on the obtained results, improvements will be implemented to offer a new design that is more optimal while still ensuring durability.

Keywords: Drum brake · Design · Thermal stability test · Stress · Optimization

1 Introduction

According to a survey by IMR Inc, it is estimated that 0.001% of vehicle crashes involving brakes will cause 5,000 deaths in the US alone [1]. Another study found that passengers were 45% more likely to die in a crash without brake assist in the same old-fashioned vehicle [2]. Brake failure accounts for 0.44% of accidents in the US, the probability of a vehicle accident is 1 in 400 due to brake system failure. An average of 264,000 car accidents occurs every year due to brake system failure in the US [3]. In Vietnam, in 2022, there will be more than 11,000 traffic accidents [4], as well as in the world, the number of accidents caused by errors in car systems, especially the brake system, is not small. Research on brake systems is always a matter of interest to researchers.

D. C. Nguyen et al. (Eds.): ICERA 2023, LNNS 944, pp. 390–398, 2024.
https://doi.org/10.1007/978-3-031-62235-9_39

The brake system is a crucial component of a car, operating in high intensity conditions. Therefore, it is regularly checked and maintained to meet technical requirements, minimizing the risk of safety issues during the vehicle's movement process. A brake is a device that inhibits the movement of a vehicle. The brake absorbs the kinetic energy of the vehicle and reduces the vehicle's movement speed [5]. The drum brake mechanism is the brake mechanism commonly used on vehicles: passenger cars, trucks,…

In the study "Structural and Thermal Analysis of Brake" [6], the author investigated four common materials: stainless steel, gray cast iron, carbon fiber, and aluminum alloy. Find the most suitable material. Moreover, in this study, the author conducted separate simulations for the static strength test and thermal analysis. The thermal analysis results were not used as boundary conditions for the static stability test problem, thus the exact results are not yet available. In the study 'Structural and Thermal Analysis of Brake Drum' [7], the author used SolidWorks software to design and simulate thermal analysis, evaluating materials and thereby providing suitable materials for production. In this study, the author has provided a detailed description of the boundary conditions used for the thermal analysis problem to produce brake discs. Additionally, there are many other studies [8, 9] analyzing heat and materials for pads, discs, and drums in both disc brakes and drum brakes.

The paper uses a simulation method that builds on the pressure on the brake drum and the heat generated causing deformation, then performs the optimization and redesign process to propose a new design.

2 Theoretical Basis

Calculate the pressure in the brake drum using the formula referenced in the document [10]:

$$p = \frac{M_p}{\mu \times b \times r_t^2 \times \beta_0} = \frac{R' \times r_0\prime}{\mu \times b \times r_t^2 \times \beta_0} \tag{1}$$

$$p_1 = 95182,9\left(\frac{kG}{m^2}\right) = 0,933\ MPa; p_2 = 52328,5\left(\frac{kG}{m^2}\right) = 0,513\ MPa \tag{2}$$

Material selection for the simulation problem includes the following: structural steel, gray cast iron, aluminum alloy, and copper alloy. These materials are commonly used in various industries, including the automotive manufacturing industry (Table 1).

In mechanics and thermodynamics, thermal stress is the mechanical stress produced by any change in the temperature of a material. These stresses can lead to cracking or plastic deformation, depending on various factors of the heating process, including material types and limits. Temperature gradients, thermal expansion or contraction, and thermal shock are factors that can lead to thermal stress. Generally, the greater the temperature change, the higher the degree of stress that can occur. Thermal shock can result from rapid temperature changes, leading to cracking or breakage. For thermal expansion or contraction, this stress is calculated by multiplying the temperature change by the material's coefficient of thermal expansion and the material's Young's modulus.

$$\sigma = E\alpha\left(T_f - T_0\right) = E\alpha\Delta T \tag{3}$$

Table 1. Material specifications

Parameter	Material				
	Aluminum alloy	Structural steel	Gray cast iron	Copper alloy	Unit
Young's module	71000	200000	110000	110000	MPa
Poisson's coefficient	0.33	0.3	0.28	0.34	
Specific weight	2770	7850	7200	8300	Kg/mm^3
Limit stress	280	250	572	280	MPa
Cutting module	26692	80000	41045	47600	MPa

where: E - is Young's modulus; α - is the coefficient of thermal expansion; T_f - is the initial temperature; T_0 – is the final temperature.

According to a study "The Effect of a Variable Disc Pab Friction Coefficient for the Mechanical Brake System of a Railway Vehicle" [11], changing the temperature also changes the coefficient of friction to decrease, endangering the braking process.

The heat equation is a consequence of Fourier's law for heat conduction:

$$\frac{\partial u}{\partial t} = k\left(\frac{\partial^2 u}{\partial x^2} + \frac{\partial^2 u}{\partial y^2} + \frac{\partial^2 u}{\partial x^2}\right) = k\left(u_{xx} + u_{yy} + u_{zz}\right)$$

where: $\frac{\partial u}{\partial t}$ - is the degree of change in temperature at a certain point over time; u_{xx}, u_{yy}, u_{zz} - is the second derivative (heat flow) of temperature in the x, y, and z directions, respectively; k - is a material-dependent coefficient that depends on thermal conductivity, density, and heat capacity.

3 Model Design

3.1 Brake Drum Design

The design is done on NX Siemens software. The reference dimensions are according to the actual size of the brake drum on the Toyota Innova 2021, listed in Table 2 (Fig. 1)

3.2 Simulation

Meshing the Model: Meshing is a crucial process in simulations in general and thermal-stress analysis in particular. The mesh parameters are presented in the table below (Table 3 and Fig. 2).

Temperature: The inlet temperature (Temperature) is defined as 100 °C, here the temperature provided is used to evaluate the heat generated due to friction and the

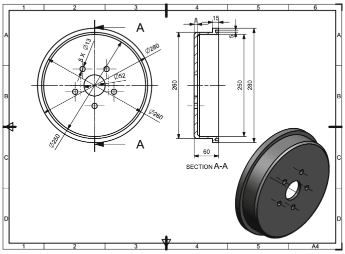

Fig. 1. Brake drum design and brake drum 3D model.

Table 2. Base size of brake drum.

Parameter	Value
Outer Diameter	280 mm
Inner Diameter	250 mm
Center hole diameter	52 mm
Small hole diameter	13 mm
Brake drum height	60 mm

Table 3. Base size of brake drum.

1	Number of elements	34615
2	Number of points	64258
3	Element size	4 mm

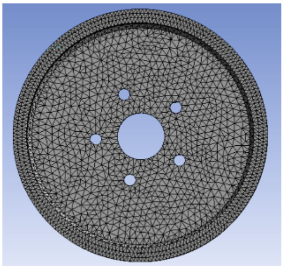

Fig. 2. Mesh Model

pressure applied during the simulation of the braking process. The temperature is applied to the inside surface of the brake drum where the brake pads are applied (Fig. 3).

Convection heat: Convection heat in this problem is heat transfer from the brake drum to the outside air, so the coefficient value will be selected according to the software

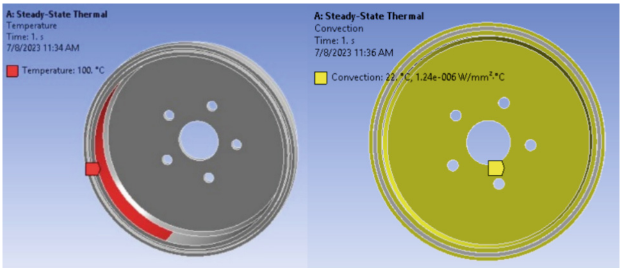

Fig. 3. Brake drum temperature and convection

standard with a value of 1.24e−6 W/mm^2.^{o}C and set at 22 °C (ambient temperature), shown in the figure above.

Pressure: is set at the position of contact with the brake pads with the value as calculated in item 2 (Fig. 4).

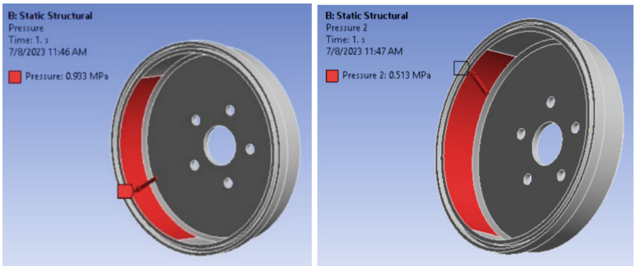

Fig. 4. Setting pressure and fixed mount

4 Results and Discussions

4.1 Simulation Results

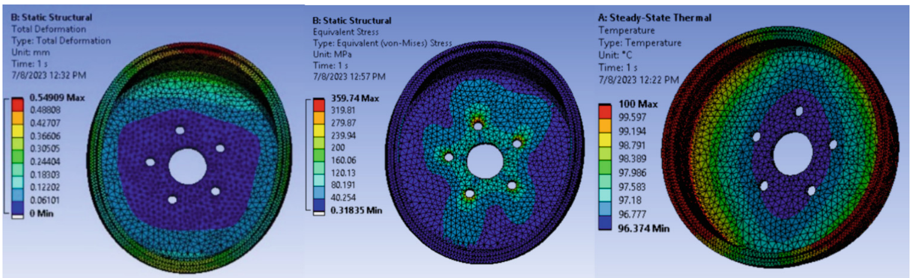

Fig. 5. Results Total strain - Equivalent stress - Heat distribution of brake drum

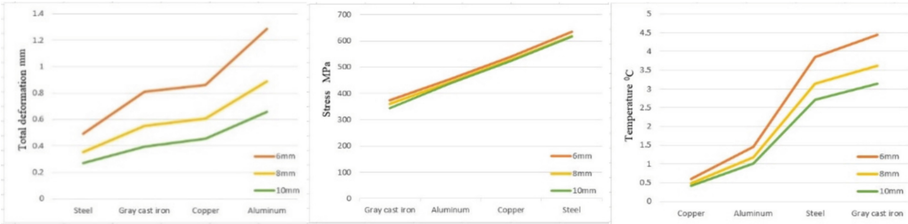

Fig. 6. Statistical graph of Deformation – Stress – Heat amplitude results with different thicknesses of brake drums.

In addition to the selection of materials, this study examines structural parameters by increasing the thickness of the brake drum with the respective brake drum wall sizes: 6 mm, 8 mm, and 10 mm, respectively. The results are shown in the graphs above. The results show that changing the thickness does not significantly affect the durability of the part. Through the above graphs, it is shown that increasing the thickness only reduces the deformation, which is understandable because the larger the thickness will reduce the deformation. However, with the criteria of temperature amplitude as well as stress, increasing the thickness does not increase the temperature amplitude as well as reduce the stress, but the obtained results are opposite. From there, it can be concluded that the factors of materials, thermal properties of materials, temperature characteristics, boundary conditions are the main factors affecting the durability of the part in the thermal problem structure (Fig. 5).

4.2 Discussion and Analysis

In terms of materials, the simulation results on the graph show that only gray cast iron is resistant to heat. Gray cast iron with a maximum stress of 373.09 MPa is less than the ultimate stress of the material Gray iron is 572 MPa and has the second smallest total strain compared to the results for other metals with a total strain of 0,54909. Simulation results show that gray cast iron meets the requirements of heat resistance, so today this material is used to manufacture brake drums. The thermal simulation results are as follows:

– Regarding temperature distribution: As a result of the table, the thermal amplitude of gray cast iron is larger than that of two other metals, aluminum and steel (3,626 > 3,137 > 1,181). This result can be assessed that the brake drum made of gray cast iron has better heat transfer ability than other materials. Good temperature distribution will avoid thermal stress causing surface deformation or warping due to material expansion when subjected to high heat, which will affect braking performance.
– Regarding the total strain: the results shown on the graph can be seen, the deformation of gray cast iron is the smallest and smaller than other materials, corresponding to the percentage of:

Regarding stress: the results of each graph show that, the maximum stress of gray cast iron is the smallest compared to the remaining materials 343.92 < 438.56 (aluminum) < 523.39 (copper) < 616, 2 (steel).

5 Optimization and Redesign

5.1 Optimization

After giving the results and analyzing the results of the process of simulating the thermal stability of the drum, we will still use Ansys software to continue to simulate the optimization process that the software offers, the process of optimization is performed with the requirement to remove 20% of the mass.

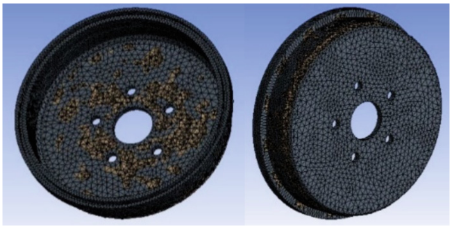

Fig. 7. Percentage of feedback and optimization constraints

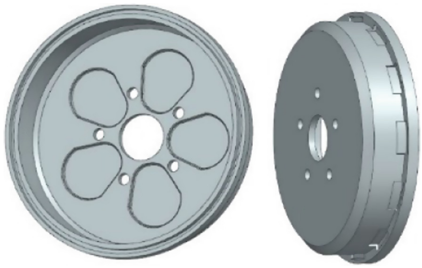

Fig. 8. New brake drum

5.2 Redesign and Simulation

Based on the results of Fig. 6, using NX Siemens to come up with a new design with a base thickness of 8 mm and reducing the thickness of some areas to holes with a thickness of 5 mm, the profile changes will rounded. The Gray Cast Iron material was used for the simulation in Ansys (Fig. 7). After redesigning and measuring, the volume was reduced by about 20% as originally planned (Fig. 9).

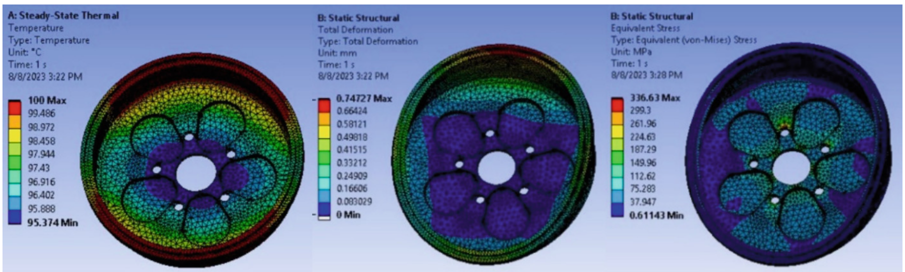

Fig. 9. Temperature, Total Strain and Stress of New Drum

From Fig. 8 we can see that the pressure has decreased from 359.74 to 336.63, the total strain has increased but not significantly from 0.54909 to 0.74727, the temperature has not changed significantly.

With the results of simulation and optimization of brakes for durability, the authors aim for further research by using CFD simulation software, surveying the cooling process and temperature changes during operation.

6 Conclusion and Suggestion

6.1 Conclude

In this study, the research team conducted simulations of Structural Optimization, Static Structural, and Steady-State Thermal issues using the Ansys software, considering five different material types, including Aluminum Alloy, Structural Steel, Gray Cast Iron, Copper Alloy, and Titanium Alloy. The simulation results provided detailed insights into the temperature distribution within these materials and their influence on the drum brake system. The research team observed that different materials significantly impact the temperature distribution and thermal performance of the system. For instance, Aluminum Alloy demonstrated superior heat dissipation capabilities compared to other materials, while Gray Cast Iron exhibited a higher heat resistance.

Furthermore, the research team's simulations revealed variations in the materials' yield strength, necessitating the formulation of an optimization problem to propose a new drum brake design. Subsequently, the optimized design was simulated and its stress levels assessed, comparing them to the initial design.

In summary, this study has advanced the research team's understanding of how different materials affect thermal performance and temperature distribution within the system. These findings can be valuable for manufacturers and designers seeking to optimize designs and select materials for various thermodynamic applications in the field of mechanical engineering.

6.2 Suggestions

Based on the research results, the research team has put forward the following recommendations for further in-depth investigation and practical application, especially for manufacturers:

Material Selection: Due to the significant influence of material properties on thermal performance, stress, and deformation, further studies should explore a broader range of materials, especially emerging materials in the field of advanced materials, to further optimize mechanical systems.

Structural Optimization: The structural optimization process leads to new design proposals, but a more in-depth exploration of this aspect is necessary to identify potential design enhancements and cost-effective solutions.

Real-World Testing: The findings from simulations must be validated through real-world testing to ensure the practical applicability of these recommendations, serving as a basis for further research and practical implementation in the field of mechanical engineering and for manufacturers, with the goal of continuing to optimize mechanical systems and design solutions.

References

1. Calvin, Safe braking, You Are More Likely to Die from Bad Brakes (2020). https://safebraking.com/you-are-more-likely-to-die-from-bad-brakes-than-covid-19-corona-virus/
2. Los Angeles Times, Study Says Death More Likely with Anti-Lock Brakes (1996). https://www.latimes.com/archives/la-xpm-1996-12-12-mn-8435-story.html
3. Arthur, J.L.: Look up a plate, 13 Shocking Brake Failure Statistics That Drivers Can't Ignore (2023). https://www.lookupaplate.com/blog/brake-failure-statistics/
4. Government electronic newspaper, Handling more than 2.8 million cases of traffic violations, fined more than VND 4,124 billion (2022). https://by.tn/thong-ke-TNGT-2022
5. Kiran, C.S., Kumar, M.R., Reddy, P.S., Venkatesh, T.: Modelling and Analysis of Brake Drum using ANSYS Workbench, December 2020
6. Subhani, S.: Structural and thermal analysis of brake. Int. J. Mod. Trends Sci. Technol. (2020)
7. Kumar, A., Sabarish, R.: Department of Mechanical Engineering, Structural and Thermal Analysis of Brake Drum (2014)
8. Parab, V., Naik, K., Dhale, A.D.: Structural and thermal analysis of brake disc **2**(2) (2014)
9. Chouhan, Y.S., Tiwari, S.: Static structural and thermal analysis of disc brake pad model, 13 June 2020
10. Quân, V.H., Ngọc, N.A., Quỳnh, L.V., Khoa, N.X., Tiến, N.M.: Modelling and simulation of automatic brake system of vehicle. ARPN J. Eng. Appl. Sci. **18**(7) (2023). http://www.arpnjournals.org/jeas/research_papers/rp_2023/jeas_0423_9171.pdf
11. Quân, V.H., Ngọc, N.A., Quân, L.H., Tiến, N.M.: A Comparison of the Performance of Anti-Lock Braking System (ABS) Using Fuzzy and PID Controllers. https://ieeexplore.ieee.org/document/9989135/

Robust Optimal Tracking Control Using Adaptive Disturbance Observer for Wheeled Mobile Robot

Nam D. Nguyen and Nam H. Nguyen(✉)

Department of Automation Engineering, School of Electrical and Electronic Engineering, Hanoi University of Science and Technology, Hanoi, Vietnam
nam.nguyenhoai@hust.edu.vn

Abstract. This paper presents an advanced control approach for wheeled mobile robots to address the challenges of slipping, skidding, and input disturbance. The proposed method combines the synchronous online adaptive algorithm with an adaptive nonlinear disturbance observer to achieve robust trajectory tracking. The synchronous online adaptive (SOA) algorithm is utilized to approximate the Hamilton-Jacobi-Bellman (HJB) solution for the robot's nonlinear dynamics, facilitating the design of a controller that can effectively compensate for uncertainties and disturbances. To address slipping and skidding, an adaptive nonlinear disturbance observer (ANDO) is incorporated into the control scheme. The ANDO accurately estimates the unknown slipping and skidding disturbances, enabling precise compensation and enhancing the robot's overall tracking performance. The proposed approach is validated through extensive simulation studies. The results demonstrate that the controller bases on the synchronous online adaptive algorithm, coupled with the adaptive nonlinear disturbance observer, achieves uniform boundedness for all signals in the closed-loop system and guarantees convergence of point tracking errors to an adjustable neighborhood of the origin.

Keywords: Synchronous online adaptive algorithm · disturbance observer

1 Introduction

In recent years, the development of mobile robots has made significant breakthroughs and has been applied in various fields. However, in this relentless quest for perfection, a persistent challenge has emerged: lateral and longitudinal sliding phenomena, causing instability and undesirable deviations from desired trajectories. To surmount this obstacle, the brightest minds in the field have engaged in rigorous analysis and model development, focusing on lateral and longitudinal sliding dynamics [1, 2]. A pivotal breakthrough came with the introduction of adaptive control methods, which enabled vehicles to adapt to changing conditions without prior knowledge of sliding effects [3, 4]. With great strides, researchers introduced robust adaptive control mechanisms featuring extended state observers [5] and disturbance estimation observers [6]. These innovations dramatically improved control quality, noise rejection capabilities, and the overall

D. C. Nguyen et al. (Eds.): ICERA 2023, LNNS 944, pp. 399–406, 2024.
https://doi.org/10.1007/978-3-031-62235-9_40

handling of sliding effects. Neural networks revolutionized autonomous vehicles with innovative adaptive control strategies [7], and robust controllers using Gaussian networks [8]. These advancements effortlessly approximate uncertain and unknown components, enabling precise trajectory execution and exceptional stability.

Simultaneously, the realm of control strategies saw a new frontier through the innovative application of reinforcement learning [9] using four neural networks. With a lot of neural networks, the algorithm makes the system complex with a significant number of weights to update, leading to reduced quality and increased computational burden. In response, ingenious researchers sought streamlined control structures with fewer neural networks, resulting in remarkable developments, such as the critic-actor dual neural network structure [10, 11]. In this paper, we introduce an innovative control structure that integrates the synchronous online adaptive (SOA) algorithm. This innovative approach employs a single neural network in conjunction with an adaptive nonlinear disturbance observer [12], and a state feedback controller. The rest of this work is organized as follows: the model of wheeled mobile robot is introduced in the next section; the disturbance observer and controller design are proposed in Sect. 3; simulations and results are given in Sect. 4; and conclusions are made in the final section.

2 Wheeled Mobile Robot Model

2.1 Kinematic Model with Skidding and Slipping

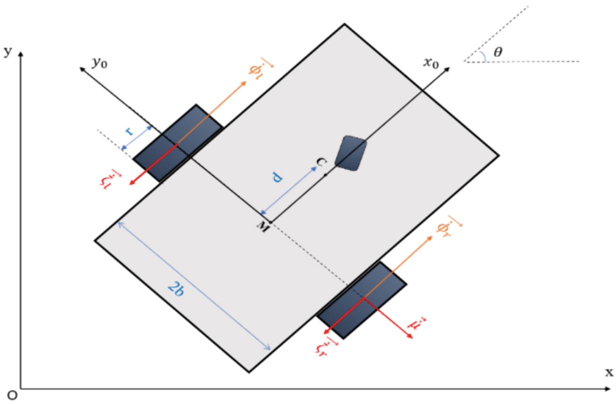

Fig. 1. A structure diagram of the wheeled mobile robot.

Figure 1 illustrates the model of a wheeled mobile robot. This robot is propelled by two driving wheels located at the back, each with a radius of r. The distance between these two driving wheels is $2b$. M is the intersection of the symmetric axis and the driving wheel axis. C is the centre of mass of the platform, d is the distance from M to C. The position of C in the global coordinate is represented by $q_C = \left[x_C, y_C, \theta, \phi_r, \phi_l\right]$, where x_C and y_C represent the transverse and vertical coordinates of C, respectively. θ

denotes the angle between the symmetric axis and the Ox axis, while ϕ_r and ϕ_l indicate the angular positions of the right and left driving wheels, respectively. The reference signals for the coordinates $q = \left[x_C, y_C\right]^T$ are denoted by $q_d = \left[x_d, y_d\right]^T$.

We are examining the perturbed non-holonomic constraints that involve skidding and slipping effects [5], in which the kinematic equations of the mobile robot:

$$\dot{q}_c = g_q(\theta)v + g_d(\theta)d_q \tag{1}$$

where $g_q(\theta) = \begin{bmatrix} \cos\theta & -d\sin\theta \\ \sin\theta & d\cos\theta \\ 0 & 1 \end{bmatrix}$, $g_d(\theta) = \begin{bmatrix} -\sin\theta & -\cos\theta & d\sin\theta \\ \cos\theta & -\sin\theta & -d\cos\theta \\ 0 & 0 & -1 \end{bmatrix}$

$d_q = \left[\dot{\mu}, \dot{\zeta}_\vartheta, \dot{\zeta}_\omega\right]^T$, $v = [\vartheta, \omega]$ with $\vartheta = \frac{r}{2}\left(\dot{\phi}_r + \dot{\phi}_l\right)$ is the forward linear velocity, $\omega = \frac{r}{2b}\left(\dot{\phi}_r - \dot{\phi}_l\right)$ is the angular velocity, $\dot{\mu}$ is the lateral skidding velocity of the wheeled mobile robot, $\dot{\zeta} = \left[\dot{\zeta}_r, \dot{\zeta}_l\right]^T$ represents the perturbed angular velocities caused by the slipping of the two actuated wheels. $\dot{\zeta}_\vartheta = \frac{r}{2}\left(\dot{\zeta}_r + \dot{\zeta}_l\right)$, $\dot{\zeta}_\omega = \frac{r}{2b}\left(\dot{\zeta}_r - \dot{\zeta}_l\right)$.

Assumption 1. $\left\|d_q\right\| \le \beta_1$, $\left\|\dot{d}_q\right\| \le \beta_2$ with β_1, β_2 are unknown positive constants.

2.2 Dynamic Model with Skidding and Slipping

Using the Euler-Lagrange equation and referring to the dynamic equations from [5], we construct the following dynamic equations:

$$\ddot{\phi} = f_{\dot{\phi}}(\dot{\phi})\dot{\phi} + g_{\dot{\phi}}\tau + d_{\dot{\phi}} \tag{2}$$

where $d_{\dot{\phi}} = -\overline{M}^{-1}\left(-\overline{M}\ddot{\zeta} + \overline{V}_2\left(\dot{\zeta}\right)\dot{\phi} - \overline{V}(q, \dot{q})\dot{\zeta} + \overline{D}_{\dot{\mu}}\dot{\mu} + \overline{D}_{\ddot{\mu}}\ddot{\mu} - \tau_d\right)$, $f_{\dot{\phi}}(\dot{\phi}) = -\overline{M}^{-1}\overline{V}_1\left(\dot{\phi}\right)$, $g_{\dot{\phi}} = \overline{M}^{-1}$ with the matrices are defined:

$$\overline{M}(q) = \begin{bmatrix} I_w + \frac{r^2}{4b^2}\left(mb^2 + I\right) & \frac{r^2}{4b^2}\left(mb^2 - I\right) \\ \frac{r^2}{4b^2}\left(mb^2 - I\right) & I_w + \frac{r^2}{4b^2}\left(mb^2 + I\right) \end{bmatrix}, \overline{D}_{\dot{\mu}} = -\frac{mr\dot{\theta}}{2}\begin{bmatrix} 1 \\ 1 \end{bmatrix}, \overline{D}_{\ddot{\mu}} = \begin{bmatrix} 0 \\ 0 \end{bmatrix}$$

$$\overline{V}(q, \dot{q}) = \frac{r^2}{2b}m_c d\dot{\theta}\begin{bmatrix} 0 & 1 \\ -1 & 0 \end{bmatrix}, \overline{B} = \begin{bmatrix} 1 & 0 \\ 0 & 1 \end{bmatrix}, \overline{V}_2\left(\dot{\zeta}\right) = -\frac{r^3}{4b^2}m_c d\left(\dot{\zeta}_r - \dot{\zeta}_l\right)\begin{bmatrix} 0 & 1 \\ -1 & 0 \end{bmatrix}$$

$\overline{V}_1\left(\dot{\phi}\right) = \frac{r^3}{4b^2}m_c d\left(\dot{\phi}_r - \dot{\phi}_l\right)\begin{bmatrix} 0 & 1 \\ -1 & 0 \end{bmatrix}$, $\tau_d = [\tau_{d1}, \tau_{d2}]$ is the disturbance input, where $m = m_c + 2m_w$, $I = I_c + m_c d^2 + 2m_w b^2 + 2I_m$, m_c is the mass of the platform, m_w is the combined mass of each driving wheel and the rotor of its respective motor, I_c is the moment of inertia of the platform with respect to a vertical axis passing through point M. I_w is the moment of inertia of each wheel and the motor rotor about the wheel axis, I_m is the moment of inertia of each wheel and the rotor of its motor with respect to the wheel's diameter.

3 Disturbance Observer and Controller Design

The control diagram of the paper consists of two control loops, with an outer loop controlling the kinematic model using a state-feedback controller, and an inner loop controlling the dynamic model using a controller based on the OADP algorithm. Two adaptive nonlinear disturbance observers are utilized to estimate the disturbance for these control loops.

3.1 Outer Loop Controller

State-Feedback Controller
In the Oxy coordinate system, the position error between the point $C(x_C, y_C)$ and the target point $C_d(x_d, y_d)$ is computed as follows:

$$e_q = \begin{bmatrix} e_x \\ e_y \end{bmatrix} = \begin{bmatrix} \cos\theta & \sin\theta \\ -\sin\theta & \cos\theta \end{bmatrix} \begin{bmatrix} x_d - x_c \\ y_d - y_c \end{bmatrix} \tag{3}$$

The first derivative of (3) along with time is:

$$\dot{e}_q = \begin{bmatrix} -1 & e_y \\ 0 & -d - e_x \end{bmatrix} v + \begin{bmatrix} 0 & 1 & -e_y \\ -1 & 0 & d + e_x \end{bmatrix} \begin{bmatrix} \dot{\mu} \\ \dot{\zeta}_\vartheta \\ \dot{\zeta}_\omega \end{bmatrix} + \begin{bmatrix} \cos\theta & \sin\theta \\ -\sin\theta & \cos\theta \end{bmatrix} \begin{bmatrix} \dot{x}_d \\ \dot{y}_d \end{bmatrix} \tag{4}$$

Define a Lyapunov function: $V = \frac{1}{2} e_q^T e_q \geq 0, \forall e_q \in \mathbb{R}^2$, and its first derivative is:

$$\dot{V} = e_q^T \dot{e}_q \tag{5}$$

Substitute (3), (4) and control law: $v_c = \begin{bmatrix} \beta_1 e_x + \dot{\zeta}_\vartheta + \cos\theta \dot{x}_d + \sin\theta \dot{y}_d \\ \left(\beta_2 e_y - \dot{\mu} + d\dot{\zeta}_\omega - \sin\theta \dot{x}_d + \cos\theta \dot{y}_d\right)/d \end{bmatrix}$ with $\alpha_1 > 0$, $\alpha_2 > 0$, into Eq. (5) to have:

$$\dot{V} = -\beta_1 e_x^2 - \beta_2 e_y^2 \leq 0 \forall e_x, e_y \in \mathbb{R} \tag{6}$$

When $e_x \neq 0$ or $e_y \neq 0 : \dot{V} < 0 \rightarrow$ the system is asymptotically stable.

Adaptive Nonlinear Disturbance Observer
Since the slipping and skidding component d_q is unknown, a disturbance observer is applied to estimate them. There exist some disturbance observers [12–14] in the literature. With the kinematic Eq. (1), the ANDO [12] is selected to design as follows:

$$\begin{cases} \dot{z} = -lz - l\left(lq_c + g_q(\theta)v\right) + (kl - \gamma)q_c \\ \hat{d} = z + lq_c \\ \dot{l} = -kl + \gamma, \end{cases} \tag{7}$$

where $z \in \mathbb{R}^3$ is the state vector, $l = diag([l_1, l_2, l_3])$ is the adaptive function, $k = diag([k_1, k_2, k_3])and\gamma = diag\left(\left[\gamma_1, \gamma_2, \gamma_3\right]\right)$ are two parameter matrices with $k_i, \gamma_i > 0$, $i = 1, 2, 3$. Then, d_q is estimated by using a formula: $\hat{d}_q = g_d^{-1}(\theta)\hat{d}$ where $\hat{d}_q = \left[\hat{\mu}, \hat{\dot{\zeta}}_r, \hat{\dot{\zeta}}_l\right]^T$ is the estimated skidding and slipping disturbances.

3.2 Inner Loop Controller

With the velocity already designed as mentioned above, the desired angular velocity for each wheel is as follows:

$$\dot{\phi}_c = \begin{bmatrix} 1/r & b/r \\ 1/r & -b/r \end{bmatrix} v_c \tag{8}$$

Set $e_{\dot{\phi}} = \dot{\phi}_c - \dot{\phi}$ is the angular velocity tracking error, combine with (3), the first derivative of the angular velocity tracking error is:

$$\dot{e}_{\dot{\phi}} = f_e + g_e \tau + d_e \tag{9}$$

where $f_e = f_{\dot{\phi}}(\dot{\phi}) e_{\dot{\phi}}$, $g_e = -g_{\dot{\phi}}$, $d_e = \ddot{\phi}_c - f_{\dot{\phi}}(\dot{\phi})\dot{\phi}_c - d_{\dot{\phi}}$.

Consider $d_e = [00]^T$.

It is commonly assumed that system (8) has a solution that depends on the initial values x_0. Let $\Omega \in \mathbb{R}^2$ be defined as the set comprising all possible solutions of (8). In other words, Ω represents the working space of (8) and encompasses all existing trajectories x, including the origin.

Assumption 2. f_e satisfies the Lipschitz continuous condition over the set Ω.

Define Hamilton function:

$$H(e, \tau, V_e) = \frac{\partial V^T}{\partial e}(f_e + g_e \tau) + e^T Q e + \tau^T R \tau \tag{10}$$

where $V(e, \tau) = \int\limits_t^\infty r(e, \tau) dt$, $r(e, u) = \tau^T R \tau + e^T Q e$, $Q \in \mathbb{R}^{2x2}$, $R \in \mathbb{R}^{2x2}$ are symmetric positive definite matrices.

The optimal control signal τ_r^* is calculated by $\tau_r^* = \arg\min_{\tau_r} H(e, \tau, V_e^*)$, after some calculations it becomes:

$$\tau_r^* = -\frac{1}{2} R^{-1} g_e^T V_e^* \tag{11}$$

With control signal (11), we define the HJB equation as:

$$e^T Q e + V_e^{*T} f_e - \frac{1}{4} V_e^{*T} g_e R^{-1} g_e^T V_e^* = 0 \tag{12}$$

As $V^*(e)$ of the HJB equation can't be directly obtained, $V(e, \tau)$ is approximated using a neural network: $V = W^T \phi(e) + \varepsilon(e)$ with W is the weight matrix, $\phi(e)$ is the activation function, $\varepsilon(e)$ is residual error. Since the ideal weights of the neural network are not determined, V is approximated as: $\hat{V}(e) = \hat{W}_1^T \phi(e)$ (Critic network).

The approximated control law with Actor network is determined:

$$\hat{\tau} = -\frac{1}{2} R^{-1} g_e^T \hat{V}_e(e) = -\frac{1}{2} R^{-1} g_e^T \partial \phi(e_{\dot{\phi}})^T / \partial e_{\dot{\phi}}(e) \hat{W}_2, \tag{13}$$

in which, the actor network approximates the neuron network W_1. To guarantee that the weight matrix converges to the optimal value, the tuning laws are:

$$\dot{\hat{W}}_1 = -\alpha_1 \frac{\hat{\sigma}}{\left(1 + \hat{\sigma}^T \hat{\sigma}\right)^2} \left(\hat{\sigma}^T \hat{W}_1 + Q\left(e_{\dot{\phi}}\right) + \tau_r^T R \tau_r\right) \tag{14}$$

$$\dot{\hat{W}}_{12} = -\frac{\alpha_2}{2} \left(\overline{D}_1\left(\hat{W}_2 - \hat{W}_1\right) - \frac{1}{2}\overline{D}_1 \hat{W}_2 \frac{\hat{\sigma}^T}{\left(1 + \hat{\sigma}^T \hat{\sigma}\right)^2} \hat{W}_1\right) \tag{15}$$

where $\hat{\sigma} = \phi_e(f_e + g_e\hat{\tau})$, $\overline{D}_1 = \phi_e g_e R^{-1} g_e^T \phi_e^T$, $\alpha_1, \alpha_2 > 0$.

Because $d_e \neq [00]^T$ and unknown then, d_e is estimated by $\hat{d}$ in Eq. (9) with: $z \in \mathbb{R}^2$ is the state vector, $l = diag([l_4, l_5])$ is the adaptive function, $k = diag([k_4, k_5])$ and $\gamma = diag\left(\left[\gamma_4, \gamma_5\right]\right)$ are two matrices with $k_i, \gamma_i > 0$, $i = 4, 5$.

Finally, the control signal with disturbance d_e is computed as follows:

$$\tau = \hat{\tau} - g_e^{-1}\hat{d}_e. \tag{16}$$

4 Numerical Simulation and Results

The parameters of the wheeled mobile robot: $r = 0.15$ (m), $d = 0.2$ (m), $b = 0.3$ (m), $m_c = 10$ (kg), $m_w = 0.5$ (kg), $I_c = 4$(kg.m^2), $I_w = 0.1$ (kg.m^2), $I_m = 0.05$ (kg.m^2), $\dot{\mu} = 0.5$ (m/s), $\dot{\zeta}_r = 3sin(0.5t)$ (m/s), $\dot{\zeta}_l = 3cos(0.5t)$ (m/s), $\tau_d = [2 + sin(t), 1 + cos(t)]$ (N.m), $q_0 = \left[1,\ 1,\ \frac{\pi}{4}\right]^T$, $\dot{\phi}_0 = [0,\ 0]^T$, the limit of the input torque: $-300 \le \tau \le 300$(N.m).

The parameter of controller and observer: $\beta_1 = 2$, $\beta_2 = 1.5$, $k_1 = k_2 = k_3 = k_4 = k_5 =$

1, $\gamma_1 = 30$, $\gamma_2 = 25$, $\gamma_3 = 10$, $\gamma_4 = 40$, $\gamma_5 = 80$, $R = 0.5\begin{bmatrix} 1 & 0 \\ 0 & 1 \end{bmatrix}$, $Q = \begin{bmatrix} 1 & 0 \\ 0 & 1 \end{bmatrix}$, $\alpha_1 = \alpha_2 = 0.05$, $\hat{W}_{10} = [0.6,\ 0.2,\ 0.8]^T$, $\hat{W}_{20} = [1,\ 1,\ 1]^T$, $\phi(e) = \left[e_{\dot{\phi}}^2(1),\ e_{\dot{\phi}}(1)e_{\dot{\phi}}(2),\ e_{\dot{\phi}}^2(2)\right]^T$.

To evaluate the control performance, the system is simulated with three predefined trajectories: a horizontal eight-shaped trajectory and a circular trajectory. To evaluate the proposed controller, we compare it with the sliding mode controller (SMC). The evaluation of the control quality is based on the following formula: $E = \int_0^{t_0} e_q dt$ (trajectory error) and $U = \int_0^{t_0} \tau dt$ (Energy consumption).

Case 1. Horizontal eight-shaped trajectory: $q_d = \left[\ \frac{9\cos t/3}{1+(\sin t/3)^2}\ \ \frac{12\sin t/3\cos t/3}{1+(\sin t/3)^2}\ \right]^T$.

Case 2. Circle trajectory: $q_d = \left[\ 5\sin t\ \ -5\cos t\ \right]^T$.

Case 3. Straight-line trajectory: $q_d = \left[\ t\ \ t + 5\ \right]^T$ (Fig. 4).

The detailed comparison results are presented in Fig. 2, Fig. 3, Fig. 4, and Table 1, indicating that the control system based on the synchronous online adaptive algorithm enables the mobile robot to track the trajectory much faster than the sliding mode controller and consumes less energy.

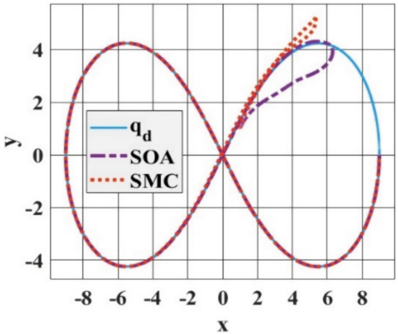

Fig. 2. Horizontal eight-shaped trajectory

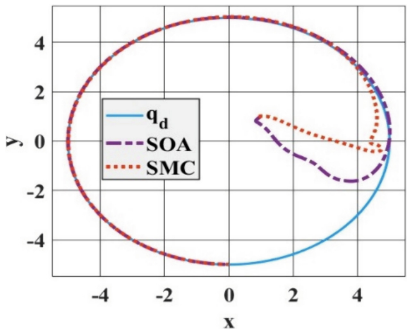

Fig. 3. Circular trajectory

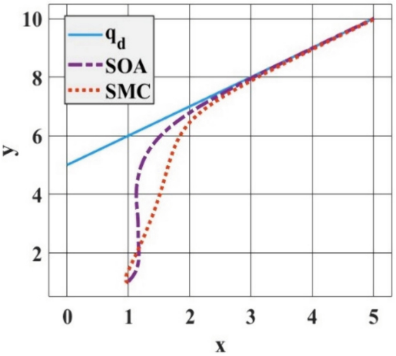

Fig. 4. Straight-line trajectory

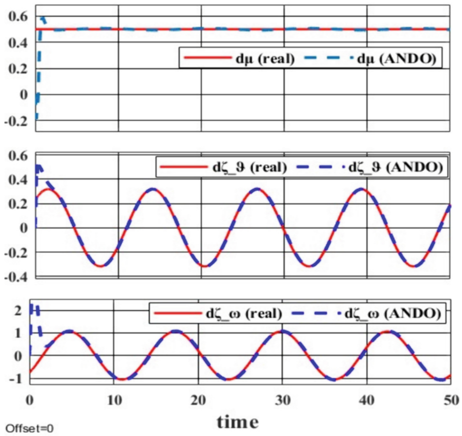

Fig. 5. Estimation of d_q

Table 1. The evaluation of the tracking error E with $t_0 = 1000$ s.

Controller	Case 1		Case 2		Case 3	
$t_0 = 1000$	E	U	E	U	E	U
AC-2NN	16.54	4965	19.19	5996	9.328	4276
SMC	32.98	5073	38.83	6381	16.94	4319

5 Conclusions and Future Works

With the proposed control structure, the stability is ensured and the desired trajectory is achieved in a short period. Especially, the two neural networks structure reduces computational load and the number of weights compared to the Actor-Critic structure with three neural networks. In addition, it outperformed the sliding mode controller. With its strong adaptability, the proposed controller holds great promise for future development and application to various objects.

Acknowledgements. This work was supported by the Ministry of Education and Training (MOET) under the Grant B2022-BKA-01.

References

1. Danwei, W., Chang, B.L.: Modeling and analysis of skidding and slipping in wheeled mobile robots control design perspective. IEEE Trans. Robotics **24**(3), 676–687 (2008)
2. Rached, D., Ahmad, A.H.: Dynamic modelling of differential-drive mobile robots using Lagrange and Newton-Euler methodologies: a unified framework. Adv. Robot. Autom. **2**(2) (2013)
3. Cui, M., Huang, R., Liu, H.: Adaptive tracking control of wheeled mobile robots with unknown longitudinal and lateral slipping parameters. Nonlinear Dyn. **78**, 1811–1826 (2014)
4. Yoo, S.J.: Adaptive tracking control for a class of wheeled mobile robots with unknown skidding and slipping. Control Theory Appl. **4**(10), 2019–2119 (2010)
5. Hyo-Seok, K., Yong-Tae, K., Chang-Ho, H., Mignon, P.: Generalized extended state observer approach to robust tracking control for wheeled mobile robot with skidding and slipping. Int. J. Adv. Robot. Syst. **10**(3), 155 (2013)
6. Mou, C.: Disturbance attenuation tracking control for wheeled mobile robots with skidding and slipping. IEEE Trans. Industr. Electron. **64**(4), 3359–3368 (2016)
7. Ngoc-Bach, H., Hee-Jun, K.: Neural network-based adaptive tracking control of mobile robots in the presence of wheel slip and external disturbance force. Neurocomputing **188**, 12–22 (2015)
8. Nguyen, T., Hoang, T., Pham, M.T., Dao, P.N.: A Gaussian wavelet network-based robust adaptive tracking controller for a wheeled mobile robot with unknown wheel slips. Int. J. Control. **92**(11), 2681–2692 (2019)
9. Shu, L., Liang, D., Haibo, G., Chao, C., Zhen, L., Zongquan, D.: Adaptive neural network tracking control-based reinforcement learning for wheeled mobile robots with skidding and slipping. Neurocomputing **238**, 20–30 (2018)
10. Vamvoudakis, G., Lewis, F.L.: Online actor critic algorithm to solve the continuous-time infinite horizon optimal control problem. Automatica **46**(5), 878–888 (2009)
11. Lewis, F.L., Derong, L.: Reinforcement Learning and Approximate Dynamic Programming for Feedback Control. Wiley-IEEE Press (2012)
12. Zongyi, G., Guo, J., Xinming, W., Jing, C., He, H.: Sliding mode control for systems subjected to unmatched disturbances/unknown control direction and its application. Int. J. Robust and Nonlinear Control **31**(4), 1303–1323 (2021)
13. Nguyen, P.D., Nguyen, N.H.: A simple approach to estimate unmatched disturbances for nonlinear non-autonomous systems. Int. J. Robust Nonlinear Control **32**(17), 9160–9173 (2022)
14. Nguyen, P.D., Nguyen, N.H.: Adaptive control for nonlinear non-autonomous systems with unknown input disturbance. Int. J. Control. **95**(12), 3416–3426 (2022)

Using WASPAS Method for Scissors Mechanism Selection

Trieu Quy Huy[1], Dinh Van Thanh[2], Tran Minh Tan[3], Tran Huu Danh[4], Nguyen Thi Thanh Nga[5], and Nguyen Ngoc Thieu[5](✉)

[1] University of Economics - Technology for Industries, Hanoi, Vietnam
[2] East Asia University of Technology, Hanoi, Vietnam
[3] Nguyen Tat Thanh University, Ho Chi Minh City, Vietnam
[4] Vinh Long University of Technology Education, Vinh Long, Vietnam
[5] Thai Nguyen University of Technology, Thai Nguyen, Vietnam
ngthieu@tnut.edu.vn

Abstract. Commonly seen in industrial and production equipment is a lift table which is used a scissors mechanism to kick objects. Numerous structures (or schematics) have been presented in the scissors mechanism. Each structure will generate a unique set of results while having the same initial variables. Consequently, selecting the right system is crucial when developing an ideal lift device. This study employed the multi-criteria decision making (MCDM) method for selecting the optimal layout of the machine that would simultaneously satisfy the goals of the minimal lifting time and the highest lifting force. Also, the weighted aggregates sum product assessment (WASPAS) technique has been applied for conducting the MCDM task for nine lift table schema using the entropy manner to determine the criterion weights. The greatest lift device structure was finally introduced.

Keywords: Lift table · Optimization · MCDM · WASPAS · Entropy

1 Introduction

A lift table (Fig. 1) is a machine that is used to elevate and lower items using a scissors mechanism. This tool is frequently used in manufacturing plants, workshops, factories, warehouses, and storage areas, among other places. As consequence, a lot of researchers are interested in optimizing scissors mechanisms or lift tables.

Until now, many investigations on scissor lifts have been carried out. M.T. Islam et al. [1] conducted general multibody system behavior of a scissor lift system using a bond graph illustrating framework. In this work, a number of application-specific requirements, including dynamics and location precision, were assessed. Hydraulic scissor lifts were the subject of optimization the device by Arunkumar et al. [2]. The main components and elements affecting the stability of scissor lifts were studied by Ren G. Dong et al. [3]. Wei Zhang et al. [4] have studied the static stiffness of six different kinds of the mechanism of this device.

D. C. Nguyen et al. (Eds.): ICERA 2023, LNNS 944, pp. 407–414, 2024.
https://doi.org/10.1007/978-3-031-62235-9_41

A MCDM analysis was presented by Nguyen N.H. et al. [5] for finding the optimal method of building a double lift desk which simultaneously get minimal lift time and maximal lift strength. In [6], Danh T.H. et al. applied the MOORA technique to select the best design for a double lift table. The authors in [7] proposed a new scissor lift mechanism. Dang A.T. [8] presented the way for identifying specifications for double lift table in order to enhance its performance. For tiny plots in hilly terrain, Xu B. et al. [9] recently presented an autonomous twin scissor sugarcane field transporter.

Fig. 1. Lift table [10]

This study used MCDM to tackle the issue of choosing the optimal lifting table system for designing. Nine different lift table structures have been found to deal with this issue. Apart from that, the mechanism diagram was determined by taking into account the minimal lifting time and the maximal lifting force. Moreover, the Entropy technique has been applied to estimate the criterion weights and the WASPAS technique was applied for solving MCDM problem.

2 Methodology

The WASPAS approach has been applied for addressing the requirement issue by using the following stages [11]:

Step 1: Creating the initial decision-making matrix:

$$X = \begin{bmatrix} r_{11} \cdots r_{1j} \cdots r_{1n} \\ \vdots \ddots \vdots \ddots \vdots \\ r_1 \cdots r_{ij} \cdots r_{in} \\ \vdots \ddots \vdots \ddots \vdots \\ r_{m1} \cdots r_{mj} \cdots r_{mn} \end{bmatrix}_{m\times n} \quad (1)$$

where *m* and *n* are the alternative and criterion numbers.

Step 2: Establishing the decision matrix's normalized numbers:

$$\mathrm{r}_{ij}^{*} = \frac{r_{ij}}{\max\limits_{i} r_{ij}} \tag{2}$$

$$\mathrm{r}_{ij}^{*} = \frac{\min\limits_{i} r_{ij}}{r_{ij}} \tag{3}$$

Noted that (2) is used for lifting time and (3) is used for lifting weight.

Step 3: Obtaining the additive significance of each solution in weighted normalized data:

$$A_i = \sum_{j=1}^{n} \mathrm{r}_{ij}^{*} \cdot w_j \tag{4}$$

wherein w_j is the weight of criterion j; i = 1 ÷ m.

Step 4: In the weighted, normalized data, determining the multiplicative relative relevance of each option:

$$\mathrm{M}_i = \prod_{j=1}^{n} \left(\mathrm{r}_{ij}^{*}\right)^{w_j} \tag{5}$$

Step 5: Identifying the combined generalizad criterion Q_i through:

$$\mathrm{Q}_i = \lambda \cdot A_i + (1 - \lambda) \cdot \mathrm{M}_i \tag{6}$$

Step 6: The alternatives are ranked from highest to lowest, with the highest number getting the highest position.

2.1 Way of Finding Criterion Weights

For getting criterion weights, the Entropy approach has been implemented in this study using the following stages [12]:

Step 1: Computing the normalized values of the indicator through:

$$p_{\mathrm{ij}} = \frac{x_{\mathrm{ij}}}{m + \sum_{i=1}^{m} x_{\mathrm{ij}}^{2}} \tag{7}$$

Step 2: Identifying the Entropy for every indicator through:

$$me_j = -\sum_{i=1}^{m}\left[p_{ij} \times ln\left(p_{ij}\right)\right] - \left(1 - \sum_{i=1}^{m} p_{ij}\right) \times ln\left(1 - \sum_{i=1}^{m} p_{ij}\right) \tag{8}$$

Step 3: Determining each indicator's weight:

$$w_j = \frac{1 - me_j}{\sum_{j=1}^{m}\left(1 - me_j\right)} \tag{9}$$

2.2 Method for Determination of Schema of Scissors Mechanism

The alternatives for raising table schema are actually quite varied. In this study, nine different scissors mechanism schemas (Fig. 2) were investigated. Each structure will produce numerous outcomes (lifting time and lifting force). Finding a scissors mechanism diagram with the same input variables is difficult since it is important for the constructed lifting table to have the quickest lifting time and most powerful lifting force. The major sizes of the lift device, the highest lift height possible, the force F_p, and the speed V_p of piston are the input parameters for this scenario.

The following is a description of the calculating process used to determine the optimum alternative of the lift mechanism: Calculate the output factors for each of the nine possibilities on the lift table. Then, employ the WASPAS approach to identify the optimal solution, that is, the one that satisfies the minimal lifting time and maximal lifting force requirements.

3 Determining the Output Responses of Scissors Mechanism

Figure 3.a depicts solution 2 of the scissors mechanism (as shown in Fig. 2.2). Where, $F_p = 2000$ (N) is the piston's force; $V_p = 10$ (mm/s) is the piston's velocity; $h_m = 866$ (mm) is the maximum lifting height are the input information. W_m (N) (maximum lifting force) and t_l (s) (lift time) are the output results.

From Figs. 3.a and 3.b, the force calculation can be shown by:

$$F_A = F_B = F_C = F_D = W/2 \tag{10}$$

It can be seen from Fig. 3.d that $F_{Gx} = 0$; $F_{Gy} = 0$. Also, from Fig. 3.c: $\sum M_A = 0$. As a result, we have:

$$\sum M_A = -F_C \cdot L_x + F_{Gx} \cdot cos\beta \cdot \frac{L_y}{2} + F_{Gx} \cdot sin\beta \cdot \frac{L_x}{2} = 0 \tag{11}$$

With $L_x = L \cdot cos\alpha$, $L_y = L \cdot sin\alpha$ and $F_C = L_x \cdot W/2$.
From (18) it can be written that:

$$W = F_P \cdot sin(\alpha + \beta)/cos\alpha \tag{12}$$

Setting $L_{AE} = a$, $L_{AF} = b$, $L_{EF} = \mathrm{c}$.
From ΔAFE:

$$c^2 = a^2 + b^2 - 2 \cdot a \cdot b \cdot cos\alpha \tag{13}$$

And:

$$\mathrm{c} = \sqrt{\mathrm{a}^2 + \mathrm{b}^2 - 2 \cdot \mathrm{a} \cdot \mathrm{b} \cdot \cos\alpha} \tag{14}$$

We get:

$$\mathrm{H} = \mathrm{c}_{\alpha\max} - \mathrm{c}_{\alpha\min} \tag{15}$$

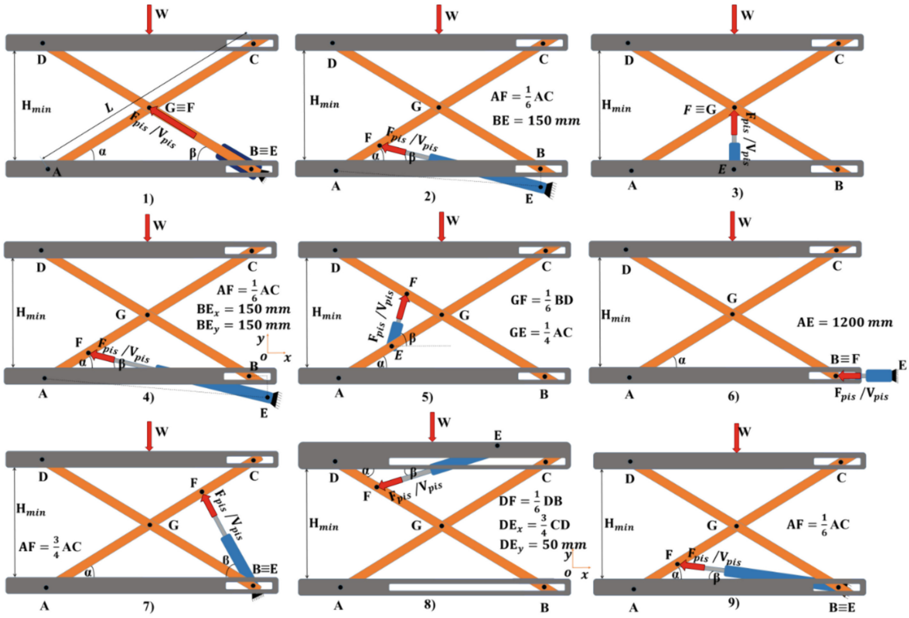

Fig. 2. Different schemas for lift table design

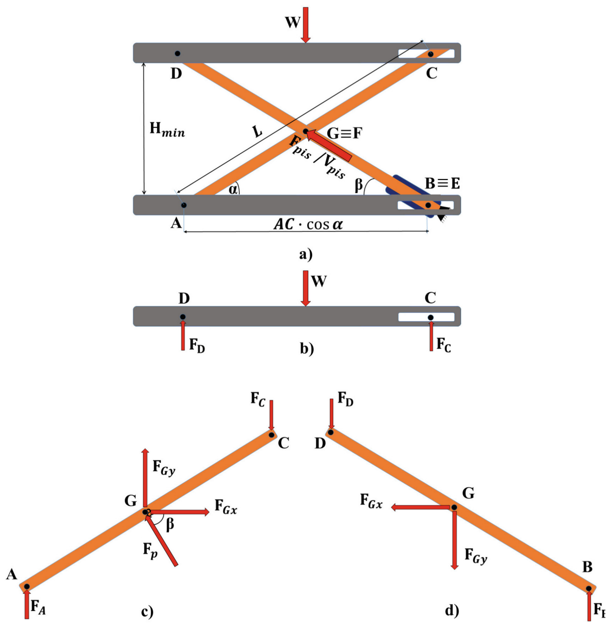

Fig. 3. Calculated schema

From ΔAFE it can be found that:

$$b^2 = a^2 + c^2 - 2 \cdot a \cdot c \cdot \cos\beta \tag{16}$$

From (22):

$$\beta = \arccos\left(\frac{a^2 + c^2 - b^2}{2 \cdot a \cdot c}\right) \tag{17}$$

The piston stroke, indicated as H, is calculated by:

$$H = c_{max} - c_{min} \tag{18}$$

In which c_{max} and c_{min} represent the maximum and minimum piston locations, correspondingly. They are calculated using Eq. (20).

The time of lifting t_l is found by:

$$t_l = H/V_P \tag{19}$$

The determination of the output results in the rest of the structures in Fig. 2 is comparable to the aforementioned. The output of ten schemas generated from initial data can be displayed on Table 1.

Table 1. Output responses of various solution of scissors mechanism

Solution	t_l (s)	W_m (N)
1	36.27	348.62
2	45.55	2000.00
3	27.26	320.62
4	64.13	1015.47
5	9.39	69.98
6	11.28	186.82
7	10.90	167.88
8	49.62	174.98
9	10.70	770.07

4 Selecting the Ideal Scissors Mechanism Schema

4.1 Calculating the Criteria's Weights

The entropy approach is applied for getting criterion weights (for more information, see Sect. 2.2): Using Eq. (7), the normalized values p_{ij} are produced. Equation (8) was used to obtain each indicator's Entropy value me_j. The criteria's w_j weight is then determined using Eq. (9). The weights of t_l and W_m have been found as 0.5249 and 0.4751, respectively.

4.2 Identifying Ideal Scissors Mechanism Schema

In the following activities (see Sect. 2.1), the WASPAS technique was employed in this study to address the MCDM problem: Through Eqs. (2) and (3) for lifting time and lifting weight, respectively, determine the normalized values of the decision matrix r_{ij}*. After that, using Eq. (4), compute the additive value of each solution in the weighted normalized data. Next, using Eq. (5), decide which variables in the weighted, normalized data have a multiplicative relative relevance. Following that, the joint generalized criterion Q_i is derived using formula (6). Lastly, arrange Q_i in order of descending to rank the alternatives. Table 2 indicates a number results from calculations in addition to the alternative's ranking. Figure 4 also depicts the relationship among solutions and Q_i.

Table 2. Numerous computed outcomes and a solution rating

Trial	r_{ij}^*		A_i	M_i	Q_i	Rank
	t_l	W_m				
1	0.2589	0.1743	0.2187	0.0113	0.1150	8
2	0.2062	1.0000	0.5833	0.0514	0.3174	2
3	0.3445	0.1603	0.2570	0.0138	0.1354	7
4	0.1464	0.5077	0.3181	0.0185	0.1683	6
5	1.0000	0.0350	0.5416	0.0087	0.2751	3
6	0.8323	0.0934	0.4813	0.0194	0.2503	5
7	0.8617	0.0839	0.4922	0.0180	0.2551	4
8	0.1893	0.0875	0.1409	0.0041	0.0725	9
9	**0.8778**	**0.3850**	**0.6437**	**0.0843**	**0.3640**	**1**

The best choice in Table 3 was discovered to be Option 9 (also in Fig. 4) as it has the maximal value of Q_i ($Q_i = 0.364$). Hence, the ideal schema for scissors mechanism is solution 9.

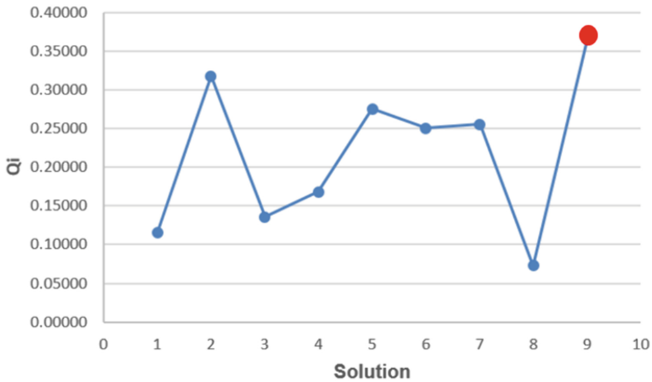

Fig. 4. Relation between solution and Q_i

5 Conclusions

The findings of a research to identify the best scissors mechanism schema for lift tables in order to simultaneously acquire the greatest lift force and the shortest lift time have been introduced in this article. In this work, the Entropy technique has been applied to estimate the weight of the criterion and the WASPAS task has been implemented for solving the MCDM task. The following recommendations are prompted by the investigation's findings:

- For this initial instance, an MCDM work was tackled with the help of the WASPAS approach, and the objective was to determine the optimal lift device schema in order to concurrently satisfy two conflicting demands: minimal lifting time and maximal lifting force.
- Alternative 9 has the highest Qi value (0.364), making it the best scissors mechanism structure.
- The best scissors mechanism structure (solution 9) has resulted in 10.7 (s) of lifting time and in 770.07 (N) of lifting force.

Acknowledgment. This article has been funded by Thai Nguyen University of Technology.

References

1. Islam, M.T., et al.: Dynamic analysis of scissor lift mechanism through bond graph modeling. In: 2014 IEEE/ASME International Conference on Advanced Intelligent Mechatronics. IEEE (2014)
2. Arunkumar, G., Kartheeshwaran, R., Siva, J.: Investigation on design, analysis and topological optimization of hydraulic scissor lift. J. Phys. Conf. Ser. (2021)
3. Dong, R.G., et al.: An investigation on the dynamic stability of scissor lift. Open J. Saf. Sci. Technol. **2**(01), 8 (2012)
4. Zhang, W., et al.: A study on the static stability of scissor lift. Open Mech. Eng. J. **9**(1) (2015)
5. Linh, N.H., et al.: Application of MCDM method in selection of schema for optimal design of double scissor lift tables. In: Nguyen, D.C., Vu, N.P., Long, B.T., Puta, H., Sattler, K.U. (eds.) Advances in Engineering Research and Application. ICERA 2022. LNNS, vol. 602, pp. 244–253. Springer, Cham (2023). https://doi.org/10.1007/978-3-031-22200-9_26
6. Danh, T.H., et al.: Application of MOORA and MEREC methods to select the best schema of scissors mechanisms. J. Military Sci. Technol. **2022**(FEE), 177–184 (2022)
7. Stawinski, L., et al.: A new approach for control the velocity of the hydrostatic system for scissor lift with fixed displacement pump. Arch. Civil Mech. Eng. **19**, 1104–1115 (2019)
8. Dang, A.-T., Nguyen, D.-V., Nguyen, D.-N.: Applying parametric analysis in enhancing performance for double-layer scissor lifts. Strojniški vestnik-J. Mech. Eng. **69**(7–8), 299–307 (2023)
9. Xu, B., et al.: Design and Experiment of Double Scissor Sugarcane Field Transporter, pp. 1–10. Sugar Tech. (2023)
10. ULINE, Electric Lift Table. https://www.uline.com/Product/Detail/H-3935/Lift-Tables/Electric-Lift-Table-2000-lb-48-x-36. Accessed 20 May 2022
11. Alinezhad, A.: New Methods and Applications in Multiple Attribute Decision Making (MADM). Springer, Cham (2019). https://doi.org/10.1007/978-3-030-15009-9
12. Hieu, T.T., Thao, N.X., Thuy, L.: Application of MOORA and COPRAS models to select materials for mushroom cultivation. Vietnam J. Agric. Sci. **17**(4), 322–331 (2019)

Signal Communication Solution in Controlling Building Electrical Equipments Applying BMS Technology

Trung Dang Ngoc(✉) and Duc Ngo Minh

Thai Nguyen University of Technology, Thai Nguyen, Vietnam
trungcsktd@tnut.edu.vn

Abstract. This paper introduces an overview of the building management system (BMS) over the internet, thereby proposing a control and communication framework for electrical equipment in the building. To be more detailed, the main communication protocol is designed based on different techniques such as Modbus RS-485, CC-Link, and the Internet. The central controller is built up from the PLC (Programmable Logic Controller) to ensure stability, high accuracy, and the ability to expand flexible peripheral modules. In addition, the combination of open source software such as Visual Studio, AT Driver Server, Itag Builder, etc. is applied to establish the intuitive monitoring interface, allowing one to operate and observe the status of the equipment. The real-time data of the electrical equipment in the building as well as the environmental parameters are collected from the sensors. Through an illustrative experimental model, the problem of operating electrical equipment in a hotel with a monitoring interface can be solved through real-time data access such as report output, incident warning, and management. The experimental results have proved the accuracy and practical applicability of the control and monitoring structure of the building or hotel proposed in this paper.

Keywords: Wireless Remote Control · Building Management System · Smart Building

1 Introduction

Nowadays, urbanization is developing rapidly in countries, and one of the important highlights is the appearance of countless buildings, hotels, etc., adorning the overall picture of urban life. Most of the buildings and hotels are equipped with modern equipment and complex service systems but are still operating independently. Therefore, it is necessary to research an integrated solution to monitor, operate, and manage the building comprehensively. The BMS system has been born and is becoming useful not only for the management and operation of buildings and hotels but also as a criterion for evaluating and checking the quality of those buildings and hotels [1–5]. Currently on the market, there are many companies that have been offering different versions of BMS systems, such as Siemens, Honeywell, Johnson Controls, Delta Control, PSA, DalyTech, etc. Figure 1 depicted the illustration of the building management system.

D. C. Nguyen et al. (Eds.): ICERA 2023, LNNS 944, pp. 415–425, 2024.
https://doi.org/10.1007/978-3-031-62235-9_42

Fig. 1. Illustrated image of building management systems – BMS.

The BMS system as the same Fig. 1 is a synchronous system that allows for the control and management of all technical systems in the building or hotel, such as lighting, electricity systems, domestic water supply systems, air conditioning, ventilation, environmental warning, alarm systems, security alarms, fire alarms, etc. The BMS system ensures the correct and efficient operation of electrical equipment in buildings and hotels while saving energy and operating costs through the local network or Internet/Ethernet. A BMS system is a synchronous, real-time, online multimedia system with a central processing system including software and hardware, input and output equipment, sensors, a controller, and the dot matrix control method [2, 5–7].

The concept of building management system - BMS is no longer strange, it was born in 1970. Up to now, there have been many research works and application of modern techniques for BMS such as: In the study [1], the author focused on designing a multi-agent building management system, that is, breaking down the building management system into processing subsystems at different levels, thereby optimizing data that is processed at the central controller via wifi. The authors in [2] have introduced the architecture and communication protocols in building management today such as: BACnet, KNX, Dali, Bluetooth, Zigbee, Z-Wave… Besides, the content of the paper focuses on to compare and predict the applicability between protocols in the near future. In [3, 8–13] the author proposes techniques for wireless sensor systems, multi-point sensors based on the internet to coordinate clean energy sources, helping to save energy and operating costs in buildings. Research [4] analyzes technical trends and challenges for future smart building technology. The authors in [6] provide an overview of the research on building energy management. The topic approaches building energy management from aspects of data science, computing, communications, control, optimization, and system storage. The content of the paper [7] proposes a solution to combine forecasting algorithms and an artificial intelligence platform to improve the control quality of control engineering systems and detect operating errors of the building. In [10, 14] the authors focus on building management system architecture for large building automation systems and optimal solutions for operating buildings with many interdependent equipments. The research [15] presents the technique of building a mobile wireless network with the ability to overcome obstacles and good transmission quality for communication in buildings. The author in [16] focuses on communication protocols to ensure data security in building management.

Thus, it can be seen that studying the direction of renovation as well as proposing new solutions to build control methods, monitoring, and management of buildings, hotels, etc. is an inevitable direction in order to provide applications. Used in the operation and management of buildings and hotels in an open direction, increasing efficiency during operation.

In particular, the construction of control and monitoring structures as well as data communication solutions for most of the technological problems of buildings, hotels, commercial and service centers, etc. are always open problems and can have many different solutions to implement. By combining the communication solution, the central controller and sensors such as temperature sensors, humidity sensors, smoke sensors, level sensors, etc. will bring automatic and intelligent technologies to operate the various functions of a building or hotel. The proposed control and communication structure is considered the key issue for each project.

Therefore, the paper focuses on proposing new solutions for control, monitoring, and signal communication in buildings, hotels, etc. according to BMS technology. In particular, the system uses a combination of several communication protocols, such as Internet/Ethernet, Modbus RS485, CC-Link, etc. Monitoring interfaces are designed on Visual Studio software, Itag Builder, AT driver servers, etc., and the central controller of choice is the PLC. The new point that the article shows is that it has coordinated the internet communication protocol with protocols such as: Modbus RS485, CC-Link, allowing control and monitoring of the building in a multi-point master-slave manner with unlimited distance. At the same time, combined with the use of PLC and expansion modules, it allows to expand the scale of system control accurately in real time.

2 The Structure of Management and Operation for BMS

The BMS has the management and operation structure of a distributed control system. The system is divided into four basic levels, as shown in Fig. 2.

- Actuator Level: Including input systems such as sensor systems, cameras, magnetic card switches, etc. Output systems include actuators such as ventilation fans, air conditioners, lights, sirens, pumps, etc. This level has the function of measuring, driving, and converting signals.
- Control Level: Including DDC, PLC, PAC controllers, etc. The control level is responsible for receiving information from sensors, processing it according to certain algorithms, and then sending control signals to the executing equipment.
- Control and monitoring Level: This level has the function of monitoring and operating the technical process, assisting users in installing applications, and monitoring the operation process to solve unexpected problems. The supervisory control does not require too much equipment and is easy to operate via ordinary computers.
- Management Level: This is the highest level of all levels and is the department that monitors, supervises, operates, and makes strategic decisions for the system. The main function of the management level is to collect, store, and process data such as statistics

of energy usage data, operating costs, history of warnings and arising incidents, etc. After that, the system generates reports for the management and exploitation of the technical infrastructure system in an efficient and sustainable manner.

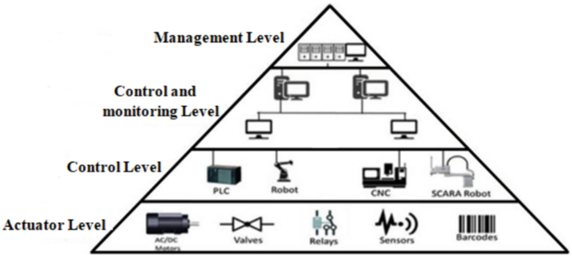

Fig. 2. Basic structure of Building Management System

3 The Basic Structure of Signal Communication in Building Management Systems

Currently, there is no universal set of rules on component or functional standards for signal communication solutions in BMS. That is, each building has its own unique technological solution. Most BMS systems will change themselves over the life of the building, adding or removing input and output units at different levels as needed. Being able to do this without changing the main infrastructure of the BMS is a prerequisite for a sustainable BMS. Using communication protocols and communication equipment that is able to adapt and scale the system is perhaps the most important factor to consider in this problem.

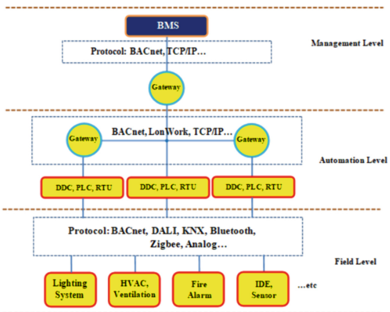

Fig. 3. Illustrated the basic communication structure in Building Management Systems

By coordinating international standard communication protocols for buildings, hotels will bring unique advantages and features to that communication solution [2, 4, 5, 16–19]. In addition, with this approach, building management systems can flexibly coordinate control equipment, measuring equipment, and actuators of different brands that have the same communication protocol. Therefore, this will be a trend for researchers to deploy their communication solutions for this BMS. Figure 3 illustrates the basic and common communication structure of an actual BMS.

4 Proposing Supervisory Control Structure and Signal Communication in BMSs

Actually searching for solutions for operation and management systems in buildings, hotels, etc. as follows the brands on the market today, combined with the study of some solutions to build the building management system in scientific research around the world Realizing that the equipment of the manufacturers is integrated as an exclusive module of each company, it is difficult to combine the equipment of the manufacturers together. Therefore, the system is not open for users and operations during the process of replacing, renovating, and expanding the system.

From those obstacles, the paper focuses on proposing control structures and monitoring electrical equipment in buildings, hotels, etc. using an Ethernet or Internet network. In which there is a combination of Modbus RS485 or CC-Link communication protocols for electrical equipment in buildings, hotels, etc. and PLC applications as the central control unit for the system. The advantage of this structure is that it allows the system to scale up and flexibly coordinate the equipment of other manufacturers with the same communication protocol. The following content will propose two structures to control and monitor electrical equipment in buildings and hotels, as follows:

4.1 Control and Monitoring Structure Using Mitsubishi FX Series PLCs Combined with Modbus RS485 Communication

In the Modbus RS485 communication network between Mitsubishi FX series PLCs, it is possible to connect up to 32 PLC Slave stations to one PLC Master station. The control structure for monitoring electrical equipment via Modbus RS485 communication between PLC stations is illustrated in Fig. 4. In which Master stations (of each building or hotel) are PLCs (FX series) acting as the central controller, other Slave stations are also PLCs (FX series) acting as receiving points. Collect signals from sensors as well as process signals at the field level, such as light sensors, temperature sensors, smoke sensors, control lighting equipment, water pump systems, ventilation fans, etc., of rooms, floors, buildings, and hotels via the Modbus communication network.

In Fig. 4, Slave stations collect and process signals from sensors and electrical equipment. These signals are then sent to the Master station. Here, through the setting algorithms, the signals are processed to issue control commands down to the Slave stations. Simultaneously, data from Master stations through the USR-TCP-N520 module converts signals from RS422/RS485 to Ethernet and then transmits the signal to the Web Server via LAN to display and monitor the status of electrical equipment, environmental parameters, etc. on the computer located in the technical area of the building or hotel via the Internet or Ethernet. In addition, the monitoring interface programmed by open source software such as Itag Builder, AT Driver Server, Visual Studio, etc. allows the operator to observe and intuitively control the equipment in those buildings, hotels, etc.

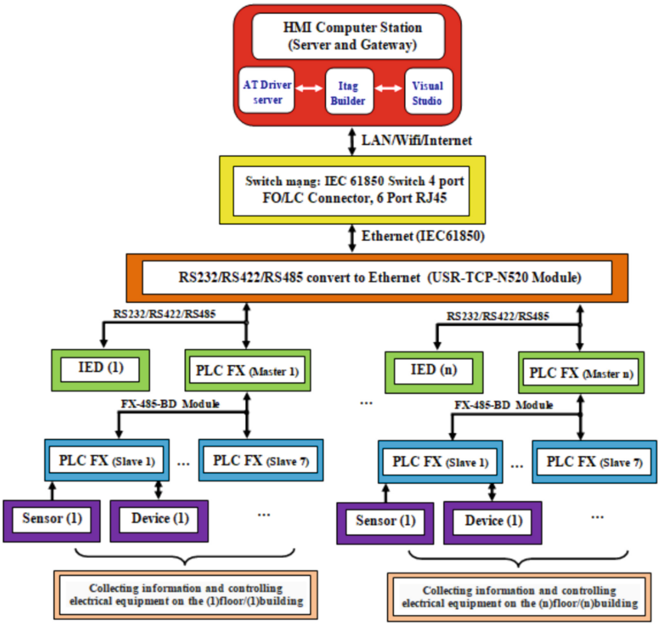

Fig. 4. Control and monitoring structure of electrical equipment according to BMS technology using Mitsubishi PLC FX series and Modbus RS485 communication

Attention: With the control and monitoring structure as shown in Fig. 4. The Modbus RS485 communication module between Slave stations and Master stations is the FX-485-BD (or FX-485-ADP) module, so each Master station (Central controller) can control up to seven Slave stations, and the distance from the master station to Slave stations is from 50m to 500 m.

4.2 Control and Monitoring Structure Using Mitsubishi Q Series PLCs Combined with CC-Link Communication

The structure for controlling and monitoring electrical equipment via CC-Link communication is illustrated in Fig. 5. In which the Master station is a Mitsubishi PLC (Q-series) acting as the central controller, other Slave stations include: PLC (Q-series); I/O Remote (AJ65SBTB1-32DT); Analog Remote (AJ65BT-64AD)… Plays the role of collecting points for signals from sensors and processing signals at field level, such as light sensors, temperature sensors, smoke sensors, projection equipment, control lighting, water pumping systems, ventilation fans, etc., of rooms, floors, buildings, and hotels through the CC-Link communication network.

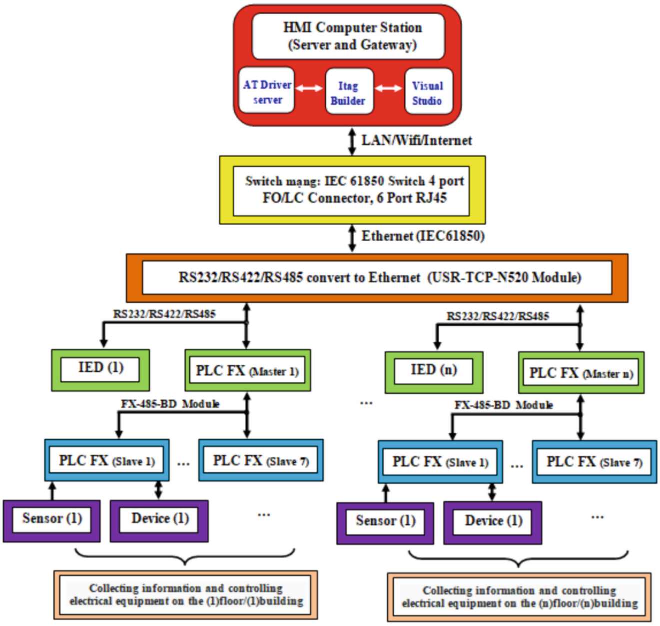

Fig. 5. Control and monitoring structure of electrical equipment according to BMS technology using Mitsubishi PLC Q series and CC-Link communication

According to the structure in Fig. 5, to ensure the connection between stations continuously in a CC-Link communication network, the stations must have the same baud rate and be configured in the correct order of stations (according to the physical connection diagram). Through GX-Works2 software. After the Slave stations collect and process the signal at the field level, the data will be sent to the Master station. Then, the data is processed by the Master station, which sends a control signal to the Slave stations. At the same time, the data from the Master is also sent to the web server to be displayed on the monitoring interface of the computers, like the structure in Fig. 4.

Attention: With the control and monitoring structure as shown in Fig. 5. Using the CC-Link communication module between Slave stations and Master stations (QJ61BT11N module), each Master station (Central controller) can control up to 64 Slave stations, and the total distance between master and slave stations can be up to 1200 m.

5 Experimental Models and Discussion

To evaluate the applicability of the structures presented in Figs. 4 and 5, the real models in Figs. 6 and 7 are designed to illustrate the problem of controlling and monitoring electrical equipment in buildings and hotels, applying the structure of Figs. 4 and 5 as follows:

The 1st Problem: Build a control model for electrical equipment in a hotel consisting of 2 floors with corresponding rooms: 1st floor (P101, P102, P103, P104); 2nd floor

(P201, P202, P203, P204). To supply power to a floor or room, it can be done through a monitoring interface located at the reception of that hotel. The communication of control data in the hotel is coordinated between Modbus RS485 communication and the Internet. The model can perform some functions in real time, as illustrated as follows:

+ Security, decentralization of management.
+ Control and monitor hotel lighting system.
+ Control and monitor automatic water pumping system.
+ Control and monitor the corridor ventilation fan system.
+ Monitor hotel fire alarm system.
+ Update and automatically calculate the time guests enter and leave the hotel room.
+ Export real-time data reports

The main equipment serving the model includes:

+ 02 PLCs Mitsubishi FX1S
+ 02 Modbus RS485 communication modules (FX1S-485-BD)
+ 01 module to convert RS422/RS485 signals to Ethernet (USR-TCP-N520)
+ 01 network switch
+ Contactor, Relay, magnetic card switch, light, fan, water pump…

The 2nd Problem: Build a control model for electrical equipment in a building consisting of four floors. In which, with each floor, there are 4 light bulbs. To supply power to a floor, it can be done through a monitoring interface located at the reception of that building. The communication of control data in the building is coordinated between CC-Link communication and the Ethernet network. The model can perform some functions in real time, as illustrated as follows:

+ Security, decentralization of management.
+ Control and monitor building lighting system.
+ Control and monitor the corridor ventilation fan system using inverter.
+ Export real-time data reports…

The main equipment serving the model includes:

+ 02 PLCs Mitsubishi Q-CPU
+ 02 CC-Link communication modules (QJ61BT11N)
+ 01 Mitsubishi Inverter E720 and CC-Link Fr-A7NC module
+ 01 network switch
+ Contactor, Relay, magnetic card switch, light, fan, water pump…

After running two tests corresponding to the models in Figs. 6 and 7, it shows that the quality of control and monitoring is accurate and stable. The equipment in the building and the hotel is controlled through a combination of Modbus RS485 communication types with the Internet and CC-Link communication with the Ethernet network. With the control and monitoring structure shown in Fig. 4, one master station can control seven slave stations; Fig. 5 allows a master station to control up to 64 slave stations. Thus, the number of electrical equipment controlled in the buildings and hotels under these two structures can be expanded arbitrarily depending on the expansion of the input and output modules in each structure. Figure 8 and Fig. 9 show features on the monitoring interface such as: notification of room entry and exit times, fire alarm, ventilation fan system status…; Export data reports in real time… designed through open source software such as: Visual studio, Itag Builder, AT-Driver server… allowing intuitive operation of equipment in the building and convenience.

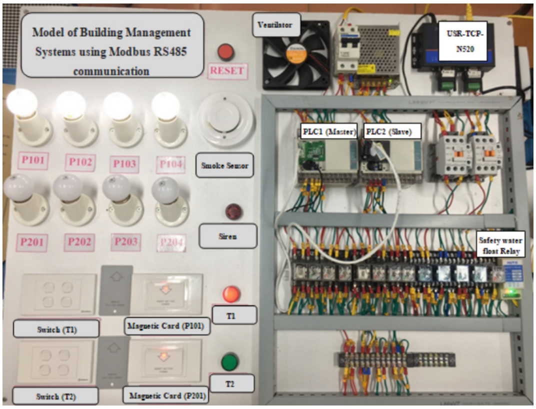

Fig. 6. Experimental model that combines Modbus RS485 and Internet communication

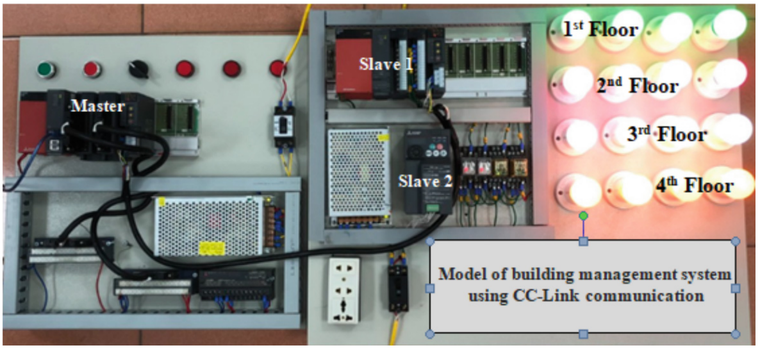

Fig. 7. Experimental model that combines CC-Link and Ethernet communication

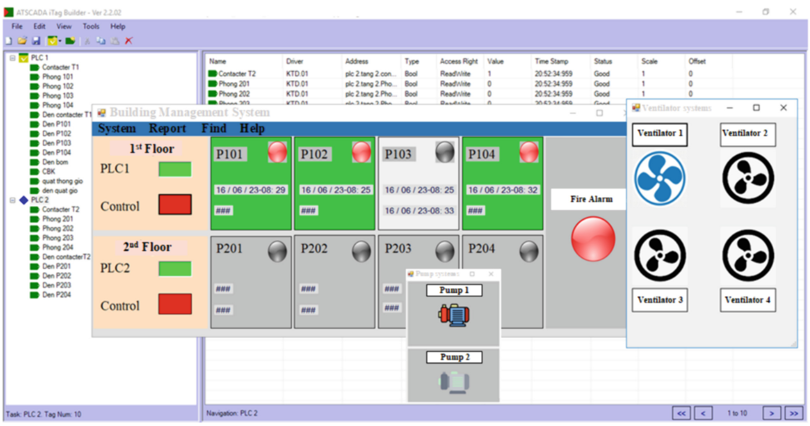

Fig. 8. Monitoring interface built on Visual studio software odder to control electrical equipments

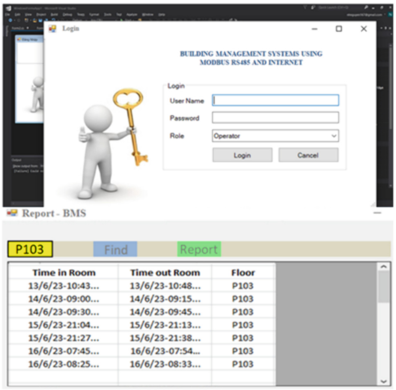

Fig. 9. Interface of Login and Report in Visual studio software

6 Conclusion

This paper introduces an overview of the application and control structure of the Building Management System (BMS). From there, a solution is proposed to build a control structure and monitor remote electrical equipment in building and hotel systems on the basis of the application of a central controller, which is a PLC. The system monitoring interface is designed for Visual Studio, Itag Builder, AT driver server software, etc. By combining communication types such as Modbus RS485, CC-Link, and Internet/Ethernet to help operate devices in the building remotely and flexibly, With the two structures proposed in the paper and the results of running experiments on the model, the accuracy and reliability of the proposed solution are shown. With the achieved results, it will open a new direction for controlling and monitoring electrical equipment in the building, putting the hotel application for building management systems into practice.

Acknowledgements. This research was supported by Research Foundation funded by Thai Nguyen University of Technology.

References

1. Priyadarshana, H.V.V., Madushanaka, W.K.I., Anuruddha, L.L.L., Chathura, G.T., Hettiarachchi, H.W.D., Hemapala, K.T.M.U.: Multi-agent controlled building management system. In: IEEE 2017 Innovations in Power and Advanced Computing Technologies (i-PACT) - Vellore (2017.4.21–2017.4.22), pp 1–5 (2017)
2. Nerland, R.: Communication Protocols in Building Management Systems, State of the Art Assessment and the Future Influence of the Internet of Things. Master's Thesis, Norwegian University of Science and Technology (2018)
3. Sutedy, V., Wang, P., Koh, L.H., Choo, F.H.: Intelligent eco-building management system. In: IEEE 2015 IEEE International Conference on CYBER Technology in Automation, Control, and Intelligent Systems (CYBER) - Shenyang (2015.6.8–2015.6.12), pp. 229–233 (2015)
4. Minoli, D., Sohraby, K., Occhiogrosso, B.: IoT considerations, requirements, and architectures for smart buildings. IEEE Internet Things J. **4**(1), 1–16 (2017)

5. Hayduk, G., Kwasnowski, P., Mikos, Z.: Building management system architecture for large building automation systems. In: IEEE 2016 17th International Carpathian Control Conference (ICCC) - High Tatras, Slovakia (2016.5.29–2016.6.1)] 2016 17th International Carpathian Control Conference (ICCC), pp. 232–235 (2016)
6. Alhashmi, S.A., et al.: Building energy management system: an overview of recent literature research. In: 2019 Advances in Science and Engineering Technology International Conferences (ASET), pp. 1–5 (2019)
7. Bogdanovs, N., Belinskis, R., Jeralovics, V., Krumins, A., Afonicevs, V., Ipatovs, A.: Intelligence system of building management system for energy efficiency in the test facility. In: IEEE 2018 Advances in Wireless and Optical Communications (RTUWO) - Riga (2018.11.15–2018.11.16) 2018 Advances in Wireless and Optical Communications (RTUWO), pp. 100–105 (2018)
8. Yoddumnern, A., Chaisricharoen, R., Yooyativong, T.: Cloud based WiFi multi-sensor network. Int. J. Online Eng. **14**(08), 35–51 (2018). https://doi.org/10.3991/ijoe.v14i08.8536
9. Dang, T.N., Le, L.T.H: An improvement of remote control panel for numerous electrical devices in smart homes using RF and Wifi. Int. J. Online Biomed. Eng. **15**(15), 127–133 (2019). https://doi.org/10.3991/ijoe.v15i15.11668
10. Li, T., Fong, S., Li, X., Lu, Z., Gandomi, A.H.: Swarm decision table and ensemble search methods in fog computing environment: case of dayahead prediction of building energy demands using IoT sensors. In: IEEE Internet Things J. **7**(3), 2321–2342 (2020)
11. Metallidou, C.K., Psannis, K.E., Egyptiadou, E.A.: Energy efficiency in smart buildings: IoT approaches. IEEE Access **8**, 63679–63699 (2020)
12. Wang, Y.: Design and implementation of a wireless sensor network node based on arduino. iJOE **13**(11), 128–135 (2017)
13. Salzmann, C., Govaerts, S., Halimi, W., Gillet, D.: The smart device specification for remote labs. Int. J. Online Biomed. Eng. **11**(4), 20–29 (2015)
14. Mauser, I., Feder, J., Müller, J., Schmeck, H.: Evolutionary optimization of smart buildings with interdependent devices. In: Applications of Evolutionary Computation. LNCS, vol. 9028, pp. 239–251. Springer, Cham (2015). https://doi.org/10.1007/978-3-319-16549-3_20
15. Li, G., Su, Y.: Intelligent building control system based on mobile wireless Internet of Things. Int. J. Online Biomed. Eng. **13**(10), 63–72 (2017)
16. Adiono, T., Tandiawan, B., Fuada, S.: Device protocol design for security on Internet of Things based smart home. Int. J. Online Biomed. Eng. **14**(07), 161–170 (2018)
17. Oddumnern, A., Chaisricharoen, R., Yooyativong, T.: Cloud based WiFi Multi-Sensor Network. Int. J. Online Biomed. Eng. 14(08), 35–51 (2018)
18. https://www.johnsoncontrols.com/building-automation-and-controls/building-management
19. https://www.siemens.com/global/en/products/buildings/automation.htmlAuthor

Singularity Analysis and Singularity Crossing Control of a Five-Bar Parallel Manipulator

Nguyen Quang Hoang[1] and Vu Duc Vuong[2](✉)

[1] Hanoi University of Science and Technology, Hanoi, Vietnam
[2] Thai Nguyen University of Technology, Thai Nguyen, Vietnam
vuducvuong@tnut.edu.vn

Abstract. This paper presents singularity analysis and singularity of type 2 crossing control of a two-degrees-of-freedom five-bar parallel manipulator. Firstly, the kinematics constraint equations of the manipulator is established, the velocity Jacobian matrix is obtained by differentiating the equation with respect to time. Based on jacobian matrices the forward and inverse singular loci are presented in the workspace. Secondly, the dynamic model of the closed loop systems is established in matrix form by applying the Lagrangian equation with multipliers. The trajectory tracking controller is designed based on the inverse dynamics and simple PD in operational space. Numerical simulations are carried out to verify the efficiencies of the proposed method.

Keywords: planar parallel manipulators · singularity · singularity crossing control · numerical simulation

1 Introduction

In the current decades, the parallel robot manipulators are found in several applications such as in medical and industrial robotics, flight and automobile simulators, mechatronic systems due to high positioning accuracy, rigidity, stiffness, fast response speed, and high force-to-weight ratio. However, a main drawback of such mechanisms is the small workspace to installation space ratio, which is further reduced by singularities occurring within the workspace [1, 2, 6].

The singularity loci of parallel robot manipulators have been extensively studied within the recent years. In some cases the singularity curves can be determined analytically and numerically [2, 18, 19]. With singularity loci shown in workspace, we can design non-singular trajectories.

In order to expand the non-singular working area, some authors have deeply studied the optimal design to choose a set of parameters such as the length of the links [13]. Some authors study the control so that the robot is able to cross through the singular configuration. The control is based on two models: the full model used when the robot is far from the singular configuration, the approximate reduced model when the robot is in the vicinity of the singular configuration [14, 15]. This method requires a switch

D. C. Nguyen et al. (Eds.): ICERA 2023, LNNS 944, pp. 426–438, 2024.
https://doi.org/10.1007/978-3-031-62235-9_43

between the two models. Moreover, the reduced model used in switching control is only approximate in order to be non-degenerating model around singularities [16].

Control based on inverse dynamics is a very basic and easy to implement. When crossing the singular configuration, the driving torques become very large and can go to infinity. Some authors have dealt with this problem by designing suitable motion law so that the driving torque is limited [17, 20, 21]. The idea of the method is to make the inertial and external forces reduced to the endpoint be perpendicular to the displacement of the endpoint at the singular configuration [12]. This makes the trajectory planning become quite complicated. In addition, several simulations have shown that the endpoint velocity near the singularity decreases. This reduces the ability to control the singularity.

This paper focuses on designing a controller based on inverse dynamics for parallel manipulators to force it move through singular configurations. To do this, the configurations and endpoint loci at which the singularity can occur are first plotted. Then, the dynamic equations for parallel manipulators are established in form of redundant generalized coordinate. Based on the dynamic equation, the driving torque corresponding to the desired motion needs to be determined in all singular and non-singular configurations.

The remainder of this paper is organized as follows: Sect. 2 is kinematic model and singularity analysis. Section 3 presents a forward and inverse dynamics. Motion control and some numerical simulations are shown in Sect. 4. Finally, the conclusion is given in Sect. 5.

2 Kinematics and Singularity of a 5 Bar Parallel Manipulator

Let's consider a five-bar parallel robotic manipulator as shown in Fig. 1. All links are considered to be absolutely rigid with length $l_1, l_2, l_3, l_4,$, ($l_3 = l_1$, $l_4 = l_2$) and L_0 is the distance between the actuated joints.

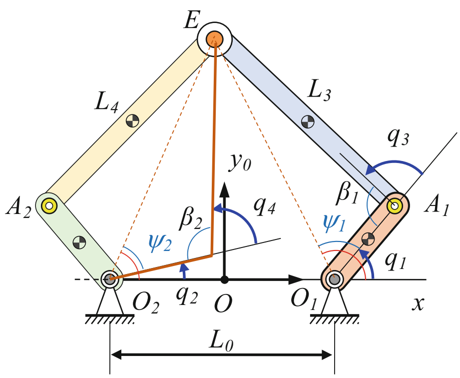

Fig. 1. Five-bar parallel robotic manipulator

Let $\mathbf{q} = [q_1, q_2, q_3, q_4]^T$ be the redudant generalized coordinates of the manipulator (Fig. 1), in which the actuated variables are $\mathbf{q}_a = [q_1, q_2]^T$. Let $\mathbf{x} = [x, y]^T$ be the position of end-efector E which is detemined as:

$$\begin{aligned} x &= \tfrac{1}{2}L_0 + l_1 \cos q_1 + l_3 \cos(q_1 + q_3), \\ y &= l_1 \sin q_1 + l_3 \sin(q_1 + q_3), \end{aligned} \tag{1}$$

Or

$$\begin{aligned} x &= -\tfrac{1}{2}L_0 + l_2 \cos q_2 + l_4 \cos(q_2 + q_4), \\ y &= l_2 \sin q_2 + l_4 \sin(q_2 + q_4), \end{aligned} \tag{2}$$

Inverse Kinematics

At each position of the end point E, the five-bar manipulator can have four configurations (−+, −−, ++, and +−) as shown in Fig. 2. Each sign indicate the sign of the passive joint variables q_4 and q_3. Configurations in which one or both of the arms become fully extended cause the end effector to lose at least one of its degrees of freedom. These configurations correspond to kinematic singularities and occur when the robot changes from one configuration to another.

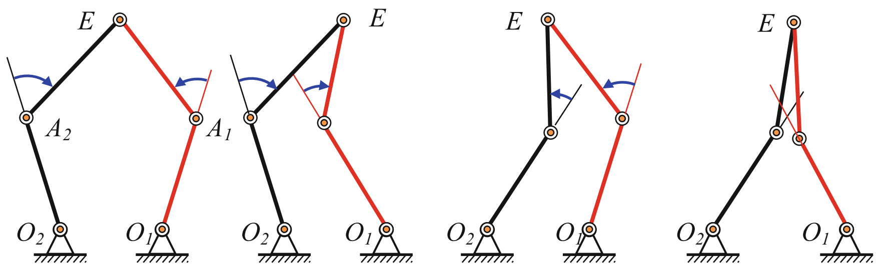

Fig. 2. Four configurations of inverse kinematics

In the following, the configuration (++) will be considered for the inverse kinematics. All joint variables will be determined for the given position of end-effector E. By analysis two triangles O_1A_1E and O_2A_2E, we have:

$$\begin{aligned} d_{O_1E} &= \sqrt{(x_E - x_{O1})^2 + (y_E - y_{O1})^2}, \\ \psi_1 &= \arccos \frac{L_1^2 + d_{O_1E}^2 - L_3^2}{2L_1 d_{O_1E}}, \quad \beta_1 = \arccos \frac{L_1^2 + L_3^2 - d_{O_1E}^2}{2L_1L_3} \\ \measuredangle xO_1E &= (q_1 + \psi_1) = a\tan 2(y_E - y_{O1}, x_E - x_{O1}) \\ q_1 &= \measuredangle xO_1E - \psi_1, \quad q_3 = \pi - \beta_1 \end{aligned}$$

Similarly, we have:

$$d_{O_2E} = \sqrt{(x_E - x_{O2})^2 + (y_E - y_{O2})^2},$$

$$\psi_2 = \arccos \frac{L_1^2 + d_{O_2E}^2 - L_3^2}{2L_1 d_{O_2E}}, \quad \beta_2 = \arccos \frac{L_1^2 + L_3^2 - d_{O_2E}^2}{2L_1 L_3}$$

$$\measuredangle xO_2E = \operatorname{atan}(y_E - y_{O2}, x_E - x_{O2})$$
$$\Rightarrow q_2 = \measuredangle xO_2E - \psi_2, \quad q_4 = \pi - \beta_2$$

Corresponding to four configuarations, we have four sets of solution of inverse kinematics as following:

1. Configuration

$$q_1 = \measuredangle xO_1E - \psi_1,\ q_3 = \pi - \beta_1\ q_2 = \measuredangle xO_2E + \psi_2,\ q_4 = -(\pi - \beta_2) \tag{3}$$

2. Configuration

$$q_1 = \measuredangle xO_1E + \psi_1,\ q_3 = -(\pi - \beta_1),\ q_2 = \measuredangle xO_2E + \psi_2,\ q_4 = -(\pi - \beta_2) \tag{4}$$

3. Configuration

$$q_1 = \measuredangle xO_1E - \psi_1,\ q_3 = \pi - \beta_1\ q_2 = \measuredangle xO_2E - \psi_2,\ q_4 = \pi - \beta_2 \tag{5}$$

4. Configuration

$$q_1 = \measuredangle xO_1E + \psi_1,\ q_3 = -(\pi - \beta_1)\ q_2 = \measuredangle xO_2E - \psi_2,\ q_4 = \pi - \beta_2 \tag{6}$$

Jacobian Matrices and Singularity

The constraint equation describes the relationship between active joint variables and position of the end-effector is given based on the constant distance from E to $A_{1,2}$. So, we have:

$$f_k(\mathbf{q}_a, \mathbf{x}) = (x - \tfrac{1}{2}L_0 - l_k \cos q_k)^2 + (y - l_k \sin q_k)^2 - l_{k+2}^2 = 0, \quad k = 1, 2 \tag{7}$$

Taking time derivative the constraint equations we get:

$$\mathbf{J}_x(\mathbf{q}_a, \mathbf{x})\dot{\mathbf{x}} + \mathbf{J}_q(\mathbf{q}_a, \mathbf{x})\dot{\mathbf{q}}_a = 0 \tag{8}$$

where

$$\mathbf{J}_x(\mathbf{q}_a, \mathbf{x}) = \begin{bmatrix} 2x - L_0 - 2l_1 \cos q_1 & 2y - 2l_1 \sin q_1 \\ 2x - L_0 - 2l_1 \cos q_2 & 2y - 2l_1 \sin q_2 \end{bmatrix} \tag{9}$$

$$\mathbf{J}_q(\mathbf{q}_a, \mathbf{x}) = \begin{bmatrix} J_{x11} & 0 \\ 0 & J_{x22} \end{bmatrix} \tag{10}$$

with $J_{x11} = -l_1((L_0 - 2x)\sin q_1 + 2y \cos q_1)$, $J_{x22} = l_1((L_0 + 2x)\sin q_2 + 2y \cos q_2)$.

Substituting (1) and (2) into (9) and (10) one obtains

$$\mathbf{J}_x(\mathbf{q}_a, \mathbf{x}) = \begin{bmatrix} 2l_3 \cos(q_1 + q_3) & 2l_3 \sin(q_1 + q_3) \\ 2l_3 \cos(q_2 + q_4) & 2l_3 \sin(q_2 + q_4) \end{bmatrix} \tag{11}$$

$$\mathbf{J}_q(\mathbf{q}_a, \mathbf{x}) = \begin{bmatrix} -2l_1 l_3 \sin q_3 & 0 \\ 0 & -2l_1 l_3 \sin q_4 \end{bmatrix} \tag{12}$$

So, the constraint equations at velocity level becomes:

$$\begin{bmatrix} l_3 \cos(q_1 + q_3) & l_3 \sin(q_1 + q_3) \\ l_3 \cos(q_2 + q_4) & l_3 \sin(q_2 + q_4) \end{bmatrix} \dot{\mathbf{x}} + \begin{bmatrix} -l_1 l_3 \sin q_3 & 0 \\ 0 & -l_1 l_3 \sin q_4 \end{bmatrix} \dot{\mathbf{q}}_a = 0$$

Determinant of two Jacobian matrices are calculated:

$$\det[\mathbf{J}_x(\mathbf{q}_a, \mathbf{x})] = -2l_3^2 \sin(q_1 + q_3 - q_2 - q_4)$$

$$\det[\mathbf{J}_q(\mathbf{q}_a, \mathbf{x})] = -2^2 l_1^2 l_3^2 \sin q_3 \sin q_4$$

Based on jacobian matrices in (8), there are three types of singularities as following:

Type 1 singularities or inverse singularities occur when the manipulator is in a position such as $\det[\mathbf{J}_q(\mathbf{q}_a, \mathbf{x})] = 0$. In such configurations, the manipulator loses the ability to move in one given direction. This singularities occur when $q_3 = 0$ or $q_3 = \pi$ or $q_4 = 0$ or $q_4 = \pi$, , (Fig. 3c,d). At this configurations, the end-effector E is at the boundary of the work space.

Type 2 singularities or forward singularities occur when the manipulator is in a position such as $\det[\mathbf{J}_x(\mathbf{q}_a, \mathbf{x})] = 0$. This singularities occur when $q_1 + q_3 - q_2 - q_4 = 0$ or π, (two links A_1E and A_2E are in a line), (Fig. 3a,b). At this configuration, one degree of freedom of the end point becomes uncontrollable. Moreover, the driving torques increase very fast when the manipulator moves closed to and crossing this configuration.

Type 3 singularities are configurations where both Type 1 and Type 2 singular configurations appear at the same time, $\det[\mathbf{J}_x(\mathbf{q}_a, \mathbf{x})] = \det[\mathbf{J}_q(\mathbf{q}_a, \mathbf{x})] = 0$, (Fig. 3e,f).

To show the nonsingular workspace corresponding to a set of solution of the inverse kinematics, the singular loci of the endpoint E is given. With the chosen parameters $l_0 = 0.275$, $l_1 = l_2 = 0.23$, $l_3 = l_4 = 0.23$ m, the workspace and forward singular loci are shown in Fig. 4. This figures show the workspace boundaries, the the singular loci of the forward kinematics and a typical configuration of the manipulator. The values shown in the figure is the determinant of the jacobian matrix $\mathbf{J}_x$. The bold blue line is the loci of the end point E when the manipulator is at singular configurations. We can see that this bold line separates the workspace into some regular areas.

3 Forward and Inverse Dynamics

3.1 Dynamic Model

Let's consider the parallel robot having two degrees of freedom as shown in Fig. 1. The system dynamic model is derived by applying Lagrangian equation with multipliers. For a closed loop multibody system, the redundant generalized coordinate will be used and the dynamic equation is described in form of DAEs as follows [3, 11]:

$$\mathbf{M}(\mathbf{q})\ddot{\mathbf{q}} + \mathbf{C}(\mathbf{q}, \dot{\mathbf{q}})\dot{\mathbf{q}} + \mathbf{g}(\mathbf{q}) + \mathbf{D}\dot{\mathbf{q}} + \mathbf{\Phi}^T(\mathbf{q})\boldsymbol{\lambda} = \mathbf{B}\mathbf{u}, \tag{13}$$

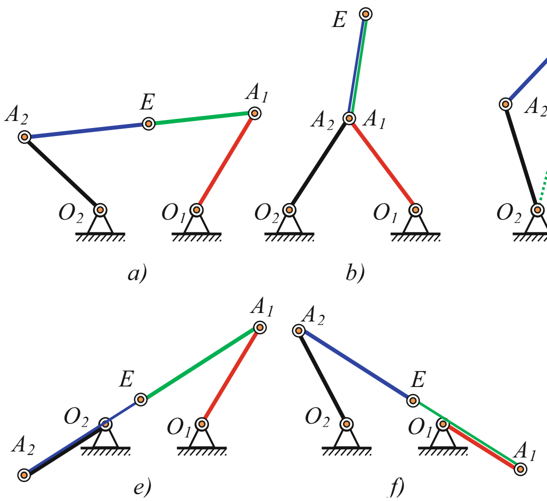

Fig. 3. Some singular configurations

$$\boldsymbol{\phi}(\mathbf{q}) = \mathbf{0}, \tag{14}$$

where $\mathbf{M}(\mathbf{q})$ is the mass matrix; $\mathbf{g}(\mathbf{q})$ the potential generalized force vector; $\mathbf{D}\dot{\mathbf{q}}$ is the vector of generalized forces of non-conservative forces (linear damping force); $\boldsymbol{\phi}(\mathbf{q}) = \mathbf{0}$ is the vector of constraint equations; $\boldsymbol{\Phi}(\mathbf{q}) = \partial\boldsymbol{\phi}/\partial\mathbf{q}$ is the Jacobian matrix; $\mathbf{B} = [\mathbf{E}_{n\times n}, \mathbf{0}^T_{m-n,n}]^T$ is the matrix related to the control input arrangement; the coriolis and centrifugal matrix $\mathbf{C}(\mathbf{q}, \dot{\mathbf{q}})$ can be determined from the mass matrix by using the Christoffel formula [7, 10].

If the generalized coordinates are divided into two groups of active and passive: $\mathbf{q} = [\mathbf{q}_a^T, \mathbf{q}_p^T]^T$, with $\mathbf{q}_a \in R^n$, $\mathbf{q}_p \in R^{m-n}$, matrix $\mathbf{B}$ has a block form $\mathbf{B} = [\,\mathbf{E}_{n\times n}\ \mathbf{0}_{n,m-n}\,]^T$.

The number of Lagrangian multipliers is $r = m - n$ equal to the number of constraint equations, $\boldsymbol{\lambda} = [\lambda_1, ..., \lambda_r]^T$.

3.2 Forward Dynamics

There are many ways to determine generalized acceleration vectors from differential equations of motion. The following is a plan to use the elemination matrix $\mathbf{R}$ satisfying $\mathbf{R}^T\boldsymbol{\Phi}^T = \mathbf{0}$ to eleminate the Lagrange multiplier, and at the same time combine it with the constraint equation at the acceleration level including the Baumgarte stabilization technique [5]:

$$\begin{aligned}
\mathbf{R}^T\mathbf{M}(\mathbf{q})\ddot{\mathbf{q}} &= \mathbf{R}^T(\mathbf{B}\mathbf{u} - \mathbf{h}(\mathbf{q}, \dot{\mathbf{q}})),\\
\boldsymbol{\Phi}(\mathbf{q})\ddot{\mathbf{q}} &= -\dot{\Phi}(\mathbf{q})\dot{\mathbf{q}} - 2\omega\boldsymbol{\Phi}(\mathbf{q})\dot{\mathbf{q}} - \omega^2\phi(\mathbf{q}), \quad \omega > 0.
\end{aligned}$$

with $\mathbf{h}(\mathbf{q}, \dot{\mathbf{q}}) = \mathbf{C}(\mathbf{q}, \dot{\mathbf{q}})\dot{\mathbf{q}} + \mathbf{D}\dot{\mathbf{q}} + \mathbf{g}(\mathbf{q})$.

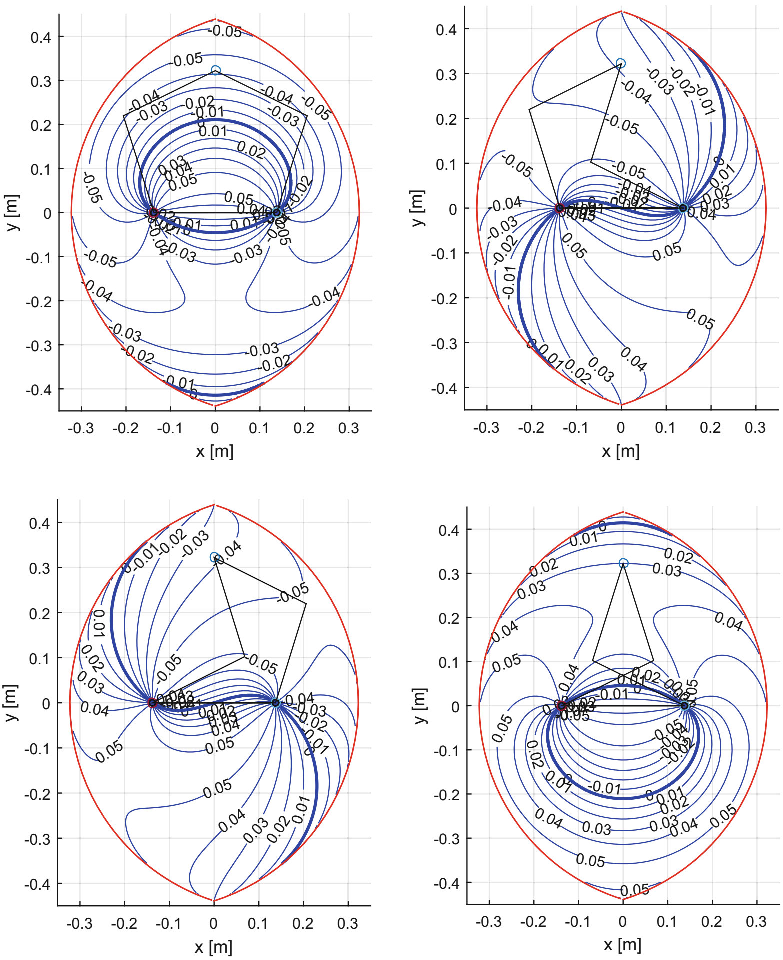

Fig. 4. Singular loci of the end point coresponding to four configurations

Solving for generalized acceleration vectors gives:

$$\ddot{\mathbf{q}} = \begin{bmatrix} \mathbf{R}^T \mathbf{M}(\mathbf{q}) \\ \boldsymbol{\Phi}(\mathbf{q}) \end{bmatrix}^{-1} \begin{bmatrix} \mathbf{R}^T(\mathbf{B}\mathbf{u} - \mathbf{h}(\mathbf{q}, \dot{\mathbf{q}})) \\ -\dot{\Phi}(\mathbf{q})\dot{\mathbf{q}} - 2\omega\boldsymbol{\Phi}(\mathbf{q})\dot{\mathbf{q}} - \omega^2\phi(\mathbf{q}) \end{bmatrix} \tag{15}$$

Equations (15) will be integrated with consistent initial conditions for $\mathbf{q}(0)$ and $\dot{\mathbf{q}}(0)$, which have to satisfy the contraint equations at position and velocity levels.

3.3 Inverse Dynamics

Assuming that the motion of the robot is known, we need to determine the torques applied to the driven joints. In this section, we will show how to determine torque $\mathbf{u}$

from the equations of motion (15). The Eq. (16) is rewritten as following:

$$\mathbf{Bu} = \mathbf{b}(\mathbf{q}, \dot{\mathbf{q}}, \ddot{\mathbf{q}}) + \mathbf{\Phi}^T(\mathbf{q})\boldsymbol{\lambda} \tag{16}$$

with $\mathbf{b}(\mathbf{q}, \dot{\mathbf{q}}, \ddot{\mathbf{q}}) = \mathbf{M}(\mathbf{q})\ddot{\mathbf{q}} + \mathbf{C}(\mathbf{q}, \dot{\mathbf{q}})\dot{\mathbf{q}} + \mathbf{D}\dot{\mathbf{q}} + \mathbf{g}(\mathbf{q})$.

Let's introduce an elemination matrix defined by

$$\mathbf{R} = \begin{bmatrix} \mathbf{E} \\ -[\mathbf{\Phi}_d^{-1}(\mathbf{q})\mathbf{\Phi}_i(\mathbf{q})] \end{bmatrix} \tag{17}$$

with $\mathbf{q}_i \equiv \mathbf{q}_a, \mathbf{q}_d$ are active and passive joint variables, $\mathbf{\Phi}_i = \partial\boldsymbol{\phi}/\partial\mathbf{q}_i$, $\mathbf{\Phi}_d = \partial\boldsymbol{\phi}/\partial\mathbf{q}_d$ are Jacobian matrices. It is clear that matrix $\mathbf{R}$ satisfied $\mathbf{\Phi}(\mathbf{q})\mathbf{R} = \mathbf{0}$ or $\mathbf{R}^T\mathbf{\Phi}^T(\mathbf{q}) = \mathbf{0}$.

Multiplying from the left of the matrix by $\mathbf{R}^T$ both sides of the Eq. (18) and rearranging, we get the equation to solve $\mathbf{u}$:

$$\mathbf{R}^T\mathbf{Bu} = \mathbf{R}^T[\mathbf{b}(\mathbf{q}, \dot{\mathbf{q}}, \ddot{\mathbf{q}})]. \tag{18}$$

In case matrix $\mathbf{\Phi}_d$ is not singular, then the product $\mathbf{R}^T\mathbf{B}$ is a unit matrix. So, in the nonsingular case, the driven torque is determined from the desired motion as following:

$$\mathbf{u} = [\mathbf{R}^T\mathbf{B}]^{-1}\mathbf{R}^T\mathbf{b}(\mathbf{q}, \dot{\mathbf{q}}, \ddot{\mathbf{q}}) = \mathbf{R}^T\mathbf{b}(\mathbf{q}, \dot{\mathbf{q}}, \ddot{\mathbf{q}}). \tag{19}$$

Passing Through Singularity

In the case of the robot moving through singular configurations, in order for the computation to be smooth, we need to find a way to reconstruct the elemination matrix $\mathbf{R}$ Using the pseudo-inverse matrix, we can build this matrix as follows [8, 9]:

$$\mathbf{R} = [\mathbf{E}_m - \mathbf{\Phi}^+(\mathbf{q})\mathbf{\Phi}(\mathbf{q})] \text{ or } \mathbf{R} = \text{null}(\mathbf{\Phi}(\mathbf{q})), \tag{20}$$

with $\mathbf{\Phi}^+$ is pseudo-inverse of $\mathbf{\Phi}$ satisfying $\Phi\Phi^+\mathbf{\Phi} = \mathbf{\Phi}$. It is clear that:

$$\mathbf{\Phi}(\mathbf{q})\mathbf{R} = \mathbf{\Phi}(\mathbf{q})[\mathbf{E}_m - \mathbf{\Phi}^+(\mathbf{q})\mathbf{\Phi}(\mathbf{q})] = [\mathbf{\Phi}(\mathbf{q}) - \mathbf{\Phi}(\mathbf{q})] = \mathbf{0}$$

With this elemination matrix, the matrix in front of $\mathbf{u}$ in Eq. (21) will no longer be square.

By introducing $\mathbf{A} = \mathbf{R}^T\mathbf{B}$, the Eq. (21) will be:

$$\mathbf{Au} = \mathbf{R}^T\mathbf{b}(\mathbf{q}, \dot{\mathbf{q}}, \ddot{\mathbf{q}})$$

Therefore, at singular configurations, we calculate by the following formula

$$\mathbf{u} = \mathbf{A}^+\mathbf{R}^T\mathbf{b}(\mathbf{q}, \dot{\mathbf{q}}, \ddot{\mathbf{q}}) \tag{21}$$

Note that formulas (21) and (22) hold even when the robot is not in the singular configuration. It should be emphasized that, at the kinematic singular configuration, the rank of matrix $\mathbf{A}$ is reduced, it is not possible to determine the correct driving current satisfying (22). Here, we can use SVD to find $\mathbf{A}^+$ or use the approximate formula (damped least-squares inverse) for $\mathbf{u}$:

$$\mathbf{Au} = \mathbf{R}^T\mathbf{b}(\mathbf{q}, \dot{\mathbf{q}}, \ddot{\mathbf{q}}) \;\;\Rightarrow\;\; \mathbf{u} = (\mathbf{A}^T\mathbf{A} + k\,\mathbf{E})^{-1}\mathbf{A}^T\mathbf{R}^T\mathbf{b}(\mathbf{q}, \dot{\mathbf{q}}, \ddot{\mathbf{q}}). \tag{22}$$

Parameter k can be chosen depending on determinant of Jacobian matrix or matrix **A**. One can choose k depending on $w = \sqrt{\det(\mathbf{A}^T\mathbf{A})}$ as following:

$$k = \begin{cases} \varepsilon_0(1 - w/w_0)^2, & \text{if } w < w_0 \\ 0, & \text{if } w \geq w_0 \end{cases}$$

Two parameters w_0, ε_0 will be choose by designer, w_0 is related to the distance to the singular configuration and ε_0 is related to the regularization of the matrix to be inverted.

4 Control Design and Numerical Simulations

4.1 Position Control

In case of position control, we apply PD controller + gravity compensation, the driving torque is calculated as

$$\mathbf{u} = \mathbf{A}^{+}\mathbf{R}^{T}\mathbf{g}(\mathbf{q}) + (\mathbf{K}_p\tilde{\mathbf{q}}_a + \mathbf{K}_d\dot{\tilde{\mathbf{q}}}_a) \tag{23}$$

in which the position error in operational space $\tilde{\mathbf{x}} = \mathbf{x}_d - \mathbf{x}$ is converted to the position error in active joint variables based on (8) as:

$$\tilde{\mathbf{q}}_a = -\mathbf{J}_q^{-1}(\mathbf{q}_a, \mathbf{x})\mathbf{J}_x(\mathbf{q}_a, \mathbf{x})\tilde{\mathbf{x}} = -\mathbf{J}_q^{-1}(\mathbf{q}_a, \mathbf{x})\mathbf{J}_x(\mathbf{q}_a, \mathbf{x})(\mathbf{x}_d - \mathbf{x})$$

$$\dot{\tilde{\mathbf{q}}}_a = -\mathbf{J}_q^{-1}(\mathbf{q}_a, \mathbf{x})\mathbf{J}_x(\mathbf{q}_a, \mathbf{x})\dot{\tilde{\mathbf{x}}} = -\mathbf{J}_q^{-1}(\mathbf{q}_a, \mathbf{x})\mathbf{J}_x(\mathbf{q}_a, \mathbf{x})(0 - \dot{\mathbf{x}})$$

The gain matrices $\mathbf{K}_p$, $\mathbf{K}_d$ are positive diagonal ones.

4.2 Tracking Control Based on Inverse Dynamics

Let $\mathbf{x}_d(t)$ be the desired trajectory of the end-effector, then the desired torques $\mathbf{u}_d$ is computed based on the inverse kinematics and inverse dynamics Fig. 5. A simple PD controller is also added to stabilize the desired trajectory. The control diagram is shown in Fig. 5.

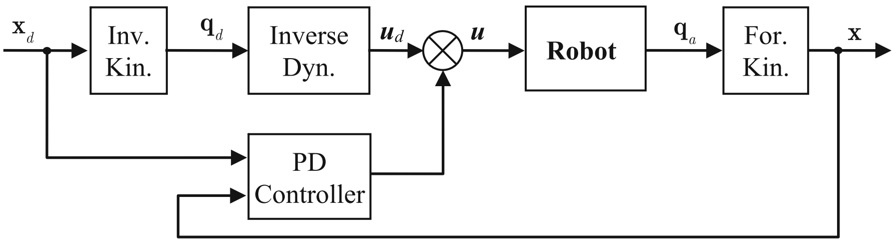

Fig. 5. Control diagram

4.3 Numerical Simulations

Let's consider a five-bar parallel robotic manipulator as shown in Fig. 1. All links are considered to be absolutely rigid. Together with the length shown above, the mass, center of mass and moment of inertia about the center of mass of these four links are given:

$$\begin{aligned} m_1 &= m_2 = 0.66, \quad m_3 = m_4 = 0.36\,\text{kg}, \\ s_1 &= s_2 = 0.5\,l_1; \quad s_3 = s_4 = 0.5 l_3; \\ s_3 &= s_4 = 0.029, \quad I_{C3} = I_{C4} = 0.016\,\text{kgm}^2. \end{aligned}$$

In these simulations, the endpoint E will be moved along three lines connecting three points. To show the ability crossing the singularity of type 2, these three points are chosen in two regions of workspace separated by singular loci, Fig. 6:

$$\mathbf{r}_{E1} = [-0.18,\ 0.3]^T; \quad \mathbf{r}_{E2} = [0.0,\ 0.1]^T; \quad \mathbf{r}_{E3} = [0.18,\ 0.3]^T\ (\text{m}).$$

Along each path is a quintic polynomial with zero velocities and acceleration at two ends. The time for three segments are chosen $T_1 = T_2 = T_3 = 1$ s, respectively.

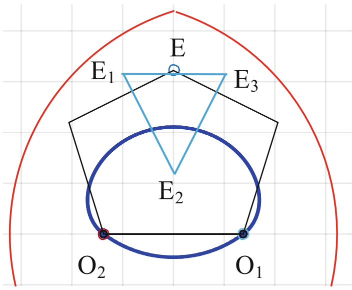

Fig. 6. Three points E_1, E_2 and E_3 in the workspace

The parameters of PD controller are chosen as:

$$\mathbf{K}_P = 500\text{diag}([1, \quad 1]); \quad \mathbf{K}_D = 50\text{diag}([1, \quad 1]).$$

Simulation results including time history of endpoint E, joint variables, driving torques and configurations of the manipulator are shown in Fig. 7 and Fig. 8.

In the simulations, the endpoint E departs from a position near the first point E_1. The results shows that the motion of the endpoint E tracks the desired trajectory after about 0.25 s (Fig. 8). The manipulator configurations show its endpoint E track the desired trajectories along three edges of the triangle $E_1E_2E_3$. The driving torques increase fast near the singular position and change the sign at forward singular configurations. Theroretically, the driving torques can increase to infinity at singular position, however, they are limited by maximum values depending on the actuators.

Thus, with a travel time of 1 s on each edge of the triangle $E_1E_2E_3$, the manipulator easily crosses its singular configuration. This is appropriate to reality. The manipulator

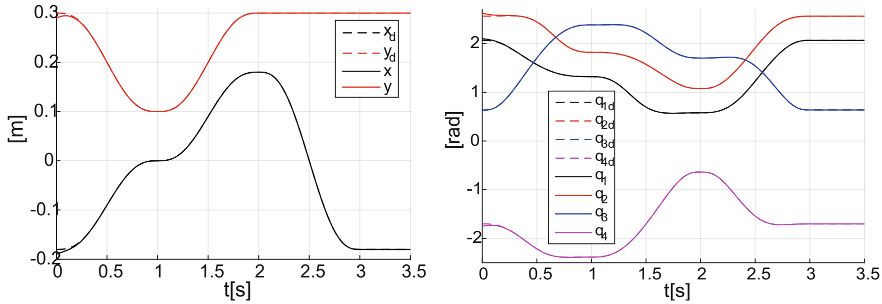

Fig. 7. Time history of endpoint E and of joint variables

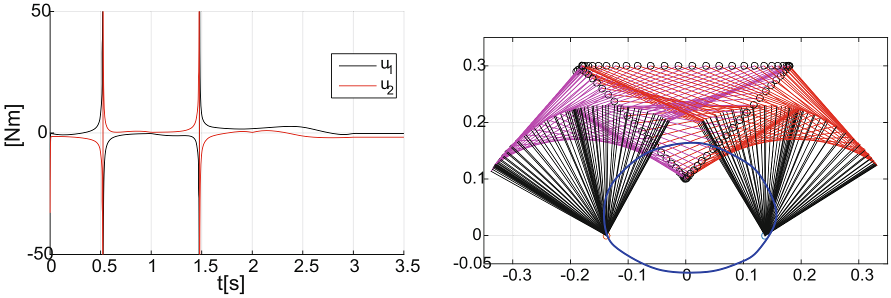

Fig. 8. Time history of driving torques and configurations of the manipulator

can only passes the singularity when it has a sufficiently large velocity when approaching the forward kinematic singularity configuration.

The following is one more simulation result in which the point endpoint E has a low velocity. In this simulation, the travel time from E_1 to E_2 is set $T_1 = 2$ s and from E_2 to E_3 is $T_2 = 5$ s. In the first edge E_1E_2, the manipulator still crosses the singularity. While on edge E_2E_3, due to increasing motion time the velocity of endpoint E is reduced. As a result, the manipulator was unable to passes the singular configuration ($t = 5.5$ s). After time point 5.5 s, the endpoint E can not track the desired trajectory (Fig. 9). Noncrossing singularity is shown more clearly in Fig. 10.

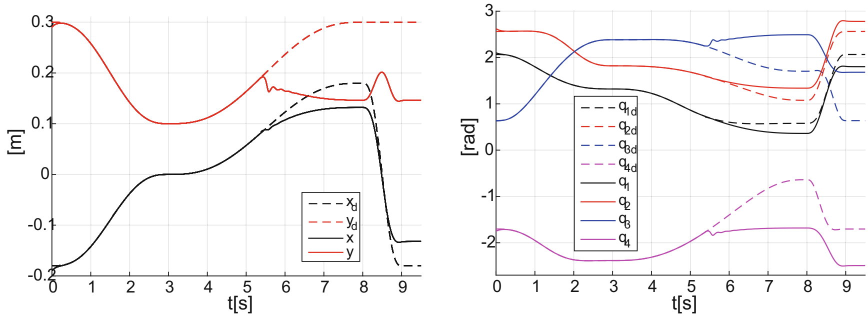

Fig. 9. Time history of endpoint E and of joint variables

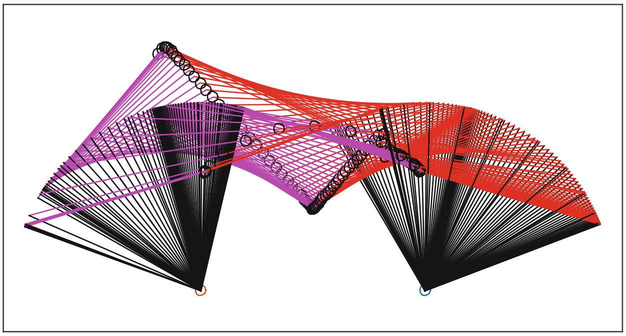

Fig. 10. Configurations of the manipulator

5 Conclusions

This paper presented the singularity analysis and singular crossing control a five-bar parallel manipulator. Four configurations of inverse kinematics and singularity loci of the endpoint were shown geometrically. The equations of motion for parallel manipulator were derived by using the redundant generalized coordinates and the Lagrangian multipliers. The inverse dynamics of the parallel manipulator was solved by pseudo-inverse of Jacobian matrix. An PD controller plus inverse dynamics were designed for trajectory tracking of the endpoint. Simulation results have shown that the approach design were effective to trajectory control of the parallel manipulator. Simulations have also shown that the ability of singularity crossing depends not only controller, but also the motion law along desired trajectory.

References

1. Merlet, J.-P.: Parallel Robots, 2nd edn. Springer, Berlin (2006)
2. Gosselin, C.M., Wang, J.: Singularity loci of planar parallel manipulators with revolute actuators. Robot. Auton. Syst. **21**(4), 377–398 (1997)
3. Van Khang, N.: Dynamics of Multibody Systems (in Vietnamese). Science and Technics Publishing House, Hanoi (2007)

4. de Jalón, J.G., Bayo, E.: Kinematic and Dynamic Simulation of Multibody Systems, The Real-Time Challenge. Springer, New York (1994)
5. Baumgarte, J.: Stabilization of constraints and integrals of motion in dynamical systems. Comput. Methods Appl. Mech. Eng. **1**(1), 1–16 (1972)
6. Tsai, L.-W.: Robot Analysis - The Mechanics of Serial and Parallel Manipulators. Wiley, New York (1999)
7. Murray, R.M., Li, Z., Sastry, S.S.: A Mathematical Introduction to Robotic Manipulation. CRC Press, Boca Raton (1994)
8. Nakamura, Y.: Advanced Robotics/Redundancy and Optimization. Addison-Wesley Publishing Company, Reading (1991)
9. Meyer, C.D.: Matrix Analysis and Applied Linear Algebra. Society for Industrial and Applied Mathematics, SIAM (2001)
10. Sciavicco, L., Siciliano, B.: Modelling and Control of Robot Manipulators, 2nd edn. Springer, London (2000)
11. Shabana, A.A.: Dynamics of Multibody Systems, 2nd edn. Cambridge University Press, Cambridge (1998)
12. Hill, R.B., Six, D., Chriette, A., Briot, S., Martinet, P.: Crossing type 2 singularities of parallel robots without pre-planned trajectory with a virtual-constraint based controller. In: 2017 IEEE International Conference on Robotics and Automation (ICRA 2017), Singapore (2017)
13. Campos, L., Bourbonnais, F., Bonev, I.A., Bigras, P.: Development of a five-bar parallel robot with large workspace. In: Proceedings of the ASME 2010 International Design Engineering Technical Conferences & Computers and Information in Engineering Conference IDETC/CIE, Montreal (2010)
14. Pagis, G., Bouton, N., Briot, S., Martinet, P.: Design of a controller for enlarging parallel robots workspace through type 2 singularity crossing. In: Proceedings of the IEEE International Conference on Robotics and Automation (2014)
15. Pagis, G., Bouton, N., Briot, S., Martinet, P.: Enlarging parallel robot workspace through Type-2 singularity crossing. Control. Eng. Pract. **39**, 1–11 (2015)
16. Arakelian, V., Wenger, P. (eds.): ROMANSY 22 – Robot Design, Dynamics and Control. CICMS, vol. 584. Springer, Cham (2019). https://doi.org/10.1007/978-3-319-78963-7
17. Ider, S.K.: Inverse dynamics of parallel manipulators in the presence of drive singularities. Mech. Mach. Theory **40**, 33–44 (2005)
18. Liu, S., Qiu, Z.-C., Zhang, X.-M.: Singularity and path-planning with the working mode conversion of a 3-DOF 3-RRR planar parallel manipulator. Mech. Mach. Theory **107**, 166–182 (2017)
19. Kotlarski, J., de Nijs, R., Abdellatif, H., Heimann, B.: New Interval-based approach to determine the guaranteed singularity-free workspace of parallel robots. In: IEEE International Conference on Robotics and Automation, Kobe, pp. 1256–1261 (2009)
20. Kemal Ider, S.: Inverse dynamics of parallel manipulators in the presence of drive singularities. Mechan. Mach. Theory **40**, 33–44 (2005)
21. Kemal Ider, S.: Singularity robust inverse dynamics of planar 2-RPR parallel manipulators. In: Proceedings of the Institution of Mechanical Engineers, Part C: Journal of Mechanical Engineering Science (2004)

STAR-Reconfigurable Intelligent Surface-Assisted Mobile Edge Computing Network with NOMA and RF Energy Harvesting

Van-Truong Truong[1,2], Mage Mikhail[3], Van-Nhan Vo[4], and Dac-Binh Ha[1,2](✉)

[1] Faculty of Electrical-Electronic Engineering, Duy Tan University, Da Nang 550000, Vietnam
hadacbinh@duytan.edu.vn

[2] Institute of Research and Development, Duy Tan University, Da Nang 550000, Vietnam

[3] Faculty of Engineering Technology, Purdue University Northwest, Hammond, IN, USA

[4] School of Computer Science, Duy Tan University, Da Nang 550000, Vietnam

Abstract. Simultaneous transmitting and reflecting reconfigurable intelligent surface (STAR-RIS) can make the wireless communication environment more intelligent in 6G networks. In this paper, we present the performance analysis for a STAR-RIS-aided mobile edge computing (MEC) network that applied non-orthogonal multiple access (NOMA) schemes with radio frequency energy harvesting (RF EH). Specifically, this system comprises an energy-constrained user, a STAR-RIS, and a pair of access points that equipped MEC servers. One of them, hybrid access point, can transfer the RF power to the user. To investigate the performance of this system, we derive the closed-form expression of successful computation probability by using statistical characteristics of signal-to-noise ratio (SNR). Furthermore, based on this expression, we investigate the behaviors of this considered system according to its key parameters, such as average transmit signal-to-noise ratio, power allocation ratio, and the number of elements of STAR-RIS. Finally, our analysis is verified by the Monte-Carlo simulation results.

Keywords: Simultaneous transmitting and reflecting reconfigurable intelligent surface · mobile edge computing · non-orthogonal multiple access · RF energy harvesting · successful computation probability

1 Introduction

The demand for high-speed and reliable wireless communication has witnessed exponential growth in recent years due to the proliferation of mobile devices (MD) and the increasing popularity of data-intensive applications [1]. To meet these demands, researchers and industry experts have been exploring innovative technologies that can enhance the capacity and efficiency of wireless networks. Non-orthogonal multiple access (NOMA) and mobile edge computing (MEC) have gained significant attention among these emerging technologies [2].

D. C. Nguyen et al. (Eds.): ICERA 2023, LNNS 944, pp. 439–448, 2024.
https://doi.org/10.1007/978-3-031-62235-9_44

NOMA is a promising multiple-access technique that allows multiple users to share the same time-frequency resource, thereby increasing the system's spectral efficiency [3]. By employing power domain multiplexing and successive interference cancellation (SIC) at the receiver, NOMA improves the system capacity and supports many connected devices. On the other hand, MEC brings computation and storage capabilities closer to the network edge, enabling low-latency and high-bandwidth services [4–6]. By offloading computationally intensive tasks from MD to edge servers, MEC reduces the processing burden on the user equipment and provides real-time response for latency-sensitive applications such as virtual reality, augmented reality, and autonomous vehicles. Furthermore, radio frequency energy harvesting (RF EH) techniques can be applied in the network to improve the performance of MDs. Accordingly, the MDs collect energy from power beacons or hybrid access points (HAPs) to operate continuously [7].

While both NOMA and MEC have shown tremendous potential in enhancing the performance of wireless networks individually, their integration can further amplify the benefits and pave the way for next-generation wireless systems. In this context, a powerful solution has emerged as a novel concept known as the simultaneously transmitting and reflecting reconfigurable intelligent surface (STAR-RIS) assisted NOMA MEC system [8, 9]. The STAR-RIS-assisted NOMA MEC system leverages the collective intelligence of intelligent reflecting surfaces (IRS) and the capabilities of MEC servers to optimize resource allocation, enhance spectral efficiency, reduce latency, and improve the overall quality of service (QoS). The STAR-RIS elements are deployed in the propagation environment to manipulate the wireless signals by controlling their amplitude, phase, and direction [10]. By intelligently configuring the elements, the system can enhance signal strength, mitigate interference, and improve the coverage and capacity of the wireless network.

This paper aims to provide an in-depth exploration of the RF EH STAR-RIS-assisted NOMA MEC system, highlighting its successful computation probability (SCP) features. We summarize the contributions of this paper as follows:

- We propose an RF EH STAR-RIS-assisted NOMA MEC system model and offloading protocol for this system.
- We derive the closed-form expression of the system's successful computation probability (SCP).
- We thoroughly analyze the SCP by considering its essential system parameters to understand the system's behavior comprehensively. These parameters include the time switching ratio, power allocation coefficient, number of RIS' elements, task length, bandwidth, and CPU operating frequency.

The remainder of this paper is organized as follows: Sect. 2 presents the system and channel model. The performance of the considered system is analyzed in Sect. 3. The numerical results are shown in Sect. 4. We conclude our work in Sect. 5.

2 System and Channel Models

We investigate a model of an RF EH NOMA MEC system with the support of STAR-RIS, as shown in Fig. 1. This system consists of a user (UE), a hybrid access point (HAP), an access point (AP), and a STAR-RIS with N_1 elements for full transmission and N_2 elements for full reflection. Each element is composed of passive electronic devices which consume deficient power. Because the quality of transmission channels from user to access points is poor and unstable, it needs the help of STAR-RIS to deal with the channel fading. The controller in Fig. 1 controls the transmission and reflecting elements and adjusts their amplitude/phase of transmission and reflection in real time. For simplicity, we assume there is no mutual signal influence in the transmission and reflection between adjacent STAR-RIS elements, i.e., all STAR-RIS elements transmit and reflect the incoming signals independently. Due to the effect of attenuation, we consider only the signals reflected by the STAR-RIS for the first time and ignore those reflected by it two or more times.

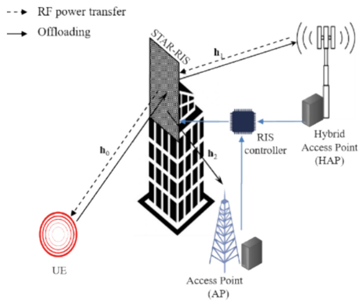

Fig. 1. System model of STAR-RIS NOMA MEC network

Thus, the signal received from all STAR-RIS elements can be modeled as a combination of their transmitted or reflected signals. Therefore, the baseband signal models, calculated for N_1 and N_2 elements of STAR-RIS, are expressed as follows:

$$y_t(t) = \left(\sum_{n=1}^{N_1} \alpha_n e^{j\theta_{1,n}} h_{01,n} h_{1,n}\right) x(t) = \mathbf{h}_{01}^H \mathbf{\Theta}_t \mathbf{h}_1 x(t), \tag{1}$$

$$y_r(t) = \left(\sum_{n=1}^{N_2} \beta_n e^{j\theta_{2,n}} h_{02,n} h_{2,n}\right) x(t) = \mathbf{h}_{02}^H \mathbf{\Theta}_r \mathbf{h}_2 x(t), \tag{2}$$

where $x(t)$ stands for the baseband transmits signal, $\mathbf{h}_{01}^H \triangleq \left[h_{01,1}, h_{01,2}, \cdots, h_{01,N_1}\right]$, $\mathbf{h}_{02}^H \triangleq \left[h_{02,1}, h_{02,2}, \cdots, h_{02,N_2}\right]$, $\mathbf{h}_1 \triangleq \left[h_{1,1}, h_{1,2}, \cdots, h_{1,N_1}\right]^T$, $\mathbf{h}_2 \triangleq \left[h_{2,1}, h_{2,2}, \cdots, h_{2,N_2}\right]^T$ with $h_{i,n},\ \ i \in \{0,\ 1,\ 2\}$, denote the channel coefficients followed to Nakagami-m distribution. $\Theta_t \triangleq diag\left[\alpha_1 e^{j\theta_{1,1}}, \alpha_2 e^{j\theta_{1,2}}, \cdots, \alpha_N e^{j\theta_{1,N_1}}\right]$, $\Theta_r \triangleq diag\left[\beta_1 e^{j\theta_{2,1}}, \beta_2 e^{j\theta_{2,2}}, \cdots, \beta_N e^{j\theta_{2,N_2}}\right]$ with $j = \sqrt{-1}$, α_n and β_n stand for the transmission and reflection amplitudes, respectively. $\theta_{1,n}$ and $\theta_{2,n}$ denote the shift phases of the n^{th} element which can be adjusted by the STAR-RIS controller. For simplicity, we assume that $\alpha_n = \alpha,\ \ \beta_n = \beta,\ \ \forall n$.

We propose the working cycle of an offloading process for this considered STAR-RIS-aided MEC network, as shown in Fig. 2. The whole process stays for the time T_{th} and is divided into four-time slots as follows:

- In the first time slot $\tau_1 = \delta T$, the user harvests RF energy from HAP with the help of STAR-RIS.
- In the next time slot $\tau_2 = (1\text{-}\delta)T$, it performs the offloading to HAP and AP by dividing the task into two subtasks (L_1-bit subtask for HAP and L_2-bit subtask for AP) and applying the NOMA scheme with the help of STAR-RIS.
- In the third time slot, the HAP decodes the UE signal sent to it, denoted by x_A, by considering the UE signal sent to the AP, denoted by x_B, as interference. At AP, by applying successive interference cancellation (SIC), it first decodes x_A by treating x_B as interference and then subtracts x_A from the received signal to obtain x_B. The server at HAP and AP processes the tasks during the period τ_3.
- In the last time slot, namely the feedback phase, HAP, and AP return the computation results to the user during the period τ_4.

In our work, τ_4 is assumed that very small compared to transmission time as well as computation time and thus is ignored [11, 12].

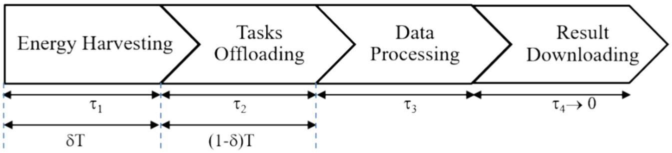

Fig. 2. The working cycle for the STAR-RIS NOMA MEC system

Next, we present the steps of the above protocol mathematically as follows.

The harvested energy of UE during the duration of δT are respectively written as

$$E = \eta P_0 |\mathbf{h}_{01}^H \mathbf{\Theta}_t \mathbf{h}_1|^2 \delta T, \tag{3}$$

where $0 < \eta \leq 1$ stands for the energy conversion efficiency of the receiver, and P_0 denotes the transmit power of HAP.

Assuming that UE uses all harvested energy for transmission. Thus, the transmit power of UE is written as

$$P_U = \frac{\eta P_0 |\mathbf{h}_{01}^H \mathbf{\Theta}_t \mathbf{h}_1|^2 \delta T}{(1-\delta)T} = a P_0 X, \tag{4}$$

where $X \triangleq \left|\mathbf{h}_{01}^H \mathbf{\Theta}_t \mathbf{h}_1\right|^2$, $a \triangleq \frac{\eta\delta}{(1-\delta)}$.

The signals received at HAP and AP are respectively given by

$$y_1 = \mathbf{h}_{01}^H \mathbf{\Theta}_t \mathbf{h}_1 \sqrt{P_U}\left[\sqrt{\rho} x_1 + \sqrt{(1-\rho)} x_2\right] + n_1, \tag{5}$$

$$y_2 = \mathbf{h}_{02}^H \mathbf{\Theta}_r \mathbf{h}_2 \sqrt{P_U}\left[\sqrt{\rho} x_1 + \sqrt{(1-\rho)} x_2\right] + n_2, \tag{6}$$

where ρ is the power allocation ratio, $n_1, n_2 \sim \mathcal{CN}\left(0, \sigma^2\right)$ are additive white Gaussian noises (AWGN) which have zero mean and σ^2 variance.

According to (5) and (6), the signal-to-interference-plus-noise ratio (SINR) at HAP and signal-to-noise ratio (SNR) at AP (applying SIC) are respectively obtained as

$$\gamma_1 = \frac{\rho a \gamma_0 X^2}{(1-\rho)a\gamma_0 X^2 + 1}, \tag{7}$$

$$\gamma_2 = (1-\rho)a\gamma_0 XY, \tag{8}$$

where $\gamma_0 \triangleq \frac{P_0}{\sigma^2}$, $Y \triangleq |\mathbf{h}_{02}^H \mathbf{\Theta}_r \mathbf{h}_2|^2$.

To assist UE offloading, SATR-RIS is configured to the maximum value, i.e., $X_{\max} = |\mathbf{h}_{01}^H \mathbf{\Theta}_t \mathbf{h}_1|^2 = \left(\alpha \sum\limits_{n=1}^{N_t} \left|h_{01,n}\right|\left|h_{1,n}\right|\right)^2$, $Y_{\max} = |\mathbf{h}_{02}^H \mathbf{\Theta}_r \mathbf{h}_2|^2 = \left(\beta \sum\limits_{n=1}^{N_r} \left|h_{02,n}\right|\left|h_{2,n}\right|\right)^2$. According to [17], the CDF and PDF of the random variables $V_t \triangleq X_{\max}$ and $V_r \triangleq Y_{\max}$ are as follows.

$$F_{V_k}(x) = \frac{m_k^{N_k}(4m_{sk}m_{lk})^{-m_{sk}N_k}}{\Gamma(2m_{sk}N_k)} \gamma\left(2m_{sk}N_k, \frac{2\sqrt{m_{sk}m_{lk}x}}{\omega}\right), \tag{9}$$

$$f_{V_k}(x) = \frac{m_k^{N_k}}{2\Gamma(2m_{sk}N_k)\omega^{2m_{sk}N_k}} x^{m_{sk}N_k - 1} e^{-\frac{2\sqrt{m_{sk}m_{lk}x}}{\omega}}, \tag{10}$$

where $\omega \in \{\alpha, \ \beta\}$, $m_{st} = \min\{m_0, m_1\}$, $m_{lt} = \max\{m_0, m_1\}$, $m_{sr} = \min\{m_0, m_2\}$, $m_{lr} = \max\{m_0, m_2\}$, $m_k = \frac{\sqrt{\pi}4^{m_{sk}-m_{lk}+1}(m_{sk}m_{lk})^{m_{sk}}\Gamma(2m_{sk})\Gamma(2m_{lk}-2m_{sk})}{\Gamma(m_{sk})\Gamma(m_{lk})\Gamma(m_{lk}-m_{sk}+\frac{1}{2})}$, $k \in \{t, r\}$.

3 Performance Analysis

The instantaneous channel capacity of the transmission path is written as

$$C_1 = W\log_2(1+\gamma_1), \tag{11}$$

where W denotes the channel bandwidth.

Similarly, the instantaneous channel capacity of the reflection path is expressed as

$$C_2 = W\log_2(1+\gamma_2), \tag{12}$$

The latency of this proposed system is given by

$$\tau = \tau_1 + \max\left\{\frac{L_1}{C_1} + \frac{c_1 L_1}{f_1}, \frac{L_2}{C_2} + \frac{c_2 L_2}{f_2}\right\}. \tag{13}$$

where c_i and f_i stand for the number of CPU cycles needed for executing each bit and the CPU-cycle frequency of the MEC servers at HAP and AP, respectively, $i \in \{1, 2\}$. Here we design the energy harvesting time as follows:

$$\tau_1 = \delta T = \delta\left(T_{th} - \max\left\{\frac{c_1 L_1}{f_1}, \frac{c_2 L_2}{f_2}\right\}\right). \tag{14}$$

The successful computation probability (SCP), denoted by Φ_s, is used as an important metric to describe the performance of a MEC system. Specifically, Φ_s is defined as the probability that all offloading tasks are finished within the maximum allowable system delay T_{th} as follows:

$$\Phi_s = \Pr(\tau < T_{th}). \tag{15}$$

According to this considered system, we obtain the following theorem.

Theorem 1
The closed-form expression of the SCP of UE, for the considered STAR-RIS-aided NOMA MEC system under quasi-static Nakagami-m fading is written as follows:

$$\Phi_s = \begin{cases} 0, & 2^{\frac{L_1}{W\Omega_1}} - 1 > \frac{\rho}{1-\rho} \\ 1 - F_{V_t}(b_1) \\ -\frac{\pi b_3 G}{4Q}\sum_{q=1}^{Q}(-\ln v_q)^{m_{st}N_t-1} e^{-\frac{\mu_t\sqrt{-\ln v_q}}{\alpha}} \gamma\left(2m_{sr}N_r, \frac{\mu_r\sqrt{b_2}}{\beta\sqrt{-\ln v_q}}\right)\sqrt{\frac{1-\varphi_q}{1+\varphi_q}}, & 2^{\frac{L_1}{W\Omega_1}} - 1 < \frac{\rho}{1-\rho} \end{cases} \tag{16}$$

where $b_1 = \sqrt{\frac{2^{\frac{L_1}{W\Omega_1}}-1}{[\rho-(2^{\frac{L_1}{W\Omega_1}}-1)(1-\rho)]a\gamma_0}}$, $b_2 = \frac{2^{\frac{L_2}{W\Omega_2}}-1}{(1-\rho)a\gamma_0}$, $b_3 = e^{-b_1}$, $G = \frac{m_t^{N_t} m_r^{N_r} \mu_r^{-2m_{sr}N_r}}{\Gamma(2m_{st}N_t)\Gamma(2m_{sr}N_r)\alpha^{2m_{st}N_t}}$, $\mu_t = 2\sqrt{m_{st}m_{lt}}$, $\mu_r = 2\sqrt{m_{sr}m_{lr}}$, $\Omega_1 = T_{th} - \tau_1 - \frac{c_1L_1}{f_1}$, $\Omega_2 = T_{th} - \tau_1 - \frac{c_2L_2}{f_2}$, $v_q = -\ln\left[\frac{(\varphi_q+1)b_3}{2}\right]$, $\varphi_q = \cos\left(\frac{2q-1}{2Q}\pi\right)$ with Q is the complexity versus accuracy trade-off coefficient of the Gaussian-Chebyshev quadrature method.

4 Numerical Results and Discussion

In this Section, we present the simulation and analytical results in terms of SCP. The simulation parameters are given in Table 1.

In the first experiment, we consider the impact of the power allocation coefficient (ρ) on system performance, as Fig. 3. We have set $N_1 = 18$, $N_2 = 12$, $W = 10^7$ Hz, and $\delta = 0.3$. The results show that SCP tends to be very low when the ρ is too small or too high, while SCP reaches its maximum value with a suitable ρ. It proves that the system's behavior highly depends on the optimal power allocation decision for the user's tasks. In other words, the system needs to be deployed with an optimal algorithm to find the suitable ρ value, so the system SCP is the largest.

In the next experiment, we look at the impact of the time switching ratio (δ) on system performance, as Fig. 4. We keep the previous experiment's settings and let $\rho = 0.6$. Simulation results show that when δ gradually increases from 0 to 1, SCP tends to be low, gradually increases to a maximum value, and gradually decreases. It proves that a suitable value δ exists such that the system performance is optimal.

In the final experiment, we investigate the effect of varying the number of the transmission elements (N_1) and reflection elements (N_2). We set the total number of IRS

Table 1. Simulation Parameters.

Parameters	Notation	Typical Values
Environment		Nakagami-m
Nakagami fading parameters	m_0, m_1, m_2	3,1,2
Number of transmission elements	N_1	0–30
Number of reflection elements	N_2	0–30
The transmit power	P_0	10 dB
The CPU-cycle frequency of the MEC server	f_1, f_2	10^9 Hz
The number of CPU cycles of the MEC server for executing each bit	c_1, c_2	2
The channel bandwidth	W	10^6–10^7 Hz
The threshold of latency	T_{th}	0.04 s
The total data bits for HAP	L_1	3.10^5 bit
The total data bits for AP	L_2	7.10^5 bit
The energy conversion efficiency	H	0.6
The power allocation ratio	P	0–1
The time - switching ratio	Δ	0–1

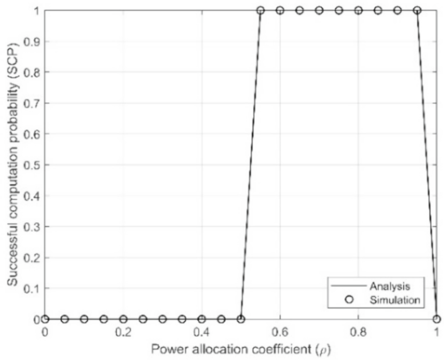

Fig. 3. SCP vs. the power allocation coefficient

elements to 30. Let ξ be the ratio of the number transmission element and reflection element. The simulation results clearly show the superiority of STAR-RIS over fully direct transmission IRS ($N_2 = 0$) or fully reflective transmission IRS ($N_1 = 0$). Indeed, with the ξ indexes other than 0 and 1, STAR-RIS brings outstanding performance to the proposed RF EH NOMA-based MEC system. To implement the system in the real world, we need an optimal algorithm to ensure that the number of elements on the RIS is set appropriately for the system to reach its maximum value.

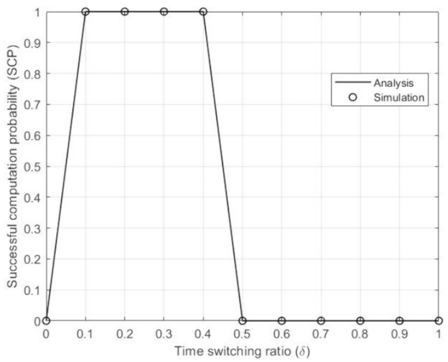

Fig. 4. SCP vs. time switching ratio

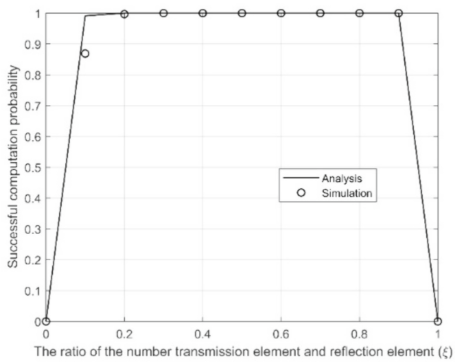

Fig. 5. SCP vs. the ratio of the number of transmission elements and reflection element

Figures 3, 4, and 5 demonstrate a consistent match between the simulated values and the computational theory, providing evidence for the correctness of our study.

5 Conclusion

In this paper, we have analyzed the system performance of an RF EH STAR-RIS-aided NOMA MEC network by deriving the closed-form expression for system SCP. Specifically, the system includes a STAR-RIS, which can flexibly control the number of transmission and reflection elements to assist a single user in harvesting radio energy from the HAP and offloading its task to the MEC servers. Accordingly, the 4-phase operation protocol ensures the system delay time is proposed. We investigated the impact of system parameters on the SCP. The numerical results have shown that the system performance can be improved by selecting an optimal value of the power allocation coefficient, the time switching ratio, or the ratio of the number transmission element and reflection element of STAR-RIS. The optimization problem will be solved in our future work.

Acknowledgment. This research is funded by Vietnam National Foundation for Science and Technology Development (NAFOSTED) under grant number 102.04-2021.11.

Appendix A: Proof of Theorem 1

$$\begin{aligned}
\Phi_s &= \Pr\left(\max\left\{\frac{L_1}{C_1}+\frac{c_1L_1}{f_1},\ \frac{L_2}{C_2}+\frac{c_2L_2}{f_2}\right\} < T_{th}-\tau_1\right)\\
&= \Pr\left(\frac{L_1}{C_1}+\frac{c_1L_1}{f_1} < T_{th}-\tau_1,\ \frac{L_2}{C_2}+\frac{c_2L_2}{f_2} < T_{th}-\tau_1\right)\\
&= \Pr\left(\frac{L_1}{C_1} < \Omega_1,\ \frac{L_2}{C_2} < \Omega_2\right)\\
&= \Pr\left(\frac{\rho a\gamma_0 V_t^2}{(1-\rho)a\gamma_0 V_t^2+1} > 2^{\frac{L_1}{W\Omega_1}}-1,\ (1-\rho)a\gamma_0 V_t V_r > 2^{\frac{L_2}{W\Omega_2}}-1\right)\\
&= \Pr\left(\left[\rho-(2^{\frac{L_1}{W\Omega_1}}-1)(1-\rho)\right]a\gamma_0 V_t^2 > 2^{\frac{L_1}{W\Omega_1}}-1,\ V_r > \frac{2^{\frac{L_2}{W\Omega_2}}-1}{(1-\rho)a\gamma_0 V_t}\right)\\
&= \begin{cases} 0, & 2^{\frac{L_1}{W\Omega_1}}-1 > \frac{\rho}{1-\rho}\\ \Pr\left(V_t > b_1, V_r > \frac{b_2}{V_t}\right), & 2^{\frac{L_1}{W\Omega_1}}-1 < \frac{\rho}{1-\rho}\end{cases}\\
&= \begin{cases} 0, & 2^{\frac{L_1}{W\Omega_1}}-1 > \frac{\rho}{1-\rho}\\ \int\limits_{b_1}^{\infty}\left[1-F_{V_r}\left(\frac{b_2}{x}\right)\right]f_{V_t}(x)dx = 1-F_{V_t}(b_1)-\int\limits_{b_1}^{\infty}F_{V_r}\left(\frac{b_2}{x}\right)f_{V_t}(x)dx, & 2^{\frac{L_1}{W\Omega_1}}-1 < \frac{\rho}{1-\rho}\end{cases}
\end{aligned} \tag{A.1}$$

By substituting (13) and (14) into the above equations, after some manipulations and by applying the Gaussian-Chebyshev quadrature method, we obtain the result as (16). This concludes our proof.

References

1. Wang, C.-X., et al.: On the road to 6G: visions, requirements, key technologies, testbeds. IEEE Commun. Surv. Tutor. **25**(2), 905–974 (2023). https://doi.org/10.1109/COMST.2023.3249835
2. Akbar, A., Jangsher, S., Bhatti, F.A.: NOMA and 5G emerging technologies: a survey on issues and solution techniques. Comput. Netw. **190**, 107950 (2021)
3. A survey on IRS NOMA integrated communication networks. https://doi.org/10.1007/s11235-022-00898-y. Accessed 21 Aug 2023
4. Du, J., et al.: When Mobile-Edge Computing (MEC) Meets Nonorthogonal Multiple Access (NOMA) for the Internet of Things (IoT): system design and optimization. IEEE Internet Things J. **8**(10), 7849–7862 (2020)
5. Li, X., Liu, Z., Dong, X., Yue, X., Tang, W.: Performance analysis of IRS-aided cooperative NOMA-MEC system. IET Commun. **16**(16), 1934–1945 (2022)
6. Ha, D.-B., Truong, V.-T., Lee, Y.: Performance analysis for RF energy harvesting mobile edge computing networks with SIMO/MISO-NOMA schemes. EAI Endors. Trans. Ind. Netw. Intell. Syst. **8**(27), e2 (2021)

7. Nguyen, M.T., Nguyen, C.V., Tran, H.T., Viola, F.: Energy harvesting for mobile agents supporting wireless sensor networks. Energy Harvest. Syst. (2022). https://doi.org/10.1515/ehs-2022-0086
8. Guo, L., Jia, J., Chen, J., Du, A., Wang, X.: Joint task offloading and resource allocation in STAR-RIS assisted NOMA system. In: 2022 IEEE 96th Vehicular Technology Conference (VTC2022-Fall) , pp. 1–5 (2022). https://doi.org/10.1109/VTC2022-Fall57202.2022.10013059
9. Zhang, Q., Wang, Y., Li, H., Hou, S., Song, Z.: Resource allocation for energy efficient STAR-RIS aided MEC systems. IEEE Wirel. Commun. Lett. **12**(4), 610–614 (2023). https://doi.org/10.1109/LWC.2023.3236411
10. Qin, X., Song, Z., Hou, T., Yu, W., Wang, J., Sun, X.: Joint resource allocation and configuration design for STAR-RIS-enhanced wireless-powered MEC. IEEE Trans. Commun. **71**(4), 2381–2395 (2023). https://doi.org/10.1109/TCOMM.2023.3241176
11. Truong, V.-T., Vo, M.-T., Ha, D.-B.: Performance analysis of mobile edge computing network applied uplink NOMA with RF energy harvesting. In: Vo, N.-S., Hoang, V.-P., Vien, Q.-T. (eds.) INISCOM 2021. LNCS, vol. 379, pp. 57–72. Springer, Cham (2021). https://doi.org/10.1007/978-3-030-77424-0_6
12. Truong, V.-T., Ha, D.-B., Truong, T.-V., Nayyar, A.: Performance analysis of RF energy harvesting NOMA mobile edge computing in multiple devices IIoT networks. In: Vo, N.-S., Vien, Q.-T., Ha, D.-B. (eds.) INISCOM 2022, pp. 62–76. Springer, Cham (2022). https://doi.org/10.1007/978-3-031-08878-0_5

Stiffness Prediction of 3D Printed Lattice Designs with Continuous Carbon Fibers Based Polylactic Acid Resin

Nguyen Ba Thuan[1], Van Du Nguyen[2], Ngo Nhu Khoa[3], Nguyen Thi Thu Dung[4], Vu Van Dam[2], Nguyen Quoc Tuan[5], Nguyen Dang Viet[6], Khairul Salleh Basaruddin[7], and Tien-Dat Hoang[5](✉)

[1] Faculty of Mechanical Engineering, Vinh University of Technology Education, Vinh, Vietnam
[2] Thai Nguyen University, Thai Nguyen, Vietnam
[3] Faculty of Mechanical Engineering, Thai Nguyen University of Technology, Thai Nguyen, Vietnam
[4] Faculty of Mechanical, Electrical and Electronic Technology, Thai Nguyen University of Technology, Thai Nguyen, Vietnam
[5] Research Development Institute of Advanced Industrial Technologies (RIAT), Thai Nguyen University of Technology, Thai Nguyen, Vietnam
hoangdat@tnut.edu.vn
[6] Faculty of International Training, Thai Nguyen University of Technology, Thai Nguyen, Vietnam
[7] Faculty of Mechanical Engineering and Technology, Universiti Malaysia Perlis, Arau, Malaysia

Abstract. This research paper explores the influence of infill patterns on the tension and compression strength of 3D printed parts using polylactic acid (PLA) material. The study utilized an ASTM D638 and 50 × 50 × 50 mm cube as investigated models with three different infill patterns in each case. The infill patterns that were investigated included line lattice (0/0), grid (0/90), grid (−45/45), and triangle (−30,30). The ASTM D638 models will be tested by tension force whereas the cubic models will be tested by compression force. The results of the study showed that the infill pattern, line (0/0) in case of ASTM D638 and triangle (−30/30) in case of the cube, provided higher tension and compression strength compared to other patterns. It was revealed that each pattern's microstructure is a crucial factor determining the mechanical properties of the printed parts. The findings of this study suggest that selecting the appropriate infill pattern could enhance the mechanical performance of 3D printed parts made from PLA material. Additionally, this research provides valuable insights into how selecting different infill patterns could influence the tension and compression strength of 3D printed parts produced from PLA material. Moreover, combining continuous carbon fiber (CCF) reinforcement with PLA resin can greatly enhance the strength of the models. It is the first step to expand the application of 3D printed parts with CCF.

Keywords: Additive manufacturing · Printing lattice · Continuous Carbon Fiber · Stiffness prediction · Finite element method

D. C. Nguyen et al. (Eds.): ICERA 2023, LNNS 944, pp. 449–457, 2024.
https://doi.org/10.1007/978-3-031-62235-9_45

1 Introduction

3D printing, commonly referred to as additive manufacturing, is a cutting-edge manufacturing process that makes it possible to produce intricate objects with extreme precision and adaptability. Numerous industries, including aerospace, biomedicine, automotive, and consumer goods have used this technology. The qualities and behaviors of the printed parts in 3D printing are greatly influenced by the lattice structure [1] or reinforcement [2]. A regular configuration of joined struts that create a porous network inside the printed item is referred to as a lattice structure. The internal architecture of the part is shaped by the lattice structure, which also affects the mechanical, thermal, and surface characteristics. Researchers and experts in the industry have paid close attention to the lattice structure because of its potential to improve the functionality of 3D printed products. Over solid pieces, the lattice structure has a number of advantages, including lighter weight, better energy absorption, and a larger surface area (which can help with cooling or fluid movement). Furthermore, by adjusting the geometry and topology of the struts, lattice structures can be created to have particular mechanical characteristics like stiffness, strength, and damping. A variety of lattice patterns, including conventional lattices such as cubic, tetrahedral, and octahedral, atypical lattices, and biomimetic lattices, can be used in 3D printing [3]. The qualities of the material, printing settings (such as layer thickness, infill density, and printing speed), and post-processing methods (such as annealing or surface polishing) all affect how well the lattice structure performs [4]. Thus, in addition to the development of various analytical and numerical methods for the design of lattice structures, the characterization of a wide range of lattice configurations produced using various 3D printing methods such as fused deposition modeling (FDM) stereolithography (SLA), jet fusion, and selective laser sintering (SLS) is currently a very active research topic. Due to the acceptable accuracy and price of FDM technique, it is often used in creating self-supporting, functional micro lattice structures with a wide range of unit cell types.

Several research have evaluated the compressive behavior of four different types of body centered cubic lattices produced using FDM and investigated the influence of geometric aspects in these lattices. Recognizing the impact of vertical support struts on the mechanical characteristics of lattice structures, stiffness, failure loads, and energy absorption capacity under quasi-static compression were reported. Likewise, produced and examined body-centered cubic lattices [5, 6]. The results of compressive tests showed that manufacturing process irregularities in the struts cause lower mechanical properties of polymer lattice structures. Some other researches investigate the effects of cell size, strut cross-section shape and area, cell arrangement, and strut filleting on the behavior of the structures [7, 8]. The impact of the variables and their interactions were studied using a factorial design of experiments, which showed that strut thickness and cell width had the biggest impacts on the plateau stress and energy absorption capacity and characterized the compressive behavior of various miniature lattice structures made using FDM. Several studies have looked into ways to forecast how strut abnormalities may affect the mechanical response of lattices, they are thought to be an inevitable byproduct of the 3D printing processes [9]. However, research on prediction the stiffness of structures with different lattices made with FDM and continuous carbon fibers is also quite rare. The prediction can help designer reduce failed printing, cost and improve the quality of printed parts.

In this paper, the stiffnesses of two printed cases with different lattices and materials are predicted. The finite element method is applied to solve six 3D printing models using materials PLA, PLA with continuous carbon fibers. In each case study, three lattices including solid, triangle, grid with the same infill density, layer thickness, and printing process parameters are simulated to predict their stiffnesses and peak loads. The results show that the lattice pattern has significant effect on the printed stiffness. Moreover, the lattice printed by carbon continuous fibers can highly improve the stiffness and peak load of the printing structure. It can extend the application of FDM printing for fabricating not only prototype models but also end-using parts.

2 Printing Models

Two case studies including ASTM-D638 models and cubic models with volume 50 $\times$ 50 $\times$ 50 mm designed by Solidworks software and used for the simulation. The software Aura of Anisoprint and Cura of Ultimake Company, printing slicers, were used to generate the lattice patterns with the selected printing parameters in each case study. This software can simulate and show the printed model like the same real printed model. Thus, based on that results, the 3D model will be design by Solidwork with nearly the same real printed model. PLA and PLA combining with CCF are used for these simulation. The material properties are given in Table 1. Additionally, the printing process parameters are provided in Table 2. With each case study, the infill density and lattice pattern are design defferently. The layer height is different from plastic printing and fiber printing because the diameter of CCF bundle is 0.36 mm. If this height is smaller than 0.34, the bundle is stretched out and ragged. To keep the fiber bundle strongly bonded together, the printing speed of CCF bundle is slower than the normal plastic printing speed.

Table 1. Printing material properties

Material	Young's modulus (GPa)	Poisson ratio	Density (g/cm^3)	Elongation at break (%)	Tensile strength (MPa)
PLA - ESUN	2.69	0.35	1.24	12	35
Continuous carbon fiber (CCF) - Anisoprint	150	0.26	1.45	–	2200

2.1 Model 1 (ASTM D638)

Three ASTM D638 models are selected for the first case study as show in Fig. 1. All printed models are printed along with the glass plate to achieve good bonding between

Table 2. Printing process parameters

CCF layer thickness (mm)	PLA layer thickness (mm)	CCF printing speed (mm/s)	PLA printing speed (mm/s)	CCF temperature (°C)	PLA temperature (°C)
0.36	0.15	20	60	250	200
Buiding plate temperature (°C)	CCF line width (mm)	PLA line width (mm)	Flowrate (%)	Wall line of model 1 (−)	Wall line of model 2 (−)
50	0.8	0.4	100	5	3

them and the plate. Aura software was used to slice the 3D models of specimens. This software allows for the generation of the different raster, infill, and fiber patterns such as solid, triangle, insogrid, anisogrid, etc. Especially, it can combine two patterns within layers to create complex lattices. The direction of fibers can be set at any given angle. The fiber path is controlled to avoid being close to the specimen wall whereas the fiber volume still is qualified. Figure 2 shows a schematic view of three specimens including pure solid plastic infill (model 1.1), +45/−45 fiber infill patterns (model 1.2), and unidirectional fiber infill (model 1.3). Figure 2 also shows the simulation of three printed models which can be used to 3D redesign in Solidworks software. The material properties and printing process parameters are used as in Tables 1 and 2. These models are imported to Abaqus software for solving finite element problems. The masses of models 1.1, 1.2, and 1.3 are 25 g, 15 g, and 30 g, respectively.

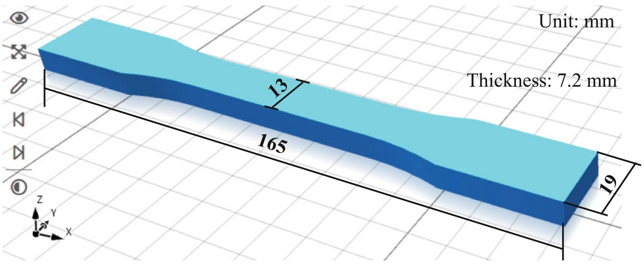

Fig. 1. ASTM – D638 model

2.2 Model 2 (Cubic Box)

For the second case study, three cubic boxes with different infill lacttice including triangle with −60/60 raster (model 2.1), grid with 0/90 raster (model 2.2), and grid with −45/45 raster (model 2.3). Each model has 10% infill density, three wall line, and double line infill. The simulated printing models in Cura software are showed in Fig. 3. These models are also redesign by Solidwork software and imported to Abaqus software for solving finite element problems. The material properties and printing process parameters are

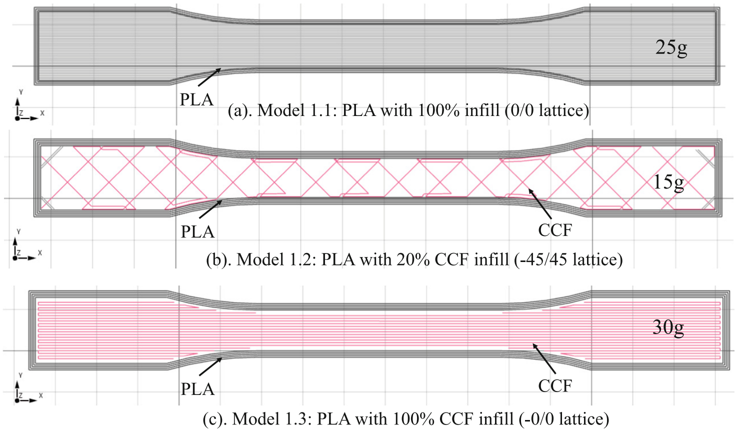

Fig. 2. Slicing structures of three models

used as in Tables 1 and 2. The masses of model 2.1, 2.2, 2.3 are 43 g, 39 g, and 41 g, respectively.

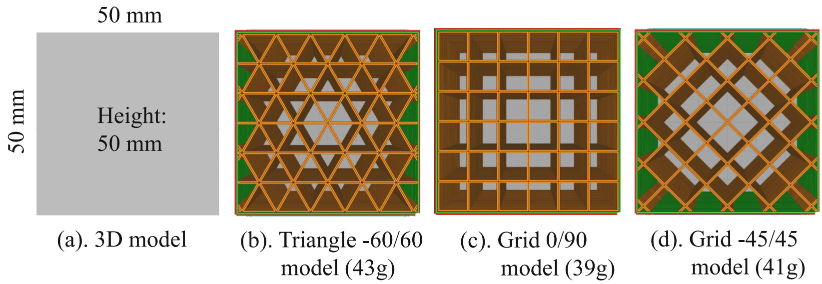

Fig. 3. Cubic models with three slicing lattice structures

3 Simulation and Results

3.1 Case Study 1 (ASTM D638)

The stiffness and deformation of models are solved by Abaqus software. The tetrahedral element is used for meshing process. The von Mises stress of model 1.1 (13,422 elements 28,446 nodes), model 1.2 (10,422 elements 22,087 nodes), and model 1.3 (6,711 elements 14,223 nodes) have showed in Fig. 4. The model 1.2 with +45/−45 fiber infill patterns is cut a haft to see the deformation of the printing model with CCF and PLA. Figure 5 shows the load-displacement curve. It can be pointed out that the CCF significant increase the stiffness and the load peak of the printing model, especially due to the longitudinal loading.

Form the load-displacement curves, the stiffness of each model can be obtained with 1466 N/mm, 2670 N/mm and 7503 N/mm corresponding to models 1.1, 1.2, and 1.3. *u* is the displacement of the moving crosshead which is set at 5 mm. It obviously shows that the peak load in the case of the model 1.3 is largest. Remarkably, the peak load of the model 1.3 is 16 times larger than that of the specimen 1. It can be pointed out that the printed continuous fiber composite material has significantly higher stiffness or specific stiffness (ration of stiffness over mass) than that of the printed pure plastic material. In further research, a larger number of specimens should be simulated to point out the variability of stiffnesses in all of the cases.

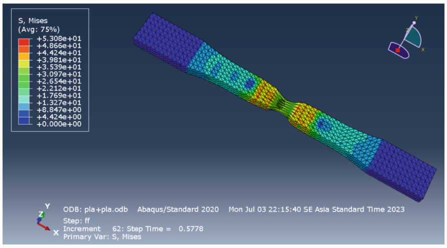

(a). Model 1.1: PLA with 100% infill (0/0 lattice)

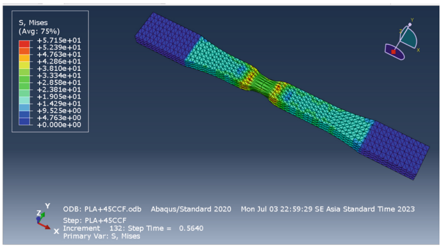

(b1). Model 1.2: PLA with 20% CCF infill (-45/45 lattice)

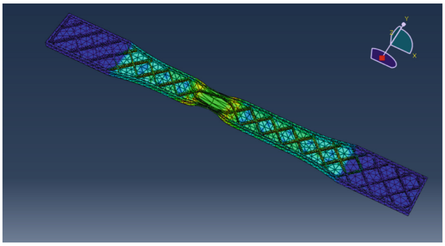

(b2). Model 1.2: PLA with 20% CCF infill (-45/45 lattice)

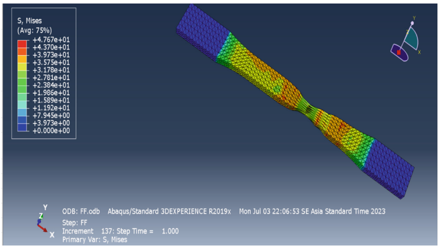

(c). Model 1.3: PLA with 100% CCF infill (-0/0 lattice)

Fig. 4. Von Mises stress and deformed shape of three models under tension loading

3.2 Model 2 (Cubic Box)

Three cubes with different lattices are investigated in the second case study. The hexagonal element is used for meshing. The von Mises stress of three models including model 2.1 (26,925 elements 37,934 nodes), model 2.2 (7,525 elements 13,832 nodes), and model 2.3 (14,200 elements 21,840 nodes) have showed in Fig. 6.

The load-deformation curves for compression testing of the three lattice designs are shown in Fig. 7. A vertical load was applied to the top surface of each model to imitate the compressive testing. The compression deformation is set 2 mm. In contrast to the load-deformation curves for models 2.2 and 2.3, which were rapidly failed and stopped saving data, the load-deformation curve for model 2.1 exhibited longer and revealed a higher stiffness. Peak loads were seen at 3,200 N for model 2.1, 4,500 N for model 2.2, and 86,000 N for model 2.3. Additionally, the stiffnesses of three models are calculated with 7.1 KN/mm (model 2.1), 5.8 KN/mm (model 2.2), and 6.3 KN/mm (model 2.3).

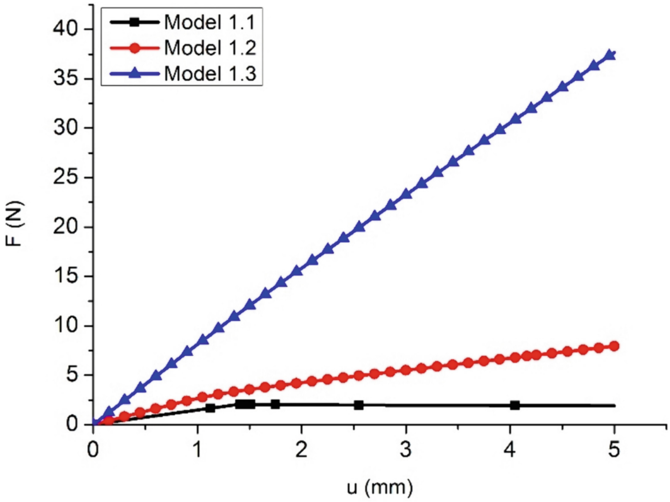

Fig. 5. Load and displacement curve

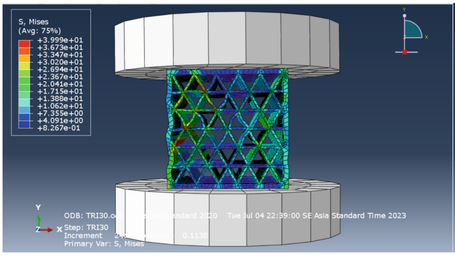

(a). Model 2.1

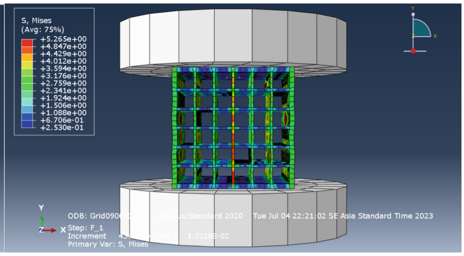

(b). Model 2.2

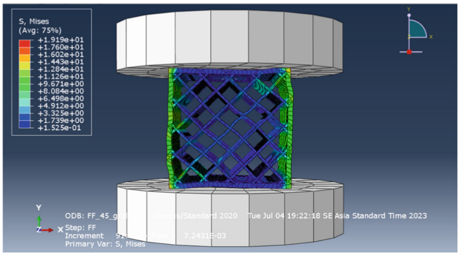

(c). Model 23

Fig. 6. Von Mises stress of three deformed models

Figure 7 depicts the three models' distorted configurations at a loading step right before their peak loads. The three models underwent various forms of deformation and failure, as shown in the images. The vertical collapse failure mode of model 2.3 was characterized by homogenous distortion across the structure. The maximum load-carrying capability was demonstrated by model 2.1. Figure 7 also displays significant local buckling in the diagonal strut.

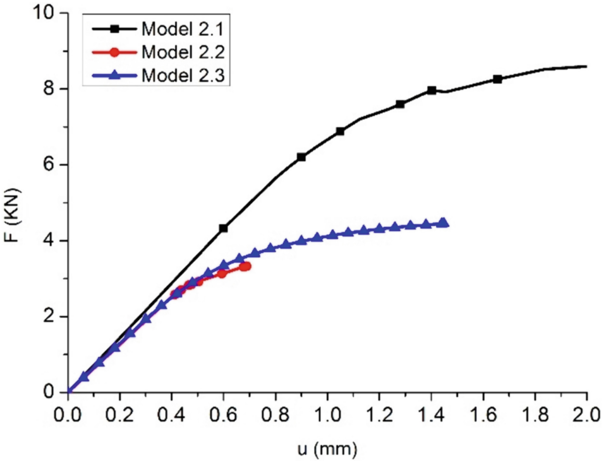

Fig. 7. Load and deformation curve

4 Conclusion

In this study, we looked at how different infill patterns affected how 3D-printed structures behaved in tension and compression. To do this, we investigated the outcomes of six distinct models including three models for tension (ASTM-D638 model) and three ones for compression tests (cubic model) with various infill patterns. The abilities of continuous fiber printing technology, different lattices in the tensile performances of printed materials are investigated for the first case study of ASTM D638 samples. Three presented models have pure solid plastic infill (model 1.1), +45/−45 fiber infill patterns with 20% of fiber volume fraction (model 1.2), and unidirectional fiber infill (model 1.3), respectively. It was shown that model 1.3 has a peak load of around 16 times larger than that of model 1.1.

In the second case study, three lattices of cubic models were preformed. The model 2.1, triangle (−60/60) infill design, in particular, had the best overall load-carrying capability but also had considerable local buckling vulnerability, as we specifically discovered. In contrast, the infill patterns for the model 2.2-grid (0/90) and model 2.3-grid (−45/45) and patterns showed a comparable mode of deformation and cause of failure, but had a lower total load-carrying capacity than the model 2.1 design. These findings have significant ramifications for sectors like aircraft and automobile, where cost-effective, lightweight, yet sturdy constructions are needed to increase fuel economy. Our research suggests that in order to maximize the structural performance and effectiveness of the building, the infill pattern used for a 3D-printed structure should be specifically adapted depending on the application requirements. In conclusion, this work offers insightful information on how infill patterns affect the compressive behavior of 3D-printed structures. The impact of other design elements, such as layer height, material characteristics, and printing orientation, on the structural performance of 3D-printed structures has to be further studied by doing both simulation and experiment.

Acknowledgement. This research was funded by the Vietnam Ministry of Education and Training, grant number B2022-TNA-27. The authors would also like to express their thanks to Thai Nguyen University of Technology (TNUT) for supporting the research.

References

1. Bhandari, S., Lopez-Anido, R.: Finite element modeling of 3D-printed part with cellular internal structure using homogenized properties. Prog. Additive Manuf. **4**, 143–154 (2019)
2. Kumar, P.N., Rajadurai, A., Muthuramalingam, T.: Thermal and mechanical behaviour of submicron sized fly ash reinforced polyester resin composite. Mater. Res. Exp. **5**(4), 045303 (2018)
3. Niutta, C.B., et al.: Defect-driven topology optimization for fatigue design of additive manufacturing structures: application on a real industrial aerospace component. Eng. Fail. Anal. **142**, 106737 (2022)
4. Wickramasinghe, S., Do, T., Tran, P.: FDM-based 3D printing of polymer and associated composite: a review on mechanical properties, defects and treatments. Polymers **12**(7), 1529 (2020)
5. Ngo, T.D., Kashani, A., Imbalzano, G., Nguyen, K.T., Hui, D.: Additive manufacturing (3D printing): a review of materials, methods, applications and challenges. Compos. B Eng. **143**, 172–196 (2018)
6. Lozanovski, B., et al.: A Monte Carlo simulation-based approach to realistic modelling of additively manufactured lattice structures. Additive Manuf. **32**, 101092 (2020)
7. Peng, C., Tran, P., Nguyen-Xuan, H., Ferreira, A.J.M.: Mechanical performance and fatigue life prediction of lattice structures: parametric computational approach. Compos. Struct. **235**, 111821 (2020)
8. Zhu, J., Zhou, H., Wang, C., Zhou, L., Yuan, S., Zhang, W.: A review of topology optimization for additive manufacturing: status and challenges. Chin. J. Aeronaut. **34**(1), 91–110 (2021)
9. Goh, G.D., Sing, S.L., Yeong, W.Y.: A review on machine learning in 3D printing: applications, potential, and challenges. Artif. Intell. Rev. **54**(1), 63–94 (2021)

Study of the Lateral Displacement of the Bus in Crosswind Conditions

Minh-Hoang Trinh[1](✉), Tien-Quyet Do[2], Duy-Suy Pham[3], Phuc-Hoa Tran[4], and Trong-Hoan Nguyen[1]

[1] Hanoi University of Science and Technology, Hanoi, Vietnam
hoang.trinhminh@hust.edu.vn
[2] Sao Do University, Hai Duong, Vietnam
[3] Vietnam Academy of Science and Technology, Hanoi, Vietnam
[4] Hanoi University of Industry, Hanoi, Vietnam

Abstract. With its large size, aerodynamic forces and moments will significantly affect the vehicle's stability when a bus moves in high wind. Therefore, studying the instability in general and the lateral displacement in particular of buses in crosswind conditions is a matter of concern. This paper focuses on studying the motion stability of a bus in the condition of crosswind, in which the aerodynamic forces and moments acting on the bus are determined by the simulation method of one source wind. The system of dynamic equations describing a bus's motion in crosswind conditions is used to evaluate the instability of the vehicle's motion, mainly to evaluate the lateral displacement of the vehicle in the following conditions: the bus speed and wind speed change. The authors used Ansys Fluent software in calculating aerodynamic forces and moments and used numerical simulation using Matlab Simulink in analyzing the motion instability of the bus. The results allow us to evaluate the level of bus lane deviation in road conditions in Vietnam.

Keywords: bus · crosswind · instability · lateral displacement

1 Introduction

Nowadays, the speed of road vehicles is increasing rapidly; when the bus moves at high speed in high wind conditions, the lateral force and yaw torque increase significantly. At that time, aerodynamic forces were one of the leading causes of vehicle instability, such as lateral displacement, body vehicle rotation, and changes in vehicle load distribution [1].

When studying the movement of the bus in crosswind conditions, scientists often divide crosswinds into unsteady wind and steady wind. A steady crosswind is valid, and the direction of the velocity does not change with time. When calculating in a steady crosswind condition, the vehicle body will be affected simultaneously by two wind sources: the wind source due to the air resistance caused by the vehicle's movement and the crosswind. Then, an equivalent wind source can be used instead [1]. Author

D. C. Nguyen et al. (Eds.): ICERA 2023, LNNS 944, pp. 458–464, 2024.
https://doi.org/10.1007/978-3-031-62235-9_46

Takuji Nakashima (2013) proposed to simulate a truck's motion with two wind sources: a front wind source and a side wind source [2]. This model needs a massive amount of computation, so it takes a lot of time and resources from the computer. The crosswind model of author Youhanna E. Williams (2013) used a simulation method where a wind source has a direction of the wind relative to the bus (β_{win}) [3]. When using an equivalent wind source, the computation will be significantly reduced compared to the simulation problem using two wind sources while still ensuring the necessary accuracy. Therefore, the authors choose the source wind model to simulate crosswind in this paper.

There are many methods to evaluate the vehicle's motion stability in crosswind conditions, such as using specialized software or building and solving equations describing vehicle dynamics in crosswind conditions, where aerodynamic force and torque values are important input parameters. Author Z. Zhang uses the TruckSim software to calculate the stability of the heavy truck's motion in crosswind conditions [4]. In another study, author X. Zhang used building and solving equations to describe vehicle dynamics in crosswind conditions [5]. In this paper, the authors use the method of constructing and solving the equations describing the dynamics to evaluate the motion stability of the bus through the assessment of the lateral displacement in the vehicle in crosswind conditions. The aerodynamic forces and torque are calculated when the origin is the vehicle's center of gravity [6].

2 Calculation of Aerodynamic Forces and Torques

In Vietnam, buses are widely used in long-distance passenger transport. Thaco bus HB120SL-H380R-14, as shown in Fig. 1, was selected as the research object. A source wind simulation model is selected to calculate the aerodynamic forces and torques acting on a bus in crosswind conditions. In the article, the authors will simulate the determination of aerodynamic forces and moments at the vehicle's center of gravity to facilitate the study of vehicle dynamic instability. The simulated condition is crosswind velocity V_{win} varying from 36 to 120 km/h; the wind's angle β_{win} relative to the bus varies from 1 °C to 90 °C.

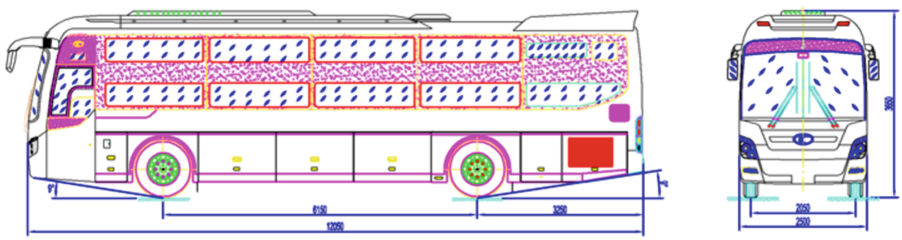

Fig. 1. Thaco bus HB120SL-H380R-14

This paper uses Ansys Fluent software to simulate aerodynamics [7]. Figure 2 shows the value of aerodynamic forces and moments according to the wind velocity values (V_{win}) and the wind's angle relative to the bus (β_{win}) changes [6, 7]. Aerodynamic forces and moments, including F_{wx}, F_{wy}, and F_{wz}, are aerodynamic forces along three axes x, y, z; M_{wx}, M_{wy}, and M_{wz}, are the aerodynamic moments that cause the body to rotate around the x, y, and z axes. These forces and moments are the essential input parameters to calculate the dynamic stability in the following section.

The results in Fig. 2 show that as wind speed (V_{win}) increases, aerodynamic forces and moments increase. As the wind's angle (β_{win}) increases, most of the aerodynamic forces and moments increase (for F_{wy}, F_{wz}, M_{wx}, and M_{wz}). However, the results for vertical force (F_{wx}) and moment about the horizontal axis (M_{wy}) differ. They increase as β_{win} increases from 0 °C to 60 °C, then gradually decrease. This rule is because the size of the bus causes the front resistance area of the vehicle compared to the wind direction to increase from 0 °C to 60 °C gradually, then gradually decrease.

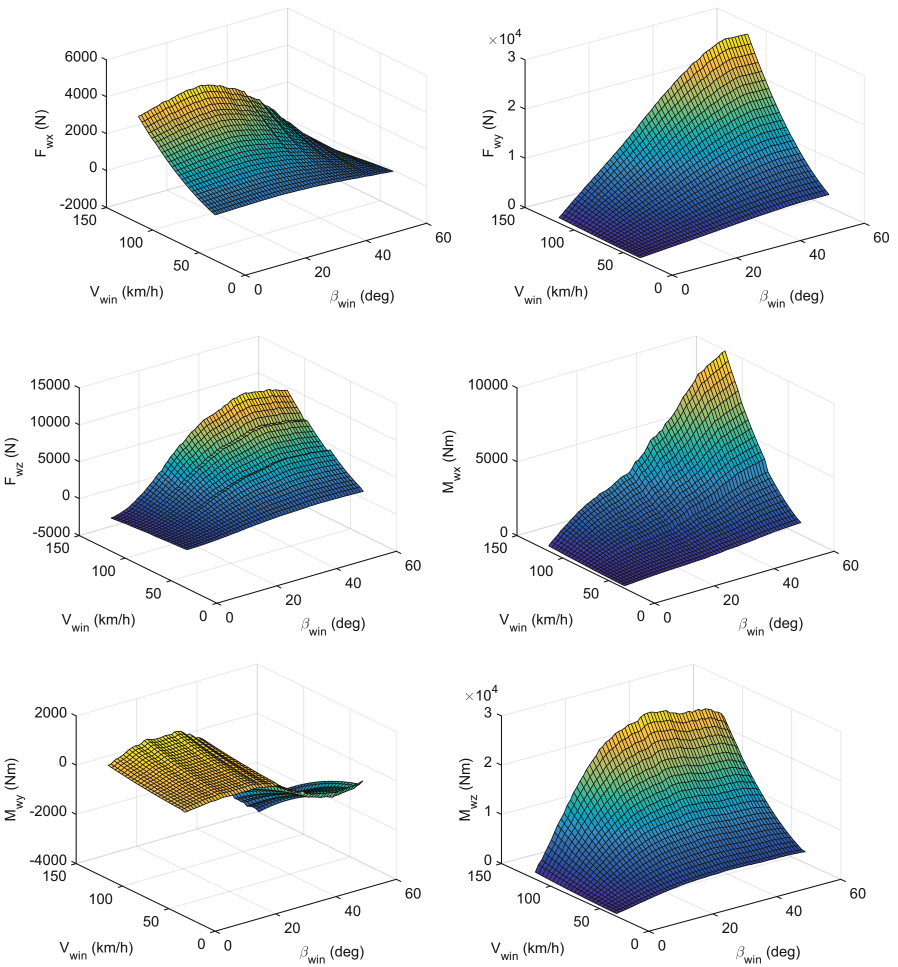

Fig. 2. Aerodynamic forces and moments acting on the bus when the velocity of crosswind and wind's angle relative to the bus change

3 Dynamic Models of the Bus

The system of differential equations describing the bus dynamics is built by separating objects and placing external forces on each object. These equations are established by balancing forces and moments acting on the body, and this is more explicit by considering the dynamical model in projection planes.

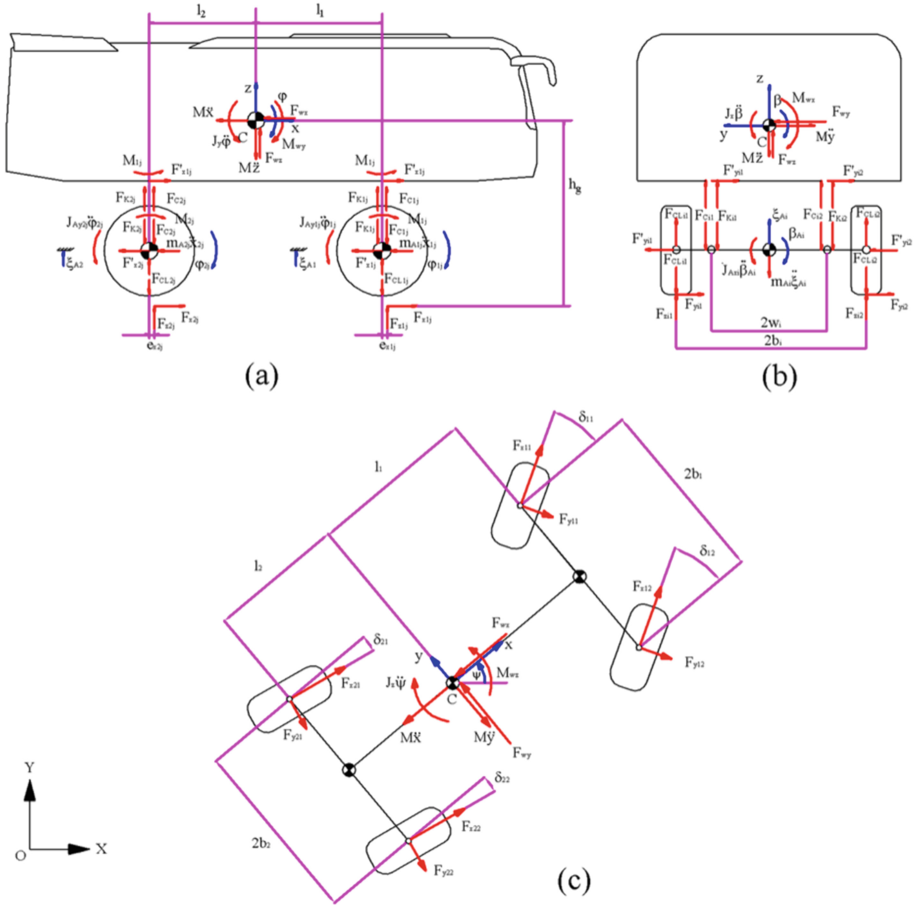

Fig. 3. Forces and moments acting on the bus: (a) in the longitudinal plane; (b) in the horizontal plane; (c) in a plane parallel to the road surface.

Figure 3 illustrates the forces and moments acting on the bus in the longitudinal, horizontal, and plane parallel to the road surface, respectively. OXYZ is the ground coordinate system, while Cxyz is the relative coordinate system located at the vehicle's center of gravity. The total mass of the vehicle (including the sprung mass and the unsprung mass) performs three motions: longitudinal (x), horizontal (y), and rotation about the vertical axis (ψ, được tính b`ăng góc quay giưa Cx v´ơi OX) (Fig. 3c). In the longitudinal plane (xCz) (Fig. 3a), the sprung mass is characterized by a mass m located at the center of gravity of the vehicle C. This center of gravity performs two motions: the vertical displacement (z) and the pitch angle (φ). J_x, J_y, and J_z are the mass moments of inertia of the vehicle body about the longitudinal x-axis, the horizontal y-axis, and the vertical z-axis. In the horizontal plane (size, Fig. 3b), the sprung mass's different motion is rolled (β). Each unsprung mass i (i = 1 with the front axle, j = 2 with the rear axle) has mass m_{Ai} which has two motions, vertical displacement (ξ_{Ai}) and roll angle (β_{Ai}), J_{Axi} is the moment of inertia of the sprung masses around the x-axis. F_{Cij} and F_{Kij} are the elastic and damping forces of the suspension system near the ijth wheels. These forces are determined from the upper and lower displacements of the suspension. The reactions forces from the road surface F_{CLij} and F_{xij}, F_{yij}, and F_{zij} are determined by the tire model. δ_{ij} is the slip angle of the ijth wheels. F_{wx}, F_{wy}, and F_{wz} are aerodynamic drag force, aerodynamic side force, and aerodynamic lift force. M_{wx}, M_{wy}, and M_{wz} are aerodynamic moments causing the body to rotate around the x, y, and z axes.

$$
\begin{aligned}
M\ddot{x} &= F_{x11}\cos\delta_{11} + F_{y11}\sin\delta_{11} + F_{x12}\cos\delta_{12} + F_{y12}\sin\delta_{12} \\
&\quad + F_{x21}\cos\delta_{21} - F_{y21}\sin\delta_{21} + F_{x22}\cos\delta_{22} - F_{y21}\sin\delta_{21} - F_{wx} + M\dot{\psi}\dot{y} \\
M\ddot{y} &= F_{x11}\sin\delta_{11} - F_{y11}\cos\delta_{11} + F_{x12}\sin\delta_{12} - F_{y12}\cos\delta_{12} \\
&\quad - F_{x21}\sin\delta_{21} - F_{y21}\cos\delta_{21} - F_{x22}\sin\delta_{22} - F_{y22}\cos\delta_{22} + F_{wy} - M\dot{\psi}\dot{x} \\
J_z\ddot{\psi} &= b_1(-F_{x11}\cos\delta_{11} - F_{y11}\sin\delta_{11} + F_{x12}\cos\delta_{12} + F_{y12}\sin\delta_{12}) \\
&\quad + b_2(-F_{x21}\cos\delta_{21} + F_{y21}\sin\delta_{21} + F_{x22}\cos\delta_{22} - F_{y22}\sin\delta_{22}) \\
&\quad + l_2(F_{x21}\sin\delta_{21} + F_{y21}\cos\delta_{21} + F_{x22}\sin\delta_{22} + F_{y22}\cos\delta_{22}) \\
&\quad + l_1(F_{x11}\sin\delta_{11} - F_{y11}\cos\delta_{11} + F_{x12}\cos\delta_{12} - F_{y12}\cos\delta_{12}) + M_{wz} \\
m\ddot{z} &= F_{C11} + F_{K11} + F_{C12} + F_{K12} + F_{C21} + F_{K21} + F_{C22} + F_{K22} + F_{wz} \\
J_y\ddot{\varphi} &= -l_1(F_{C11} + F_{K11} + F_{C12} + F_{K12}) + l_2(F_{C21} + F_{K21} + F_{C22} + F_{K22}) - (M_{1j} + M_{2j}) \\
&\quad - (h_g - r_1)(F_{x11}\cos\delta_{11} + F_{y11}\sin\delta_{11} + F_{x12}\cos\delta_{12} + F_{y12}\sin\delta_{12}) \\
&\quad - (h_g - r_2)(F_{x21}\cos\delta_{21} - F_{y21}\sin\delta_{21} + F_{x22}\cos\delta_{22} - F_{y22}\sin\delta_{22}) + M_{wy} \\
J_x\ddot{\beta} &= (F_{C11} + F_{K11} - F_{C12} - F_{K12})w_1 + (F_{C21} + F_{K21} - F_{C22} - F_{K22})w_2 + M_{wx} \\
m_{A1}\ddot{\xi}_{A1} &= (F_{CL11} + F_{CL12} + F_{KL11} + F_{KL12}) + (F_{C11} + F_{K11} + F_{C12} + F_{K12}) \\
J_{Ax1}\ddot{\beta}_{A1} &= (F_{C12} + F_{K12} - F_{C11} - F_{K11})w_1 + (F_{CL11} + F_{KL11} - F_{CL12} - F_{KL12})b_2 \\
&\quad + (F_{y11}\cos\delta_{11} + F_{x11}\sin\delta_{11} + F_{y12}\cos\delta_{12} + F_{x12}\sin\delta_{12})r_1 \\
m_{A2}\ddot{\xi}_{A2} &= (F_{CL21} + F_{CL22} + F_{KL21} + F_{KL22}) - (F_{C21} + F_{K21} - F_{C22} - F_{K22}) \\
J_{Ax2}\ddot{\beta}_{A2} &= (F_{C22} + F_{K22} - F_{C21} - F_{K21})w_2 + (F_{CL21} + F_{KL21} - F_{CL22} - F_{KL22})b_2 \\
&\quad + (-F_{y21}\cos\delta_{21} - F_{x21}\sin\delta_{21} - F_{y22}\cos\delta_{22} - F_{x22}\sin\delta_{22})r_2 \\
J_{Ayij}\ddot{\varphi}_{ij} &= M_{ij} - \left(F_{xij} + F_{zij}f_{ij}\right)\left[r_{0ij} - \left(h_0 - \xi_{Aij}\right)\right]
\end{aligned}
\tag{1}
$$

The system of equations describing the vehicle's motion includes 14 differential equations shown in formula (1), corresponding to 14 degrees of freedom. They include 6 DOF of sprung mass (x, y, z, β, φ, ψ), 2 DOF of front unsprung mass (ξ_{A1}, β_{A1}), 2 DOF of rear unsprung mass (ξ_{A2}, β_{A2}), and 4 DOF of the wheels (φ_{11}, φ_{12}, φ_{21}, φ_{22}). Besides, a Pacejka tire model is used to determine the longitudinal and lateral forces of the tire. The Pacejka tire model is used to determine the longitudinal and lateral forces of the tire.

4 Assessment of Motion Stability of the Bus in Crosswind Conditions

When the bus moves in high crosswind conditions, the aerodynamic forces and moments can cause instability in the bus's movement. ISO 12021-2010 provides three important parameters when the vehicle moves with crosswind under actual test conditions (without changing the steering angle), including lateral displacement, lateral acceleration, and yaw rate. One of the main criteria to evaluate the stability of a large passenger car is the deviation of the vehicle's trajectory. Therefore, in this paper, the lateral displacement is interesting to be evaluated. Simulation conditions are when the vehicle moves in a straight line at constant speed on a smooth, flat road without changing the steering angle. The bus moves at speeds from 40 to 120 km/h, and the crosswind has a direction perpendicular to the direction of vehicle movement at speeds of 40 to 100 km/h. The simulation time is 5 s. The aerodynamic forces and moments acting on the bus in this case of crosswind (Fig. 4) are determined from the calculation results in Sect. 2.

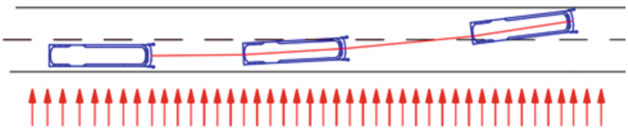

Fig. 4. Simulation diagram of passenger car moving in crosswind conditions.

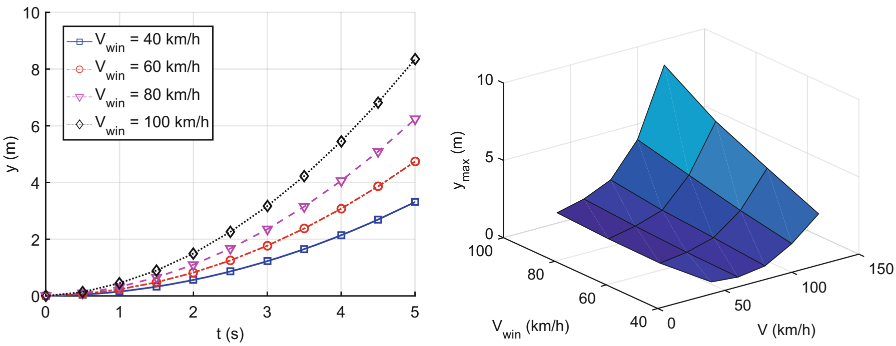

Fig. 5. (a) When the bus moves at 120 km/h, the speed crosswind changes; (b) The max of lateral displacement when the bus speed and wind speed change.

Figure 5a shows the results of the lateral displacement of the bus when moving speed $V_v = 120$ km/h and in the cases where the crosswind speed varies from 40 km/h to 100 km/h in a time survey is 5 s. The results show that when the wind speed increases, the lateral displacement increases rapidly. After 5 s, the maximum lateral displacement when the wind is 40 km/h is 3.83 m. At wind speeds of 60 km/h, 80 km/h, and 100 km/h, the maximum of displacement reached is 4.739 m, 6.2367 m, and 8.348 m, respectively. The width of the lane in Vietnam is 3.75 m, and the width of passenger cars is 2.5 m. Therefore, a lane violation occurs after 5 s when the bus moves at a speed of 120 km/h and different wind levels from 40 km/h to 100 km/h. Figure 5b shows the maximum lateral displacement of the bus according to the values of vehicle movement speed from 40 to 120 km/h and wind speed from 40 to 100 km/h. The results show that when wind and vehicle speed increase, the lateral displacement value increases accordingly.

5 Conclusion

The article has investigated the lateral displacement in case the bus moves at 40 to 120 km/h through the crosswind speed of 40 to 100 km/h. At the same time, a dynamic model has been built to describe the motion characteristics of the bus in crosswind conditions. In the model, the aerodynamic forces and moments acting on the bus are calculated in other CFD models using a source wind simulation method. The results on lateral displacement are of great significance in the problem of assessing lateral displacement of movement, leading to the possibility of lane violation of the vehicle. This result can serve as reference data for building a warning mode for the driver when driving the vehicle in crosswind conditions.

References

1. Hucho, W.H.: Aerodynamics of Road Vehicle, 4th edn. SAE Int, Warrendale (1998)
2. Nakashima, T., Tsubokura, M., Vázquez, M., Owen, H., Doi, Y.: Coupled analysis of unsteady aerodynamics and vehicle motion of a road vehicle in windy conditions. Comput. Fluids **80**(2013), 1–9 (2013)
3. William, Y.E., Mohamed, M.H., Oraby, W.A.H.: Investigation of crosswind aerodynamics for road vehicles using CFD technique. In: Eleventh International Conference of Fluid Dynamics 19–21 December (2013)
4. Zhang, Z., Li, J., Guo, W.: Combined simulation of heavy truck stability under sudden and discontinuous direction change of crosswind with computational fluid dynamics and multi-body system vehicle dynamics software. Adv. Mech. Eng. **10**, 1–10 (2018)
5. Eng, M., Zhang, X.: Crosswind Stability of Vehicles Under Nonstationary Wind Excitation. Doktor der Ingenieurwissenschaften. Karlsruher Institutfür Technologie (2015)
6. Trinh, M.H., Do, T.Q., Nguyen, T.H.: Study on the dynamic instability of a bus in crosswind conditions. J. Sci. Technol. Eng. Technol. Sustain. Develop. **32**(1), 043–051 (2022)
7. Quyet, D.T., Hoan, N.T., Hoang, T.M.: Study on computation of aerodynamic force acting on bus in crosswind conditions by using CFD. In: International Conference on Fluid Machinery and Automation Systems ICFMAS2018, vol. 1, pp. 522–527. Bach Khoa Publishing House, Vietnam (2018)

Technological Factors Contribute to Enhancing Energy Efficiency in Manufacturing Enterprises: Evidence from the Technology of Switching and Restructuring Solar Panel in Viet Nam

Nhung Tang Cam[1(✉)], Tuan Do Anh[2], Kiet Ngo Tuan[3], and Tung-Nguyen Thanh[4]

[1] Thai Nguyen University of Technology, Thainguyen, Vietnam
tangcamnhung@tnut.edu.vn
[2] Thanh Dong University, Hai Duong, Vietnam
[3] Electric Power University, Hanoi, Vietnam
[4] Faculty of Engineering Physics and Nanotechnology, VNU University of Engineering and Technology, Vietnam National University, Hanoi, Vietnam

Abstract. The article delves into the pivotal role of technology in optimizing energy efficiency within the manufacturing business realm. By showcasing a specific example from the technology of switching and restructuring solar energy panel cells, the article underscores the positive impact of advanced technology in enhancing energy utilization. This technology serves to optimize the process of converting sunlight into electrical power while minimizing energy losses. Through the amalgamation of energy efficiency and environmental preservation, the switching and restructuring technology has yielded substantial benefits for businesses, spanning from operational cost reduction to making a positive imprint in environmental conservation. The article encapsulates how the application of advanced technology can significantly contribute to the construction of a sustainable future through intelligent and effective utilization of energy resources.

Keywords: Efficient energy using · Photovoltaic panel · Switching for restructuring

1 Introduction

Nowadays, when energy resources are becoming more precious than ever, and the impacts of climate change are becoming increasingly evident, the use of energy efficiently is a crucial part of global economic progress. Small and medium-sized enterprises (SMEs) play a significant role in promoting energy conservation and environmental protection. They can harness the unlimited potential of solar energy to enhance their production efficiency and minimize negative impacts on the environment.

Why is energy efficiency important for SMEs? The primary benefit is cost savings. In the fiercely competitive business landscape, every opportunity to reduce production

D. C. Nguyen et al. (Eds.): ICERA 2023, LNNS 944, pp. 465–479, 2024.
https://doi.org/10.1007/978-3-031-62235-9_47

and operation costs is invaluable. Utilizing energy efficiently means reducing energy consumption and electricity bills, which can significantly contribute to a business's cost considerations. However, energy savings also offer long-term benefits, improving a business's competitiveness in the market.

In the effort to promote energy savings, solar energy stands out as a prominent factor when applied to the roofs of production workshops and buildings of SMEs. Solar energy, generated from sunlight, is not only a clean and non-polluting energy source but also widely available and free. This helps SMEs reduce their dependence on traditional energy sources and minimize negative environmental impacts.

When applying solar energy to their production activities, SMEs can harness this resource to provide energy for their manufacturing processes, making their business operations more sustainable. Installing solar energy systems not only helps reduce energy costs but also creates a stable and backup energy supply, ensuring that production is not disrupted due to energy supply issues.

Integrating solar energy into their business can become part of their communication and marketing strategy. Customers and partners are increasingly concerned about social responsibility and environmental protection. Using solar energy is not only a significant step in environmental care but also an opportunity to build trust and confidence among customers. Businesses can use their adoption of solar energy as a part of their branding strategy to attract environmentally conscious customers.

Furthermore, using solar energy can bring financial benefits through government policies and incentives. Many countries have implemented solar energy promotion programs by providing financial support, tax reductions, or purchasing excess energy from solar systems. This can help businesses reduce their initial investment costs and quickly recover these investments through energy savings and other benefits.

However, to maximize the potential of solar energy, SMEs in Vietnam need a comprehensive strategy and appropriate investment in suitable systems and equipment. This includes assessing the energy needs of the business, designing suitable solar energy systems, and ensuring the efficient maintenance and operation of these systems.

Alongside the development of solar energy systems, photovoltaic (PV) systems are also being installed in various locations, particularly in areas with abundant sunlight. The continuous relative movement between the sun-facing surface of PV elements and the sun itself leads to fluctuations in power output. Additionally, random shading elements also influence the system's output power. To optimize power output, researchers propose several solutions:

Firstly, controlling the movement of the PV array to follow the sun's trajectory, ensuring that the sunlight direction remains perpendicular to the surface of PV modules. This approach can also involve fixed trajectory tracking over time, or more complex solutions incorporating feedback-based control systems.

Secondly, when the orientation of the fixed PV array is determined, power optimization needs to be achieved through control algorithms based on feedback signals of current and voltage from the PV modules. Numerous Maximum Power Point Tracker (MPPT) algorithms have been studied and applied, such as those in [5, 6]. Algorithms like Incremental Conductance (Inc) and Perturb and Observe (P&O) [1, 3, 4] are frequently used.

The fuzzy adaptive P&O algorithm represents an advancement over traditional P&O, having demonstrated greater efficacy [2, 7–10].

Thirdly, a highly effective solution proposed by the authors in [11] involves restructuring the interconnection of PV modules to optimize the power output of the entire PV array.

2 Factors Influencing the Efficiency of Photovoltaic Panel Power Extraction and Remedial Solutions

2.1 Factors Affecting the Efficiency of Photovoltaic Panel Power Extraction

In practical usage, the operational efficiency of photovoltaic panels is influenced by various external factors. Depending on the real environmental conditions, these diverse factors can diminish both the panel efficiency and the overall system performance. The key factors impacting efficiency are listed as follows (Fig. 1):

– Irradiance (W/m2): The power curves shown above highlight the relationship between irradiance and the electrical output of the panel.

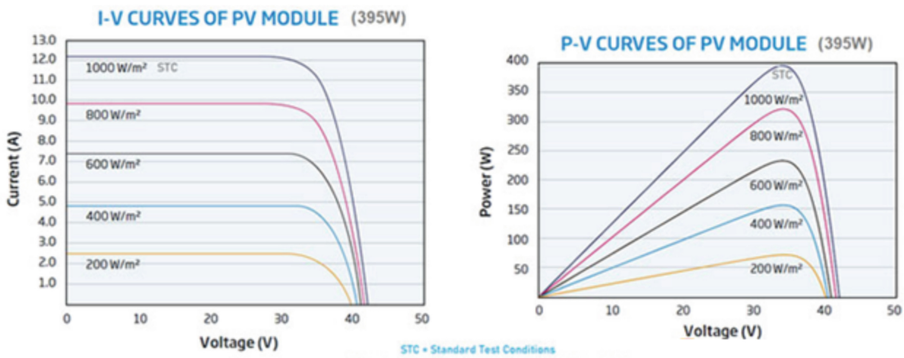

Fig. 1. Current-Voltage and Power Curves of the Solar Panel Dependent on Solar Irradiance

The level of solar irradiance, measured in watts per square meter (W/m2), is influenced by atmospheric conditions such as clouds and fog, latitude, and the time of year.

– Shadowing: Solar cells within a solar panel are interconnected to generate voltage values Voc and Vmp as specified in the panel's datasheet. A system is composed of individual photovoltaic panels connected in a chain. Because of this, even if the smallest segment becomes inactive due to shadowing, the performance of the entire system will be affected. The weakest cell tends to bring down the efficiency of the other cells to the same level.

While some cells stop functioning, the rest continue to operate. Therefore, if 30% of cells are heavily shaded, the overall energy output will decrease by 30% compared to normal operation under full sunlight. Over an extended period, if solar panels remain in the shadow, they may generate less energy.

– Installation Orientation: The orientation of solar panels, particularly the angle of inclination or tilt, significantly influences their energy output from the sun. To optimize the reception of solar radiation throughout the year, panel placement needs to consider the panel's orientation. Ideally, panels should be oriented toward the equator to receive direct sunlight during daylight hours.
– Temperature: The operational efficiency of photovoltaic panels is influenced by temperature. Therefore, photovoltaic panels are less efficient on extremely hot summer days but perform better on days with moderate temperatures.
– Dust and Debris: In the climate of Vietnam, allowing the surfaces of photovoltaic panels to accumulate dirt or other debris can impede the process of converting light energy into electricity, thereby reducing the operational efficiency of the panels. Therefore, cleaning photovoltaic panels once or twice a year is necessary to maintain their cleanliness.

The most significant factors impacting utilization efficiency are irradiance, shading, orientation, dust and debris, and temperature.

2.2 Solutions

As analyzed in Sect. 2.1, factors such as irradiance, time of year, and location (latitude) impact the operational efficiency of solar panels. However, when installing a practical photovoltaic system at a specific location, these factors cannot be easily adjusted or intervened.

Among these factors, shading, orientation, and dust and debris can be adjusted or intervened during the installation and use of solar panels. Making adjustments or changes to shading, orientation, and cleanliness can help mitigate unfavorable effects on the operational efficiency of the panels, ultimately enhancing their operational power.

To enhance the operational power of solar panels, the following solutions should be implemented:

Solutions for Installation and Maintenance

– Regarding Installation Orientation: To maximize the time of receiving solar irradiance throughout the year, solar panels should be oriented towards the Equator, allowing them to directly face sunlight during the daytime.

  The tilt angle of the solar panels also holds significant importance. The simplest approach is to tilt the panels at an angle equal to the latitude of the installation location.

  Based on studies, the optimal tilt angle in Vietnam ranges from 15 to 45 °, with decreasing inclination towards the South. For the Southern region, the recommended tilt angle is 16–18 ° to achieve the highest operational efficiency. In Hanoi, the most suitable tilt angle is approximately 20–22 °.
– Regarding the Issue of Cleaning Solar Panels: There are numerous solutions for cleaning solar panels. Below, we will present several solutions along with their advantages and disadvantages:

Traditional Manual Cleaning Solution: This method relies on labor equipped with specialized cleaning equipment combined with water to manually clean the surface of the solar panels.

Water Pressure Robot Cleaning Solution: This method involves using a robot equipped with a nozzle that utilizes high-pressure water to clean dust and dirt from the surface of the panels.

Water-Based Robot Cleaning Solution: This method employs a robot that uses water to clean stains and dirt from the surface of the solar panels.

Solutions to Mitigate the Effects of Shadows

- Installing solar energy systems in shadow-free locations would be an ideal solution, but this is not feasible in all cases. We can modify the installation structure of the solar panels, calculate the number of sunlight rays reaching the panels, or trim branches of trees, but we cannot control the presence of clouds. Additionally, there are several ways to minimize the impact of shadows, as follows: Bypass Diodes, Arranging the Array, Micro Inverters, Power Optimizer, MPPT, Restructuring Solar Panel Connections, Reconfiguration of Solar Panel Connections

2.3 Reconfiguration of Solar Panel Connections

The concept of restructuring the circuit connections of PV modules was first proposed by Salameh and colleagues [15, 16], and it has been applied to the operation and acceleration of electric vehicles using PV modules [17]. In [18], Sherif and Boutros introduced a reconfiguration scheme for PV modules using diodes and circuit breakers. In [14], Nguyen and Lehman proposed an internal reconfiguration scheme for PV modules and presented two optimal control algorithms for reconfiguration. However, Nguyen and Lehman did not provide any mathematical models to find the optimal configuration. To determine the optimal configuration, Nguyen and Lehman divided PV modules into two parts: fixed and reconfigurable positions using a switch matrix.

Nguyen and Lehman employed a single group of reconfigurable PV modules to minimize the number of sensors and circuit breakers required for efficient operation over a large shading area. Nonetheless, they did not address changes required in their algorithm when dealing with a larger number of reconfigurable groups and did not test the system under purely resistive loads, omitting the Maximum Power Point Tracking (MPPT) function. In [19–21], Velasco and colleagues applied the reconfiguration method to grid-connected systems and developed mathematical models for them. However, their optimization was limited to local optimization, lacking a globally optimal configuration. Velasco proposed an Equalization Index (EI) to measure the difference in solar irradiance between rows of PV modules, and the configuration with the lowest EI value was considered the global optimal configuration. The optimal configuration required the smallest disparity in illuminance received by PV modules in each parallel circuit. The number of possible connection configurations can be proportional to the number of PV modules; for a PV system with 6 modules, there are 15 connection configurations, and for a system with 9 modules, there are 280 configurations. The number of configurations could grow significantly with an increasing number of PV modules, making it challenging to find the optimal configuration quickly. Velasco proposed algorithms to identify optimal configurations [19–21], but these algorithms are suitable for systems with a small number of PV modules and may not yield truly optimal configurations.

The reconfiguration strategy can be applied to the following systems: firstly, Non-Linear Multi-Terminal (NLMT) systems with fixed PV modules, often installed in areas with ample sunlight, such as rooftops and fields. In general design, PV modules are placed away from obstructions like chimneys, buildings, and power lines. However, in some specific cases, a few PV modules might become damaged, broken, or experience reduced efficiency. In such cases, they are automatically disconnected from the system using a reconfiguration array. Secondly, for large NLMT plants, shading caused by widespread cloud cover could significantly impact plant performance. Depending on cloud speed, light intensity, sudden changes in plant output may result, posing substantial effects on the power grid.

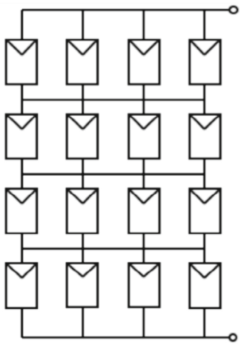

Fig. 2. TCT Connection Circuit

The power generated by Photovoltaic Quasi-Diodes (PVQDs) in real conditions is usually lower than under standard working conditions. The main reasons for reduced PVQD efficiency are solar irradiance, temperature, and aging. The effects of solar irradiance on the operation of Solar Energy Systems (NLMT) and the reconfiguration strategy for enhancing NLMT system performance under non-uniform irradiance conditions are addressed. For instance, the configuration of the restructured Total Current Terminal (TCT) circuit involves PVQDs connected in parallel, and the parallel circuits are connected in series (Fig. 2), characterized by:

– The maximum voltage of parallel-connected circuits (within the TCT circuit) is not affected by the received light intensity of each Photovoltaic Quantum Dot (PVQD).
– The current generated by a series of parallel-connected circuits will be proportional to the received light intensity of each PVQD.

During operation, PVQDs are influenced by partial shading issues, possibly caused by building shadows, cloud cover, snow, or nearby object shadows, resulting in varying solar irradiance received by each PVQD. The method of irradiance balancing for the TCT or main SP circuit involves rearranging the connection positions During operation, PVQDs are influenced by partial shading issues, possibly caused by building shadows, cloud cover, snow, or nearby object shadows, resulting in varying solar irradiance received by each PVQD. The method of irradiance balancing for the TCT or main SP circuit involves rearranging the connection positions of PVQDs to balance the total solar irradiance across parallel connections in the TCT circuit or SP circuit, as illustrated in Fig. 3

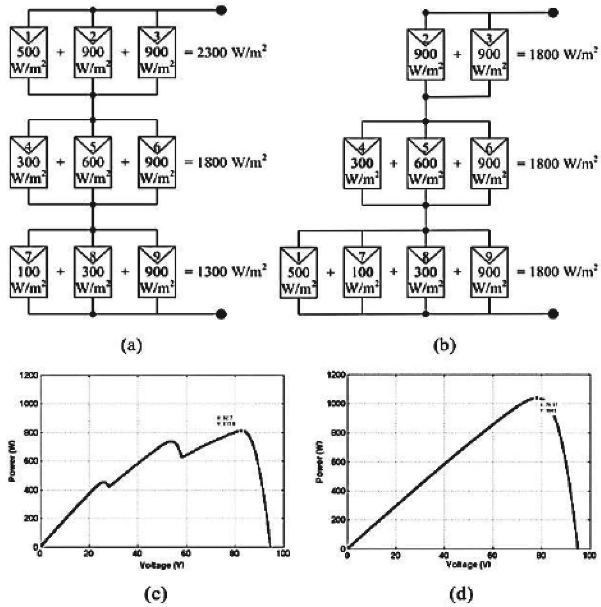

Fig. 3. Radiation balance simulation. (a) before balancing; (b) after balancing; (c) Power output chart before balancing with misleading phenomenon; (d) Power output chart after balancing without misleading phenomenon.

In Fig. 3, before radiation balancing, the TCT circuit with the total radiation in each row is 2300 W/m2, 1800 W/m2, 1300 W/m2, respectively (Fig. 3a). After changing the module positions as shown in the figure (module 1 moving from row 1 to row 3), the balanced total irradiance is 1800 W/m2 in all rows (Fig. 3b). The maximum power output before balancing is 811.9 W with a misleading phenomenon (Fig. 3c), and after balancing, the maximum system power output increases to 1041 W (a 28.2% efficiency increase) with only one maximum point, avoiding the misleading phenomenon (Fig. 3d).

3 Photovoltaic Panel Interconnection Structure

Currently, when installing photovoltaic panels (PVQDs), there are three basic interconnection methods designed to serve specific purposes. The three most common methods of interconnecting PVQDs are:

– Series Interconnection

– Parallel Interconnection
– Hybrid Interconnection

3.1 Series Interconnection Method

Interconnecting PVQDs in a series configuration primarily serves to increase the total voltage for the entire solar power system. To interconnect the photovoltaic panels, the positive terminal of one panel is connected to the negative terminal of another panel so that when the panel array is fully interconnected, they will have a single positive and a single negative terminal remaining (Fig. 4).

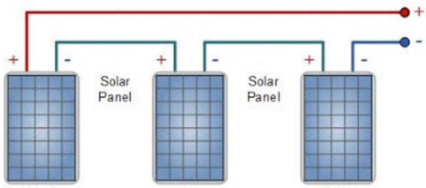

Fig. 4. Series Connection Method for Photovoltaic Panels

The advantage of a series-connected circuit is that the voltage is the total voltage of the PVQDs:

$$V_{out} = V_1 + V_2 + ... + V_n \tag{1}$$

The advantage of a series-connected circuit is that the voltage is the total voltage of the PVQDs:

$$I_{out} = \min(I_1, I_2, ..., I_n) \tag{2}$$

The output power of the series-connected circuit:

$$P_{out} = V_{out} I_{out} \tag{3}$$

where: n is the number of PVQDs in the series-connected circuit; Ii, Vi (i = 1..n): Correspondingly, the current and voltage of the i-th PVQD; Iout: The output current of the series-connected circuit; Vout: The output voltage of the series-connected circuit; Pout: The output power of the series-connected circuit.

3.2 Parallel PVQD Interconnection Method

Interconnecting PVQDs in a parallel configuration serves to increase the total power output of the entire photovoltaic panel system. To connect PVQDs in parallel, one simply connects all the positive terminals of the PVQDs into one line and all the negative terminals into another line. This results in two main connections, representing the positive and negative poles of the entire panel system.

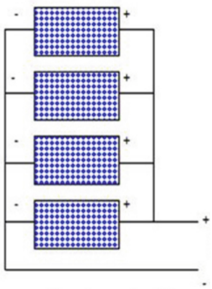

Fig. 5. Parallel Connection of PV Panels with Matching Parameters

When interconnecting PVQDs in this manner, the resulting photovoltaic panel system will have a power output equal to the sum of the power outputs of all the individual PVQDs within the system. Conclustion.

The advantage of parallel connection is that the current is equal to the sum of the currents of the PV panels.

$$I_{out} = I_1 + \mathrm{I}_2 + \ldots + \mathrm{I}_n \tag{4}$$

The drawback of parallel connection is that the circuit voltage is equal to the voltage of the PV panel with the lowest voltage.

$$V_{out} = \min(V_1, V_2, \ldots, V_n) \tag{5}$$

The output power of the parallel connection circuit

$$P_{out} = V_{out} I_{out} \tag{6}$$

where: n is the number of PVQDs in the series circuit; Ii, Vi (i = 1..n): Corresponding current and voltage of PVQD I; Iout: Output current of the parallel connection circuit; Vout: Output voltage of the parallel connection circuit; Pout: Output power of the parallel connection circuit.

3.3 Mixed Photovoltaic Module Connection Method

In [21], Damiamo La Manna introduced various connection structures for PVQDs with the purpose of ensuring the system's power output. Figure 5 presents six different connection methods commonly used for PVQDs.

Figure 5a and b depict the series and parallel connection circuits, respectively, which are fundamental connection configurations for PVQDs. During operation, when partially shaded, the elements in the parallel connection circuit have a voltage equal to the PVQD with the lowest voltage, while the elements in the series connection circuit have a current equal to the PVQD with the lowest current. Therefore, the primary drawback of these two connection methods is that the corresponding current and voltage of the series and parallel connection circuits always fall below the desired practical values.

In practical solar power plants, the series-parallel (SP) connection circuit in Fig. 5c is the most common. Next is the parallel-series (TCT) connection circuit in Figure dd. Although under standard conditions, the SP and TCT connections have the same rated power, under non-uniform conditions, the TCT connection has an advantage in minimizing power degradation and is more convenient for restructuring.

Fig. 2e illustrates the bridge-linked (BL) connection circuit, which reduces half the number of connections compared to the TCT circuit, thus minimizing conductor losses and installation time. The advantages of the TCT and BL connection configurations are combined to form the honeycomb-connected (HC) circuit in Fig. 5f. Despite the numerous specialized connection structures with various advantages that have been researched and implemented, the most widely exploited solution in practice today remains the SP and TCT connection circuits (Fig. 6).

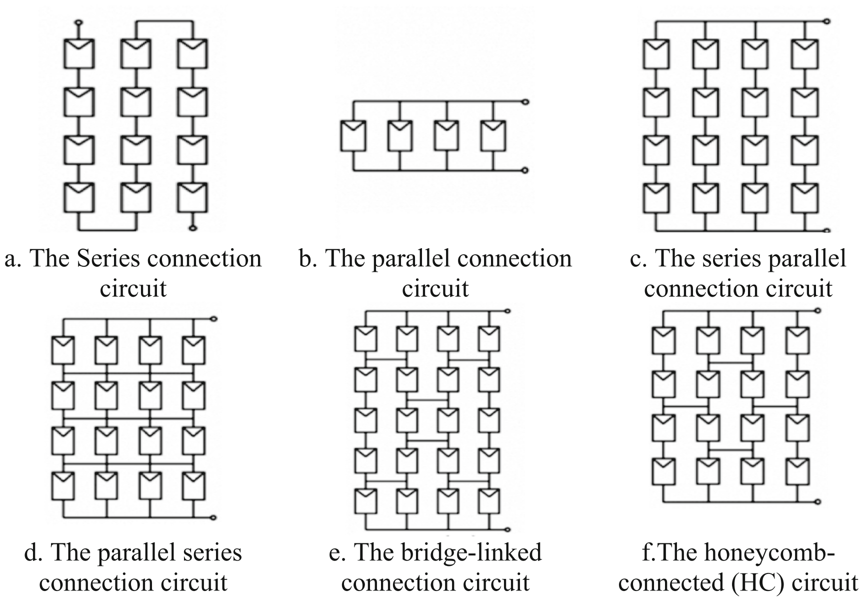

a. The Series connection circuit

b. The parallel connection circuit

c. The series parallel connection circuit

d. The parallel series connection circuit

e. The bridge-linked connection circuit

f.The honeycomb-connected (HC) circuit

Fig. 6. The six different connection methods commonly used for PVQDs.

4 Developing the Principle of Restructuring Photovoltaic Panels

To address the issue of shading, we opted for a solution of restructuring the interconnection of solar panels based on a fixed panel-to-Inverter connection configuration.

Restructuring strategy includes the following steps:

Step 1: Measure current and voltage of each PV module.
Step 2: Based on the measured current and voltage, estimate the solar radiation received by each PV module.

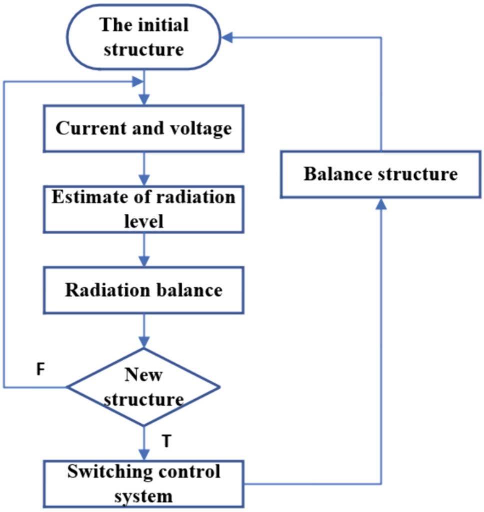

Fig. 7. Restructuring Strategy Flowchart

Step 3: Apply the radiation balance algorithm to find a balanced interconnection configuration of the PV modules.
Step 4: Compare the new interconnection configuration with the initial configuration. If it matches the initial configuration, return to step 1. If it differs from the initial configuration, proceed to step 5.
Step 5: Control the switching matrix to open or close the connections to achieve the new interconnection configuration for optimal system performance.

Thus, the PV module interconnection restructuring strategy involves two main problems: the radiation balance problem and the switching control problem. In essence, system restructuring involves changing the interconnections of PV modules to achieve a balanced configuration that maximizes system power output.

Given that the input voltage range of the Inverter's Maximum Power Point Tracking (MPPT) is 100–480 VDC with 2 MPPT channels, we choose the fixed interconnection configuration of PV modules with the Inverter as follows (Fig. 8):

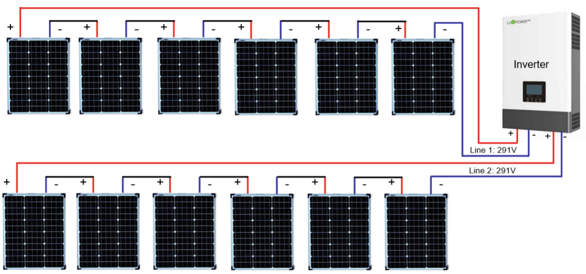

Fig. 8. Fixed PV Module Interconnection Structure

The interconnection configuration will consist of 2 strings: Each string comprising 6 PV Modules connected in series, the open-circuit voltage of each string under standard conditions is 291V. With this connection method, each string will optimize Maximum Power Point Tracking (MPPT) in case of non-uniform operation of the PV Modules, as each series of connected PV Modules will operate at a different Maximum Power Point (MPP), helping to minimize losses and increase system efficiency.

In the configuration shown in Fig. 7, each PV Module will have 2 connection options: connecting to string 1 (line 1) or connecting to string 2 (line 2). To determine which string a PV Module will connect to out of the 2 strings, we rely on the irradiance balance method. The irradiance balance method is performed to ensure that the solar PV system operates with the most appropriate efficiency and is iteratively carried out over a certain period of time.

Each irradiance balance calculation involves the following steps:

Step 1: Measure the current and voltage of each PV Module.
Step 2: Estimate the received solar irradiance at each PV Module.
Step 3: Determine the appropriate connection configuration of the PV Modules (assigning a PV Module to either Line 1 or Line 2, determining the number of PV Modules in each Line) based on the principle of irradiance balance among the PV Modules in the Lines.
Step 4: Compare the new connection configuration with the initial configuration. If it is the initial configuration, return to Step 1. If it is a different configuration from the initial one, proceed to Step 5.
Step 5: Control the switch matrix to open or close connections to achieve a new connection configuration for optimal system performance.

To implement the irradiance balance strategy, it is necessary to estimate the solar irradiance on each PV Module. Solar irradiance is calculated based on measured current, voltage, and rated parameters of the PV Module, considering the influence of the temperature of the PV Module (T_c). The formula for calculating solar irradiance is as follows:

$$G_s = \frac{G_{STC}}{I_{L_{STC}} + \mu_{1_{SC}}\left(T_c - T_{C_{STC}}\right)}\left[I + I_0\left(e^{\frac{U+IR_S}{n_S A_d k \frac{T_c}{q}}} - 1\right) + \frac{U + IR_S}{R_{Sh}}\right] \tag{7}$$

Where:

G_S : solar irradiance, unit W/m²;

I, U : alues of measured current and voltage at the PV Module;

G_{STC} : solar irradiance value at standard conditions (1000 W/m²);

$I_{L_{STC}}$: current generated by the PV Module at standard conditions;

$\mu_{1_{SC}}$: short-circuit current temperature coefficient;

T_c : temperature of the PV Module;

$T_{C_{STC}}$: temperature at standard conditions (298.15 K);

I_0: saturation current;

R_S: series resistance;

R_{SH}: shunt resistance;

n_S: number of PV Modules connected in series within the PV Module;

A_d: quality factor of semiconductor material;

k: Boltzmann's constant;

q: electron charge.

With the following parameter values:

GSTC = 1000 W/m2; $T_{C_{STC}} = 298{,}15\ ^0K$

$\mu_{1_{SC}} = 0{,}004$ Lookup the photovoltaic panel specifications table.

$T_c = 35 + 271{,}15 = 308{,}15\ ^0K$

$n_S = 72$ (according to the actual number of cells on the solar panel)

$I_0 = 10^{-9}$ A

$R_S = 0{,}01\ \Omega$ [26]

$R_{SH} = 100\ \Omega$ [26]

$A_d = 1{,}2$

$k = 1{,}3806.10^{-23}\ J/^0K$

$q = 1{,}6022.10^{-19}$ C

5 Conclusion

Solar panel restructuring brings many significant advantages. First, they could optimize the efficiency of solar energy collection by adjusting the installation angle and direction, saving energy, and reducing electricity costs. Second, the use of restructured solar panels contributes to environmental protection by reducing greenhouse gas emissions and using clean energy. Third, they have a long lifespan and can withstand harsh weather conditions. Fourth, restructured solar panels are flexible and can be integrated into the architecture of manufacturing facilities and buildings, saving space, and creating innovative energy solutions. Fifth, they can be customized to meet the specific requirements of businesses or projects. Furthermore, using restructured solar panels reduces dependence on traditional energy sources and ensures that production activities are not disrupted due to energy supply issues. Finally, businesses can leverage the adoption of this technology to build their brand and attract environmentally conscious customers, contributing to their marketing and communication efforts.

In subsequent papers, we will elaborate on the aspects not fully covered in this article, while also presenting concrete comparative data on the efficient energy utilization when applying this technology.

Acknowledgments. This research is funded by Thai Nguyen University of Technology (Tnut).

References

1. Ngư, N.V., Tâm, L.T.M., Thư`ơng, T.T., Trư`ơng, N.X.: So sánh hai thuật toán Inc và P&O trong điều khiển bám điểm công suất cực đại của hệ thống pin quang điện cấp điện độc lập. Tạp chí Khoa học và Phát triển **13**(8), 1452–1463 (2015)
2. Phương, H.T.T., Thư, N.T., Ánh, H.P.H., Kiên, C.V.: Tối ưu công suất MPPT nguồn quang năng PV dùng thuật toán P&O m`ơ thích nghi. Hội nghị toàn quốc lần th´ư 8 về Cơ Điện tử - VCM-2016 (2016)
3. Tế, Đ.H.Đ., Hải, T. and Quốc, T.: Cải tiến thuật toán Inc trong điều khiển bám điểm công suất cực đại hệ thống Pin quang điện cấp điện độc lập. Tạp chí KH Nông nghiệp Việt Nam **14**(5), 785–798 (2016)
4. Văn Tấn, N., Quân, D.M., Tuấn, T.A., Văn Kiên, P., Lâm, L.H., Long, H.H.: So sánh các thuật toán b´ăt điểm công suất cực đại b`ăng phương pháp mô phỏng và thực nghiệm. Tạp chí khoa hoc và công nghệ Đại học Đà N˜ăng, Số **11**(132), 64–68 (2018)
5. Chưởng, T.T., Huy, B.V.: Nghiên c´ưu, thiết kế hệ thống biến đổi điện tử công suất ´ưng dụng trong hệ thống năng lượng mặt tr`ơi kết nối lư´ơi điện phân phối. Tạp chí Khoa học & Công Nghệ, Số Đặc biệt, pp. 28–35 (2018)
6. Văn Hiền, B., Anh, T.V., Hải, Q.T.: Tối ưu điểm phát công suất cực đại của pin quang điện làm việc trong điều kiện bóng che. Tạp chí Phát triển Khoa học và Công nghệ – Kĩ thuật và Công nghệ **3**(1), 326–338 (2020)
7. Bounechbaa, H., Bouzida, A., Nabtib, K., Benalla, H..: Comparison of perturb & observe and fuzzy logic in maximum power point tracker for PV systems. In: The International Conference on Technologies and Materials for Renewable Energy, Environment and Sustainability, TMREES14, Energy Procedia, vol. 50, pp. 677–684 (2014)
8. Boukezata, B., Chaoui, A., Gaubert, J.-P., Hachemi, M.: An improved fuzzy logic control MPPT based P&O method to solve fast irradiation change problem. J. Renew. Sustain. Energy **8**, 043505 (2016)
9. Andrianantenaina, C., Victorien, D.B., Razafinjaka, J.N.: MPPT P&O algorithm optimization by fuzzy logic. Int. J. Eng. Res. Manage. (IJERM) **04**(11) (2017)
10. Haji, D., Genc, N.: Fuzzy and P&O based MPPT controllers under different conditions. In: 7th International Conference on Renewable Energy Research and Applications (ICRERA), pp. 649–655 (2018)
11. Ngo Ngoc, T., et al.: A hierarchical architecture for increasing efficiency of large photovoltaic plants under non-homogeneous solar irradiation. Solar Energy **188**, 1306–1319 (2019)
12. Ngô Ngọc Thành, Đề xuất các thuật toán điều khiển tối ưu cho bài toán tái cấu trúc hệ thống pin quang điện, Luận án tiến sĩ, Viện Khoa học và Công nghệ, Hà Nội, 2020
13. Trends in photovoltaic applications. Survey report of selected IEA countries between 1992 and 2012. International Energy Agency (2013)
14. Nguyen, D., Lehman, B.: An adaptive solar photovoltaic array using model-based reconfiguration algorithm. IEEE Trans. Industr. Electron. **55**(7), 266–2616 (2008)
15. Salameh, Z.M., Liang, C.: Optimum switching point for array reconfiguration controllers. In: Proceedings of IEEE 21st Photovoltaic Specialist Conference, vol. 2, pp. 971–976 (1990)
16. Salameh, Z.M., Dagher, F.: The effect of electrical array reconfiguration on the performance of a PV-powered volumetric water pump. IEEE Trans. Energy Convers. **5**, 615–658 (1990)
17. Auttawaitkul, Y., Pungsiri, B., Chammongthai, K., Okuda, M.: A method of appropriate electric array reconfiguration management for photovoltaic powered car. In: Proceedings of 1998 IEEE Asia-Pacific Conference on Circuits and Systems (APCCAS 98), pp. 201–204 (1998)

18. Sherif, R.A., Boutros, K.S.: Solar module array with reconfigurable tile. U.S. Patent 6350944B1 (2002)
19. Velasco, G., Guinjoan, F., Pique, R.: Electrical PV array reconfiguration strategy for energy extraction improvement in grid-connected PV systems. IEEE Trans. Industr. Electron. **56**(11), 4319–4331 (2009)
20. Velasco, G., Negroni, J.J., Guinjoan, F., Piqué, R.: Energy generation in PV grid-connected systems: a comparative study depending on the PV generator configuration. Proc. IEEE Int. Symp. Indust. Electron. **3**, 1025–1030 (2005)
21. Velasco, G., Negroni, J.J., Guinjoan, F., Piqué, R.: Grid-connected PV systems energy extraction improvement by means of an electric array reconfiguration (EAR) strategy: operating principle and experimental results. In: Proceedings of IEEE 39th Power Electronics Specialists Conference (2008)

The Efficiency of Changing Traditional Vehicle by EVs on Taxi Service: A Case Study on the Energy Consumption and Emission Levels in Hanoi City

Le Van Nghia, Le Hue Tai Minh(✉), Dam Hoang Phuc, Duong Ngoc Khanh, and Bui The Dat

Department of Vehicle and Energy Conversion Engineering, School of Mechanical Engineering, Hanoi University of Science and Technology, Hanoi, Vietnam
minh.lht210001d@sis.hust.edu.vn

Abstract. The green transition is becoming inevitable in many places worldwide, including Vietnam. To evaluate the energy consumption and emission levels of the taxi service in Hanoi when transferring from traditional to electrical taxis, the article presents an average model to calculate energy consumption and carbon emissions, considering two typical driving cycles (DC): urban in light traffic and urban in rush hour. Two calculation scenarios are provided: one using traditional taxis with internal combustion engines and the other using electric taxis. Additionally, greenhouse gas emissions were evaluated to highlight the advantages of applying electric vehicles in the taxi service sector in Hanoi.

Keywords: average model · energy consumption · emission level · taxi service

1 Introduction

Greenhouse gas emissions, along with fossil fuel consumption, are always a matter of global and local concern, both on a worldwide scale and in the context of Vietnam. During the COP 26 conference in December 2021, Vietnam pledged to achieve net-zero emissions by 2050. The green transition within the transportation sector, which accounts for 21% of Vietnam's greenhouse gas emissions, is a critical component of this commitment. A pragmatic approach to government policy could be to concentrate on state-managed public transportation, such as buses and taxis [1]. This demonstrates Vietnam's increasing concern regarding issues related to fuel consumption and greenhouse gas emissions.

One of the major contributors to greenhouse gas emissions is the transportation sector, including public transportation vehicles like taxis. According to the Vietnam Taxi Market Report provided by Mondor Intelligence, the Vietnamese taxi market was estimated at 410 million USD in 2021 and is forecasted to reach 790 million USD in 2027, with a compound annual growth rate of 10.25% during this period [2]. This indicates

D. C. Nguyen et al. (Eds.): ICERA 2023, LNNS 944, pp. 480–488, 2024.
https://doi.org/10.1007/978-3-031-62235-9_48

the substantial size of the domestic taxi market. The global surge in green automotive technology has significantly influenced the taxi service industry. Transitioning to environmentally friendly operating models has become imperative. According to Decision No. 876/QĐ-TTg issued on July 7th, 2022, by the Prime Minister approving the action program on green energy transition, it is mandated that all road and construction vehicles participating in traffic must be powered by electricity and green energy [3]. Consequently, numerous taxi companies have begun employing environmentally friendly electric vehicles. To facilitate this trend, governmental support predicated on energy consumption (EC) and emission levels in the taxi transportation sector is essential during the transition to electric vehicles. As a result, it also requires methods to assess the energy efficiency and emissions impact of this conversion process.

Two primary methods exist for determining vehicle energy consumption: experimental procedures and simulation models of vehicle operations. The experimental method is time-consuming and requires extensive measuring devices. Moreover, fluctuating environmental factors can influence the experimental results. This study opts for a simulation method due to its advantages in terms of time efficiency, equipment requirements, cost-effectiveness, and convenience. Dynamic modeling is a prevalent tool that offers relatively high accuracy. Currently, validated tools include ADVISOR and PSAT. However, all vehicle dynamic modeling methods have limitations such as the need for detailed input data (often unavailable), complex computations, and dependence on defined DC.

This study employs a modified averaging model to compare and evaluate the fuel consumption and emissions efficiency of converting traditional taxi vehicles to electric taxis. The average modeling is a simpler simulation method that uses estimates of engine characteristics (including internal combustion engines and electric motors), parameters averaged over a DC, and empirical correlations. Unlike dynamic modeling, average models employ multiple sets of averaged parameters, facilitating their use and enabling straightforward analysis of energy usage on vehicles without necessitating detailed component models or performance charts. The average parameter sets can be derived from real driving cycle data.

2 Methods

The energy consumption and emissions of the taxi transportation industry in Hanoi when transferring from traditional taxis to electric taxis were calculated using the average energy calculation method to determine the energy consumption per kilometer traveled by vehicles. Experimental tests and real-world surveys, combined with social media platform surveys, were conducted to identify the characteristic parameters for the urban driving cycle in Hanoi and calculate the average distance traveled by taxis per day. The results showed a significant improvement in energy efficiency and emissions reduction for the taxi transportation industry if the transition from traditional taxis to electric taxis is conducted.

The proposed average model [4, 5] is based on the average power method and reverse calculation from the wheels to the engine. According to the automotive theory [6], the equation for calculating power at the wheels can be averaged as follows:

$$\overline{P}_{road} = \overline{P}_{roll} + \overline{P}_{aero} + \overline{P}_{accel} = C_{RR} m_{total} g v_{avg} + \frac{1}{2} \rho C_D A v_{rmc}^3 + k_m m_{total}\, a v_{avg} \quad (1)$$

where: $\overline{P}_{road}$ – Average road load power (W), $\overline{P}_{roll}$– Average rolling resistance power (W), $\overline{P}_{aero}$ – Average aerodynamic power (W), $\overline{P}_{accel}$ – Average accelerating power (W), C_{RR} – Rolling resistance coefficient, m_{total} – Total mass of the vehicle (kg), g - Gravitational acceleration (9,81 m/s^2), ρ – Air density (1,2 kg/m^3), C_D – Aerodynamic coefficient, A – Frontal area of the vehicle (m^2), k_m – coefficient accounting for the rotational inertia of the powertrain system (k_m= 1,05).

In Eq. (1), there are three representative parameters of driving cycles: average velocity (v_{avg}), root-mean-cubed velocity (v_{rmc}), and characteristic acceleration ($\tilde{a}$) [5]. Description and calculations of those parameters are demonstrated below:

- Average speed [4, 5]: This is the most common parameter to describe a driving pattern. The fundamental driving pattern attribute that describes how quickly a vehicle will complete its journey is calculated as follows:

$$v_{avg} = \frac{1}{T}\int_0^T v dt \tag{2}$$

- Root-mean-cubed velocity [4, 5]: This parameter characterizes the range of vehicle speed changes during the journey, calculated as follows:

$$v_{rmc} = \sqrt[3]{\frac{1}{T}\int_0^T v^3 dt} \tag{3}$$

- Characteristic acceleration [4, 5]: This parameter quantifies the rate at which vehicle speed changes throughout the journey without providing any information regarding the range of speeds at which the vehicle travels. The minimum possible value for characteristic acceleration is zero, corresponding to constant speed driving. This parameter is calculated as follows:

$$\tilde{a} = \frac{1}{2}\frac{\sum(v_{final}{}^2 - v_{initial}{}^2)}{v_{avg}T} \tag{4}$$

The computational method of the model is generalized as shown in Fig. 1.

For Vehicles Using Internal Combustion Engines:
The average power of the internal combustion engine is calculated as:

$$\overline{P}_{ICE} = \overline{P}_{drive-out} + \overline{P}_{drive-loss} + \overline{P}_{accessory} \tag{5}$$

The average energy consumption of a vehicle using an internal combustion engine (kWh/km) is calculated as:

$$\overline{E}_{ICE} = \frac{\overline{P}_{ICE}}{\eta_{ICE}.v_{avg}.3600} \tag{6}$$

where: η_{ICE} - is the fuel conversion efficiency of the engine.

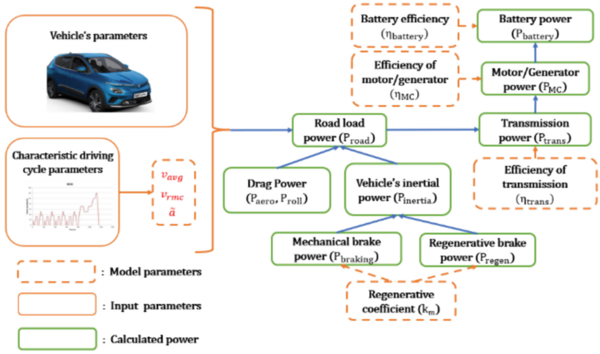

Fig. 1. Calculation diagram according to the parameter averaging model

For Vehicles Using an Electric Motor:

The average power that the battery needs to provide for vehicle operation during the DC is:

$$\overline{P}_{battery} = \overline{P}_{drive-out} + \overline{P}_{drive-loss} + \overline{P}_{battery-loss} + \overline{P}_{accessory} \tag{7}$$

The average energy consumption for an electric vehicle (kWh/km):

$$\overline{E}_{EV} = \frac{\overline{P}_{battery}}{\eta_{changer}.\eta_{battery}.v_{avg}.3600} \tag{8}$$

where : $\eta_{changer}$- is the efficiency of the charger; $\eta_{battery}$ - is the efficiency of the battery.

Basic vehicle specifications and DC parameters are required to calculate the energy consumption-related results using the model. The article constructs a representative DC for the inner-city area of Hanoi, as described below.

There are three main steps in constructing a DC: route selection, data collection, and cycle construction. The routes are selected to represent typical driving patterns based on evaluations by researchers, such as trips from home to work, population density differences, and road classifications. The results yield two representative routes for inner-city traffic in Hanoi, including the inner-city peak hours cycle and off-peak hours cycle, as shown in Figs. 2 and 3 below.

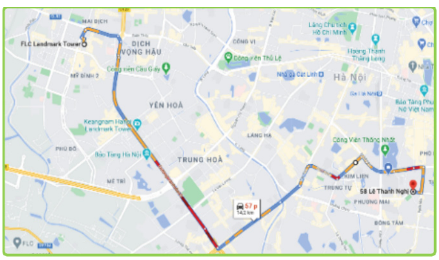

Fig. 2. Peak hours route

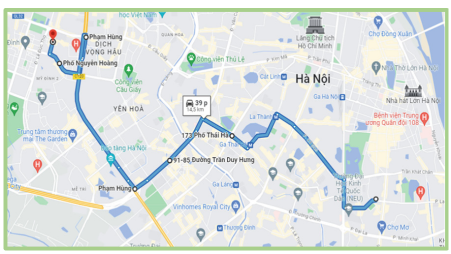

Fig. 3. Off-peak hours route

The inner city during peak hours cycle consists of urban roads with multiple intersections, high population density, poor traffic conditions, potential congestion, vehicle speeds below 20 km/h, and frequent braking and stopping (Fig. 2). Typical examples include ring roads and radial roads. The off-peak hours cycle consists of urban roads with multiple intersections, good traffic conditions, no significant delays, and vehicle speeds ranging from 20–50 km/h (Fig. 3). The report selects two routes with the same starting and ending points and equal lengths. One represents inner-city in peak hours cycle characteristics, and the other represents inner-city in off-peak hours cycle characteristics. The experiments were conducted over two months, with a total of 15 peak hours cycles and 15 off-peak hours cycles.

The experimental vehicle speed data was recorded via the OBD-II ports and GPS sensor, and shown in Figs. 4 and 5:

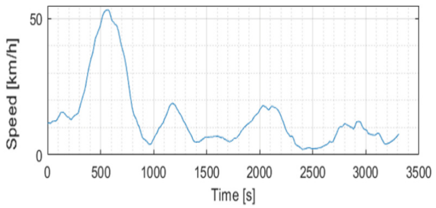

Fig. 4. Peak hours driving cycle

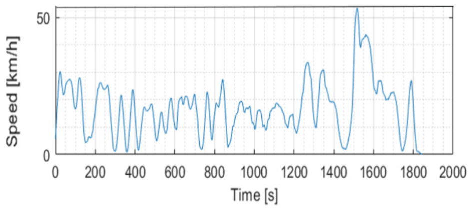

Fig. 5. Off-peak hours driving cycle

Since taxis operate regularly, the travel time is evenly distributed between peak and off-peak hours. Therefore, the distance ratio between these urban driving cycles is taken as 50%–50%. Based on this, the report calculates the characteristic parameters for each experimental run and then takes the average value over 15 experiments, resulting in the following results (Table 1):

Table 1. Specific parameters of the urban driving cycle in Hanoi city

Basic parameters of driving cycles	Values	Units
The average velocity	8,128	m/s
The root-mean-cubed velocity	11,357	m/s
The velocity ratio	1,397	–
The characteristic acceleration	0,237	m/s^2

With the averaging model method and the characteristic parameters of the driving cycle in the central area of Hanoi city, the average energy consumption per kilometer traveled for both electric and traditional taxis could be calculated.

The survey results have shown that the most common traditional taxi model in Hanoi is the Hyundai Grand i10, while the electric taxi model is the VF e34 by Vinfast. The article conducted calculations on the energy consumption for these representative vehicle models using the input parameters shown in Table 2 and obtained the results as presented in Table 3, as follows:

Table 2. Basic specifications table for the Hyundai Grand i10 and VF e34 [7–9]

Basic parameters of surveyed vehicles	Grand i10	VF e34
The total vehicle mass (kg)	1020	1490
The drag coefficient	0,35	0,29
The frontal area of the vehicle (m^2)	2,043	2,424
The rolling drag coefficient	0,008	0,008
The average efficiency of transmission	87%	95%
The energy exchange efficiency	16,67%	–
The battery efficiency ($\eta_{battery}$)	–	96%
The charger efficiency ($\eta_{changer}$)	–	86%
The average efficiency of the electric motor/controller	–	92,8%
The coefficient of energy regeneration in the transmission system	–	0,8

Table 3. The calculation results of loss-power for the Hyundai Grand i10 and VF e34

Parameters	Grand i10	VF e34
The average battery power ($P_{battery}$)	–	3824
The average electric power charging (P_{elec})	–	4681
The average power of the engine (W)	30545	–
The average fuel energy input requirement (W)	18326	–
The loss of energy per kilometer (kWh)	0,63	0,16

According to the test results by Vinfast, with a long-distance journey of 1970 km, the VF e34 electric vehicle required a total of 11 charging sessions, averaging 30 kWh per session, resulting in a total of 330 kWh [9]. The calculated energy consumption rate was 0,1675 kWh/km and this low value can be explained by using a regenerative braking system on the electric vehicle [10]. The 4,69% deviation between the average model calculation and real experimental results demonstrates the accuracy of the model and its applicability in calculating energy consumption and emissions in the taxi transportation sector.

3 The Evaluation of Emissions of Traditional Taxis and Electric Taxis

Based on the statistical data from the Hanoi Department of Transportation in 2022, there are 19,625 taxis in Hanoi City [11]. The graph below shows the percentage of taxis with a travel distance range per day in the central of Hanoi, according to social media and face-to-face surveys (Fig. 6):

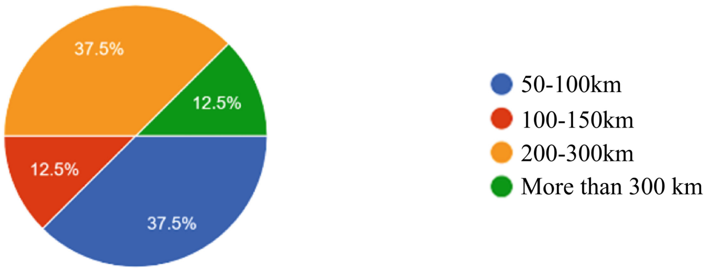

Fig. 6. Daily distance traveled by taxis in Hanoi's urban area

The average number of kilometers traveled by taxi in a day (S) could be calculated with a lower limit *(S_{min})* and an upper limit (S_{max})*:*

$$S = \frac{S_{min} + S_{max}}{2} = \frac{\sum \partial.\Delta S_{min} + \sum \partial.\Delta S_{max}}{2.100} \quad (9)$$

where: ∂ is the percentage of taxis with each travel distance range per day (%), ΔS_{max} is the maximum distance in each travel distance range (km), ΔS_{min} is the minimum distance in each travel distance range (km).

Based on the energy conversion table provided by the National Fuel Efficiency Research and Development Center of Vietnam, every 1000 kWh of electricity produced in Vietnam is equivalent to 0,1543 metric tons of oil equivalent (*TOE*) and emits 0,7221 metric tons of CO_2 into the atmosphere [12].

According to the Arbor Day Foundation, a non-profit organization specializing in tree planting in the United States, a mature tree absorbs over 48 lb (approximately 21,77 kg) of carbon dioxide from the atmosphere and releases oxygen through exchange [13].

The emission of the taxi industry in Hanoi was calculated based on the bellow formulas.

Energy consumption per day (kWh):

$$E_{day} = E_{onekm} \times S \times Vehicle\_num \quad (10)$$

Annual emissions - greenhouse gas of the taxi industry in Hanoi per year GHG (tons):

$$GHG = 0{,}7221 \times \frac{E_{day}.365}{1000} \quad (11)$$

The number of trees required to absorb the emitted CO_2 per year:

$$Tr\_num = \frac{GHG \times 1000}{21{,}77} \tag{12}$$

The emissions results of traditional taxis and electric taxis were compared as shown in Table 4:

Table 4. The emissions results of traditional taxis and electric taxis

	S (km)	E_{onekm} (kWh)	E_{day} (kWh)	EC *per year* (kWh)	GHG (tons)	Tr_num (trees)
Grand i10	175	0,63	110,25	2163656	1562,38	71767
VF e34	175	0,16	28,01	549500	396,79	18227

Therefore, in the scenario of replacing all traditional taxis with electric taxis, the taxi industry in Hanoi can reduce its CO_2 emissions into the environment by 74,6%. This transition is equivalent to planting 53541 trees (while the 12 central districts of Hanoi have approximately 75000 trees). The proposed scenario will significantly improve air pollution in the city's urban area.

In terms of energy, electric taxis demonstrate their superior advantage in urban traffic conditions, with energy consumption per kilometer only amounting to 25,4% compared to traditional taxis. The total energy consumption in the Hanoi taxi industry will decrease from 2163656 kWh/year to 549500 kWh/year. This allows the taxi industry to utilize energy more efficiently (reducing total energy consumption while maintaining the total distance traveled). There are limitations in data collection for input parameters such as distance traveled. A more enormous nationwide data source would enhance the accuracy of the calculation method and allow for the expansion of its calculations to regional and national levels.

4 Conclusion

The article has presented the development of a model designed to calculate the average energy consumption and carbon emissions in the taxi transportation sector in Hanoi. Two real-time driving cycles were taken into account: the inner city road during peak hours and off-peak hours. The results show that electric taxis have an energy consumption level of approximately 25,4% compared to traditional ones. The complete transition from traditional to electric taxis could potentially decrease the industry's CO_2 emissions by 74,6%, a reduction equivalent to the carbon sequestration of newly planted trees covering 71,4% of the area in Hanoi's twelve inner districts. These results show the superior advantage of electric taxis in urban traffic conditions.

References

1. Socialist Republic of Vietnam Government News: Make the best use of the current opportunity to implement drastically, effectively and substantively the commitments at COP26. https://shorturl.at/lmqwI. Accessed 25 Jun 2023
2. CAR BACK: the development of taxi transport services during the 4.0 revolution. https://carback.vn/su-phat-trien-cua-dich-vu-van-tai-bang-taxi-trong-cuoc-cach-mang-4-0. Accessed 25 Jun 2023
3. Socialist Republic of Vietnam: Decision No. 876/QĐ-TTg dated July 7th, 2022 by Prime Minister on approving the action program on green energy transition, reducing carbon and methane emissions of the transport sector, https://vanban.chinhphu.vn/?pageid=27160&docid=206188. Accessed 25 Jun 2023
4. Mordor Intelligence: Vietnam Taxi Market size Analysis - Growth forecast trend (2023–2028), https://www.mordorintelligence.com/vi/industry-reports/vietnam-taxi-market. Accessed 25 Jun 2023
5. Nghia, L.V., Phuc, D.H., Khanh, D.N., Hoang, T.M., Hai, H.H.: An average method for calculating the vehicle energy consumption on driving cycles. Int. Rev. Mech. Eng. **16**, 610–619 (2022)
6. Tuan, L.V.: Automotive Theory. Vietnam Education Publishing House Limited Company, Hanoi (2019)
7. Hyundai/TC Motor: Grand i10 Hatchback specification. https://huyndainamdinh.com.vn/hyundai-grand-i10-hatchback-tskt/. Accessed 25 Jun 2023
8. Vinfast Auto: VFe34 – Technical parameters. https://vinfastauto.com/vn_vi/thong-so-ky-thuat-o-dien-vinfast-vf-e34-chi-tiet-nhat. Accessed 25 Jun 2023
9. Vinfast Auto: Evaluate VinFast VF-e34 across Vietnam with more economical costs than petrol cars, https://vinfastauto.com/vn_vi/vf-e34-xuyen-viet-tiet-kiem-hon-xe-xang, last accessed 2023/06/25
10. Le, V.N., Dam, H.P., Nguyen, T.H., Kharitonchik, S.V., Kusyak, V.A.: Research of regenerative braking strategy for electric vehicles. Energetika **66**(2), 105–123 (2023)
11. Do, P.A.: Assessing the current status of environmentally friendly public passenger transport in Hanoi, developed according to the roadmap of green energy transformation in the transport sector. Consultation workshop on technical support to develop a national program to develop environmentally friendly public transport, p. 14 (2023)
12. ENERTEAM: Energy to TOE conversion table. http://enerteam.org/quy-doi-nang-luong-sang-toe.html. Accessed 25 Jun 2023
13. U.S. Department of agriculture: the power of one tree - the very air we breathe. https://shorturl.at/qwyC3. Accessed 25 Jun 2023

The Study of Effective Regenerative Brakes on Battery Electric Vehicles

Le Hoang Long[1,2](✉), Khong Vu Quang[2](✉), Pham Huu Nam[1], Pham Van Thoan[3], and Pham Minh Hieu[3]

[1] Faculty of Mechatronics and Automobile, Hanoi University of Business and Technology, Hanoi, Vietnam
long.lh230007d@sis.hust.edu.vn
[2] Department of Vehicle and Energy Conversion Engineering, School of Mechanical Engineering, Hanoi University of Science and Technology, Hanoi, Vietnam
[3] Faculty of Automobile Technology, Hanoi University of Industry, Hanoi, Vietnam

Abstract. The regenerative brake system is a standard to increase hybrid or battery-electric vehicles' range per charge period. According to some research, the system can extend up to 16% of the range [1]. There are several studies on different configurations or strategies of control to improve the efficiency of regenerative brakes. Most of them use specifications from hybrid or battery electric vehicles that have a gross weight of more than 1 ton [2, 3]. More and more mini-battery electric vehicles have been introduced around the world, including in Vietnam. Therefore, the combination of regenerative and mechanical brakes on mini-battery electric vehicles that use low-power motors and batteries needs more consideration. This paper presents research on effective regenerative brakes on mini-battery electric vehicles (gross weight lower than 1 ton) equipped with BLDC motors in different conditions (initial SoCs and accelerations). The simulation on MATLAB Simulink showed that the efficiency can reach 24% per braking period under special brake conditions.

Keywords: Electric vehicle · Regenerative brake · BLDC

1 Introduction

At present, there are some research directions to improve the efficiency of energy use on battery electric vehicles (BEV) as increasing the specific capacity and power of the battery [4]; improving the electric motor [5]; increasing the efficiency of electric converter and motor algorithms [6]; regenerative energy from brake or suspension system [7]. In an ordinary car, kinetic energy is dispatched by friction in the brake process can up to 50% of the necessary energy to accelerate again [8]. There are already high-power electric motors, controllers, and batteries in a BEV. They are the main components of the regenerative brake system. The efficiency of regenerating energy can reach 16% of BEV's kinetic energy in some testing cycles [1].

The regenerative brake system is a hybrid brake system (HBS) between mechanical and electric motor-based brake systems. The system must ensure the effectiveness and

D. C. Nguyen et al. (Eds.): ICERA 2023, LNNS 944, pp. 489–496, 2024.
https://doi.org/10.1007/978-3-031-62235-9_49

stability of the brake system while converting as much of BEV's kinetic energy to electric energy and then storing the regenerative energy in the battery.

The modeling used in the research on the regenerative brake system is almost based on BEV which has a gross weight of more than 1 ton and uses a high voltage system up to 400 V. In contrast, mini BEVs that use low-power motors and batteries are more consistent for urban transportation. A quarter mathematical model of the regenerative brake system of a mini-BEV was used to analyze the effects of different conditions of urban transportation in Vietnam on the efficiency of the regenerative brake.

2 Mathematical Model of Regenerative Brake System

2.1 Dynamic of Regenerative Brake System

This paper uses a quarter model of a regenerative brake system to simulate a brake process without considering the effect of the brake distribution, the friction force, the wind drag force, and the difference in road-tire adhesion between the tires. The system is presented in Fig. 1.

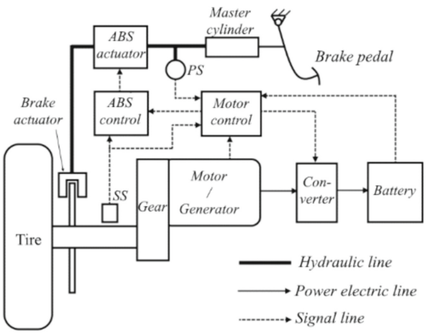

Fig. 1. Quarter model of a regenerative brake system

The pressure after the master cylinder is measured by the pressure sensor (PS) corresponding with the level of the brake pedal. The motor controller uses the level signal to control the regeneration process. The speed sensor measures the speed of the wheel as an input signal for the ABS and motor controllers. The friction torque (M_{ABS}) in the brake actuator depends on the hydraulic pressure, which is controlled by the ABS actuator. The torque produced by the regenerative system (M_{RB}) depends on its construction and the charge current to the battery. The charge current depends on the state of charge (SoC), the maximum allowed current, and other parameters of the battery. It is controlled by the electric converter.

When braking, the wheel speed ω_{whl} is decreased under the effect of the M_{ABS} and M_{RB}. The dynamic of the wheel is described in Fig. 2. The vertical reaction force Z is a constant. The angular acceleration of the wheel depends on braking torques and the longitudinal force F_x, as in Eq. 1.

$$\varepsilon_{whl} = \dot{\omega}_{whl} = \frac{-M_{ABS} - M_{RB} + F_x r_{whl}}{I_{whl}} \tag{1}$$

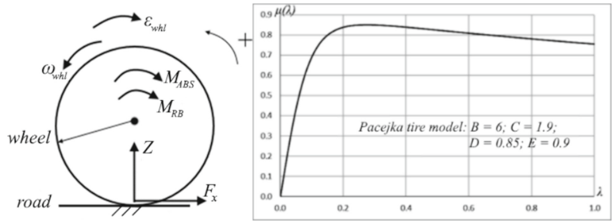

Fig. 2. Wheel dynamic and Pacejka tire model

M_{ABS} depends on the parameters of the brake actuator and the hydraulic pressure p. The derivative of M_{ABS} concerning time depends on the control signal *u(s),* as in Eq. 2 [9].

$$H(s) = \frac{\dot{M}_{ABS}(s)}{u(s)} = \frac{600}{0.001s + 0{,}15} \tag{2}$$

The value of the *u(s)* variable in the range [−1, 1] concerning the decrease and increase cycles of the hydraulic pressure. The factors in Eq. 2 are determined by experiment. In this paper, p is controlled by a Bang-Bang controller [9]. M_{RB} depends on the torque on the motor's rotor M_{em} and the gear ratio in Eq. 3.

$$M_{RB} = M_{em} * i_{tl} \tag{3}$$

M_{em} depends on the dimensions, the electric parameters, the flux characteristic, the rotor's speed ω_r, and the phase current. The motor speed is given in Eq. 4.

$$\omega_r = \omega_{whl} i_G \tag{4}$$

The brake force F_x depends on Z, m, the acceleration of gravity g, the BEV's velocity v, and the adhesion characteristic $\mu(\lambda)$ between road and tire as Eq. 5.

$$F_x = \mu(\lambda)Z = \mu(\lambda)mg \tag{5}$$

λ is the slip between tire and road, given in Eq. 6.

$$\lambda = 1 - \frac{\omega_{whl} r_{whl}}{v} \tag{6}$$

In this paper, the Magic Formula with constant factors is used to calculate the characteristic of the $\mu(\lambda)$ as presented in Fig. 2. The braking acceleration is given in Eq. 7.

$$a_{brk} = \frac{F_x}{m} \tag{7}$$

This paper uses several basic parameters of a mini-BEV for modeling as Table 1.

Table 1. Modeling parameters.

Parameter	Value
Mass m (kg)	245
The momentum of the inertial of the wheel I_{whl} (kg.m^2)	1.7
Motor type	BLDC
Max. output (kW)/torque (Nm) of the motor	5/22
Max. speed of the motor (rpm)	17,000
Wheel radial r_{whl} (m)	0.236
Gear ratio i_G	16

2.2 Electric System and Control

The construction of the BLDC motor is similar to the permanent magnet DC motor [10]. The BLDC used in the BEVs usually consists of 3 phases (A, B, and C) on the stator and permanent magnets on the rotor, as Fig. 3.

The BLDC uses hall sensors (H1, H2, and H3) to determine the rotor's position. When working in generating mode, BLDC can be considered a permanent magnet synchronous 3-phase generator. The RMS value of the back-EMF of the BLDC generator is given in Eq. 8.

$$E_0 = 4{,}44 \times f \times n \times k_n \times \Phi_0 = 4{,}44 \times \frac{p\omega_r}{60} \times n \times k_n \times \Phi_0 = K_e\omega_r \quad (8)$$

where E_0 is the RMS value of the back-EMF; f is the frequency of the back-EMF; n is the number of rotations of the phase coil; k_n is the coil constant; ϕ_0 is the flux created by the permanent magnets; p is the number of pole pairs; and K_e is the voltage constant of the BLDC.

BEVs use batteries constructed from Lithium-Ion cells. Cells are connected in parallel to increase the charge/discharge current and in serial to increase the voltage of the batteries. The batteries can be charged only when:

$$E_0 > E_{OCV} \quad (9)$$

where E_{OCV} is the open circuit voltage of the battery. The E_{OCV}-SoC curve of the 96 V Lithium-Ion battery is presented in Fig. 3. If the BEV's velocity v is lower than

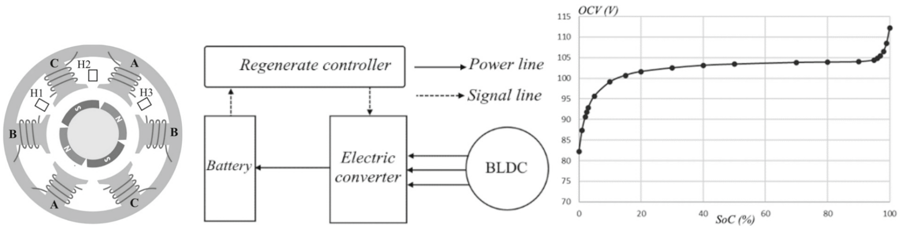

Fig. 3. Construction of BLDC, the regenerate control, and the E_{OCV}-SoC of battery.

a threshold v_{th} then $E_0 < E_{OCV}$, so the regenerate current will decrease to zero. The threshold v_{th} can be determined by using Eqs. 8 and 9.

In Fig. 3, the electric converter converts the voltage of three phases of the BLDC to a DC voltage. A PWM signal from the regenerate controller is used to control the charge current under the upper limit of $I_{RB\,max}$. In this paper, the charge current is controlled by a PID controller and a non-isolated drop-down converter.

The efficiency of the regeneration R in a braking process is used to determine the efficiency of the system. The value of R is given by Eq. 10.

$$R = \frac{e_r}{T_0} = \frac{(SoC_0 - SoC_t) \times e_0}{\frac{1}{2}mv_0^2 + \frac{1}{2}I_{whl}\left(\frac{v_0}{r_{whl}}\right)^2} \tag{10}$$

where e_r is the energy regenerated and charged into the battery; T_0 and v_0 are the kinetic energy and the velocity of the BEV at the beginning moment of the braking with respect; e_0 is the rated energy of the battery at its $SoC = 100\%$; SoC_0 and SoC_t are the states of charge of the battery at the beginning and the ending of the braking. SoC_t is determined using the coulomb counting method in Eq. 11.

$$SoC_t = SoC_0 - \frac{1}{Q_n}\int idt \tag{11}$$

where: Q_n is the rated capacity of the battery; i is the instantaneous charging current into the battery.

3 Simulation

3.1 Modelling

The parameters of the motor and the battery are given in Table 2.

Table 2. Parameters of the motor and the battery

Parameters	Value
Battery type	Li-ion
Nominal Voltage (V)/Capacity (Ah)	96/25
Max. charge current of the battery (A)	20
Torque constant of the motor (Nm/A)	0.3
Number of pole pairs	4

Based on equations from (1) to (11), the regenerative braking system is modeled using the MATLAB Simulink environment as presented in Fig. 4.

The level of the brake pedal is respected with the desired brake acceleration and slip, given in Eqs. 5, 6, and 7.

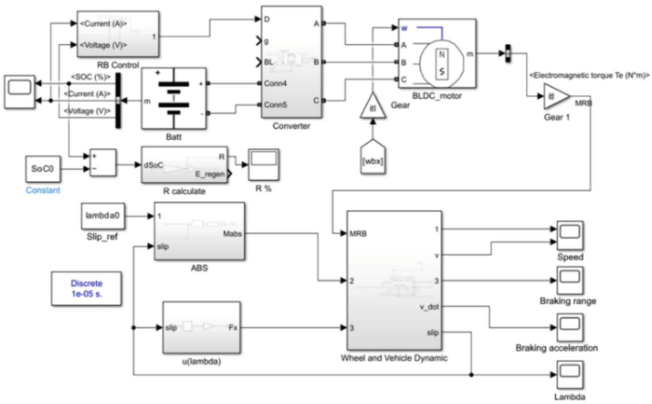

Fig. 4. Modeling the regenerative brake system using MATLAB Simulink.

3.2 Results

As a result of this study, a mathematical model of a regenerative brake system is applied and simulated. The system is simulated at an initial speed of $v_0 = 80$ km/h (maximum permitted in the urban transport system of Vietnam), different average braking accelerations a_{ave}, and different initial states of charge SoC_0.

In the MATLAB Simulink program, the efficiency of regeneration R changes inversely with the a_{ave} and SoC_0, as presented in Fig. 5.

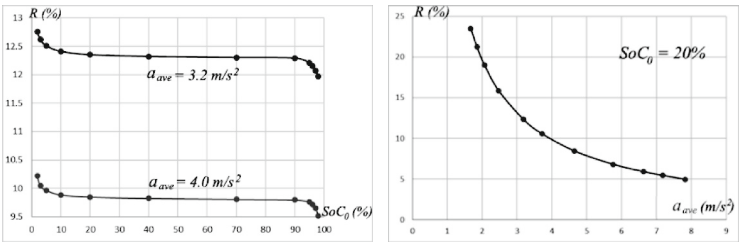

Fig. 5. The efficiency of regeneration R is affected by a) the initial state of charge SoC_0 and b) the average brake acceleration a_{ave}

When the initial state of charge SoC_0's value changes from 20 to 90%, the value of R does not change so much and is in linear form. A dramatic decrease in the value of R when the SoC0 is above 90%. It leads to the conclusion that it is better to keep the state of charge of the battery lower than 90% to achieve a high efficiency of regeneration. It's because at a high level of charge, the battery's open circuit voltage increases and the regeneration current decreases.

At the condition of the initial state of charge $SoC_0 = 20\%$, the R-a_{ave} curve is in the form of a function given in Eq. 12.

$$R = \frac{K_R}{a_{ave}} \tag{12}$$

where K_R is a constant (≈ 44.5 in Fig. 5). The value of R can reach 24% when braking at very low brake acceleration (1.7 m/s^2). To maximize the value of R, the regeneration must be activated at very low acceleration, such as when the driver releases the accelerator pedal.

4 Conclusion

In this paper, a regenerative brake system using a low-power electric motor, and a battery is simulated. The efficiency of regeneration is determined by using the state of charge of the battery in one brake cycle. The results of the simulation show that the efficiency of regeneration is relative to the initial state of charge of the battery and the average acceleration.

There are several other factors that contribute to the efficiency, such as the threshold velocity v_{th}, the control algorithm of ABS and the electric converter; the temperature, and the aging effect of the battery. They can be analyzed in future studies using these model parameters and simulations of the study.

References

1. Berjoza, D., Pirs, V., Jurgena, I.: Research into the regenerative braking of an electric car in urban driving. World Electr. Veh. J. **13**(11), 202 (2022). https://doi.org/10.3390/wevj13110202
2. Duong, T.T., Huynh, P.S., Ho, D.A.D., Ngo, Q.T.: Research on simulation of regenerative braking system based on actual driving cycle. J. Tech. Educ. Sci. (76), 76–85 (2023). https://doi.org/10.54644/jte.76.2023.1271.
3. Tuan, T.D., Do Van, D., Truong, T.N.: Research on using PSO algorithm to optimize controlling of regenerative braking force distribution in automobile. In: 2020 5th International Conference on Green Technology and Sustainable Development (GTSD), Ho Chi Minh City, Vietnam, pp. 418–423 (2020). https://doi.org/10.1109/GTSD50082.2020.9303155.
4. Chen, W., Liang, J., Yang, Z., Li, G.: A review of lithium-ion battery for electric vehicle applications and beyond. Energy Procedia **158**, 4363–4368 (2019). https://doi.org/10.1016/j.egypro.2019.01.783
5. Cao, Z., Mahmoudi, A., Kahourzade, S., Soong, W. L.:An overview of electric motors for electric vehicles. In: 2021 31st Australasian Universities Power Engineering Conference (AUPEC), Perth, Australia, pp. 1–6 (2021). https://doi.org/10.1109/AUPEC52110.2021.9597739
6. Ma, H., Tan, Y., Du, L., Han, X., Ji, J.:An integrated design of power converters for electric vehicles. In: 2017 IEEE 26th International Symposium on Industrial Electronics (ISIE), Edinburgh, UK, pp. 600–605 (2017). https://doi.org/10.1109/ISIE.2017.8001314
7. Wang, Z., Zhang, T., Zhang, Z., Yuan, Y., Liu, Y.: A high-efficiency regenerative shock absorber considering twin ball screws transmissions for application in range-extended electric vehicles. Energy Built Environ. **1**(1), 36–49 (2020). https://doi.org/10.1016/j.enbenv.2019.09.004

8. Ehsani, M., Gao, Y., Emadi, A.: Modern Electric, Hybrid Electric, and Fuel Cell Vehicles - Fundamentals, Theory, and Design, 3rd edn. CRC Press, Boca Raton (2018)
9. Chen, C., Chiang, M.: Mathematical simulations and analyses of proportional electro-hydraulic brakes and anti-lock braking systems in motorcycles. Actuators **7**(3), 34 (2018). https://doi.org/10.3390/act7030034
10. Chau, K.T.: Electric Vehicle Machines and Drives Design, Analysis and Application. Wiley, Singapore (2015)

The Use of a Combined Power Source Vehicles When Converting an Internal Combustion Engine to an Alternative Fuel to Reduce Emissions from Exhaust Gases of Carbon Compounds

Van Dung Nguyen[1], Andrey Y. Dunin[1], Thin Quynh Nguyen[2], Khac Minh Nguyen[3](✉), Dinh Thi Luong[4], and Huy Truong Thai[5]

[1] Department of Heat Engineering and Automotive Engines, Moscow Automobile and Road Construction State Technical University (MADI), Moscow, Russia

[2] Faculty of Mechanical Engineering, University of Transport and Communications, Hanoi, Vietnam

[3] Automotive and Power Machinery Faculty, Thai Nguyen University of Technology, Thai Nguyen, Vietnam

khacminhcdl@tnut.edu.vn

[4] Institute of Vehicle and Energy Engineering, Military Technical Academy, Hanoi, Vietnam

[5] Logistic Commanding Faculty, Air Defense-Air Force Academy, Hanoi, Vietnam

Abstract. In this paper, this research was carried out using the spark ignition engine (SI engine) when it is operated on alternative fuels as part of a Combined Power Source Vehicles (hybrids drivers). Using the SI engine as a part of a Combined Power Source Vehicles allows to reduce the working volume of the internal combustion engine, to reduce the amount of heat added to the cycle with the fuel at medium and high load conditions while maintaining the full specified power. In this case, it becomes necessary to choose a rational combination of the required power of the engine and electric machine and the capacity of the battery.

Keywords: Combined Power Source Vehicles (hybrids drivers) · spark ignition engine (SI engine) · alternative fuel

1 Introduction

The desire to reduce the negative impact of transport on the environment is forcing automakers to improve existing areas and look for new ways to reduce the proportion of toxic substances in the exhaust gases (EG) of internal combustion engines (ICEs). Decades of research have focused on the modification of fuel injection and boost systems, the application of electronic control and exhaust gas after treatment. Simultaneously with the improvement of the design of internal combustion engines, the situation of expanding the amount of motor fuels with a partial or complete transition to renewable energy sources was considered.

D. C. Nguyen et al. (Eds.): ICERA 2023, LNNS 944, pp. 497–508, 2024.
https://doi.org/10.1007/978-3-031-62235-9_50

A joint solution to these problems is the use of alternative fuels, that is, fuels of non-petroleum origin [1–3]. These fuels are obtained from various raw materials and have different physical and chemical properties from diesel fuel and gasoline.

Alternative fuels (see Fig. 1) can be divided into four main groups [1].

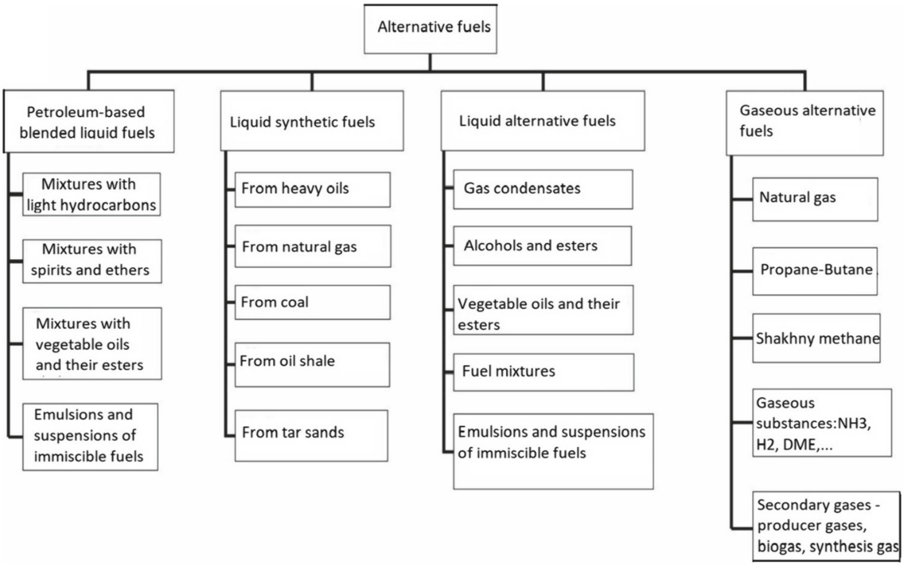

Fig. 1. Classification of alternative motor fuels [1]

The first group of alternative fuels includes petroleum-based fuels with additives of non-petroleum origin (alcohols, ethers, vegetable oils and their esters, water, solutions of chemically active substances) or other hydrocarbons. Such additives can be very significant and exceed the amount of fuel oil. These mixtures are called mixed or composite fuels. Blended fuels can be close to petroleum distillate fuels in terms of their operational properties, especially with a small amount of the addition of an alternative component.

The second group consists of synthetic liquid fuels that are identical or close in composition to traditional petroleum fuels. They are obtained by processing liquid, gaseous or solid raw materials, for example, natural bitumen, hard and brown coal, oil shale, and also from methanol. By their properties, these fuels are close to petroleum fuels.

The third group of alternative fuels includes liquid non-petroleum fuels, which differ significantly in physical and chemical properties from traditional motor fuels. These are alcohols, esters, vegetable oils and their esters. The same group of fuels includes alcohol-water-fuel emulsions, water-coal suspensions, and various compositions of other immiscible fuels.

The fourth group includes fuels that are under normal physical conditions in a gaseous state. These are natural gas (up to 95… 99% consisting of CH_4 methane), petroleum gas (propane-butane mixtures), hydrogen (H_2), ammonia (NH_3), dimethyl ether (DME), secondary gases (generator gas, biogas, synthesis gas). Gas fuels differ significantly in their characteristics from traditional fuels, which requires more careful adaptation of convertible internal combustion engines (see Fig. 2).

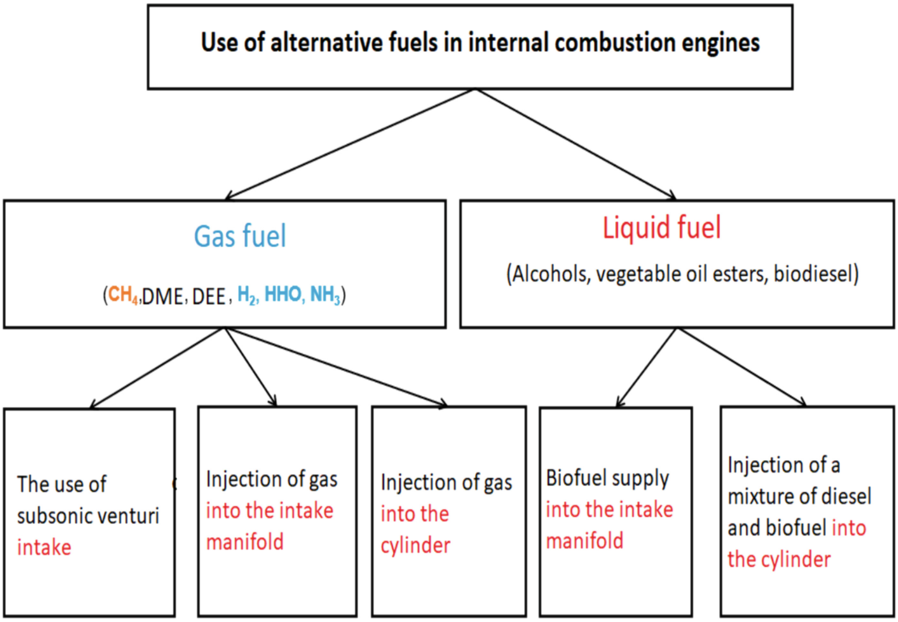

Fig. 2. Methods for supplying alternative fuels to internal combustion engine cylinders

The attractiveness of alternative fuels is determined by their renewability and the presence of oxygen in the molecule (alcohols and ethers). Recently, these features have been supplemented by the idea of using fuels whose chemical formulas are characterized by the absence of carbon or its relatively low content (H_2, explosive gas HHO, NH_3, CH_4, DME, DEE diethyl ether, etc.). Such an approach, according to its supporters, significantly reduces or completely eliminates the presence of carbon-containing compounds in exhaust gases: carbon dioxide CO_2, carbon monoxide CO, hydrocarbons CH and dispersed particles.

In Table 1 compares the physicochemical properties that affect the operation of internal combustion engines running on some alternative fuels with those of conventional fuels.

All presented in Table 1 alternative fuel sources for H_2 and NH_3 this figure is zero.

For use in a compression ignition engine, DME is best suited. The cetane number is higher than that of diesel fuel.

NH_3 and CH_4 are superior in octane to gasoline and can be used in spark ignition (SI) engines provided the compression ratio is increased and the ignition system is improved.

H_2 has the highest lower heating value of all those listed in Table 1. However, the use of hydrogen is associated with the use of expensive technologies that do not guarantee its complete safety. In this regard, from the point of view of the complete absence of

Table 1. Physical and chemical properties of some fuels that affect the working process of internal combustion engines.

Property	Petrol	Diesel fuel	H_2	NH_3	CH_4	DME
Mass fraction of hydrogen	0,145	0,128	1	0,176	0,25	0,13
Mass fraction of carbon	0,855	0,872	0	0	0,75	0,522
Mass fraction of oxygen	0	0	0	0	0	0,348
Lower heating value (LHV)MJ/kg	44	42,6	120	17,1	48,9	27,6
Octane number	92 … 100	3	70	130	110 … 115	—
Cetane number	8 … 14	45 … 55	—	—	3 … 8	more 55

carbon in the chemical formula of the fuel, the supply of spark ignition engines with ammonia looks more attractive.

Ammonia in the air is highly soluble in water, which makes it possible to control its leakage, avoiding the danger of fire or explosion. The low viscosity of ammonia is of higher quality compared to gasoline, spraying and mixing with air [4, 5].

Over the past few decades, NH_3 oxidation reactions have been well studied. This was facilitated by its use as a fuel and a decrease in the content of nitrogen oxides in the exhaust gas of diesel engines due to its use as a reducing agent in selective neutralization [6–8].

Ammonia can be used directly as a fuel in single-fuel or dual-fuel modes. Moreover, in the dual-fuel mode, it is possible to use ammonia with hydrogen obtained by decomposition of ammonia (Fig. 3).

Among the significant attempts to describe the oxidation of NH_3 are the works of Miller and co-workers [4, 5]. Miller et al. [9–11] investigated computationally a variety of burner-stabilized and freely propagating NH_3/O_2 and $NH_3/H_2/O_2$ flames and proposed detailed kinetics of NH_3 oxidation with 22 species and 98 elementary reactions. At lean and moderately rich conditions, their model satisfactorily predicts the species profiles measured by MacLean and Wagner [12], Green and Miller [13], Fenimore and Jones [14], and the burning velocity measured by Murray and Hall [15]. Cannot provide satisfactory accuracy in the conditions of combustion of rich air-fuel mixtures due to an insufficiently accurate description of the NH_3 pyrolysis mechanism.

According to Fig. 4. The 4 OH and H radicals first react with NH_{i+1} and form NH_i, where $i = 0, 1, 2$ [16].

The NH_i radicals will follow either one of the pathways leading to the formation of NO as a result of oxidation, or to the formation of nitrogen as a result of the reaction with NO.

The mechanism of the NH_3 combustion reaction was first proposed by Miller. in 1983 [16] by carrying out numerical and experimental studies of a flame based on ammonia at low pressure. This limits the applicability of this mechanism to cases of pressure increase and non-stoichiometric flame conditions [17]. The researchers proposed various modifications to the reaction mechanism to improve the predictability of the ammonia flame structure over a wide range of temperatures and air ratios.

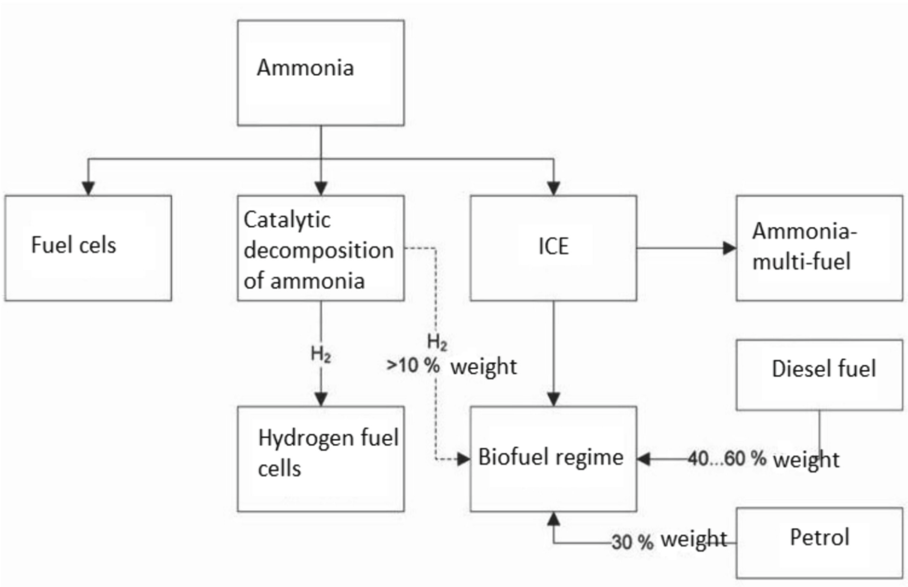

Fig. 3. Possibilities of using ammonia in vehicles

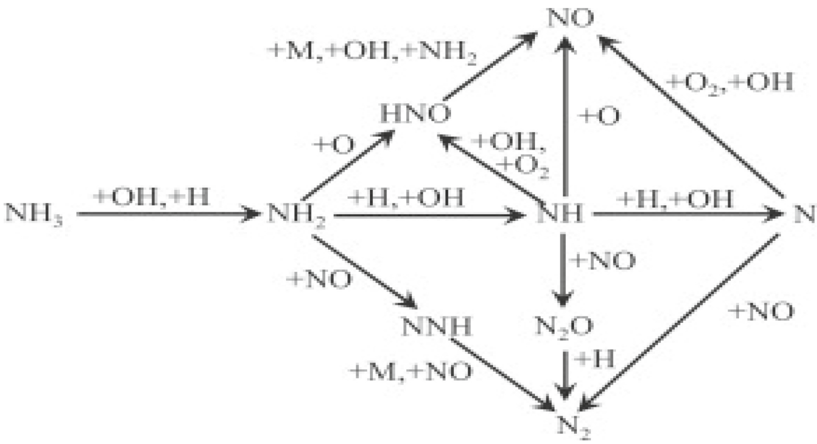

Fig. 4. NH3 oxidation mechanism proposed by Miller [14]

2 Research Model

To compensate for the power losses of spark ignition (SI) engines on NH_3 (because of the lower calorific value, it is less than that of gasoline and CH_4, Table 1) when operating at increased loads, it is proposed to use it as part of a Combined Power Source Vehicles (hybrids drivers). In this case, it becomes necessary to choose a rational combination of the required power of spark ignition (SI) engines and electric machines (generator and electric motor), battery capacity (see Fig. 5).

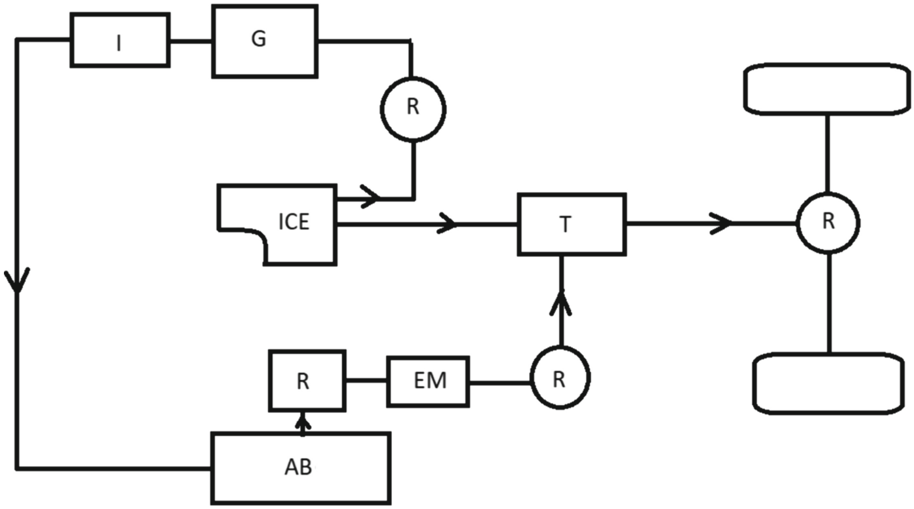

Fig. 5. Rice. 5. The proposed scheme of a car with a Combined Power Source Vehicles (hybrids drivers)

ICE - Internal Combustion Engine; T - Transmission; R - Reducer; EM - Asynchronous Electric Motor; I - Inverter; G - Asynchronous Generator; AB - Accumulator Battery.

The use of Combined Power Source Vehicles (hybrids drivers) allows to reduce the working volume of the internal combustion engine, for example, by reducing the number of engine cylinders, and thereby ensure its operation in modes with a large throttle opening, which will reduce the work of gas exchange (Table 2).

Table 2. Main parameters of the experimental engine and vehicle

Model	4CHN 8.2/7
Displacement	370 mm^3
Diameter	82 mm
Stroke	70 mm
Compression ratio	9.0
Minimum engine speed	1400 min^{-1}
The frequency of rotation of the crankshaft of the engine at nominal mode	5400 min^{-1}
Vehicle weight	900 kg

3 Research Results

The mechanical characteristics of electrical induction machines are reflected by the dependences of the electromagnetic moments of the electric motor and generator on the crankshaft speed (see Figs. 6 and 7), as well as their effective efficiency on the crankshaft speed (see Figs. 8 and 9).

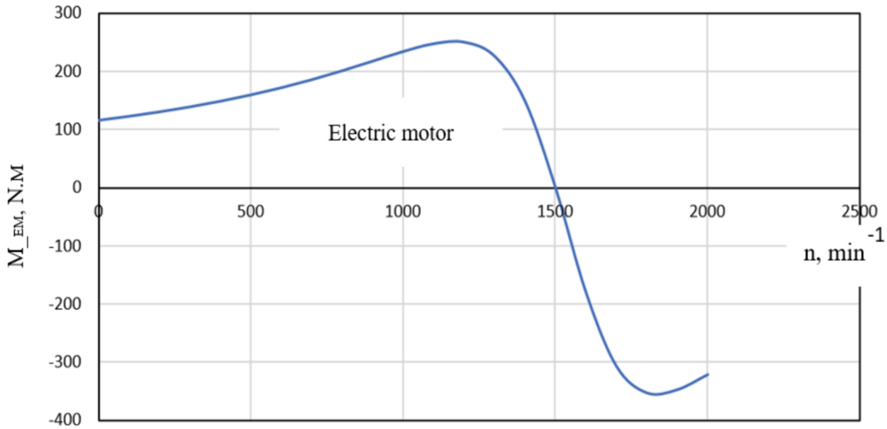

Fig. 6. The dependence of the electromagnetic torque of the electric motor on the crankshaft speed

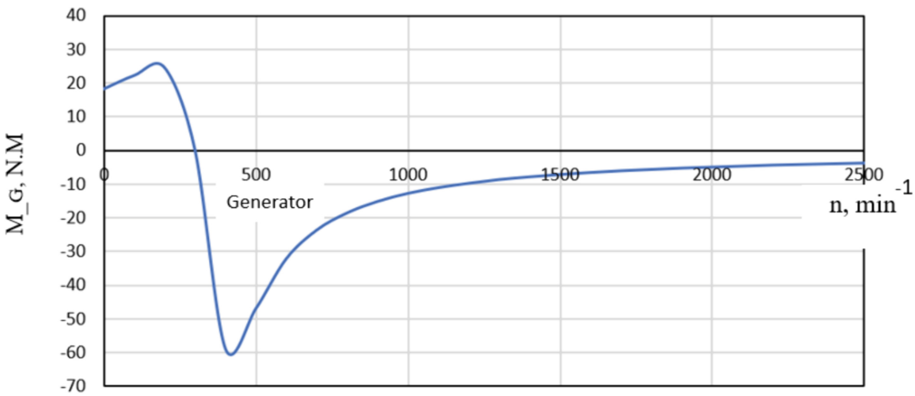

Fig. 7. The dependence of the electromagnetic torque of the generator on the crankshaft speed

For type tests of the vehicle, a new European cycle (NEDC - New European Driving Cycle) was adopted in a small cycle (see Fig. 10).

M_ICE: ICE torque; M_EM: Asynchronous electric motor torque; M_G: Asynchronous generator torque; M_W: Wheel torque.

During the test period, the sum of the torques is: M_ICE + M_EM + M_G + M_W = 0 (see Fig. 11).

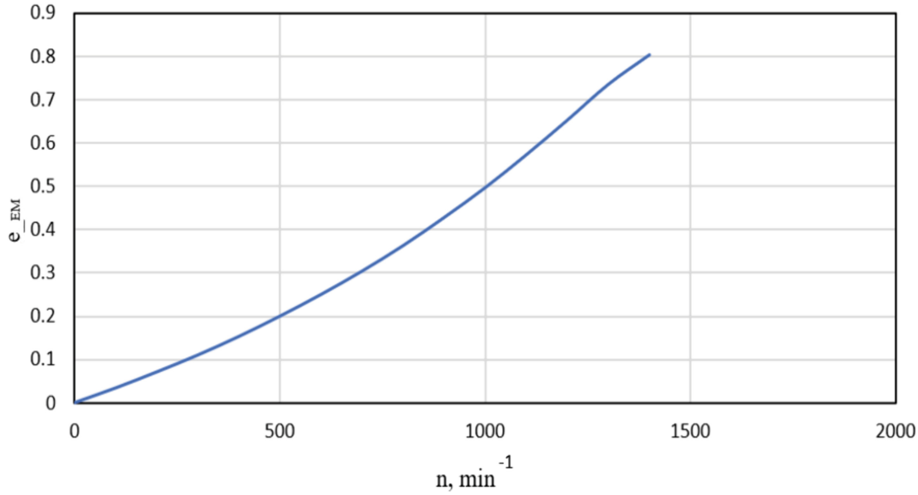

Fig. 8. The dependence of the effective efficiency of the electric motor on the crankshaft speed

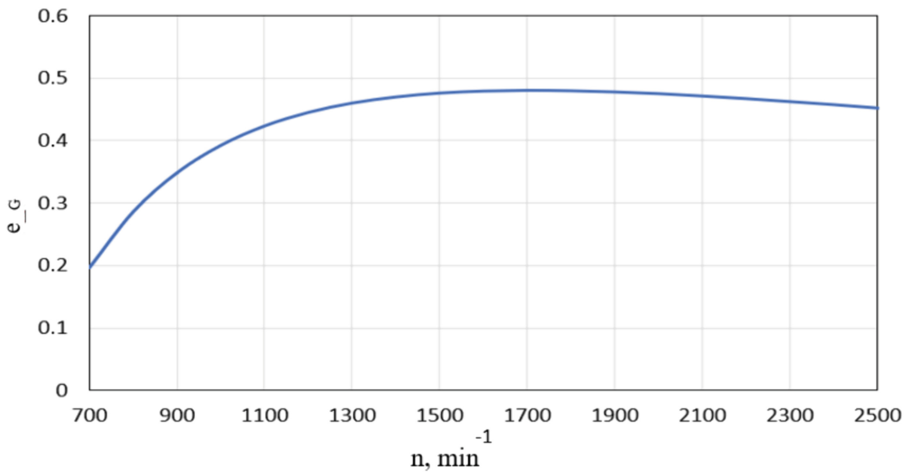

Fig. 9. The dependence of the effective efficiency of the generator on the crankshaft speed

While the car is moving, the electric motor takes electrical energy from the battery and generates mechanical energy to transfer the movement to the wheels, in the opposite direction to the electric motor, the generator takes excess energy from the internal combustion engine and recharges the battery. The effective efficiencies of which are shown in Fig. 12.

The car works with engines having 2, 3 and 4 cylinders, respectively (see Fig. 13). The results show that with 2 cylinders the engine gives a higher efficiency, this explains why the engine operates with a larger throttle opening than with 3 or 4 cylinders (see Fig. 14). ICE with 2 cylinders operates at low crankshaft speed from 1500 to 3000 rpm

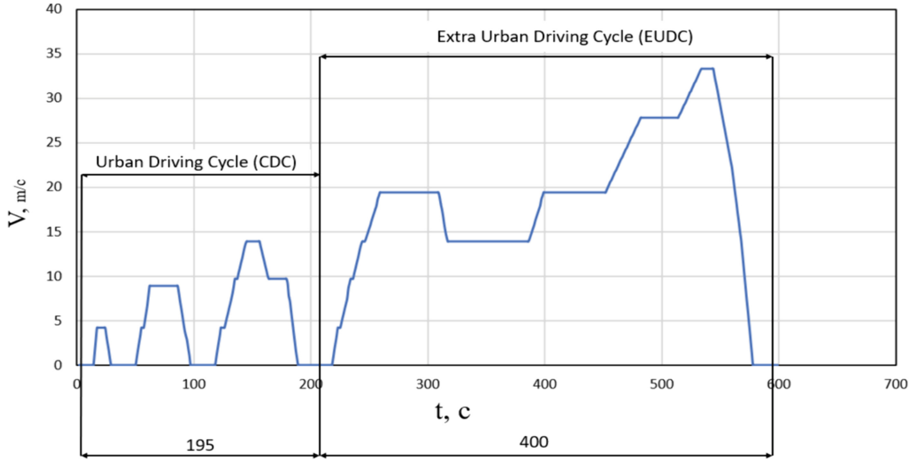

Fig. 10. Small driving cycle for testing a car (NEDC - New European Driving Cycle - a new European driving cycle). The duration of the small cycle is 595 s (1x195 + 1x400)

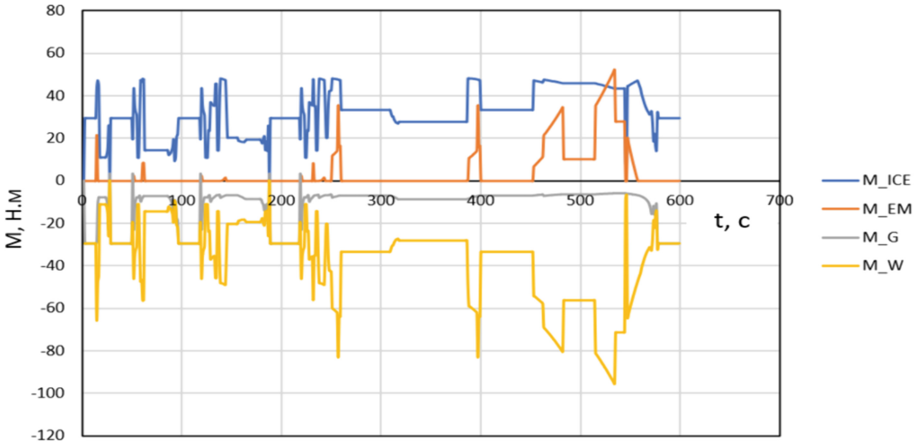

Fig. 11. The balance of moments of the Combined Power Source Vehicles (hybrids drivers) during the operation of the internal combustion engine on NH_3

together with a greater degree of throttle opening, the possibility of detonation ranges from 25–30% (see Fig. 15).

This shows that we can reduce the displacement of an internal combustion engine by reducing the number of cylinders from 4 to 2, and this also leads to a decrease in the mass of the car.

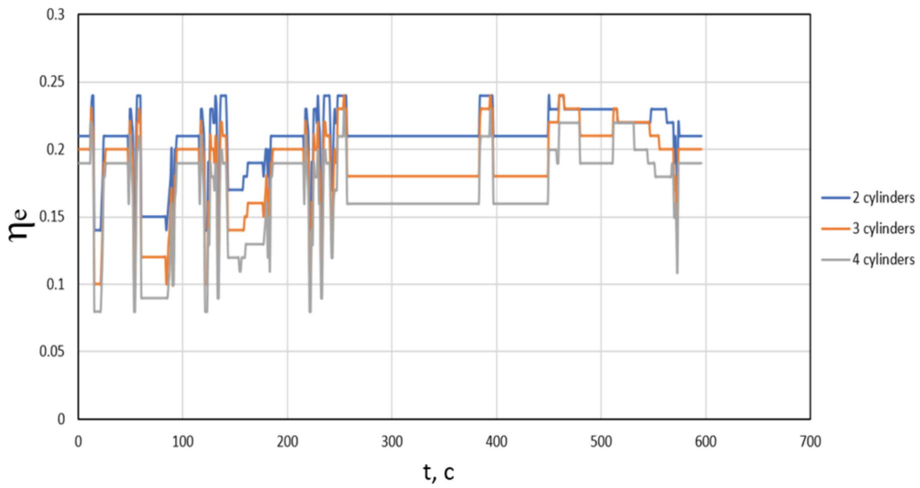

Fig. 12. Effective efficiency of the electric motor and generator according to the driving cycle when the internal combustion engine is running on NH_3

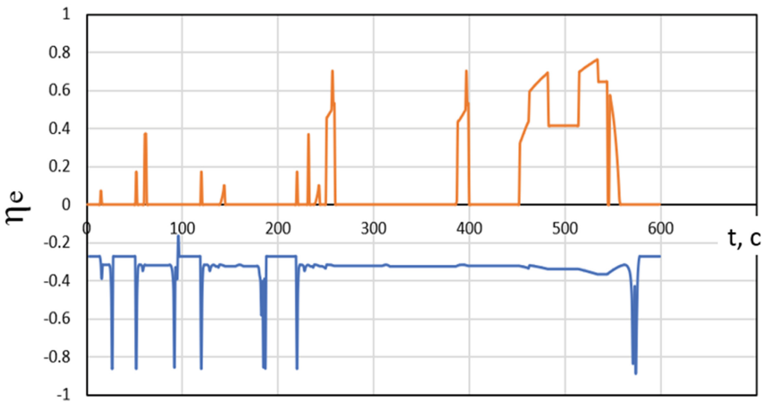

Fig. 13. Effective efficiency of the internal combustion engine according to the driving cycle when the internal combustion engine is running on NH_3

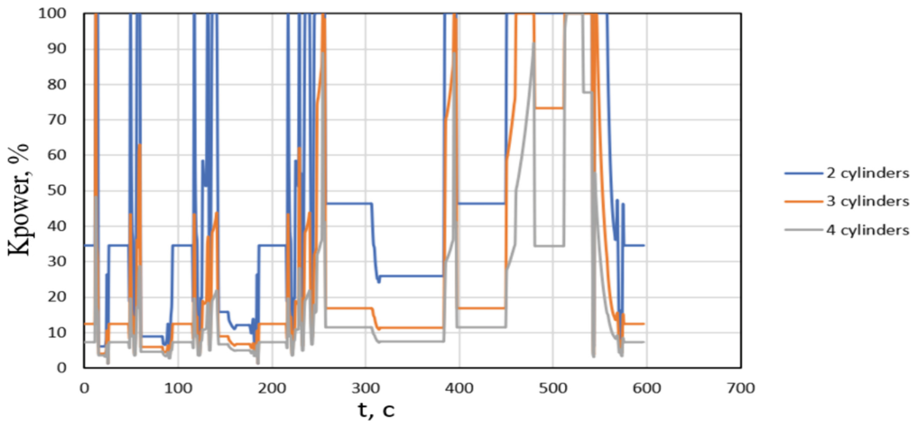

Fig. 14. The coefficient of utilization of the ICE's power when ICE is running on gasoline as part of the Combined Power Source Vehicles

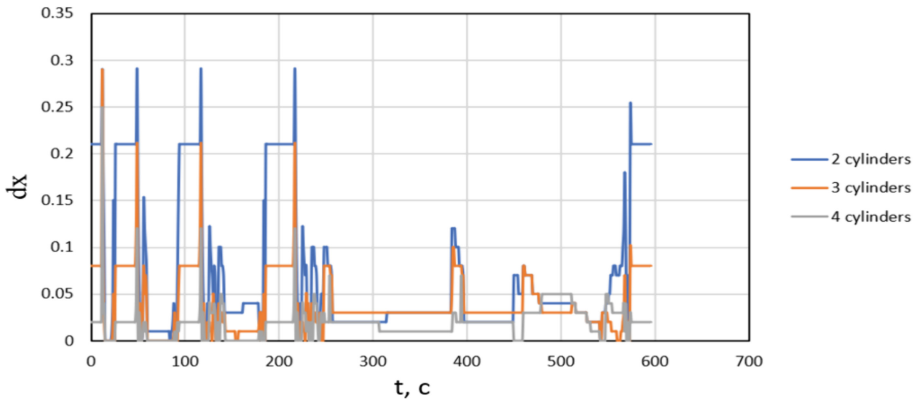

Fig. 15. Proportion of detonation during operation of internal combustion engines on gasoline as part of a Combined Power Source Vehicles for a different number of engine cylinders

4 Conclusion

A study was carried out of the working process of a modern spark ignition engine (SI) when it runs on alternative fuel as part of a Combined Power Source Vehicles (hybrids drivers):

– Among other alternative fuels with a low-carbon compound in the exhaust gases during combustion, from the point of view of the complete absence of carbon in the chemical formula of the fuel, one suitable option is the use of ammonia.
– Using the SI engine as a part of a Combined Power Source Vehicles allows to reduce the working volume of the internal combustion engine, to reduce the amount of heat added to the cycle with the fuel at medium and high load conditions while maintaining the full specified power.

References

1. Aleksandrov, A.A., et al.: Alternative fuels for internal combustion engines. OOO NITs "Inzhener", OOO "Oniko-M, 791 (2012)
2. Markov, V. A., Devyanin, S.N., Semenov, V.G., Shakhov, A.V., Bagrov, V.V.: The use of vegetable oils and fuels based on them in diesel engines. OOO NITs "Engineer", OOO "Oniko-M", 536 (2011)
3. Markov, V.A., Bebenin, E.V., Pozdnyakov, E.F.: Comparative evaluation of alternative fuels for diesel engines. Transp. Altern. Fuel. No. **5**, 24–29 (2013)
4. Miller, J.A., Branch, M.S., Kee, R.J.: A chemical kinetic model for the selective reduction of nitric oxide by ammonia. Combust. Flame **43**, 81–98 (1981)
5. Miller, J.A., Smooke, M.D., Green, R.M., Kee, R.J.: Kinetic modeling of the oxidation of ammonia in flames. Combust. Sci. Technol. **34**(1–6), 149–176 (1983). https://doi.org/10.1080/00102208308923691
6. Cremer, M.A., Montgomery, C.J., Wang, D.H., Heap, M.P., Chen, J.-Y.: Development and implementation of reduced chemistry for computional fluid dynamics modeling of selective non-catalytic reduction. Proc. Combust. Inst. **28**(2), 2427–2434 (2000). https://doi.org/10.1016/S0082-0784(00)80656-6
7. Charles, L., Pierre, B., Francesco, C., Christine, M.R.: Experimental study on ammonia/hydrogen/air combustion in spark ignition engine conditions. Fuel **269**, 117448 (2020)
8. Haynes, B.S.: Reactions of ammonia and nitric oxide in the burnt gases of fuel-rich hydrocarbon-air flames. Combust. Flame **28**, 81–91 (1977). https://doi.org/10.1016/0010-2180(77)90010-4
9. Miller, J.A., Bowman, C.T.: Mechanism and modeling of nitrogen chemistry in combustion. Prog. Energy Combust. Sci. **15**(4), 287–338 (1989). https://doi.org/10.1016/0360-1285(89)90017-8
10. Kobayashi, H., Hayakawa, A., Somarathne, K.A., Okafor, E.C.: Science and technology of ammonia combustion. Proc. Comsust. Int. **37**(1), 109–133 (2019)
11. Duynslaegher, C., Contino, F., Vandooren, J., Jeanmart, H.: Modeling of ammonia combustion at low pressure. Combust. Flame **159**(9), 2799–2805 (2012)
12. Maclean, D.I., Wagner, H.G.: The structure of the reaction zones of ammonia-oxygen and hydrazine-decomposition flames. Symp. (Int.) Combust. **11**(1), 871–878 (1967). https://doi.org/10.1016/S0082-0784(67)80213-3
13. Green, R.M., Miller, J.A.: The measurement of relative concentration profiles of NH2 using laser absorption spectroscopy. J. Quant. Spectrosc. Radiat. Transfer **26**(4), 313–327 (1981). https://doi.org/10.1016/0022-4073(81)90126-6
14. Fenimore, C.P., Jones, G.W.: Oxidation of ammonia in flames. J. Phys. Chem. **65**(2), 298–303 (1961). https://doi.org/10.1021/j100820a027
15. Murray, R.C., Hall, A.R.: Flame speeds in hydrazine vapour and in mixtures of hydrazine and ammonia with oxygen. Trans. Faraday Soc. **47**, 743 (1951). https://doi.org/10.1039/tf9514700743
16. Miller, J.A., Smooke, M.D., Green, R.M., Kee, R.J.: Kinetic modeling of the oxidation of ammonia in flames. Combust. Sci. Technol. **34**(1–6), 149–176 (1983)
17. Miller, J.A., Bowman, C.T.: Mechanism and modeling of nitrogen chemistry in combustion. Prog. Energy Combust. Sci. **15**(4), 287–338 (1989)

Theoretical Study for Apple Slice Drying in Superheated Steam

Thi Thu Hang Tran and Kieu Hiep Le(✉)

School of Mechanical Engineering,
Hanoi University of Science and Technology, Hanoi, Vietnam
hiep.lekieu@hust.edu.vn

Abstract. A theoretical model for superheated steam drying of apple slice is presented, in which the spatial distributions of temperature and moisture inside the product layer are considered. The model is built based on the diffusion theory in which the effective diffusivity is a function of moisture content and it is calculated by fitting with experimental data. There is good agreement between the experimental moisture content and the simulated average moisture content. The moisture and temperature distributions show that the moisture gradient is high while the temperature gradient is small. Moisture content on the surface reduces dramatically at the beginning of drying while this at the center spends several minutes to start to evaporate. Temperatures witnesses the constant period corresponding with the first drying stage then temperature increases continuously to the gas temperature. Results of the study can be used for simulating for dryer scale in the computational fluid dynamics in the next step.

Keywords: superheated steam drying · apple slice · diffusivity

1 Introduction

Recently, superheated steam (SSD) has appeared in various drying fields due to the avoiding of oxidative reaction, recycle ability, faster evaporation speed than hot air drying at temperature above the inversion temperature [1]. Apple is the sensitive product under the hot air drying because in the drying agent containing oxygen, product is brown, shrinks and loses nutrition [2]. Thus, superheated steam can be a potential drying agent replacing hot air in the drying process of apple. Most of studies for SSD are experimental studies regarding the product quality comparisons among various drying methods and experimental models [3].

Studying of apple drying in air can be categorized in the experiment work [4]; the analytical models [5–7] and numerical model [8]. Experimental models are simple but the distributions of moisture and temperature may not presented in these models. The analytical models can give the clear results but these need a series of assumptions, in which the effective diffusivity of moisture is assumed as a constant. The numerical modelling concerns apple as porous medium including pore and solid, pores are filled by water vapor, water liquid and air. This numerical model is complicated model with

D. C. Nguyen et al. (Eds.): ICERA 2023, LNNS 944, pp. 509–515, 2024.
https://doi.org/10.1007/978-3-031-62235-9_51

empirical parameters like porosity, permeability are setup parameters which need to determine by complicated procedure.

Fick's law has been applied widely for modelling of fruit layer drying [9]. In which, the water movement from the center to the surface is described by vapor diffusion. By this, the evolutions of spatial temperature and moisture distributions versus time can be presented. In this work, the Fick's law model is applied for apple slice drying in SSD. In which the changes physical properties of products during drying will be concerned, the moisture diffusivity is determined by fitting with the own experimental data. The model is successfully validated by comparison with the experiment, then this will be applied to simulate to examine the evolutions of spatial moisture and temperature distributions.

2 Theoretical Model

2.1 Model Description

A model will be developed for drying an apple slice which is shown in Fig. 1. l is assigned as thickness; d is the diameter. It is assumed that the thickness is small in compared with the diameter so the model is the one dimensional model.

Mass transfer process includes the vapor diffusivity from the center to the surface and the vapor diffuses from the surface to the vapor bulk. The continuous moisture diffusion inside the apple is described as [10]:

$$\frac{\partial(\rho_0 X)}{\partial\tau} - \nabla.[-D_{eff}\nabla(\rho_0 X) = 0 \tag{1}$$

In which, X (kg water/kg solid) is moisture content on dry basis, ρ_0 (kg/m^3) is the density of dry apple, D_{eff} is the effective diffusivity which is a function of temperature and it is determined by fitting with experimental data.

Heat transfer is described by the convective heat transfer from the gas to the surface and heat conduction from the surface to the center as follows:

$$\rho_{eff} C_{eff} \frac{\partial T}{\partial\tau} - \nabla.\left(\lambda_{eff}\nabla T\right) = 0 \tag{2}$$

where T^oC is the temperature, ρ_{eff} (kg/m^3), C_{eff} (J/kgK), λ_{eff} (W/mK) are effective density, effective thermal conductivity respectively.

The boundary conditions are written as:

$$\rho_s D_{eff} \frac{\partial X}{\partial x} = \beta\left(\rho_{v,surf} - \rho_{v,b}\right) \tag{3}$$

In which $\alpha\left(W/m^2\right)$, $\beta(m/s)$ are the heat and mass transfer coefficient, T_g°C is the gas temperature, T_{surf}°C is the surface temperature, Δh_v is the latent heat, $\rho_{v,surf}$ and $\rho_{v,b}$ are the vapor densities (kg/m^3) on the surface and in bulk gas.

The vapor density on the surface is determined by [11]:

$$\rho_{v,surf} = \rho_{sat}(T)\frac{P_{v,surf}}{P_{sat}(T)} \tag{4}$$

$$\frac{P_{v,surf}}{P_{v,sat(T)}} = \begin{cases} 1 \text{ if } X \geq X_{irr} \\ \frac{X}{X_{irr}}\left[\left(1 + a - a.\frac{X}{X_{irr}}\right)\right] \text{ if } X < X_{irr} \end{cases} \quad (5)$$

X_{irr} will be correlated from experimental data. $P_{v,sat}(T)$ is calculated by:

$$P_{v,sat} = 133.32.\exp\left(18.5848 - \frac{3984.2}{233.426 + T}\right) \quad (6)$$

Heat and mass transfer coefficients are computed from [12]:

$$Sh = 2 + 0.6.\mathrm{Re}^{1/2}Sc^{1/3} \quad (7)$$

$$Nu = 2 + 0.6.\mathrm{Re}^{1/2}\,\mathrm{Pr}^{1/3} \quad (8)$$

In which, gas flow across the surface of apple slice so the characteristic length is calculated as the ratio of surface area per the perimeter of projection perpendicular to the flow [13]. For apple slice with the dimensions presented in Fig. 1, the characteristic length is:

$$d_s = \frac{2.\pi d^2}{4.2.(l + d)} \quad (9)$$

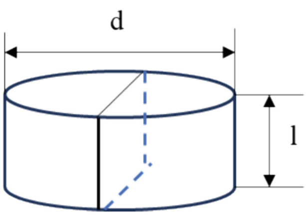

Fig. 1. Objective of model

2.2 Determination of Model Parameters

Parameters D_{eff} and X_{irr} are determined by fitting with own experiment data. The own experiment system is briefly presented in Fig. 2. Breeze New Zealand apple is bought from local market to do experiment. Firstly, the apples are cleaned and cut to slices of 2 mm thickness. After the temperature reaches the setup temperature, drying slices are put onto the tray. One sensitive balance records continuously the sample mass until the sample mass is constant. The initial moisture content of sample is also determined by placing the sample in the Themos-plus drying chamber (GMP500) at high temperature for a long time until getting only dried solid. By comparison between the initial mass m_i and final mass m_s, the initial moisture content is calculated as:

$$X_i = \frac{m_i - m_s}{m_s} \tag{10}$$

By comparison between the temporal mass and the solid mass at each time, the temporal moisture content can be calculated:

$$X = \frac{m - m_s}{m_s} \tag{11}$$

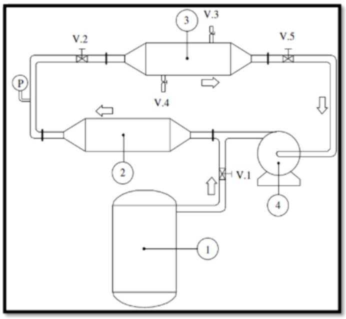

Fig. 2. Schematics of experimental system (1): boiler, (2) resistance bar, (3) dryer, (4) centrifugal fan

The model is implemented in Matlab and the experiment data is used to fit by reversion method for finding effective diffusivity. For all cases, results show that the effective diffusivity is a function of temperature by following function:

$$D_{eff} = 113.10^{-11} \exp\left(-\frac{2.1}{RT}\right) \tag{12}$$

$$X_{irr} = 2.$$

3 Result of Modelling

3.1 Model Validation

The selective comparisons of moisture content versus time calculated by simulation and experiments are shown in Fig. 3. In which the continuous line represents for simulated moisture content and points are the experimental points. It can be seen the good agreements between the experiment and simulation results for all cases. The theoretical model will be applied to yield the evolutions of moisture and temperature versus time.

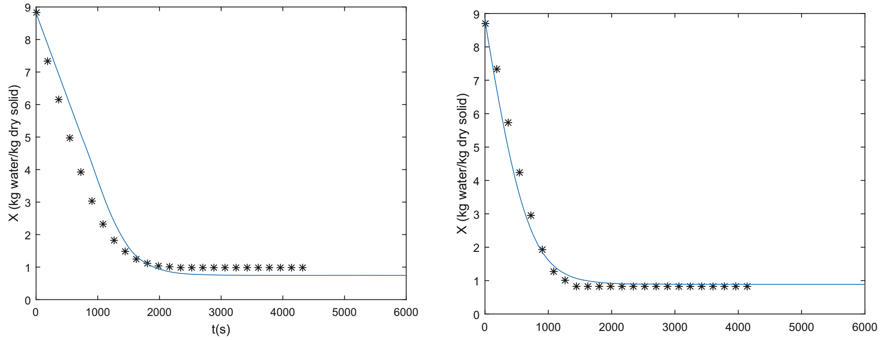

a, $v_g = 6$ (m/s), $T_g = 120$°C   b, $v_g = 5$ (m/s), $T_g = 150$°C

Fig. 3. Evaporation of apple slice *continuous line*: simulation; *points*: experiment

3.2 Spatial Distributions of Moisture and Temperature

Theoretical model is implemented to examine the evaluations of moisture and temperature as shown in Fig. 4. For all time, the difference between moisture content on the surface and at the center can be seen clearly while the temperature is almost uniform. These are because the thermal conductivity is high while the thermal diffusivity is low result in the high moisture gradient but the small temperature gradient appears inside the dried sample. In terms of moisture content, moisture content on the surface drops quickly while the center starts to dry after several minutes. In terms of temperature, temperature remains constant during the first drying period then it increases gradually to the gas temperature after long time.

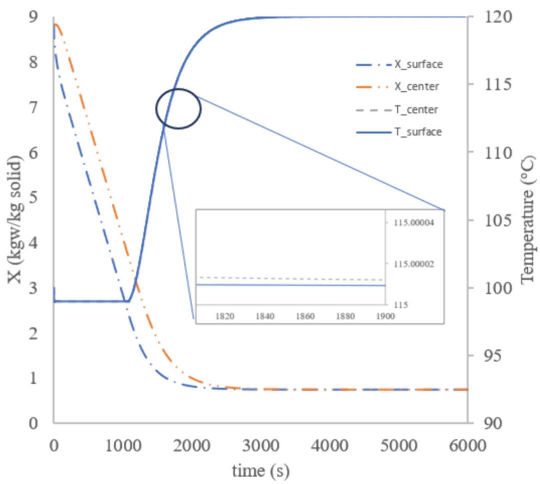

Fig. 4. Evolutions of moisture and temperature of surface and center versus time $T_g = 120$ °C, $v_g = 5$ (m/s)

4 Conclusion

This work presents the results of theoretical model for drying of apple slice in the superheated steam. The model considers the moisture and temperature distribution inside the sample. In which, the moisture transport is due to the diffusion with the diffusivity is determined by experiment data. The simulated average moisture contents are compared with experiment giving the high accuracy. After that the model is implemented to get the evolutions of spatial moisture and temperature. The results show that the moisture gradient is big with a clear difference while the temperature is almost uniform.

The built model with high accuracy results can be the basic tool for simulation of macro scale modelling for the dryer. This can be extended for other agricultural products in order optimize the drying processing in terms of energy efficiency.

Acknowledgement. This research is funded by the Vietnamese Ministry of Education and Training under grant number B2022-BKA-11.

References

1. Mujumdar, A.S., Law, C.L.: Drying technology: trends and applications in postharvest processing. Food Bioprocess Technol. **3**(6), 843–852 (2010). https://doi.org/10.1007/s11947-010-0353-1
2. Hawlader, M., Perera, C.O., Tian, M.: Properties of modified atmosphere heat pump dried foods. J. Food Eng. **74**(3), 392–401 (2006)
3. Alfy, A., Kiran, B.V., Jeevitha, G.C., Hebbar, H.U.: Recent developments in superheated steam processing of foods—a review. Crit. Rev. Food Sci. Nutr. **56**(13), 2191–2208 (2016). https://doi.org/10.1080/10408398.2012.740641
4. Zhu, J., Liu, Y., Zhu, C., Wei, M.: Effects of different drying methods on the physical properties and sensory characteristics of apple chip snacks. LWT **154**, 112829 (2022). https://doi.org/10.1016/j.lwt.2021.112829
5. Elustondo, D., Elustondo, M.P., Urbicain, M.J.: Mathematical modeling of moisture evaporation from foodstuffs exposed to subatmospheric pressure superheated steam. J. Food Eng. **49**(1), 15–24 (2001). https://doi.org/10.1016/S0260-8774(00)00180-1
6. Zlatanović, I., Komatina, M., Antonijević, D.: Low-temperature convective drying of apple cubes. Appl. Therm. Eng. **53**(1), 114–123 (2013)
7. Kaya, A., Aydın, O., Demirtaş, C.: Drying kinetics of red delicious apple. Biosyst. Eng. **96**(4), 517–524 (2007). https://doi.org/10.1016/j.biosystemseng.2006.12.009
8. Kumar, C., Joardder, M.U.H., Farrell, T.W., Millar, G.J., Karim, A.: A porous media transport model for apple drying. Biosyst. Eng. **176**, 12–25 (2018). https://doi.org/10.1016/j.biosystemseng.2018.06.021
9. Ghazanfari, A., Emami, S., Tabil, L.G., Panigrahi, S.: Thin-layer drying of flax fiber: I. Analysis of modeling using fick's second law of diffusion. Drying Technol. **24**(12), 1631–1635 (2006). https://doi.org/10.1080/07373930601031430
10. Agrawal, S.G., Methekar, R.N.: Mathematical model for heat and mass transfer during convective drying of pumpkin. Food Bioprod. Process. **101**, 68–73 (2017). https://doi.org/10.1016/j.fbp.2016.10.005
11. Le, K.H., Tran, T.T.H., Nguyen, N.A., Kharaghani, A.: Multiscale modeling of superheated steam drying of particulate materials. Chem. Eng. Technol. **43**(5), 913–922 (2020)

12. Stephan, P.: VDI Heat Atlas. Springer, Berlin Heidelberg (2010). https://doi.org/10.1007/978-3-540-77877-6
13. Le, K.H., Tsotsas, E., Kharaghani, A.: Continuum-scale modeling of superheated steam drying of cellular plant porous media. Int. J. Heat Mass Transfer **124**, 1033–1044 (2018). https://doi.org/10.1016/j.ijheatmasstransfer.2018.04.032

Author Index

D. C. Nguyen et al. (Eds.): ICERA 2023, LNNS 944, pp. 517–519, 2024.
https://doi.org/10.1007/978-3-031-62235-9

V

Z